Switch-mode High Voltage Drivers for Dielectric Electro Active Polymer (DEAP) Incremental Actuators

Thummala, Prasanth

Publication date:
2014

Document Version
Publisher's PDF, also known as Version of record

Technical University of Denmark

Prasanth Thummala

Switch-mode High Voltage Drivers for Dielectric Electro Active Polymer (DEAP) Incremental Actuators

PhD Thesis, November 2014

DTU Electrical Engineering
Department of Electrical Engineering

Prasanth Thummala

Switch-mode High Voltage Drivers for Dielectric Electro Active Polymer (DEAP) Incremental Actuators

PhD Thesis, November 2014

Switch-mode High Voltage Drivers for Dielectric Electro Active Polymer (DEAP) Incremental Actuators

This PhD Thesis was prepared by
Prasanth Thummala

Supervisors
Prof. Michael A. E. Andersen
Assoc. Prof. Zhe Zhang

Release date:	14^{th} November 2014
Category:	1 (public)
Edition:	Final
Comments:	This thesis is submitted in partial fulfillment of the requirements for obtaining the PhD degree at the Technical University of Denmark.

Department of Electrical Engineering
Electronics Group (ELE)
Technical University of Denmark
Oersteds Plads bygning 349
DK-2800 Kgs. Lyngby
Denmark
www.ele.elektro.dtu.dk
Tel: (+45) 45 25 25 25
Fax: (+45) 45 88 01 17

Preface and Acknowledgment

This PhD thesis "Switch-mode high voltage drivers for dielectric electro active polymer (DEAP) incremental actuators" has been carried out at the Electronics group, Department of Electrical Engineering, Technical University of Denmark (DTU) during the period November 2011 to November 2014. The PhD work was funded by the Danish National Advanced Technology Foundation (ATF), and has been a part of the "ATF DEAP Actuator and Generator Project", managed by Danfoss PolyPower A/S. The research work was conducted in close collaboration between DTU Electrical Engineering and the industry partner Danfoss PolyPower A/S. During the PhD work, a research visit was carried out in "Colorado Power Electronics Center (CoPEC)", at Department of Electrical, Computer and Energy Engineering, University of Colorado at Boulder, USA.

It is a matter of great pleasure and privilege for me to be able to express my deep sense of gratitude to my PhD supervisors Prof. Michael A. E. Andersen and Assoc. Prof. Zhe Zhang for their unwavering support, insightful suggestions, incessant encouragement, and innumerable fruitful discussions throughout my PhD. Their time to time advice was immensely helpful for me in carrying out my research.

I would like to thank all colleagues involved in work packages 6 and 4 (WP6 and WP4) of ATF project, especially Dr. Sarban Rahimullah for his constructive suggestions and discussions during my PhD.

I would like to appreciate and thank Henrik Schneider with whom I have had a great collaboration throughout my PhD. He has always made himself available for any sort of discussion.

I would like to express my sincere gratitude to Prof. Dragan Maksimovic, for accepting me as a visiting PhD student in his research group, and for his valuable discussions and suggestions during my 4 months stay in CoPEC. Thanks to all colleagues in CoPEC, especially, Hua Chen and Hein Nguyen for their help and discussions.

Special thanks to Technical University of Denmark for providing me with the resources and facilities required to conduct very exciting research.

I am very thankful to many people at DTU Electronics group both former and current, especially Dr. Ziwei Ouyang, Lina Huang, Riccardo Pittini, Khiem Nguyen-Duy, Milovan Kovacevic, Juan Carlos, and Maria C. Mira who all contributed to

a pleasant and great working environment. Special thanks to our group secretary Henritte D. Wolff and Bertil Morelli, for their care and kind assistance during my PhD.

I am indebted to my father Basaveswara Rao, mother Ratna Kumari, and my elder brother Sudhakar for their never fading love, support and encouragement from India during my PhD in Denmark. I thank my friend Rama Krishna Challa for his valuable suggestions and help during my PhD. Finally, I express my gratitude to all those who helped me directly or indirectly in the successful completion of my PhD.

Abstract

Actuators based on dielectric electro active polymers (DEAPs) have attracted special attention in the recent years. The unique characteristics of DEAP are large strain (5-100%), light weight (7 times lighter than steel and copper), high flexibility (100,000 times less stiff than steel), low noise operation, and low power consumption. DEAP actuators require very high voltage (2-2.5 kV) to fully elongate them. In general, the elongation or stroke length of a DEAP actuator is of the order of mm. DEAP actuators can be configured to provide incremental motion, thus overcoming the inherent size-to-stroke implications of conventional linear actuators, where the stroke is limited by their size. In incremental mode, DEAP actuators are several orders of magnitude shorter in their length compared to the stroke/elongation they provide.

The dissertation presents design, control and implementation of switch-mode high voltage DC-DC converters for driving the DEAP based incremental actuators. The DEAP incremental actuator technology has the potential to be used in various industries, e.g., automotive, space and medicine. The DEAP incremental actuator consists of three electrically isolated and mechanically connected capacitive actuators. To accomplish the incremental motion, each capacitive actuator needs to be independently charged (from 0 V to 2.5 kV, within 40-60 ms) and discharged (from 2.5 kV to 0 V, within 40-60 ms) by a high voltage bidirectional DC-DC converter.

This thesis investigates a low input voltage (24 V) and high output voltage (0-2.5 kV) bidirectional flyback converter toplology for driving the capacitive actuators. Due to very high step-up ratio requirement, the transformer design becomes very complex for charging and discharging the capacitive load at very high voltage. Hence, the thesis particularly focuses on design and optimization of high voltage flyback transformer. The energy efficiency of the bidirectional flyback converter is optimized using a proposed new automatic winding layout (AWL) technique and a comprehensive loss model. Different transformer winding architectures such as non-interleaved and non-sectioned, interleaved and non-sectioned, non-interleaved and sectioned, and interleaved and sectioned have been investigated and implemented.

A digital control technique to achieve the valley switching (variable frequency control) during both charge and discharge operations in a bidirectional flyback converter, has been proposed and implemented. Using the proposed digital control scheme, the converter achieved good charge and discharge energy efficiencies in the entire output voltage range, and was able to charge and discharge the capacitive

load with in a minimum time period. This digital control scheme is very useful to control and change the charging and discharging profiles of the three high voltage drivers.

The DEAP incremental actuator concept has been designed, built and tested. It is demonstrated that the DEAP is feasible for providing incremental motion with variable speed and bidirectional motion. The system integration has been performed by driving the three capacitive actuators (each having a capacitance of 400 nF) up to a maximum voltage of 1.8 kV. Each high voltage driver is able to charge and discharge the 400 nF capacitive actuator within 23 ms and 36 ms, respectively.

Finally, a new bidirectional flyback converter topology with multiple series connected outputs is proposed. A theoretical comparison showed that the proposed converter could improve the overall energy efficiency, lower the cost and reduce the volume of high voltage driver.

Key words: high voltage, switch-mode power converters, capacitive loads, flyback, transformer design, energy efficiency, dielectric electro active polymer actuators, digital control

Resumé

Aktuatorer baseret på dielektriske elektro aktive polymerer (DEAPs) har tiltrukket særlig opmærksomhed i de seneste år. De unikke egenskaber ved DEAP er store stamme (5-100%), lette vægt (7 gange lettere end stål og kobber), høj fleksibilitet (100.000 gange mindre stiv end stål), støjsvag drift og lavt strømforbrug. DEAP aktuatorer kræver meget høj spænding (2-2,5 kV) til fuldt ud at forlænge dem. Almindeligvius er forlængelsen eller slaglængden for en DEAP aktuator af størrelsesordenen mm. DEAP aktuatorer kan konfigureres til at give trinvis bevægelse, og dermed overvinde det iboende størrelse-til-slag forhold for konventionelle lineære aktuatorer, hvor slaglængden er begrænset af deres størrelse. I trinvis tilstand er DEAP aktuatorer flere størrelsesordener kortere i deres længde i forhold til den slagtilfælde/forlængelse, de leverer.

Afhandlingen præsenterer design, kontrol og gennemførelse af switch-mode højspænding DC-DC konvertere til drivning af DEAP baserede trinvise aktuatorer. Den DEAP inkremental aktuator teknologi har potentialet til at blive brugt i forskellige industrier, fx bilindustrien, rumfart og medicin. Den DEAP inkremental aktuator består af tre elektrisk isolerede og mekanisk forbundne kapacitive aktuatorer. For at opnå den trinvise bevægelse, behov hver kapacitiv aktuatoren til uafhængigt opladet (fra 0 V til 2,5 kV, inden 40-60 ms) og afladet (fra 2,5 kV til 0 V, inden for 40-60 ms) ved en høj spænding tovejs DC-DC konverter.

Denne afhandling undersøger en lav indgangsspænding (24 V) og høj udgangsspænding (0-2,5 kV) tovejs flybackkonverter topologi til at drive de kapacitive aktuatorer. På grund af meget høj step-up forholdet krav bliver transformerdesignet meget kompleks for opladning og afladning af kapacitive belastning til meget høj spænding. Derfor fokusere afhandlingen især på design og optimering af højspændings flybacktransformeren. Energieffektiviteten af tovejs flybackkonverteren er optimeret ved hjælp af en foreslået ny automatisk afvikling layout (AWL) teknik og en omfattende tabsmodel. Forskellige transformerviklingsarkitekturer, såsom ikke-sammenflettet og ikke-sektionaliseret, sammenflettet og ikke-sektionaliseret, ikke-sammenflettet og sektionaliseret, og sammenflettet og sektionaliseret, er blevet undersøgt og implementeret.

En digital kontrol teknik, til at opnå minimum skiftetab (med variabel frekvensstyring) under både op- og afladningsoperationer i en tovejs flybackkonverter, er blevet foreslået og implementeret. Ved brug af den foreslåede digitale kontrol har konverteren opnået gode energieffektiviteter ved både opladning og afladning i hele

udgangsspændingsområdet, og var i stand til at oplade og aflade kapacitive belastning indenfor kort tidperiode. Denne digitale kontrolmetode er meget nyttigt til at styre opladnings- og afladningsprofilerne for de tre højspændingskonvertere.

DEAP inkremental aktuatorkonceptet er blevet designet, bygget og testet. Det er påvist, at DEAP i stand til at give trinvis bevægelser med variabel hastighed og i begge retninger. Systemintegrationen er blevet udført ved at drive tre kapacitive aktuatorer (der hver har en kapacitet på 400 nF) op til en maksimal spænding på 1,8 kV. Hver højspændingskonverter er i stand til at oplade og aflade 400 nF kapacitive aktuator inden for hhv. 23 ms og 36 ms.

Endelig foreslås der en ny tovejs flybackkonvertertopologi med flere serieforbundne udgange. En teoretisk sammenligning viste, at den foreslåede konverteringskoncept kan forbedre den samlede energieffektivitet, sænke omkostningerne og reducere-volumenet af højspændingskonverteren driver.

Nøgleord: højspænding, switch-mode strømforsyninger omformere, kapacitive belastninger, flyback, transformer design, energieffektivitet, dielektriske elektro aktiv polymer aktuatorer, digital kontrol

Contents

List of Figures

List of Tables

Chapter 1

Introduction

1.1 Background and Motivation

Actuators providing linear motion are used in a vast variety of applications ranging from large size machineries (e.g., cranes) to small scale micro-electro-mechanical system (MEMS) devices used for micro positioning. Linear actuators are typically characterized by their maximum stroke length, force, speed, and precision (or resolution). The stroke of many linear actuators is limited to their initial geometrical dimensions. This characteristic of conventional linear actuators limits their use in applications where large strokes, and low size and weight of the actuators are desired. Incremental linear motors are an alternative to potentially overcome these limitations by providing an inchworm-like actuation. Dielectric Electro Active Polymer (DEAP) can act as an artificial muscle and furthermore, DEAP has the ability to act as an actuator without using the mechanical parts like bearings or rotational joints. DEAP technology, inherently capable of providing novel actuations needed for an inchworm-like movement, can potentially provide novel solutions for the incremental motor design.

The concept of an incremental linear motor based on the DEAP technology is inspired by the inchworm type of actuators. The incremental motor performs the elongation in the direction of the movement by using one or more push/pull linear actuators, in combination with two or more actuators for clamping/holding the motor in position. As shown in Figure 1.1, the incremental actuator with 3 sub-actuators (1 actuator for push/pull operation and 2 actuators for clamping/holding) achieves 1 incremental stroke/movement within 6 steps.

The relative high strain level of DEAP actuator (compared to Piezo actuator) combined with its relatively high frequency of operation provides the opportunity to design a linear positioner capable of moving with relatively high speed. The combination of the relative high speed and the high force density of the DEAP transducer can potentially result in an extremely high power density of the system (densities based on weight). Moreover, combining high efficiency charge and discharge circuits with the principle of energy recovery during discharge, as a part of the electrical

driver, can provide low level of electrical energy consumption. The combination of a highly efficient DEAP motor and an energy efficient electrical driver can result in a system with extremely high energy efficiency.

The DEAP incremental motor/actuator concept consists of a system of DEAP transducers mounted in the linear motor structure and electrical drivers. The drivers monitor the movement of the motor, charge and discharge the DEAP transducers, and recover the electrical energy from the discharge cycles.

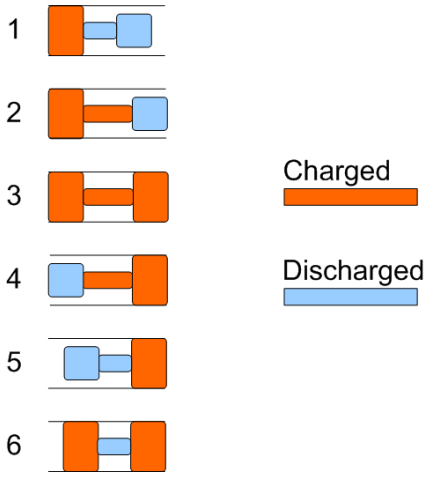

Figure 1.1: Incremental actuation schematics.

1.2 Thesis Scope

Since the early 1990s, a new type of smart material called, dielectric electro active polymer (DEAP) has gradually attracted the attention of scientists and engineers from various disciplines. Danfoss Group perceived the bright prospect of DEAP and started the research within this field since 1995. A separate company within Danfoss Group, called Danfoss PolyPower A/S, was established in 2008 to design and manufacture the DEAP film and elements for the customers.

A platform project entitled "Highly efficient low cost energy generation and actuation using disruptive DEAP technology" was proposed by Danfoss PolyPower A/S and has gained great financial support from the Danish National Advanced Technology Foundation. 7 companies, 3 universities and 8 PhD students are involved in this platform project, which is organized with 9 work packages (WPs).

The overall success criterions of this project are, First:

- to mature the DEAP material from version 2 to 5 successively, measured by improved material properties as shown in Figure 1.2.
- to increase the DEAP material's dielectric constant to >10, dielectric strength to >100 V/μm, and tear strength to >25 N/mm.
- to optimize the production processes, to reduce film imperfections, and to enable film width to >1 m and thickness to <20 μm.

Second, to demonstrate DEAP solutions on four key applications:

- as trailing edge flaps for wind turbine blades (to achieve >10% improved blade efficiency, and reduced loads and fatigues on blades, turbine and structure). The partner in this project LM Wind Power has withdrawn from the project due to some reasons. So, the project has been changed to DEAP based incremental actuators (to set new standards for weight, energy efficiency, and cost, for replacing the existing conventional linear actuators on mobile applications).

- in wave energy systems (to achieve an efficiency of 80-85% compared to 25-50% now at grid parity costs).

- as compact in-line heating valves (better and cheaper valves without mechanical parts and with battery life of more than 10 years).

- and as flat screen loudspeakers (with a goal of 10 times smaller and 100 times more energy efficient compared to current state-of-the-art).

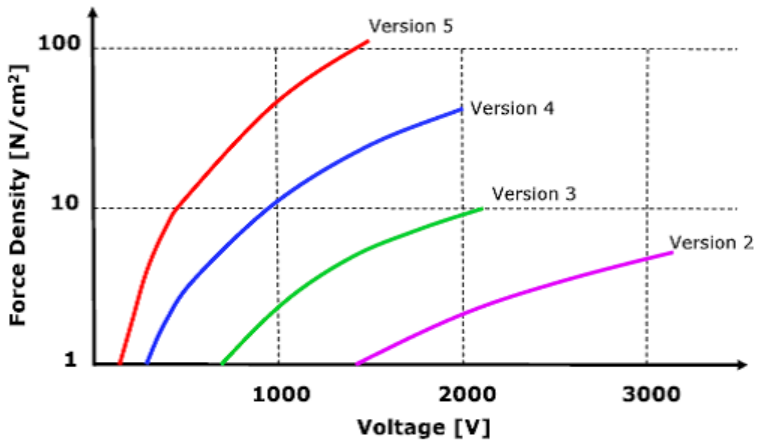

Figure 1.2: Performance roadmap of DEAP material for actuator operation [1].

In WP1, Department of Chemical Engineering at Technical University of Denmark (DTU) and Danfoss PolyPower A/S are cooperating to optimize the characteristics of DEAP film. In WP2, Polyteknik A/S, ESS Technology A/S, Danfoss PolyPower A/S and DTU Chemical Engineering are involved to optimize and improve the DEAP production processes. In WP3, DTU Management Engineering and Danfoss PolyPower A/S are focusing on investigating DEAP elements with various configurations and building high-level block diagrams for 4 application work packages. DTU Electrical Engineering, Department of Energy Technology at Aalborg University (AAU), and Noliac A/S are working together to provide electrical solutions inside the platform project. University of Southern Denmark (SDU) Mads Clausen Institute and Danfoss PolyPower A/S are developing design and simulation tools for DEAP film and elements.

The WP6 to WP9 are 4 work packages based on applications, and are led by WP4. In WP6, DTU Electrical Engineering and Danfoss PolyPower A/S are demonstrat-

ing a DEAP based incremental motor. In WP7, AAU and Wave Star A/S are investigating a wave energy harvester using DEAP technology. In WP8, DTU Electrical Engineering and Danfoss A/S Heating Solutions are investigating a potential DEAP based in-line heating valve. In WP9, a flat screen loudspeaker is under development by DTU Electrical Engineering and Bang & Olufsen A/S. The platform project structure with the information of corresponding work packages is illustrated in Figure 1.3.

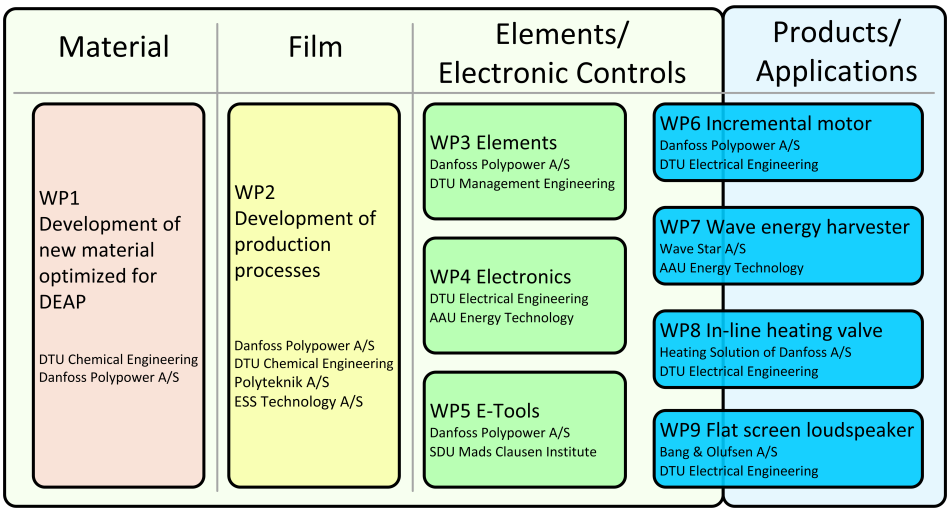

Figure 1.3: The configuration of DEAP platform project.

This PhD thesis "Switch-mode high voltage drivers for dielectric electro active polymer (DEAP) incremental actuators" is based on WP6 and the goal is to develop the necessary power electronic converters for driving an incremental motor. The DEAP actuators and the incremental actuator mechanical setp-up for system integration are provided by Danfoss Polypower A/S.

The scope of this thesis is to present the research work carried out during the PhD period from November 2011 to November 2014. Most of the scientific results of the research have been published or submitted in the form of peer reviewed conference and journal papers. The publications form a major part of this thesis and are included in Appendix. The thesis supplements already published information and thereby present a more coherent and complete overview of the research work and results obtained in during the PhD research.

Furthermore, the thesis particularly focuses on the design and optimization of magnetic transformer for high voltage capacitor charge and discharge application. It is expected that this thesis will be useful for the power electronics engineers who want to design, optimize and control the converters for high input and/or high output voltage applications.

1.3 Thesis Objectives

The primary objective of this PhD thesis is to develop the necessary power electronic drivers for WP6 in DEAP platform project, i.e. to investigate energy efficient,

and highly flexible, high voltage bidirectional DC-DC converters for driving DEAP incremental actuators. To achieve the main objective of the research, the following sub goals are proposed:

- The DEAP incremental actuator consists of three electrically isolated and mechanically connected capacitive actuators. To accomplish the incremental motion, each actuator needs to be independently charged and discharged by a high voltage bidirectional DC-DC converter. A suitable bidirectional power converter topology needs to be selected to meet the specifications of the DEAP incremental actuator.

- For battery powered applications, high energy efficiency of the high voltage driver is extremely important. Hence, another major objective is to optimize the high voltage bidirectional DC-DC converter, to obtain high charge and discharge energy efficiencies, using the commercially available high voltage MOSFETs on the secondary high voltage side.

- The low input voltage can be boosted to very high output voltage required by the actuator, using a high-voltage, high-frequency transformer. The parasitics of the transformer can significantly affect the performance of the converter. Therefore, the transformer design needs to be optimized, and different transformer architectures and winding configurations need to be investigated for better energy efficiency.

- The parasitics of the high voltage MOSFETs and diodes, on the secondary high voltage side can significantly influence the energy efficiency and performance of the converter, while charging and discharging the capacitive actuator at very high output voltage. Hence, new control techniques and new converter configurations need to be investigated and implemented to minimize the loss in the high voltage active components.

1.4 Thesis Structure and Content

The structure and contents of this PhD project are visualized in the flow chart as shown in Figure 1.4. The first chapter briefly introduces the background and motivation, scope as well as the objectives of the project. The overview and state-of-the art are discussed in Chapter 2.

Chapter 3 discusses the research related to the high voltage flyback converter, including the efficiency optimization, investigation of different transformer winding architectures (TWAs), digital control implementation, the system level integration, and investigation of a new topology.

The thesis is finalized with conclusions and future works. Furthermore, the published or submitted conference and journal papers are illustrated in the flow chart as well (Figure 1.4). The purpose of this thesis is to provide a condensed and coherent overview of the research and results obtained in the thesis.

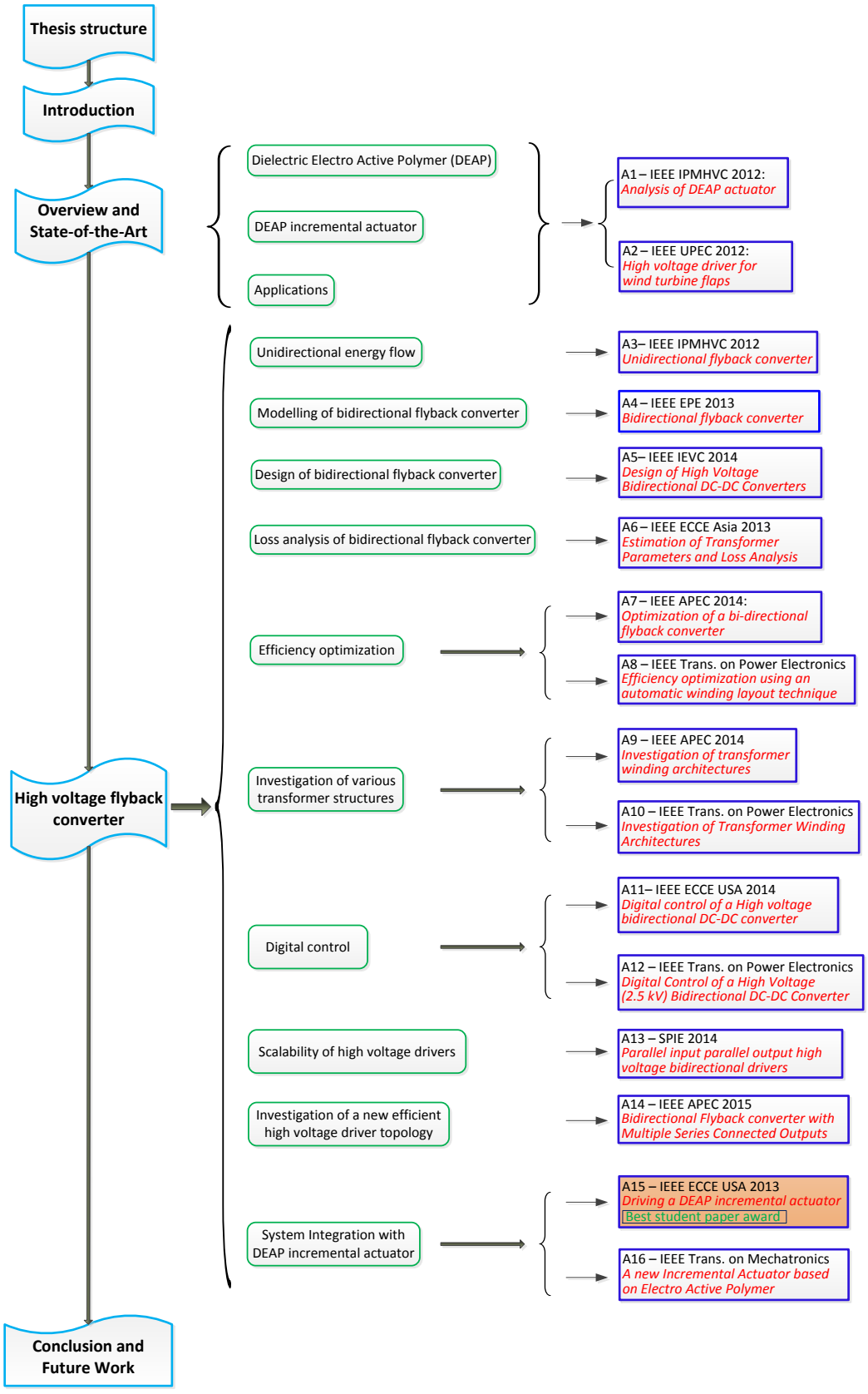

Figure 1.4: PhD thesis structure.

Chapter 2

Overview and State-of-the-art

The research topic of the thesis is design and development of high voltage drivers for DEAP incremental actuators. In this chapter, an overview and state-of-the-art for the DEAP incremental actuators, and the high voltage driving solutions are presented. The information about some applications of DEAP actuator and its high voltage drivers can be obtained from Appendix A and B.

2.1 Linear Actuators

Actuators providing linear motion are used in a vast variety of applications ranging from large size machineries (e.g., cranes) to small scale micro-electro-mechanical system (MEMS) devices used for micro positioning. Linear actuators are typically characterized by their maximum stroke length, force, speed, and precision (or resolution). The typical linear actuators [2] include mechanical, electro-mechanical, hydraulic, pneumatic, and piezo, etc. Several well-known linear actuators are provided in Figure 2.1.

Mechanical linear actuator operates by converting the rotary motion into linear motion. The advantages of mechanical actuators are low price, precision positioning, and no need of a power source. The disadvantage is that they have to be operated manually. The electromechanical linear actuators use DC motors and stepper motors to control a linear-action shaft output. Rotary motion of the motor is converted to linear displacement. These actuators are heavier than their motor counterparts due to the addition of actuator assembly. Piezoelectric actuators can achieve extremely fine positioning resolution, but have a very short range of motion. The piezo actuators are expensive and fragile. Pneumatic linear actuators operate with an external source of compressed air. They are efficient, but relatively complex to control via pressure valves and compressor manipulation. Hydraulic linear actuators are used in many industrial applications requiring higher levels of force than provided through equivalently sized electromechanical systems. Hydraulic linear actuators require an external source for fluid pressurization. Unlike pneumatic actuators, a leak from hydraulic equivalents can foul equipment and require addi-

tional clean up procedures depending on the type of fluid used. Control is complex, involving compressor control and hydraulic valves.

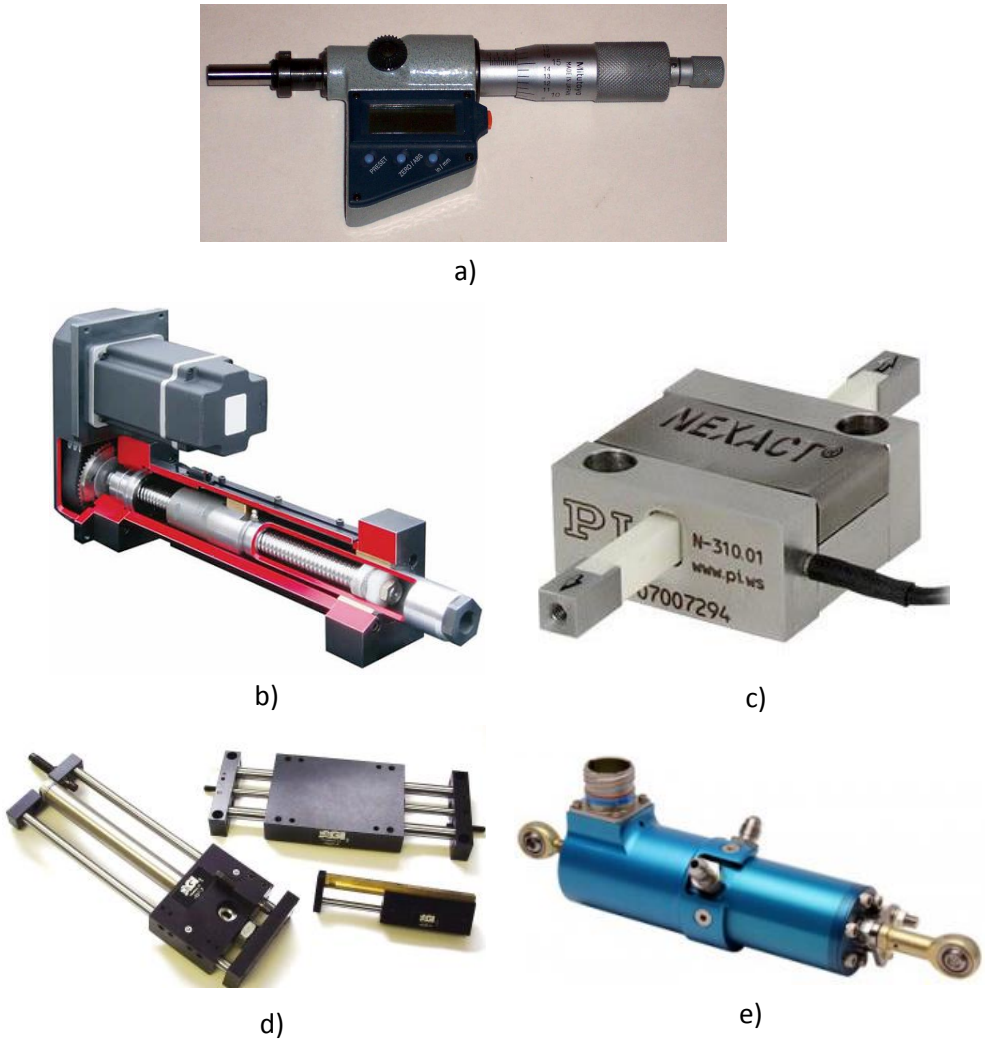

Figure 2.1: Linear actuators from different technologies: a) a mechanical linear actuator [3]; b) an electro-mechanical linear actuator [4]; c) a piezo linear actuator [5]; d) a pneumatic linear actuator [6]; e) a hydraulic linear actuator [7];

2.2 Dielectric Electro Active Polymer

Smart materials which respond to external stimuli like light, temperature, pressure, pH, magnetic and electric fields by changing their shape or size have been a particular focus in the past decade [8]. The intelligent materials include, shape memory alloys, piezoelectric materials, etc., and deforming active polymers include, hydro gels, dielectric elastomers, carbon-nano tubes, and liquid crystalline elastomers.

The beginning of the Electro Active Polymer (EAP) field can be traced back to an 1880 experiment that was conducted out by Roentgen, using a rubber band that was charged and discharged with fixed end and a mass attached to the free end [9], [10]. This discovery had been verified by Sacerdote in 1899, who formulated the relationship between strain response and electric field excitation [11].

Electro Active Polymers (EAPs) are categorized into two major classes: Ionic and Dielectric (DEAP). An electric field or coulomb forces drive DEAPs, while the actuation mechanism for ionic EAPs is through the diffusion or mobility of ions. The DEAPs generally require high electric fields (>30 V/μm) and the ionic EAPs require low driving voltages, nearly equal to 1-5 V. Dielectric electro active polymer (DEAP) is an emerging smart material technology that has experienced substantial development and has gained increasing attention by scientists and engineers [8], [12], [13].

The DEAP material is a very thin (40 μm) incompressible elastomer film having a compliant electrode layer on both sides [1], [14], [15]. The unique properties of DEAP are, light weight, high flexibility, large elastic strain, fast electromechanical response, etc, due to which it can be applied in a wide range of applications [8]. An actuator is a mechanical device for moving or controlling a mechanism or a system. A laminate of PolyPower DEAP material with corrugated surface and electrode is shown in Figure2.2. The basic operation of the DEAP is the reduction in the polymer's thickness and increase in its area, due to an applied electric field. Figure2.2 shows the actuation direction when a high voltage is applied to its electrodes. The prototye of a linear DEAP actuator is shown in Figure 2.3.

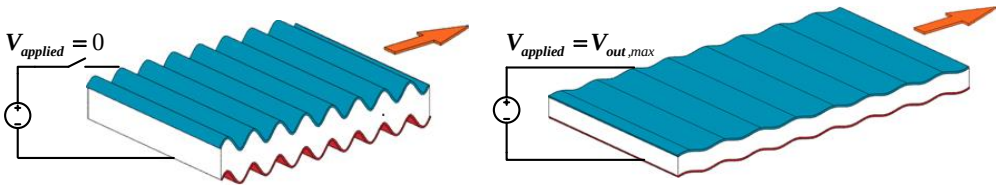

Figure 2.2: Basic principle of PolyPower [1] DEAP material.

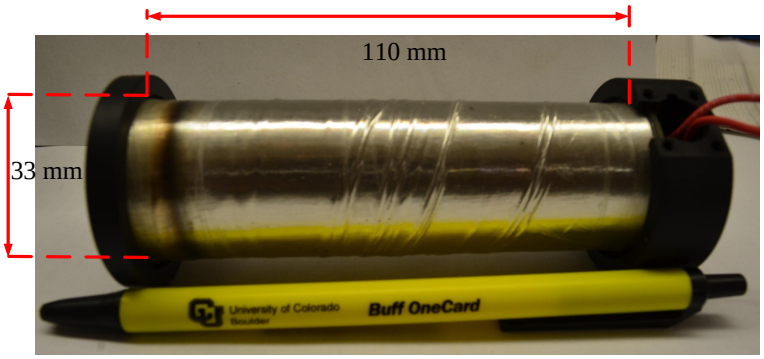

Figure 2.3: A prototype of linear DEAP actuator.

DEAPs can be used as actuators in active structures, in particular when large

deformations are required. Such EAP actuators convert electrical energy into mechanical energy and produce large strains. DEAP actuators have the capability to outperform the piezo, pneumatic and electromagnetic actuators in many ways, one of which is presented in Figure 2.9 showing actuation stress vs. strain. The dynamical electro mechanical model of DEAs is discussed in [16]. Several applications of DEAP actuators are discussed in [17], [18], [19], [20], [21], [22].

2.3 DEAP Incremental Actuator

2.3.1 Literature on Sliding Dielectric Elastomer Actuators

Several researchers have investigated and implemented electro active polymer based linear and rotary type actuators. Numerous applications of dielectric elastomers including inchworm robot and rotary motors have been described in [17]. The robotic inchworm as shown in Figure 2.4 uses electrostatic clamps which enable it to travel over both vertical and horizontal surfaces, for tasks such as inspection in narrow pipes [17].

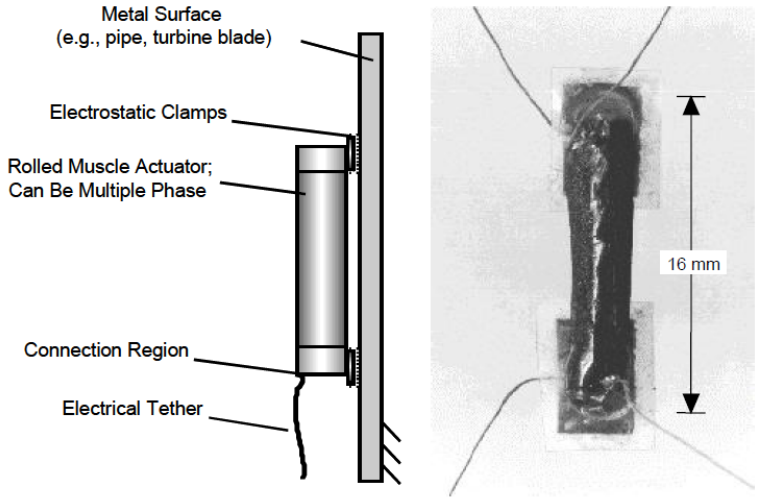

Figure 2.4: An inchworm robot with a dielectric elastomer body [17].

The walking robot using a multifunctional electroelastomer (MER) spring roll as each of the robot's six legs is shown in Figure 2.5 [18]. Each spring roll leg was a linear actuator, with 3-6 mm stroke at 1-10 Hz frequency. The speed was as high as 2.7 in/s. A rotary motor made with a pair of bow tie elastomer actuators as shown in Figure 2.6, with an output power of 4 W at 100 RPM has been demonstrated in [17]. The emerging DE technology has been thoroughly reviewed presents exciting possibilities across a wide range of applications including soft robotics [19]. An earthworm robot as shown in Figure 2.7, has been made using a novel soft actuator based on a dielectric elastomer. It has been demonstrated that the actuator moved with 1 mm/s at 5 Hz [20]. A simple rotary motor based on dielectric elastomers as shown in Figure 2.8, has been proposed in [21]. A new way to achieve the rotary motion using the DEAP actuators has been reported in [23]. Furthermore, several

researchers have investigated piezo, pneumatic and hydraulic based actuators. The gain scheduling control of a walking piezo actuator is proposed in [24]. Bipolar piezo electric actuators are proposed in [25]. High-accuracy tracking control of hydraulic actuators is discussed in [26].

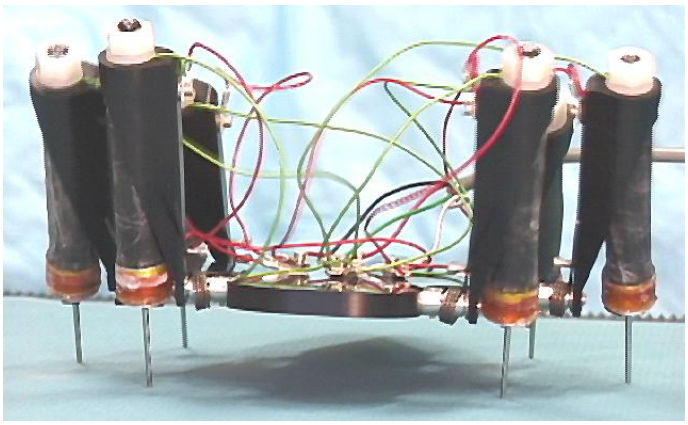

Figure 2.5: A walking robot with MER spring rolls as legs [18].

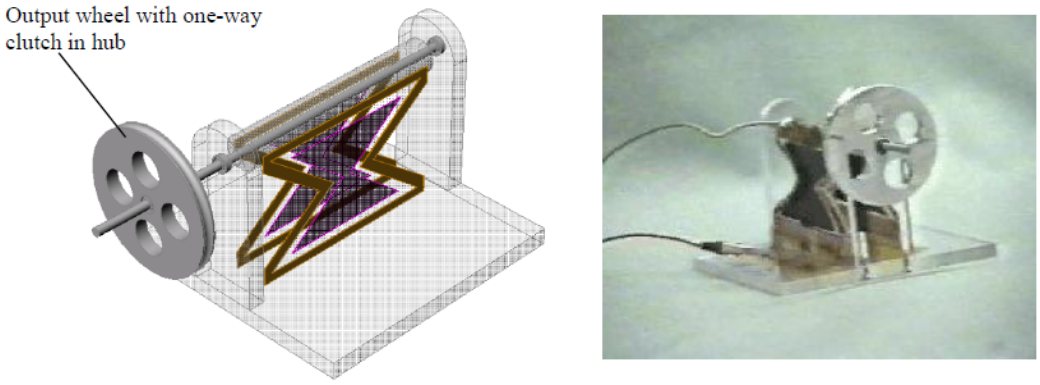

Figure 2.6: A simple rotary motor based on dielectric elastomers [17].

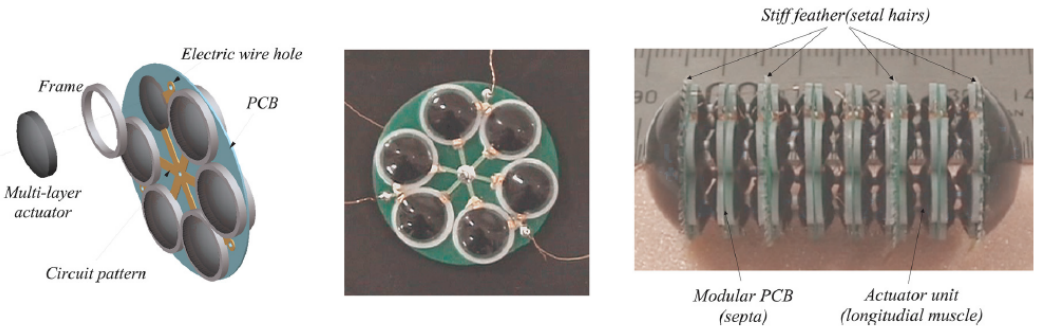

Figure 2.7: An earthworm robot with the actuator module [17].

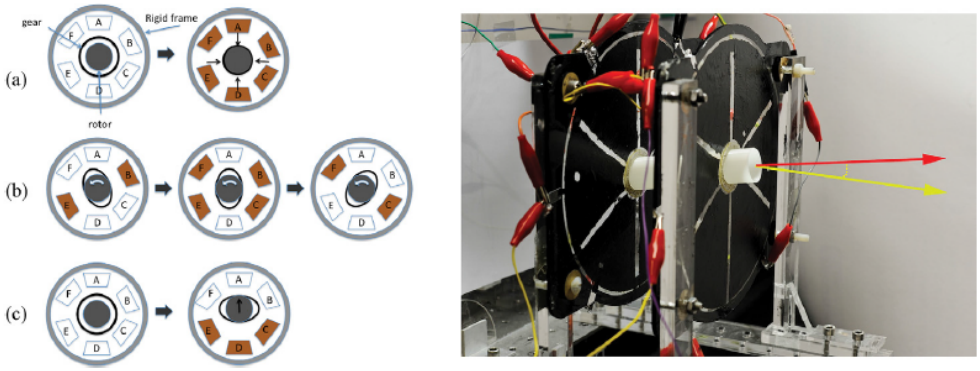

Figure 2.8: A simple rotary motor based on dielectric elastomers [21].

2.3.2 Advantages and Figure of Merits of DEAP Incremental Actuator

DEAP actuators exhibit large elastic strains, reasonable actuation pressures, relatively high electro-mechanical coupling and actuation speeds as compared to other known smart material technologies [8, 12]. DEAP actuators are very silent, can be of relatively light weight. DEAP actuators are potentially capable of outperforming pneumatics and electromagnetics in many ways, one of which is presented in Figure 2.9 showing actuation stress versus actuation strain.

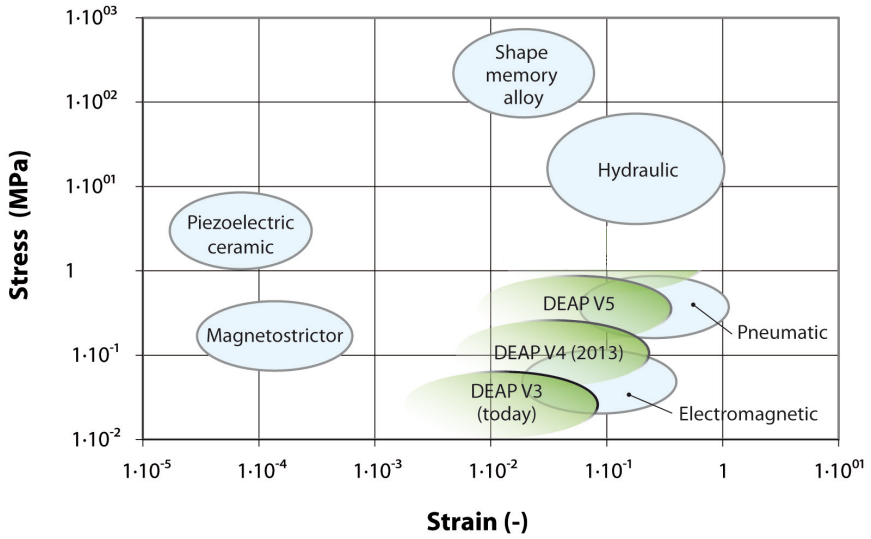

Figure 2.9: Typical stress-strain performance ranges for several actuator technologies [1].

The design and implementation of high voltage drivers for the DEAP based capacitive actuators is a new area of research [27–42]. DEAP, when utilized as linear actuators, has the potential to be an effective replacement for many conventional actuators.

Replacement of conventional actuators with DEAP actuators is able to provide the

following advantages:

- DEAP is seven times lighter than copper and steel by which the conventional actuators are made of. Reducing the weight in any application can result in better overall efficiency.

- DEAP actuators are capacitive devices, i.e., a large portion of the energy is reactive and can be harvested and reused in cyclic motions. This will require less energy from the main power source, once again increasing its efficiency.

- DEAP actuators are entirely made of rubbery material which is inherently tolerant to shock and vibration which exist in some applications (e.g., electric vehicles). Moreover, a DEAP actuator does not incorporate any moving and sliding parts such as bearings, gearing and similar. All these characteristics result in improved lifetime, cost, and efficiency.

- DEAP actuators can be configured to provide incremental motion, thus overcoming the inherent size-to-stroke implications of conventional linear actuators, where the stroke is limited by their size. In incremental mode, DEAP actuators are several orders of magnitude shorter in their length compared to the stroke they provide. This will once again reduce the size and weight of the actuation mechanism resulting in better system efficiency.

There are two types of operational modes of incremental actuators viz., Pusher mode and Walker mode. In Pusher mode an incremental actuator is stationary and it pushes a shaft or rotates a disk. In Walker mode, as the name employs, the incremental actuator is mobile and it carry a load on either a guided path or a random path depending on the applications. For example, in industrial manufacturing the path is generally guided, while in search and rescue operations the path is random. Figure 2.10 illustrates these fundamental operational modes.

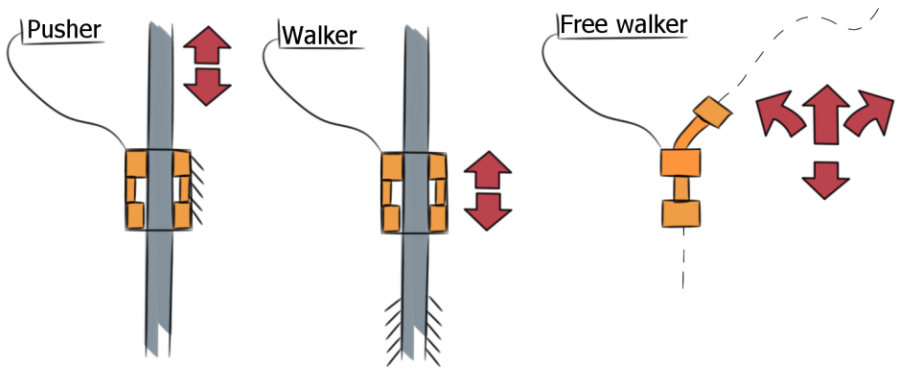

Figure 2.10: An incremental actuator can either be of a pusher type, where another object is moved, or of a walker type, where the incremental actuator itself moves. A walker type can either be guided or unguided [1].

Two existing technologies i.e. Piezo and Pneumatics, with good potentials in pro-

viding incremental motion are being compared with DEAP technology. Table 2.1 shows the results of comparison study between the three technologies and the two motion types. This initial study indicates that DEAP has its value proposition for mobile applications requiring low weight and form factor (simple and flexible design).

Table 2.1: Figure of merits of three technologies for two motion types of incremental actuators

FoM	Suited for Pusher mode	Suited for Walker mode
Stroke	DEAP, Piezo, Pneumatics	DEAP, Piezo, Pneumatics
Force	Piezo, Pneumatics	DEAP, Piezo, Pneumatics
Speed (frequency)	DEAP, Piezo	DEAP, Piezo
Precision	Piezo	DEAP, Piezo
Weight in mobile products	**DEAP**	**DEAP**
Simple design	DEAP, Piezo	**DEAP**
Flexible	DEAP, Piezo, Pneumatics	**DEAP**
Autonomous	DEAP, Piezo, Pneumatics	**DEAP**
Compact	DEAP, Piezo	DEAP, Piezo
Energy efficient	DEAP, Piezo, Pneumatics	DEAP, Piezo

2.3.3 Conceptual Development of DEAP Incremental Actuator

The conceptual design of electro active polymer based linear DEAP actuators is provided in Appendix P. The generic concept of an incremental actuator is an assembly of sub-mechanism capable of gripping, releasing and extending. As DEAP showed most potential in Walker operation (Table 2.1), the incremental actuator concepts are developed for this type of motion. The static guiding structures on which the actuator performs its motion are chosen to be rods and pipes. The concepts used to design DEAP incremental actuator have two grippers and one extender. A gripper should be able to maintain its position with a certain force, while the extender should be able to displace a gripper at its released state. The incremental motion is then performed by activating the grippers and extender at a certain pattern. Figures 2.11, 2.12, 2.13 and 2.14 show various conceptual drawings for the DEAP incremental actuator.

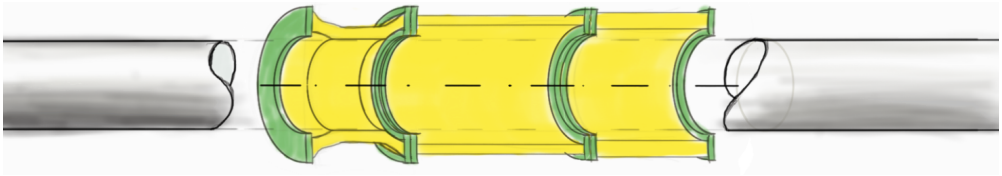

Figure 2.11: Concept 1 of DEAP incremental actuator [1].

Concept 1 is designed to operate outside a cylindrical rod. It consists of three sub components, namely one extender and two grippers at either end. When in operation, one gripper holds the bar while the other gripper is in the released

position. The extender either pushes or pulls the released gripper. The grippers and extender are joined by gluing or screwing their mechanical connections together (green plates in Figure 2.11).

Concept 2 is designed to operate inside a cylindrical tube as opposed to Concept 1. Concept 2 consists of one extender and two grippers on either end. Both the grippers and the extender of Concept 2 are realized by using axial DEAP actuators. Additional gripping mechanisms are applied to the grippers (red structures in Figure 2.12). The gripping mechanism extends or contracts radially when the grippers are, respectively, contracting or extending axially as illustrated by the arrows in Figure 2.12. The three axial actuators are joined together, at their mechanical connections, by gluing or by screws.

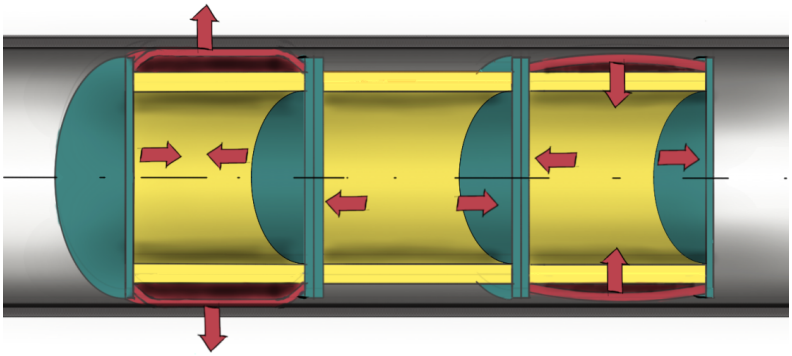

Figure 2.12: Concept 2 of DEAP incremental actuator [1].

The concept 3 as shown in Figure 2.13 is based on 3 DEAPs in axial configuration 1 extender and 2 blocking DEAPs. When the blocking DEAP is extended the wedges are driven toward the guide rod thereby create a blocking force.

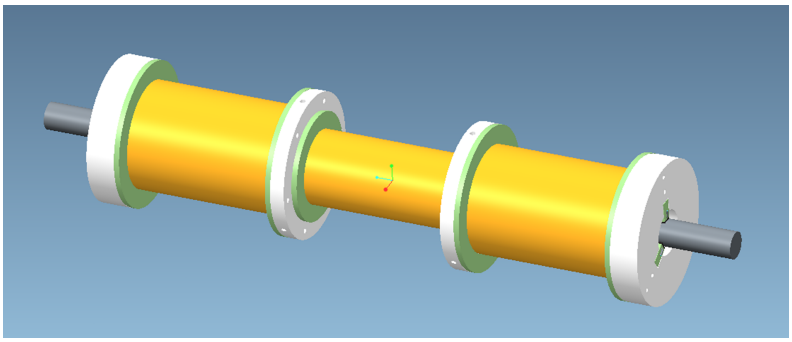

Figure 2.13: Concept 3 of DEAP incremental actuator [1].

The concept 4 as shown in Figure 2.14 [38] is chosen as the first iteration of this feasibility study, due to its transparent motion which can be easily understood and demonstrated. Here three Axial-1 type transducers are used to facilitate the incremental motion. Auxiliary mechanics are attached to the transducer enabling them to grip, release and extend on a solid rod.

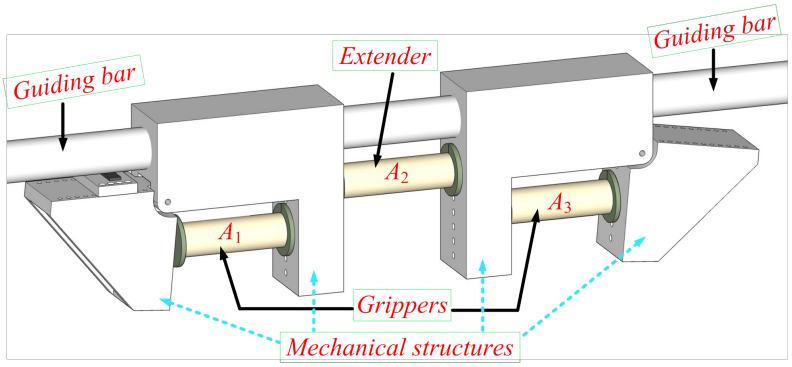

Figure 2.14: Concept 4 of DEAP incremental actuator [38].

2.4 High Voltage Driver Solutions for Incremental Actuator

As explained in Section 2.3.3 the DEAP incremental actuator consists of three mechanically connected and electrically isolated linear DEAP actuators. Driving the DEAP incremental actuator has three main challenges from a power electronics standpoint. Firstly, it requires high voltages (2-2.5 kV), to generate sufficient force and stroke (or elongation) from each linear DEAP actuator. Suitable energy sources for this application are lithium batteries with a voltage range: 9-24 V DC. This necessitates the need of high voltage step-up circuits as a driving mechanism for the DEAP actuator. Secondly, DEAP actuators convert only a small fraction of the input electrical energy into mechanical work, while they store the remainder in the capacitive structure of the actuator, and can be recovered to maximize the system efficiency. This necessitates the need of bidirectional converters [43]. Finally, to move the incremental actuator with the required speed and direction, the three DEAP actuators need to be driven by a specific sequence of high voltage signals [38].

The design specifications and requirement of high voltage (HV) driver are summarized in Table 2.2. The average charging power needed for the design is 25 W (during 50 ms). Due to very high step-up voltage ratio (104) and low power requirements for the HV driver, the piezo transformer based converter [44–55] and magnetic transformer based flyback converter [37, 38, 43, 56–65] are the potential candidates for generating high maximum output voltage (2.5 kV) from low input voltage (24 V) source. However, in this research the main focus is only on the flyback converter based HV drivers.

2.4.1 High Voltage Bidirectional Flyback Converter

High voltage switch-mode power supplies for charging the capacitive loads are implemented in [52, 66, 67]. Bidirectional DC-DC power converters are needed for the DEAP based capacitive actuators [64, 68], to increase the lifetime of the battery, and to discharge the high voltage across them. Bidirectional flyback converter [43, 61, 62, 69, 70], and a forward-flyback bidirectional converter [71] are imple-

Table 2.2: Design specifications and requirements of high voltage converter

Parameters	Target Specifications
Input voltage / Output voltage	24 V / 0-2.5 kV
Capacitance of DEAP actuator	400 nF
Charging time to reach 2.5 kV from 0 V	50 ms
Average charging power	25 W
Discharging time to reach 0 V from 2.5 kV	50 ms
Linear velocity of DEAP incremental actuator	0-5 mm/s
Charge energy efficiency to charge the capacitive actuator from 0 V to 2.5 kV	$> 90\%$
Discharge energy efficiency to discharge the capacitive actuator from 2.5 kV to 0 V	$> 85\%$

mented for various applications. The schematic of the conventional bidirectional flyback converter is shown in Figure 2.15. Due to high reverse recovery time (2.6 μs) of body diode of high voltage (4 kV) MOSFET, a modified high voltage bidirectional flyback converter topology [37] as shown in Figure 2.16, is proposed and implemented for driving a DEAP actuator.

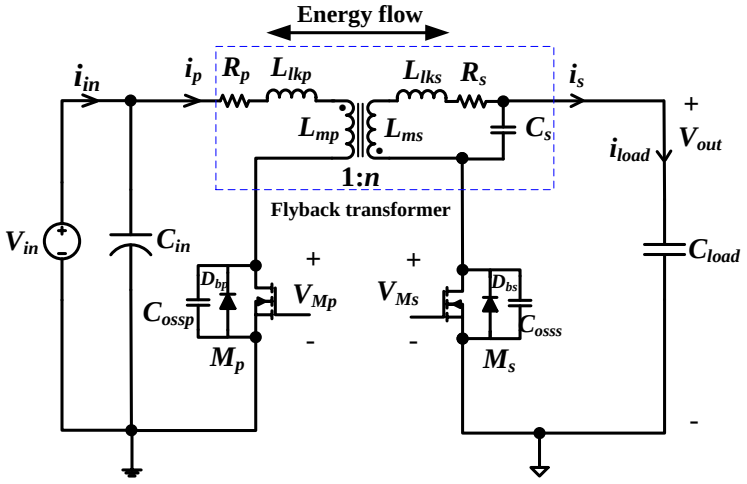

Figure 2.15: Schematic of the conventional bidirectional flyback converter.

The loss analysis of the same converter is performed in [42]. More details about the analysis of the bidirectional flyback converter can be found in Appendix D. The detailed design of the bidirectional flyback converter for driving a capacitive load is presented in Appendix E. The discharge energy efficiency is limited by the parasitics of the high voltage components which prevent full utilization of valley switching as described in Appendix K. A new implementation is therefore proposed in Appendix N, where the secondary transformer winding is split into multiple windings which are connected in series by lower voltage rating MOSFETs driven by a gate drive transformer which is shown in Figure 2.17. For more details about the new proposed topology refer to Appendix N.

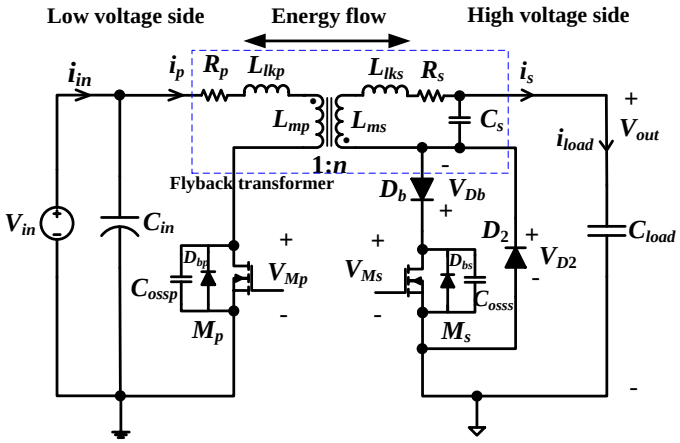

Figure 2.16: Schematic of the high voltage bidirectional flyback converter for driving a high voltage capacitive load.

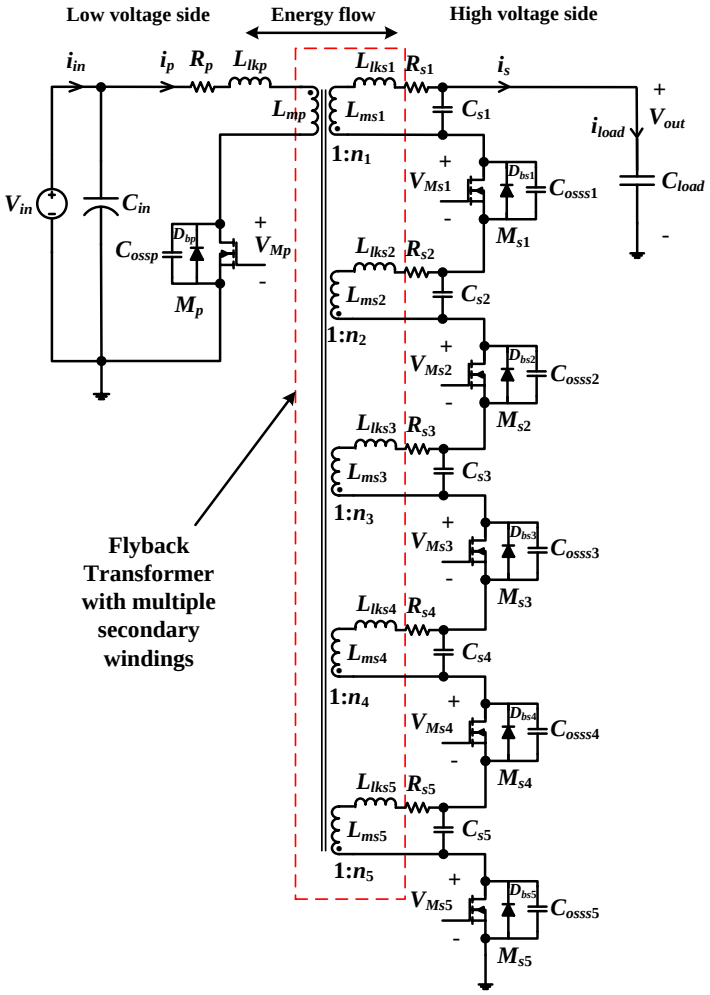

Figure 2.17: Proposed HV bidirectional flyback converter with 5 transformer stages on the secondary side.

2.4.2 HV Drivers for DEAP Incremental Actuator

The detailed driving voltage waveforms for the DEAP incremental actuator are given in Appendix O, from which it is clear that the 3 linear DEAP actuators need to be charged and discharged independently. Different solutions for driving the DEAP incremental actuator are provided in Figures 2.18, 2.19, 2.20. The concept 1 is to drive the system of DEAP incremental actuator having 3 linear actuators, with 3 independent HV drivers with the same input power source. Concept 2 is to drive the 3 linear actuators, with a single HV driver. For this concept a series combination of diode and a transistor/IGBT, is connected in series with each actuator, during both charge and discharge modes. The concept 3 is to drive the 3 linear actuators, with a single HV driver with a transformer having multiple secondary windings. For this concept a transistor/IGBT is connected in series with each actuator during charge mode, and a diode is connected in series with each actuator during discharge mode. The concept 4 is to drive the 3 linear actuators, with a single HV driver having a bidirectional relay in series with each actuator.

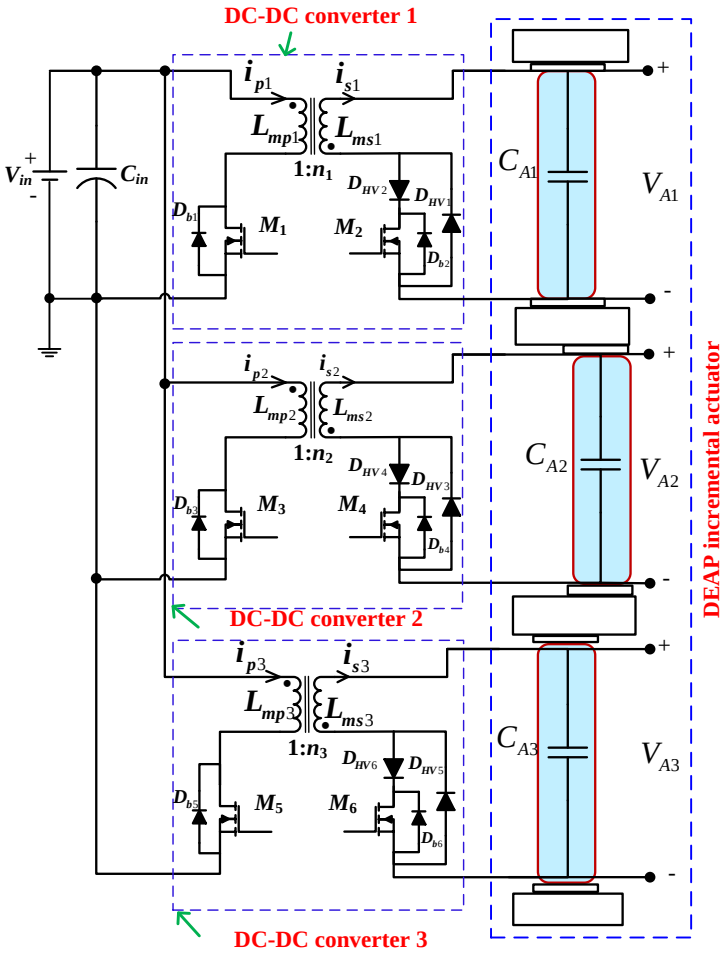

Figure 2.18: Driving multiple actuators in the DEAP incremental actuator with multiple converters.

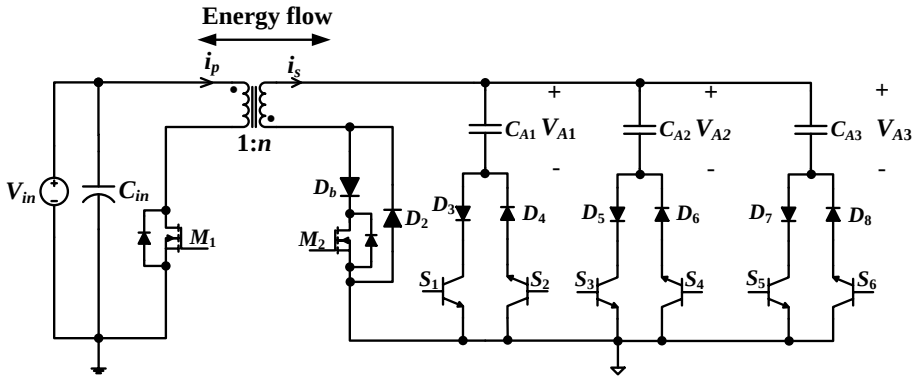

Figure 2.19: Driving multiple actuators with a single converter.

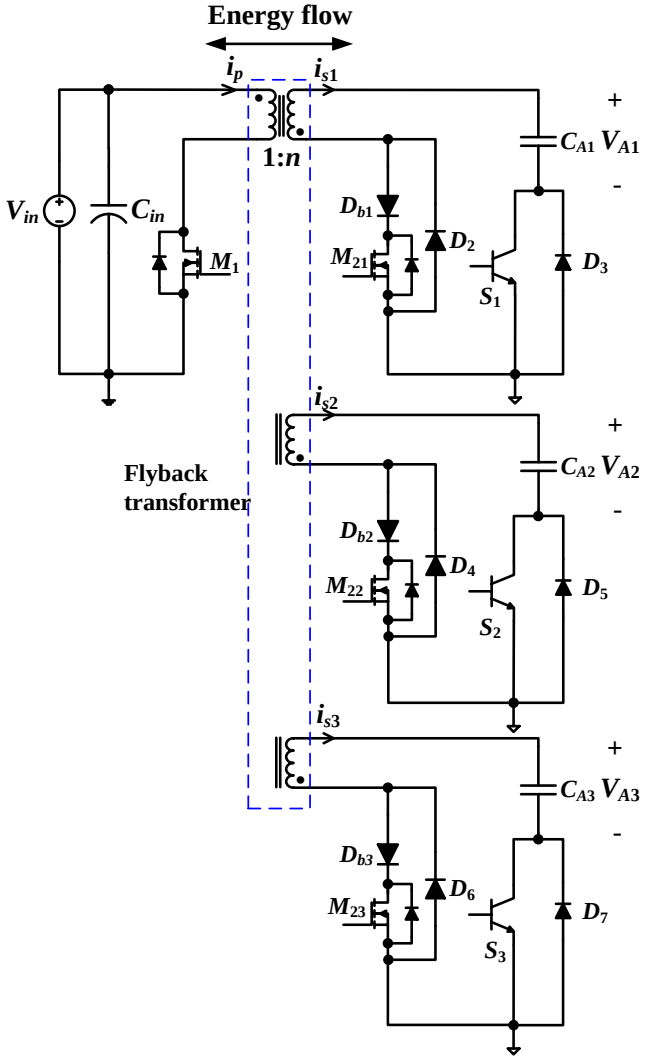

Figure 2.20: Driving multiple actuators with a single converter having multiple transformer windings.

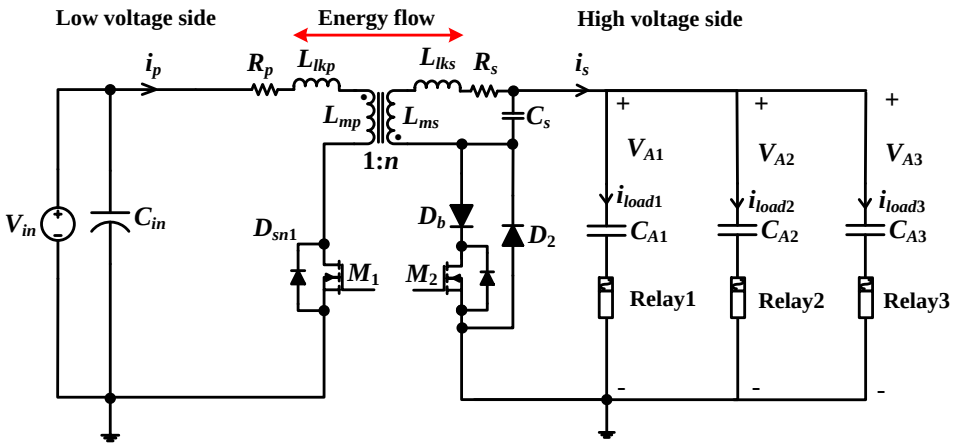

Figure 2.21: Driving multiple actuators with a single converter having a bidirectional relay in series with each actuator/capacitive load.

The comparison among all HV driver concepts is provided in Table 2.3.

Table 2.3: Comparison of HV driver concepts for the DEAP incremental actuator

Comparing item	Concept 1	Concept 2	Concept 3	Concept 4
Low voltage switches	1	1	1	1
High voltage switches	3	7	6	1
High voltage relays	0	0	0	3
High voltage diodes	6	8	9	2
Primary low side gate drivers	1	1	1	1
Secondary low side gate drivers	3	4	6	1
Secondary high side gate drivers	0	3	0	0
Control complexity	Low	Very High	High	Low
Cost of HV driver	Moderate	Very High	High	Low
Volume of HV driver	Moderate	Moderate	High	Small

The concept 1 is simple to implement and it is easy to charge and discharge the 3 capacitive actuators at very high voltage (2.5 kV). Use of a single magnetic component (flyback transformer) in Concept 2 has the potential to reduce the system cost, weight and dimensions while maximizing the system efficiency by recovering the unused energy from the capacitive loads. These qualities make the drive circuit attractive for mobile and embedded systems, as well as any weight and power-critical designs. However, Concept 2 is very complex and expensive to implement, since more HV diodes, HV switches, and high-side gate drivers are needed. Concept 3 consists of a flyback transformer with multiple secondary windings. This concept

is simple to implement, but, it is expensive. Furthermore, in Concept 3, it is very difficult to achieve perfect coupling among the 3 secondary windings. The Concept 4 has a bidirectional relay in series with each actuator. The commercially available solid state bidirectional relay is provided in [72]. But, the maximum rating of the relay is 1.5 kV and 20 mA. Hence, even though the Concept 4 is cheap to implement, it is impossible to drive the capacitive load at very high voltage (2.5 kV).

2.5 Summary

In this chapter, an overview of several linear actuators, literature review on sliding dielectric elastomer actuators, and different conceptual designs for DEAP incremental actuator are presented. The flyback converter is chosen as a suitable topology for the HV driver due to its simple structure and a low component count. Several flyback converter based HV driver solutions are presented for DEAP incremental actuator to accomplish the incremental motion. Out of the 4 concepts, the concept 1 is chosen as a reliable and simple solution.

Chapter 3

High Voltage Bidirectional Flyback Converter

3.1 Efficiency Optimization

The DEAP incremental actuator technology has the potential to be used in various industries, e.g. automotive, aeronautics, and medicine. For using the DEAP actuators in such applications, the high voltage drivers should have low volume to fit inside or together with the actuators. The overall energy efficiency of battery powered high voltage drivers influence, the distance travelled by the incremental actuator. Hence, for DEAP actuator applications, both the volume and energy efficiency of high voltage drivers are extremely important and need to be optimized.

Transformer design plays a very important role in high voltage DC-DC power converters employed in low, medium and high power applications. The design methodologies for transformers used in conventional switch-mode power supplies are well documented [56, 73–75]. Often, a transformer for a given application is designed based on some assumptions such as, constant switching frequency, maximum temperature rise, estimated converter efficiency, winding fill factor, and winding current density. However, those assumptions are not valid or suitable for some applications. Hence, more customized procedures are needed to design efficient transformers, for specific applications. In a high voltage capacitor charge and discharge application, the high voltage transformer will have a large amount of (> 200) secondary turns. For such application, it is very difficult to select an optimum winding diameter and number of winding layers beforehand, which decide the values of the transformer parasitics. To avoid this difficulty, an automatic winding layout (AWL) technique is introduced in [41] and Appendix G, for the winding design of a high voltage transformer. The high voltage flyback converter operation is very sensitive to the transformer parasitics. The proposed AWL technique, utilizes the entire available space in a given transformer bobbin and provides an optimum winding diameter that minimizes the total loss due to the transformer parasitics.

In the initial design phase, it is difficult to predict which core type is optimal for a given application. In a flyback converter, a long transformer window width is

often preferred, in order to minimize the leakage inductance and AC resistance by providing a close coupling between windings, and to decrease the number of winding layers. For high output or input voltage flyback converters, this could be different, since the self-capacitance of the high voltage winding has significant impact on the performance of the converter. During this research, an efficiency optimization algorithm is proposed, which provides an optimum solution for a given transformer core, by using the proposed AWL technique and the comprehensive loss model. Different transformer winding architectures (TWAs) for the high voltage capacitor charge and discharge application are investigated in [40] and Appendix I. In [39] and Appendix K, a digital control technique is proposed for improving the energy efficiency and charge/discharge speed. Control algorithms for optimal-flyback charging of a capacitive load are proposed in [65]. A number of switch-mode power supply design optimization methods have been described in the literature [76–81].

The proposed efficiency optimization technique has the following features:

- an automatic winding layout (AWL) technique, which produces the information about winding diameters, number of layers, and number of parallel windings, for both primary and secondary windings.
- an accurate calculation of transformer parasitics using the outputs of AWL technique.
- calculation of energy losses during charge and discharge modes using a comprehensive loss model.
- an objective function that minimizes the sum of energy losses during charge and discharge modes, over a range of operating points.

More details about the efficiency optimization can be found in Appendix H and G.

3.1.1 Automatic Winding Layout (AWL) Technique

The transformer design using the proposed AWL technique is described in Figure 3.1. The inputs to AWL technique are fixed number of primary and secondary turns, and the dimensions of core/bobbin (window height and width). The outputs of AWL technique are various winding implementations, including specific winding details such as, diameters of primary and secondary windings, number of primary and secondary winding layers, and insulation thicknesses for placing between secondary winding layers.

The outputs of the AWL technique are used to calculate the transformer parasitics [42, 82–87], such as DC resistance, leakage inductance and self-capacitance. In Figure 3.2, one output of AWL technique such as the insulation thickness ($d_{insulation}$) for a PQ 20/20 core, and calculated transformer parasitics are shown with respect to square width (W_{sqs}) of secondary winding. As the width of the secondary square (or secondary winding) decreases, the insulation spacing $d_{insulation}$ between secondary winding layers increases, DC resistance R_s increases, leakage inductance L_{lkp} slightly decreases, and the self-capacitance C_s decreases.

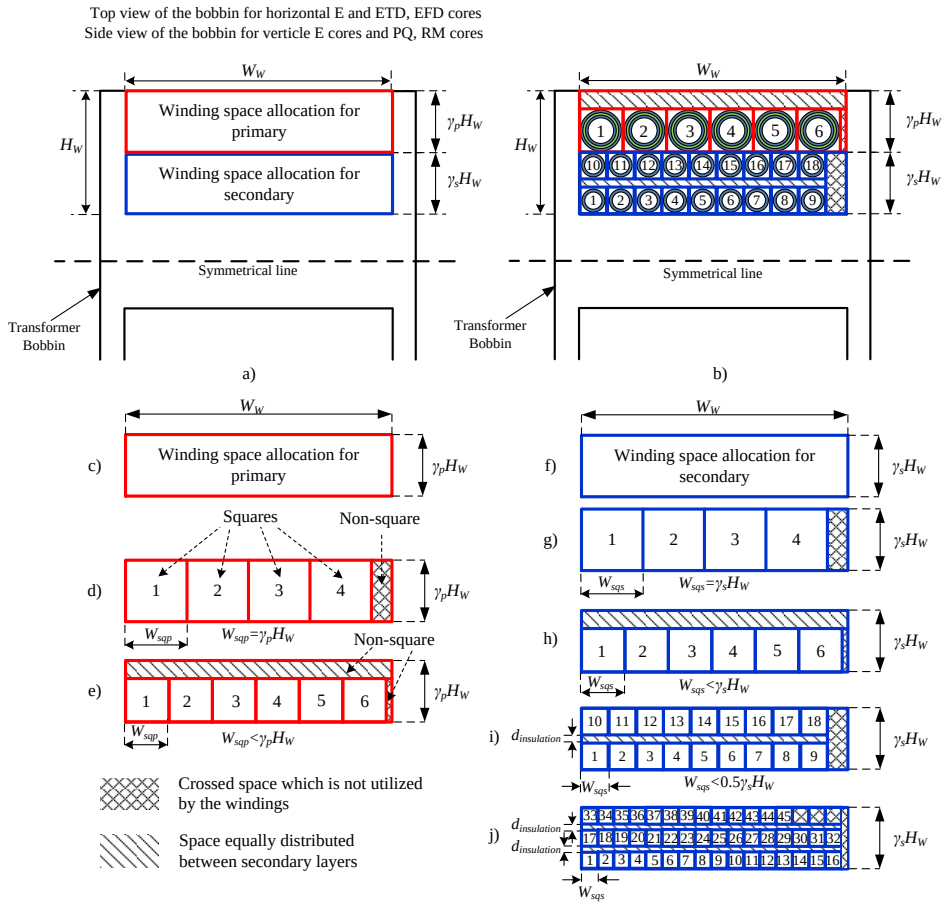

Figure 3.1: a) Allocated winding space a) before applying AWL technique; b) after applying AWL technique; c) - e) Different steps involved in AWL technique for primary winding; f) - j) Different steps involved in AWL technique for secondary winding;.

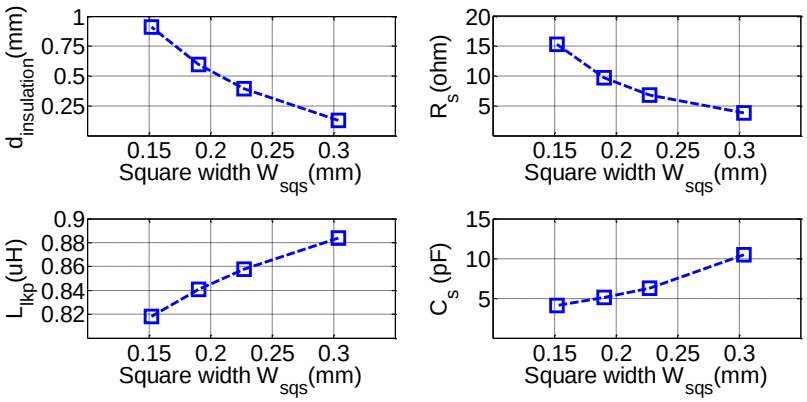

Figure 3.2: Variation of transformer parasitics with the diameter of secondary winding, for PQ 20/20 core (when γ_s=0.8).

3.1.2 Efficiency Optimization Procedure

The flow chart of the proposed optimization routine is shown in Figure 3.3. The proposed optimization routine is described in the following steps:

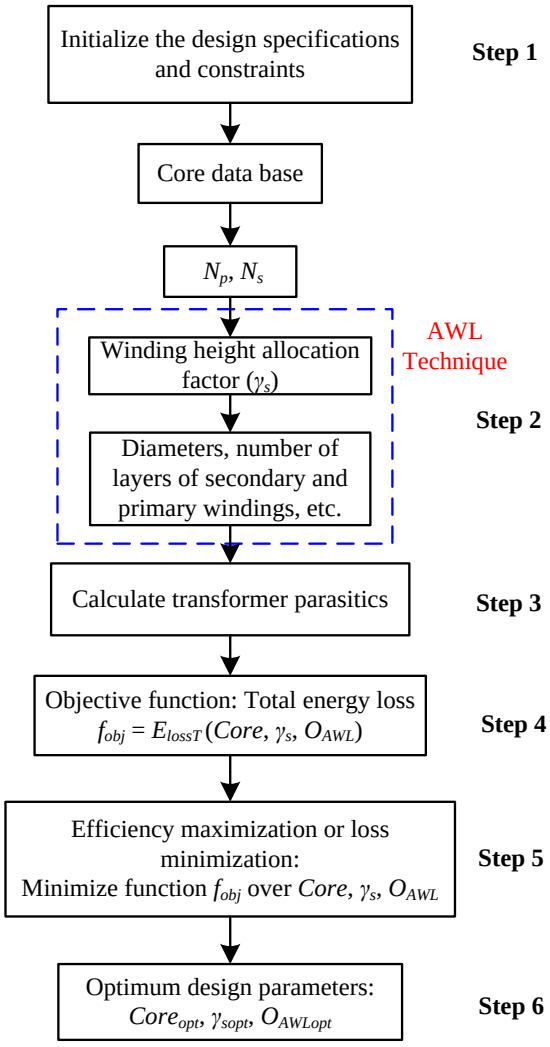

Figure 3.3: Flow chart of the proposed efficiency optimization procedure.

- Transformer turns ratio, peak currents (for charge and discharge operations), magnetizing inductance are selected from the design specifications and constraints. Number of primary and secondary turns are calculated for a given transformer core.
- The proposed AWL technique is applied to calculate an array of the outputs (diameter, number of layers, turns per layer, number of parallel wires, for both primary and secondary windings). The condition for the last layer fill factor (FF_{LL}) is FF_{LL}>0.85, this is to approximately make, equal number of

turns per layer in final secondary layer and remaining secondary layers).

- The transformer parasitics are calculated for each set of outputs resulted from AWL technique.
- The objective function is defined as sum of the total energy losses in the bidirectional flyback converter over a set of operating points.
- The end results of the optimization routine are the set of parameters which contributes to the minimum total energy loss. Finally, the optimum charge and discharge energy efficiencies are calculated as a function of output voltage.

3.1.3 Results of Optimization

The optimum secondary height allocation factor γ_s, for each core is provided in Figure 3.4. Figure 3.5 provides the results of the optimum charge, discharge and overall (product of charge and discharge) energy efficiencies, and an overall energy efficiency of a typical design where 50% space is allocated for primary and secondary windings, at an output voltage of 2.5 kV, with respect to different core volumes. The most efficient and smallest transformer (or core) designs are two important outcomes of the proposed efficiency optimization routine.

The smallest and optimized core designs are described below:

3.1.3.1 Smallest Core Design (SCD)

The smallest core is selected as the core whose temperature rise is less than the maximum temperature limit of 130 °C (with an estimated ambient temperature of 35 °C). Several small cores such as, EFD 12, EFD 15, E 16 have been used in the optimization routine, out of those E 16 is the smallest core with a maximum temperature rise of 94 °C (in a single bidirectional charge and discharge cycle).

3.1.3.2 Optimized Core Design (OCD)

The core which has a lower volume and a better overall energy efficiency compared to other cores is selected as an optimized core. In Figure 3.5, most of the cores whose volume is above 2.85 cm^3 have an overall energy efficiency between 74% and 76%. The EFD 25 core with volume 3.3 cm^3 has lower discharge efficiency (hence lower overall efficiency), since its window height H_W is less compared with the neighboring cores, such as EF 25 and RM 10. For a better trade-off between the core volume and overall efficiency, the cores whose volume is between 2.85 and 4 cm^3 could be more suitable for the high voltage driver. The cores with volumes 4 cm^3 (E 30) and 2.85 cm^3 (PQ 20/20) have overall efficiencies of 75% and 74%, respectively. However, PQ 20/20 core is selected as an optimized core, as 40% increase in the core volume provides only 1% increase in the overall energy efficiency. More details about the results of efficiency optimization can be found in Appendix H.

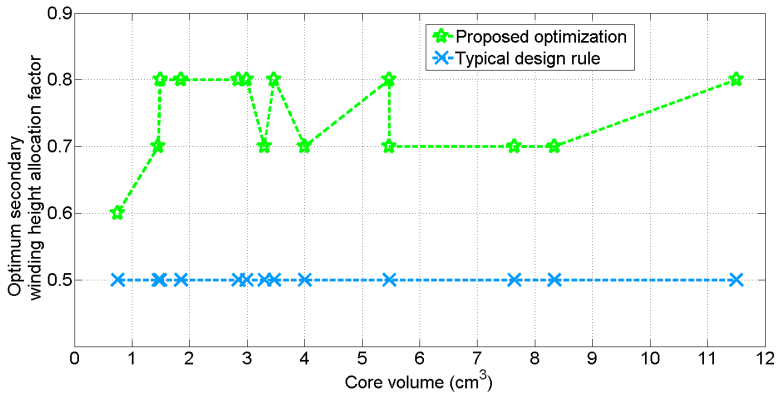

Figure 3.4: Optimum secondary winding height allocation factor γ_s vs. core volume.

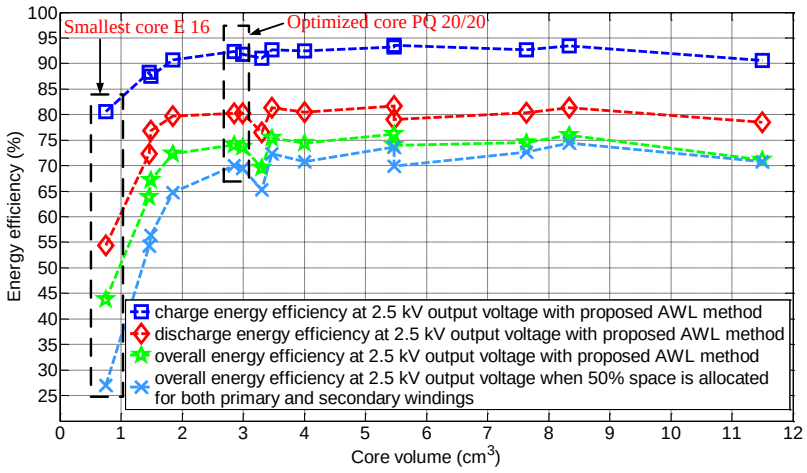

Figure 3.5: Calculated optimized energy efficiencies at an output voltage of 2.5 kV vs. core volume. The sequence of the 14 cores is: [E 16, EFD 20, E 20, RM 8, PQ 20/20, E 25, EFD 25, RM 10, E 30, PQ 26/20, ETD 29, ETD 34, RM 12, ETD 39].

3.2 Investigation of Transformer Winding Architectures

Transformer parameters such as leakage inductance and self-capacitance are rarely calculated in advance during the design phase, because of the complexity and huge analytical error margins caused by practical winding implementation issues. Thus, choosing one transformer architecture over another for a given design is usually based on experience or a trial and error approach. The leakage inductance, self-capacitance and AC resistance calculations in several transformer winding architectures, ranging from the common non-interleaved primary/secondary winding architecture, to an interleaved, sectionalized and bank winded architectures are presented in [40] and Appendix I.

Four winding schemes (A, B, C and D) are shown in Figure 3.6. Winding scheme

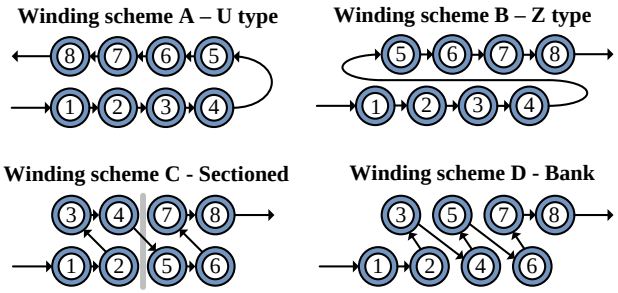

Figure 3.6: An overview of different winding schemes.

A is the most simple to implement since the next layer starts where the previous layer ended. In winding scheme B, the next layer starts just above the starting point of the previous layer. Winding scheme C split the winding into a number of sections that is individually wounded like winding scheme A. In winding scheme D, the turns progress in a vertical back angled way where turns are built on top of previous turns. It seems like winding scheme D achieves as many angled sections as there are turns in a layer without the penalty of reducing the fill factor due to the thickness of the section walls. Another advantage is that winding scheme D can be easily interleaved which is not the case for winding scheme C since it is hard to add section walls in-between windings. The difference in self-capacitance due to the winding schemes is severe [82, 86, 87] because of change in the voltage potentials between the turns in the winding.

3.2.1 Investigation using RM8 Core

Several winding buildups (S/P, S/P/S, S/P/S/P/S/P/S; where S and P are the secondary and primary windings) are investigated - see Figure 3.7.

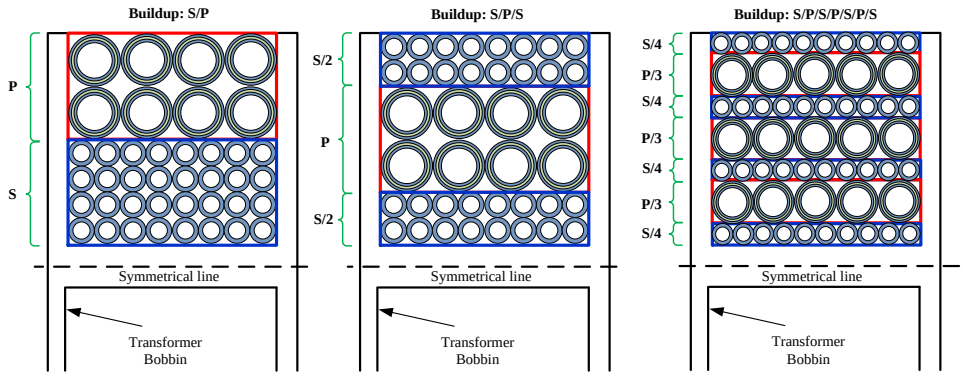

Figure 3.7: An overview of different winding buildups (just an example, here the number of primary or secondary windings are not the same as those shown in Table 3.1 or Table 3.2).

In order to simplify the implementation of the windings a low turns ratio of 10 is selected. Based on these configurations, seven high voltage transformer winding architectures (W_1-W_7) are derived and the winding information is summarized in Table 3.1. The TWAs W_1-W_6 are wound with 10 primary turns and 100 secondary turns. W_7 deviates since it is only implemented with 9 primary turns due to the nature of the winding architecture. For more details about the TWAs refer to Appendix I.

Table 3.1: Details of the transformer with a turns ratio of 10 for W_1-W_6

Parameter	**Value**
Number of primary / secondary turns	10 / 100
Diameter of primary / secondary winding	0.8 mm / 0.32 mm
Number of layers of primary / secondary winding	2 / 4
Number of parallel wires of primary / secondary	2 / 1
Type of core / material	RM8 / N41
Space allocation for primary / secondary	50% / 50%

Table 3.2: Details of the transformer for W_7

Parameter	**Value**
Number of primary / secondary turns	9 / 100
Diameter of primary / secondary winding	0.5 mm / 0.32 mm
Number of layers of primary / secondary winding	3 / 4
Number of parallel wires of primary / secondary	5 / 1
Type of core / material	RM8 / N41
Space allocation for primary / secondary	50% / 50%

The different winding architectures are simulated in Ansoft Maxwell [88] to extract the values of the leakage inductances, self-capacitances and AC resistances. In Figure 3.8 the electrostatic energy between the windings is shown for winding schemes B and D. It is noted that the energy density is high between layer to layer and low between turn to turn as expected in winding scheme B. In winding scheme D there is less electrostatic energy and thus it has lower self-capacitance.

The simulated, calculated and measured (using the impedance analyzer PSM1735) values of the self-capacitance, leakage inductance and AC resistance for the 7 transformer winding architectures (TWAs) are shown in the Tables 3.3, 3.4, 3.5, respectively, from which it is clear that the measured, calculated and simulated transformer parameters for most of the TWAs closely matches. However, the differences in winding parameters such as an average layer to layer distance and mean length turn may cause errors around ±20%. In Appendix I, from the approximate loss model it was concluded that W_6 has the lowest loss among all TWAs followed by W_4, W_7 and W_3. This analysis is based on calculated parasitics values. However, if measured values are used in the loss calculations, then W_4 will have lowest loss due to transformer parasitics, followed by W_3 and W_6.

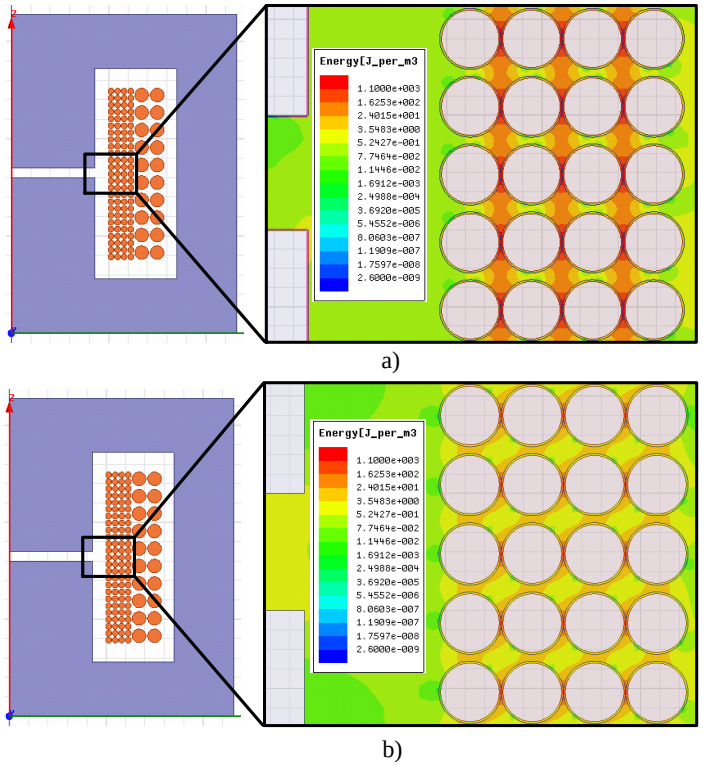

Figure 3.8: Plots from simulation of self-capacitance. a) Energy distribution for winding scheme B:Z-type. b) Energy distribution for winding scheme D: Bank-type.

Table 3.3: Self-capacitance of secondary winding

TWA	**Buildup**	**Winding scheme**	**sim.** (pF)	**Cal.** (pF)	**Mea.** (pF)
W_1	S/P	A	33	32	28
W_2	S/P	B	25	24	26
W_3	S/P	C	2.4	2	4.2
W_4	S/P	D	1.9	1	1.3
W_5	S/P/S	B	10	20	22
W_6	S/P/S	D	3.3	2.1	6
W_7	S/P/S/P/S/P/S	B	5	3.6	15

3.2.2 Investigation using EF25 Core

The transformer winding architectures (TWAs) investigated in Section 3.2.1 using RM8 core are not suitable for generating the maximum voltage of 2.5 kV to drive the DEAP actuators. Hence, it is needed to investigate the parameters of the transformer further with a high turns ratio. From Section 3.2.1, the interesting TWAs are W_3, W_4, and W_6. When the secondary turns are very high, implementing the TWAs with bank winding scheme (W_4 and W_6) in the laboratory was extremely

Table 3.4: Leakage inductance referred to primary

TWA	Buildup	Winding scheme	sim. (nH)	Cal. (nH)	Mea. (nH)
W_1	S/P	A	526	590	550
W_2	S/P	B			520
W_3	S/P	C			725
W_4	S/P	D			580
W_5	S/P/S	B			181
W_6	S/P/S	D	150	150	208
W_7	S/P/S/P/S/P/S	B	30	22	74

Table 3.5: AC resistance referred to primary at 100 kHz

TWA	Buildup	Winding scheme	sim. (mΩ)	Cal. (mΩ)	Mea. (mΩ)
W_1	S/P	A	102	110	130
W_2	S/P	B			127
W_3	S/P	C			135
W_4	S/P	D			84
W_5	S/P/S	B			39
W_6	S/P/S	D	35	37	42
W_7	S/P/S/P/S/P/S	B	23	18	22

difficult, and hence it was not considered. Table 3.6 provides the details of transformer design using EF20 core. Four different TWAs such as non-interleaved and non-sectioned (W_2), interleaved and non-sectioned (W_5), non-interleaved and sectioned (W_3), and interleaved and sectioned (W_8, which is a new TWA) have been practically implemented. The measured parameters of the transformer for each TWA are provided in Tables 3.7, 3.8, 3.9, and 3.10, respectively.

Table 3.6: Details of the transformer with a turns ratio of 20

Parameter	Value
Number of primary / secondary turns	18 / 360
Diameter of primary / secondary winding	0.4 mm (TEX [89]) / 0.14 mm
Number of layers of primary / secondary winding	3 / 4
Number of parallel wires of primary / secondary	3 / 1
Type of core / material	EF25 / N87

3.2.3 Discussion

This research work is summarized in Appendix J. By comparing the transformer parasitics of all TWAs for EF25 core, the TWA non-interleaved and sectioned (W_3) has lowest self and interwinding capacitances, followed by the interleaved and sectioned (W_8) TWA. The self-capacitances of TWAs W_8 and W_3 are comparable. Even though, the leakage inductance of W_8 is approximately half of W_3, due to

Table 3.7: Parameters for non-interleaved (P/S) and non-sectioned transformer [W_2]

Parameter	Value
Magnetizing inductance of primary / secondary	53 μH / 23 mH
Leakage inductance referred to primary / secondary	1.2 μH / 490 μH
DC resistance of primary / secondary winding	42 mΩ / 16 Ω
AC resistance referred to primary / secondary winding at 50 kHz	98 mΩ / 39 Ω
AC resistance referred to primary / secondary winding at 100 kHz	130 mΩ / 52 Ω
Self-capacitance of high voltage winding	42 pF
Interwinding capacitance	59 pF

Table 3.8: Parameters for interleaved (S/P/S) and non-sectioned transformer [W_5]

Parameter	Value
Magnetizing inductance of primary / secondary	47 μH / 20 mH
Leakage inductance referred to primary / secondary	590 nH / 236 μH
DC resistance of primary / secondary winding	43 mΩ / 19 Ω
AC resistance referred to primary / secondary winding at 50 kHz	98 mΩ / 38 Ω
AC resistance referred to primary / secondary winding at 100 kHz	108 mΩ / 43 Ω
Self-capacitance of high voltage winding	21.5 pF
Interwinding capacitance	160 pF

Table 3.9: Parameters for non-interleaved (P/S) and sectioned (4 sections) transformer [W_3]

Parameter	Value
Magnetizing inductance of primary / secondary	49 μH / 21 mH
Leakage inductance referred to primary / secondary	1 μH / 357 μH
DC resistance of primary / secondary winding	39 mΩ / 14 Ω
AC resistance referred to primary / secondary winding at 50 kHz	91 mΩ / 38 Ω
AC resistance referred to primary / secondary winding at 100 kHz	117 mΩ / 43 Ω
Self-capacitance of high voltage winding	4.3 pF
Interwinding capacitance	44 pF

very high interwinding capacitance, it might not be recommended for high voltage capacitor charge and discharge applications, due to conducted and radiated electromagnetic interference (EMI) problems.

Table 3.10: Parameters for interleaved (S/P/S) and sectioned (4 sections) transformer [W_8]

Parameter	Value
Magnetizing inductance of primary / secondary	49 μH / 21.5 mH
Leakage inductance referred to primary / secondary	420 nH / 175 μH
DC resistance of primary / secondary winding	43 mΩ / 19 Ω
AC resistance referred to primary / secondary winding at 50 kHz	90 mΩ / 39 Ω
AC resistance referred to primary / secondary winding at 100 kHz	100 mΩ / 43 Ω
Self-capacitance of high voltage winding	6.8 pF
Interwinding capacitance	150 pF

3.3 Digital Control of High Voltage Bidirectional Flyback Converter

Valley switching/quasi resonant (QR) control has been used in [90–93], to improve the efficiency of the switch mode power supplies by reducing the capacitive turn-on/switching losses, and to reduce EMI. For the high voltage capacitor charging application, the capacitive switching losses [42, 78] due to the equivalent lumped capacitance, at the drain node of the primary MOSFET during charge process, and at the drain node of the HV MOSFET during discharge process dominates the total losses in the converter. Therefore, the capacitive switching losses can be reduced by implementing the valley switching control for charging as well as discharging the capacitive load. The proposed valley switching technique requires only sensing of the low voltage side voltages (supply voltage and drain voltage) without the need to sense any HV side signals. The converter specifications are provided in Table 3.11.

Table 3.11: Specifications of the bidirectional flyback converter

Parameter	Value
Input / Output voltage	24 V / 0-2.5 kV
On-time of low voltage MOSFET during charge process	9 μs
On-time of high voltage MOSFET during discharge process	[2 μs, 3 μs, 5 μs, 10 μs, 20 μs, 150 μs, 200 μs]

The bidirectional flyback converter with the control circuit to achieve the valley switching during charge and discharge processes is shown in Figure 3.9. The input voltage and the drain voltage of primary MOSFET M_1, each scaled by a resistor divider network H_1 (3 $k\Omega$ and 90 $k\Omega$), are compared using a high speed comparator TLV3501A. The comparator output becomes low ($V_{comp} = 0$), when the drain voltage of M_1 is lower than the input voltage V_{in}. The output signal of the comparator V_{comp} is sent to the 16-bit microcontroller (PIC18F45K22) which detects the comparator output change, and produces a fixed on-time pulse to enable the gate driver 1 to drive the MOSFET M_1. The experimental prototype of the HV

bidirectional flyback converter is shown in Figure 3.10. The bidirectional operation of the HV converter at 2.5 kV output voltage is shown in the Figure 3.11. Due to constant turn on-time t_{onC} for M_1 during charge process, the primary current I_{ppkC} is constant. During discharge process, employing variable turn on-time t_{onD} for M_2 makes the secondary current (hence the primary current) I_{spkC} almost constant.

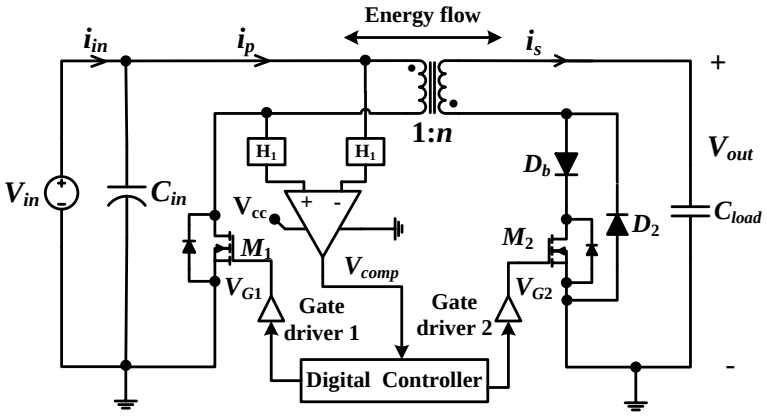

Figure 3.9: Schematic of the bidirectional flyback converter with the control circuit to achieve valley switching.

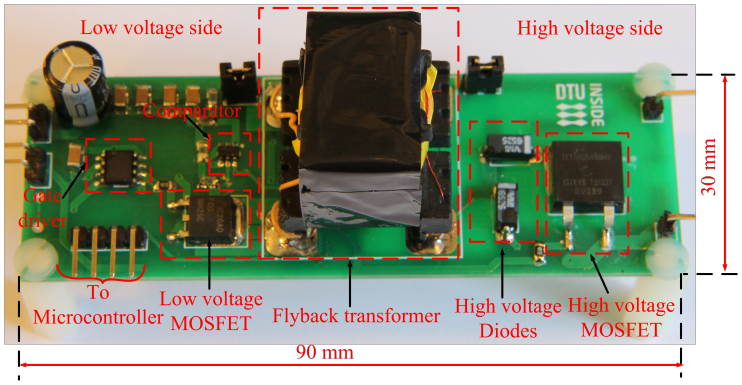

Figure 3.10: Experimental prototype of the HV bidirectional flyback converter with a 4.5 kV MOSFET on the HV side [94].

The experimental results when the converter, tested with a film capacitive load of 400 nF, to validate the proposed valley switching technique are shown in Figures 3.12, 3.13, 3.14. In Figures 3.12, 3.13, successful valley-switching operation at different output voltages during the charge process is shown. From Figure 3.14, it is clear that the converter operates with zero voltage switching (ZVS) turn-on, and the primary current is negative before the switch is turned-on. The energy efficiency measurements during charge and discharge processes with 4 kV and 4.5 kV MOSFETs on the HV side are shown in Figure 3.15. The charge energy efficiency for both 4 kV and 4.5 kV MOSFETs is above 90%, for the output voltage range 750 V$<V_{out}<$2.2 kV, with a maximum efficiency of 92%. The charge energy efficiency for the output voltage range 2.2 kV$<V_{out}<$2.5 kV is between 88-90%. The discharge

energy efficiency for 4 kV MOSFET is lower than the charge efficiency due to the fact that valley voltage in V_{M2} is not equal to valley voltage in V_{D2} during DCM. Some of the reasons for very low discharge energy efficiency for 4.5 kV MOSFET are due to its high on resistance (750 Ω), high gate input resistance (76 Ω). More details about this work can be found in Appendix K.

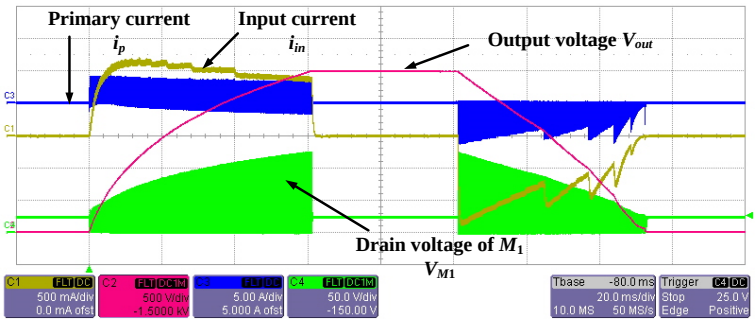

Figure 3.11: Experimental charge and discharge cycle of the HV bidirectional flyback converter with a 4.5 kV MOSFET on the HV side; CH1: 500 mA/div, CH2: 500 V/div, CH3: 5 A/div, CH4: 50 V/div, Time scale: 20 ms/div.

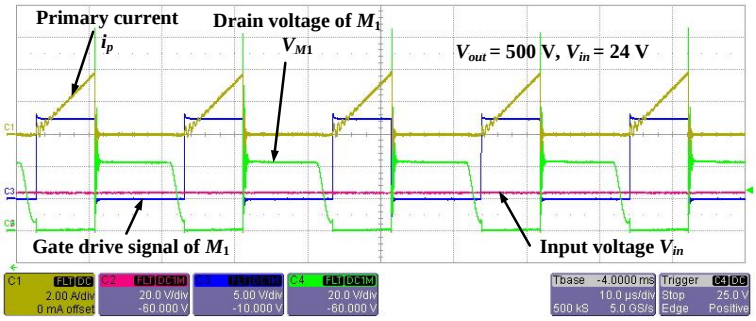

Figure 3.12: Experimental results when the converter is operated with valley switching during charge process; CH1: 2 A/div, CH2: 20 V/div, CH3: 5 V/div, CH4: 20 V/div, Time scale: 10 μs/div.

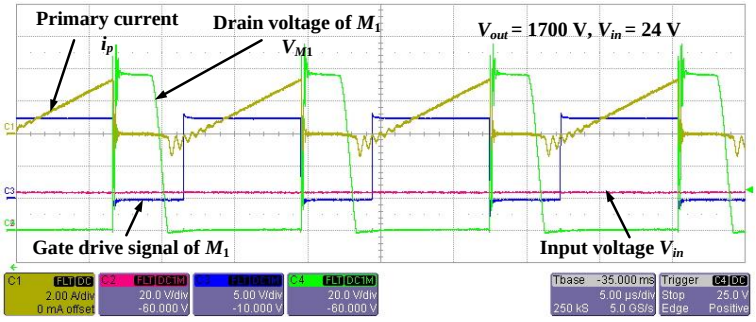

Figure 3.13: Experimental results when the converter is operated with valley switching during charge process; CH1: 2 A/div, CH2: 20 V/div, CH3: 5 V/div, CH4: 20 V/div, Time scale: 5 μs/div.

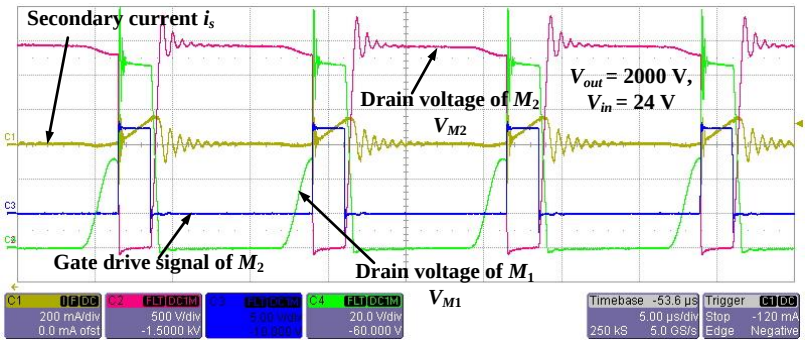

Figure 3.14: Experimental results when the converter is operated with valley switching during discharge process; CH1: 200 mA/div, CH2: 500 V/div, CH3: 5 V/div, CH4: 20 V/div, Time scale: 5 μs/div.

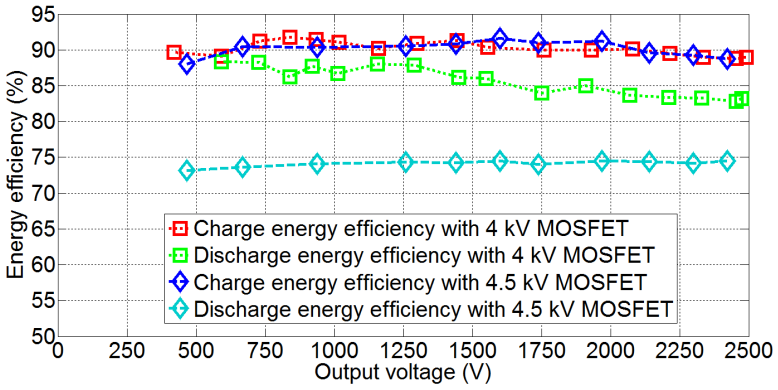

Figure 3.15: Energy efficiency measurements.

3.4 Scalability of HV Drivers

Dielectric electroactive polymer (DEAP) actuators are capacitive devices which provide mechanical motions when charged electrically. The charging characteristics of a DEAP actuator depends on its size, voltage applied to its electrodes, and its operating frequency. The conventional bidirectional flyback DC-DC converter incorporates commercially available high voltage MOSFETs (4 kV [95]) and high voltage diodes (5 kV [96]). The average current of the aforementioned devices is limited to 300 mA and 150 mA, respectively. Connecting the outputs of multiple converters in parallel can provide a scalable design. This enables operating the DEAP actuators in various static and dynamic applications, e.g. positioning, vibration generation or damping, and pumps. The capacitive actuator can be charged and discharged quickly by employing the converter as shown in Figure 3.16, in which the HV semiconductors are connected in parallel on the secondary side. The same can be achieved by employing two parallel input parallel output high voltage bidirectional converters as shown in Figure 3.17. More details about this topic can be found in Appendix M.

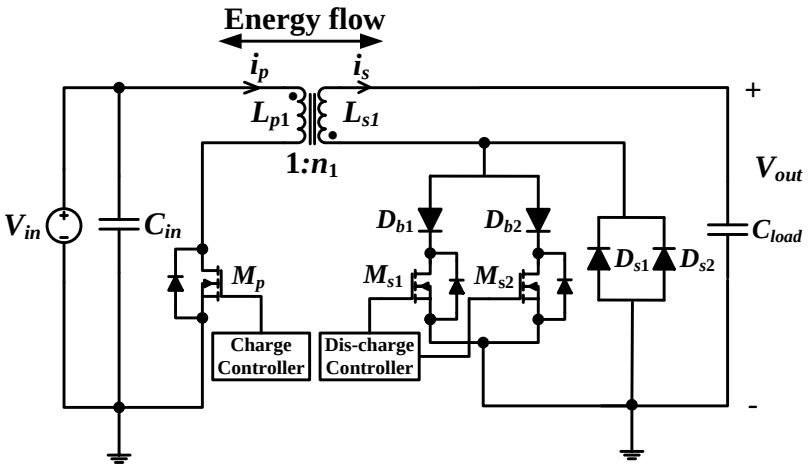

Figure 3.16: Circuit diagram of a bi-directional flyback with high voltage semiconductors connected in parallel on the secondary side to drive a capacitive load.

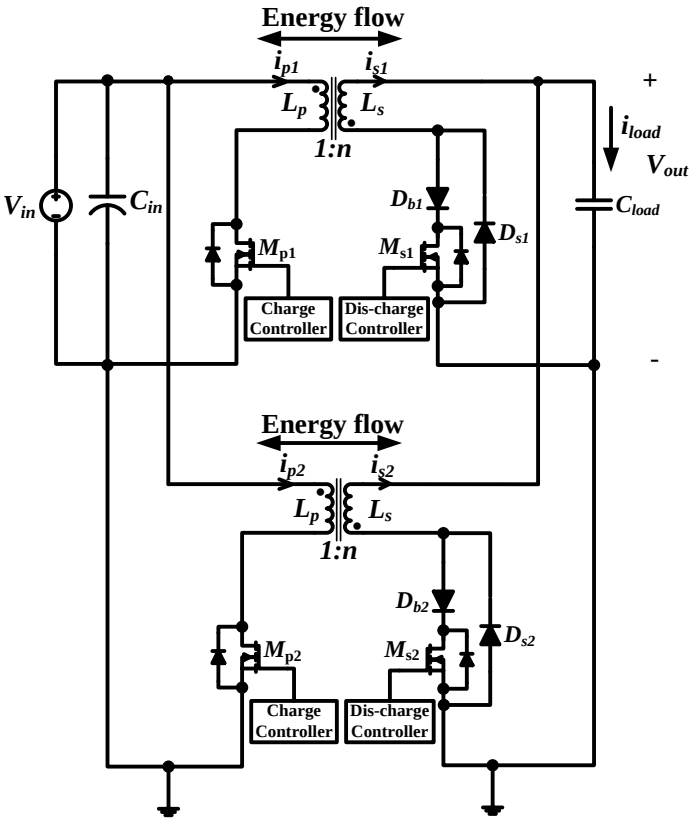

Figure 3.17: Circuit diagram of two parallel input parallel output high voltage bidirectional converters to drive a single capacitive load.

Experimental results of driving a single DEAP actuator/capacitive load with three parallel connected high voltage converters is shown in Figure 3.18. Practically, a single converter is able to charge and discharge the actuator to and from 2 kV within 15 ms and 18 ms, respectively. The 3 parallel input, parallel output HV modules are able to charge and discharge the actuator to and from 2 kV within 4.5 ms and 6 ms, respectively. This can increase the maximum operating frequency of the DEAP actuator from 30 Hz to 90 Hz with an assumption of zero delay time between charge and discharge processes.

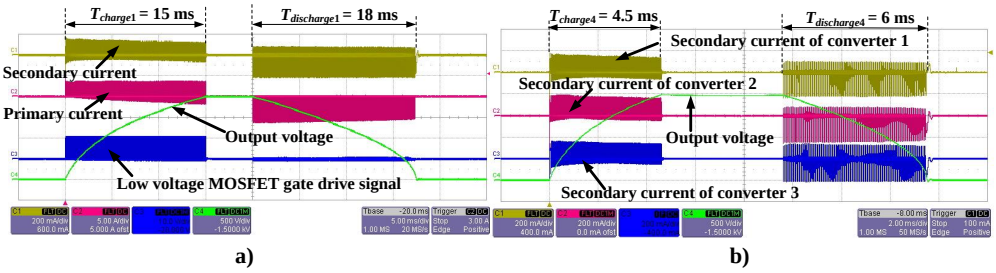

Figure 3.18: a) Experimental results of a single HV bidirectional converter; CH1: 200 mA/div, CH2: 5 A/div, CH3: 10 V/div, CH4: 500 V/div, Time scale: 5 ms/div., and b) 3 parallel connected bidirectional converters; CH1: 200 mA/div, CH2: 200 mA/div, CH3: 200 mA/div, CH4: 500 V/div, Time scale: 2 ms/div.

3.5 Investigation of a New Topology: Bidirectional Flyback Converter with Multiple Series Connected Outputs

A high voltage MOSFET (4 kV) in series with a blocking diode is added in parallel with the high voltage output diode of a conventional flyback topology (see Figure 2.16) to enable bidirectional operation. Experimental results from a digitally controlled bidirectional flyback converter show that the discharge energy efficiency is limited by the parasitics of the high voltage components which prevent full utilization of valley switching. A new implementation is therefore proposed, where the secondary transformer winding is split into multiple windings which are connected in series by lower voltage rating MOSFETs driven by a gate drive transformer. The proposed HV bidirectional flyback converter is shown in Figure 2.17. Using this topology, it is possible to series connect several lower voltage (< 4 kV) rated MOSFETs each having a better body diode (having less reverse recovery time). For more details about the proposed topology refer to Appendix N.

The advantages of the proposed topology are reduction in the voltage rating and price of the HV MOSFET, possible to achieve perfect valley switching of HV MOSFET, unlike the semi-valley switching [39], and improved energy efficiency. However, the difficulties associated with the proposed converter are the need of high side gate drivers, synchronous switching of secondary MOSFETs, and the voltage sharing among the secondary windings and the secondary MOSFETs.

3.6 Implementation of Incremental Pattern on Film Capacitor Loads

The DEAP incremental actuator consists of three linear DEAP actuators (one extender and two grippers). The incremental actuation steps and the driving voltage waveforms for the grippers and extender are shown in Figures 3.19, 3.20, respectively. Each gripper is connected to mechanical supports on either side. It expands and clamps to the guiding bar (e.g., a rod) surface when charged (with high voltage), and unclamps from it, when discharged. The extender expands along the axis of guiding bar. During the operation, one gripper holds the guiding bar while the other gripper is in a released position. The extender either pushes or pulls the released gripper. The incremental actuator performs 6 different steps, to achieve a single incremental actuation stroke Δx as shown in Figure 3.19.

The moving sequence of steps for the linear incremental motion towards the positive x-axis (right) direction:

- Start: All actuators are in the discharged state.
- Step 0: A_1 is charged and clamps to the guiding bar. A_2 and A_3 are in the discharged state.
- Step 1: A_1 remains in the charged state. A_2 is charged and pushes the mechanical structure towards right, and A_3 remains in the discharged state.
- Step 2: A_1 is charged and clamps to the guiding bar. A_2 and A_3 are in the discharged state.
- Step 3: A_1 is discharged and is in the released position. A_2 and A_3 still remain in the charged state.
- Step 4: A_1 remains in the discharged state. A_2 is discharged, and A_3 remains in the charged state.
- Step 5: A_1 is charged. A_2 remains in the discharged, and A_3 in the charged state.
- Step 6: A_1 remains in the charged state. A_2 remains in the discharged state, and A_3 is discharged.
- End: All actuators are discharged at the end. The Step 0 is used only for charging the actuator A_1. The Steps 1-6 repeat for achieving continuous incremental actuations.

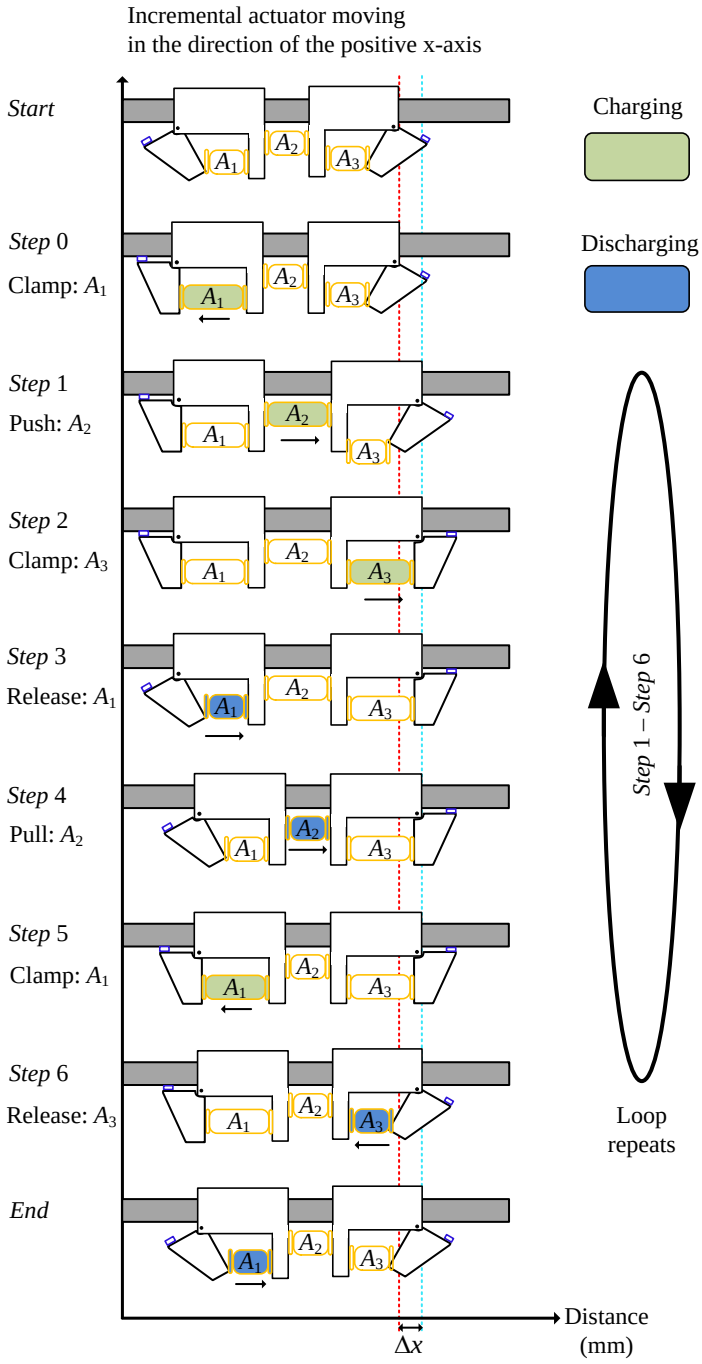

Figure 3.19: Moving sequence of the DEAP incremental actuator for incremental motion towards the positive x-axis direction.

For more details about the DEAP incremental actuator operation refer to Appendix O and Appendix P. The proposed DEAP incremental actuator control scheme is experimentally verified on film capacitive loads. The experimental set-up of 3 HV converters for driving 3 capacitive loads is provided in Figure 3.21. Each capacitive load is driven by a bidirectional flyback converter. One of the experimental result is provided in Figure 3.22. The maximum voltage across each load is 2.5 kV, and

the incremental sequence is repeated for several cycles.

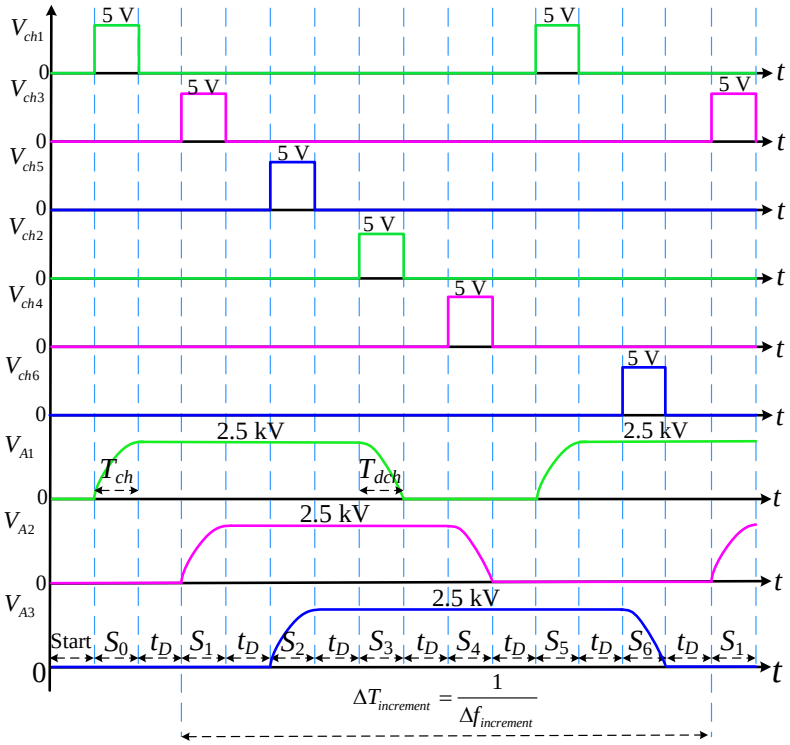

Figure 3.20: Enable signals and driving voltages of all DEAP actuators, to achieve the incremental motion with variable speed, towards the positive x-axis direction [38] (Appendix O).

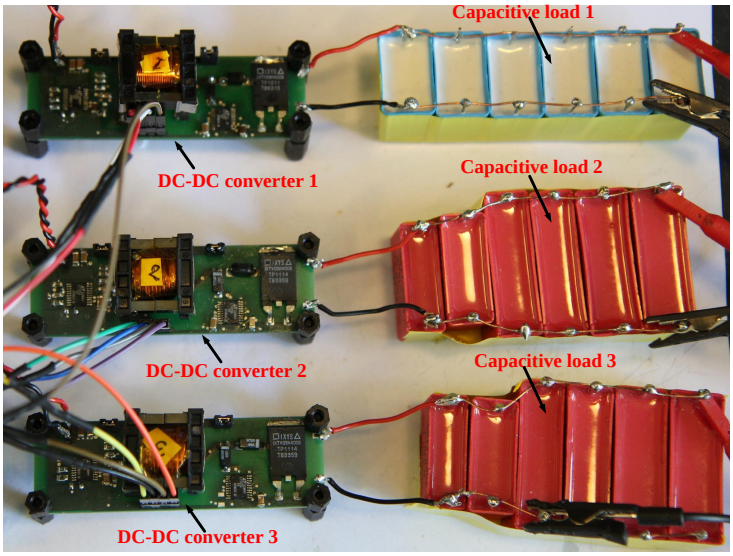

Figure 3.21: Experimental setup picture.

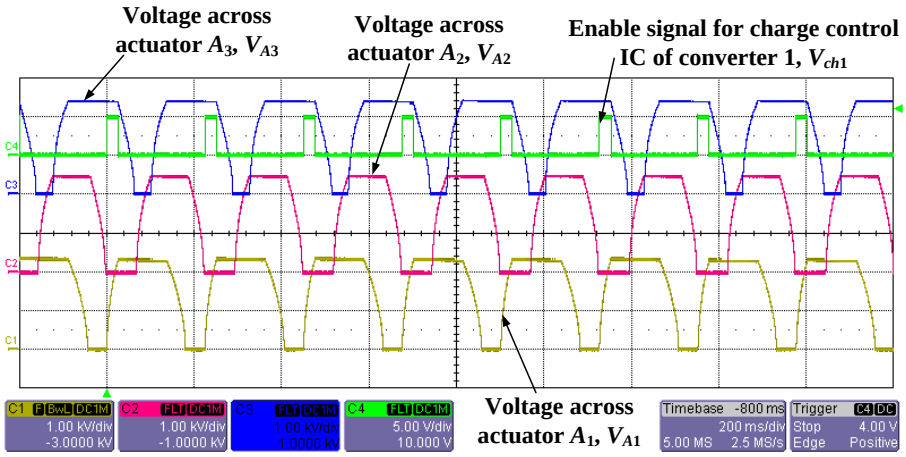

Figure 3.22: Experimental result with the 3 DC-DC converters with several incremental actuation cycles; CH1: 1 kV/div, CH2: 1 kV/div, CH3: 1 kV/div, CH4: 5 V/div, Time scale: 200 ms/div.

3.7 System Integration with DEAP Incremental Actuator

DEAP Axial-1 transducers are detailed designed and manufactured in Danfoss PolyPower [1] with version 3 (V3) DEAP film. The transducers are designed to provide 10 N output force at 1 mm stroke when stimulated at 2.4 kV. The auxiliary mechanical parts were designed and prototyped at IPU in DTU and Danfoss PolyPower. The mechanical parts were designed to adjustably amplify the transducers stroke or force. The transducers were mounted with the auxiliary mechanics and installed on the guiding rod. The rod was fixed on a table in horizontal position.

3.7.1 Incremental Motion at Different Speeds

The integrated system of Figure 3.23 is tested for its variable speed and repeatability. The height and outer diameter of each DEAP actuator are 110 mm and 33 mm, respectively. 100 increments are generated using the digital controller and the total displacement and travel time are recorded. The applied voltage level is fixed to a maximum 1.8 kV to avoid any potential damage to the DEAP actuators. Table 3.12 shows the acquired data of the experiments. It can be seen that the system has repeatability within 5% (of stroke) for different speed levels. Moreover, the speed of the system could have been doubled if the maximum operating voltage (2.4 kV) is applied to all actuators, i.e. a maximum speed of 3 mm/s could be achieved.

3.7.2 Bidirectional Motion

The above test is repeated with a maximum voltage of 1.7 kV for bidirectional motion at three different speed settings (delay times t_D) in the controller. Table

3.13 shows the results which indicate a larger total displacement in the forward motion compared to the reverse motion. In Table 3.13, Forward: positive x-axis direction, and Reverse: negative x-axis direction.

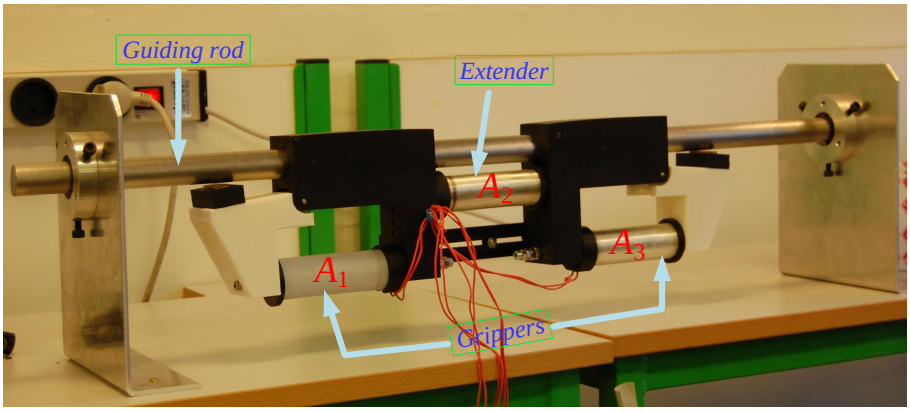

Figure 3.23: System integration with DEAP incremental actuator.

Table 3.12: Experimental data of DEAP incremental actuator moving with different speeds to achieve 100 increments/steps

Total stroke (mm)	**Actuator total travel time (s)**	**Delay time t_D (ms)**	**Average speed (mm/s)**	**Increment size/ stroke per step (mm)**	**Increment actuation frequency (Hz)**
39	50	50	0.78	0.39	1.53
39	45	40	0.86	0.39	1.68
39	40	30	0.97	0.39	1.87
38	35	20	1.07	0.38	2.11
40	30	10	1.33	0.40	2.41
40	28	5	1.43	0.40	2.6
39	25	2	1.56	0.39	2.73
39	26	1	1.5	0.39	2.78

3.7.3 Discussion

The DEAP incremental actuator system indicated a non-repeatable motion when operated bidirectional, resulting in a drift from the original position. This drift increased with the number of bidirectional iterations resulting in an even larger drift from original position. Such drift might be primarily caused by non-identical grippers differing in their gripping force. As the extending transducer is activated, it excites both grippers with the same force. The activated gripper should have enough gripping force to not slip backward due to transient forces generated by the extender. If the two grippers have different gripping forces, the one with smaller force will exhibit larger backward slipping resulting cumulatively in a drift of the whole system from the original position.

Subsequent iteration of the DEAP incremental actuator will consider improved mechanical and electronics concepts. Specific attention will be given to the design of the grippers to, i) achieve a more identical performance, and ii) have enough grip force to overcome the inertial effects and as such increased speed and repeatability. The weight and form factor of DEAP are to be exploited and demonstrated. This is potentially achieved by reducing the actuator size, redesigning the auxiliary mechanics, and integrating the electronics on a single PCB print. Moreover, the form factor can be demonstrated by developing a concept which can travel on curved and inclined paths as shown in Figure 3.24, which is challenging for other technologies to achieve.

Table 3.13: Experimental data from bidirectional DEAP incremental actuator tests for 100 increments

Total stroke (mm)	**Actuator total travel time (s)**	**Delay time t_D (ms)**	**Average speed (mm/s)**	**Increment size/ stroke per step (mm)**	**Increment actuation frequency (Hz)**
Forward	40	71	100	0.56	1.08
Forward	44	35	10	1.26	2.60
Forward	43.7	32	1	1.36	3.03
Reverse	37	71	100	0.52	1.08
Reverse	41	41	10	1.00	2.60
Reverse	35	37	1	0.94	3.03

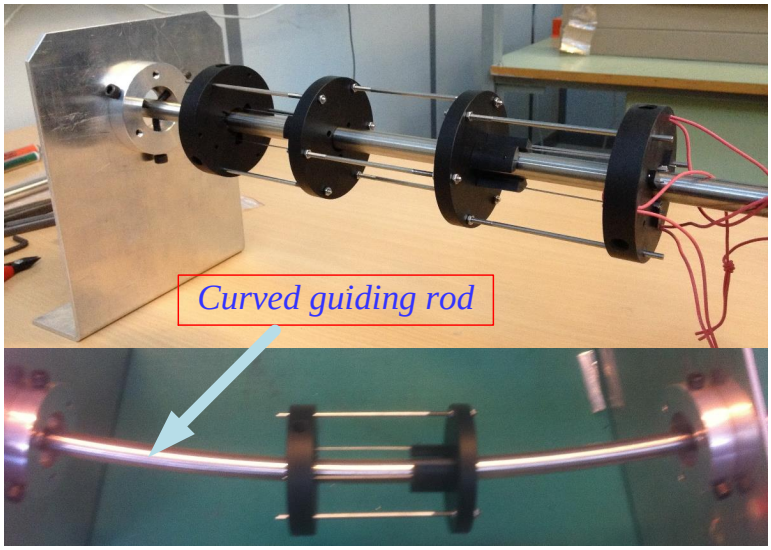

Figure 3.24: Mechanical set-up to demonstrate the incremental motion on a curved path with a new DEAP incremental actuator concept.

Chapter 4

Conclusions and Future Works

4.1 Conclusions

This work has investigated the 24 V input voltage and 0-2.5 kV output voltage, high voltage, bidirectional DC-DC converters for driving the DEAP based incremental actuator.

The major parts of this thesis and the associated publications correspond to the following contributions:

- The detailed mathematical analysis of high voltage bidirectional flyback converter is presented. The converter operates in boundary conduction mode (BCM) control with variable switching frequency during the charge process and in discontinuous conduction mode (DCM) control with constant switching frequency during the discharge process.

- The power losses in the bidirectional flyback converter for the capacitor charging application has been analyzed in detail. Due to the variable switching frequency and non-sinusoidal waveforms, it is very difficult to accurately compute the core and winding losses. The core loss was accurately calculated during charge and discharge operations, using piecewise linear approximation of the IGSE model. Estimation of the leakage inductance for a non-interleaved structure and interleaved winding structures has been discussed. Stray capacitance calculation for a typical HV winding structure is discussed.

- The detailed power stage design of the high voltage bidirectional flyback converter for driving a dielectric electro active polymer (DEAP) based capacitive actuator is described. Experimental results are provided to show the bidirectional operation (charge and discharge) of the high voltage converter. Even though the flyback transformer is designed for a high peak charging flux density of 0.35 T, thermal measurement results show that the maximum temperature rise in the transformer is 33 °C (with an ambient temperature of 28 °C). Therefore, for a high voltage capacitor charge and discharge applications

it is possible to minimize the number of transformer turns on the secondary high voltage side, by choosing a higher flux density.

- The energy efficiency is optimized using a proposed new automatic winding layout (AWL) technique and a comprehensive loss model. The proposed optimization technique is experimentally validated on a 25 W (charging power) high voltage bidirectional flyback converter. The measured charge and discharge energy efficiencies of the converter, with PQ 20/20 core at an output voltage of 2.5 kV are 88% and 77%, respectively. For both optimized and smallest core designs, energy efficiency during discharge process is less compared to that during charge process, mostly due to the switching loss of output capacitance of high voltage MOSFET.

- The proposed automatic winding layout (AWL) technique is highly recommended for high input or high output voltage applications which need a transformer with many turns (primary or secondary). It automatically calculates and provides the necessary winding design data such as wire sizes, number of winding layers, number of turns per layer, and number of parallel wires.

- The analytical equations for calculating the transformer AC resistance, leakage inductance and self-capacitance for seven different winding architectures have been presented and evaluated experimentally and with FEA simulations for a RM8 core with a turns ratio of 10. The main contribution to the errors is due to practical winding issues which are not accounted for in the equations. The transformer loss distribution is based on the calculated values, and it clearly shows that transformer winding architectures where the self-capacitance is lowest are particularly suitable for high voltage charging applications. Another investigation has been made for EF25 core with a turns ratio of 25. Non-interleaved and Sectioned transformer could be most suitable for HV capacitor charge and discharge application as a good balance between the efficiency and EMI.

- The valley switching technique for a bidirectional flyback converter, driving a capacitive load has been successfully implemented using a 16-bit microcontroller, during charge and discharge processes, respectively. Using the proposed simple valley switching technique, the flyback converter is able to charge and discharge the capacitor load/actuator within minimum time (or with maximum speed). To charge and discharge from 2.4 kV output voltage using a 4 kV MOSFET, the flyback converter has charge and discharge energy efficiencies of 89% and 84%, respectively.

- Parallel-input and parallel-output high voltage bidirectional flyback converters have been implemented, and their operation has been successfully verified with both film capacitive load and the DEAP actuator. The proposed idea of reducing/scaling the charge and discharge times is verified by connecting a maximum of 3 modules in parallel. With the practical experience, it is expected that even more modules (> 3) could be easily connected in parallel. Practically, a single converter was able to charge and discharge the actuator to and from 2 kV within 15 ms and 17.5 ms, respectively. The 3 parallel-

input and parallel-output HV modules were able to charge and discharge the actuator to and from 2 kV within 4.5 ms and 6 ms, respectively.

- A bidirectional flyback converter with multiple series connected outputs is proposed, for high voltage drive of capacitive DEAP actuators. Simulation results (output voltages and voltage stresses across the secondary MOSFETs-/diodes) during both charge and discharge processes are provided, to show a comparison between the proposed and the conventional implementation. A theoretical comparison shows that the proposed converter has the potential to improve the energy efficiency, lower the cost and reduce the volume of high voltage driver.

- The DEAP incremental actuator concept has been designed, built and tested. It was demonstrated that the DEAP is feasible for providing incremental motion with variable speed and bidirectional motion. Control and high voltage electronics demonstrated good performance in providing the appropriate stimuli to the transducers with reasonable efficiency and compactness. The proposed DEAP incremental actuator moves with a maximum velocity of 1.5 mm/s, when all actuators are driven with 1.8 kV. It is possible to achieve a speed of 3 mm/s, when the actuators are driven by 2.4 kV.

4.2 Future Works

- Driving the three actuators in the DEAP incremental actuator using a single high voltage converter needs to be investigated.

- The proposed automatic winding layout (AWL) technique to design a high voltage tramsformer, can be further extended for interleaved transformer configurations.

- If the future applications demand that the HV drivers should be integrated inside the DEAP incremental actuators, then further research needs to be carried out to accomplish this.

- Special research needs to be carried out to design high side gate drivers for this challenging high voltage capacitor charge and discharge application.

- The proposed digital control technique can be further extended to improve the energy efficiency of the converter by optimizing the switching frequency of the converter. This is possible by switching the converter at other valley points in the drain voltage of the MOSFETs.

- Further investigation of proposed digital control technique with 4.5 kV MOSFET on the secondary HV side needs to be carried out.

- The energy efficiency can be further improved by utilizing the leakage energy stored in the transformer by implementing the active clamp circuits both on high voltage and low voltage sides.

- The DEAP incremental actuator should be tested for incremental motion along the curved path, using the digitally controlled HV drivers.

Bibliography

[1] "Danfoss polypower." http://www.polypower.com/, November 2014.

[2] "Linear actuator." http://en.wikipedia.org/wiki/Linear_actuator, November 2014.

[3] "Ok coil." http://www.haydonkerk.com/Resources/StepperMotorTheory/tabid/192/Default.aspx, November 2014.

[4] "jenatec." http://www.jena-tec.co.uk/linear-actuators.php, November 2014.

[5] "Pi." http://www.linear-actuator.net/Vacuum_Linear_Actuators.php, November 2014.

[6] "Local automation." http://localautomation.com/featured/agi-pneumatic-linear-actuator-agi-american-grippers-inc.html, November 2014.

[7] "Stemulate." http://www.stemulate.org/2012/07/02/solid-learning-robot-linear-actuators/, November 2014.

[8] Y. Bar-Cohen, *Electroactive polymer (EAP) actuators as artificial muscles : reality, potential, and challenges*. SPIE Press, 2004.

[9] W. C. Roentgen, "About the changes in shape and volume of dielectrics caused by electricity," *Annual Review of Physical Chemistry*, vol. 31, pp. 771–786, 1880.

[10] P. Brochu and Q. Pei, "Advances in dielectric elastomers for actuators and artificial muscles," *Macromolecular Rapid Communications*, vol. 31, no. 1, pp. 10–36, 2010.

[11] Y. Bar-Cohen, "Electroactive polymers as artificial muscles - reality and challenges," *Collection of Technical Papers - AIAA/ASME/ASCE/AHS/ASC Structures, Structural Dynamics and Materials Conference*, vol. 4, pp. 2313–2321, 2001.

[12] F. Carpi, D. D. Rossi, R. Kornbluh, R. Pelrine, and P. Sommer-Larsen, *Dielectric Elastomers as Electromechanical Transducers*. Amsterdam: Elsevier, 2008.

[13] R. Pelrine, R. Kornbluh, Q. Pei, and J. Joseph, "High-speed electrically actuated elastomers with strain greater than 100%," *SCIENCE*, vol. 287, no. 5454, pp. 836–839, 2000.

[14] "Leap technology." `http://leaptechnology.com/`, November 2014.

[15] M. Tryson, H.-E. Kiil, and M. Benslimane, "Powerful tubular core free dielectric electro activate polymer (DEAP) push actuator," in *Proceedings of SPIE*, vol. 7287, pp. 72871F–1 – 72871F–11, March 2009.

[16] R. Sarban, B. Lassen, and M. Willatzen, "Dynamic electromechanical modeling of dielectric elastomer actuators with metallic electrodes," *Mechatronics, IEEE/ASME Transactions on*, vol. 17, pp. 960 –967, October 2012.

[17] R. D. Kornbluh, R. Pelrine, Q. Pei, R. Heydt, S. Stanford, S. Oh, and J. Eckerle, "Electroelastomers: applications of dielectric elastomer transducers for actuation, generation, and smart structures," in *Proc. SPIE*, vol. 4698, pp. 254–270, 2002.

[18] Q. Pei, R. Pelrine, S. Stanford, R. D. Kornbluh, M. S. Rosenthal, K. Meijer, and R. J. Full, "Multifunctional electroelastomer rolls and their application for biomimetic walking robots," in *Proc. SPIE*, vol. 4698, pp. 246–253, 2002.

[19] I. A. Anderson, T. A. Gisby, T. G. McKay, B. M. O Brien, and E. P. Calius, "Multi-functional dielectric elastomer artificial muscles for soft and smart machines," *Journal of Applied Physics*, vol. 112, no. 4, pp. –, 2012.

[20] K. Jung, J. C. Koo, J. do Nam, Y. K. Lee, and H. R. Choi, "Artificial annelid robot driven by soft actuators," *Bioinspiration & Biomimetics*, vol. 2, no. 2, p. S42, 2007.

[21] I. A. Anderson, T. C. H. Tse, T. Inamura, B. M. O Brien, T. McKay, and T. Gisby, "A soft and dexterous motor," *Applied Physics Letters*, vol. 98, no. 12, pp. –, 2011.

[22] A. T. Conn, A. D. Hinitt, and P. Wang, "Soft segmented inchworm robot with dielectric elastomer muscles," in *Proc. SPIE*, vol. 9056, pp. 90562L–90562L–10, 2014.

[23] R. Wache, D. McCarthy, S. Risse, and G. Kofod, "Rotary motion achieved by new torsional dielectric elastomer actuators design," *Mechatronics, IEEE/ASME Transactions on*, vol. 20, pp. 975–977, April 2015.

[24] R. Merry, J. Holierhoek, M. van de Molengraft, and M. Steinbuch, "Gain scheduling control of a walking piezo actuator," *Mechatronics, IEEE/ASME Transactions on*, vol. 19, pp. 954–962, June 2014.

[25] D. Neal and H. Asada, "Bipolar piezoelectric buckling actuators," *Mechatronics, IEEE/ASME Transactions on*, vol. 19, pp. 9–19, Feb 2014.

[26] J. Yao, Z. Jiao, D. Ma, and L. Yan, "High-accuracy tracking control of hydraulic rotary actuators with modeling uncertainties," *Mechatronics, IEEE/ASME Transactions on*, vol. 19, pp. 633–641, April 2014.

[27] D. Nielsen, A. Knott, and M. Andersen, "Hysteretic self-oscillating bandpass current mode control for class d audio amplifiers driving capacitive transducers," in *ECCE Asia Downunder (ECCE Asia), 2013 IEEE*, pp. 971–975, June 2013.

[28] D. Nielsen, A. Knott, and M. Andersen, "A high-voltage class d audio amplifier for dielectric elastomer transducers," in *Applied Power Electronics Conference and Exposition (APEC), 2014 Twenty-Ninth Annual IEEE*, pp. 3278–3283, March 2014.

[29] D. Nielsen, A. Knott, and M. A. E. Andersen, "Class d audio amplifier with 4th order output filter and self-oscillating full-state hysteresis based feedback driving capacitive transducers," in *Proceedings of Epe'14-ecce*, 2014.

[30] D. Nielsen, A. Knott, and M. A. E. Andersen, "Multilevel inverter based class d audio amplifier for capacitive transducers," in *Proceedings of Epe'14-ecce*, 2014.

[31] D. Nielsen, M. B. Moller, R. Sarban, B. Lassen, A. Knott, and M. A. E. Andersen, "Characterization of dielectric electroactive polymer transducers," in *Proc. SPIE*, vol. 9056, pp. 90560L–90560L–9, 2014.

[32] L. Huang, Z. Zhang, and M. Andersen, "A review of high voltage drive amplifiers for capacitive actuators," in *Universities Power Engineering Conference (UPEC), 2012 47th International*, pp. 1–6, Sept 2012.

[33] L. Huang, Z. Zhang, and M. Andersen, "Detailed behavior analysis for high voltage bidirectional flyback converter driving deap actuator," in *Industrial Electronics Society, IECON 2013 - 39th Annual Conference of the IEEE*, pp. 625–630, Nov 2013.

[34] L. Huang, L. F. Normolle, R. Sarban, E. N. Christiansen, Z. Zhang, and M. A. E. Andersen, "Deap actuator and its high voltage driver for heating valve application," in *Proc. SPIE*, vol. 9056, pp. 90562U–90562U–13, 2014.

[35] R. Pittini, L. Huang, Z. Zhang, and M. Andersen, "Primary parallel secondary series flyback converter (ppssfc) with multiple transformers for very high step-up ratio in capacitive load charging applications," in *Applied Power Electronics Conference and Exposition (APEC), 2014 Twenty-Ninth Annual IEEE*, pp. 1440–1447, March 2014.

[36] L. Huang, Z. Zhang, and M. Andersen, "Design and development of autonomous high voltage driving system for deap actuator in radiator thermostat," in *Applied Power Electronics Conference and Exposition (APEC), 2014 Twenty-Ninth Annual IEEE*, pp. 1633–1640, March 2014.

[37] P. Thummala, Z. Zhang, and M. Andersen, "High voltage bi-directional flyback converter for capacitive actuator," in *Power Electronics and Applications (EPE), 2013 15th European Conference on*, pp. 1–10, Sept 2013.

[38] P. Thummala, Z. Zhang, M. Andersen, and S. Rahimullah, "Dielectric electro active polymer incremental actuator driven by multiple high-voltage bidirectional dc-dc converters," in *Energy Conversion Congress and Exposition (ECCE), 2013 IEEE*, pp. 3837–3844, Sept. 2013.

[39] P. Thummala, D. Maksimovic, Z. Zhang, and M. Andersen, "Digital control of a high-voltage (2.5 kv) bidirectional dc-dc converter for driving a dielectric electro active polymer (deap) based capacitive actuator," in *Energy Conversion Congress and Exposition (ECCE), 2014 IEEE*, pp. 3435–3442, Sept 2014.

[40] H. Schneider, P. Thummala, L. Huang, Z. Ouyang, A. Knott, Z. Zhang, and M. Andersen, "Investigation of transformer winding architectures for high voltage capacitor charging applications," in *Applied Power Electronics Conference and Exposition (APEC), 2014 Twenty-Ninth Annual IEEE*, pp. 334–341, March 2014.

[41] P. Thummala, H. Schneider, Z. Zhang, A. Knott, and M. Andersen, "Optimization of bi-directional flyback converter for a high voltage capacitor charging application," in *Applied Power Electronics Conference and Exposition (APEC), 2014 Twenty-Ninth Annual IEEE*, pp. 2556–2563, March 2014.

[42] P. Thummala, H. Schneider, Z. Ouyang, Z. Zhang, and M. Andersen, "Estimation of transformer parameters and loss analysis for high voltage capacitor charging application," in *ECCE Asia Downunder (ECCE Asia), 2013 IEEE*, pp. 704–710, June 2013.

[43] M. Karpelson, G.-Y. Wei, and R. J. Wood, "Driving high voltage piezoelectric actuators in microrobotic applications," *SENSORS AND ACTUATORS A-PHYSICAL*, vol. 176, pp. 78–89, 2012.

[44] E. Horsley, M. Foster, and D. Stone, "State-of-the-art piezoelectric transformer technology," in *Power Electronics and Applications, 2007 European Conference on*, pp. 1–10, Sept 2007.

[45] C.-Y. Lin, *Design and analysis of piezoelectric transformer converters.* PhD thesis, Virginia Polytechnic Institute and State University, 1997.

[46] M. S. Roedgaard, *Piezoelectric transformer based power converters; design and control.* PhD thesis, Technical University of Denmark, Department of Electrical Engineering, 2012.

[47] T. Andersen, *Piezoelectric transformer based power supply for dielectric electro active polymers.* PhD thesis, Technical University of Denmark, Department of Electrical Engineering, 2012.

[48] E. Horsley, A. Carazo, M. Foster, and D. Stone, "A lumped equivalent circuit model for the radial mode piezoelectric transformer," in *Applied Power Electronics Conference and Exposition, 2009. APEC 2009. Twenty-Fourth Annual IEEE*, pp. 1747–1753, Feb 2009.

[49] Y. Liu, D. Vasic, F. Costa, and D. Schwander, "Improvement of burst-mode controlled piezoelectric transformers," in *Power Electronics and Motion Control Conference (EPE/PEMC), 2012 15th International*, pp. DS2c.7–1–DS2c.7–6, September 2012.

[50] M. S. Roedgaard, T. Andersen, K. S. Meyer, and M. A. E. Andersen, "Design of interleaved multi layer rosen type piezoelectric transformer for high voltage dc/dc applications," in *Power Electronics, Machines and Drives (PEMD 2012), 6th IET International Conference on*, pp. 1 –6, March 2012.

[51] E. Baker, W. Huang, D. Chen, and F. Lee, "Radial mode piezoelectric transformer design for fluorescent lamp ballast applications," *Power Electronics, IEEE Transactions on*, vol. 20, pp. 1213–1220, Sept 2005.

[52] T. Andersen, M. S. Roegaard, O. C. Thomsen, and M. A. E. Andersen, "Low voltage driven dielectric electro active polymer actuator with integrated piezoelectric transformer based driver," in *Proceedings of SPIE*, pp. 79762N–1 – 79762N–12, March 2011.

[53] E. Horsley, N. Nguyen-Quang, M. Foster, and D. Stone, "Achieving zvs in inductor-less half-bridge piezoelectric transformer based resonant converters," in *Power Electronics and Drive Systems, 2009. PEDS 2009. International Conference on*, pp. 446–451, Nov 2009.

[54] K. S. Meyer, M. S. Roedgaard, M. A. E. Andersen, and T. Andersen, "Piezoelectric power converter with bi-directional power transfer," 2014. Patent WO2013083679.

[55] M. S. Roedgaard, M. A. E. Andersen, and K. S. Meyer, "Self-oscillating loop based piezoelectric power converter," 2013. Patent WO2013083678 A3.

[56] R. Erickson and D. Maksimovic, *Fundamentals of Power Electronics*. Power electronics, Springer, 2001.

[57] A. Abramovitz, C.-S. Liao, and K. Smedley, "State-plane analysis of regenerative snubber for flyback converters," *Power Electronics, IEEE Transactions on*, vol. 28, pp. 5323–5332, Nov 2013.

[58] J.-H. Jung and S. Ahmed, "Flyback converter with novel active clamp control and secondary side post regulator for low standby power consumption under high-efficiency operation," *Power Electronics, IET*, vol. 4, pp. 1058–1067, November 2011.

[59] P. Davari, F. Zare, A. Ghosh, and H. Akiyama, "High-voltage modular power supply using parallel and series configurations of flyback converter for pulsed power applications," *Plasma Science, IEEE Transactions on*, vol. 40, pp. 2578–2587, Oct 2012.

[60] A. Rahimi, F. Rahimi, and I. Hassanzadeh, "Analysis of high-voltage flyback converter in color tvs, and its regulation," in *Power Electronics and Drive Systems, 2003. PEDS 2003. The Fifth International Conference on*, vol. 1, pp. 353–358 Vol.1, Nov 2003.

[61] G. Chen, Y.-S. Lee, S. Hui, D. Xu, and Y. Wang, "Actively clamped bidirectional flyback converter," *Industrial Electronics, IEEE Transactions on*, vol. 47, pp. 770–779, Aug 2000.

[62] J. Park, Y.-S. Roh, Y.-J. Moon, and C. Yoo, "A ccm/dcm dual-mode synchronous rectification controller for a high-efficiency flyback converter," *Power Electronics, IEEE Transactions on*, vol. 29, pp. 768–774, Feb 2014.

[63] H.-H. Chung, W.-L. Cheung, and K. Tang, "A zcs bidirectional flyback dc/dc converter," *Power Electronics, IEEE Transactions on*, vol. 19, pp. 1426–1434, Nov 2004.

[64] L. Eitzen, C. Graf, and J. Maas, "Cascaded bidirectional flyback converter driving deap transducers," in *IECON 2011 - 37th Annual Conference on IEEE Industrial Electronics Society*, pp. 1226–1231, Nov 2011.

[65] N. Sokal and R. Redl, "Control algorithms and circuit designs for optimal flyback-charging of an energy-storage capacitor (e.g., for flash lamp or defibrillator)," *Power Electronics, IEEE Transactions on*, vol. 12, pp. 885–894, Sep 1997.

[66] J. Elmes, C. Jourdan, O. Abdel-Rahman, and I. Batarseh, "High-voltage, high-power-density dc-dc converter for capacitor charging applications," in *Applied Power Electronics Conference and Exposition, 2009. APEC 2009. Twenty-Fourth Annual IEEE*, pp. 433–439, Feb 2009.

[67] S.-K. Chung and H.-B. Shin, "High-voltage power supply for semi-active suspension system with er-fluid damper," *Vehicular Technology, IEEE Transactions on*, vol. 53, pp. 206–214, Jan 2004.

[68] L. Eitzen, T. Hoffstadt, and J. Maas, "Power electronics concepts for driving eap actuators," vol. 8687, pp. 86870D–86870D–13, 2013.

[69] K. Venkatesan, "Current mode controlled bidirectional flyback converter," in *Power Electronics Specialists Conference, 1989. PESC '89 Record., 20th Annual IEEE*, pp. 835–842 vol.2, Jun 1989.

[70] T. Bhattacharya, V. Giri, K. Mathew, and L. Umanand, "Multiphase bidirectional flyback converter topology for hybrid electric vehicles," *Industrial Electronics, IEEE Transactions on*, vol. 56, pp. 78–84, Jan 2009.

[71] F. Zhang and Y. Yan, "Novel forward-flyback hybrid bidirectional dc-dc converter," *Industrial Electronics, IEEE Transactions on*, vol. 56, pp. 1578–1584, May 2009.

[72] "Solid state relay." `http://www3.panasonic.biz/ac/e_download/control/relay/photomos/catalog/semi_eng_he1a_aqv25.pdf`, November 2014.

[73] C. McLyman, *Transformer and Inductor Design Handbook, Fourth Edition*. Electrical and Computer Engineering, Taylor & Francis, 2011.

[74] W. Hurley and W. Wölfle, *Transformers and Inductors for Power Electronics: Theory, Design and Applications*. EngineeringPro collection, Wiley, 2013.

[75] M. Kazimierczuk, *High-Frequency Magnetic Components*. Wiley, 2013.

[76] R. Prieto, J. Cobos, O. Garcia, R. Asensi, and J. Uceda, "Optimizing the winding strategy of the transformer in a flyback converter," in *Power Electronics Specialists Conference, 1996. PESC '96 Record., 27th Annual IEEE*, vol. 2, pp. 1456–1462 vol.2, Jun 1996.

[77] C. Sullivan, T. Abdallah, and T. Fujiwara, "Optimization of a flyback transformer winding considering two-dimensional field effects, cost and loss," in *Applied Power Electronics Conference and Exposition, 2001. APEC 2001. Sixteenth Annual IEEE*, vol. 1, pp. 116–122 vol.1, 2001.

[78] S. H. Kang, D. Maksimovic, and I. Cohen, "Efficiency optimization in digitally controlled flyback dc-dc converters over wide ranges of operating conditions," *IEEE TRANSACTIONS ON POWER ELECTRONICS*, vol. 27, no. 8, pp. 3734–3748, 2012.

[79] A. C. Nanakos, E. C. Tatakis, and N. P. Papanikolaou, "A weighted-efficiency-oriented design methodology of flyback inverter for ac photovoltaic modules," *IEEE TRANSACTIONS ON POWER ELECTRONICS*, vol. 27, no. 7, pp. 3221–3233, 2012.

[80] X. Zhou, T. Wang, and F. Lee, "Optimizing design for low voltage dc-dc converters," in *Applied Power Electronics Conference and Exposition, 1997. APEC '97 Conference Proceedings 1997., Twelfth Annual*, vol. 2, pp. 612–616 vol.2, Feb 1997.

[81] J. Biela, U. Badstuebner, and J. Kolar, "Impact of power density maximization on efficiency of dc-dc converter systems," *Power Electronics, IEEE Transactions on*, vol. 24, pp. 288–300, Jan 2009.

[82] E. Snelling, *Soft ferrites : Properties and applications*. Butterworths, 1988.

[83] W. Hurley and D. Wilcox, "Calculation of leakage inductance in transformer windings," *Power Electronics, IEEE Transactions on*, vol. 9, pp. 121–126, Jan 1994.

[84] F. Blache, J.-P. Keradec, and B. Cogitore, "Stray capacitances of two winding transformers: equivalent circuit, measurements, calculation and lowering," in *Industry Applications Society Annual Meeting, 1994., Conference Record of the 1994 IEEE*, pp. 1211–1217 vol.2, Oct 1994.

[85] A. Massarini and M. Kazimierczuk, "Self-capacitance of inductors," *Power Electronics, IEEE Transactions on*, vol. 12, pp. 671–676, Jul 1997.

[86] J. Biela and J. Kolar, "Using transformer parasitics for resonant converters - a review of the calculation of the stray capacitance of transformers," in *Industry Applications Conference, 2005. Fourtieth IAS Annual Meeting. Conference Record of the 2005*, vol. 3, pp. 1868–1875, 2005.

[87] L. Dalessandro, F. da Silveira Cavalcante, and J. Kolar, "Self-capacitance of high-voltage transformers," *Power Electronics, IEEE Transactions on*, vol. 22, no. 5, pp. 2081–2092, 2007.

[88] "Ansoft maxwell." `http://ansoft-maxwell.narod.ru/english.html`, November 2014.

[89] "Furukawa." `http://www.furukawa.co.jp/makisen/eng/product/texe_feature.htm`, November 2014.

[90] Y. Panov and M. Jovanovic, "Adaptive off-time control for variable-frequency, soft-switched flyback converter at light loads," *Power Electronics, IEEE Transactions on*, vol. 17, pp. 596–603, Jul 2002.

[91] Y. Panov and M. Jovanovic, "Performance evaluation of 70-w two-stage adapters for notebook computers," in *Applied Power Electronics Conference and Exposition, 1999. APEC '99. Fourteenth Annual*, vol. 2, pp. 1059–1065 vol.2, Mar 1999.

[92] Y.-B. Park and H.-S. Choi, "A efficiency improvement methodology for active mode efficiency regulation," in *Electronics and the Environment, 2008. ISEE 2008. IEEE International Symposium on*, pp. 1–5, May 2008.

[93] Z.-S. Ling, T.-J. Liang, L.-S. Yang, and T.-H. Li, "Design and implementation of interleaved quasi-resonant dc-dc flyback converter," in *Power Electronics and Drive Systems, 2009. PEDS 2009. International Conference on*, pp. 429–433, Nov 2009.

[94] "Ixys 4.5 kv mosfet." `http://ixapps.ixys.com/DataSheet/DS100498(IXTA-T02N450HV).pdf`, November 2014.

[95] "Ixys 4 kv mosfet." `http://ixapps.ixys.com/DataSheet/DS100214A-(IXTH_V03N400_S).pdf`, November 2014.

[96] "Vmi 5 kv diode." `http://www.voltagemultipliers.com/pdf/SXF6521_25.pdf`, November 2014.

List of Publications

The overview of publications accomplished during the PhD study are given below. The publications are located in Appendix A-P.

A **Prasanth Thummala**, Lina Huang, Zhe Zhang and Michael A. E. Andersen, "Analysis of Dielectric Electro Active Polymer Actuator and its High Voltage Driving Circuits," in *Proc. 2012 IEEE International Power Modulator and High Voltage Conference (IPMHVC 2012)*, Jun. 2012, pp. 458–461.

B **Prasanth Thummala**, Zhe Zhang, Michael A. E. Andersen and Ole C. Thomsen, "A high voltage DC-DC converter driving a Dielectric Electro Active Polymer actuator for wind turbine flaps," in *Proc.* 47^{th} *International Universities' Power Engineering Conference (UPEC 2012)*, Sept. 2012, pp. 1–7.

C Lina Huang, **Prasanth Thummala**, Zhe Zhang and Michael A. E. Andersen, "Battery Powered High Output Voltage Bidirectional Flyback Converter for Cylindrical DEAP Actuator," in *Proc. 2012 IEEE International Power Modulator and High Voltage Conference (IPMHVC 2012)*, Jun. 2012, pp. 454–457.

D **Prasanth Thummala**, Zhe Zhang and Michael A. E. Andersen, "High Voltage Bi-directional Flyback Converter for Capacitive Actuator," in *Proc.* 15^{th} *European Conference on Power Electronics and Applications (EPE ECCE Europe 2013)*, Sept. 2013, pp. 1–10.

E **Prasanth Thummala**, Dragan Maksimovic, Zhe Zhang and Michael A. E. Andersen, "Design of a High Voltage Bidirectional DC-DC Converter for Driving Capacitive Incremental Actuators usable in Electric Vehicles (EVs)," in *Proc. 2014 IEEE International Electric Vehicle Conference (IEVC 2014)*, Nov. 2014.

F **Prasanth Thummala**, Henrik Schneider, Zhe Zhang and Michael A. E. Andersen, "Estimation of Transformer Parameters and Loss Analysis for High Voltage Capacitor Charging Application," in *Proc. 2013 IEEE Energy Conversion Congress and Exposition ASIA (ECCE ASIA 2013)*, Jun. 2013, pp. 704–710.

G **Prasanth Thummala**, Henrik Schneider, Zhe Zhang, Arnold Knott and Michael A. E. Andersen, "Optimization of bi-directional flyback converter for a high voltage capacitor charging application," in *Proc. 2014 IEEE Applied Power Electronics Conference and Exposition (APEC 2014)*, Mar. 2014, pp. 2556–2563.

H **Prasanth Thummala**, Henrik Schneider, Zhe Zhang, Ziwei Ouyang, Arnold Knott and Michael A. E. Andersen, "Efficiency Optimization by Considering the High Voltage Flyback Transformer Parasitics using an Automatic Winding Layout Technique," *IEEE Trans. Power Electronics*, DOI: 10.1109/TPEL.2014.2379439, 2014.

I Henrik Schneider, **Prasanth Thummala**, Lina Huang, Ziwei Ouyang, Arnold Knott, Zhe Zhang and Michael A. E. Andersen, "Investigation of transformer winding architectures for high voltage capacitor charging applications," in *Proc. 2014 IEEE Applied Power Electronics Conference and Exposition (APEC 2014)*, Mar. 2014, pp. 334–341.

J **Prasanth Thummala**, Henrik Schneider, Zhe Zhang and Michael A. E. Andersen, "Investigation of Transformer Winding Architectures for High Voltage (2.5 kV) Capacitor Charging and Discharging Applications," *IEEE Trans. Power Electronics, about to submit*, 2014.

K **Prasanth Thummala**, Dragan Maksimovic, Zhe Zhang and Michael A. E. Andersen, "Digital control of a high-voltage (2.5 kV) bidirectional DC-DC converter for driving a dielectric electro active polymer (DEAP) based capacitive actuator," in *Proc. 2014 IEEE Energy Conversion Congress and Exposition USA (ECCE USA 2014)*, Sept. 2014, pp. 3435–3442.

L **Prasanth Thummala**, Dragan Maksimovic, Zhe Zhang and Michael A. E. Andersen, "Digital Control of a High Voltage (2.5 kV) Bidirectional DC-DC Converter for Driving a Capacitive Incremental Actuator," *IEEE Trans. Power Electronics, about to submit*, 2014.

M **Prasanth Thummala**, Zhe Zhang, Michael A. E. Andersen and Sarban Rahimullah, "Parallel input parallel output high voltage bi-directional converters for driving dielectric electro active polymer actuators," in *Proc. SPIE Smart Structures/NDE on Electroactive Polymer Actuators and Devices (EAPAD) 2014*, Mar. 2014, pp. 90561N(1–15).

N **Prasanth Thummala**, Henrik Schneider, Zhe Zhang and Michael A. E. Andersen, "Bidirectional Flyback Converter with Multiple Series Connected Outputs for High Voltage Capacitive Charge and Discharge Applications," in *Proc. 2015 IEEE Applied Power Electronics Conference and Exposition (APEC 2015)*, Mar. 2015.

O **Prasanth Thummala**, Zhe Zhang, Michael A. E. Andersen and Sarban Rahimullah, "Dielectric Electro Active Polymer Incremental Actuator Driven by Multiple High-Voltage Bi-directional DC-DC Converters," in *2013 IEEE Energy Conversion Congress and Exposition USA (ECCE USA 2013)*, Sept. 2013, pp. 3837–3844.
→ *Best Student Paper Award*

P **Prasanth Thummala**, Henrik Schneider, Zhe Zhang, Michael A. E. Andersen and Sarban Rahimullah, "A new Incremental Actuator based on Electro Active Polymer: Conceptual, Control and Driver Design Considerations," *IEEE Trans. Mechatronics, revision submitted*, 2015.

Appendix A

Analysis of Dielectric Electro Active Polymer Actuator and its High Voltage Driving Circuits

---

2012 IEEE International Power Modulator and High Voltage Conference (IPMHVC 2012)

Analysis of Dielectric Electro Active Polymer Actuator and its High Voltage Driving Circuits

Prasanth Thummala, Lina Huang, Zhe Zhang and Michael A. E. Andersen

Technical University of Denmark, Department of Electrical Engineering, DK-2800 Kongens Lyngby, Denmark
Email: {pthu, huang, zz, ma}@elektro.dtu.dk

ABSTRACT

Actuators based on dielectric elastomers have promising applications in artificial muscles, space robotics, mechatronics, micro-air vehicles, pneumatic and electric automation technology, heating valves, loud speakers, tissue engineering, surgical tools, wind turbine flaps, toys, rotary motors, and grippers for material handling, etc. This paper focuses on the application of Dielectric Electro Active Polymer (DEAP) technology as an actuation mechanism for different applications. The DEAP material requires very high voltage (~2.5 kV DC) to fully utilize it as an actuator. In this paper the DEAP actuator is analyzed in detail and the actuator structures, for the wind turbine flap and the heating valve applications are shown. Different high voltage switch mode power supply topologies for driving the DEAP actuator are discussed. The simulation and experimental results are discussed.

Index Terms — **Dielectric electro active polymer (DEAP), actuator, high voltage (HV), dc-dc converter, power electronics, heating valves, wind turbine flaps, PolyPower**

1 INTRODUCTION

Smart materials which respond to external stimuli like light, temperature, pressure, pH, magnetic and electric fields by changing their shape or size have been a particular focus in the past decade [1]. The intelligent materials include, shape memory alloys, piezoelectric materials, etc. and deforming active polymers include hydro gels, dielectric elastomers, carbon-nano tubes and liquid crystalline elastomers. Electro Active Polymers (EAPs) that undergoes force and deformation when electrically stimulated were strongly focused in the last years.

An actuator is a mechanical device for moving or controlling a mechanism or a system. EAPs can be used as actuators in active structures, in particular when large deformations are required. Such EAP actuators convert electrical energy into mechanical energy and produce large strains. Several applications of dielectric elastomer actuators were discussed in [2]. From the electrical standpoint, DEAP actuators are capacitive loads. In [3] a low voltage driven DEAP actuator was developed using piezoelectric transformer. A novel activation strategy for dielectric elastomer actuators was proposed in [4]. Section 2 discusses the detailed analysis of the DEAP actuator and its electrical, mechanical, and electromechanical modeling, and the actuator structures for the heating valves and wind turbine flaps applications. We discuss the high voltage DC-DC converter topologies in Section 3, followed by the conclusion in Section 4.

2 DIELECTRIC ELASTOMERS AS ACTUATORS

Electro Active Polymers (EAPs) are categorized into two major classes: ionic and electronic. An electric field or coulomb forces drive electronic EAPs, while the actuation mechanism for ionic EAPs is through the diffusion or mobility of ions. The electronic EAPs generally require high electric fields (>100 V/μm) and the ionic EAPs requires low driving voltages, nearly equal to 1-5V. Typical driving voltages for dielectric elastomer actuators lie in the range between 2 kV and 4 kV, depending on the polymer breakdown field and thickness of the polymer film. The operating principle of a dielectric elastomer actuator is shown in Figure 1. The DEAP material is a very thin (~40 μm) incompressible elastomer film with a compliant electrode layer on both sides [5]. A dielectric elastomer is basically a compliant capacitor. The electrodes are designed to be able to comply with the deformations of the elastomer. As for any capacitor, when an electric field is applied to the electrodes, positive charges appear on one electrode, and negative charges on the other. This gives rise to coulomb forces between opposite charges, generating a pressure, known as the Maxwell stress. The Maxwell stress forces the electrodes to move closer, thereby squeezing the polymer. As the polymer is thinned, it elongates in the directions perpendicular to the applied force [6]. The electro static pressure (or stress) σ generated by the actuator is

$$\sigma = \varepsilon_o \varepsilon_r \left(\frac{v_{DEAP}}{x} \right)^2 = \varepsilon_o \varepsilon_r E^2 \qquad (1)$$

where E is the imposed electrical field, x is the final thickness, v_{DEAP} is the voltage across the DEAP material, and ε_o and ε_r are the permittivity of the free space (8.85×10^{-12} F/m) and the relative permittivity of the polymer, respectively. The mechanical strain S of the DE is given by

$$S = -\frac{\varepsilon_o \varepsilon_r}{Y} \left(\frac{v_{DEAP}}{x_o / (1+S)} \right)^2 = -\frac{\varepsilon_o \varepsilon_r}{Y} \left(\frac{v_{DEAP}(1+S)}{x_o} \right)^2 \qquad (2)$$

where Y is the Young's modulus and d_o is the initial thickness of the material. Using the capacitive behavior of the polymer, DEAP can be used as an actuator, mechano-electrical sensor, as well as energy harvester to generate electricity. When operated as an actuator DEAP show unique properties, such as very low electrical power consumption, high specific elastic energy density, high speed of response, no noise, flexibility, high power density, large bandwidth, higher performance than competing technologies and light weight, hence it has the potential to be an effective replacement for conventional actuators.

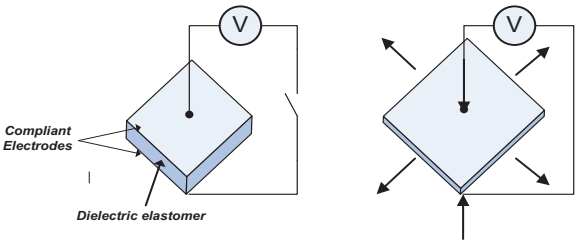

Figure 1. Schematic showing the principle of operation of DEAP actuator. Right: Voltage is ON; Left: Voltage is OFF;

1.1 POLYPOWER DEAP ACTUATOR

Figure 2. PolyPower DE tubular actuator

PolyPower™ dielectric elastomer (DE) is a silicone DE manufactured by Danfoss PolyPower A/S, Denmark. PolyPower DEAP actuator (Figure 2) is produced in thin sheets of 40 μm thickness. Table 1 shows the properties of the Danfoss PolyPower DEAP material. A DE sheet can be modeled as a strain dependent variable plate capacitor (3). For the unidirectional actuation shown in Figure 3, the capacitance of the DEAP actuator as a function of strain S is

$$C = \varepsilon_o \varepsilon_r \frac{A}{x} = \varepsilon_o \varepsilon_r \frac{A_o(1+S)}{x_o/(1+S)} = \varepsilon_o \varepsilon_r \frac{A_o}{x_o}(1+S)^2 \qquad (3)$$

Table 1. Material properties of Danfoss PolyPower DEAP material

Film thickness	40 μm
Dielectric field strength	40 V/μm
Dielectric constant	3.1

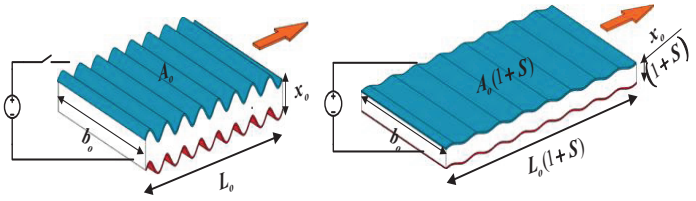

Figure 3. Left: A laminate of PolyPower DE material with corrugated surface and electrode, Right: Actuation direction of the DE material.

1.2 DEAP ELECTRICAL MODELLING

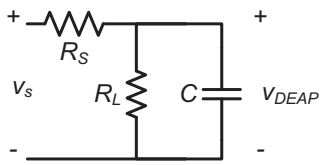

Figure 4a. Electric-circuit model of DEAP actuator

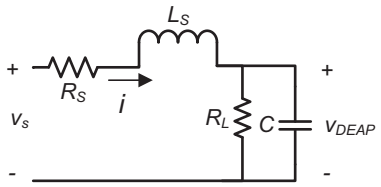

Figure 4b. Electric-circuit model of DEAP actuator including the inductance of the high voltage cables and the compliant electrodes

Figures 4a and 4b show the circuit representation of the electrical model for the DE system employed in this paper. In the figures, R_S is the resistance of the electrodes and the wiring, R_L is the resistance of the DE material, C is the capacitance of the DE sheet, L_S is the equivalent inductance of the electrodes and the high voltage cables, v_s is the voltage of the power source, and v_{DEAP} is the voltage over the DE sheet.

For the circuit shown in Figure 4a, the quasi-electrostatic pressure (1) at the surface of the DE sheet is induced by v_{DEAP}, which is given by

$$\frac{dv_{DEAP}(t)}{dt} + \left(\frac{R_L + R_S}{R_L R_S C}\right) v_{DEAP}(t) = \left(\frac{1}{R_S C}\right) v_s(t) \qquad (4)$$

Similarly for the circuit shown in Figure 4b, the differential equations are given as,

$$v_s(t) = R_S i + L_S \frac{di}{dt} + v_{DEAP}(t) \qquad (5)$$

$$i = \frac{v_{DEAP}(t)}{R_L} + C\frac{dv_{DEAP}(t)}{dt} \qquad (6)$$

Figures 5a and 5b are the block diagram representations for the electrical equivalents of the DEAP actuator.

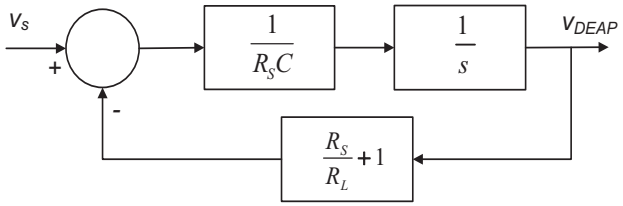

Figure 5a. Block diagram for the electrical circuit of the EAP actuator shown in Figure 4a

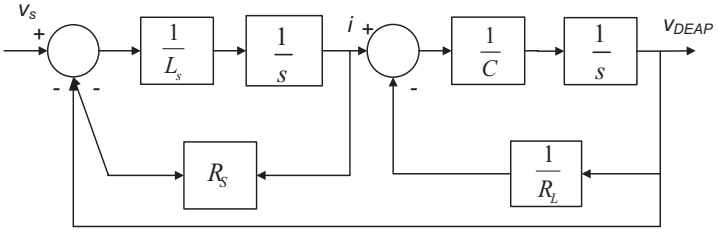

Figure 5b. State block diagram for the electrical circuit of the EAP actuator shown in Figure 4b

1.3 DEAP MECHANICAL MODELLING

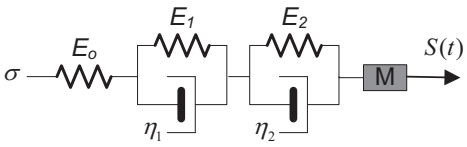

Figure 6. Voigt–Kelvin's viscoelastic model with inertial force.

Dielectric polymers exhibit both elastic solid and viscous fluid characteristics. The viscoelastic behavior of the polymers can be modeled as linear elastic spring (E_0, E_1 and E_2) and dashpot networks (η_1 and η_2). The viscoelastic behavior of the DE actuators can be predicted by a Voigt–Kelvin five-parameter model (Figure 6) [7]. The strain response $S(t)$ to a step-stress input σ of the five-parameter Voigt–Kelvin model is

$$S(t) = \sigma\left(\frac{1}{E_o} + \sum_{n=1}^{2}\frac{1}{E_n}\left(1-\exp\left(-\frac{t}{\tau_n}\right)\right)\right) \quad (7)$$

where $\tau_n = \eta_n / E_n$ are the retardation time constants.

1.4 DEAP ELECTRO-MECHANICAL MODELLING

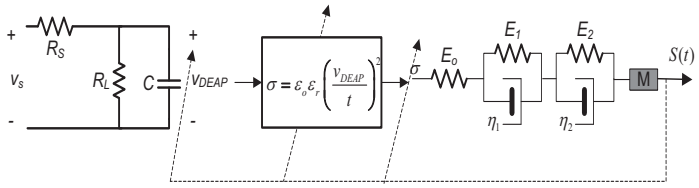

Figure 7. Electro-mechanical modeling of DEAP actuator

Figure 7 shows the electro-mechanical model of DEAP actuator. The input voltage v_s generate a voltage across the DEAP capacitor v_{DEAP}, which induces an electrostatic pressure σ. The mechanical part input viz., the electrostatic pressure σ is the input that results in a mechanical strain S. If the actuation strain S is large, it changes the capacitance C, thickness t, and the stiffness of the material

2.5 DIFFERENT STRUCTURES OF DEAP ACTUATORS

In this paper we focus on the application of DEAP actuator technology to two challenging applications, viz., heating valves and wind turbine flaps. The actuator structures for the two applications are discussed below.

2.5.1 WIND TURBINE FLAP APPLICATION

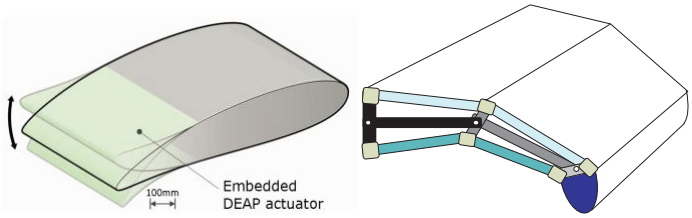

Figure 8. Left: Embedded DEAP actuator into the wing flap; Right: actuated flap structure with DEAP actuators.

Implementing DEAP actuator in the wind turbine flaps will result in improved blade efficiency, reduced loads and fatigues on the blades and turbine. Figure 8 shows the typical structure of the wind turbine flap with embedded DEAP actuators.

2.5.2 HEATING VALVE APPLICATION

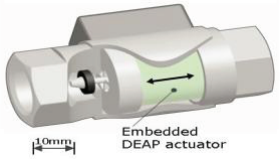

Figure 9. The heating valve containing the DEAP actuator

The current heating valve actuators in the market are thermal actuators, being noiseless but consuming significant power, and electrical gear motors which are relatively energy efficient, but inherently prone to noise issues. The compact in-line heating valves based on DEAP actuator will make better, cheaper and noiseless valves without mechanical parts.

3 HIGH VOLTAGE POWER CONVERTERS TO DRIVE THE DEAP ACTUATOR

To drive the DEAP actuator a high voltage in the range of kilovolts is required [3, 4]. For the systematic control of the DEAP actuators that are implemented in a specific application, special high voltage power electronic (HVPE) converters with advanced control techniques are required. Simulation and experimental results for a unidirectional flyback converter are shown.

3.1 DIFFERENT TOPOLOGIES

Flyback and full bridge converters shown in Figures 10a and 10b, are some of the suitable DC-DC converter topologies for high voltage applications. However, the choice of the converter topology depends on the specific requirements of the application, which are shown in Table 2.

Table 2. Specifications of the applications and choice of converter topology

Application	Input voltage	Charging Time of Actuator
Wind turbine flap	24 V(from battery)	50-100 ms
	400 V (from wind turbine)	
Heating valve	3 V (from battery)	5-10 min

Table 3. Parameters of the flyback converter used in the experiment

Parameters	Values
Rated input voltage	24 V
Rated output voltage	2.5 kV
Magnetizing inductance L_p	35 µH
Flyback transformer core	EF20, N87
Primary turns/ Turns ratio	10/ 20
Leakage inductance L_{lk}	800 nH
Capacitance of DEAP actuator	145 nF
Primary peak current	5.3 A

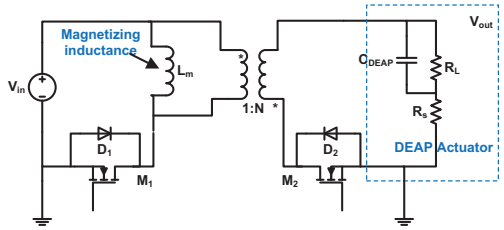

Figure 10a. Schematic of bi-directional flyback converter

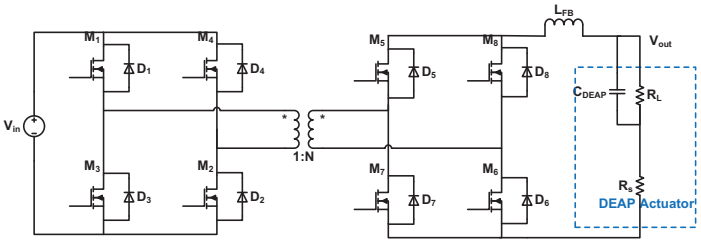

Figure 10b. Schematic of isolated bi-directional full bridge converter.

In this paper we focus only on the flyback topology, for both applications. We used LT3751 capacitor charger controller to generate high voltage. However, for wind turbine flap application, if the output power requirement is too high, isolated full bridge converter is the good choice.

3.2 SIMULATION AND EXPERIMENTAL RESULTS

The simulation has been done using LTSpice software. The simulation results for a uni-directional flyback are shown below for different input voltages (V_{in} = 3V, 24V and 400V).

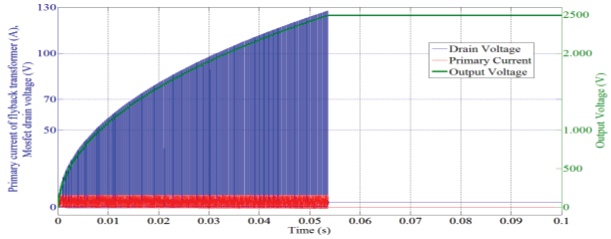

Figure 11. Simulation results of flyback converter for V_{in} = 3 V

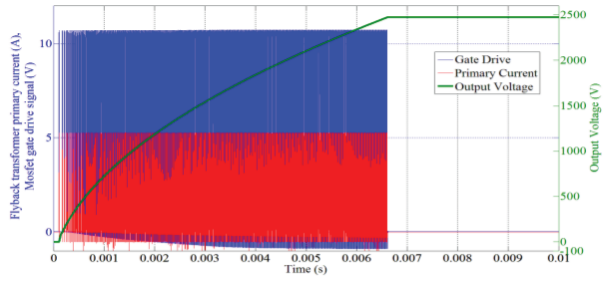

Figure 12. Simulation results of flyback converter for V_{in} = 24 V

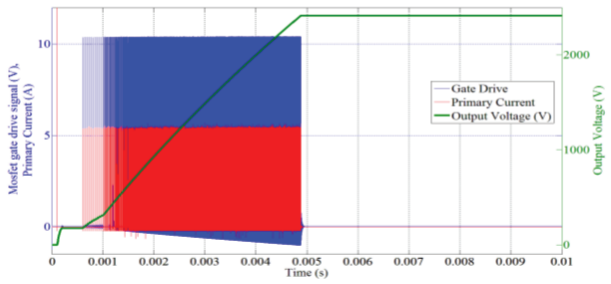

Figure 13. Simulation results of flyback converter for V_{in} = 400 V

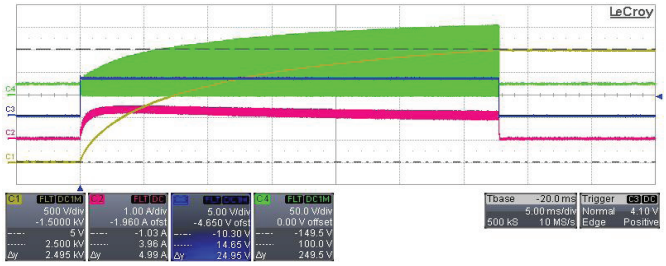

Figure 14. Experimental waveforms (CH1-Output voltage; CH2-Input current; CH3-Charge signal to the converter; CH4-Mosfet drain voltage)

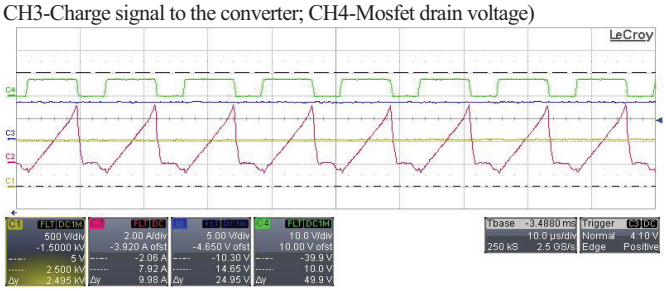

Figure 15. Experimental waveforms (CH1-Output voltage; CH2-Flyback primary current; CH3-Charge signal to the converter; CH4-Mosfet gate voltage)

Figures 14 and 15 are the experimental results for the uni-directional flyback converter.

4 CONCLUSION

The DEAP actuator is analyzed in detail. And the modeling of the DEAP actuator is presented. Different structures of the DEAP actuators that can be implemented in two different applications are shown. Some high voltage converter topologies for driving the capacitive loads are presented. Finally, simulation and experimental results are shown for a uni-directional flyback converter.

REFERENCES

[1] Y. Bar-Cohen, *Electroactive Polymer (EAP) Actuators as Artificial Muscles: Reality, Potential, and Challenges*. SPIE Press, Bellingham, Washington, USA, 2001.

[2] R. Pelrine, P. Sommer-Larsen, R. Kornbluh, R. Heydt, G. Kofod, Q. Pei, P. Gravesen, "Applications of dielectric elastomer actuators", Proc. of SPIE, Smart structures and materials 2001: Electroactive polymer actuators and devices, Vol. 4329, pp. 335-349, 2001.

[3] T. Andersen, M. S. Rødgaard, O. C. Thomsen and M. A. E. Andersen, "Low voltage driven dielectric electro active polymer actuator with integrated piezoelectric transformer based driver," *Proceedings of SPIE*, vol. 7976, p. 79762N, 2011.

[4] M. Babič, R. Vertechy, G. Berselli, J. Lenarčič, V. Parenti Castelli, G. Vassura, "An electronic driver for improving the open and closed loop electro-mechanical response of Dielectric Elastomer actuators", Mechatronics, Vol. 20, pp. 201-212, 2010.

[5] M. Benslimane, P. Gravesen, P. Sommer-Larsen, "Mechanical properties of dielectric elastomers with smart metallic compliant electrodes", In. Proc. of SPIE Int Soc. Opt. Eng., 4695, pp. 150-157, 2002.

[6] R.E. Pelrine, R.D. Kornbluh, J.P. Joseph, "Electrostriction of polymer dielectrics with compliant electrodes as a means of actuation," Sensors and Actuators, Vol. A 64, pp. 77-85, 1998.

[7] R. Sarban, B. Lassen, M. Willatzen, "Dynamic Electromechanical Modeling of Dielectric Elastomer Actuators With Metallic Electrodes," IEEE/ASME Transactions on Mechatronics, Vol. PP, no.99, pp.1-8, 2011.

Appendix B

A high voltage DC-DC converter driving a Dielectric Electro Active Polymer actuator for wind turbine flaps

---

47^{th} *International Universities' Power Engineering Conference (UPEC 2012)*

A high voltage DC-DC converter driving a Dielectric Electro Active Polymer actuator for wind turbine flaps

Prasanth Thummala
Dept. of Electrical Engineering, Technical University of Denmark
pthu@elektro.dtu.dk

Zhe Zhang
Dept. of Electrical Engineering, Technical University of Denmark
zz@elektro.dtu.dk

Michael A. E. Andersen
Dept. of Electrical Engineering, Technical University of Denmark
ma@elektro.dtu.dk

Ole C. Thomsen
Dept. of Electrical Engineering, Technical University of Denmark
oct@elektro.dtu.dk

***Abstract*-The Dielectric Electro Active Polymer (DEAP) material is a very thin (~80 µm) silicone elastomer film with a compliant metallic electrode layer on both sides. The DEAP is fundamentally a capacitor that is capable of very high strain. The property that the polymer changes its shape, as a result of the electrostatic forces generated by an applied voltage, can be used in actuators, for instance to adapt the trailing edges of wind turbine blades, for maximum efficiency and increased energy output. Conventional actuator technologies have not proven feasible solutions for driving the wind turbine flaps. With the DEAP based high power actuator, it is expected to make a reliable and light solution with superior controllability. The current DEAP technology requires high DC voltage in the range of kV to fully utilize the DEAP material as an actuator. In this paper we propose a flyback converter topology to obtain high voltage at low current, for driving the DEAP actuator. Simulation and experimental results for uni-directional flyback converter topology are shown.**

***Index Terms*--Dielectric Electro Active Polymer (DEAP), high voltage, capacitive load, actuator, wind turbine, flaps, flyback, PolyPower**

I. INTRODUCTION

Nowadays the world's main focus is on how to best utilize the energy from the natural energy resources such as sunlight, wind and tides etc. One of the reasons is due to the fact that the fossil fuels will not last forever. But the energy production from fossil fuel is relatively cheaper when compared to sustainable energy. Engineers are doing extensive research to face the challenge of making the equipment that catches the energy from nature more efficient. Wind turbines and in particular their wings/blades are subject to loads varying greatly because of wind gusts and turbulences occurring at passing the tower. The varying loads on the wings may cause them to oscillate and collide with the tower. So it is very important to control these blade loads along the length of the blade body, to protect the turbine from being damaged. This can be achieved with aerodynamic control devices such as flaps [1].

A flap mounted on the wing can control the lift on certain sections of the wing. A wing flap covering ten percent of the airfoil can change its lift coefficient (C_l) by twenty percent at an angular deflection (δ) of five degrees. The effect of the changing lift coefficient is a change in the force acting on the wing. Being able to control this force makes it feasible to avoid oscillation of the wing. The flaps may also be used to increase the energy output of a wind turbine. Piezoelectric [2], hydraulic [3]-[6], pneumatic [7]-[10] and electro-mechanical actuators [11]-[12] are the most common types of actuators used in various engineering applications and in existing wind turbines for traditional control purposes. Among the above actuators, piezoelectric and pneumatic actuators had already been implemented for controlling the trailing edge flaps in the wind turbine blades [2], [10].

In this paper, we aim to utilize the DEAP material as an actuation mechanism for the wing flap. The unique properties of the DEAP material such as, very low electrical power consumption, no noise, flexibility, large bandwidth, self sensing ability, higher performance than competing technologies and light weight, allows it to operate as an actuator [13]. The basic behaviour of the DEAP material is the reduction in the polymer's thickness and increment in its area, due to an applied electric field. The DEAP material can be used for actuation, sensing and energy harvesting [14], [15]. The limited thickness of the polymer film in the range of 20-80 µm, together with the requirement of high operating electric field strength in the range 40-100 V/µm, created the requirement of high voltage power electronics to drive the DEAP actuators.

Prior work in the high voltage DC-DC converters for capacitive load applications is given hereinafter; in [16] a low voltage driven DEAP actuator is developed using a piezoelectric transformer. In [17] a diode converter approach is suggested for harvesting the mechanical energy using DEAP. Cascaded bi-directional flyback topology for generating high voltage is discussed in [18]. A DC-DC converter topology for charging high voltage bulk capacitors for pulsed load applications is given in [19]. Bidirectional power converters for driving dielectric elastomer transducers are given in [20]. A high voltage power supply is developed for ER-fluid application in [21].

The goal of this paper is to discuss, how the high voltage DC-DC converter topology can be used to drive DEAP actuator, which can be as an actuation mechanism for the wind turbine flaps. Section II discusses the advantage of a flap in the wind turbine blade. We discuss the closed loop control of wind turbine flap with DEAP actuator in Section III. In Section IV we discuss about the proposed high voltage power converter topology. In Section V we show the

simulation results and in Section VI we describe the experimental results and choice of high-voltage components. The efficiency analysis is given in Section VII, followed by the conclusion in Section VIII.

II. Wind Turbine Blade: Requirement and Advantage of a Flap

By providing the wind turbine blade with a movable trailing edge, it is possible to control the loads on the blade and extend the life time of the wind turbine components. This is similar to the technique used on aircrafts, where flaps regulate the lift during the most critical times such as at take-off and landing. The latest wind turbine designs increase the rotor diameter to reduce the cost of energy. Rotor diameters for onshore turbines currently exceed 120 m, and some offshore turbines use rotor diameters of up to 164 m.

Wind turbine blades experience aerodynamically induced fatigue loads from yaw error, wind shear and wind turbulence etc. Extreme operating conditions like strong gusts, emergency shutdown, and parked conditions in high wind further generate large extreme loads on their structure. Both fatigue and extreme loads are also transferred to all major wind turbine components, causing damage and thereby influencing or driving the components design.

The use of smart rotor systems, for future generations of wind turbines is perceived as a promising way to decrease the cost of wind energy [22]. Such systems use distributed sensing and span-wise distributed aerodynamic control surfaces to reduce changes in the aerodynamic loads. This reduction then enables e.g. larger rotor diameters, reduction in the tower bill of material or placement in complex terrain with extreme turbulence levels. The research in the area has amongst others been surveyed in [22], [23].

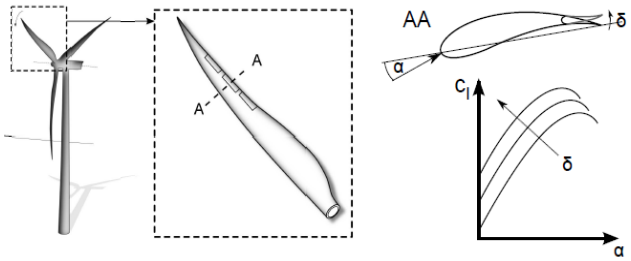

Fig. 1. Smart rotor concept level: Turbine, Blade and Airfoil [30].

In general, the smart rotor concept can be divided into three different levels (illustrated in Fig. 1): full turbine, full blade and two dimensional airfoil. In the Fig. 1, α is the angle of attack, C_l is the lift coefficient and δ is the flap deflection angle. Fig. 2 shows four popular concepts for active aerodynamic control surfaces. These concepts all change the effective camber of the airfoil by directly modifying the airfoil geometry. The trailing edge flap (TEF) and the nose droop are considered to be the most common ones, with a wide area of applications in aerospace technology. The use of flaps on wind turbines is more similar to aircraft ailerons, which control the aircraft's roll state.

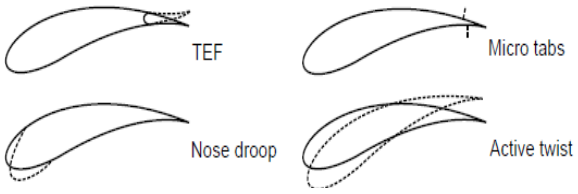

Fig. 2. Control Surface Concepts [30].

The choice of any aerodynamic control surface directly leads to strict requirements for the choice of actuation. A fundamental distinction arises for nearly all actuator types. Slow actuators can apply large forces and strokes, while fast actuators are limited to small strokes or small forces. A trade-off is usually possible between stroke and force by for instance mechanical levers. Actuators based on pneumatics/hydraulic systems have been applied to wind tunnel experiments in a smart rotor context. Examples are the full rubber structure in [24], or the linear pneumatic artificial muscle (PAM) actuators presented in [25]. Shape memory alloy (SMA) actuators consist of alloy wires that contract when being heated, mostly by an electrical current. They are attributed with being light weight, using less space and operating quietly. The larger the wire diameter the longer it takes the wire to cool down again, before the next motion cycle can be started. This restricts the actuators to low frequencies at reasonable forces. Magnetostrictively actuated flaps for vibration reduction in helicopter rotors are presented in [26]. These actuators produce strain when a magnetic field is applied (e.g. by a surrounding wire coil). Piezo electric benders as actuators have been presented in wind tunnel tests of airfoil sections [27] and rotating turbine models [28].

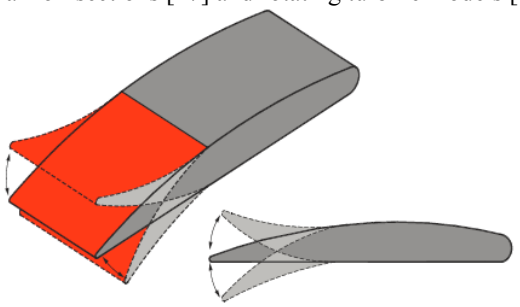

Fig. 3. Adaptive airfoil structure [13].

Nowadays the challenge for the actuators that are to be embedded in the trailing edge flaps are: to have a long life span, having no moving parts and being highly robust. The previous actuator configurations that have been implemented so far, in the trailing edge flaps of wind turbine blades or aircraft wings, fails to show the long life span and they contain the moving parts (like rotational joints, and such actuators are expensive due to regular maintenance). The Inslator actuators developed by Danfoss PolyPower have the potential for integration into the airfoil structure as well as performing the above mentioned challenges, due to the unique properties of the polymer material. Fig. 3 shows structure of the typical adaptive airfoil.

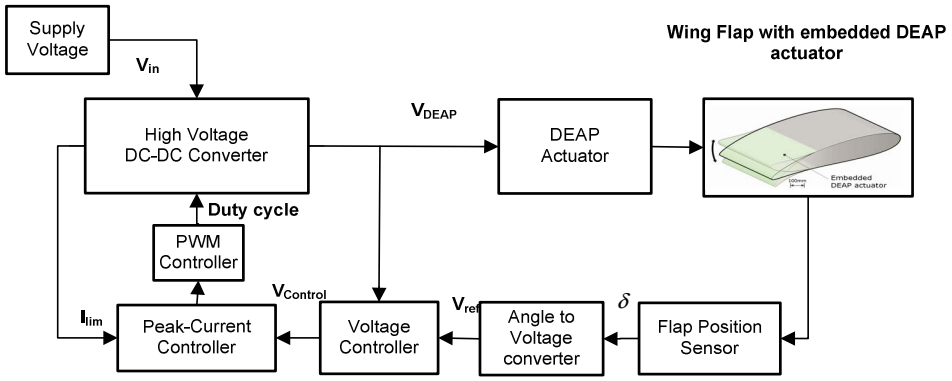

Fig. 4. Closed Loop block diagram of the DEAP actuator controlling the wind turbine flap.

III. Closed Loop Control of Wind Turbine Flap with DEAP Actuator

If the DEAP material is used as an actuation mechanism for the flap, the actuator has to be supplied with very high voltage. In this paper we present a flyback converter topology, to supply required voltage to the DEAP actuator. Fig. 4 shows the closed loop block diagram of the wind turbine flaps actuated by DEAP actuator.

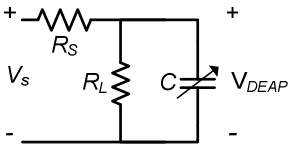

Fig. 5. Electrical equivalent of DEAP actuator.

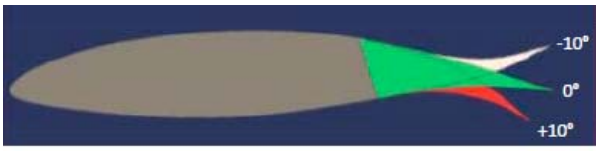

Fig. 6. Angular deflections in a typical wind turbine blade with a flap [31].

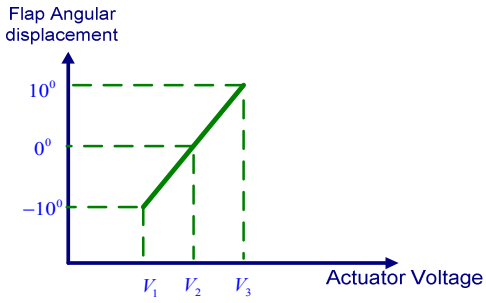

Fig. 7. Graph showing flap angular displacement of the flap with respect to actuator voltage.

In Fig. 5 we show the electrical equivalent circuit of DEAP material, C is the capacitance of the DEAP film. R_S is the resistance of the electrodes and the wiring, R_L is the resistance of the DEAP material and V_{DEAP} is the voltage across the DEAP actuator. V_s is the voltage of the power source. The electrical time constant of the DEAP actuator is given as

$$\tau_e = \frac{R_L R_S C}{R_L + R_S} \tag{1}$$

When the DEAP actuator is supplied with a certain voltage, the wing flap should perform a certain angular displacement. Fig. 6 shows the angular deflections in a typical wind turbine blade with the trailing edge flap, and Fig. 7 shows the variation of the actuator voltage with respect to the flap angle. The voltage required by the actuator to achieve a stroke r is given by [32]

$$V = \sqrt{\frac{r \times x^2 \times k}{A \times \varepsilon_o \times \varepsilon_r}} \tag{2}$$

The stroke r is a function of the flap angle i.e. $r = f(\delta)$. In (2) k is the spring constant (assuming DEAP actuator as a spring, with small strain) with $k = (Y \times A)/L$, Y is the Young's modulus, A is the cross-sectional area and L is the length of the active DEAP material, x is the film thickness and ε_o and ε_r are the permittivity of the free space (8.85×10^{-12} F/m) and the relative permittivity of the polymer, respectively.

So by sensing the flap angular deflection, the stroke required to deflect the flap to such an angle will be estimated. From the stroke, the voltage required to actuate the flap will be calculated, which acts as a reference voltage for voltage controller. The voltage controller together with peak current controller generates a Pulse Width Modulation (PWM) signal to drive the high voltage DC-DC converter.

The challenge in the wing flap application is, to sense the real time behaviour of the wing. So it is required to develop a system to detect the real time behaviour of the wing to estimate the flap angle. The DEAP actuator has to be charged to a specified voltage, in a specified time, to achieve a certain flap deflection; and it has to be discharged, through a load or by using a bi-directional topology, to achieve another flap deflection. The power rating of the DC-DC converter depends on how fast the actuator has to be charged or discharged and the size of the actuator. Depending on the power rating of the converter, suitable topology has to be chosen.

IV. PROPOSED TOPOLOGY: FLY-BACK CONVERTER

Due to simple structure, fast dynamic performance and magnetic isolation, flyback converter is utilized in conventional HV applications. The uni-directional flyback converter is shown in Fig. 8. Boundary current mode controller LT3751 [29] has been employed to obtain high voltage. The output capacitors will be charged till the output voltage reaches the high target voltage and after that the voltage remains constant; and the converter stops switching. The specifications of the flyback converter are shown in Table 1.

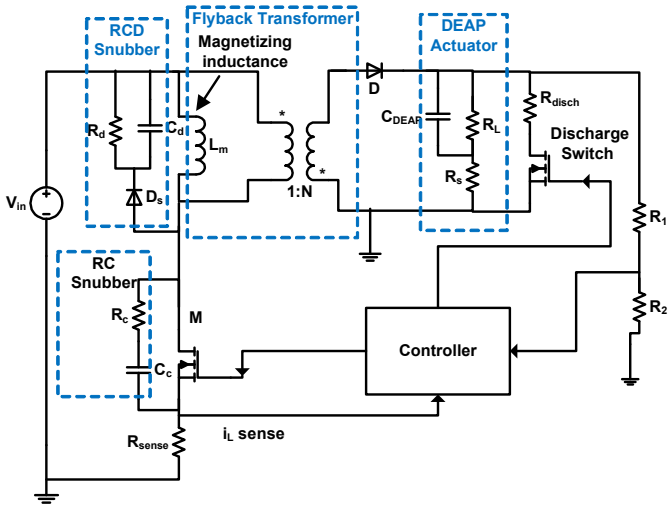

Fig. 8. Schematic of the flyback converter charging the DEAP actuator.

TABLE 1. Specifications of flyback converter

Parameters	Values
Rated input voltage	24 V
Rated output voltage	2.275 kV
Primary inductance L_p	35 µH
Flyback transformer core	EF20, N87
Primary turns (N_p) / Turns ratio (N)	10 / 20
Primary leakage inductance L_{lk}	800 nH
Capacitance of DEAP actuator (C_{DEAP}) / Capacitance of film capacitive load (used for comparison with DEAP actuator)	145 nF / 147 nF
Primary peak current	5.3 A
RC snubber: R_c, C_c	10 Ω, 50 pF
RCD snubber: R_d, C_d	8 kΩ, 400 nF

V. SIMULATION RESULTS

The flyback converter is simulated using LTSpice software. The same parameters shown in Table 2 are used for the simulation. However, stray capacitances of the primary and secondary windings, and inter winding capacitances of the transformer are neglected in the simulation. The simulation results for the output voltage of 1 kV are shown in Figs. 9-10. The control IC LT3751 [29] employs peak current mode control (current limit is fixed at 106mV/R_{SENSE}), and it is operated in the charge mode by connecting the feedback pin to the ground. By proper choice of the transformer turns ratio, and three external resistors (RV_{OUT}, R_{BG} and RV_{TRANS}) one can achieve high output voltage. By proper choice of the resistor R_{DCM}, discontinuous mode is sensed when the MOSFET drain voltage falls to V_{TRANS}+20µA*R_{DCM} during the off-state, and initiates next switching cycle.

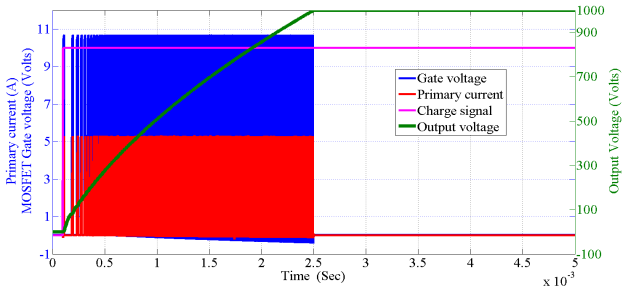

Fig. 9. Simulation results of flyback converter for output voltage of 1 kV.

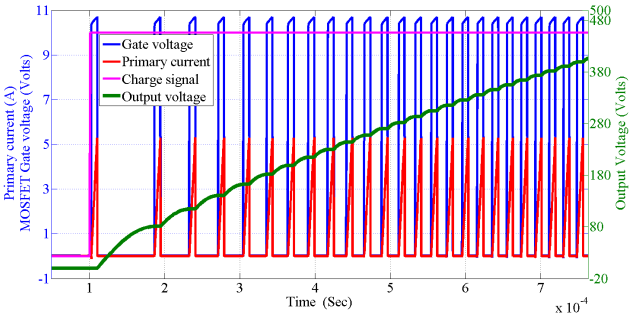

Fig. 10. Zoomed view of Fig. 9.

VI. EXPERIMENTAL RESULTS

A. *Results*

The uni-directional flyback converter is implemented in the laboratory. The DEAP actuator and the film capacitive loads are tested separately. The experimental results for film capacitive load and DEAP actuator are shown in Figs. 11-18. In Fig. 11, CH3 is the charge signal for the controller, where as in Fig. 12, CH3 is the flyback primary current. It is clear from the both the figures that the MOSFET drain voltage (V_{DRAIN} =V_{TRANS}+ [V_{OUT}+V_{DIODE}]/N), increases as the output voltage increases.

Figures 13 and 14 are the experimental waveforms for output voltage of 2kV for both capacitive loads respectively. The results for the maximum tested output voltage (2.275kV) are shown in Figs. 15 and 16; CH2 in both figures is the MOSFET gate drive signal. The zoomed waveforms for 2kV output voltage for both the loads are shown in the Figs. 17 and 18.

In Fig. 18 the CH3 is the flyback primary current at the steady state of the output voltage, the primary current becomes slightly negative at the turn-on instant, this is due to conduction of the intrinsic body diode of the MOSFET. When the secondary diode stops forward conduction, the energy stored in the secondary winding capacitance ($0.5C_{SEC}V_{OUT}^2$)

is reflected to the primary. The drain of the MOSFET became negative, when the reflected capacitance was greater than the MOSFET drain capacitance, so the body diode of the MOSFET is conducted. This created a propagation delay, and due to this the charging times in the simulation and in the experiment did not match some times.

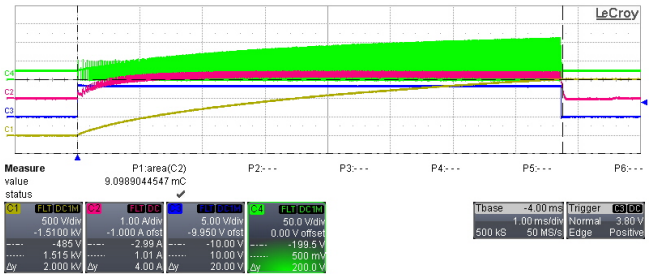

Fig. 11. Flyback converter wave forms for output voltage V_{out} = 1.5kV with Film capacitive load; CH1: Output voltage; CH2: Input current; CH3: Charge signal for the controller; CH4: MOSFET drain voltage.

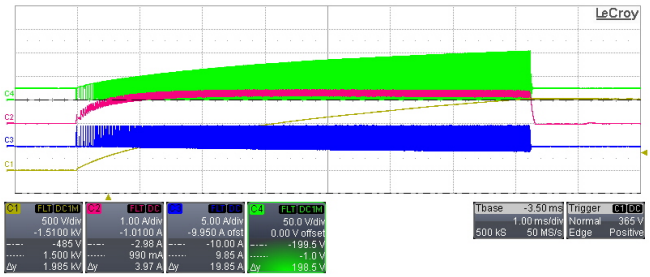

Fig. 12. Flyback converter wave forms for output voltage V_{out} = 1.5kV with DEAP actuator as load; CH1: Output voltage; CH2: Input current; CH3: Primary current of flyback transformer; CH4: MOSFET drain voltage.

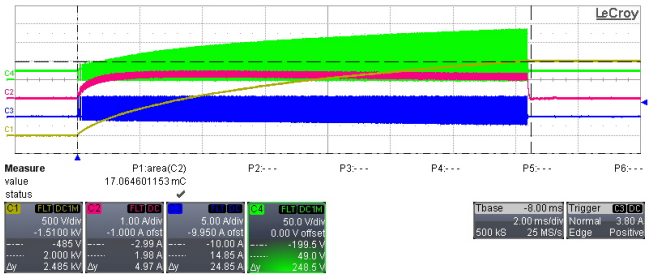

Fig. 13. Flyback converter wave forms for output voltage V_{out} = 2kV with Film capacitive load; CH1: Output voltage; CH2: Input current; CH3: Primary current of the flyback transformer; CH4: MOSFET drain voltage.

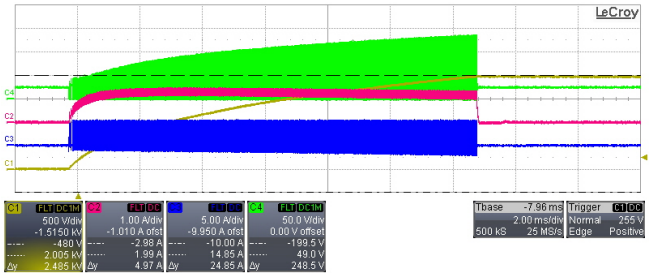

Fig. 14. Flyback converter wave forms for output voltage V_{out} = 2kV with DEAP actuator as load; CH1: Output voltage; CH2: Input current; CH3: Primary current of the flyback transformer; CH4: MOSFET drain voltage.

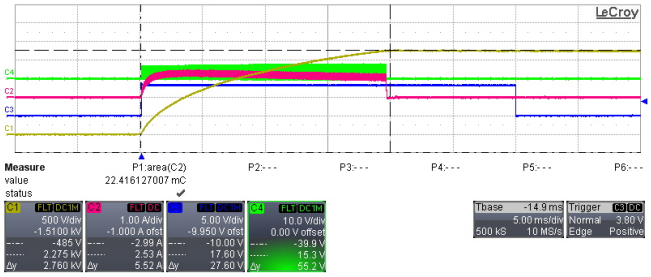

Fig. 15. Flyback converter wave forms for output voltage V_{out} = 2.275kV with Film capacitive load; CH1: Output voltage; CH2: Input current; CH3: Charge signal for the controller; CH4: MOSFET gate drive signal.

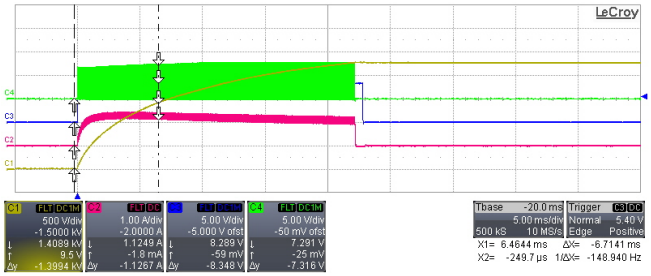

Fig. 16. Flyback converter wave forms for output voltage V_{out} = 2.275kV with DEAP actuator as load; CH1: Output voltage; CH2: Input current; CH3: Primary current of flyback converter; CH4: MOSFET drain voltage.

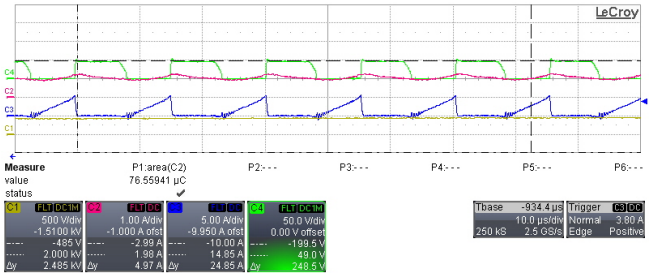

Fig. 17. Zoomed wave forms (in the starting) for output voltage V_{out} = 2kV with Film capacitive load; CH1: Output voltage; CH2: Input current; CH3: Primary current of flyback transformer; CH4: MOSFET drain voltage

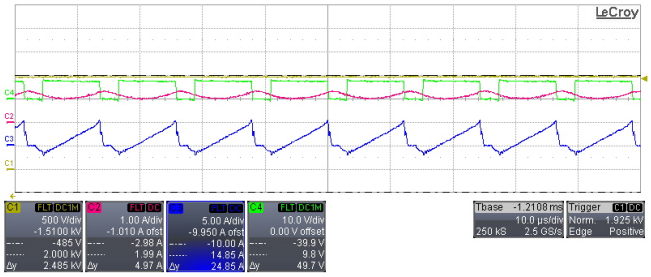

Fig. 18. Zoomed wave forms (in the steady state) for output voltage V_{out} = 2kV with DEAP actuator as load; CH1: Output voltage; CH2: Input current; CH3: Primary current of flyback transformer; CH4: MOSFET drain voltage

B. Choice of the high voltage components

We used the high voltage diode VMI SM6525 (5kV and 150 mA) as a secondary diode and the high voltage pulse capacitors RIFA PHE 450 (3000V) as a film capacitive load. The DEAP actuator (PolyPower Push Inslator actuator) rated maximum voltage is 2500V [13].

VII. EFFICIENCY ANALYSIS

Since the flyback converter driving the DEAP actuator is, driving a pure capacitive load. There is no power consumption in the capacitive load. So the energy efficiency can be calculated as the ratio of energy stored in the capacitive load to the energy input to the converter, and is given below

$$\eta = \frac{\frac{1}{2} C_{OUT} V_{OUT}^{2}}{\int_{0}^{T_{charge}} V_{in} \times i_{in} \, dt} \quad (3)$$

where T_{charge} is the charging time and is defined as: the time taken by the output to reach the target value, C_{OUT} is the capacitance of the load, V_{OUT} is the steady state output voltage, V_{in} is the input voltage and i_{in} is the input current into the flyback capacitor.

The efficiency comparison for the film capacitive load and the DEAP actuator is given in Fig. 19. There is sudden drop in the efficiency for the DEAP actuator at 2.275kV; this is due to the fact that, at very high voltage there is significant increase in the strain of the DEAP actuator, since the capacitance is directly proportional to the strain for uni-directional actuation [33], the capacitance of the DEAP actuator increases at high voltage. For the DEAP actuator efficiency calculations, we assumed constant DEAP actuator capacitance. That means at very high voltage, we find the efficiency at less output capacitance, this reduces the efficiency for the DEAP actuator at very high voltage.

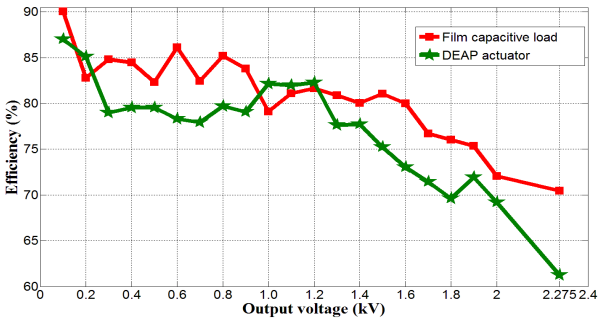

Fig. 19. Energy efficiency comparison for DEAP actuator and Film capacitive load

VIII. CONCLUSIONS

The requirement of a flap in a wind turbine blade is discussed. The closed loop control concept of wind turbine flap, with DEAP actuator as an actuation mechanism, which is driven by high voltage DC-DC converter is discussed. The uni-directional flyback converter is implemented in the lab and the experimental results are shown along with simulation results. The energy efficiency is calculated for the DEAP actuator and for the film capacitive load. The bi-directional flyback will be implemented as a future work, to discharge the output capacitors as well as for the energy recovery.

ACKNOWLEDGEMENTS

The authors would like to acknowledge the financial support from the Danfoss PolyPower A/S and the Danish National Advanced Technology Foundation.

REFERENCES

[1] S. Daynes and P. M. Weaver, "A shape adaptive airfoil for a wind turbine blade," *Proc. SPIE, Industrial and Commercial Applications of Smart Structures Technologies*, vol. 7979, p. 79790H, 2011.

[2] S. Narasimalu, "Wind turbine blade comprising a trailing edge flaps and a piezo electric actuator," U.S. Patent, 7 992 450, Apr. 12, 2011.

[3] M. H. Hansen and B. S. Kallesøe, "Servo-Elastic Dynamics of a Hydraulic Actuator Pitching a Blade with Large Deflections," J. Phys.: Conf. Ser. 75 012077, 2007.

[4] S.D. Hughes and W.D. Musial, "Implementation of a Two-Axis Servo-Hydraulic System for Full-Scale Fatigue Testing of Wind Turbine Blades," presented at Wind power '99 Burlington, Vermont June 20–23, 1999.

[5] C. H. Westergaard, "Flap control for wind turbine blades," U.K. Patent, GB 2475694 A, 2011.

[6] P. Malhotra, "Advanced blade testing methods," M.S. Thesis, Dept. of Mech. and Ind. Eng., University of Massachusetts Amherst, Amherst, MA, 2010.

[7] B. K. S. Woods, C. S. Kothera, J. Sirohi and N. M. Wereley, "Pneumatic artificial muscles for trailing edge flap actuation: a feasibility study*," Smart Mater. Struct.*, vol. 20**,** pp. 1-15, 2011.

[8] N. T. Yerkes and N. M. Wereley, "Pneumatic Artificial Muscle Activation for Trailing Edge Flaps," *46th AIAA Aerospace Sciences Meeting*, Reno, NV, AIAA-2008-1418 (2008)

[9] G. Andrikopoulos, G. Nikolakopoulos and S. Manesis, "A Survey on Applications of Pneumatic Artificial Muscles," *19th Mediterranean Conference on Control and Automation*, Corfu, Greece, pp. 1439-1446, 2011.

[10] B. K. S. Woods, C. S. Kothera and N. M. Wereley, "Wind Tunnel Testing of a Helicopter Rotor Trailing Edge Flap Actuated via Pneumatic Artificial Muscles," *ASME Conf. Proc.*, pp. 515-524, 2010.

[11] B. Joshuna, "Method and apparatus for reducing fluid flow induced forces produced by vortex shedding on a wind turbine rotor blade," International application published under the patent cooperation treaty (PCT), WO 2011/147422 A2.

[12] S. Kota, "Active control surfaces for the wind turbine blades," U.S. Patent, 0259046 A1, 2010.

[13] www.polypower.com

[14] R. Pelrine, R. Kornbluh, J. Eckerle, P. Jeuck, S. Oh, Q. Pei, S. Stanford, "Dielectric elastomers: generators mode fundamentals and its applications," *Proc. of SPIE Electroactive Polymer Actuators and Devices (EAPAD),* vol. 4329, pp. 148-156, 2001.

[15] R. Pelrine, P. S. Larsen, R. Kornbluh, R. Heydt, G. Kofod, Q. Pei, P. Gravesen, "Applications of dielectric elastomer actuators," *Proc. of SPIE Electroactive Polymer Actuators and Devices (EAPAD)*, vol. 4329, pp. 335-349, 2001.

[16] T. Andersen, M. S. Rødgaard, O. C. Thomsen and M. A. E. Andersen, "Low voltage driven dielectric electro active polymer actuator with integrated piezoelectric transformer based driver," *Proc. of SPIE Electroactive Polymer Actuators and Devices (EAPAD),* vol. 7976, p. 79762N, 2011.

[17] D. Jens, S. M. Nielsen, R. O. Nielsen, "Energy harvesting with Di-Electro Active Polymers," 5th *IET Int. Con. Power Electronics, Machines and Drives (PEMD)*, pp. 1-6, 19-21 April 2010.

[18] L. Eitzen, C. Graf, J. Maas, "Cascaded bidirectional flyback converter driving DEAP transducers," *37th Annual Conference on IEEE Industrial Electronics Society (IECON),* pp. 1226-1231, 7-10 Nov. 2011.

[19] J. Elmes, C. Jourdan, O. A. Rahman, I. Batarseh, "High-Voltage, High-Power-Density DC-DC Converter for Capacitor Charging Applications," *24th Annual IEEE Applied Power Electronics Conference and Exposition (APEC)*, pp. 433-439, 15-19 Feb. 2009.

[20] L. Eitzen, C. Graf, J. Maas, "Bidirectional power electronics for driving dielectric elastomer transducers," *Proc. of SPIE Electroactive Polymer Actuators and Devices (EAPAD), vol.* 8340, 834018, 2012.

[21] S. K. Chung, H. B. Shin, "High-voltage power supply for semi-active suspension system with ER-fluid damper," *IEEE Trans. on Vehi. Tech.,* vol.53, no.1, pp. 206- 214, Jan. 2004.
[22] T. Barlas and G. V. Kuik, "Review of state of the art in smart rotor control research for wind turbines," *Progress in Aerospace Sciences*, vol. 46(1), pp. 1 – 27, 2010.
[23] S. J. Johnson, C. V. Dam, and D. E. Berg. "Active load control techniques for wind turbines," Technical Report SAND2008-4809, Sandia National Laboratories, 2008.
[24] H. A. Madsen, "The potentials of the controllable rubber trailing edge flap (CRTEF)," in EWEC 2010 proc. online, pp. 1-11, 2010.
[25] C. S. Kothera and N. M. Wereley, "Wind Tunnel Testing of Pneumatic Artificial Muscles for Control Surface Actuation," in *Wind Tunnels* InTech, 2011, pp. 105-120.
[26] P. P. Friedmann, G. P. Carman, and T. A. Millott, "Magnetostrictively actuated control flaps for vibration reduction in helicopter rotors– design considerations for implementation," *Int. J. Mathematical and Computer Modelling*, vol. 33(10-11), pp. 1203 –1217, 2001.
[27] P. B. Andersen "Advanced Load Alleviation for Wind Turbines using Adaptive Trailing Edge Flaps: Sensoring and Control" PhD thesis, Risø-DTU – National Laboratory for Sustainable Energy, Technical University of Denmark, Denmark, 2010.
[28] J. W. V. Wingerden, A. Hulskamp, T. Barlas, I. Houtzager, H. Bersee, G. V. Kuik, and M. Verhaegen "Two-Degree-of-Freedom Active Vibration Control of a Prototyped Smart Rotor," *IEEE Trans. Contr. Sys. Tech.,* vol. 19, no. 2, pp. 284-296, March 2011.
[29] "LT3751 High Voltage Capacitor Charger with Regulation Datasheet," Linear Technology Corporation, USA.
[30] T. Behrens, "Simulation of Moving Trailing Edge Flaps on a Wind Turbine Blade using a Navier-Stokes based Immersed Boundary Method," Ph.D. thesis, Dept. Mech. Eng., Technical University of Denmark, Denmark, 2011.
[31] http://www.flxsys.com/wind-energy/
[32] A. Bargum, "Adaptive wing flap," B.S. Thesis, Dept. of Mechatronic Eng., University of Southern Denmark, Sønderborg, Denmark, 2010.
[33] P. Thummala, L. Huang, Z. Zhang and M. A. E. Andersen, "Analysis of Dielectric Electro Active Polymer Actuator and its High Voltage Driving Circuits," *IEEE International Power Modulator and High Voltage Conference (IPMHVC)*, San Diego, CA, pp. , Jun. 4-7, 2012.

Appendix C

Battery Powered High Output Voltage Bidirectional Flyback Converter for Cylindrical DEAP Actuator

---

2012 IEEE International Power Modulator and High Voltage Conference (IPMHVC 2012)

Battery Powered High Output Voltage Bidirectional Flyback Converter for Cylindrical DEAP Actuator

Lina Huang, Prasanth Thummala, Zhe Zhang, Michael A. E. Andersen
huang@elektro.dtu.dk, pthu@elektro.dtu.dk, zz@elektro.dtu.dk, ma@elektro.dtu.dk
Technical University of Denmark, Department of Electrical Engineering, DK-2800 Kgs. Lyngby, Denmark

ABSTRACT

DEAP (Dielectric Electro Active Polymer) actuator is essentially a capacitive load and can be applied in various actuation occasions. However, high voltage is needed to actuate it. In this paper, a high voltage bidirectional flyback converter with low input voltage is presented. The fundamental operating principle for both energy transfer process and energy recovery process is analyzed in detail. In order to verify the analysis, critical simulation results are provided. So far, a unidirectional flyback converter, which can realize the energy transfer process, has been implemented in the lab. The design parameters for flyback transformer and snubber circuits are illustrated. Moreover, the experimental waveforms are provided.

Index Terms — **DEAP actuator, high voltage, flyback, bidirectional**

1 INTRODUCTION

DEAP (Dielectric Electro Active Polymer) is a new type of polymer material, which consists of a soft silicone polymer, sandwiched between two compliant metallic electrodes [1]. The similar structure to a capacitor enables DEAP to be fundamentally considered as a capacitive load. Figure 1 shows the measured impedance of DEAP material at low frequency. The -90 degrees phase angle can sufficiently illustrate the capacitive property of DEAP.

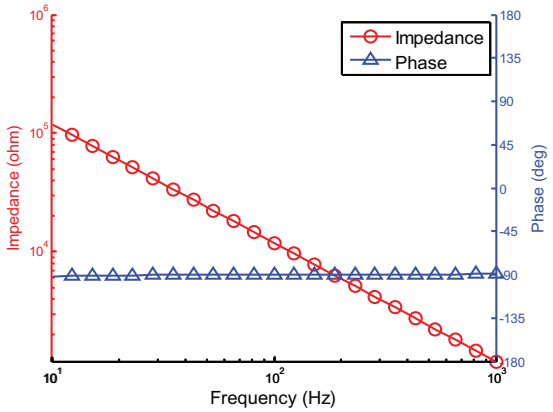

Figure 1. Impedance measurement of DEAP material

When a voltage is applied to DEAP material, the polymer will compress in thickness and expand in area due to the electric field [2]; therefore, DEAP can be used as an actuator. Compared to traditional electro-magnetic, pneumatic or hydraulic actuators, capacitive actuator possesses many advantages, such as high power density, low weight, fast and direct actuation, high actuating precision, extremely low steady-state power consumption, low noise, etc.

Because of the simple design and immense applicable occasions, cylindrical DEAP actuator, which only performs linear motion, will be an effective replacement for many conventional actuators. Figure 2 shows a cylindrical DEAP actuator [3].

Figure 2. Cylindrical DEAP actuator

The stroke-voltage response of cylindrical DEAP actuator shown in Figure 2, is demonstrated in Figure 3 [4]. It is obvious that DEAP actuator needs high voltage to be fully elongated.

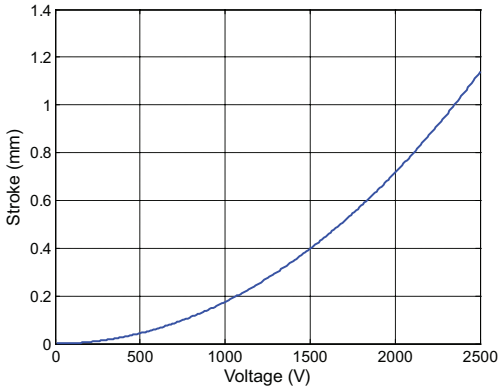

Figure 3. Stroke-voltage characteristic of cylindrical DEAP actuator

Owing to the low weight of DEAP actuator, it can be used in the portable or autonomous systems, where the battery will be the only power source. Therefore, for stimulating DEAP, a DC-DC converter which can convert low input voltage to high output voltage will be necessary. Combined with the capacitive property

of DEAP material and the objective to extend the lifetime of battery, a bidirectional flyback converter can be a good choice, which can not only boost the low voltage to several thousand volts, but also can recover the stored electrical energy when DEAP actuator is released. Furthermore, due to the simple topology of flyback, the converter can be realized in small size, which is vital in the portable or autonomous applications.

This paper analyzes the working principle of bidirectional flyback converter to drive cylindrical DEAP actuator and validates the feasibility through simulation in Section 2. Until now, only the unidirectional flyback converter was realized in the lab, which can boost the output voltage to 2.5kV from a 3V battery and will be addressed in Section 3. And conclusion is drawn in Section 4.

2 BIDIRECTIONAL FLYBACK ANALYSIS

For DEAP actuator, only a small portion of stored electrical energy is converted into mechanical response [5]; therefore, it can approximately be considered as a pure capacitor load in order to simplify the analysis.

2.1 TOPOLOGY AND WORKING PRINCIPLE

The bidirectional flyback converter is shown in Figure 4, consisting of coupled inductors in the middle and active power switches in both primary and secondary side.

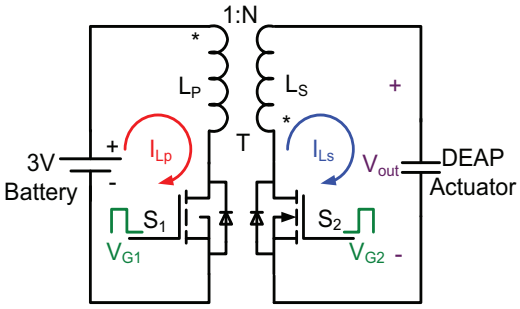

Figure 4. The topology of bidirectional flyback converter

a) Energy transfer process analysis

When driving DEAP actuator, the electrical energy is transferred to capacitive load from battery. Actually, the energy transfer process includes a series of switching cycles. For each cycle, the primary inductor L_P is magnetized in the on-time of S_1 to accumulate magnetic energy. Then in the off-time of S_1, through body diode of S_2, the stored energy will be transferred to DEAP actuator from coupled secondary inductor L_S. Ideally, the magnetic energy of L_S is totally transformed into electrical energy in the capacitive actuator. Moreover, based on the basic principle of LC resonant circuit, in every off-time of S_1, inductor current of L_S and output voltage V_{out} can be expressed in (1) and (2), respectively.

$$i_{L_S}(t) = i_{L_S}(0)\cdot\cos\left(\frac{t}{\sqrt{L_S\cdot C_{DEAP}}}\right) - V_{out}(0)\cdot\sqrt{\frac{C_{DEAP}}{L_S}}\cdot\sin\left(\frac{t}{\sqrt{L_S\cdot C_{DEAP}}}\right) \quad (1)$$

$$V_{out}(t) = V_{out}(0)\cdot\cos\left(\frac{t}{\sqrt{L_S\cdot C_{DEAP}}}\right) + i_{L_S}(0)\cdot\sqrt{\frac{L_S}{C_{DEAP}}}\cdot\sin\left(\frac{t}{\sqrt{L_S\cdot C_{DEAP}}}\right) \quad (2)$$

where L_S is the inductance of secondary coupled inductor, C_{DEAP} is the capacitance of DEAP actuator, and $i_{Ls}(0)$, $V_{out}(0)$ are the initial current and voltage for inductor and actuator, respectively.

In order to reduce the charge time of fully elongating DEAP actuator and completely transfer the energy stored in the flyback transformer in each cycle, a boundary mode control strategy can be used [6]. When the current through the body diode of S_2 accomplishes freewheeling in the previous cycle, the next cycle immediately starts. In addition, primary peak current control is employed to guarantee the sufficient utilization of magnetic core as well as to avoid its saturation. The fixed input voltage from battery and the application of peak current control make primary conduction time a constant value. However, with the increasing of output voltage, the freewheeling time in secondary side will decrease. That means the switching frequency is variable, and in the early stage of charge, the converter operates in low frequency, whereas at the end, the working frequency becomes high. Although the unfixed operating frequency accelerates the charging process, it also brings some challenges in designing the transformer and analyzing the power loss. The waveforms of first several cycles in charging process are shown in Figure 5.

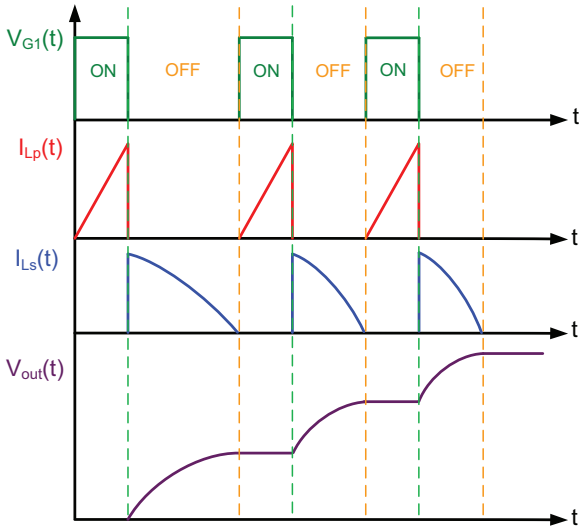

Figure 5. Waveforms in the energy transfer process

b) Energy recovery process analysis

For the purpose of increasing the service life of battery, it is pivotal to recover the energy stored in DEAP actuator when it is released. Like the charge process, the energy recovery process also consists of many successive switching cycles. Only S_2 and the body diode of S_1 work in the discharging process. In each cycle, L_S obtains magnetic energy from DEAP actuator in the on-time of S_2 and releases the stored energy to primary side in the off-time of S_2.

Similar to energy transfer stage, boundary mode control scheme and secondary peak current control are also adopted in discharge process. The waveforms of first several cycles in the energy recovery process are shown in Figure 6.

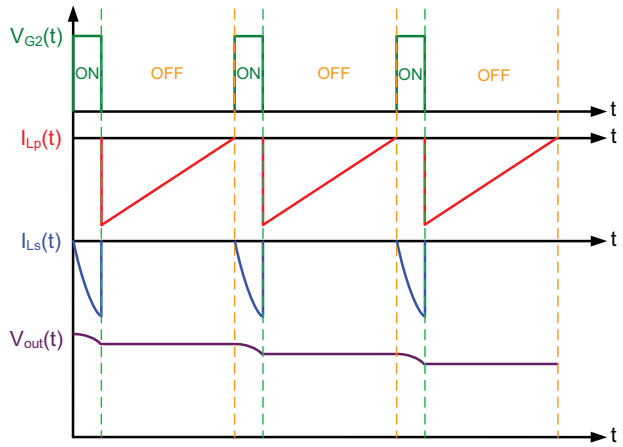

Figure 6. Waveforms in energy recovery process

2.2 SIMULATION VERIFICATION

For validating the analysis mentioned above, a bidirectional flyback converter simulation model has been established with PLECS (Piecewise Linear Electrical Circuit Simulation) software. In addition, a boundary operation mode and peak current control module is also built up. The detailed simulations parameters are shown in Table 1.

Table 1. Simulation parameters for bidirectional flyback converter

Simulation Parameters	Values
L_P	9 μH
L_S	21.36 mH
Capacitance of DEAP actuator	142 nF
Vin	3 V
Primary peak current	3.9 A
Secondary peak current	80 mA
N	48.7

a) Energy transfer process simulation

Figure 7 shows the whole charge process, in which the output voltage increases from 0 to 2.5kV.

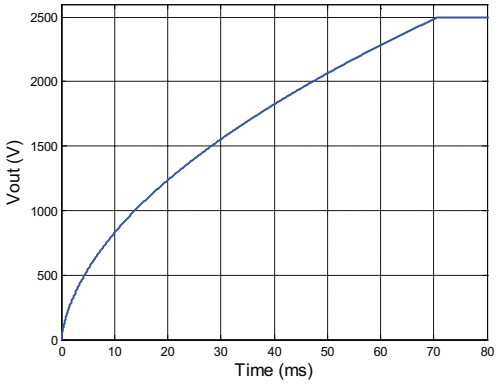

Figure 7. Simulated output voltage waveform in the energy transfer process

In the first several cycles, the current waveforms for both primary and secondary side are shown in Figure 8, which indicates that the boundary mode operation is achieved. Owing to the employment of boundary mode, the charge time is short, only less than 80ms.

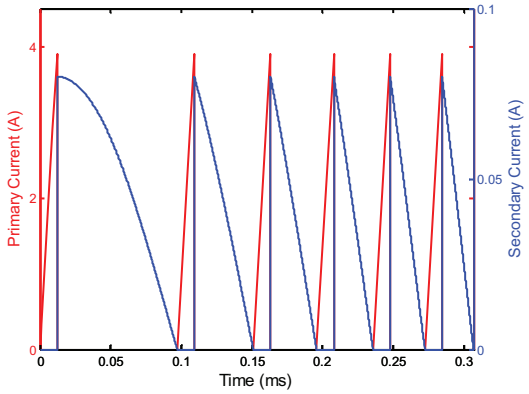

Figure 8. Simulated current waveform in the energy transfer process

b) Energy recovery process simulation

The output voltage decreases from 2.5kV to 0 in the energy recovery process, shown in Figure 9. And the current waveforms are provided in Figure 10, which also demonstrates the realization of boundary mode in discharge process.

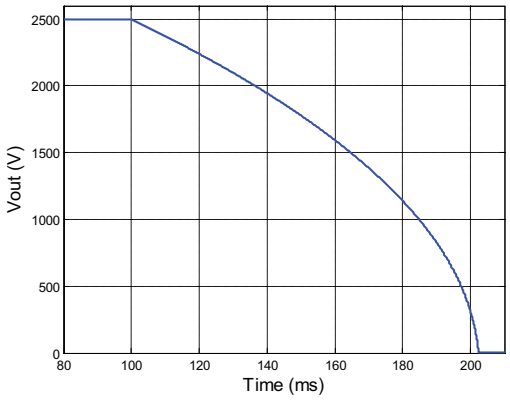

Figure 9. Simulated output voltage waveform in the energy recovery process

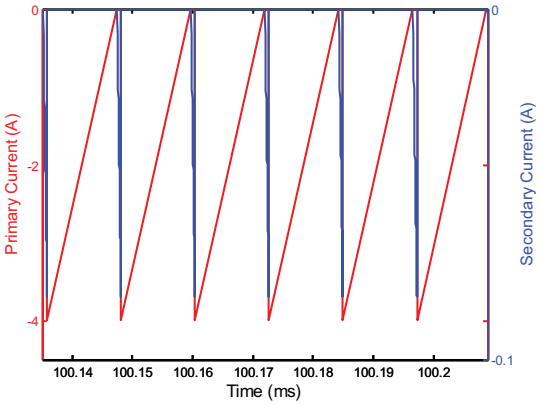

Figure 10. Simulated current waveform in the energy recovery process

3 UNIDIRECTIONAL FLYBACK DESIGN AND REALIZATION

A unidirectional flyback converter to drive DEAP actuator, shown in Figure 11, has been realized in the lab. Because of the voltage stress issue of S_1, a RC snubber and a RCD clamp circuits are employed [7].

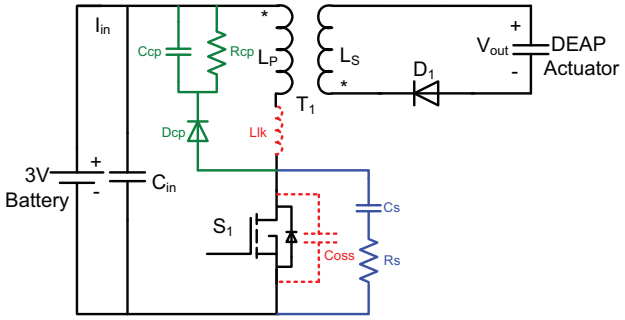

Figure 11. Unidirectional flyback converter

3.1 DESIGN PARAMETERS

The detailed design parameters are shown in Table 2, including the parameters of transformer, RC and RCD circuit.

Table 2. Design parameters for unidirectional flyback converter

Parameters	Values
Turns ratio (primary turns : secondary turns)	7:341
Core type (Core material)	EF20 (N67)
Air gap length	250 μm
Lp	9 μH
Ls	21.36 mH
Leakage inductance L_{lk}	750 nH
Capacitance of DEAP actuator	142 nF
Rs of RC snubber circuit	68.1 Ω
Cs of RC snubber circuit	220 pF
Rcp of RCD clamp circuit	20 kΩ
Ccp of RCD clamp circuit	1 μF

3.2 EXPERIMENTAL WAVEFORMS

The experimental waveforms are shown in Figure 12, Figure 13 and Figure 14. From Figure 12, it is clear to see the variable switching frequency which is caused by the boundary mode operation.

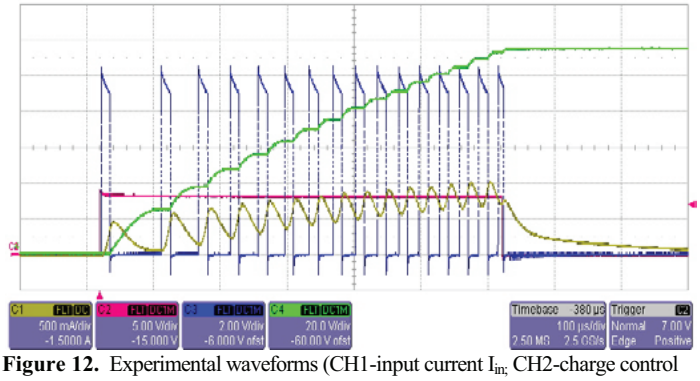

Figure 12. Experimental waveforms (CH1-input current I_{in}; CH2-charge control signal for converter; CH3-gate signal of S_1; CH4-output voltage)

The peak current control can be validated in Figure 13 and the whole energy transfer process is shown in Figure 14.

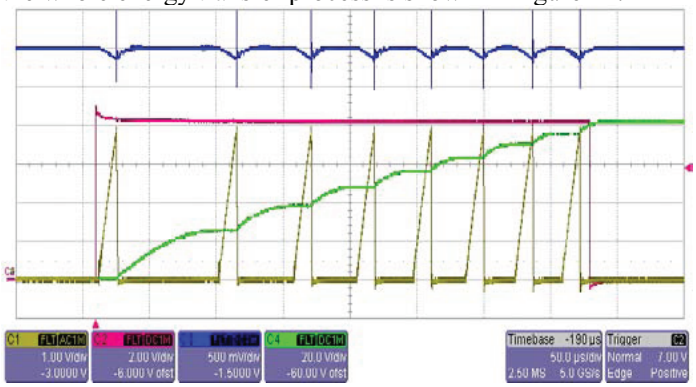

Figure 13. Experimental waveforms (CH1-primary winding current; CH2-charge control signal for converter; CH3-input voltage; CH4-output voltage)

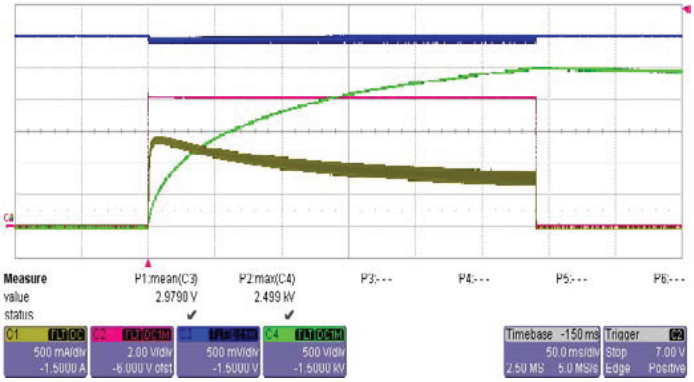

Figure 14. Experimental waveforms (CH1-input current I_{in}; CH2-charge control signal for converter; CH3-input voltage; CH4-output voltage)

4 CONCLUSION

A high voltage bidirectional flyback converter driving DEAP actuator is presented. The detailed analysis for both the energy transfer and the recovery process is discussed. The simulation results are provided to support analysis. In addition, a unidirectional flyback prototype has been implemented in the lab, which can charge DEAP actuator to 2.5kV.

REFERENCES

[1] M. Y. Benslimane, H. E. Kiil and M. J. Tryson, "Electro-mechanical properties of novel large strain PolyPower film and laminate components for DEAP actuator and sensor applications", Proceedings of SPIE, Vol. 7642, 2010.

[2] M. Y. Benslimane, H. E. Kiil and M. J. Tryson, "Dielectric electro-active polymer push actuators: performance and challenges", Polymer International, Vol. 59, No. 3, pp. 415-421, 2010.

[3] T. Andersen, M. S. Rødgaard, O. C. Thomsen and M. A. E. Andersen, "Low voltage driven dielectric electro active polymer actuator with integrated piezoelectric transformer based driver", Proceedings of SPIE, Vol. 7976, 2011.

[4] R. Sarban, R. W. Jones, B. R. Mace and E. Rustighi, "A tubular dielectric elastomer actuator: Fabrication, characterization and active vibration isolation", Mechanical Systems and Signal Processing, Vol.25 No. 8. , pp. 2879-2891, 2011.

[5] M. J. Tryson, R. Sarban, K. P. Lorenzen, "The dynamic properties of tubular DEAP actuators", Proceedings of SPIE, Vol. 7642, 2010.

[6] "LT3750 Capacitor Charger Controller Datasheet", Linear Technology Corporation, USA.

[7] "Application Note AN-4147 Design Guidelines for RCD Snubber of Flyback Converters", Fairchild Semiconductor Corporation, USA, 2006.

Appendix D

High Voltage Bi-directional Flyback Converter for Capacitive Actuator

---

15^{th} *European Conference on Power Electronics and Applications (EPE ECCE Europe 2013)*

High Voltage Bi-directional Flyback Converter for Capacitive Actuator

Prasanth Thummala, Zhe Zhang and Michael A. E. Andersen
TECHNICAL UNIVERSITY OF DENMARK
Oersteds Plads, Building 349
Kongens Lyngby, Denmark
Tel.: +45–45255764.
E-Mail: pthu@elektro.dtu.dk
URL: http://www.ele.elektro.dtu.dk

Keywords

«High voltage power converters», «Switched-mode power supply », «Energy efficiency», «Actuator», «Electroactive materials».

Abstract

This paper presents a high voltage DC-DC converter topology for bi-directional energy transfer between a low voltage DC source and a high voltage capacitive load. The topology is a bi-directional flyback converter with variable switching frequency control during the charge mode, and constant switching frequency control during the discharge mode. The converter is capable of charging the capacitive load from 24 V DC source to 2.5 kV, and discharges it to 0 V. The flyback converter has been analyzed in detail during both charge and discharge modes, by considering all the parasitic elements in the converter, including the most dominating parameters of the high voltage transformer viz., self-capacitance and leakage inductance. The specific capacitive load for this converter is a dielectric electro active polymer (DEAP) actuator, which can be used as an effective replacement for conventional actuators in a number of applications. In this paper, the discharging energy efficiency definition is introduced. The proposed converter has been experimentally tested with the film capacitive load and the DEAP actuator, and the experimental results are shown together with the efficiency measurements.

Introduction

High voltage power converters are widely used in medical, airborne and space applications with voltage range from 5 kV to 100 kV and with a power level of few tens of watts to several hundred kilowatts. A number of applications require a capacitive load to be charged to several thousands of volts. Such applications include pulsed lasers, pulsed sonar equipment, photo flash systems, electric fences, and plasma research, which require high voltage DC power supplies to efficiently charge a large capacitive load to high voltage. Design of efficient high voltage power supplies is very vital in terms of selection of converter configuration, switching frequency, and control strategy. All these vital aspects are very closely related to the high voltage transformer used in the power converter.

The focus of our research is to develop high voltage DC power supplies for DEAP actuators, which are a special type of capacitive actuators made with dielectric electro active material, and require high voltage (~2.5 kV) at relatively low current, to fully actuate them. The dielectric electro active polymer is a thin silicon elastomer film (~20-80 µm) sandwiched between two metallic electrodes. Due to requirement of very high electric field strength of >40 V/µm, the material needs high operating voltage to completely elongate the actuator [1]. DEAP technology has a wide potential in actuator, energy harvesting and sensor applications [2], [3] due to the material unique properties such as light weight, very low electrical power consumption, flexible nature, low noise and higher performance than competing technologies. DEAP actuators have some interesting applications in linear incremental motors, loud speakers, in-line heating valves, and wind turbine flaps, etc. [4], [5].

High voltage switch-mode power supplies for charging the capacitive loads have been implemented in [4]-[8]. In most of the papers the high output voltage was discharged by using a resistive load [7], an active discharge circuit [8], or with the high voltage probes (4 kV, 50 MΩ, <6 pF) [4], [5]. With these discharging methods, the reactive energy stored in the load capacitance is lost. If the output energy stored in the capacitive load is transferred back to the source, the lifetime of the source can be increased for battery powered applications. The energy stored in the load can be transferred to the source by discharging the capacitive load using a bi-directional DC-DC converter. The bi-directional flyback converters proposed in [9]-[11] perform the synchronous bi-directional operation to transfer the power in both directions. The operation and control of bi-directional flyback converter for charging and discharging a DEAP actuator is different from that of [9]-[11]. For this application, a new bi-directional flyback converter has been proposed and implemented to transfer the energy in both directions. It is to be noted that bi-directional in this application means either the energy flows from the source to the load or vice versa, but not at the same time.

Table I: Specifications of the proposed bi-directional flyback converter

Parameter	Target	Achieved
Input voltage (V_{in})	24 V	10-24 V
Output voltage (V_{out})	0-2500 V	0-2500 V
Peak charging efficiency (η_{cpk})	~ 90 %	~ 85 %
Peak discharging efficiency (η_{dpk})	~ 80 %	~ 79 %
117 nF capacitive load charging time to charge from 0 V to 2.5 kV (t_{ch1})	20 ms	21 ms
DEAP actuator charging time to charge from 0 V to 2.5 kV (t_{ch2})	20 ms	22 ms
117 nF capacitive load discharging time to discharge from 2.5 kV to 0 V (t_{dch1})	20 ms	16 ms
DEAP actuator discharging time to discharge from 2.5 kV to 0 V (t_{dch2})	20 ms	17 ms
DEAP actuator capacitance (C_{DEAP})	NA	117 nF
Charging switching frequency (f_{swc})	NA	~ 10-60 kHz
Discharging switching frequency (f_{swd})	NA	~ 25.6 kHz
Primary peak current during charging process (I_{ppk_ch}) / discharging process (I_{ppk_dch})	NA	4.24 A / 5.3 A
Stored energy in the capacitive load @ 2.5 kV	NA	0.37 J [Equivalent to 16 W charging power during 21 ms, and 22 W discharging power during 16 ms]

This paper focuses on the accurate analysis, design, component selection, and implementation of the 0-2.5 kV, low power bi-directional flyback converter. This paper illustrates a hard switched flyback converter topology that is capable of operating with reasonably good charging and discharging energy efficiencies over a wide operating output voltage range. The specifications of the bi-directional flyback converter are provided in Table I.

Converter design and analysis

In this section the high voltage bi-directional DC-DC converter, shown in Fig. 1 is discussed. High voltage unidirectional flyback converter for a normal resistive load is analyzed in [12] without considering all parasitic elements in the flyback converter. The converter operation during the charge and the discharge modes including all parasitic elements is analyzed in detail in this paper. Loss modeling of the proposed converter has been performed in [13] using the proposed accurate analysis. The approximated model of the flyback transformer from [14] either referred to primary or secondary is used in this paper for the analysis in each stage of charging and discharging processes (Fig. 3).

Topology

Flyback converter topology had been widely used because of its relatively simple structure and better performance for single or multiple output applications. It can save the cost and volume compared with the other converters. Flyback converter is a well-suited topology for low power (< 200 W) and high output voltage applications. Some high voltage applications of flyback converter are in cathode ray tube (CRT) for televisions, monitors and in xenon flash lamps for exciting the xenon gas.

The power stage of Fig. 1a can be divided into three parts: primary stage, high voltage flyback transformer and secondary stage. The primary stage consists of a DC voltage source, input capacitor C_{in}, and low voltage MOSFET M_1. The flyback transformer with 1: n turns ratio is provided with an air gap, to store the energy in the magnetizing winding when the switch M_1 is turned ON. In the transformer model shown in Fig. 1b, L_{mp}, C_p, C_{int}, C_s, L_{lkp}, L_{lks}, R_p, and R_s represent the primary magnetizing inductance, primary self-capacitance, interwinding capacitance, secondary self-capacitance, primary and secondary leakage inductances, primary DC resistance, and secondary DC resistances, respectively. The secondary stage consists of high voltage MOSFET M_2, high voltage diode D_2, which is required as the body diode of M_2 has very high reverse recovery time (t_{rr}=2.8 µs), another high voltage diode D_b added in series with the drain of M_2, to block the body diode of M_2 during the discharging process, and a high voltage capacitive load C_{out}.

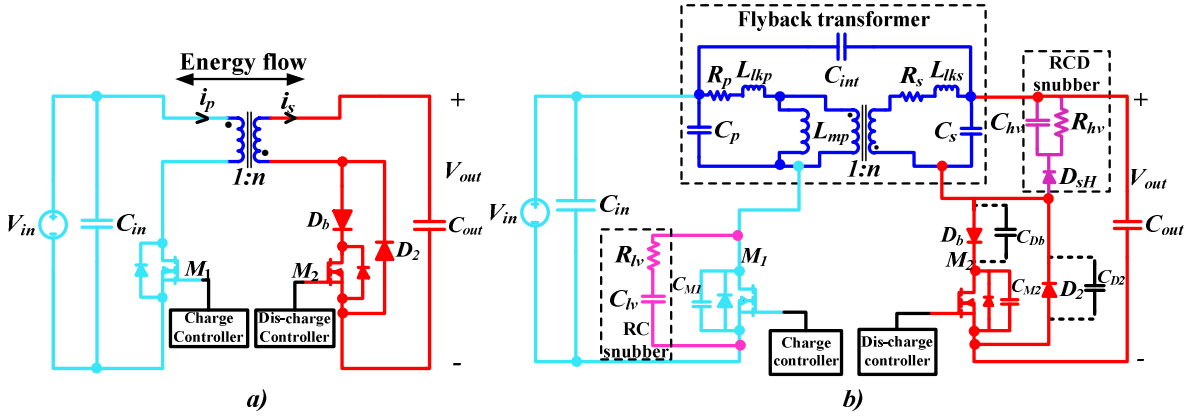

Fig. 1: Circuit configuration of the high voltage bi-directional flyback converter (*a*); with equivalent transformer model, and RC snubber on low voltage side and RCD snubber on high voltage side (*b*).

If a snubber circuit is not used in the flyback converter, then the stored energy in the leakage inductance is dissipated in the MOSFET resulting in large voltage spikes across it. In this capacitor charging application, on the primary side only a RC snubber has been used which can damp the high frequency oscillations in the drain voltage waveform, when the switch is OFF. The RCD snubber on the low voltage side can be skipped by either using an overrated low voltage MOSFET M_1 or by reducing the transformer leakage inductance. The stray capacitance of the transformer contributes to capacitive switching loss. We are investigating how to reduce both the leakage inductance and stray capacitance of the flyback transformer, and to make a trade-off between them for this high voltage capacitor charging application [13]. On the high voltage side a RCD snubber has been used to protect the high voltage MOSFET M_2 from the voltage spikes due to the secondary leakage inductance during discharging. As the maximum drain voltage of M_2 used in the converter is 4 kV, and with 24 V as input voltage and n=25 as the turns ratio, the maximum drain voltage of M_2 excluding the voltage increase due to secondary leakage inductance, at 2.5 kV output voltage is 3.1 kV. If the leakage inductance of the flyback transformer secondary is considered, the voltage seen by the drain of M_2 will be higher than by a factor of $\left[I_{spk} \cdot \left(\sqrt{\frac{C_{\sec 2}}{L_{lks}} - \left(\frac{R_s}{2L_{lks}} \right)^2 C_{\sec 2}^{\,2}} \right)^{-1} \right]$ (see (12)). Even though a passive snubber (RC or RCD) protects the MOSFET, it results in high power loss. To eliminate this power loss, active snubber circuits can be used at the cost of extra components. The circuit configuration of the practical

flyback converter with the transformer equivalent model and the low and high voltage snubber circuits is shown in Fig. 1b.

Converter analysis during charging process

A soft-switched flyback converter is analyzed in [6] for high voltage capacitor charging application. While charging the capacitive load the proposed converter operates in the boundary mode (boundary between CCM and DCM), with peak current control using LT3751 [15]. The MOSFET M_1 is turned OFF when the primary current reaches the peak current I_{ppk}. The waveforms of the converter during the charge operation are shown in Fig. 2a. In general, self-capacitance of the transformer low voltage winding (C_p) is very small compared to that of the high voltage winding, and hence can be neglected. One complete switching period T_s, during the charge mode can be divided into four stages. These stages operate continuously until the desired output voltage is reached. The first stage will begin after the transformer primary has finished storing the energy or when the primary MOSFET is turned OFF.

Stage 1 [$t_0 < t \leq t_1$]

During this stage the MOSFET M_1 is OFF and the high voltage diode D_2 is blocked. The equivalent parasitic capacitance referred to the primary side (C_{pri}) when both the switch M_1 and the diode D_2 are OFF, is the parallel combination of the output capacitance of M_1, the transformer secondary self-capacitance referred to the primary side, and the equivalent reflected parasitic capacitance of high voltage diodes (M_2 is OFF during the charging process), and is given by

$$C_{pri} = \left[C_{M_1} + \left(C_s + C_{D_2} + \frac{C_{D_b} C_{M_2}}{C_{D_b} + C_{M_2}} \right) n^2 \right] \tag{1}$$

The magnetizing current i_p charges the equivalent parasitic capacitance C_{pri1}=C_{pri} in a resonant manner. The current through the magnetizing inductance L_{mp} is $\left(i_{C_{pri1}}(t) = -i_p(t) \right)$

$$i_p(t) = -C_{pri1}\, e^{-\alpha_{0C}(t-t_0)} \left[\left(K_{0C}\beta_{0C} - V_{in}\alpha_{0C} \right) \cos\left(\beta_{0C}(t-t_0) \right) - \left(K_{0C}\alpha_{0C} + V_{in}\beta_{0C} \right) \sin\left(\beta_{0C}(t-t_0) \right) \right] \tag{2}$$

The voltage across the transformer primary winding is

$$\begin{gathered} V_{C_{pri1}}(t) = e^{-\alpha_{0C}(t-t_0)} \left[V_{in} \cos\left(\beta_{0C}(t-t_0) \right) + K_{0C} \sin\left(\beta_{0C}(t-t_0) \right) \right];\; V_{C_{pri1}}(t_0) = V_{in};\; V_{C_{pri1}}(t_1) = \frac{-\left(V_{out}(t_0) + V_{HVd} \right)}{n} \\ \alpha_{0C} = \frac{R_P}{2L_{mp}};\; \beta_{0C} = \sqrt{\left(\frac{1}{L_{mp} C_{pri1}} - \alpha_{0C}^2 \right)};\; K_{0C} = \frac{1}{\beta_{0C}} \left(V_{in}\alpha_{0C} - \frac{I_{ppk}}{C_{pri1}} \right);\; i_p(t_0) = i_p(t_1) = i_{M_1}(t_0) = I_{ppk};\; i_{M_1}(t_1) = 0 \end{gathered} \tag{3}$$

Stage 2 [$t_1 < t \leq t_2$]

During this stage the voltage across the primary winding of the transformer is clamped to the reflected voltage of $-\left(V_{out}(t_0) + V_{HVd} \right)/n$. The diode in the secondary side is turned-ON and the magnetizing current flows to the secondary side, and delivers the energy stored in L_{mp} to the output capacitor C_{out}.

The primary leakage and secondary currents, and voltage across drain of M_1, and the output voltage are

$$\begin{gathered} i_{lkp}(t) = I_{ppk} e^{-\alpha_{2C}(t-t_1)} \left[\cos\left(\beta_{2C}(t-t_1) \right) - \frac{\alpha_{2C}}{\beta_{2C}} \sin\left(\beta_{2C}(t-t_1) \right) \right];\; V_{M_1}(t) = V_{in} + \frac{\left(V_{out}(t_1) + V_{HVd} \right)}{n} + \frac{I_{ppk}}{\beta_{2C} C_{M_1}} e^{-\alpha_{2C}(t-t_1)} \sin\left(\beta_{2C}(t-t_1) \right) \\ i_s(t) = C_{out}\, e^{-\alpha_{1C}(t-t_1)} \left[\left(K_{1C}\beta_{1C} - \left(V_{out}(t_1) + V_{HVd} \right)\alpha_{1C} \right) \cos\left(\beta_{1C}(t-t_1) \right) - \left(K_{1C}\alpha_{1C} + \left(V_{out}(t_1) + V_{HVd} \right)\beta_{1C} \right) \sin\left(\beta_{1C}(t-t_1) \right) \right] + \frac{i_{lkp}(t)}{n} \\ V_{out}(t) = \left\{ e^{-\alpha_{1C}(t-t_1)} \left[\left(V_{out}(t_1) + V_{HVd} \right) \cos\left(\beta_{1C}(t-t_1) \right) + K_{1C} \sin\left(\beta_{1C}(t-t_1) \right) \right] - V_{HVd} \right\};\; \alpha_{1C} = \frac{R_s + r_{HVd}}{2\left(L_{ms} + L_{lks} \right)};\; \alpha_{2C} = \frac{R_p}{2L_{lkp}} \\ \beta_{1C} = \sqrt{\left(\frac{1}{\left(L_{ms} + L_{lks} \right) C_{out}} - \alpha_{1C}^2 \right)};\; \beta_{2C} = \sqrt{\left(\frac{1}{L_{lkp} C_{M_1}} - \alpha_{2C}^2 \right)};\; K_{1C} = \frac{1}{\beta_{1C}} \left(\left(V_{out}(t_1) + V_{HVd} \right)\alpha_{1C} + \frac{I_{spk}}{C_{out}} \right) \end{gathered} \tag{4}$$

where V_{HVd} and r_{HVd} are the voltage drop and resistance of the high voltage diode $(D_2$ or $D_b)$ respectively. This stage ends when the secondary current falls to 0 A, and $C_{pri2} = C_{M_1}$ (Fig. 3).

Stage 3 [$t_2 < t \leq t_3$]

This stage occurs after the energy stored in L_{mp} is completely transferred to the output capacitor C_{out}. In this stage the output capacitance of M_1 resonates with the magnetizing inductance L_{mp} by bringing the voltage across M_1 close to 0 V. In this stage, the equivalent reflected capacitance C_{pri3}=C_{pri1}=C_{pri} discharges through M_1 and $i_{C_{pri3}}(t) = -i_p(t)$.

The current through the magnetizing inductance and voltage across the primary winding are

$$\begin{aligned} i_p(t) &= e^{-\alpha_{0C}(t-t_2)}\left(\frac{-\left(V_{out}(t_2)+V_{HVd}\right)}{n}\right)\left[\frac{1}{L_{mp}\beta_{0C}}\sin\left(\beta_{0C}(t-t_2)\right)\right] \\ V_{C_{pri3}}(t) &= e^{-\alpha_{0C}(t-t_2)}\left(\frac{-\left(V_{out}(t_2)+V_{HVd}\right)}{n}\right)\left[\cos\left(\beta_{0C}(t-t_2)\right)+\frac{\alpha_{0C}}{\beta_{0C}}\sin\left(\beta_{0C}(t-t_2)\right)\right];\ V_{C_{pri3}}(t_3) = V_{in} \end{aligned} \tag{5}$$

The voltage across MOSFET M_1 is

$$V_{M_1}(t) = V_{in} + V_{C_{pri3}}(t);\ V_{M_1}(t_3) = 0 \tag{6}$$

By solving (5) and (6), and using α_{0C} and β_{0C} from (3)

$$\sin\left(\beta_{0C}(t_3-t_2)\right) = G\cdot\frac{\beta_{0C}}{w_{0C}^2}\left[\alpha_{0C}+\sqrt{\frac{w_{0C}^2}{G^2}-\beta_{0C}^2}\right];\ G = \frac{V_{in}\cdot n}{\left(V_{out}(t_2)+V_{HVd}\right)e^{-\alpha_{0C}(t_3-t_2)}};\ w_{0C} = \sqrt{\frac{1}{L_{mp}C_{pri3}}} \tag{7}$$

The peak negative amplitude of the equivalent capacitor C_{pri3} current at the time t_3 is

$$\left|i_{C_{pri3}}(t_3)\right| = \frac{V_{in}}{L_{mp}}\left[\frac{R_P C_{pri3}}{2}+\frac{1}{w_{0C}}\sqrt{G^2-\frac{\beta_{0C}^2}{w_{0C}^2}}\right] \tag{8}$$

Stage 4 [$t_3 < t \leq T_s$]

Stage 4 begins when M_1 is turned-ON by the controller under ZVS conditions. The current through the MOSFET M_1 flows in the negative direction (Fig. 2a) through its body diode for a short time, and then it continue to flow through M_1. The currents through C_{pri4}, transformer primary and MOSFET M_1 are

$$\begin{aligned} i_{C_{pri4}}(t) &= C_{pri4}\ e^{-\alpha_{3C}(t-t_3)}\left[\frac{i_{C_{pri3}}(t_3)}{C_{pri4}}\cos\left(\beta_{3C}(t-t_3)\right)-\left(K_{3C}\alpha_{3C}+\left(V_{C_{pri}}(t_3)-V_{in}\right)\beta_{3C}\right)\sin\left(\beta_{3C}(t-t_3)\right)\right] \\ i_p(t) &= \left[\frac{V_{in}}{R_p+r_{dson1}}+\left(i_p(t_3)-\frac{V_{in}}{R_p+r_{dson1}}\right)e^{-\frac{R_p+r_{dson1}}{L_{mp}+L_{lkp}}(t-t_3)}\right]-\frac{L_{lkp}}{L_{mp}}i_{C_{pri4}}(t)\ ;\ i_{M_1}(t) = i_p(t)+i_{C_{pri4}}(t) \\ \alpha_{3C} &= \frac{r_{dson1}}{2L_{lkp}};\ \beta_{3C} = \sqrt{\left(\frac{1}{L_{lkp}C_{pri4}}-\alpha_{3C}^2\right)};\ K_{3C} = \frac{1}{\beta_{3C}}\left(\left(V_{C_{pri3}}(t_3)-V_{in}\right)\alpha_{3C}+\frac{i_{C_{pri3}}(t_3)}{C_{pri4}}\right);\ C_{pri4} = n^2\cdot\left(C_s+C_{M_2}+C_{D_2}\right) \end{aligned} \tag{9}$$

Converter analysis during discharging process

The same controller LT3751 [15] is used in the proposed bi-directional flyback converter for discharging the capacitive load. During discharging process, the converter operates in the discontinuous conduction mode (DCM) with constant switching frequency. The converter waveforms during the discharging operation are shown in Fig. 2b. The capacitive load is discharged when the high voltage MOSFET M_2 is turned ON, and transfer the energy stored in the secondary magnetizing winding L_{ms} to the source, through the body diode of M_1, when M_2 is OFF. As the output voltage discharges, the ON-

time of the high voltage MOSFET M_2 increases, and OFF-time is constant with a value of $L_{mp}i_{ppk\_dch}/V_{in}$. At the end of the discharging process M_2 is completely turned ON. The switching period T_s during discharging operation can be divided into 5 stages. The Stage 1 begins once the secondary magnetizing inductance L_{ms} of the transformer has finished storing the energy.

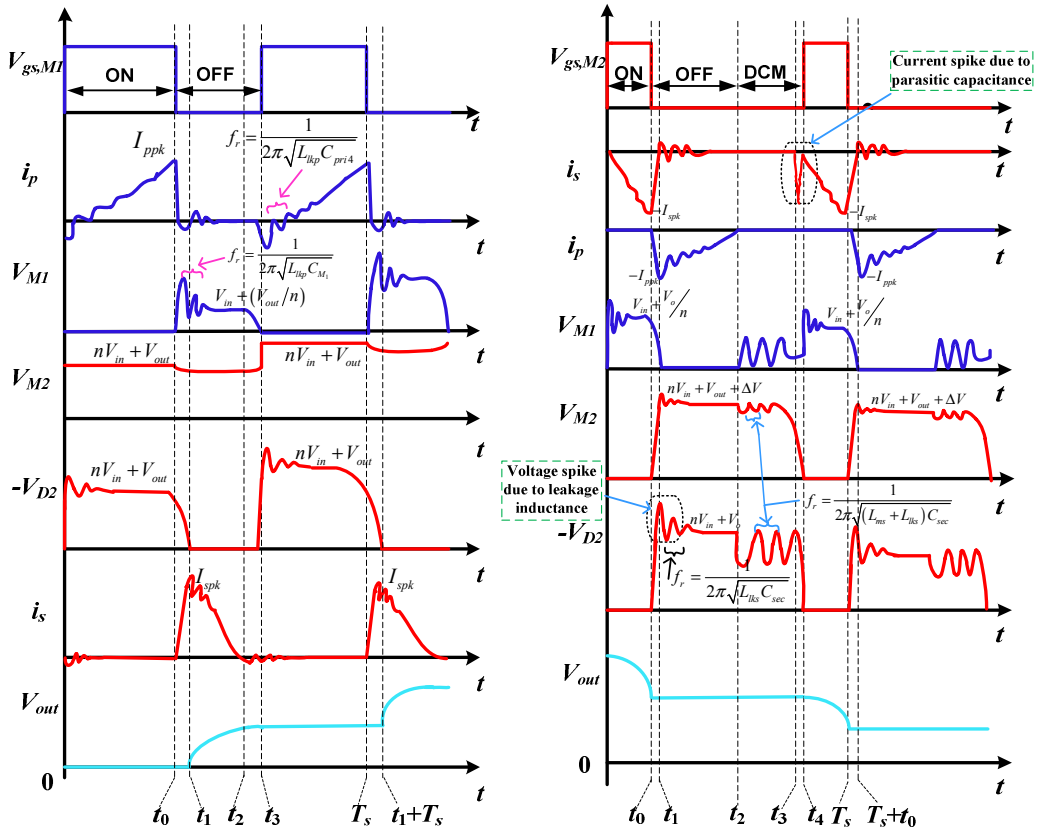

Fig. 2: Charging (a) and discharging (b) waveforms of the proposed converter.

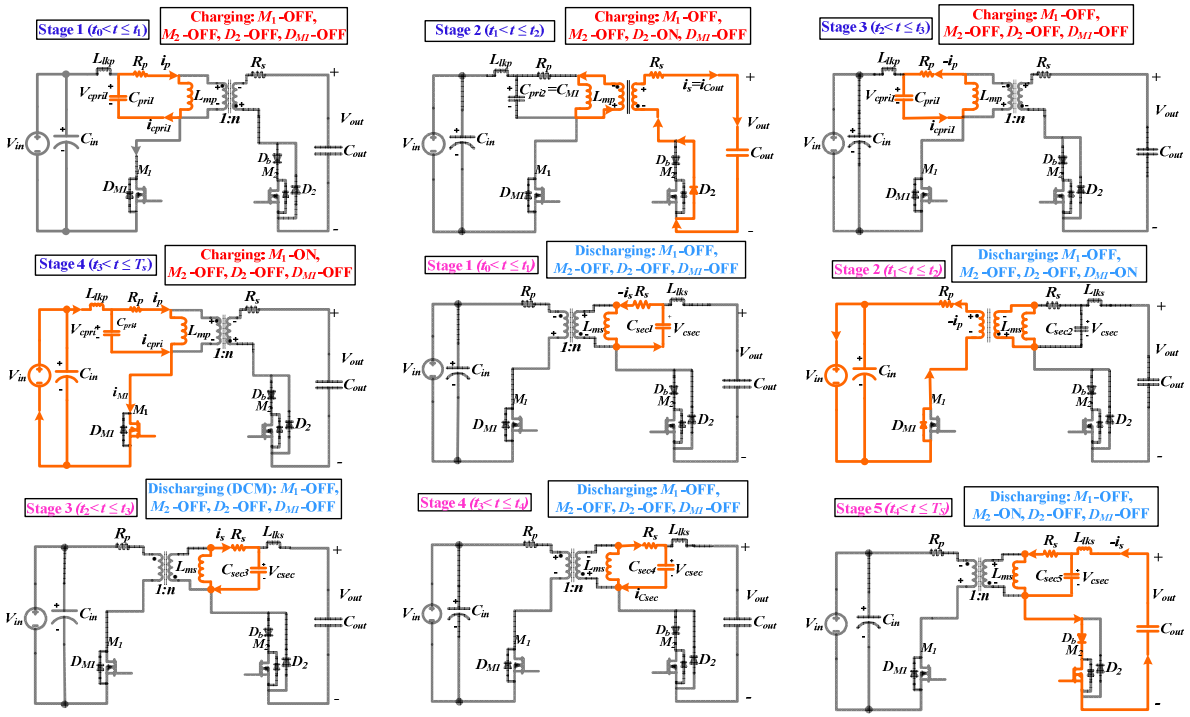

Fig. 3: All charging and discharging stages in one respective charging and discharging switching cycle

Stage 1 [$t_0 < t \le t_1$]

The high voltage MOSFET M_2 is turned OFF at time $t=t_0$. The secondary magnetizing inductance (L_{ms}) in series with the secondary leakage inductance (L_{lks}) resonates with the equivalent parasitic capacitance referred to the secondary side C_{sec}.

$$C_{sec} = C_{M_2} + C_s + C_{D_2} + \frac{C_{D_b} C_{M_2}}{C_{D_b} + C_{M_2}} \tag{10}$$

The voltage across the transformer secondary winding and peak secondary current are

$$\begin{aligned} &V_{C_{\sec}}(t) = e^{-\alpha_{0D}(t-t_o)}\left[V_{out}(t_0)\cos\left(\beta_{0D}(t-t_o)\right) + K_{0D}\sin\left(\beta_{0D}(t-t_o)\right)\right];\ V_{C_{\sec}}(t_1) = -nV_{in} \\ &\alpha_{0D} = \frac{R_S}{2L_{ms}};\ \beta_{0D} = \sqrt{\left(\frac{1}{L_{ms}\,\mathrm{C}_{\sec}} - \alpha_{0D}^2\right)};\ K_{0D} = \frac{1}{\beta_{0D}}\left(V_{out}(t_0)\alpha_{0D} + \frac{I_{spk}}{C_{\sec}}\right) \\ &I_{spk} = \sqrt{I_{spk\_design}^2 + \left(C_{\sec}/L_{ms}\right)V_{out}^2} \end{aligned} \tag{11}$$

where I_{spk} is the actual secondary peak current, I_{spk_design} is the design value of the secondary peak current or M_2 turn OFF current. If the energy stored in the equivalent parasitic capacitance C_{sec} $\left(0.5 \cdot C_{sec} V_{out}^2\right)$, is higher than the energy stored in the secondary winding inductance L_{ms} $\left(0.5 \cdot L_{ms} I_{spk\_des}^2\right)$, then the secondary peak current will be greater than the M_2 turn OFF current.

Stage 2 [$t_1 < t \le t_2$]

During this stage the voltage across the secondary winding of the transformer is clamped to $-nV_{in}$. The body diode of M_1 in the primary side conducts and the magnetizing current flows to the primary side, in the reverse direction delivering the output energy to the source. The stage ends when the primary current falls to 0 A.

The secondary leakage and primary currents, and voltage across diode D_2 are

$$\begin{aligned} &i_{lks}(t) = I_{spk} e^{-\alpha_{1D}(t-t_1)}\left[\cos\left(\beta_{1D}(t-t_1)\right) - \frac{\alpha_{1D}}{\beta_{1D}}\sin\left(\beta_{1D}(t-t_1)\right)\right];\ \alpha_{1D} = \frac{R_s}{2L_{lks}} \\ &V_{D_2}(t) = nV_{in} + V_{out}(t_1) + \frac{I_{spk}}{\beta_{1D} C_{\sec 2}} e^{-\alpha_{1D}(t-t_1)}\sin\left(\beta_{1D}(t-t_1)\right);\ \beta_{1D} = \sqrt{\left(\frac{1}{L_{lks} C_{\sec 2}} - \alpha_{1D}^2\right)} \\ &i_p(t) = \left[\frac{V_{in} + V_{LVd}}{R_p}\left(1 - e^{-\frac{R_p}{L_{mp}+L_{lkp}}(t-t_1)}\right)\right] - n \cdot i_{lks}(t);\ V_{out}(t_1) = V_{out}(t_0);\ \mathrm{C}_{\sec 2} = \mathrm{C}_{\mathrm{M}_2} + \mathrm{C}_s + \mathrm{C}_{\mathrm{D}_2} \end{aligned} \tag{12}$$

Stage 3 [$t_2 < t \le t_3$]

This stage occurs when the primary current becomes zero. In this stage the converter operates in DCM. The secondary inductance (L_{ms}) resonates with the equivalent secondary parasitic capacitance $C_{sec3}=C_{sec}$. The voltage V_{LVd} in (13) is the voltage drop of the body diode of M_1.

The voltages across C_{sec3} and the drain of M_2, and the current through C_{sec3} are

$$\begin{aligned} &V_{C_{\sec}}(t) = -\left[n\left(V_{in} + V_{LVd}\right)\right] \cdot e^{-\alpha_{2D}(t-t_2)}\left[\cos\left(\beta_{2D}(t-t_2)\right) + \frac{\alpha_{2D}}{\beta_{2D}}\sin\left(\beta_{2D}(t-t_2)\right)\right];\ i_{C_{\sec}}(t) = C_{\sec 3}\frac{dV_{C_{\sec}}(t)}{dt} \\ &V_{M_2}(t) = V_{out}(t_1) + V_{C_{\sec}}(t) - V_{D_b}(t);\ V_{M_1} = V_{in} + \left(\frac{V_{C_{\sec}}(t)}{n}\right);\ \alpha_{2D} = \alpha_{0D};\ \beta_{2D} = \sqrt{\left(\frac{1}{L_{ms} C_{\sec 3}}\right)^2 - \alpha_{2D}^2} \end{aligned} \tag{13}$$

Stage 4 [$t_3 < t \le t_4$]

In this stage the equivalent parasitic capacitance $C_{sec4}=C_{sec}$ resonates with the secondary magnetizing inductance L_{ms} by bringing the voltage across M_2 to 0 V.

The current through the equivalent parasitic capacitance C_{sec4} is given by

$$i_{C_{sec}}(t) = -e^{-\alpha_{0D}(t-t_3)}\left[\frac{V_{C_{sec}}(t_3)}{L_{ms}\beta_{0D}}\sin\left(\beta_{0D}(t-t_3)\right)\right] \tag{14}$$

Stage 5 [$t_4 < t \le T_s$]

This stage begins when M_2 is turned-ON by the controller. The current not only flows through the magnetizing inductance L_{ms}, but also through the equivalent parasitic capacitance $C_{\sec 5} = C_s + C_{D_2}$.

The currents through C_{sec5}, L_{ms} and the MOSFET M_2, and the output voltage are

$$\begin{aligned}
&i_{C_{sec}}(t) = -C_{pri5}\, e^{-\alpha_{5D}(t-t_4)}\left[\left(K_{5D}\beta_{5D} - V_{out}(t_1)\alpha_{5D}\right)\cos\left(\beta_{5D}(t-t_4)\right) - \left(K_{5D}\alpha_{5D} + V_{out}(t_1)\beta_{5D}\right)\sin\left(\beta_{5D}(t-t_4)\right)\right]\\
&V_{out}(t) = e^{-\alpha_{4D}(t-t_4)}\left[\left(V_{out}(t_1) - V_{HVd}\right)\cos\left(\beta_{4D}(t-t_4)\right) + K_{4D}\sin\left(\beta_{4D}(t-t_4)\right)\right] + V_{HVd}\\
&i_s(t) = \left[-C_{out}\frac{dV_{out}(t)}{dt} - \frac{L_{lks}}{L_{ms}}i_{C_{sec}}(t)\right];\ i_{M_2}(t) = i_s(t) + i_{C_{sec}}(t);\ V_{out}(t_4) = V_{out}(t_3) = V_{out}(t_2) = V_{out}(t_1)\\
&\alpha_{4D} = \frac{r_{dson2} + R_S + r_{HVd}}{2\left(L_{ms} + L_{lks}\right)};\ \beta_{4D} = \sqrt{\left(\frac{1}{\left(L_{ms} + L_{lks}\right)C_{out}} - \alpha_{4D}^2\right)};\ K_{4D} = \frac{1}{\beta_{4D}}\left(\left(V_{out}(t_1) - V_{HVd}\right)\alpha_{4D} - \frac{i_{C_{sec}}(t_4)}{C_{out}}\right)\\
&\alpha_{5D} = \alpha_{1D},\ \beta_{5D} = \sqrt{\left(\frac{1}{L_{lks}C_{\sec 5}} - \alpha_{5D}^2\right)};\ K_{5D} = \frac{1}{\beta_{5D}}\left(V_{out}(t_1)\alpha_{5D} - \frac{i_{C_{sec}}(t_4)}{C_{\sec 5}}\right)
\end{aligned} \tag{15}$$

These stages operate continuously until the output voltage is discharged to $I_{spk\_dch}\sqrt{L_{ms}/C_{out}}$, which is the minimum voltage required to store the energy in L_{ms} during the discharging process. At this point the MOSFET M_2 is completely ON, since the secondary current becomes zero, and L_{ms} resonates with C_{out}.

Controller description, component selection and transformer design

Possible control techniques for the capacitor charging flyback converter have been discussed in [16]. For achieving 2.5 kV bi-directional operation, the capacitor charger controller from Linear Technology [15] has been chosen as charge and discharge controllers.

Variable frequency during charging and Constant frequency during discharging

The primary inductance store the energy with constant ON-time at low output voltages, and with variable ON-time at high output voltages. The discharging time of M_1 decreases with the increase in the output voltage, which increases the switching frequency during the charging process. During discharging process, the control IC needs to sense the output voltage to operate in the boundary mode. But the controller LT3751 is not designed for wide input voltage variations (2.5 kV to 0 V is too wide operating range). So, we operated the IC in the start-up protection mode without giving the output voltage feedback to it, and the IC is operated with a constant switching frequency of ~ 25.6 kHz.

Component selection and Transformer design

The components used for the implementation of the bi-directional flyback converter are given Table 2. The flyback transformer is designed with the ETD 29 core and the measured parameters of the transformer are provided in Table 3. The transformer should be designed without saturating the magnetic core during both the charging as well as the discharging processes.

Experimental results

The experimental results of the bi-directional flyback converter are shown in Figs. 4 and 5. Fig. 4 shows the zoomed waveforms during charging and discharging operations respectively, and Fig. 5 shows the waveforms of the continuous charging and discharging operation of the flyback converter for

the film capacitive load and the DEAP actuator respectively. The charging energy efficiency is defined as, the ratio of energy stored in the capacitive load, to the energy input to the converter during charging process [17]. The discharging energy efficiency is defined as, the ratio of energy recovered back to the source, to the energy input during the discharging process (which is the energy stored in the capacitive load). The charging η_{charge} and discharging $\eta_{discharge}$ energy efficiency expressions are given below.

$$\eta_{charge} = \frac{0.5 \cdot C_{out} V_{out}^2}{\int_0^{T_{charge}} V_{in}\ i_{in\_charge}\ dt} \tag{17}$$

$$\eta_{discharge} = \frac{\int_{T_{charge}+T_{delay}}^{T_{discharge}} V_{in}\ i_{in\_discharge}\ dt}{0.5 \cdot C_{out} V_{out}^2} \tag{18}$$

where T_{charge} and $T_{discharge}$ are the charging and discharging times of the capacitive load respectively (T_{delay} is a delay between the charging and discharging processes). The input supply current during charging is i_{in_charge} and the recovered input current during discharging is $i_{in\_discharge}$. The energy efficiency curves are given in Fig. 6.

Table II: Components used in the converter

Component	Name
Low voltage / High voltage MOSFET	STB50NF25 [250 V, 45 A, 55 mΩ] / IXTV03N400S [4 kV, 300 mA, 290 Ω]
High voltage diode	SXF6525 [5 kV, 150 mA, 70 ns (t_{rr})]

Table III: Flyback transformer parameters

Parameter	Value
Primary (L_{mp}) / Secondary magnetizing inductance (L_{ms})	44 µH / 28 mH
Flyback transformer core / Material	ETD 29 / N87
Primary turns (N_p) / Turns ratio (n)	10 / 25
Leakage inductance of transformer primary (L_{lkp}) / secondary winding (L_{lks})	930 nH / 647 µH
Secondary winding (C_s) / Inter-winding stray capacitance (C_{int})	26 pF / 26.2 pF
DC resistance of primary (R_p) / secondary winding (R_s)	60 mΩ / 7.6 Ω

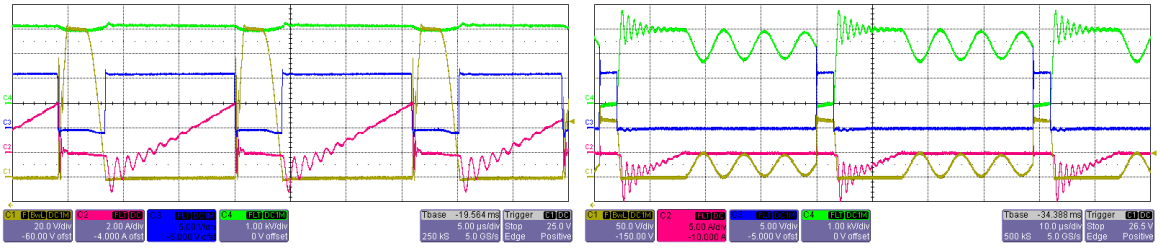

Fig. 4: Zoomed waveforms during charging operation (left)- CH1:$V_{drainM1}$; CH2: i_p ; CH3: V_{GateM1}; CH4: $V_{drainM2}$ and discharge operation (right)- CH1:$V_{drainM1}$; CH2: i_p ; CH3: V_{GateM2}; CH4: V_{D2}

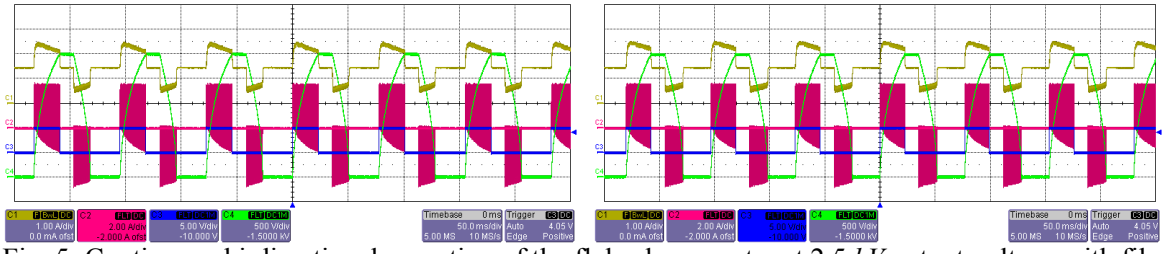

Fig. 5: Continuous bi-directional operation of the flyback converter at 2.5 kV output voltage with film capacitive load (left), and with DEAP actuator (right) - CH1: i_{in} ; CH2:i_p ; CH3:$V_{charge1}$; CH4: V_{out}

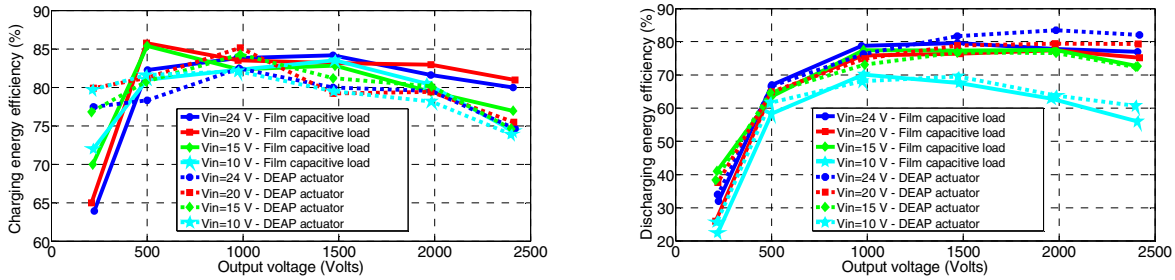

Fig. 6: Charging energy efficiency (left) and discharging energy efficiency curves (right)

Conclusion

The bi-directional flyback converter was successfully implemented for high voltage capacitor charging application. The converter was operating with 80-85% charging and 70-80% discharging energy efficiencies. Careful design of the flyback transformer is required for successful implementation of high voltage bi-directional flyback converter, without damaging the high voltage 4 kV MOSFET.

References

[1] M. Tryson, H. E. Kiil, M. Benslimane, "Powerful tubular core free dielectric electro activate polymer (DEAP) push actuator," in *Proc. SPIE*, vol. 7287, p. 72871F, 2009.

[2] R. Pelrine, P. Sommer-Larsen, R. Kornbluh, R. Heydt, G. Kofod, Q. Pei, P. Gravesen, "Applications of dielectric elastomer actuators," in *Proc. SPIE*, vol. 4329, pp. 335-349, 2001.

[3] http://www.polypower.com

[4] P. Thummala, L. Huang, Z. Zhang, M. A. E. Andersen, "Analysis of Dielectric Electro Active Polymer Actuator and its High Voltage Driving Circuits," in *Proc. IEEE IPMHVC,* pp. 458-461, Jun. 4-7, 2012.

[5] P. Thummala, Z. Zhang, M. A. E. Andersen, O. C. Thomsen, "A high voltage DC-DC converter driving a Dielectric Electro Active Polymer actuator for wind turbine flaps," in *Proc. IEEE UPEC,* pp.1-7, 4-7 Sept. 2012.

[6] J. Elmes, C. Jourdan, O. Abdel-Rahman, I. Batarseh, "High-Voltage, High-Power-Density DC-DC Converter for Capacitor Charging Applications," in *Proc. IEEE APEC*, pp. 433-439, 2009.

[7] T. Andersen, M. S. Rødgaard, O. C. Thomsen, M. A. E. Andersen, "Low voltage driven dielectric electro active polymer actuator with integrated piezoelectric transformer based driver," in *Proc. SPIE*, vol. 7976, p. 79762N, 2011.

[8] S. K. Chung, H. B. Shin, "High-voltage power supply for semi-active suspension system with ER-fluid damper," in *Proc. IEEE Transactions on Vehicular Technology*, vol. 53, no. 1, pp. 206- 214, Jan. 2004.

[9] K. Venkatesan, "Current Mode Controlled Bidirectional Flyback Converter," in *Proc. IEEE PESC*, pp. 835-842, 1989.

[10] T. Bhattacharya, V. S. Giri, K. Mathew, L. Umanand, "Multiphase Bidirectional Flyback Converter Topology for Hybrid Electric Vehicles,", in *Proc. IEEE Transactions on Industrial Electronics*, vol. 56, no.1, pp.78-84, Jan. 2009.

[11] G. Chen, Y.-S. Lee, S.Y.R. Hui, D. Xu, Y. Wang, "Actively clamped bidirectional flyback converter," in *Proc. IEEE Transactions on Industrial Electronics*, vol. 47, no. 4, pp. 770-779, Aug. 2000.

[12] S.-S. Hong, S.-K. Ji, Y.-J. Jung, C.-W. Roh, "Analysis and Design of a High Voltage Flyback Converter with Resonant Elements," in *Proc. Journal of Power Electronics*, vol. 10, no. 2, pp. 107-114, Mar. 2010.

[13] P. Thummala, H. Schneider, Z. Ouyang, Z. Zhang, M. A. E. Andersen, "Estimation of Transformer Parameters and Loss Analysis for High Voltage Capacitor Charging Application," in *Proc. IEEE ECCE Asia,* pp. 704-710, 3-6 Jun. 2013.

[14] S.–K, Chung, "Transient characteristics of high-voltage flyback transformer operating in discontinuous conduction mode," in *IEE Proc. Electric Power Applications,* vol.151, no.5, pp.628-634, 9 Sept. 2004.

[15] Linear Technology, "LT3751 High Voltage Capacitor Charger with Regulation", Linear Technology Corporation, USA. http://cds.linear.com/docs/en/datasheet/3751fc.pdf

[16] N. O. Sokal, R. Redl, "Control algorithms and circuit designs for optimal flyback-charging of an energy-storage capacitor (e.g., for flash lamp or defibrillator)," in *Proc. IEEE Transactions on Power Electronics*, vol. 12, no. 5, pp. 885-894, Sep. 1997.

[17] T. Andersen, L. Huang, M. A. E. Andersen, O. C. Thomsen, "Efficiency of capacitively loaded converters," in *Proc. IEEE IECON*, pp. 367-372, 2012.

Appendix E

Design of a High Voltage Bidirectional DC-DC Converter for Driving Capacitive Incremental Actuators usable in Electric Vehicles (EVs)

2014 IEEE International Electric Vehicle Conference (IEVC 2014)

Design of a High Voltage Bidirectional DC-DC Converter for Driving Capacitive Incremental Actuators Usable in Electric Vehicles (EVs)

Prasanth Thummala, Zhe Zhang, Michael A. E. Andersen
Department of Electrical Engineering
Technical University of Denmark
DK-2800 Kongens Lyngby, Denmark
pthu@elektro.dtu.dk

Dragan Maksimovic
Colorado Power Electronics Center
Department of Electrical, Computer, and Energy Engineering
University of Colorado at Boulder
Boulder, Colorado, USA-80309
maksimov@colorado.edu

Rahimullah Sarban
LEAP Technology
Science and Technology Park,
Diplomvej 381,
DK-2800 Kongens Lyngby,
Denmark
rahim@leaptechnology.com

***Abstract*—This paper presents the design of a low input (24 V) and variable high output voltage (0-2.5 kV) bidirectional dc-dc converter for driving a capacitive actuator. The topology is a digitally controlled bidirectional flyback converter with a variable frequency control. The objective is, to design the converter for efficiently charging and discharging the capacitive actuator from 0 V to 2.5 kV and vice versa, respectively. The converter is used to drive a dielectric electro active polymer (DEAP) based capacitive incremental actuator, which has the potential to be used in automotive (e.g., EVs), space and medical industries. The design of the bidirectional flyback converter to charge and discharge a 400 nF capacitive actuator is presented, when 4 kV and 4.5 kV high voltage MOSFETs are used on the secondary high voltage side. The experimental results and efficiency measurements of the converter with the proposed design are provided.**

Keywords—switch mode power converters, electric vehicles, capacitive actuators, high voltage, dc-dc converters

NOMENCLATURE

A_c	Cross sectional area of the core
B_{maxC}/B_{maxD}	Maximum flux density during charge/discharge process
C_{in}/C_{load}	Input capacitance/Load or actuator capacitance
D_2/D_b	High voltage (5 kV) diode which conducts during charge/discharge process
D_{b1}/D_{b2}	Body diodes of MOSFET M_1/M_2
$D_{onC,min}$	Minimum on-duty cycle of M_1
$D_{offC,max}$	Maximum off-duty cycle of M_1
$D_{onD,max}$	Maximum on-duty cycle of M_2
f_{swC}/f_{swD}	Switching frequency during charge/discharge process
$i_{in}/i_p/i_s$	Input/Primary/Secondary current
I_{ppkC}/I_{spkD}	Primary charging peak current/secondary discharging peak current
I_{D2}/I_{Db}	Rated average current of diode D_2/D_b
I_{M2}	Rated average current of MOSFET M_2
L_{mp}/L_{ms}	Primary/secondary magnetizing inductance
L_{lkp}/L_{lks}	Leakage inductance of transformer referred to primary side/secondary side
M_1	Low voltage MOSFET
M_2	High voltage (4 kV/4.5 kV) MOSFET
n	Turns ratio of the transformer from secondary to primary
N_p/N_s	Number of primary/secondary turns
R_p/R_s	Primary/Secondary dc resistance of transformer
T_{ch}	Charging time to reach the target output voltage
t_{onC}/t_{offC}	On-time/Off-time of M_1 during charge process
t_{onD}/t_{offD}	On-time/Off-time of M_2 during discharge process
$V_{in}/\Delta V_{inD}$	Input voltage/Increment in the input voltage during discharge process
$V_{o,max}$	Maximum or target output voltage
V_{outC}/V_{outD}	Variable load voltage during charge process (0 V-2.5 kV)/discharge process (2.5 kV-0 V)
V_{M1}/V_{M2}	Drain-to-source voltage of MOSFET M_1/M_2
V_{D2}/V_{Db}	Reverse voltage across high voltage diode D_2/D_b
V_{onD2}/V_{onDb}	Voltage drop of high voltage diode D_2/D_b
V_{BVM1}/V_{BVM2}	Breakdown voltage of MOSFET M_1/M_2
V_{BVD2}	Breakdown voltage of high voltage diode D_2 (or D_b)
$\beta_{M1}/\beta_{M2}/\beta_{D2}$	Margin factor (< 1) for $V_{BVM1}/V_{BVM2}/V_{BVD2}$
η	Power efficiency of the converter

I. Introduction

Dielectric electro active polymer (DEAP) is an emerging smart material technology that has experienced substantial growth and has gained significant attention over the last decade [1]-[3]. The DEAP material is a very thin (~40 μm) incompressible elastomer film having a compliant electrode layer on both sides [4]-[6]. The basic operation of the DEAP is the reduction in the polymer's thickness and increase in its area, due to an applied electric field. DEAP, when utilized as linear actuators (Fig. 1), has the potential to be an effective replacement for many conventional actuators. Several applications of DEAP actuators are discussed in [7]-[14].

978-1-4799-6075-0/14/$31.00 ©2014 IEEE

Fig. 1. A prototype of linear DEAP actuator.

Linear actuators are increasingly used in the automotive industry, for providing various functions. Some of them include, a piezo actuator drive (PAD) to control the door of a car [15], electric actuators to control and move the headlights of vehicles [16], linear motors to replace the conventional shock absorbers in cars [17] (see Fig. 2), digital linear actuators to adjust the air flow in the throttle by pass valve [18], and actuators for the central locking system [19]. However, some of these linear actuators can be very heavy, inefficient, rigid, and can have limited performance (force, stroke, and speed).

Therefore, DEAP actuators have their highest value proposition in automotive and specifically for electric vehicles (EVs) where system efficiency is of highest importance. Replacement of conventional actuators with DEAP actuators is able to provide the following advantages for electric vehicles:

1. DEAP is seven times lighter than copper and steel by which the conventional actuators are made of. Reducing the weight in electric vehicles can result in better overall efficiency.
2. DEAP actuators are capacitive devices, i.e., a large portion of the energy is reactive and can be harvested and reused in cyclic motions. This will require less energy from the main power source of an electric vehicle, once again increasing its efficiency.
3. DEAP actuators are entirely made of rubbery material which is inherently tolerant to shock and vibration which exist in every vehicle. Moreover, a DEAP actuator does not incorporate any moving and sliding parts such as bearings, gearing and similar. All these characteristics result in improved lifetime, cost, and efficiency.
4. DEAP actuators can be configured to provide incremental motion, thus overcoming the inherent size-to-stroke implications of conventional linear actuators, where the stroke is limited by their size. In incremental mode, DEAP actuators are several orders of magnitude shorter in its length compared to the stroke they provide. This will once again reduce the size and weight of the actuation mechanism resulting in vehicle efficiency.

The DEAP incremental actuator concept [20] consists of two grippers (to enable gripping operation) and an extender (to move the grippers), see Fig. (3). These grippers connect with the extender using the mechanical structures, so the incremental actuator is equivalent to three independent capacitive actuators with electrical isolation between them.

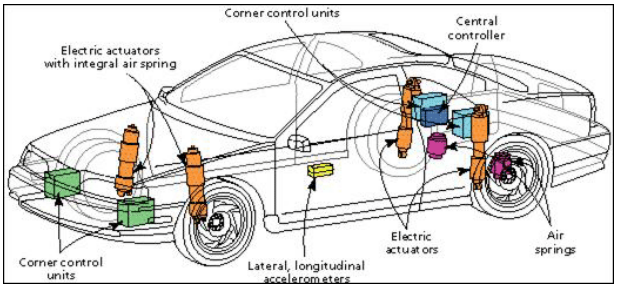

Fig. 2. Replacing the shock absorbers in a car with linear motors [17].

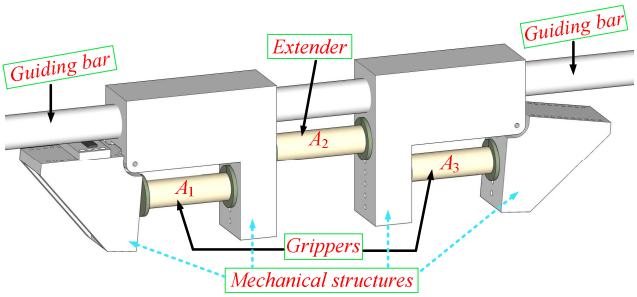

Fig. 3. Conceptual diagram of the DEAP incremental actuator.

Due to the requirement of high electric field strength (40-60 V/μm), DEAP actuator needs high voltage (2.5 kV) to fully elongate the actuator. Hence, high voltage dc-dc converters are needed to drive the DEAP actuators. The flyback converter is suitable for high voltage and low power applications due to its simple structure and low component count [21]. Efficiency optimization of the flyback converter for wide range of operating conditions is discussed in [22]. Control algorithms for optimal-flyback charging of a capacitive load have been proposed in [23]. High voltage switch-mode power supplies for charging the capacitive loads have been implemented in [24], [25]. The bidirectional flyback converters are proposed in [26]-[28] to transfer the power in both directions. Prior work on the high voltage drivers for the DEAP actuators demonstrated a low voltage piezoelectric transformer based DEAP solution, and it was inserted inside a coreless DEAP actuator [29], and a bidirectional flyback converter topology to drive the PolyPower Push Inlastor DEAP actuator [30]. In [31] an efficiency optimization technique is proposed for a bidirectional flyback converter used to drive capacitive actuator. Several transformer winding architectures have been investigated in [32] for the high voltage capacitor charge and discharge application. A digital control technique to achieve the valley switching in a bidirectional flyback converter is proposed in [33]. This paper focuses on the power stage design of a bidirectional flyback converter, which is used to drive the incremental DEAP actuator as shown in Fig. 3.

This paper is organized as follows: Section II describes the converter design considerations. Section III provides the experimental results followed by the conclusions in Section IV.

II. Bidirectional DC-DC Converter Design Considerations

The schematic of the bidirectional flyback converter is shown in Fig. 4. Due to very high reverse recovery time of the high voltage (HV) MOSFET M_2 (e.g., 2.6 μs for a 4 kV MOSFET), a blocking diode D_b is added in series with it. The converter design considerations are discussed in this section. Specifications of the converter and power stage components are provided in Tables I and II, respectively. The main focus of this paper is the design of flyback transformer, as it a critical component in the converter.

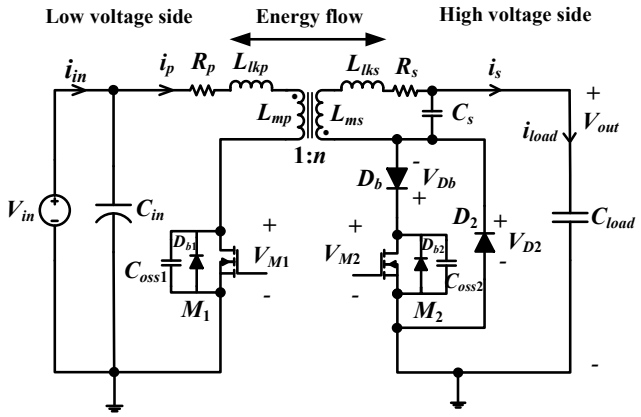

Fig. 4. Schematic of the high voltage bidirectional flyback converter for driving a high voltage capacitive load.

TABLE I. Specifications of Bidirectional Flyback Converter

Parameter	Value
Input V_{in}	24 V
Output voltage V_{out}	0-2.5 kV ($V_{o,max}$=2.5 kV)
Capacitance of the load C_{load}	400 nF
On time during charge process t_{onC}	9 μs
Target charging time T_{ch}	50 ms
Maximum flux density B_{maxC}	0.35 T

TABLE II. Components Used in the Converter

Component	Value
Primary MOSFET M_1	250V, 25A, 60 mΩ [IPD600N25N3 G]
HV MOSFET M_2	4.5 kV, 200 mA, 750 Ω [IXTA02N450HV] and 4 kV, 300 mA, 290 Ω [IXTV03N400S/ IXTH03N400]
HV diode D_b / D_2	5 kV, 150 mA [SXF6525]

A. Choice of turns ratio of the flyback transformer

For the capacitor charging application, the turns ratio is selected based on the maximum charging voltage of the capacitive load $V_{o,max}$. The typical voltage stress waveforms across MOSFETs M_1, M_2, and HV freewheeling diode D_2 are shown in Figs. 5a), 5b) and 5c), respectively.

1) Charge process: The minimum and maximum turns ratios, from secondary to primary of the flyback transformer during charge process can be calculated to meet the device breakdown voltage constraints.

The voltage stress across the primary MOSFET M_1 when turned off, should be less than its breakdown voltage V_{BVM1} (Fig. 5a)), so

$$\left[V_{in}+\frac{\left[V_{o,max}+V_{onD2}\right]}{n}+V_{leakP}\right]<\beta_1 V_{BVM1} \qquad (1)$$

where V_{leakP} is the increase in the drain voltage of primary MOSFET due to the leakage inductance L_{lkP}.

From (1), the transformer turns ratio

$$n > n_{min} \qquad (2)$$

where n_{min} is the minimum turns ratio needed, to charge the capacitive load to $V_{o,max}$ and is given by

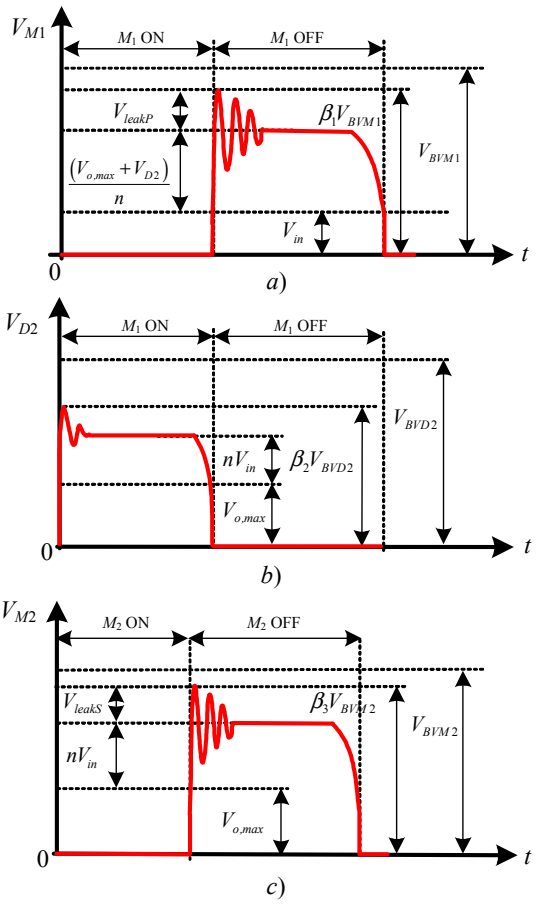

Fig. 5. Voltage stress when target output voltage ($V_{o,max}$) is reached across, a) M_1 during charge process (BCM), b) D_2 during charge process (BCM), c) M_2 during discharge process (BCM); BCM: Boundary Conduction Mode.

$$n_{min} = \frac{\left[V_{o,max} + V_{onD2}\right]}{\left[\left(\beta_1 V_{BVM1}\right) - V_{in} - V_{leakP}\right]} \tag{3}$$

For the given input specifications provided in Table I, by choosing V_{leakP}=70 V (this design value can be changed depending on the possible value of the leakage inductance referred to primary L_{lkP}), and choosing a margin factor of β_1=0.9 for a 250 V primary MOSFET (see Table II), with a high voltage diode drop V_{onD2}=7 V, the minimum turns ratio is n_{min}=20.

The voltage stress across the high voltage freewheeling diode D_2 when M_1 is turned on must be less than its breakdown voltage V_{BVD2} (Fig. 5b)), so

$$\left[V_{o,max} + nV_{in}\right] < \beta_2 V_{BVD2} \tag{4}$$

From (4), the transformer turns ratio

$$n < n_{maxC} \tag{5}$$

where n_{maxC} is the maximum turns ratio needed for the charge process, and is given by

$$n_{maxC} = \left\lfloor \frac{\beta_2 V_{BVD2} - V_{o,max}}{V_{in}} \right\rfloor \tag{6}$$

By choosing a margin factor of β_2=0.8 for a 5 kV high voltage diode D_2, the maximum turns ratio is n_{maxC}=62. Since the charge and discharge processes are independent, the turns ratio during the discharge process needs to be calculated separately, and is described below.

2) Discharge process: The turns ratio limit of the flyback transformer during discharge process can be calculated from the breakdown voltage of the secondary HV MOSFET M_2. The voltage stress across M_2 when turned off should be less than its breakdown voltage V_{BVM2} (Fig. 5c)), so

$$\left[V_{o,max} + nV_{in} + V_{leakS}\right] < \beta_3 V_{BVM2} \tag{7}$$

where V_{leakS} is an increase in the drain voltage of HV MOSFET due to the leakage inductance L_{lkS}.

From (7), the transformer turns ratio

$$n < n_{maxD} \tag{8}$$

where n_{maxD} is the maximum turns ratio needed for the discharge process, and is given by

$$n_{maxD} = \left\lfloor \frac{\beta_3 V_{BVM2} - V_{o,max} - V_{leakS}}{V_{in}} \right\rfloor \tag{9}$$

Since V_{BVM2}<V_{BVD2} (see Table II), the turns ratio n should satisfy 20<n<48, for 4.5 kV HV MOSFET, and 20<n<30, for 4.5 kV HV MOSFET, respectively. To avoid complexity and difficulty in winding several secondary turns in the transformer, the turns ratio n is selected to be equal to 20. However, it is up to the designer to choose a different turns ratio, different margin factors, and different rating low voltage MOSFET for this application.

B. Design of primary and secondary turns

The design methodologies for transformers and coupled inductors used in conventional switch-mode power supplies are well documented [21], [34]-[36]. For the bidirectional flyback converter, the primary and secondary turns are selected to avoid the saturation of the core during both charge and discharge modes. The converter operates with valley switching/BCM control during both charge and discharge processes [33].

1) Charge process: The number of primary turns needed during charge process is

$$N_p = \frac{V_{in} t_{onC}}{B_{maxC} A_c} \tag{10}$$

The number of secondary turns needed is

$$N_{sC} = N_p n \tag{11}$$

By choosing an EF25 core (with N87 material) with A_c=52 mm^2, and for the specifications shown in Table I, the primary and secondary turns become N_p=12 and N_{sC}=240, respectively.

2) Discharge process: The number of secondary turns needed during discharge process is

$$N_{sD} = \frac{V_{outD}\ t_{onD}}{B_{maxD} A_c} = \frac{n\left(V_{in} + \Delta V_{inD}\right) t_{offD}}{B_{maxD} A_c} \tag{12}$$

The same secondary turns ($N_s = N_{sC} = N_{sD}$) should meet both (11) and (12). The input capacitance C_{in}=30 mF is chosen, such that the voltage increment during the discharge process ΔV_{inD} <2 V.

C. Selection of peak currents during charge and discharge processes

1) Charge process: The expression for primary peak current to charge the HV capacitive load from 0 V to $V_{o,max}$ in time T_{ch} is [23], [34]

$$I_{ppkC} = \frac{\left(2nV_{in} + V_{o,max}\right) C_{load} V_{o,max}}{\eta V_{in}\left(T_{ch} - T_{delay}\right)} \tag{13}$$

For the given input specifications shown in Table I, for a turns ratio of n=20, by choosing a power efficiency η=0.8, and for a delay time T_{delay}=5 ms, the approximate primary peak current is I_{ppkC}=4 A.

The expression for maximum secondary peak current $I_{spkC,max}$, to charge the HV capacitive load through HV diode D_2, when the converter is operating in a boundary conduction mode (BCM) is

$$I_{spkC,max} < \frac{2I_{D2}}{\left(1-D_{onC,min}\right)} < \frac{2I_{D2}}{D_{offC,max}} \tag{14}$$

Equation (14) is derived based on the average current expression across HV diode D_2 during the charge process. The maximum secondary peak charging current, when a 5 kV HV diode, with a rated current of I_{D2}=150 mA is used, and for a maximum off-duty cycle during charge process $D_{offC,max}$=0.9 is $I_{spkC,max}$=333 mA. This corresponds to a maximum primary peak current of 6.67 A, for a turns ratio of n=20.

2) Discharge process: During the discharge process, since the output voltage decreases in each switching cycle, to discharge the load with constant peak current i_{spkD}, the on-time t_{onD} should increase in each switching cycle. The expression for maximum secondary peak current $I_{spkD,max}$, to discharge the HV capacitive load, through the series combination of high voltage diode D_b and high voltage MOSFET M_2 (Fig. 4) is

$$I_{spkD,max} < \frac{2I_{SD}}{D_{onD,max}} \tag{15}$$

where I_{SD} is the average current in the secondary HV side during discharge process, and is given by:

$$I_{SD} = \begin{cases} I_{Db}, \text{if } I_{Db} < I_{M2} \\ I_{M2}, \text{if } I_{Db} > I_{M2} \end{cases} \tag{16}$$

Since average current of D_b is less than that of M_2, i.e., I_{Db}<I_{M2} (see Table II), I_{SD}=I_{Db}. The maximum secondary peak discharging current, for a maximum discharge on-duty cycle $D_{onD,max}$=0.8 is $I_{spkD,max}$=375 mA. This corresponds to a maximum primary peak discharging current of 7.5 A, for n=20.

D. Design of primary magnetizing inductance

1) Charge process: When the converter operates in BCM during charge process, selecting fixed on-time t_{onC} ensures constant peak current. In this case, the duty cycle and the switching frequency are maximum at the final switching cycle (where the output voltage is close to the maximum target output voltage ($V_{o,max}$)), and minimum in the first switching cycle (where the output voltage is minimum or 0 V). The expression for the primary magnetizing inductance needed for charge operation is

$$L_{mpC} = \frac{V_{in}t_{onC}}{I_{ppkC}} \tag{17}$$

For V_{in}=24 V, t_{onC}=9 μs, and I_{ppkC}=4 A the primary magnetizing inductance L_{mpC}=54 μH.

2) Discharge process: When the converter operates in BCM during discharge process, selecting variable on-time t_{onD} (since the output voltage is decreasing) ensures constant peak current. In this case, the duty cycle and the switching frequency are maximum at the first switching cycle (where the output voltage is close to the maximum target output voltage ($V_{o,max}$)) and minimum in the final switching cycle (where the output voltage is close to minimum discharge voltage or 0 V).

When the capacitive load transfers the energy back to the source, the input voltage slightly increases by ΔV_{inD}. The magnitude of ΔV_{inD} depends on the value of the input capacitance C_{in} used in the converter. The expression for the primary magnetizing inductance for discharge operation is

$$L_{mpD} = \frac{\left(V_{in} + \Delta V_{inD}\right)t_{offD}}{I_{ppkD}} \tag{18}$$

The same primary magnetizing inductance ($L_{mp} = L_{mpC} = L_{mpD}$) should meet both (17) and (18).

From (10)-(12) and (17), (18), it can be concluded that, if the number of secondary turns $N_s = N_{sC} = N_{sD}$ and the magnetizing inductance $L_{mp} = L_{mpC} = L_{mpD}$ then, the flux density during the discharge process is

$$B_{max\,D} = \frac{I_{ppkD}}{I_{ppkC}} B_{max\,C} = \frac{nI_{spkD}}{I_{ppkC}} B_{max\,C} \tag{19}$$

The secondary discharge peak current I_{spkD} in any switching cycle limits the peak flux density B_{maxD} during the discharge process. Hence, from (19) suppose if a secondary discharge peak current of I_{spkD}=200 mA is chosen, then the flux density during discharge process becomes (for n=20, I_{ppkC}=4 A, B_{maxC}=0.35 T) B_{maxD}=0.35 T. Hence, the secondary discharge peak current I_{spkD} needs to be selected to avoid the core saturation during discharge operation.

E. Selection of air-gap length l_g

1) If the gap is put on the center leg of the core: The expression for the air-gap length is given by [21], [37]

$$l_g = \left[\frac{\mu_0 N_p I_{ppkC}}{B_{max\,C}} - \frac{l_m}{\mu_r}\right] \tag{20}$$

If $l_g \gg \frac{l_m}{\mu_r}$, the air-gap length becomes

$$l_g = \frac{\mu_0 N_p I_{ppkC}}{B_{maxC}} \quad (21)$$

where l_m is the effective magnetic path length, and μ_0 and μ_r are the permeability of vacuum and relative permeability of the ungapped core, respectively.

2) If the air-gap is put on the outer legs of the core: The expression for the air-gap length in this case is

$$l_g = \frac{1}{2}\frac{\mu_0 N_p I_{ppkC}}{B_{maxC}} \quad (22)$$

In the practical high voltage transformer, an approximate air-gap length of l_g=0.12 mm is provided in each outer leg of EF25 core. But, practically the transformer has a primary magnetizing inductance of L_{mpC}=38 μH, so when 9 μs constant on-time is used to drive M_1, peak current I_{ppkC} becomes 5.68 A, which is less than the maximum calculated value of 6.6 A.

III. Experimental Results

The experimental prototype of the bidirectional flyback converter with E25 transformer and 4 kV through hole MOSFET (TO-247) is shown in Fig. 6. The experimental results showing a single bidirectional charge and discharge cycle at 2.42 kV output voltage is provided in Fig. 7. Figure 8 provides the experimental result when the converter is continuously charged and discharged at 1.8 kV output voltage. As shown in Fig. 8, when a diode is placed between the input dc supply and the input capacitor C_{in}, during the charge process the input voltage slightly drops, and during the discharge process the input voltage slightly increases, as expected.

A sectioned EF25 bobbin with 4 sections is used for the flyback transformer. Sectioning the transformer significantly reduces the self-capacitance of the high voltage winding [32]. A 0.5 mm triple isolated (TEX-E) solid wire is used for the primary winding, and 0.1 mm normal single insulated solid wire is used for the secondary winding.

The measured flyback transformer parameters (using Agilent 4294A Impedance analyzer) are provided in Table III. Temperature measurements are performed to verify the reliable operation of the proposed design. During the thermal measurements, instead of 250V, 25A, 60 mΩ [IPD600N25N3 G] MOSFET, another 200 V, 600 mΩ, 5 A (IRFR220N) MOSFET is used. Figure 9 provides the steady-state thermal profile of the converter when it is charged and discharged continuously for 30 min, at 2 kV output voltage. The test was performed without any delay between the charge and discharge cycles. The maximum temperature rise was across the low voltage MOSFET, because of the conduction loss due to its high on-resistance, the temperature across the flyback transformer was 61 °C. Furthermore, it is expected that the temperature across the transformer will be higher than 10 °C, if the converter is continuously charged (0 V → 2.5 kV) and discharged (2.5 kV → 0 V) at 2.5 kV. Another test was performed by putting a delay time of 100 ms between the charge and discharge cycles, the temperature profile is shown in Fig. 10. In this case, the maximum temperature across the transformer is ~46 °C, due to the low average power across it.

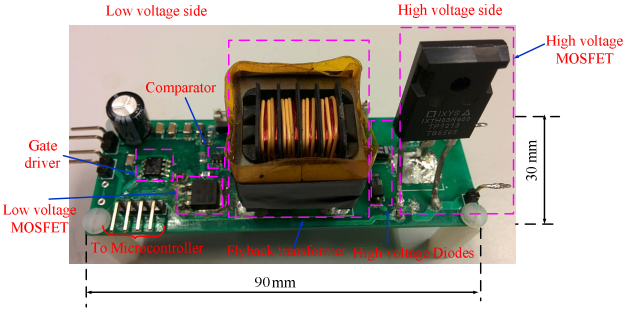

Fig. 6. Experimental prototype of the bidirectional flyback converter.

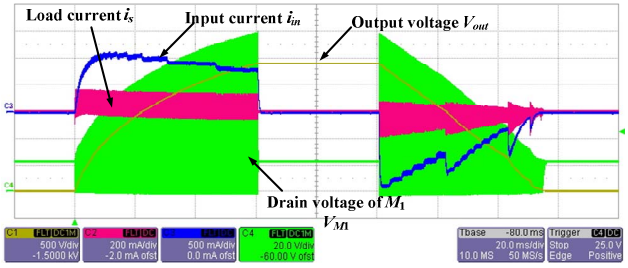

Fig. 7. Experimental waveforms showing the bidirectional operation at 2.42 kV output voltage. The 24 V dc source and the input capacitor are directly connected.

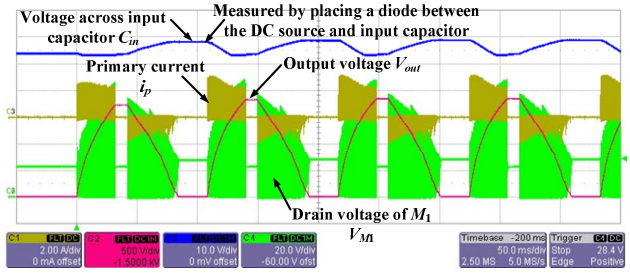

Fig. 8. Continuous bidirectional cycles at 1.8 kV output voltage. A diode is placed between the 24 V dc source and the input capacitor.

Fig. 9. Steady-state temperature measurement, when the converter is continuously charged and discharged (without any delay between the cycles) from 0 V to 2 kV, and vice versa, when 200 V, 600 mΩ, 5 A (IRFR220N) low voltage MOSFET is used.

Fig. 10. Steady-state temperature measurement, when the converter is continuously charged and discharged (without 100 ms delay between the cycles) from 0 V to 2 kV, and vice versa, when IRFR220N (200 V, 600 mΩ, 5 A) low voltage MOSFET is used.

Since the load is purely capacitive, the converter efficiency is defined as energy efficiency, instead of normal power efficiency. The charge and discharge energy efficiency measurement [30] results are provided in Table IV. During the charge process the output energy is the energy stored in the load capacitor, and the input energy is obtained by integrating the input charge current and multiplying it with the input voltage. During the discharge process, the input energy is the energy stored in the load capacitor, and the output energy is obtained by integrating the input discharge current and multiplying it with the input voltage. All components shown in Table II are used during the energy efficiency measurements. As explained earlier, the converter operates with valley switching control during charge and discharge operations. The charge and discharge efficiencies are 89.2% and 83.4%, respectively. The reasons for the lower discharge energy efficiency are explained in [33].

TABLE III. FLYBACK TRANSFORMER PARAMETERS

Parameter	Value
Core used / material used	EF25 / N87
Type of bobbin (coil former)	Sectioned with 4 sections
Number of primary N_p / secondary turns N_s	12 / 240
Primary L_{mp} / secondary magnetizing inductance L_{ms}	38 μH / 15.2 mH
Leakage inductance referred to primary L_{lkp} / secondary L_{lks}	450 nH / 185 μH
Self-capacitance of secondary winding C_s	5 pF
Dc resistance of primary R_p / secondary R_s	50 mΩ / 10.5 Ω

TABLE IV. ENERGY EFFICIENCY AT 2.4 KV OUTPUT VOLTAGE

Type of mode	Input energy (J)	Output energy (J)	Energy efficiency (%)
Charge	1.29	1.15	89.2 (to charge from 0 V to 2.4 kV)
Discharge	1.15	0.96	83.4 (to discharge from 2.4 kV to 0 V)

IV. CONCLUSIONS

This paper describes the detailed power stage design of the high voltage bidirectional flyback converter for driving a dielectric electro active polymer (DEAP) based capacitive actuator. Experimental results are provided to show the bidirectional operation (charge and discharge) of the high voltage converter. Even though the flyback transformer is designed for a high peak charging flux density of 0.35 T, thermal measurement results show that the maximum temperature across the transformer is 61 °C. Therefore, for a high voltage capacitor charge and discharge applications it is possible to minimize the number of transformer turns on the secondary high voltage side, by choosing a high flux density.

Energy efficiency measurements are provided for the charge and discharge modes using the proposed design. For driving the capacitive load at 2.4 kV, the converter attains charge and discharge energy efficiencies of 89.2% and 83.4%, respectively. It is easy to make three similar converters with the same design for driving the DEAP incremental actuator, which has an enormous potential in the automotive industry. By optimizing the flyback transformer design, it is possible to increase the power density of the high voltage driver, so that it can be easily placed in the EVs. The research on the DEAP material is still on-going, and in the future it is expected that the operating voltage ranges of the DEAP actuators may be reduced to 1.5-2 kV from the current range 2-2.5 kV.

REFERENCES

[1] Y. Bar-Cohen, "*Electroactive Polymer [EAP] Actuators as Artificial Muscles: Reality, Potential, and Challenges,"* 2nd ed. Washington, DC: SPIE, 2004.

[2] F. Carpi, D. DE Rossi, R. Kornbluh, R. Pelrine, P. Sommer-Larsen, Eds, "*Dielectric Elastomer As Electromechanical Transducers*," Amsterdam, The Netherlands: Elsevier, 2008.

[3] R. E. Pelrine, R. D. Kornbluh, Q. Pei, J. P. Joseph, "High-speed electrically actuated elastomers with strain greater than 100%," *Science*, vol. 287, pp. 836–839, 2000.

[4] Danfoss PolyPower, Denmark, Online available: http://www.polypower.com/ [accessed 20 Oct. 2014].

[5] LEAP Technology, Denmark, Online available: http://leaptechnology.com/ [accessed 20 Oct. 2014].

[6] M. Tryson, H. E. Kiil, M. Benslimane, "Powerful tubular core free dielectric electro active polymer (DEAP) push actuator," in *Proc. SPIE*, vol. 7287, 2009.

[7] R. Sarban, B. Lassen, M. Willatzen, "Dynamic Electromechanical Modeling of Dielectric Elastomer Actuators With Metallic Electrodes," *IEEE/ASME Trans. Mechatronics*, vol. 17, no. 5, pp. 960-967, Oct. 2012.

[8] R. D. Kornbluh, R. Pelrine, Q. Pei, R. Heydt, S. Stanford, S. Oh, J. Eckerle, "Electroelastomers: applications of dielectric elastomer transducers for actuation, generation, and smart structures," in *Proc. SPIE*, vol. 4698, pp. 254-270, 2002.

[9] Q. Pei, R. Pelrine, S. Stanford, R. D. Kornbluh, M. S. Rosenthal, K. Meijer, R. J. Full, "Multifunctional electroelastomer rolls and their application for biomimetic walking robots," in *Proc. SPIE*, vol. 4698, 2002.

[10] I. A. Anderson, T. A. Gisby, T. G. McKay, B. M. O'Brien, E. P. Calius, "Multi-functional dielectric elastomer artificial muscles for soft and smart machines," *Journal of Applied Physics*, 112, 041101, 2012.

[11] K. Jung, J. C. Koo, J. -do Nam, Y. K. Lee, H. R. Choi, "Artificial annelid robot driven by soft actuators," *Journal of Bioinspiration and Biomimetics*, vol. 2, pp. S42-S49, 2007.

[12] I. A. Anderson, T. C. H. Tse, T. Inamura, B. M. O'Brien, T. McKay, T. Gisby, "A soft and dexterous motor," *Journal of Applied Physics*, 98, 123704, 2011.

[13] A. T. Conn, A. D. Hinitt, P. Wang, "Soft segmented inchworm robot with dielectric elastomer muscles," in *Proc. SPIE*, Electroactive Polymer Actuators and Devices (EAPAD), vol. 9056, pp. 90562L, 2014.

[14] F. Carpi, R. Kornbluh, P. Sommer-Larsen, G. Alici, "Electroactive polymer actuators as artificial muscles: are they ready for bioinspired applications?," *Journal of Bioinspiration and Biomimetics*, vol. 6 (4), 2011.

[15] Siemens website, online available [accessed 29 Oct. 2014]: http://www.siemens.com/innovation/en/publikationen/publications_pof/pof_spring_2006/motors_articles/future_motors.htm.

[16] Helix Linear Technologies website, online available [accessed 29 Oct. 2014]: http://blog.helixlinear.com/bid/307529/How-a-Small-Electric-Actuator-Operates-Automotive-Headlights.

[17] The University of Sheffield website, online available [accessed 29 Oct. 2014]: http://www.sheffield.ac.uk/research/impact/stories/fce/7.

[18] VDO global website, online available [accessed 29 Oct. 2014]: http://www.vdo.com/generator/www/com/en/vdo/main/products_solutions/cars/replacement_parts/engine_actuators/digital_linear_actuators/digital_linear_actuators_en.html.

[19] VDO global website, online available [accessed 29 Oct. 2014]: http://www.vdo.com/generator/www/com/en/vdo/main/products_solutions/cars/replacement_parts/actuators_for_central_locking_systems/actuators_for_central_locking_systems_en.html.

[20] P. Thummala, Z. Zhang, M. A. E. Andersen, S. Rahimullah, "Dielectric electro active polymer incremental actuator driven by multiple high-voltage bi-directional DC-DC converters," in *Proc. IEEE ECCE USA,* pp. 3837-3844, 15-19 Sept. 2013.

[21] R. W. Erickson, D. Maksimovic, "Fundamentals of Power Electronics," 2nd ed. New York: Springer, 2001.

[22] H. K. Sang, D. Maksimovic, I. Cohen, "Efficiency Optimization in Digitally Controlled Flyback DC–DC Converters Over Wide Ranges of Operating Conditions," *IEEE Trans. Power Electronics*, vol. 27, no. 8, pp. 3734-3748, Aug. 2012.

[23] N. O. Sokal, R. Redl, "Control algorithms and circuit designs for optimal flyback-charging of an energy storage capacitor (e.g., for flash lamp or defibrillator)," *IEEE Trans. Power Electronics*, vol. 12, no. 5, pp. 885-894, Sep. 1997.

[24] J. Elmes, C. Jourdan, O. Abdel-Rahman, I. Batarseh, "High-Voltage, High-Power-Density DC-DC Converter for Capacitor Charging Applications," in *Proc. IEEE APEC*, pp. 433-439, 2009.

[25] S. K. Chung, H. B. Shin, "High-voltage power supply for semi-active suspension system with ER-fluid damper," *IEEE Trans. Vehicular Technology*, vol. 53, no. 1, pp. 206- 214, Jan. 2004.

[26] T. Bhattacharya, V. S. Giri, K. Mathew, L. Umanand, "Multiphase Bidirectional Flyback Converter Topology for Hybrid Electric Vehicles," *IEEE Trans. Industrial Electronics*, vol. 56, no. 1, pp. 78-84, Jan. 2009.

[27] G. Chen, Y.-S. Lee, S. Y. R. Hui, D. Xu, Y. Wang, "Actively clamped bidirectional flyback converter," *IEEE Trans. Industrial Electronics*, vol. 47, no. 4, pp. 770-779, Aug. 2000.

[28] F. Zhang, Y. Yan, "Novel Forward–Flyback Hybrid Bidirectional DC-DC Converter," *IEEE Trans. Industrial Electronics,* vol. 56, no. 5, pp. 1578-1584, May 2009.

[29] T. Andersen, M. S. Rødgaard, O. C. Thomsen, M. A. E. Andersen, "Low voltage driven dielectric electro active polymer actuator with integrated piezoelectric transformer based driver," in *Proc. SPIE EAPAD*, vol. 7976, p. 79762N, 2011.

[30] P. Thummala, Z. Zhang, M. A. E. Andersen, "High Voltage Bi-directional Flyback Converter for Capacitive Actuator," in *Proc. IEEE EPE,* pp. 3-6 Sept. 2013.

[31] P. Thummala, H. Schneider, Z. Zhang, A. Knott, M. A. E. Andersen, "Optimization of a bi-directional flyback converter for a high voltage capacitor charging application," in *Proc. IEEE APEC*, pp. 2556-2563, 16-20 March 2014.

[32] H. Schneider, P. Thummala, L. Huang, Z. Ouyang, A. Knott, Z. Zhang, M. A. E. Andersen, "Investigation of transformer winding architectures for high voltage capacitor charging applications," in *Proc. IEEE APEC*, pp. 334-341, 16-20 March 2014.

[33] P. Thummala, D. Maksimovic, Z. Zhang, M. A. E. Andersen, "Digital control of a high-voltage (2.5 kV) bidirectional DC-DC converter for driving a dielectric electro active polymer (DEAP) based capacitive actuator," in *Proc. IEEE ECCE USA*, pp. 3435-3442, 14-18 Sept. 2014.

[34] LT3751 datasheet, "High voltage capacitor charger controller with regulation," Linear Technology Corporation, USA, Online available: http://cds.linear.com/docs/en/datasheet/3751fc.pdf [accessed 16 Oct. 2014].

[35] C. W. T. McLyman, *Transformer and Inductor Design Handbook*, 3rd Ed., New York: Marcel Dekker, 2004.

[36] W. G. Hurley, W. H. Wolfle, *Transformers and Inductors for Power Electronics: Theory, Design and Applications*, 1st Ed., John Wiley and Sons Ltd., 2013.

[37] M. Kazimierczuk, *High-frequency magnetic components*, 2nd Ed., John Wiley and Sons Ltd., 2014.

Appendix F

Estimation of Transformer Parameters and Loss Analysis for High Voltage Capacitor Charging Application

---

2013 IEEE Energy Conversion Congress and Exposition ASIA (ECCE ASIA 2013)

Estimation of Transformer Parameters and Loss Analysis for High Voltage Capacitor Charging Application

Prasanth Thummala, Henrik Schneider, Ziwei Ouyang, Zhe Zhang, and Michael A. E. Andersen
Electronics Group, Department of Electrical Engineering
Technical University of Denmark
Oersteds Plads, Building 349, Kongens Lyngby, Denmark
Email: pthu@elektro.dtu.dk , Homepage: http://www.dtu.dk/centre/ele/English.aspx

Abstract—**In a bi-directional DC-DC converter for capacitive charging application, the losses associated with the transformer makes it a critical component. In order to calculate the transformer losses, its parameters such as AC resistance, leakage inductance and self capacitance of the high voltage (HV) winding has to be estimated accurately. This paper analyzes the following losses of bi-directional flyback converter namely switching loss, conduction loss, gate drive loss, transformer core loss, and snubber loss, etc. Iterative analysis of transformer parameters viz., AC resistance, leakage inductance and stray capacitance of the HV winding will lead to a considerable reduction in converter losses. In this work, a 24 V to 2.5 *k*V bi-directional flyback converter has been implemented and the same has been used for loss calculation.**

Keywords— *high voltage bi-directional converter, capacitive load, AC resistance, core loss, stray capacitance, leakage inductance*

I. INTRODUCTION

High voltage switch mode power converters are used in a wide variety of capacitive charging applications. Typical applications include pulsed lasers, dielectric electro active polymer (DEAP) actuators, pulsed sonar equipment, photo flash systems, electric fences, and plasma research. Our research focus is to develop high voltage DC-DC power supplies as a driving mechanism for DEAP actuator applications [1]-[4].

The DEAP material requires a high electric field strength of 60 V/μm and the thickness of polymer film is 40 μm therefore, a high voltage is needed for the DEAP actuator (is a pure capacitive load with very low leakage current) to achieve a reasonable actuation stroke. Thus specific component used in this study requires high voltage in the range of kilovolts (~ 2.5 *k*V) at relatively low current. However, with the advanced research and development in high voltage devices like MOSFETS and diodes, it is possible to implement efficient and compact high voltage drivers, to drive and fulfil the requirements of DEAP actuator applications. An incremental DEAP actuator (Fig. 1) which consists of 3 sub-actuators (2 grippers and 1 extender), is the load which needs to be driven by high voltage DC-DC converters.

Danish National Advanced Technology Foundation (*sponsor*).

The common goals of high voltage DC-DC power supplies are reliability, high efficiency, low cost, size and weight. The flyback topology is suitable for low power (< 150 W) and high voltage applications, as it can be made very compact with a low number of components. The magnetic transformer is the most critical component in the HV flyback converter, its leakage inductance causes undesirable voltage spikes, and winding capacitance result in the undesirable current spikes, distortions in the waveforms of the converter, and slow rise times. These non-idealities in the transformer can lead to increased capacitive switching loss, snubber loss, winding loss due to skin and proximity effects, and variable core loss at high and variable frequency of operation, which might lead to reduced converter efficiency and reliability. So, accurate estimation of the transformer parameters, and individual losses in the converter are required to achieve an optimized design for this demanding application.

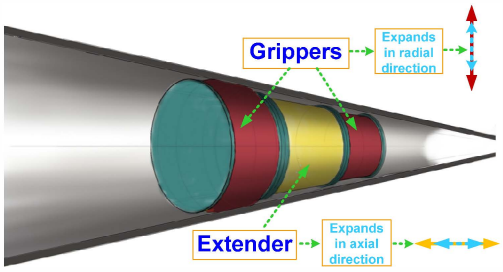

Fig. 1. Incremental DEAP actuator.

The converter efficiency can be improved by optimizing the whole converter design as well as with the proper selection of the control strategy. There is only limited research available in the literature, for an in depth optimization of a flyback transformer for the capacitive load charging and discharging application. In the future an efficiency optimization for this application will be carried out as an extension to the present research work.

This paper is organized as follows. Section II describes the estimation of the HV transformer parameters. Section III summarizes the power loss modelling. Section IV discusses the details of the HV transformer design and the calculations are validated with measured data. Section V shows the experimental and simulation results, followed by the conclusion in Section VI.

II. HV TRANSFORMER PARAMETERS ESTIMATION

A. DC and AC resistances

An increase in the switching frequency of the converter increases the transformer winding losses due to the skin and proximity effects. Since the converter operates under boundary mode during charging and in discontinuous conduction mode (DCM) during discharging, the AC conduction loss cannot be ignored and may dominate the total winding loss. The AC conduction loss is caused by high frequency skin and proximity effects, as well as the fringing effect. Due to its complexity fringing effect is not considered in this paper.

The DC resistance of the primary winding can be calculated by

$$R_{DCP} = \frac{\rho l_{TP}}{A_P},\ A_P = \frac{\pi d_P{}^2}{4} \tag{1}$$

where, ρ is the resistivity of copper at room temperature, N_P is the number of primary turns, l_{TP} is the total length of the primary winding, and d_P is the diameter of the primary winding.

The AC resistance of each harmonic in the current waveform can be calculated as [4], [5],

$$F_{RPn} = \frac{R_{ACP}}{R_{DCP}} = F_{Skin} + F_{Prox} = \varepsilon_P \sqrt{n} \left\{ \begin{array}{l} \dfrac{\sinh\left(2\varepsilon_P\sqrt{n}\right)+\sin\left(2\varepsilon_P\sqrt{n}\right)}{\cosh\left(2\varepsilon_P\sqrt{n}\right)-\cos\left(2\varepsilon_P\sqrt{n}\right)} + \\ \dfrac{2}{3}\left(m_p^2-1\right)\dfrac{\sinh\left(\varepsilon_P\sqrt{n}\right)-\sin\left(\varepsilon_P\sqrt{n}\right)}{\cosh\left(\varepsilon_P\sqrt{n}\right)+\cos\left(\varepsilon_P\sqrt{n}\right)} \end{array} \right\}$$

$$\varepsilon_P = \left(\frac{\pi}{4}\right)^{\frac{3}{4}} \left(\frac{d_P}{\delta_P}\right) \sqrt{\frac{d_i}{d_o}} \tag{2}$$

where, n is the harmonic number, m_p is the number of layers of the primary winding and ε_P is the primary winding conductor thickness normalized with respect to the conductor skin depth at the switching frequency for a round conductor, δ_P is the skin depth at the fundamental frequency, and d_i/d_o is the porosity factor of the primary winding.

B. Leakage Inductance

In the flyback converter the leakage inductance causes voltage spikes on the drain of low voltage and the high voltage MOSFETs, and may cause significant loss if the flyback transformer is not properly designed.

1) Without interleaving: The leakage inductance for the winding structure shown in Fig. 2a referred to primary is calculated using the energy stored in the magnetic field.

$$E_{Mag} = \frac{1}{2}\int_{Vol} B \cdot H \cdot dv = \frac{1}{2} L_{lk} I_{pk}{}^2 \tag{3}$$

The general expression for the leakage inductance referred to the primary winding for a non-interleaving winding structure having n_{lp} primary layers and n_{ls} secondary layers (with equal turns per layer) is derived in this work and is given by

$$L_{lkp} = \mu_o \frac{l_w}{b_w} N_p{}^2 \left[\begin{array}{l} \dfrac{n_{lp}h_p + n_{ls}h_s}{3} + \dfrac{\left(2n_{lp}-1\right)\left(n_{lp}-1\right)}{6}\left(\dfrac{h_{ip}}{n_{lp}}\right) \\ + \dfrac{\left(2n_{ls}-1\right)\left(n_{ls}-1\right)}{6}\left(\dfrac{h_{is}}{n_{ls}}\right) + h_i \end{array} \right] \tag{4}$$

where μ_o is the permeability of free air, l_w is the mean length turn (MLT), b_w is the width of the bobbin window excluding the edge isolation tape width, n_{lp}/n_{ls} is the number of primary/secondary layers, and h_{ip}/h_{is} is the insulation thickness between the primary/secondary layers, and h_i is the insulation thickness between the primary and secondary layers, and N_p is the number of primary turns.

The leakage inductance of transformer for the structure shown in Fig. 2 referred to primary is given by [6], [7]

$$L_{lkp} = \mu_o \frac{l_w}{b_w} N_p{}^2 \left[\frac{h_p + 5h_s}{3} + \frac{6}{5} h_{is} + h_i \right] \tag{5}$$

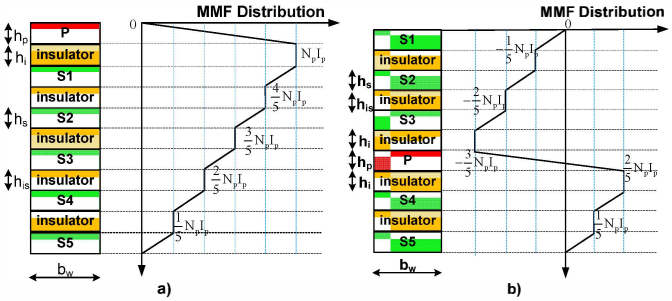

Fig. 2. Analytical MMF distribution for non-interleaving structure P-S-S-S-S-S (left) and interleaving S-S-S-P-S-S (right) structure.

2) With interleaving: Practical experience revealed that interleaving the primary and secondary windings reduces the leakage inductance, self capacitance, and increases the interwinding capacitance. A transformer that is used in the HV application will have a lot of secondary windings, the interleaving structure with the secondary windings sandwiched between the primary winding as shown in Fig. 2b is typical for the high voltage DC-DC converter application.

The general expression for the leakage inductance referred to the primary, for an interleaving winding structure where n_{ls1} and n_{ls2} secondary layers are at the top and bottom of a primary winding respectively, having n_{lp} primary layers (with equal turns per layer of both, and no insulation between the primary layers) is derived in this work and is given by

$$L_{lkp} = \frac{\mu_o l_w N_p{}^2}{b_w} \left[\begin{array}{l} \dfrac{n_{ls1}{}^3 + n_{ls2}{}^3}{3\left(n_{ls1}+n_{ls2}\right)^3}\left[n_{lp}h_p + \left(n_{ls1}+n_{ls2}\right)h_s\right] + \\ \dfrac{n_{ls1}\left(n_{ls1}-1\right)\left(2n_{ls1}-1\right) + n_{ls2}\left(n_{ls2}-1\right)\left(2n_{ls2}-1\right)}{6\left(n_{ls1}+n_{ls2}\right)^2} h_{is} \\ + \dfrac{n_{ls1}{}^2 + n_{ls2}{}^2}{\left(n_{ls1}+n_{ls2}\right)^2} h_i \end{array} \right] \tag{6}$$

The leakage inductance of the HV transformer for a simple interleaving structure shown in Fig. 2b is calculated using (7).

$$L_{lkp} = \frac{\mu_o}{2}\frac{l_w}{b_w} N_p^{\,2}\left[\frac{7h_p + 35h_s}{75} + \frac{6}{25}h_{is} + \frac{13}{25}h_i\right] \tag{7}$$

C. Stray Capacitance

The stray capacitance is another important parameter in the HV transformer because it contributes to capacitive switching loss. The stray capacitance is calculated using the energy stored in the electric field [8]

$$E_{Ele} = \frac{1}{2}\int_{Vol} D \cdot E \cdot dv = \frac{1}{2} C \cdot \Delta V^2 \tag{8}$$

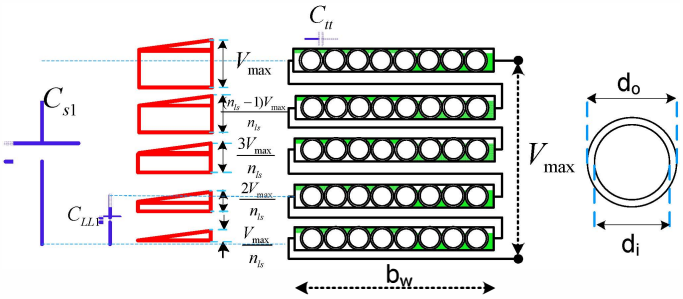

Fig. 3. Voltage distribution in the secondary HV winding with the layers wounded in the same direction

The turn to turn capacitance per unit length of the non-interleaved HV winding with a round conductor is given by

$$C_{tt} = \varepsilon_0\left(\varepsilon_r \theta \cdot \ln^{-1}\left(\frac{d_o}{d_i}\right) + \cot\left(\frac{\theta}{2}\right) - \cot\left(\frac{\pi}{12}\right)\right) \tag{9}$$

where $\theta = \cos^{-1}\left(1 - \frac{1}{\varepsilon_r}\ln\left(\frac{d_o}{d_i}\right)\right)$, ε_0 is the air permitivity, ε_r is the dielectric constant of the insulation of the winding, d_o / d_i is the outer/inner diameter of the HV winding conductor. The layer to layer capacitance is given by

$$C_{LL1} = \frac{T_{Ls}(T_{Ls}+1)(2T_{Ls}+1)}{6T_{Ls}^{\,2}} C_{tt} l_w \tag{10}$$

where T_{Ls} is the turns per layer of the HV winding.

The self capacitance of the HV winding for the winding configuration shown in Fig. 3 is given by

$$C_{S1} = \frac{C_{LL1}}{4}(n_{ls}-1)\left(\frac{2}{n_{ls}}\right)^2 \tag{11}$$

For the HV winding structure shown in Fig. 4, the layer to layer capacitance is given by [9], [10]

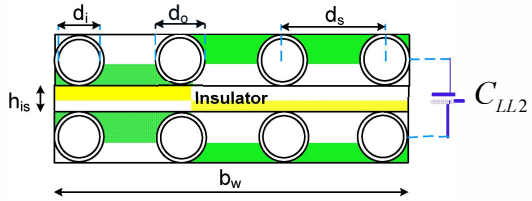

Fig. 4. A random HV winding arrangement.

$$C_{LL2} = \varepsilon_o \varepsilon_r \frac{l_w b_w}{d_{eff}} \tag{12}$$

where $d_{eff} = h_{is} + (d_o - 1.15d_i + 0.26d_s)$ is the effective distance between the two layers, d_s is the spacing between the centers of adjacent turns. The self capacitance of the HV winding for the winding structure shown in Fig. 4, and with the winding connections as shown in Fig. 3 is given by

$$C_{S2} = \frac{C_{LL2}}{4}(n_{ls}-1)\left(\frac{2}{n_{ls}}\right)^2 \tag{13}$$

D. Trade-off between AC resistance, leakage inductance and stray capacitance for HV application

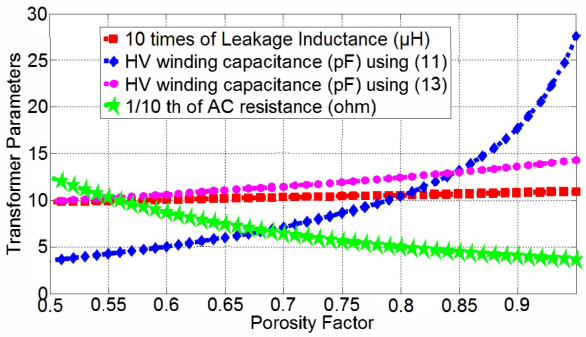

Fig. 5. Trade-off between the primary leakage inductance, secondary stray capacitance and the secondary AC resistance with a change in the porosity factor (d_i/d_o).

Fig. 5 shows the trade-off between the transformer parameters by changing the porosity factor. To show all the parameters in a single plot, the leakage inductance is multiplied by 10 and the AC resistance is divided by 10. The porosity factor (d_i / d_o) is changed from 0.95 to 0.5 and the calculated parameters are shown in Fig. 5. It is observed that the AC resistance increases, and the self capacitance of the HV winding drops as the porosity factor is decreased.

III. Loss Modeling of the Converter

In order to investigate the bi-directional converter efficiency, it is necessary to estimate the losses associated with each one of the circuit components in the converter. The schematic of the bi-directional flyback converter is shown in Fig. 6. The detailed analysis of the same converter is discussed in [13]. Different losses contributed from the transformer of the bi-directional flyback converter are given below.

A. Transformer winding loss

The flyback converter operates in boundary mode with variable switching frequency, while charging the capacitive load [13]. The primary winding power loss is given by [5]

$$P_{wP} = R_{DCP} I_{DCP}^2 + \frac{1}{2} R_{DCP} \sum_{n=1}^{\infty} F_{RPn} I_{Pn}^{\,2} \tag{14}$$

By applying the Fourier series expansion for the primary current waveform shown in Fig. 7 the following equations are obtained:

$$I_{DCP} = \frac{\left(I_{pk} - I_{min}\right)}{2} D_{onC} \tag{15}$$

$$I_{Pn} = \sqrt{a_n^{\,2} + b_n^{\,2}} \tag{16}$$

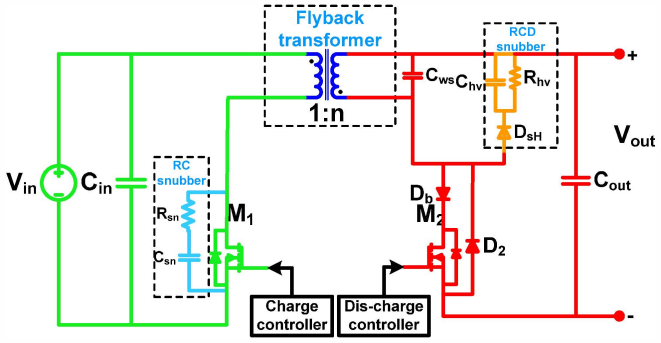

Fig. 6. Bi-directional flyback converter for capacitive load [13].

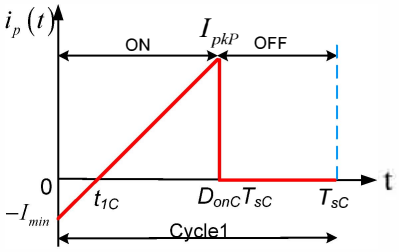

Fig. 7. Primary current waveform while charging the capacitive load.

$$a_n = \left\{ \begin{aligned} &\frac{-I_{min}}{\pi n} sin\left(2\pi n D_{onC}\right) + \frac{I_{pk} + I_{min}}{2\pi^2 n^2 D_{onC}} \times \\ &\left[cos\left(2\pi n D_{onC}\right) - 1 + \left(2\pi n D_{onC}\right) sin\left(2\pi n D_{onC}\right) \right] \end{aligned} \right\} \tag{17}$$

$$b_n = \left\{ \begin{aligned} &\frac{I_{min}}{\pi n} cos\left(2\pi n D_{onC}\right) + \frac{I_{pk} + I_{min}}{2\pi^2 n^2 D_{onC}} \times \\ &\left[sin\left(2\pi n D_{onC}\right) - \left(2\pi n D_{onC}\right) cos\left(2\pi n D_{onC}\right) \right] \end{aligned} \right\} \tag{18}$$

where I_{DCP}, I_{pkP}, I_{min}, R_{DCP}, I_{RMSP} and R_{ACP} are the primary winding DC current, peak current, negative current at the beginning of the turn-on process, DC resistance, rms current, and AC resistance (given by (2)) respectively. I_{Pn} is the current amplitude of the n^{th} harmonic. D_{onC} is the on-time duty cycle during charging process. The secondary winding power loss can also be calculated using the above approach.

The negative current at the beginning of the turn-on process (Fig. 7.) is because of the HV winding capacitance. When the secondary winding current becomes zero, the drain to source voltage tends to drop. Since the control IC LT3751 [14] that is used, operates under boundary mode control, the next switching cycle starts before the HV winding capacitance completely discharges. So current flows in the negative direction to discharge the HV winding capacitance at the start.

B. *Transformer core loss*

The core loss calculation during the charging process needs to take care of the variable switching frequency of operation. The most commonly used expression for the time-average core loss calculation per unit volume, for the sinusoidal excitation is the Steinmetz equation given by

$$P_v = k f^{\alpha} \left(\Delta B/2\right)^{\beta} \tag{19}$$

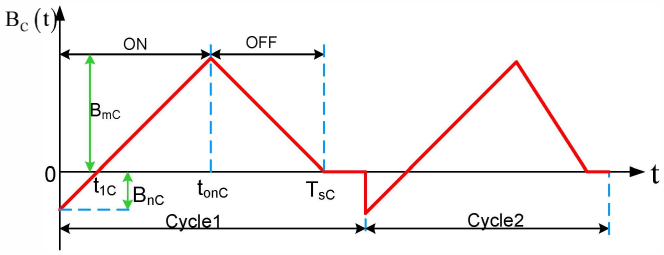

Fig. 8. Flux density waveform during the charging mode.

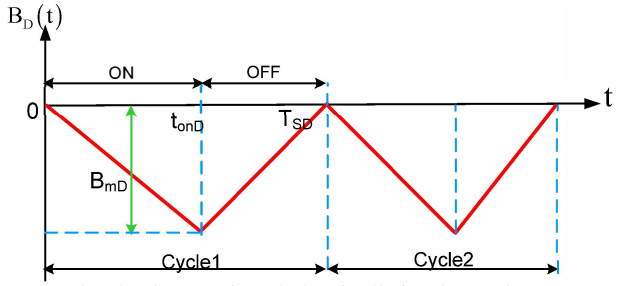

Fig. 9. Flux density waveform during the discharging mode.

The core loss per unit volume due to non-sinusoidal excitation is calculated using the improved generalized Steinmetz equation (IGSE) [10] which is given by

$$P_v = \frac{1}{T}\left[\int_0^T k_i \left|\frac{dB(t)}{dt}\right|^{\alpha} (\Delta B)^{\beta-\alpha}\, dt\right],\ k_i = \frac{k}{(2\pi)^{\alpha-1} \int_0^{2\pi} \left|cos\,\theta\right|^{\alpha} 2^{\beta-\alpha}\, d\theta} \tag{20}$$

where k, α and β are the constants provided by the manufacturer, ΔB is the peak-to-peak flux density of the current excitation. The angle θ represents the phase angle of the sinusoidal waveform. Figs. 8 and 9 show the flux density waveforms during charging and discharging modes.

The core loss per unit volume during the charge operation in each switching cycle is given by

$$P_{vC} = \frac{k_{iC}}{T_{sC}}\left[\left(B_{mC} + B_{nC}\right)^{\beta_C} \cdot t_{onC}^{\,1-\alpha_C} + B_{mC}^{\,\beta_C} \cdot t_{offC}^{\,1-\alpha_C}\right] \tag{21}$$

Similarly the core loss per unit volume during the discharge operation in each switching cycle is given by

$$P_{vD} = \frac{k_{iD} B_{mD}^{\,\beta_D}}{T_{sD}}\left[t_{onD}^{\,1-\alpha_D} + t_{offD}^{\,1-\alpha_D}\right] \tag{22}$$

with $k_{iC}, \beta_C, \alpha_C, T_{sC}, B_{mC}, t_{onC}, t_{offC}$ / $k_{iD}, \beta_D, \alpha_D, T_{sD}, B_{mD}, t_{onD}, t_{offD}$ as the core loss constants, switching period in each cycle, peak flux density, on-time and off-time in each switching cycle during charging/discharging modes respectively.

C. *Losses in the bi-directional flyback converter excluding the magnetic losses*

Different losses associated with the bi-directional flyback converter are provided in Table I. The loss distribution can be made after calculating all those losses. The results of the loss analysis are shown in Section V.

TABLE I. DIFFERENT LOSSES IN THE BI-DIRECTIONAL FLYBACK CONVERTER DURING CHARGE AND DISCHARGE OPERATIONS

Type of power loss			Power loss expression	Abbreviations *The subscript 'P' / 'S' or 'C' / 'D' in any variable represents that variable is being referred to primary / secondary side or that variable during charging and discharging modes*
Switching loss	Low voltage MOSFET		$P_{swP}=\frac{f_{swC}}{2}\left[\begin{matrix}(C_{wP}+C_{ossP})V_{dsP}^2+\\ V_{dsP}I_{pkPC}(t_{if}+t_{vr})\end{matrix}\right]$	C_{wP}/C_{wS} - self capacitance of the transformer primary/secondary C_{ossP}/C_{ossS} - output capacitance of the primary/secondary MOSFET V_{dsP}/V_{dsS} - primary/secondary MOSFET drain to source voltage $V_{dsP}=V_{in}+V_{out}/n$; $V_{dsS}=V_{out}+nV_{in}$ f_{swC} / f_{swD} - switching frequency during charging/discharging operation n - turns ratio of the transformer from secondary to primary t_{if} / t_{vr} - current fall/voltage rise transition times of the corresponding MOSFETs
	HV MOSFET		$P_{swD}=\frac{f_{swD}}{2}\left[\begin{matrix}(C_{wS}+C_{ossS})V_{dsP}^2+\\ V_{dsS}I_{pkSD}(t_{if}+t_{vr})\end{matrix}\right]$	
Conduction loss	Low voltage MOSFET		$P_{cP}=I_{RMSPC}^2 r_{dsonP}$ $I_{RMSPC}^2=\frac{I_{pkPC}^2}{3}\left(\frac{D_{onC}T_{sC}-t_1}{T_{sC}}\right)+\frac{I_{min}^2}{3}\left(\frac{t_1}{T_{sC}}\right)$	r_{dsonP}/r_{dsonS} - on-resistance of the primary/secondary MOSFET I_{RMSPC}/I_{RMSSC} - primary/secondary rms current during charging mode I_{RMSPD}/I_{RMSSD} - primary/secondary rms current during discharging mode I_{min} - negative current at the beginning of the turn-on process V_{f_D} - HV diode forward voltage drop I_{DCSC} / I_{RMSSC} - average/rms current through the HV diode D_2 during charging I_{DCSD} / I_{RMSSD} - average/rms current through the HV diode D_b during discharging r_D - HV diode on resistance $V_{f_{M_1}}$ - forward voltage drop of body diode of M_1 I_{DCPD} - average current through primary during discharging D_{onC} / D_{onD} - on-duty cycle during charging/discharging
	Sense resistor on the primary side		$P_{senePC}=I_{RMSPC}^2 r_{senseP}$ $P_{sensePD}=I_{RMSPD}^2 r_{senseP}$	
	HV MOSFET		$P_{cS}=I_{RMSSD}^2 r_{dsonS}$ $I_{RMSSD}^2=\frac{I_{pkSD}^2}{3}D_{onD}$	
	HV diode	Diode D_2	$P_{cD_2}=V_{f_D}I_{DCSC}+r_D I_{RMSSC}^2$	
		Diode D_b	$P_{cD_b}=V_{f_D}I_{DCSD}+r_D I_{RMSSD}^2$	
	Body diode of low voltage MOSFET		$P_{cBDM_1}=V_{f_{M_1}}I_{DCPD}$	
Reverse recovery loss of HV diode			$P_{rrC}=Q_{rr}(V_{out}+nV_{in})f_{swC}$ $Q_{rr}=\int_t^{t+t_{rr}}-i_s\,dt$	Q_{rr}/t_{rr} - reverse recovery charge/time in the high voltage diode D_2 i_s - secondary current, V_{out}/V_{in} - output/input voltage of flyback converter
Gate driver loss			$P_{Gate}=V_{GS}(Q_{GM_2}f_{swD}+Q_{GM_1}f_{swC})$	V_{GS} - gate drive voltage of the MOSFET Q_{GM_2}/Q_{GM_1} - gate charge for high voltage/low voltage MOSFETS
Snubber loss	RC snubber across primary MOSFET		$P_{snLV}=C_{sn}V_{dsP}^2 f_{swC}$	C_{sn} -snubber capacitance in the RC snubber V_{clamp} - clamping voltage of the RCD snubber
	RCD snubber across secondary winding		$P_{snHV}=\frac{1}{2}L_{lkS}I_{pkSD}^2\frac{V_{clamp}}{V_{clamp}-nV_{in}}f_{swD}$	
Power consumption in the two control IC's			$P_{Controller}=2V_{cc}I_Q$	V_{cc} - IC supply voltage I_Q - quiescent current of V_{cc}

IV. HV TRANSFORMER DESIGN: COMPARISON OF MEASUREMENTS AND CALCULATIONS

Since the proposed DC-DC converter operates in a wide output voltage range (0-2.5 *k*V), to charge and discharge the DEAP actuator employed in a specific application, different components of the converter have to be designed for different operating points. High voltage capacitor charging application requires proper design of the transformer, otherwise significant amount of energy is lost and efficiency will suffer.

The parameters that significantly affect the efficiency of the converter for capacitor charging application are the peak current, MOSFET type, transformer type and size, magnetizing

inductance, the turns ratio, air-gap length, AC resistance, leakage inductance, and HV winding capacitance.

V. Experimental and Simulation Results

The specifications of the bi-directional flyback converter and the components used in it are provided in Tables II and III respectively. The flyback transformer parameters are shown in Tables V. The experimental prototype is shown in Fig. 11. A boundary mode controller LT3751 has been used for performing both charging and discharging operations. The bi-directional flyback converter charge and discharge cycles are controlled using a microcontroller. Table IV presents the components used in the bi-directional flyback converter. Fig. 10 shows the comparison of the calculated and measured charging and discharging energy efficiencies of the converter. The energy efficiency definitions can be obtained from [13].

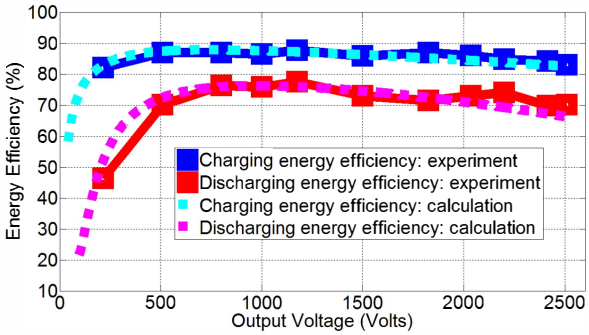

Fig. 10. Comparison of the experimental and the calculated charging and discharging energy efficiencies for a non-interleaved transformer.

TABLE II. Bi-Directional Flyback Converter Specifications

Parameter	Value
Input voltage	24 V
Output voltage	0-2500 V
Stored energy in the load at 2.5 *kV* output voltage	0.625 J
Capacitance of the film capacitive load	200 *nF*
Primary peak current during charging/discharging	4.24 A / 5.3 A

TABLE III. Components Used in the Bi-Directional Flyback Converter

Component	Name
Low voltage MOSFET	STB50NF25 [250 V, 45 A, 55 *mΩ*]
HV MOSFET	IXTV03N400S [4 *kV*, 300 *mA*, 290 Ω]
HV diode	SP5LFG [5 *kV*, 400 *mA*, 50 *ns*(t_{rr})]
Film capacitor load	WIMA [200 *nF* , 3 *kV*]
Analog control IC	LT 3751

TABLE IV. Comparison of HV Transformer Parameters

Parameter	Calculation		Measurement
DC resistance of secondary winding of transformer (Ω)	23		27.5
Leakage inductance of primary winding of transformer (*μH*)	1.09		1.11
Self capacitance of HV winding (*pF*)	**Eq. (11)**	**Eq. (13)**	16.29
	17.65	13.58	

TABLE V. Flyback Transformer Parameters with Non-Interleaving Structure

Parameter	Value
Flyback transformer core type / Material	EF20 / N87
Primary (L_{mP}) / Secondary magnetizing inductance (L_{mS})	28 *μH* / 15.3 *mH*
Primary turns (N_P) / Secondary turns (N_S)	16 / 375
Leakage inductance of transformer primary (L_{lkP}) / secondary (L_{lkS})	1.11 *μH* / 633 *μH*
Secondary winding self (C_s) / Interwinding capacitance (C_{int})	16.29 *pF* / 41 *pF*
DC resistance of primary (R_{acP}) / secondary winding (R_{acS})	62 *mΩ* / 28.5 Ω
Primary (n_{lp}) / Secondary layers (n_{ls})	1 / 5
Turns per layer of primary (T_{Lp}) / secondary (T_{Ls})	16 / 75
Each layer primary (h_p) / secondary winding thickness (h_s)	0.5 *mm* / 0.1 *mm*
Insulation thickness between secondary layers (h_{is})	0.1 *mm* (Kapton Tape)
Insulation thickness between the primary layer and the adjacent secondary layer (h_i)	0.3 *mm*
Transformer edge isolation tape width	1.6 *mm* So, $b_w = b_w - 2\times1.6$ *mm*
Dielectric constant of the insulation of the HV winding (ε_r)	3.5

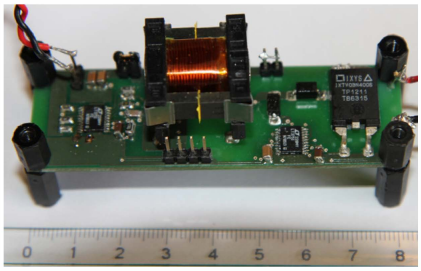

Fig. 11. Picture of the experimental setup.

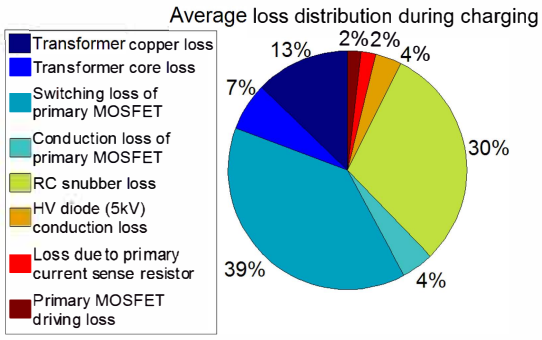

Fig. 12. Average loss distribution during charging of capacitive load.

All loss calculations are done in Matlab. The average loss distributions of the bi-directional flyback converter during charging and discharging modes are shown in Figs. 12 and 13 respectively. Fig. 14 provides the comparison of the average power losses during charging and discharging modes. The peak current of the primary MOSFET has been changed, and

the charging energy efficiency variation has been provided in Fig. 15. In Fig. 16 we show the variation of the energy efficiency with the porosity factor. At high porosity factor the HV winding capacitance is high, so the discharging energy efficiency at 2.5 *k*V is low compared to that at medium porosity factor. However, at low porosity factor, the AC/DC resistance increases, so both charging and discharging energy efficiencies will drop.

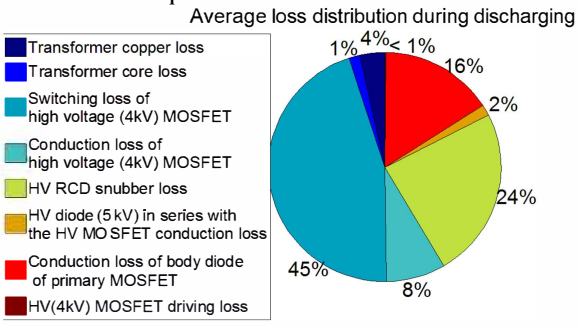

Fig. 13. Average loss distribution during discharging of capacitive load.

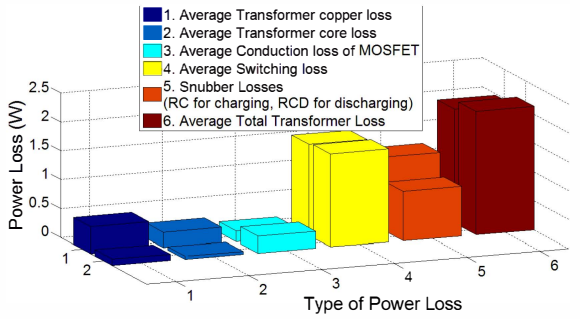

Fig. 14. Comparison of the average loss; On Y-axis, 1 and 2-corresponds to power loss during charging and discharging respectively.

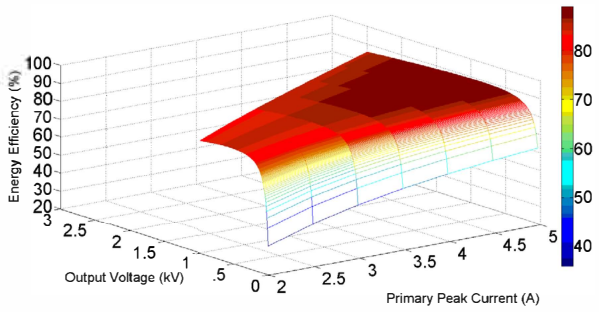

Fig. 15. 3D plot showing how the peak current affects the charging energy.

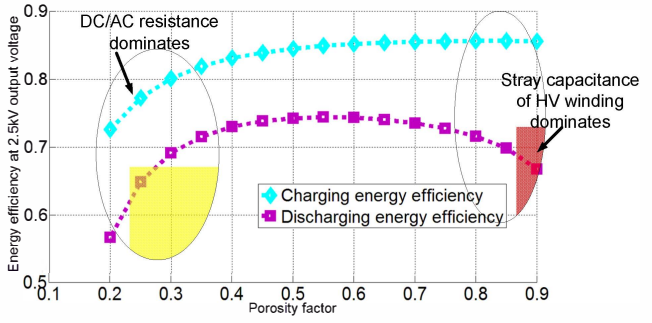

Fig. 16. Variation of energy efficiency at 2.5 *k*V with porosity factor (d_i/d_o)

VI. Conclusion

The power losses in the bi-directional flyback converter for the capacitor charging application has been analyzed in detail. Due to the variable switching frequency and non-sinusoidal waveforms, it is very difficult to accurately compute the core and winding losses. The core loss was accurately calculated during charge and discharge operations, using piecewise linear approximation of the IGSE model.

Estimation of the leakage inductance for a non-interleaved structure and an interleaved winding structure has been discussed. Stray capacitance calculation for a typical HV winding structure is discussed. Trade-off between the different transformer parameters has been made with respect to porosity factor. Comparison of the measurement efficiency and the calculated efficiency shows the accuracy of the proposed loss analysis.

The future work involves the optimization of the whole converter with mostly focusing on transformer optimization.

References

[1] R. Pelrine, P. S. Larsen, R. Kornbluh, R. Heydt, G. Kofod, Q. Pei, P. Gravesen, "Applications of dielectric elastomer actuators," in *Proc. SPIE*, vol. 4329, pp. 335-349, 2001.

[2] M. Tryson, H. E. Kiil, and M. Benslimane, "Powerful tubular core free dielectric electro activate polymer (DEAP) push actuator," in *Proc. SPIE* vol. 7287, p. 72871F, 2009.

[3] P. Thummala, L. Huang, Z. Zhang and M. A. E. Andersen, "Analysis of Dielectric Electro Active Polymer Actuator and its High Voltage Driving Circuits," in *Proc. IPMHVC*, pp. , Jun. 4-7, 2012.

[4] P. Thummala, Z. Zhang, M. A. E. Andersen, O. C. Thomsen, "A high voltage DC-DC converter driving a Dielectric Electro Active Polymer actuator for wind turbine flaps," in *Proc. UPEC* pp.1,7, 4-7 Sept. 2012.

[5] W.G. Hurley, E. Gath, J. G. Breslin, "Optimizing the AC resistance of multilayer transformer windings with arbitrary current waveforms," *IEEE Trans. Power Electronics*, vol.15, no.2, pp.369-376, Mar 2000.

[6] D. Murthy-Bellur, M. K. Kazimierczuk, "Winding losses caused by harmonics in high-frequency flyback transformers for pulse-width modulated dc-dc converters in discontinuous conduction mode," *IET Trans. Power Electronics*, vol.3, no.5, pp.804,817, September 2010.

[7] J. Zhang, Z. Ouyang, M. Duffy, M. A. E Andersen and W. G. Hurley "Leakage inductance calculation for planar transformer with magnetic shunt", in *Proc. ECCE USA* 2013 (accepted).

[8] Z. Ouyang, O. C. Thomsen, M. A. E. Andersen, "The analysis and comparison of leakage inductance in different winding arrangements for planar transformer", *in Proc. IEEE PEDS*, pp. 1143-1148, Nov. 2009.

[9] L. Dalessandro, F. da Silveira Cavalcante, J. W. Kolar, "Self-Capacitance of High-Voltage Transformers," *IEEE Trans. On Power Electronics*, Vol. 22, no.5, pp. 2081-2092, Sept. 2007.

[10] J. Biela, J. W. Kolar, "Using Transformer Parasitics for Resonant Converters—A Review of the Calculation of the Stray Capacitance of Transformers," *IEEE Trans. on Industry Applications*, , vol. 44, no.1, pp. 223-233, 2008.

[11] E. C. Snelling, *Soft Ferrites-Properties and applications*, 2nd ed. London, UK, Butterworth, 1988.

[12] K. Venkatachalam, C. R. Sullivan, T. Abdallah, and H. Tacca, "Accurate prediction of ferrite cores loss with nonsinusoidal waveforms using only Steinmetz parameters," in *Proc. IEEE Workshop Comput. Power Electron.*, pp. 36–41, 2002.

[13] P. Thummala, Z. Zhang and M. A. E. Andersen, "Bi-directional Flyback Converter for Capacitive Actuator", in *Proc. EPE* 2013 (accepted).

[14] LT3751, "High voltage capacitor charger controller with regulation," datasheet.

Appendix G

Optimization of bi-directional flyback converter for a high voltage capacitor charging application

---

2014 IEEE Applied Power Electronics Conference and Exposition (APEC 2014)

Optimization of bi-directional flyback converter for a high voltage capacitor charging application

Prasanth Thummala, Henrik Schneider, Zhe Zhang, Arnold Knott, Michael A. E. Andersen
Electronics Group, Department of Electrical Engineering
Technical University of Denmark
2800 Kongens Lyngby, Denmark
pthu@elektro.dtu.dk, hensc@elektro.dtu.dk

Abstract—This paper presents an optimization technique for a flyback converter with a bidirectional energy transfer. The main goal is to optimize the converter for driving an incremental dielectric electro active polymer actuator, which must be charged and discharged from 0 V to 2500 V DC, supplied from a 24 V battery. The proposed optimization routine sweeps through a database of low voltage switching devices, and transformer core types and sizes. For each core, important winding parameters such as, the vertical winding space allocation for primary and secondary windings, and the spacing between the secondary windings layers are also swept. This enables the optimization routine to calculate and optimize the losses caused by transformer parasitics such as leakage inductance, self-capacitance and AC resistance which is crucial in achieving a high energy efficiency and high power density required for this application. The efficiency and loss distribution results provided by the optimization routine provide a deep insight into the transformer design and its impact on total converter efficiency. Finally, experimental work on a prototype of the bi-directional flyback converter is presented. The maximum charging and discharging energy efficiencies of the optimized design, are 96.1% and 85%, respectively.

I. INTRODUCTION

Dielectric electro active polymer (DEAP) is an emerging smart material that has experienced substantial development and has gained increasing attention over the last decade [1]-[4]. The DEAP technology can be used in actuator, sensor and energy harvesting applications. Bidirectional power electronics are of particular interest in DEAP actuator applications since the potential of the material needs to be high (charged) to expand and low (discharged) to retract. In Fig. 1, an illustration of an incremental actuator using two DEAPs as grippers and one DEAP as an extender is shown. DEAP, when used as incremental actuators, has the potential to be an effective replacement for many conventional incremental actuators due to its unique properties, such as large strain, light weight, low power consumption, and high flexibility. The DEAP technology has the potential to be used in various industries, e.g. automotive, aeronautics, space and medicine. In order to take full advantage of the DEAP potential, the drivers for the DEAP's need to have a low volume to be utilized in small spaces and the weight and energy efficiency influence the achieved traveling distance when powered from a battery.

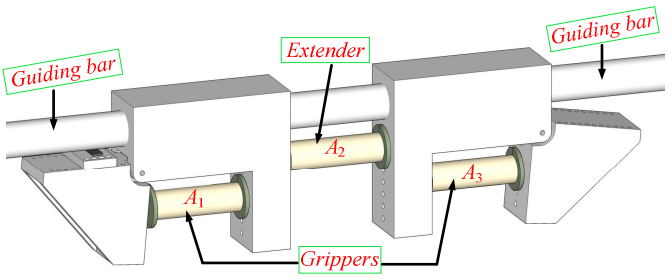

Figure 1. Incremental DEAP actuator [24].

The flyback topology is selected for the high voltage driver since it is suitable for low power (< 150 W) and has a low component count. High voltage switch-mode power supplies for charging the capacitive loads have been implemented in [5]-[12]. The design methodologies for transformers used in conventional switch mode power supplies are well documented in the literature. However, the procedures are conservative and are based on some assumptions in order to provide a simple, low risk and fast design phase. Often, the size of a suitable core is calculated based on assumptions such as constant switching frequency, a guess of the total converter efficiency, transformer conduction loss and core loss based on sinusoidal excitation and estimation of the winding current density. Thus, more complex and customized design procedures tailored for specific applications are needed to achieve efficient transformer designs. In this paper, an unconventional optimization routine is developed and tailored for bi-directional flyback converters, for high voltage capacitor charging and discharging applications, since literature regarding for this application is very limited [21]. The transformer optimization procedures for the switch-mode DC-DC converters have been discussed in [13]-[20]. The efficiency optimization method of the digitally controlled flyback converter for wide operating conditions is given in [15]. Analytical optimization of solid round wire conductors is

This work was sponsored by Danish National Advanced Technology Foundation.

proposed in [16]. In [17], a weighted efficiency oriented design methodology is proposed for a flyback inverter. The optimization routine is different from most methods since it does not depend on any guess work, estimations or rule of thumb approaches in order to achieve the transformer design. Instead, advanced algorithms for calculating the transformer parasitics are used in combination with a comprehensive loss model in order to evaluate the converter efficiency and other key parameters for a wide range of implementation possibilities. The loss model takes into account that the waveforms in the flyback converter are not sinusoidal in both the conduction and switching loss calculations. The optimization routine provides the designer with the necessary practical details of the chosen design such as core size, core material, wire sizes, number of winding layers, etc. In order to provide a high level of driver design flexibility for different DEAP applications, the driver efficiency and its size/weight can be weighted. The main idea behind the optimization routine can easily be adapted to fit other topologies and applications.

II. Optimization Routine

The optimization routine is described as follows: first, a drain to source voltage of the primary MOSFET is selected from a range of voltage levels. Then the turns ratio, magnetizing inductance, peak primary current, and primary and secondary turns are calculated using the converter specifications (input and maximum output voltages, charging time). Next, a primary MOSFET rated for the selected drain to source voltage is selected from a range of MOSFETs with varying parameters such as MOSFET package type, on-resistance and gate charge, etc. Next a transformer core is selected, followed by the choice of winding space allocation and layer to layer spacing. A dynamic winding function is used to design the transformer enabling the calculation of transformer parameters. Finally, losses in all components of the bi-directional flyback converter [6], in both charging and discharging modes are calculated [12] and added to represent the total estimated loss for that specific design. The optimization routine iterates through all design possibilities and in this case presents two solutions: one for the smallest transformer (limited by a temperature limit), and another for the most efficient solution (limited by an increase in converter efficiency vs. increase in transformer size). In the following sections, the challenges faced in the optimization routine are described, and solutions are presented.

A. Dynamic transformer design

Well into the optimization routine when the design parameters such as the number of turns and the allocated winding space is locked a winding implementation need to be found. In order to simplify that task the huge design space is limited - see Table 1. The core types are limited to 5 types. It is hard to predict which core type is most suitable for any application. In a flyback converter, a long transformer window width is often preferred to minimize the leakage inductance and AC resistance by providing a close coupling between windings and decrease the amount of winding layers. For high voltage converters, this could be different, since the winding self-capacitance on the high voltage side has a significant impact on the performance of the converter. Only the N87 core material and a simple non-interleaved winding structure (S-P) are used to limit complexity of the proposed optimization method. However, the optimization method can be easily adopted for an interleaved winding structure. Single insulated solid wire is used for the secondary winding since a

TABLE I. High voltage transformer structures and winding information

Description	Design decision	Advantages
Core type	ETD, EFD, E, RM and PQ	Round and square center leg ease the analytical complexity.
Core material	N87	Suitable for high frequency of operation.
Winding structure	P / S	Simple implementation and decreases analytical complexity.
Primary winding type	Solid wire	Flexible in terms of design and different winding structures.
Primary winding insulation	Triple insulation	Avoid edge tape to achieve a higher fill factor. More flexible in terms of implementation.
Secondary winding type	Solid wire	Suitable winding type, for a large number of turns. Flexible in terms of design, prototyping and different winding structures.
Secondary winding insulation	Single insulation	Minimum insulation thickness for a large number of turns.
Air gap	All legs	Simplifies the prototyping.
Maximum transformer temperature	140 °C	With an estimated ambient temperature of 40 °C, this enables a transformer temperature rise of 100 °C.

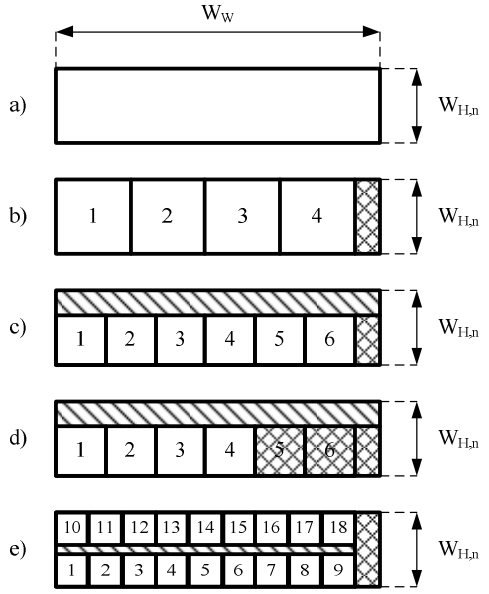

Figure 2. Cases from the dynamic transformer design. a) Allocated winding area. b) Initial starting point (Square width = area height). c) Unused space above and beside the squares (fill factor < 1). d) Squares not used (fill factor << 1). e) Close to ideal winding implementation (All squares used for the windings, horizontal space used as spacing between layers, high fill factor).

lot of turns are needed. The proper insulation between primary and secondary windings are achieved using a triple insulated solid wire for the secondary winding, which has proven to increase the winding fill factor and thus the efficiency and/or size of the transformer. The air gap is provided in all legs of the core, and the maximum air gap length is limited to 20% of the center leg length/window width, to avoid the loss due to the fringing field. A maximum transformer temperature limit of 140 °C is chosen. These limitation values can be altered based on the experience of the designer or the initial design specifications.

In this section, different cases about the dynamic transformer design are explained. The concept is best understood with the help of visualization. In Fig. 2.a, the space allocation for a given winding is shown. The width of the available area is the width of the bobbin window W_W and the height of the area is the allocated height for the winding $W_{H,n}$. The first step is to split the area into squares with a square width (W_{sq}) equal to the allocated height for the winding. It is $\alpha W_{H,n}$ for secondary and $(1-\alpha)W_{H,n}$ for the primary winding, with being the space allocation factor for secondary. In this case, it results in 4 squares and a non-square area that is considered as an unusable area as shown in Fig 2.b. In each square, a solid round wire could be placed with a diameter equal to the width of the square or a bundle of round wires with an outside bundle diameter equal to the width of the square. In this work, only the first option has been considered since the high number of needed secondary turns result in very thin wire diameter compared to the skin depth. If the number of turns required is 4 or less, this case will be considered as a valid solution and saved for later comparison with other found solutions. If a single turn is needed, then four squares could be utilized by 4 round wires in parallel and only the non-square area would not be used. The wire diameter may not be optimal compared to the skin depth which is why more solutions need to be considered and validated. This is achieved by splitting the winding area into smaller and smaller squares. The width of the squares for the secondary winding is limited by the smallest practical feasible diameter of a solid round wire (0.08 mm). In Fig. 2.c, the square size limits the use of the shaded area above the squares. However, that area can be set free for another winding thus improving the overall fill factor. The case shown in Fig. 2.d, illustrates, how the fill factor of a winding is reduced if not all squares are utilized as a turn. Fig. 2.e, illustrates how an optimum winding solution could look like if 18 turns were needed and the width of the square was optimum in terms of skin depth. Note that non-square horizontal area is utilized as spacing between the layers. The spacing distance is swept in order to balance the transformer parameters and the converter performance.

In Fig. 3, a flowchart of the dynamic transformer winding design is shown. The gray arrows point to a set of variables that are calculated during each iteration viz, squares per column (Sq_{Column}), squares per row (Sq_{Row}), total squares (Sq_{Total}), squares in parallel ($Sq_{Parallel}$), number of layers (N_{Layers}), total squares used (Sq_{Used}), last or final layer fill factor ($FF_{LastLayer}$) and spacing between the layers ($Space_{Layers}$). These variables are calculated from the equations (1)-(9). As explained earlier, the design phase starts by defining a square

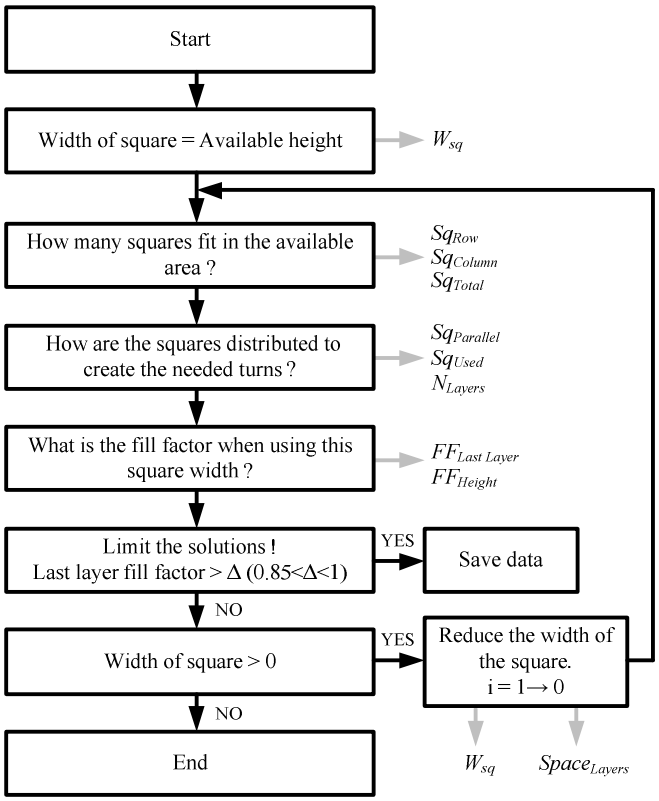

Figure 3. Flowchart of dynamic winding design.

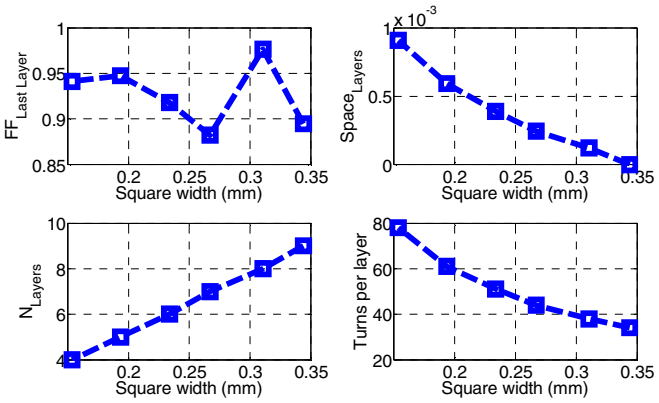

Figure 4. Results of the dynamic winding design for optimized core.

sized based on the allocated height for a given winding. Then important information about how many squares that can fit into the available area is calculated. The actual number of squares used to construct the winding is then determined based on the number of turns needed. The calculated variables are saved if the fill factor of the final layer is above 85 percent. This limit is implemented since the calculations of the transformer parameters are based on fully occupied layers.

$$W_{Sq} = \alpha \cdot W_{H,n} \cdot i \tag{1}$$

where the variable i varies from 1 to 0 in small steps.

$$Sq_{Column} = floor\left(\frac{\alpha W_{H,n}}{W_{Sq}}\right) \tag{2}$$

$$Sq_{Row} = floor\left(\frac{W_w}{W_{Sq}}\right) \tag{3}$$

$$Sq_{Total} = Sq_{Column} \cdot Sq_{Row} \tag{4}$$

$$Sq_{Parallel} = floor\left(\frac{Sq_{Total}}{N}\right) \tag{5}$$

where N is the number of turns of that particular winding for which the dynamic winding design is applied.

$$Sq_{Used} = N \cdot Sq_{Parallel} \tag{6}$$

$$N_{Layers} = ceil\left(\frac{Sq_{Used}}{Sq_{Row}}\right) \tag{7}$$

$$FF_{Last\ Layer} = \left[\frac{N}{Sq_{Row}} - floor\left(\frac{N}{Sq_{Row}}\right)\right] \tag{8}$$

$$Space_{Layers} = \frac{W_{H,n} - N_{layers}W_{sq}}{\left(N_{layers} - 1\right)} \tag{9}$$

In the above equations $ceil(x+\Delta x)=x+1$ and $floor(x+\Delta x)=x$ with $0<\Delta x<1$.

B. *Estimation of transformer parasitics and comprehensive loss model*

The outputs of the dynamic transformer design are used to calculate the transformer parasitics [12] such as DC and AC resistances, leakage inductance and self-capacitance. The loss model has been verified in [12]. In this paper, the winding loss calculations are calculated accurately, since the primary and secondary currents are 180° out of phase.

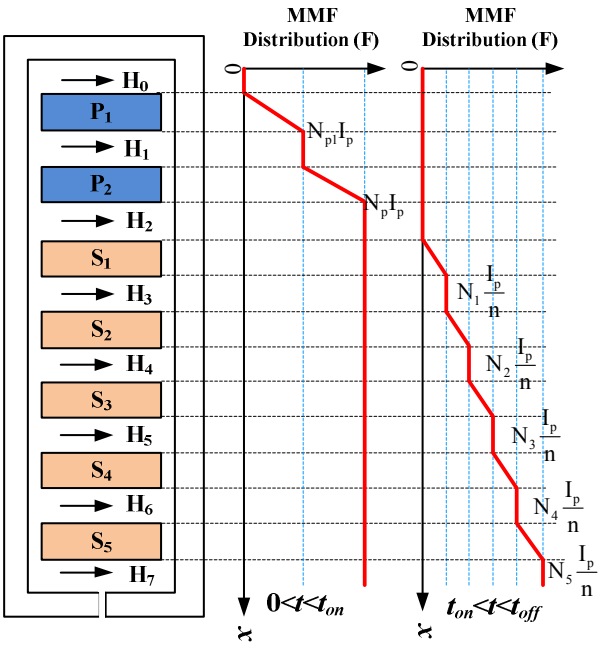

Figure 5. MMF distribution of the non-interleaved (P-P-S-S-S-S-S) structure with respect to space (secondary winding is wounded on the bobbin first).

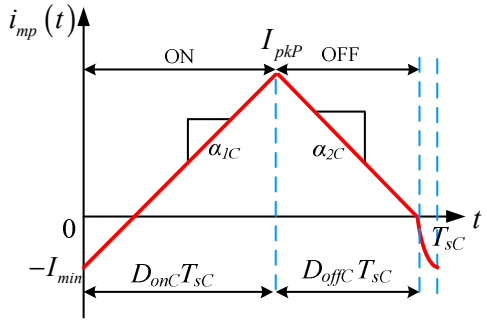

Figure 6. Magnetizing current during the charge process.

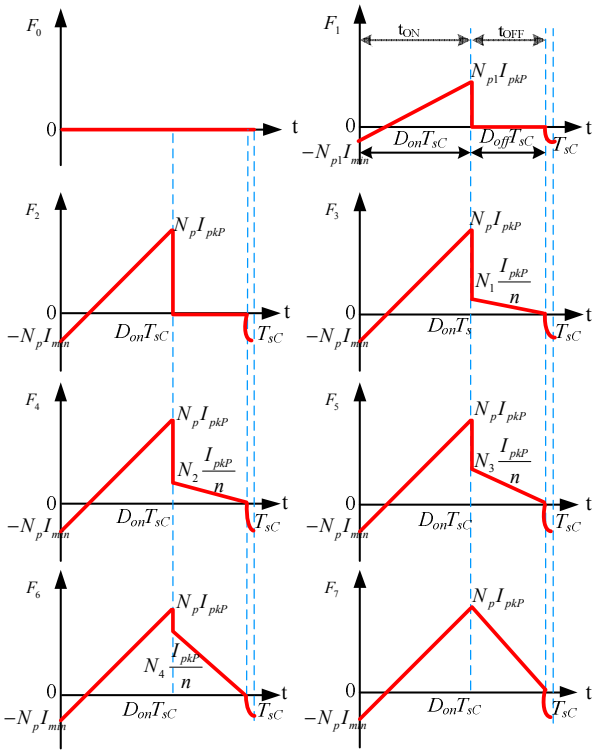

Figure 7. MMF distribution of the non-interleaved (P-P-S-S-S-S-S) structure with respect to time during the charge process.

1) Flyback transformer winding loss during charge process:

The high voltage bi-directional flyback converter proposed in [6], [12], operates in boundary conduction mode (BCM) with variable switching frequency during the charge process and in discontinuous conduction mode (DCM) during the discharge process. The winding loss in a flyback transformer is calculated using the MMF analysis presented in [22]. For the winding loss modeling, a non-interleaved transformer with 2 layers on the primary side and 5 layers on the secondary side is considered as an example. The MMF distribution in a flyback transformer is different from that of a normal transformer [22]. Fig. 5 shows different MMF distributions during both turn-on ($0<t<t_{on}$) and turn-off ($t_{on}<t<t_{off}$) periods in a non-interleaved flyback transformer. The magnetizing current and the time variation of the MMF at the boundary of each layer during the charging process are shown in Figs. 6 and 7, respectively. As the output voltage increases, the magnitude of the minimum negative current $-I_{min}$, in Fig. 6

increases with the switching frequency during the charge process [6], [12].

In Fig. 7, since the negative MMF is presented at the end of each switching cycle for very short time compared to the switching period, it can be neglected in the loss calculation. In Fig. 5, N_{p1} and N_p, are the number turns in the primary layer 1 and the total primary turns. The terms N_1, N_2, N_3, N_4, N_5 are defined as follows: $N_1=N_{s1}$, $N_2=N_{s1}+N_{s2}$, $N_3=N_{s1}+N_{s2}+N_{s3}$, $N_4=N_{s1}+N_{s2}+N_{s3}+N_{s4}$, and $N_5=N_{s1}+N_{s2}+N_{s3}+N_{s4}+N_{s5}=N_s$ where N_{s1}, N_{s2}, N_{s3}, N_{s4}, N_{s5} and N_s are the number of turns in the secondary layers 1, 2, 3, 4, 5, and total secondary turns, respectively.

The magnetizing current and the time variation of the MMFs at the boundary of each layer during the discharging process are shown in Figs. 8 and 9, respectively. Even though the magnetizing current is negative during the discharging process compared to that in the charging process, for the convenience the MMF waveforms are drawn as positive (since the power loss is a function of square of the MMFs, see (10)).

The MMF distribution in each transformer winding layer in the time domain is decomposed into sinusoidal harmonics by Fourier series analysis. The power loss is then computed for each harmonic, and the power loss densities over all harmonics are summed to find the power dissipated in each layer. The corresponding loss model in each layer (P_{layer}) is given by [22], [23]

$$P_{\text{layer}} = \frac{R_{layer}}{2N_l^2}\sum_{i=1}^{\infty}\varepsilon_i\begin{bmatrix}\left(\left|F_i(h)\right|^2+\left|F_i(0)\right|^2\right)G_1(\varepsilon_i)\\ -4\left|F_i(h)\right|\left|F_i(0)\right|\cos(\Delta\theta)G_2(\varepsilon_i)\end{bmatrix} \tag{10}$$

$$\delta_i = \sqrt{\frac{\rho}{\pi\mu_0 i f_{si}}} \tag{11}$$

$$\varepsilon_i = \left(\frac{\pi}{4}\right)^{0.75}\sqrt{\frac{N_l}{w_w}}\left(\frac{d^{1.5}}{\delta_i}\right) \tag{12}$$

$$G_1(\varepsilon_i) = \frac{\sinh(2\varepsilon_i)+\sin(2\varepsilon_i)}{\cosh(2\varepsilon_i)-\cos(2\varepsilon_i)} \tag{13}$$

$$G_2(\varepsilon_i) = \frac{\sinh(\varepsilon_i)\cos(\varepsilon_i)+\cosh(\varepsilon_i)\sin(\varepsilon_i)}{\cosh(2\varepsilon_i)-\cos(2\varepsilon_i)} \tag{14}$$

$F_i(h)$ and $F_i(0)$ are the MMF amplitudes of the i^{th} harmonic at $x=0$ and $x=h$ respectively, assuming h as the thickness of each layer, with the suffix i being the harmonic number. For example for layer 1, $F_i(h)=F_1$ and $F_i(0)=F_0$; for layer 2, $F_i(h)=F_2$ and $F_i(0)=F_1$, and so on. R_{layer} is the resistance of each layer, T_l is the number of turns in each layer, δ_i is the skin depth of the conductor material, ε_i is the ratio of conductor diameter to the effective skin depth, G_1 and G_2, which are functions of ε_i, are given by (13) and (14) [22].

The amplitude and phase of i^{th} harmonic of the MMF during the charge process are given by

$$\left|F_i\right| = \sqrt{a_i^2+b_i^2} \tag{15}$$

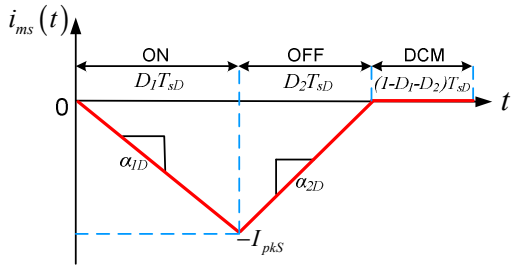

Figure 8. Magnetizing current during the discharge process.

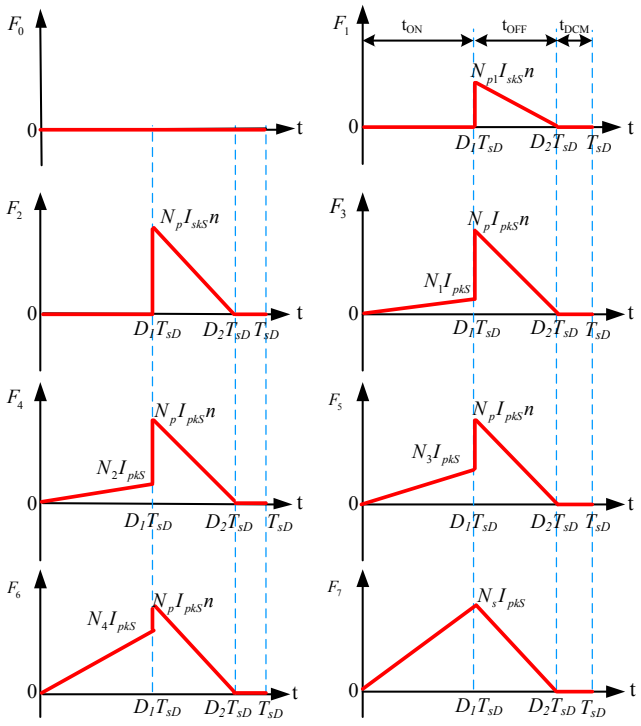

Figure 9. MMF distribution of the non-interleaved (P-P-S-S-S-S-S) structure with respect to time during the discharge process.

$$\theta_i = \begin{cases}\tan^{-1}\left(-\dfrac{b_i}{a_i}\right), & \text{if } a_i \geq 0\\ \pi+\tan^{-1}\left(-\dfrac{b_i}{a_i}\right), & \text{if } a_i < 0\end{cases} \tag{16}$$

$$\Delta\theta = \theta_i(0)-\theta_i(h) \tag{17}$$

The coefficients of the Fourier series of each MMF, during the charging process are given by

$$a_i = \frac{2}{T_{sC}^2 w_i^2}\begin{bmatrix}(\alpha_{1C}-\alpha_{2C})\cos(D_{onC}T_{sC}w_i)+\alpha_{2C}-\alpha_{1C}+\\ w_i(F_{f1}-F_{i2})\sin(D_{onC}T_{sC}w_i)\end{bmatrix} \tag{18}$$

$$b_i = \frac{2}{T_{sC}^2 w_i^2}\begin{bmatrix}(\alpha_{1C}-\alpha_{2C})\sin(D_{onC}T_{sC}w_i)-\alpha_{1C}+\\ w_i(F_{i2}-F_{f1})\cos(D_{onC}T_{sC}w_i)-w_iF_{i1}\end{bmatrix} \tag{19}$$

$$w_{iC} = \frac{2\pi i}{T_{sC}} \tag{20}$$

where w_{iC} the frequency of the i^{th} harmonic, T_{sC} is the switching period, and α_{1C}, α_{2C} are the on-time and off-time slopes of the corresponding MMFs, during the charging process, respectively. F_{i1}, F_{f1}, F_{i2} and F_{f2}, are the initial and final MMFs of the MMF waveform during the turn-on and turn-off processes, respectively.

The expression for the total winding loss in a flyback transformer during the charge process is

$$P_{winding,flyback} = I_{DC,P}^2 R_{DC,P} + I_{DC,S}^2 R_{DC,S} + \sum_{k=1}^{n_{ls}+n_{lp}} P_{\text{layer}}(k) \tag{21}$$

where n_{ls}, n_{lp}, $I_{DC,P}$, $I_{DC,S}$, and $R_{DC,P}$, $R_{DC,S}$ are the number of primary, secondary layers, primary, secondary DC current, primary, secondary DC resistances, during the charge process, respectively.

2) Flyback transformer winding loss during discharge process:

The winding loss during the discharge process is calculated similar to that of the charge process, hence equations are avoided.

C. Evaluating simulated results

Table 2 provides a comparison of the smallest core (D_1) and optimized core (D_2) designs. Dynamic winding design discussed in Section 2 has been employed for both designs D_1 and D_2. All losses in the bi-directional flyback converter have been calculated in Matlab. For the winding loss calculation, 30 harmonics are considered.

TABLE II. DESIGN SPECIFICATIONS FOR D_1 AND D_2

Design specifications: V_{in}=24V; V_{out}=2500V; C_{out}=400nF;B_{sat}=0.3T; T_{ch}=50ms	**D_1**	**D_2**
Primary MOSFET	IPB600N25N3 G 250V, 25A, 60 mΩ	IPB600N25N3 G 250V, 25A, 60 mΩ
Core type	E16	PQ 20/20
Core volume	750 mm^3	2850 mm^3
Total turns primary / secondary	29 / 720	12 / 300
Layers primary / secondary	2 / 8	1 / 4
Turns per layer of primary / secondary	15 / 90	12 / 75
Wire diameter Primary/ secondary	0.4 mm / 0.1 mm	(0.5+0.2) mm / 0.143 mm
Primary magnetizing inductance	40 µH	44 µH
Peak primary current charge / discharge	4.24 A / 5.3 A	4.24 A / 5.3 A
Space allocation secondary (α)	0.6	0.8
Spacing between the secondary layers (mm)	60 μm	0.9 mm
Transformer weight	35 grams	120 grams
Transformer maximum temperature rise (°C)	71	30

The minimum turns ratio is calculated using the following equation

$$n_{\min} = \frac{N_p}{N_s} > \frac{\left(V_{out} + V_{HVdiodedrop}\right)}{\beta_1\left[\left(V_{BVpri}\ \beta_2\right) - V_{in}\right]} \tag{22}$$

where V_{in}, $V_{HVdiodedrop}$, N_p, N_s, β_1, and β_2 are the input voltage, high voltage diode drop, number of primary and secondary turns, leakage factor for primary, and margin factor for primary MOSFET drain to source voltage, respectively. The constants, β_1 and β_2 are chosen as 1.75 and 0.8, respectively, which results $n_{\min}$ as 25. In the optimized core, for primary winding TEX-E triple insulated winding has been used. For the smallest core, normal wire with single insulation is used, as the triple isolated wire has an insulation thickness of 0.2 mm, due to which lower diameter wire needs to be used for a

TABLE III. ENERGY LOSS DISTRIBUTION FOR D_1 AND D_2

Different energy losses in the bi-directional flyback converter (mJ)	**Charging E_{lossc} (mJ)**		**Discharging E_{lossd} (mJ)**		**Total (mJ)**	
During charging: Output energy E_{out} = 1250 mJ; $\eta_{charge}=E_{out}/(E_{out}+E_{lossc})$ During discharging: Input energy E_{in}= 1250 mJ; $\eta_{discharge}=(E_{in}-E_{lossd})/E_{in}$	**D_1**	**D_2**	**D_1**	**D_2**	**D_1**	**D_2**
Energy loss due to transformer paracitics	371.6	105.8	426	96	798	201.8
Winding loss due to resistance	31	12.3	3.75	2.37	34.8	14.67
Loss due to leakage inductance	126	25.7	284	56.4	410	82.1
Capacitive switching loss due to self-capacitance	207.6	57.1	132	37.3	340	94.4
Core loss (Power loss / switching frequency)	7	10.7	5.96	13.9	13	24.6
Converter energy losses	65.4	58.7	168	154		
Primary MOSFET conduction loss	6.1	6.1	--	--		
Secondary MOSFET conduction loss	--	--	6.97	7.4		
Primary MOSFET switching loss	44	38.5	--	--		
Secondary MOSFET switching loss	--	--	129	115	233	212
HV diode conduction loss	2.3	2.5	--	--		
Primary body diode loss	--	--	14.3	16		
Gate drive loss	1	0.9	0.4	0.3		
IC power consumption	9.5	8.2	16.8	15		
Loss due to primary current sense resistor	2.5	2.5	--	--		
Total energy loss	437	164.5	594	250	1031	413.8
Energy efficiency (%)	74	88.43	52.3	80	39	70.8

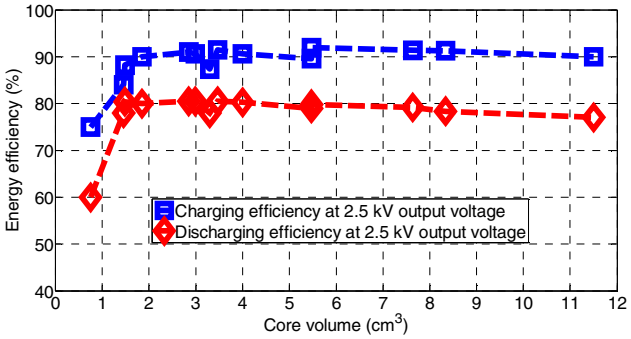

Figure 10. Calculated optimized efficiency at 2.5 kV vs. core volume.

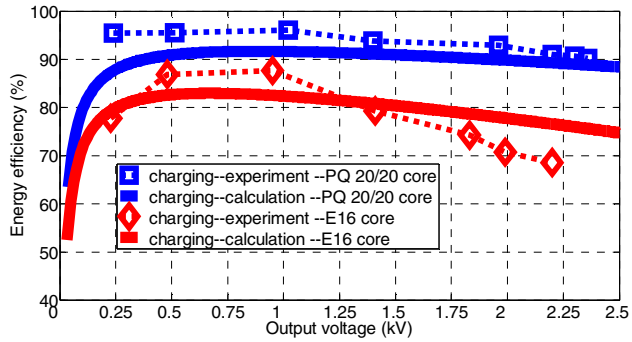

Figure 11. Comparison of calculated and measured charging energy efficiencies for optimized PQ 20/20 and smallest core E16

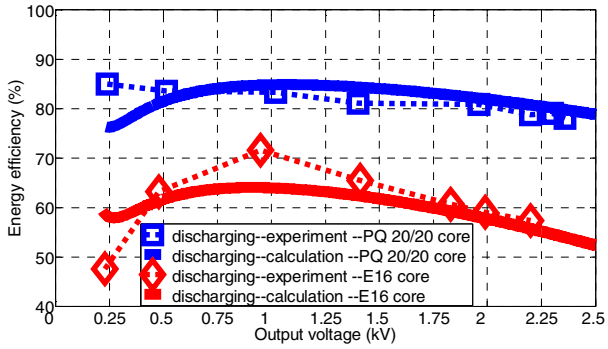

Figure 12. Comparison of calculated and measured discharging energy efficiencies for optimized PQ 20/20 and smallest core E16

given window width. But that results in higher DC resistance for the primary winding and may exceed the transformer temperature limit. Figure 10 shows the charging and discharging energy efficiency variation at 2.5 kV output voltage with respect to different core volumes. The core which has reasonably good energy efficiency with low volume is selected as the optimized core. From Fig. 10, the core which has a volume of 2.85 cm^3 is selected as an optimized core which is PQ 20/20. The smallest core is E 16, and is selected as the core which has low volume and whose temperature doesn't exceed the maximum temperature limit.

III. EXPERIMENTAL RESULTS

The comparison of the measured and calculated charging energy efficiency for the smallest and optimized cores is given in Fig. 11. Figure 12 shows the comparison of the measured and calculated discharging energy efficiency for the smallest

TABLE IV. COMPARISON OF CALCULATED AND MEASURED TRANSFORMER PARAMETERS FOR DESIGNS D_1 AND D_2

Parameter	D_1		D_2	
	Meas.	Calc.	Meas.	Calc.
Leakage inductance referred to primary (secondary shorted)	3.3 μH	3.22 μH	857 nH	804 nH
Leakage inductance referred to secondary (primary shorted)	2.23 mH	2.14 mH	550 μH	502 μH
Self-capacitance of secondary without core (primary opened)	18.61 pF	16.24 pF	3.06 pF	3.3 pF
Self-capacitance of secondary with core (primary opened)	21.62 pF	18.1 pF	6.23 pF	5.5 pF
DC resistance of primary (secondary opened)	182 mΩ	186 mΩ	74 mΩ	58.8 mΩ
DC resistance of secondary (primary opened)	44 Ω	46.54 Ω	18.2 Ω	15.3 Ω
AC resistance referred to primary at 100 kHz (secondary shorted)	370 mΩ	463 mΩ	125 mΩ	108 mΩ
AC resistance referred to secondary at 100 kHz (primary shorted)	190 Ω	358 Ω	73.6 Ω	68 Ω
AC resistance of primary at 100 kHz (secondary opened)	2.45 Ω	--	190 mΩ	--
AC resistance of secondary at 100 kHz (primary opened)	242 Ω	--	85 Ω	--
Primary resonance frequency with core	217 kHz	--	335 kHz	--
Secondary resonance frequency with core	238 kHz	--	360 kHz	--
Secondary resonance frequency without core	776 kHz	--	1.08 MHz	--

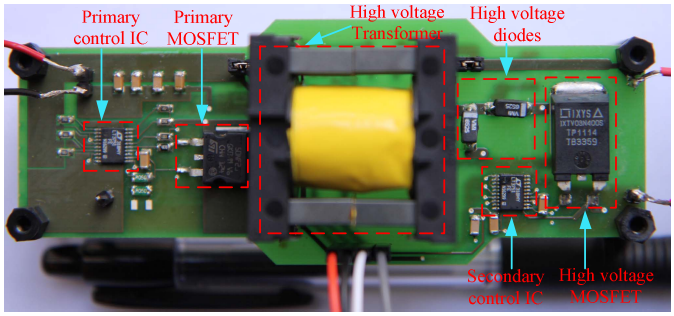

Figure 13. Experimental prototype of the bi-directional flyback converter with ETD 29 transformer

and optimized cores. The experimental prototype of the bi-directional flyback converter is shown in Figure 13. Table 3 shows the loss distribution of the optimized and smallest core designs, from which it is clear that the total losses due to transformer parasitics for design D_1 is higher than that of D_2, and the other losses from the converter remains the same for both designs. Comparison of measured and calculated transformer parameters, and resonant frequencies for both designs are provided in Table 4. The loss distributions of the

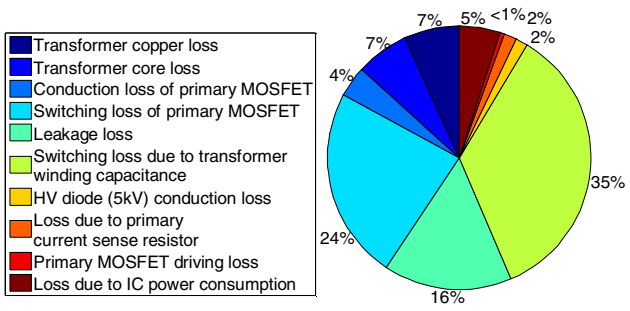

Figure 14. Energy loss distribution during charge process with optimized core.

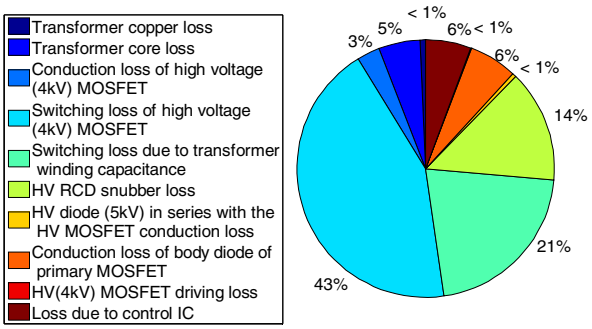

Figure 15. Energy loss distribution during discharge process with optimized core.

optimized design during charge and discharge processes are shown in Figs. 14 and 15, respectively.

IV. CONCLUSIONS

In this paper, a new dynamic transformer winding design concept is introduced. An optimization algorithm for minimizing the total energy loss of a bi-directional flyback converter for a high voltage capacitor charging application is presented. Winding loss calculation for a flyback transformer, with a simple non-interleaved structure is discussed. The proposed optimization technique is experimentally validated on a bi-directional flyback converter, and high efficiency (>90%) is achieved during the charge process. The proposed dynamic winding design can be easily extended to other transformer structures and for other applications.

REFERENCES

[1] R. E. Pelrine, R. D. Kornbluh, Q. Pei, and J. P. Joseph, "High-speed electrically actuated elastomers with strain greater than 100%," in Proc. *Science*, vol. 287, pp. 836–839, 2000.

[2] R. E. Pelrine, R. D. Kornbluh, and J. P. Joseph, "Electrostriction of polymer dielectric with compliant electrodes as a means of actuation," in Proc. *Sensors and Actuators A*, vol. 64, pp. 77–85, 1998.

[3] M. Tryson, H. E. Kiil, M. Benslimane, "Powerful tubular core free dielectric electro active polymer (DEAP) push actuator," in Proc. *SPIE Electroactive Polymer Actuators and Devices (EAPAD)*, vol. 7287, 2009.

[4] R. Sarban, B. Lassen, M. Willatzen, "Dynamic Electromechanical Modeling of Dielectric Elastomer Actuators With Metallic Electrodes," in Proc. *IEEE/ASME Transactions on Mechatronics,* vol. 17, no. 5, pp. 960-967, Oct. 2012.

[5] L. Eitzen, C. Graf, J. Maas, "Cascaded bidirectional flyback converter driving DEAP transducers," in Proc. *IECON*, pp. 1226-1231, 7-10 Nov. 2011.

[6] P. Thummala, Z. Zhang, M. A. E. Andersen, "High Voltage Bi-directional Flyback Converter for Capacitive Actuator," in Proc. *European Power Electronics Conference (EPE),* pp. 3-6th Sept. 2013.

[7] L. Eitzen, T Hoffstadt, J. Maas, "Power electronics concepts for driving EAP actuators," in Proc. *SPIE Electroactive Polymer Actuators and Devices (EAPAD)*, pp. 86870D, 2013.

[8] P. Thummala, Z. Zhang, M. A. E. Andersen, O. C. Thomsen, "A high voltage DC-DC converter driving a Dielectric Electro Active Polymer actuator for wind turbine flaps," in Proc. *IEEE UPEC,* pp. 1-7, 4-7 Sept. 2012.

[9] J. Elmes, C. Jourdan, O. Abdel-Rahman, I. Batarseh, "High-Voltage, High-Power-Density DC-DC Converter for Capacitor Charging Applications," in Proc. *IEEE APEC*, pp. 433-439, 2009.

[10] T. Andersen, M. S. Rødgaard, O. C. Thomsen, M. A. E. Andersen, "Low voltage driven dielectric electro active polymer actuator with integrated piezoelectric transformer based driver," in Proc. *SPIE Electroactive Polymer Actuators and Devices (EAPAD),* vol. 7976, pp. 79762N, 2011.

[11] S. K. Chung, H. B. Shin, "High-voltage power supply for semi-active suspension system with ER-fluid damper," in Proc. *IEEE Transactions on Vehicular Technology*, vol. 53, no. 1, pp. 206- 214, Jan. 2004.

[12] P. Thummala, H. Schneider, Z. Ouyang, Z. Zhang, M. A. E. Andersen, "Estimation of transformer parameters and loss analysis for high voltage capacitor charging application," in Proc. *IEEE ECCE Asia,* pp. 704-710, 3-6 Jun. 2013.

[13] R. Prieto, J.A. Cobos, O. Garcia, R. Asensi and J. Uceda, "Optimizing the winding strategy of the transformer in a flyback converter," in Proc. *IEEE Power Electronics Specialists Conference (PESC)*, vol. 2, pp. 1456-1462, 1996.

[14] C. R. Sullivan, T. Abdallah, T. Fujiwara, "Optimization of a flyback transformer winding considering two-dimentional field effects, cost and loss," in Proc. *IEEE APEC*, vol.1, pp.116-122, 2001.

[15] H. K. Sang, D. Maksimovic, I. Cohen, "Efficiency Optimization in Digitally Controlled Flyback DC–DC Converters Over Wide Ranges of Operating Conditions," in Proc. *IEEE Transactions on Power Electronics*, vol. 27, no. 8, pp. 3734-3748, Aug. 2012.

[16] R. P. Wojda, M. K. Kazimierczuk, "Analytical Optimization of Solid–Round-Wire Windings," in Proc. *IEEE Transactions on Industrial Electronics*, vol. 60, no. 3, pp. 1033-1041, March 2013.

[17] A.C. Nanakos, E.C. Tatakis, N.P Papanikolaou, "A Weighted-Efficiency-Oriented Design Methodology of Flyback Inverter for AC Photovoltaic Modules," in Proc. *IEEE Transactions on Power Electronics*, vol. 27, no. 7, pp. 3221-3233, July 2012.

[18] C. Marxgut, J. Muhlethaler, F. Krism, J.W. Kolar, "Multiobjective Optimization of Ultraflat Magnetic Components With PCB-Integrated Core," in Proc. *IEEE Transactions on Power Electronics*, vol. 28, no. 7, pp. 3591-3602, July 2013.

[19] J. Mühlethaler, "Modeling and Multi-Objective Optimization of Inductive Power Components,", Ph.D. Theis, Dept. Information Technology and Electrical Engineering, ETH Zurich, Switzerland 2012.

[20] Z. Ouyang, "Planar Magnetics for High Grade Converter," Ph.D. Theis, Dept. Electrical Engineering, Technical University of Denmark, Denmark 2011.

[21] N. O. Sokal, R. Redl, "Control algorithms and circuit designs for optimal flyback-charging of an energy storage capacitor (e.g., for flash lamp or defibrillator)," in *Proc. IEEE Transactions on Power Electronics*, vol. 12, no. 5, pp. 885-894, Sep. 1997.

[22] J. Vandelac, P. D. Ziogas, "A Novel Approach for Minimizing High-Frequency Transformer Copper Losses," *IEEE Trans. on Power Electronics,* vol. 3, no. 3, pp. 266-277, Jul 1988.

[23] S. H. Kang, "Efficiency Optimization in Digitally Controlled Flyback DC-DC Converters Over Wide Ranges of Operating Conditions," Ph.D. Theis, Dept. Electrical, Computer and Energy Engineering, University of Colorado Boulder, USA 2011.

[24] P. Thummala, Z. Zhang, M. A. E. Andersen, S. Rahimullah, "Dielectric electro active polymer incremental actuator driven by multiple high-voltage bi-directional DC-DC converters," in Proc. *IEEE ECCE USA,* pp. 3837-3844, 15-19 Sept. 2013.

Appendix H

Efficiency Optimization by Considering the High Voltage Flyback Transformer Parasitics using an Automatic Winding Layout Technique

---

IEEE Transactions on Power Electronics, DOI: 10.1109/TPEL.2014.2379439

This article has been accepted for publication in a future issue of this journal, but has not been fully edited. Content may change prior to final publication. Citation information: DOI 10.1109/TPEL.2014.2379439, IEEE Transactions on Power Electronics

TPEL-Reg-2014-09-1319

Efficiency Optimization by Considering the High Voltage Flyback Transformer Parasitics using an Automatic Winding Layout Technique

Prasanth Thummala*, *Student Member IEEE*, Henrik Schneider, *Student Member IEEE*, Zhe Zhang, *Member IEEE*, Ziwei Ouyang, *Member IEEE*, Arnold Knott, *Member IEEE*, and Michael A. E. Andersen, *Member, IEEE*

***Abstract*—This paper presents an efficiency optimization approach for a high voltage bidirectional flyback dc-dc converter. The main goal is to optimize the converter for driving a capacitive actuator, which must be charged and discharged from 0 V to 2.5 kV dc and vice versa, supplied from a 24 V dc supply. The energy efficiency is optimized using a proposed new automatic winding layout (AWL) technique and a comprehensive loss model. The AWL technique generates a large number of transformer winding layouts. The transformer parasitics such as dc resistance, leakage inductance and self-capacitance are calculated for each winding layout. An optimization technique is formulated to minimize the sum of energy losses during charge and discharge operations. The efficiency and energy loss distribution results from the optimization routine provide a deep insight into the high voltage transformer design and its impact on the total converter efficiency. The proposed efficiency optimization approach is experimentally verified on a 25 W (average charging power) with 100 W (peak power) flyback dc-dc prototype.**

***Index Terms*—switched-mode power supply, high voltage dc-dc power converter, transformer design, optimization, energy efficiency, actuators, dielectric films**

NOMENCLATURE

a_{uC}, b_{uC}	Coefficients of Fourier series of the magneto motive force (MMF) during charge process (AT: Ampere-turns)
B_{mC} / B_{mD}	Maximum flux density during charge / discharge process (T)
B_{nC}	Magnitude of negative flux density at the beginning of a switching cycle during charge process (T)
ΔB	Peak-to-peak flux density of the current excitation (T)
C_{in} / C_{load}	Input capacitance / Capacitance of the load or actuator (F)
C_s	Self-capacitance of secondary winding (F)
C_{ossp} / C_{osss}	Output capacitance of low voltage MOSFET M_p / high voltage MOSFET M_s (F)
C_{Db}	Junction capacitance of high voltage diode D_b (F)
d_p / d_s	Diameter of primary / secondary winding of transformer (mm)
D_2 / D_b	High voltage (5 kV) freewheeling diode / blocking diode
$d_{insulation}$	Uniform spacing or thickness of the insulating tape, between secondary layers (mm)
D_{onC} / D_{offC}	On-time / Off-time duty cycle of low voltage MOSFET M_p during charge process
D_{onD} / D_{offD}	On-time / Off-time duty cycle of high voltage MOSFET M_s during discharge process
$E_{load}(V_{out})$	Stored energy in the load at an output voltage V_{out} (J)
f_{swC} / f_{swD}	Switching frequency during charge / discharge process (kHz)
FF_{LL}	Fill factor of the last layer in the high voltage winding
$F_{uC}(0)$ / $F_{uC}(h)$	MMF amplitude of u^{th} harmonic at x=0 / x=h, h is the thickness of layer
G_1, G_2	Constants used in the power loss expressions and are functions of ε_u
H_W	Window height of transformer bobbin (mm)
i_{in} / i_p / i_s	Input current / Primary current / Secondary or load current (A)
i_{mp} / i_{ms}	Primary / Secondary magnetizing current (A)
I_{ppkC} / I_{ppkD}	Primary peak current during charge process / discharge process (A)
I_{spkC} / I_{spkD}	Secondary peak current during charge process / discharge process (A)
i_{min}	Magnitude of the negative primary current at the beginning of charge process (A)
I_{pavgC} / I_{savgC}	Primary / Secondary average current during charge process (A)
k_z	Core loss constant in the improved generalized Steinmetz equation (*i*GSE)
L_{mp} / L_{ms}	Primary / Secondary magnetizing inductance of transformer (H)
L_{lkp} / L_{lks}	Leakage inductance referred to primary / secondary side of transformer (H)
M_p / M_s	Low voltage MOSFET / High voltage (4 kV) MOSFET

Manusctipt received on 8th Sept. 2014, revised on 15th Oct. 2014, and accepted on 24th Nov. 2014. This paper has been presented at 29th Annual Applied Power Electronics Conference, Fort Worth, TX, USA, March 2014.

All authors are with the Electronics Group, Department of Electrical Engineering, Technical University of Denmark, Kongens Lyngby, DK-2800 Denmark.
E-mail: *pthu@elektro.dtu.dk, hensc@elektro.dtu.dk, zz@elektro.du.dk, zo@elektro.dtu.dk, akn@elektro.dtu.dk, ma@elektro.dtu.dk.
*Indicates the corresponding author.

This article has been accepted for publication in a future issue of this journal, but has not been fully edited. Content may change prior to final publication. Citation information: DOI 10.1109/TPEL.2014.2379439, IEEE Transactions on Power Electronics

N_p / N_s / n	Number of primary / secondary turns / Turns ratio of transformer from secondary to primary
n_{lp} / n_{ls}	Number of layers in primary / secondary winding of transformer
n_{parp} / n_{pars}	Number of parallel wires in primary / secondary winding of transformer
N_h / N_c	Total number of harmonics considered / Total number of switching cycles during charge process
P^k_{layerC}	Power loss in k^{th} layer during charge process (W)
P_{windC} / P_{TwindC}	Winding loss at each switching cycle / Total winding loss during charge process (W)
P_{swC} / P_{swD}	Capacitive switching loss due the self-capacitance during charge / discharge process (W)
P_{snC} / P_{snD}	Snubber loss due leakage inductance during charge / discharge process (W)
R_p / R_s	dc resistance of primary / secondary winding of transformer (Ω)
R_{psense} / R_{ssense}	Primary / Secondary current sense resistance (Ω)
R_{layer}	dc resistance of a given layer (Ω)
t_{onC} / t_{offC}	On-time / Off-time of low voltage MOSFET M_p during charge process (s)
t_{onD} / t_{offD}	On-time / Off-time of high voltage MOSFET M_s during discharge process (s)
T_{sC} / T_{sD}	Switching period during charge / discharge process (s)
T_{ch}	Charging time to reach the target output voltage from 0 V (s)
T_{layer}	Number of turns in a given layer (primary or secondary) of transformer
V_{leakD}	Increase in the steady state drain-to-source voltage of M_s due to leakage inductance L_{lks} (V)
V_{in} / V_{out}	Input voltage / Output or load or actuator voltage (V)
W_W	Window width of bobbin (mm)
W_{sqp} / W_{sqs}	Width of square for primary / secondary in the automatic winding layout generator routine (mm)
γ_s / γ_p	Height allocation factor for secondary / primary winding with γ_p=(1-γ_s)
δ_u / δ	Skin depth of the conductor at u^{th} harmonic frequency / fundamental (u=0) frequency (mm)
ε_u	Ratio of conductor diameter to the effective skin depth of u^{th} harmonic
$\varphi_{uC}(0)$ / $\varphi_{uC}(h)$	Phase of u^{th} harmonic of the MMF during charge process at x=0 / x=h (h is thickness of layer)
ρ / μ_0	Resistivity of copper (Ω-m) / Magnetic permeability of vacuum (H/m)
α, β, k	The constants related to core material which are provided by the core manufacturer
δ_C	Capacitance ratio factor on the high voltage side

I. Introduction

DIELETRC electro active polymer (DEAP) [1]-[3] is an evolving smart material that can be used in actuation, sensing and energy harvesting applications [4]. DEAPs, when used as linear actuators, have the potential to be an effective replacement for many conventional linear actuators because of their unique properties, including light weight, low noise operation, high flexibility, large strain, and autonomous capability. The axial DEAP actuator as shown in Fig. 1(a) is ideally equivalent to a capacitive load. When a DEAP actuator is driven with high voltage (2-2.5 kV), it converts a portion of the electrical energy into mechanical displacement, which is of the order of mm (~1-1.5 mm) [5]-[7]. Three of such axial DEAP actuators are used to create a DEAP incremental actuator [8] as shown in Fig. 1(b). The DEAP incremental actuator technology has the potential to be used in various industries, e.g. automotive, aeronautics, and medicine. For using the DEAP actuators in such applications, the high voltage drivers should have low volume to fit inside or above the actuators. The overall energy efficiency of battery powered, high voltage driver influences, the distance travelled by the incremental actuator. Hence, for DEAP actuator applications, both volume and energy efficiency of high voltage drivers are extremely important and need to be optimized.

The flyback converter is suitable for high voltage and low power applications due to its simple structure and a low component count [9]. High voltage switch-mode power supplies for charging the capacitive loads are implemented in [10]-[12]. Bidirectional dc-dc power converters are needed for the DEAP based capacitive actuators [13], to increase the lifetime of the battery, also to discharge the high voltage across them. Bidirectional flyback converter [14]-[17], and a forward-flyback bidirectional converter [18] are implemented for various applications. Due to high reverse recovery time (~2.6 μs) of high voltage MOSFET, a modified high voltage bidirectional flyback converter topology [19] as shown in Fig. 2, is proposed and implemented for driving a DEAP actuator. The loss analysis of the same converter is performed in [20].

Transformer design plays a very important role in high voltage dc-dc power converters employed in low, medium and high power applications. The design methodologies for transformers used in conventional switch-mode power supplies are well documented [9], [21]-[23]. Often, a transformer for a given application is designed based on some assumptions such as, constant switching frequency, maximum

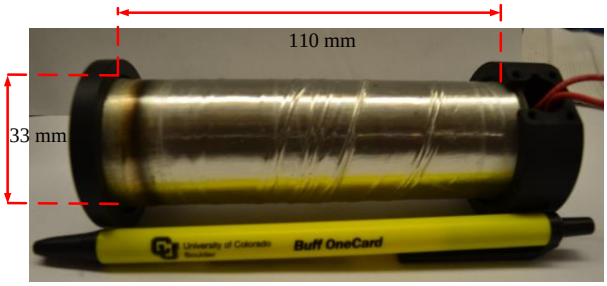

a)

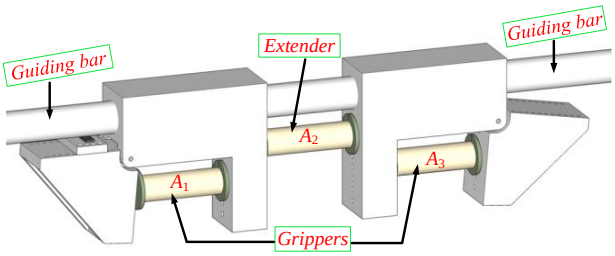

b)

Fig. 1. a) DEAP actuator; b) DEAP incremental actuator.

This article has been accepted for publication in a future issue of this journal, but has not been fully edited. Content may change prior to final publication. Citation information: DOI 10.1109/TPEL.2014.2379439, IEEE Transactions on Power Electronics

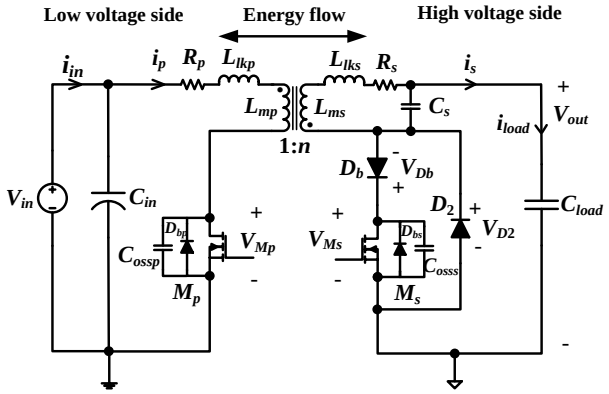

Fig. 2. Circuit configuration of the high voltage bidirectional flyback converter for driving a capacitive load.

temperature rise, estimated converter efficiency, winding fill factor, and winding current density. However, these assumptions are not valid or suitable for some applications. Hence, more customized procedures are needed to design efficient transformers, for specific applications. In a high voltage capacitor charge and discharge application, the high voltage transformer will have a large amount of (> 200) secondary turns. For such application, it is very difficult to select an optimum winding diameter and number of winding layers beforehand, which decide the values of the transformer parasitics. To avoid this difficulty, an automatic winding layout (AWL) technique is introduced in [24], for the winding design of a high voltage transformer. The high voltage flyback converter operation is very sensitive to the transformer parasitics. The proposed AWL technique, utilizes the entire available space in a given transformer bobbin and provides an optimum winding diameter that minimizes the total loss due to the transformer parasitics.

In the initial design phase, it is difficult to predict which core type is optimal for a given application. In a flyback converter, a long transformer window width is often preferred, in order to minimize the leakage inductance and ac resistance by providing a close coupling between windings, and to decrease the number of winding layers. For high output or input voltage flyback converters, this could be different, since the self-capacitance of the high voltage winding has significant impact on the performance of the converter. In this paper, an efficiency optimization algorithm is proposed, which provides an optimum solution for a given transformer core, by using the proposed AWL technique and the comprehensive loss model. Different transformer winding architectures (TWAs) for the high voltage capacitor charge and discharge application are investigated in [25]. In [26], a digital control technique is proposed for improving the energy efficiency and charge/discharge speed. Control algorithms for optimal-flyback charging of a capacitive load are proposed in [27]. A number of switch-mode power supply design optimization methods have been described in the literature [28]-[34].

The proposed efficiency optimization technique has the following features:

1) an automatic winding layout (AWL) technique, which produces the
2) information about winding diameters, number of layers, and number of parallel windings, for both primary and secondary windings;
3) an accurate calculation of transformer parasitics using the outputs of AWL technique;
4) calculation of energy losses during charge and discharge modes using a comprehensive loss model;
5) an objective function that minimizes the sum of energy losses during charge and discharge modes, over a range of operating points.

This paper is organized as follows: Section II describes the proposed automated winding layout (AWL) technique. Section III provides the loss modeling of the bidirectional flyback converter. Section IV discusses the proposed optimization routine. Section V provides the optimization and experimental results, followed by the conclusions in Section VI.

II. Automatic Winding Layout (AWL) Technique

The bidirectional flyback converter design specifications are provided in Table I. The magnetic transformer is the most critical component in the high voltage bidirectional flyback converter. The leakage inductance causes voltage spikes across the drain-to-source of the MOSFET, and this can be avoided by a dissipative snubber circuit or by using an over rated MOSFET. The self-capacitance of the secondary winding creates large resonating current spikes in the leading edge of the MOSFET current waveform [19]. Additional switching losses will be created due to those two parasitics, respectively [30]. The remaining losses in the transformer are core loss, and the winding loss due to dc and ac resistances. The losses due to the high voltage transformer need to be minimized to improve the bidirectional flyback converter efficiency and reliability.

TABLE I
Converter Design Specifications

Parameter	Value
Input voltage V_{in}	24 V
Output voltage V_{out}	0-2500 V
Capacitance of load C_{load}	400 nF
Stored energy in the load E_{load} at 2.5 kV	1.25 J
Target charging time T_{ch}	50 ms
Turns ratio of the transformer n	25
Primary magnetizing inductance L_{mp}	44 μH
Primary peak current during charge process I_{ppkC}	4.2 A
Primary peak current during discharge process I_{ppkD}	5.3 A

The transformer design decisions considered for the proposed AWL technique are given in Table II. The core types are limited to ETD, EFD, E, RM and PQ. The N87 core material is chosen for most of the cores, due to its lower core losses at high frequency up to 500 kHz. For those cores for

This article has been accepted for publication in a future issue of this journal, but has not been fully edited. Content may change prior to final publication. Citation information: DOI 10.1109/TPEL.2014.2379439, IEEE Transactions on Power Electronics

which N87 material is not available, other core materials which are suitable for operation up to 500 kHz are considered. A simple, non-interleaved winding structure (P/S; P: Primary, S: Secondary), is considered in this paper to limit the complexity of the proposed AWL technique. Nevertheless, the proposed AWL technique can be easily extended for the interleaved transformer structures (P/S/P or S/P/S). The proper insulation between the low voltage (primary) and high voltage (secondary) windings is achieved by using a triple insulated (TEX-E) solid wire for primary winding. To avoid the high insulation thickness (0.2 mm) of TEX-E wire, single insulated solid wire is used for a large number of secondary turns. A maximum transformer temperature limit of 130 °C is chosen. These limitation values can be altered based on the experience of the user or the initial design specifications.

The AWL technique is described below:

A. AWL technique:

The space allocated for the primary and secondary windings for a given transformer bobbin with winding width W_W and window height H_W are shown in Fig. 3(a). Different steps associated with the proposed AWL technique for an example of N_p=6 primary turns and N_s=18 secondary turns, are explained below:

1) The first step is, to split the available winding space for primary (see Fig. 3(a)) and secondary (Fig. 3(f)) into a number of squares, with a square width equal to height allocated for that winding. As shown in Figs. 3(d) and 3(g), it results into 4 squares and a crossed non-square, which is considered as an unusable space for both primary and secondary windings. In each square, a solid round wire could be placed with a diameter equal to the width of a square or a bundle of round wires with an outside bundle diameter equal to the width of a square.
2) Since the number of available squares is 4 in Figs. 3(d) or 3(g), which is less than the required 6 primary and 18 secondary turns, more squares are required to fill the needed turns. Hence, the width of square for primary or secondary is decreased from its maximum value of $\gamma_p H_W$ or $\gamma_s H_W$, respectively.
3) The fill factor of the last layer FF_{LL} for a given winding is defined as the ratio of the number of squares used in the final layer to the number of squares available in it. For example, in Fig. 3(i), 9 squares are available and 9 squares are occupied in the final layer, hence FF_{LL}=1. Similarly, in Fig. 3(j), 16 squares are available and 13 squares are occupied in the final layer, hence FF_{LL}=0.81. In the proposed AWL technique a maximum limit of 0.85 is set for FF_{LL}, since the calculation of transformer parasitics is based on fully occupied layers.
4) When the square width is reduced as shown in Figs. 3(e) and 3(h), the new square size limits the use of a shaded space above the squares. For primary winding since only 6 turns are needed, this will be a valid solution. However, for secondary winding, since 18 turns are needed, the shaded space can be occupied by the other windings, by reducing the square width further.
5) When the square width is reduced further as shown in Fig. 3(i), the winding space contains 18 squares in 2 layers, and a shaded space. The non-square horizontal space is utilized to provide an insulation tape (with thickness $d_{insulation}$) between the secondary layers. This is the final step of the AWL technique for 6 primary and 18 secondary turns.
6) If 45 turns are required for the secondary winding, the square width is decreased again, as shown in Fig. 3(j), the solution contains 3 layers and 16 squares in each layer. The last layer fill factor FF_{LL} in this case is 0.81, which is less than 0.85. Hence, this is not a valid solution and the square width needs to be decreased further.
7) In Fig. 3(b), a solution from the AWL technique is shown. The primary and secondary squares are filled with triple isolated and single isolated solid wires, respectively. The same steps described above apply for the real high voltage transformer design which will have more than 200 secondary turns.
8) Finally, the outputs of AWL technique are various winding implementations, including specific winding details such as, diameters of primary and secondary windings, number of primary and secondary winding layers, and insulation thicknesses for placing between secondary windings, for which FF_{LL}>0.85, respectively.

TABLE II
TRANSFORMER DESIGN DECISIONS

Description	Design decision	Comments
Ferrite core and bobbin type	ETD, EFD, E, RM and PQ	Typically used in switch-mode power supplies.
Core material	N87	Suitable for switching frequencies up to 500 kHz.
Winding structure	P/S	Simple implementation and decreases analytical complexity.
Primary winding type	Solid wire	Flexible winding type in terms of design and prototyping.
Primary winding insulation	Triple insulation (TEX-E)	Edge tape can be avoided. No need for interlayer insulation tape between the primary and secondary windings.
Secondary winding type	Solid wire	Suitable winding type, for a large number of turns. Flexible winding type in terms of design, prototyping and different winding structures.
Secondary winding insulation	Single insulation	Provides minimum insulation thickness for a large number of turns.
Air gap	All legs	Simplifies the prototyping.
Maximum transformer temperature	130 °C	With a predicted ambient temperature of 35 °C, this enables transformer temperature rise of 95 °C.

This article has been accepted for publication in a future issue of this journal, but has not been fully edited. Content may change prior to final publication. Citation information: DOI 10.1109/TPEL.2014.2379439, IEEE Transactions on Power Electronics

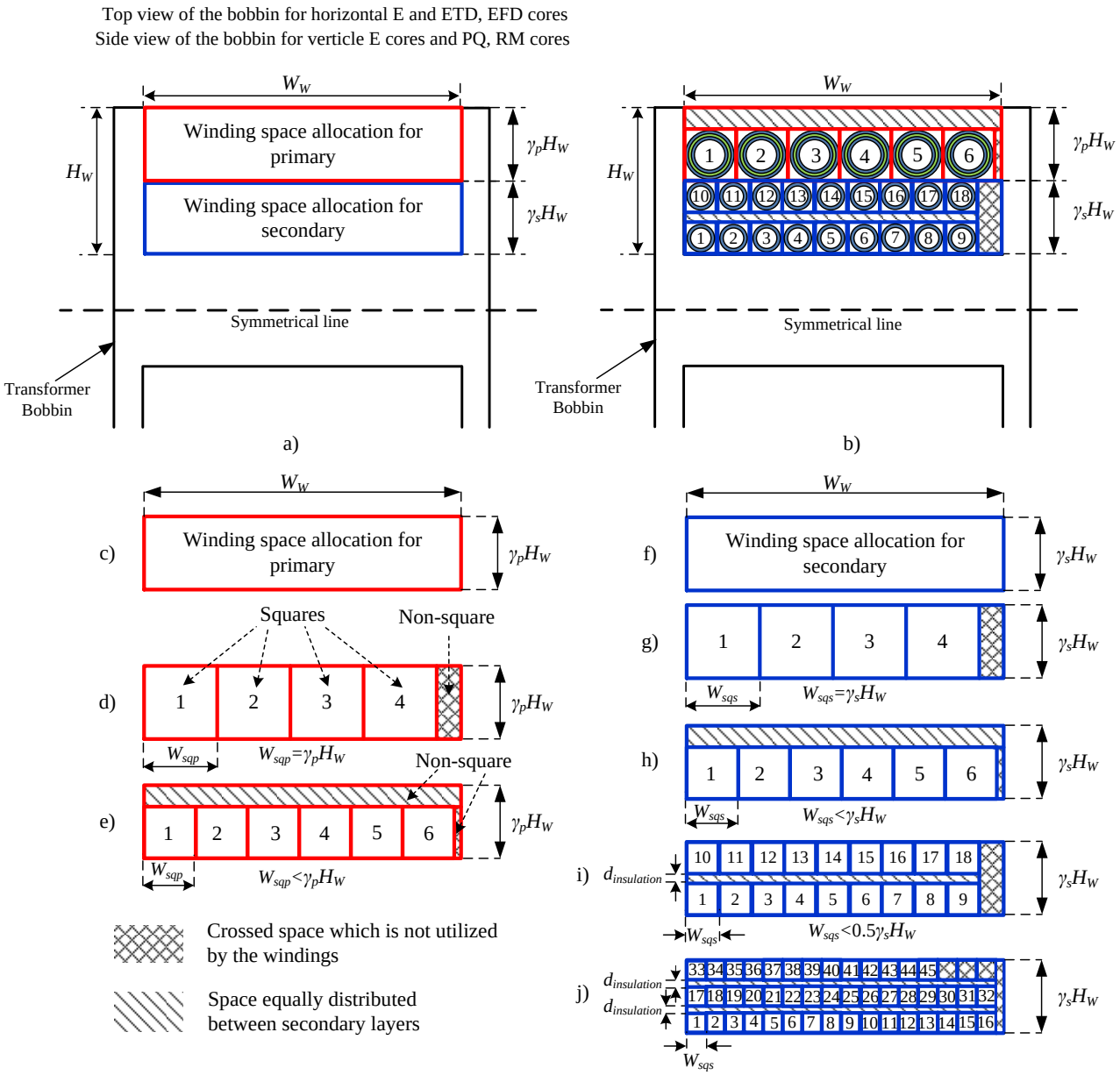

Fig. 3. a) Allocated winding space a) before applying AWL technique; b) after applying AWL technique; c) - e) Different steps involved in AWL technique for primary winding; f) - j) Different steps involved in AWL technique for secondary winding;

B. Calculation of transformer parasitics using the results of AWL technique:

The outputs of the AWL technique are used to calculate the transformer parasitics [20], [24], [35]-[37] such as dc resistance, leakage inductance and self-capacitance. In Fig. 4, one output of AWL technique such as the insulation thickness ($d_{insulation}$) for a PQ 20/20 core, and calculated transformer parasitics are shown with respect to square width (W_{sqs}) of secondary winding. As the width of the secondary square (or secondary winding) decreases, the insulation spacing $d_{insulation}$ between secondary winding layers increases, dc resistance R_s increases, leakage inductance L_{lkp} slightly decreases, and the self-capacitance C_s decreases.

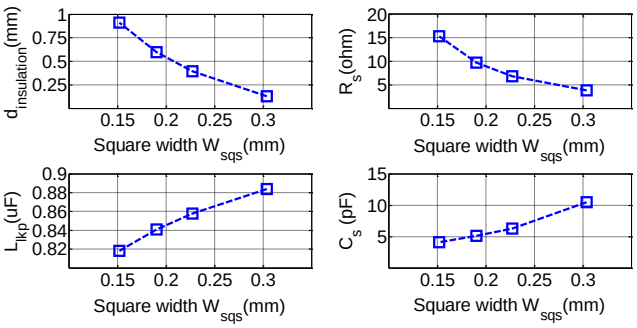

Fig. 4. Variation of transformer parasitics with the diameter of secondary winding, for PQ 20/20 core (when γ_s=0.8).

This article has been accepted for publication in a future issue of this journal, but has not been fully edited. Content may change prior to final publication. Citation information: DOI 10.1109/TPEL.2014.2379439, IEEE Transactions on Power Electronics

III. Loss Modelling

In order to investigate the bidirectional flyback converter efficiency, it is necessary to calculate the losses associated with each circuit component in the converter. The loss model is a function of transformer parasitics. Different losses in the bidirectional flyback converter are given below:

A. *Transformer winding loss:*

In a flyback converter the primary and secondary currents are 180° out of phase, hence the conventional equations cannot be used to calculate the ac resistance [38], [39]. The calculation of the total winding loss in a flyback converter using the magneto motive force (MMF) analysis [40], [41] is described below.

1) Winding loss in a flyback transformer during charge process:

For the winding loss modeling, a non-interleaved transformer with 2 layers on the primary side (P_1 and P_2) and 5 layers on the secondary side (S_1, S_2, S_3, S_4 and S_5), is considered as an example. The MMF distribution in a flyback transformer is different from that of a normal transformer [40]. Figure 5 shows different MMF distributions during both turn-on ($0<t<t_{onC}$) and turn-off ($t_{onC}<t<t_{onC}+t_{offC}$) periods in a non-interleaved flyback transformer. In Fig. 5, N_{p1} and N_p, are the number of turns in the primary layer 1 and the total primary turns, respectively, and H_0, H_1,….H_7 are the magnetic field intensities between the layers. The terms N_1, N_2, N_3, N_4, N_5 are defined as follows: $N_1=N_{s1}$, $N_2=N_{s1}+N_{s2}$, $N_3=N_{s1}+N_{s2}+N_{s3}$, $N_4=N_{s1}+N_{s2}+N_{s3}+N_{s4}$, and $N_5=N_{s1}+N_{s2}+N_{s3}+N_{s4}+N_{s5}=N_s$ where N_{s1}, N_{s2}, N_{s3}, N_{s4}, N_{s5} and N_s are the number of turns in the secondary layers 1, 2, 3, 4, 5, and the total number of secondary turns, respectively. The primary $i_{mp}(t)$ and secondary $i_{ms}(t)$ magnetizing current waveforms in a given switching cycle, during charge and discharge processes are shown in Figs. 6(a) and 6(b), respectively. The MMF distribution in each transformer winding layer in the time

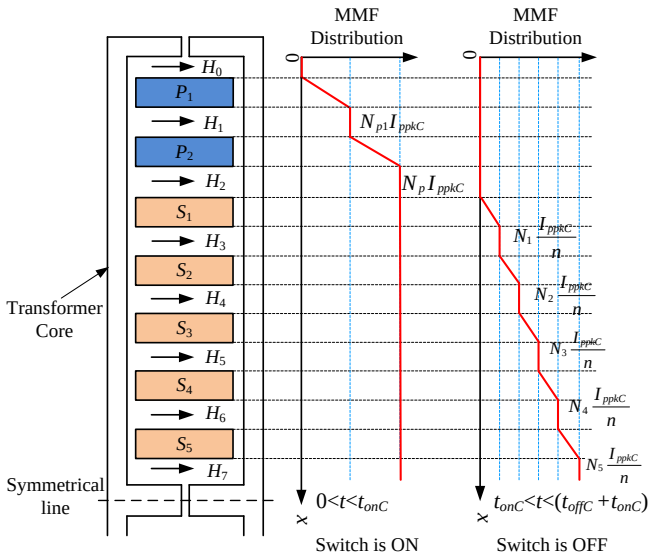

Fig. 5. MMF distribution of the non-interleaved (P-P-S-S-S-S-S) flyback transformer with respect to space.

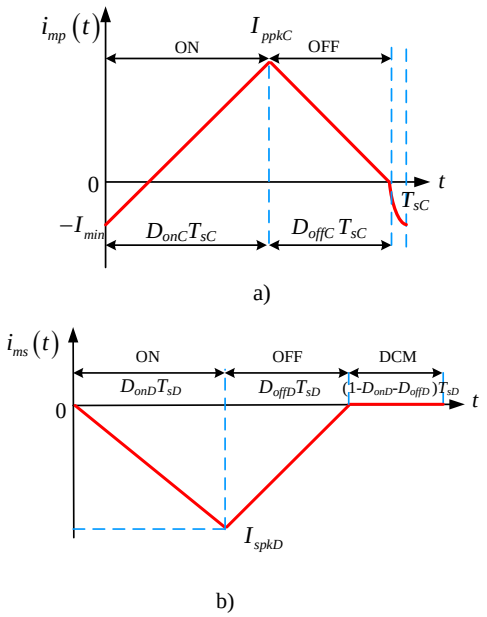

Fig. 6. a) Primary magnetizing current in a given switching cycle during charge process, and b) Secondary magnetizing current discharge process.

domain is decomposed into sinusoidal harmonics by Fourier series analysis [24]. The power loss is then computed for each harmonic, and the power loss densities over all harmonics are summed to find the power dissipated in each layer.

The power loss expression in k^{th} layer P_{layerC}^{k} is given by [24], [40], [41]

$$P_{layerC}^{k}=\frac{R_{layer}}{2T_{layer}^{2}}\sum_{u=1}^{N_h}\varepsilon_u\begin{bmatrix}\left(\left|F_{uC}(h)\right|^2+\left|F_{uC}(0)\right|^2\right)G_1(\varepsilon_u)-\\ 4\left|F_{uC}(h)\right|\left|F_{uC}(0)\right|\cos(\Delta\varphi)G_2(\varepsilon_u)\end{bmatrix} \quad (1)$$

$$\delta_u=\sqrt{\frac{\rho}{\pi\mu_0 u f_{swC}}} \quad (2)$$

$$\varepsilon_u=\left(\frac{\pi}{4}\right)^{0.75}\sqrt{\frac{T_{layer}}{W_W}}\left(\frac{d^{1.5}}{\delta_u}\right) \quad (3)$$

where $F_{uC}(0)$ and $F_{uC}(h)$ are the MMF amplitudes of the u^{th} harmonic at the beginning (x=0) and end (x=h) of a layer, respectively, d is the diameter of the given winding, h is the thickness of a given layer, with the suffix u being the harmonic number [24].

The magnitude $\left|F_{uC}\right|$ and phase φ_{uC} of u^{th} harmonic of the MMF during charge process are given by

$$\left|F_{uC}\right|=\sqrt{a_{uC}^2+b_{uC}^2} \quad (4)$$

$$\varphi_{uC}=\begin{cases}\tan^{-1}\left(-\frac{b_{uC}}{a_{uC}}\right), & \text{if } a_{uC}\geq 0\\ \pi+\tan^{-1}\left(-\frac{b_{uC}}{a_{uC}}\right), & \text{if } a_{uC}<0\end{cases} \quad (5)$$

$$\Delta\varphi=\varphi_{uC}(0)-\varphi_{uC}(h) \quad (6)$$

where a_{uC} and b_{uC} are the coefficients of the Fourier series of the MMF during charge process and are provided in [24], and $\Delta\varphi$ is the difference between the phase angles of the u^{th}

This article has been accepted for publication in a future issue of this journal, but has not been fully edited. Content may change prior to final publication. Citation information: DOI 10.1109/TPEL.2014.2379439, IEEE Transactions on Power Electronics

harmonic at the beginning (x=0) and end (x=h) of a layer, respectively.

The expression for the winding loss in a flyback transformer at each switching frequency (each switching cycle) index j during charge process is

$$P_{windC}(j) = I^2_{pavgC}(j)R_p + I^2_{savgC}(j)R_s + \sum_{k=1}^{n_{ls}+n_{lp}} P^k_{layerC}(j) \quad (7)$$

The total winding loss during charge process having N_c switching cycles is

$$P_{TwindC} = \sum_{j=1}^{N_c} P_{windC}(j) \quad (8)$$

2) Discussion:

The winding loss during discharge process is calculated similar to that during charge process. The AC loss due to air-gap fringing field [28] has not been considered because of difficulties in interfacing the 2-D/3-D finite element analysis (FEA) simulation results with the optimization process. The negative current at the beginning of the turn-on process during charge process in Fig. 6(a) is due to the high voltage winding self-capacitance. When the secondary winding current becomes zero, the drain to source voltage V_{Mp} tends to decrease. Since the control IC, LT3751 [42] operates under boundary mode control, the next switching cycle starts before the high voltage winding capacitance completely discharges. Hence, the current flows in the reverse direction to discharge the high voltage winding capacitance.

B. Transformer core loss:

The time-average core loss per unit volume P_v due to non-sinusoidal excitation is calculated using the improved generalized Steinmetz equation (*i*GSE) [43] which is given by

$$P_v = \frac{1}{T_s}\left[\int_0^{T_s} k_z \left|\frac{dB(t)}{dt}\right|^{\alpha} (\Delta B)^{\beta-\alpha}\, dt\right] \quad (9)$$

where $\left|\frac{dB(t)}{dt}\right|$ is the absolute value of the change rate of the flux density, ΔB is the peak-to-peak flux density, T_s is the switching period, and k, α and β are the constants provided by the core manufacturer. The core loss coefficient k_z in (9) is calculated using the following expression

$$k_z = \frac{k}{(2\pi)^{\alpha-1} 2^{\beta-\alpha}\left[\int_0^{2\pi} |\cos\theta|^{\alpha}\, \mathrm{d}\theta\right]} \quad (10)$$

The angle θ in (10) represents the phase angle of the sinusoidal excitation. For a given values of k, α and β, the value of coefficient k_z in (10) is fixed, irrespective of shape of the flux density waveform.

The core loss per unit volume using *i*GSE during charge operation (where $\Delta B = B_{mC} + B_{nC}$ during the turn-on period and $\Delta B = B_{mC}$ during the turn-off period), in each switching cycle is given by

$$P_{vC} = \frac{k_z}{T_{sC}}\left[(B_{mC} + B_{nC})^{\beta} \cdot {t_{onC}}^{1-\alpha} + {B_{mC}}^{\beta} \cdot {t_{offC}}^{1-\alpha}\right] \quad (11)$$

Similarly, the core loss per unit volume during discharge operation (where $\Delta B = B_{mD}$), in each switching cycle is given by

$$P_{vD} = \frac{k_z}{T_{sD}} {B_{mD}}^{\beta}\left[{t_{onD}}^{1-\alpha} + {t_{offD}}^{1-\alpha}\right] \quad (12)$$

C. Switching loss due to transformer self-capacitance

The capacitive turn-on or switching loss due the self-capacitance when the converter employs valley switching/boundary conduction mode (BCM) control during charge process is given by [26], [44], [45]

$$P_{swC} = \frac{1}{2}\left(n^2 C_s\right)\left(V_{in} - \frac{V_{out}}{n}\right)^2 f_{swC} \quad (13)$$

When the output voltage V_{out} is greater than nV_{in}, the capacitive switching loss P_{swC} is 0 W, since the converter operates with zero voltage switching (ZVS). The capacitive switching loss due the self-capacitance when the converter employs DCM control during discharge process is [26]

$$P_{swD} = \frac{1}{2} C_s (V_{Ms})^2 f_{swD} \quad (14)$$

In DCM, the drain-to-source voltage V_{Ms} at the beginning of the next switching cycle can be anywhere between $V_{out} + \delta_C n V_{in} + \delta_C V_{leakD}$ and $V_{out} + (2\delta_C - 1) n V_{in} + \delta_C V_{leakD}$. The expression for δ_c is given by [26]

$$\delta_c = \frac{C_{osss}}{C_{osss} + C_{Db}} \quad (15)$$

The output capacitance C_{osss} of M_s and junction capacitance C_{Db} of diode D_b are approximately 15 pF and 1 pF, respectively.

D. Switching loss due to transformer leakage inductance

The loss due to the dissipative RCD snubber during charge process is given by

$$P_{snC} = \frac{1}{2} L_{llkp} I^2_{ppkC} \frac{V_{snC}}{V_{snC} - \frac{V_{out}}{n}} f_{swC} \quad (16)$$

The loss due to the dissipative RCD snubber during discharge process is given by

$$P_{snD} = \frac{1}{2} L_{lks} I^2_{spkD} \frac{V_{snD}}{V_{snD} - nV_{in}} f_{swD} \quad (17)$$

where V_{snC} and V_{snD} are the snubber clamp voltages for low and high voltage MOSFETs, respectively.

E. Remaining losses in the bidirectional flyback converter

The remaining losses in the converter during charge process are: switching loss of M_p, conduction losses of M_p, D_2 and R_{psense}, gate drive loss of M_p, and power consumption of charge control IC. Similarly, the remaining losses in the converter during discharge process are: switching loss of M_s, conduction losses of M_s, D_b and R_{ssense}, gate drive loss of M_s, and power consumption of discharge control IC. Since during both charge and discharge operations the converter employs BCM and DCM control, respectively, there are no diode reverse recovery losses in both modes.

This article has been accepted for publication in a future issue of this journal, but has not been fully edited. Content may change prior to final publication. Citation information: DOI 10.1109/TPEL.2014.2379439, IEEE Transactions on Power Electronics

IV. Efficiency Optimization for a DC-DC Converter Driving Capacitive Load

Efficient design of a high voltage bidirectional flyback converter, necessitates many trade-offs and iterations with a large number of design variables. The first step of the optimization routine is to determine the design specifications of the converter. The low voltage and high voltage MOSFETs, high voltage diode, turns ratio and magnetizing inductance are used as the constraints in the optimization, and are kept constant throughout the optimization routine. The flow chart of the proposed optimization routine is shown in Fig. 7. The converter specifications are used to calculate the number of primary and secondary turns, for a given ferrite core. The outputs of AWL technique are used to calculate the transformer parasitics. The energy losses during both charge E_{lossC} and discharge E_{lossD} modes are calculated and added to represent the total energy loss for that specific core. Finally, the energy efficiencies during charge η_C and discharge η_D modes are calculated as a function of output voltage.

The design decisions presented in Table II are used, to limit the solution space of the optimization routine. The ranges for the cores and parameters to be optimized are shown in Table III. The optimization routine iterates through all design possibilities, and finally presents an optimized (most efficient) solution for each core. The outputs of the AWL technique are

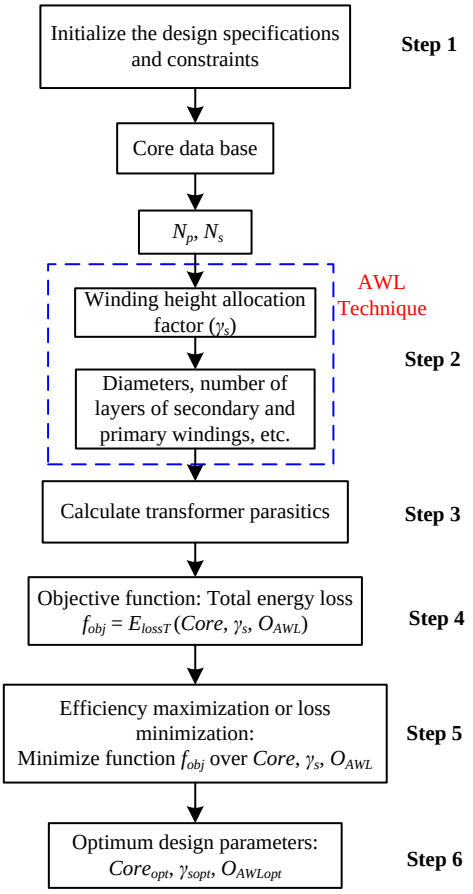

Fig. 7. Flow chart of the proposed efficiency optimization procedure.

TABLE III
Ranges of the Design Parameters

Parameters	Ranges for optimization
Transformer cores	EFD12, EFD 15, EFD 20, EFD 25, E 16, E 20, E 25, E 30, ETD 29, ETD 34, ETD 39, RM 8, RM 10, RM 12, PQ 20/20 and PQ 26/20
Height allocation factors for secondary winding (γ_s)	[0.5, 0.6, 0.7, 0.8]
Outputs from AWL technique O_{AWL}	see Section II and Figure 7

represented as O_{AWL}.

The proposed optimization routine is described in the following steps:

1) Transformer turns ratio, peak currents (for charge and discharge operations), magnetizing inductance are selected from the design specifications and constraints. Number of primary and secondary turns are calculated for a given transformer core.
2) The proposed AWL technique is applied to calculate an array of the outputs (diameter, number of layers, turns per layer, number of parallel wires, for both primary and secondary windings). The condition for the last layer fill factor is FF_{LL}>0.85, this is to approximately make, equal number of turns per layer on final secondary layer and remaining secondary layers).
3) The transformer parasitics are calculated for each set of outputs resulted from AWL technique.
4) The objective function f_{obj} is defined as the sum of the total energy losses in the bidirectional flyback converter over a set of operating points, and is given by
$$f_{obj} = E_{lossT}\left(Core,\ \gamma_s,\ O_{AWL}\right) \tag{18}$$
5) The efficiency optimization or loss minimization of function f_{obj} is
$$\min_{Core,\ \gamma_s,\ O_{AWL}}\left[f_{obj}\right] = \min_{Core,\ \gamma_s,\ O_{AWL}}\left[E_{lossT}\right] = \min_{Core,\ \gamma_s,\ O_{AWL}}\left[E_{lossC} + E_{lossD}\right] \tag{19}$$
6) The end results of the optimization routine are the set of parameters which contributes to the minimum total energy loss. Finally, the optimum charge and discharge energy efficiencies are calculated as a function of output voltage
$$\eta_C\left(V_{out}\right) = \frac{E_{load}\left(V_{out}\right)}{E_{load}\left(V_{out}\right) + E_{lossC}} = \frac{0.5C_{load}V_{out}^2}{0.5C_{load}V_{out}^2 + E_{lossC}} \tag{20}$$
$$\eta_D\left(V_{out}\right) = \frac{E_{load}\left(V_{out}\right) - E_{lossD}}{E_{load}\left(V_{out}\right)} = \frac{0.5C_{load}V_{out}^2 - E_{lossD}}{0.5C_{load}V_{out}^2} \tag{21}$$

V. Efficiency Optimization Results and Experimental Validation

A. Details of the optimization results:

The components used in the bidirectional flyback converter except the transformer are shown in Table IV. All losses in the bidirectional flyback converter are calculated in MATLAB

This article has been accepted for publication in a future issue of this journal, but has not been fully edited. Content may change prior to final publication. Citation information: DOI 10.1109/TPEL.2014.2379439, IEEE Transactions on Power Electronics

TABLE IV
COMPONENTS USED IN THE BIDIRECTIONAL FLYBACK CONVERTER

Component	Name / Manufacturer
Low voltage MOSFET M_p	IPB600N25N3 G [250 V, 25 A, 60 mΩ]
High voltage MOSFET M_s	IXTV03N400S [4 kV, 300 mA, 290 Ω]
High voltage diode D_2 or D_b	SP5LFG [5 kV, 400 mA, 50 ns (t_{rr})]
Film capacitive load C_{load}	WIMA [400 nF, 3 kV]
Analog control IC	LT3751

using the proposed comprehensive loss model. The winding loss is calculated during both charge and discharge processes, up to 100th order harmonics (N_h=100). The optimum secondary height allocation factor γ_s, for each core is provided in Fig. 8. Figure 9 provides the results of the optimum charge, discharge and overall (product of charge and discharge) energy efficiencies, and an overall energy efficiency of a typical design where 50% space is allocated for primary and secondary windings, at an output voltage of 2.5 kV, with respect to different core volumes.

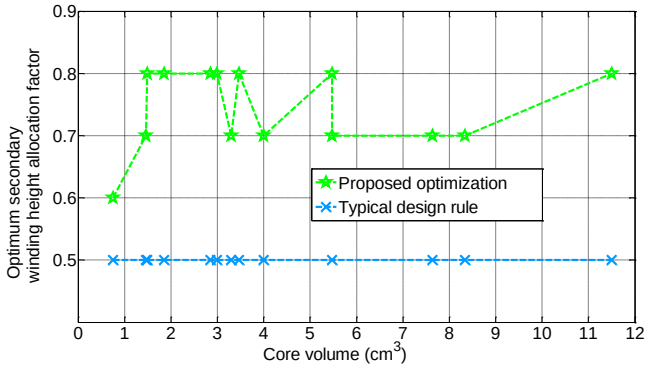

Fig. 8. Optimum secondary winding height allocation factor γ_s vs. core volume.

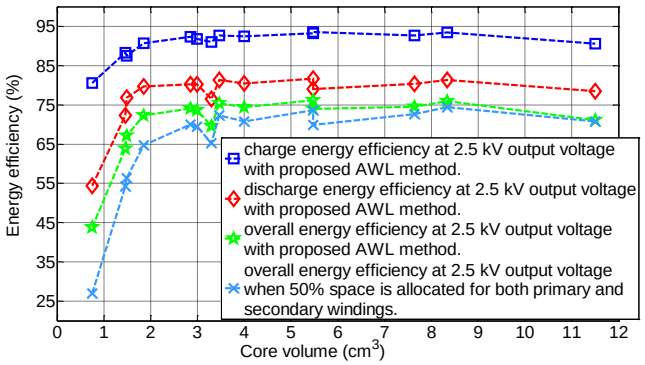

Fig. 9. Calculated optimized energy efficiencies at an output voltage of 2.5 kV vs. core volume. The sequence of the 14 cores is: [E 16, EFD 20, E 20, RM 8, PQ 20/20, E 25, EFD 25, RM 10, E 30, PQ 26/20, ETD 29, ETD 34, RM 12, ETD 39].

The total energy loss E_{lossC} at an output voltage of 2.5 kV is the loss occurred in all components of the converter, for charging the capacitive load from 0 V to 2.5 kV. Similarly, the total energy loss E_{lossD} at an output voltage of 2.5 kV is the loss occurred in all components of the converter, for discharging the capacitive load from 2.5 kV to 0 V. The most efficient and smallest transformer (or core) designs are two important outcomes of the proposed efficiency optimization routine. Table V shows a comparison of smallest core (SCD) and optimized core (OCD) designs.

The smallest and optimized core designs are described below:

1) Smallest core design (SCD)

The smallest core is selected as the core whose temperature rise is less than the maximum temperature limit (130 °C). Several small cores such as, EFD 12, EFD 15, E 16 have been used in the optimization routine, out of those E 16 is the smallest core with a maximum temperature rise of 94 °C (in a single bidirectional charge and discharge cycle). In the optimization routine, for all small cores (EFD 12, EFD 15, E 16), a maximum flux density of 0.33 T is chosen, hence for E 16, N_p becomes 29. As shown in Fig. 8, the optimum secondary height allocation factor for E 16 core is 0.6, this is for accommodating the 29 primary turns on the small core. The spacing between the secondary winding layers for SCD is 66 μm.

2) Optimized core design (OCD)

The core, which has a lower volume and a better overall energy efficiency compared with other cores, is selected as an optimized core. In Fig. 9, most of the cores whose volumes are above 2.85 cm^3 have an overall energy efficiency between 74% and 76%. The EFD 25 core with volume 3.3 cm^3 has a lower discharge efficiency (hence lower overall efficiency), since its window height H_W has been less compared with the neighboring cores, such as the EF 25 and RM 10 (see Fig. 9). For a better trade-off between the core volume and overall efficiency, the cores whose volume is between 2.85 and 4 cm^3 could be more suitable for the high voltage driver (with specifications shown in Table I). The cores with volumes 4 cm^3 (E 30) and 2.85 cm^3 (PQ 20/20) have overall efficiencies of 75% and 74%, respectively. However, PQ 20/20 core is selected as an optimized core, as a 40% increase in the core volume provides only 1% increase in the overall energy efficiency. In the optimization routine, a maximum flux density of 0.26 T is chosen for all cores whose volumes are greater than equal to 1.46 cm^3 (EFD 20). As shown in Fig. 8, for all cores except the smallest core, the optimum secondary winding height allocation factor varies between 0.7 and 0.8. For PQ 20/20 core, the secondary height allocation factor is 0.8. The spacing between the secondary winding layers for OCD is 0.9 mm.

The energy loss distributions for PQ 20/20 core during charge and discharge processes are shown in Figs. 10(a) and 10(b), respectively. During charge process, the converter operates with boundary conduction mode (BCM) control; hence the capacitive switching loss due to the self-capacitance is very low compared with other losses. The significant losses during charge process are: switching loss of low voltage MOSFET M_p, switching loss/snubber loss due to the transformer leakage inductance and transformer winding loss. During discharge process, the converter operates with discontinuous conduction mode (DCM) control; hence the capacitive switching loss due to the self-capacitance cannot be

This article has been accepted for publication in a future issue of this journal, but has not been fully edited. Content may change prior to final publication. Citation information: DOI 10.1109/TPEL.2014.2379439, IEEE Transactions on Power Electronics

TABLE V
RESULTS OF THE OPTIMIZATION FOR SMALLEST CORE DESIGN (SCD) AND OPTIMIZED CORE DESIGN (OCD)

Parameter	SCD	OCD
Core name	E 16	PQ 20/20
Core volume	0.75 cm^3	2.85 cm^3
Maximum flux density B_{mC}	0.33 T	0.26 T
Total number of turns of primary N_p / secondary N_s winding	29 / 720	12 / 300
Number of layers of primary n_{lp} / secondary n_{ls}	2 / 8	1 / 4
Number of parallel wires (or squares) of primary n_{parp} / secondary n_{pars}	1 / 1	1 / 1
Number of turns (or squares) per layer of primary / secondary	15 / 90	12 / 75
Diameter of primary d_p / secondary winding d_s	0.4 mm / 0.1 mm	(0.5+0.2) mm / 0.143 mm
Primary magnetizing inductance L_{mp}	40 μH	44 μH
Height allocation for secondary winding γ_s	0.6	0.8
Spacing (or insulation) between secondary layers $d_{insulation}$	66 μm	0.9 mm
Transformer maximum temperature rise in a single bidirectional charge and discharge cycle	94 °C	30 °C

neglected. The significant losses during discharge process are: switching loss of high voltage MOSFET M_s, switching loss due to the transformer leakage inductance, and capacitive switching loss due to the transformer self-capacitance.

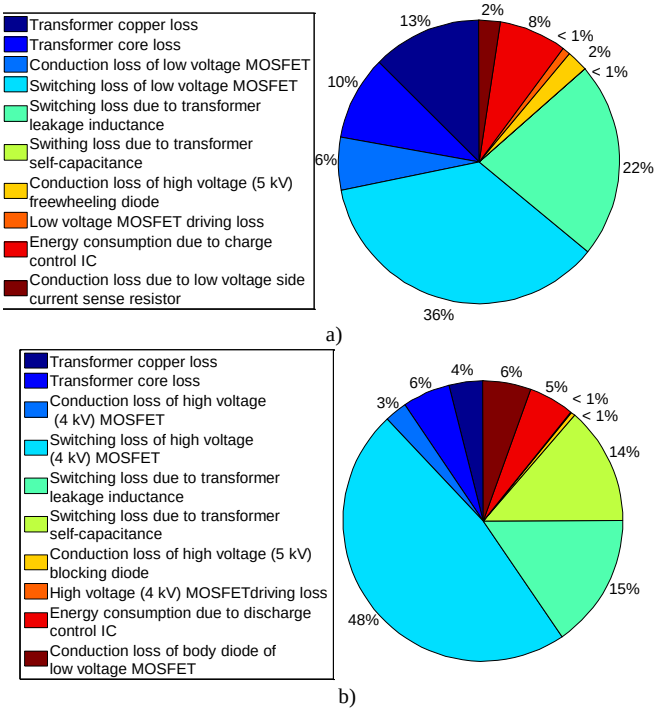

Fig. 10. Energy loss distribution of the optimized core (PQ 20/20), a) during charge and b) during discharge process.

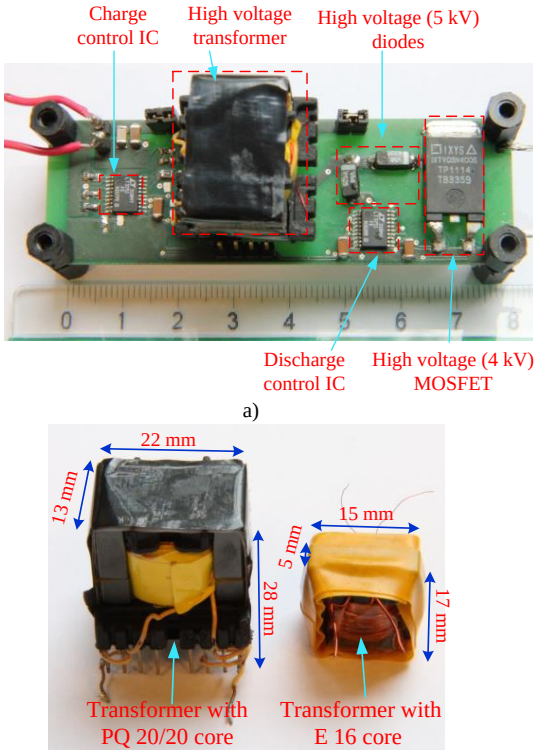

Fig. 11. a) Experimental prototype of the bidirectional flyback converter with PQ 20/20 core; b) Optimized (PQ 20/20) and smallest (E 16) transformers.

B. *Experimental Results*

The experimental prototype of the bidirectional flyback converter is shown in Fig. 11(a). The prototypes of optimized and smallest transformers are shown in Fig. 11(b). The comparison of measured [19] and calculated charge and discharge energy efficiencies for the smallest and optimized cores is provided in Figs. 12(a) and 12(b), respectively. In Figs. 12(a) and 12(b), the maximum difference between the calculated and measured energy efficiencies during charge and discharge modes is less than ±5%, except for the smallest core design at very high output voltage (>2.2 kV). The total loss due to the transformer parasitics for SCD is higher than that of OCD by 5 times, and the remaining losses in the converter, are the same for both designs.

In the bidirectional flyback converter an input capacitance C_{in} of 1800 μF (100 V) is used. The primary R_{psense} and secondary R_{ssense} sense resistors used in the converter are 25 mΩ and 0.5 Ω, respectively. The Z-type winding scheme [25] is implemented in the secondary winding of the flyback transformer, to reduce the self-capacitance. To remove the interlayer insulation tape between primary and secondary windings, triple insulated wire (TEX-E) from Furukawa [46]

This article has been accepted for publication in a future issue of this journal, but has not been fully edited. Content may change prior to final publication. Citation information: DOI 10.1109/TPEL.2014.2379439, IEEE Transactions on Power Electronics

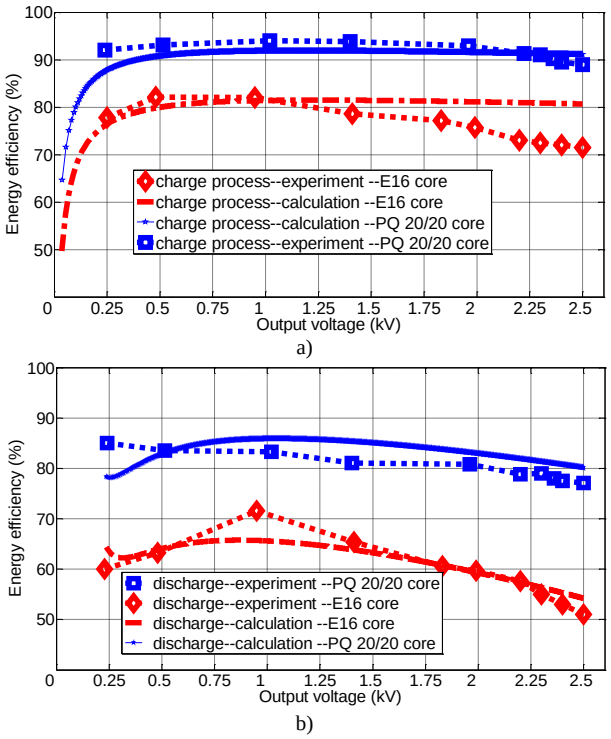

Fig. 12. Comparison of calculated and measured a) charge and b) discharge energy efficiencies for the optimized (PQ 20/20) and smallest (E 16) cores.

is used for the primary winding, and it has an insulation thickness of 0.2 mm. As shown in Table VI, 0.7 mm overall diameter wire (0.5 mm TEX-E wire) is used in the primary winding of PQ 20/20 core, and 0.4 mm overall diameter normal single insulated wire is used in the primary winding of E 16 core, due to non-availability of 0.2 mm TEX-E wire during practical implementation.

For PQ 20/20 core, no snubber is used in either low voltage or high voltage side. Since the leakage inductance of E 16 core is very high, RCD snubbers are used in both primary and secondary sides and the loss model is updated accordingly. The loss model automatically considers RCD snubbers, when the leakage inductance L_{lkp} in the optimization is higher than 1.2 μH. The low voltage V_{snC} and high voltage V_{snD} RCD snubber clamp voltages are chosen as $\frac{2V_{out,max}}{n}$ and $2nV_{in}$, respectively, with a maximum output voltage $V_{out,max}$ of 2.5 kV. The insulation between the secondary layers of transformer is provided by the Kapton tape which has a single layer thickness of 66 μm. The calculated and measured transformer parasitics for both SCD and OCD are provided in Table VI. The comparison shows that the model used for calculating the parasitics, for multiple solutions in the optimization routine is accurate enough.

VI. Conclusions

This paper presents an efficiency optimization approach for a high voltage bidirectional flyback dc–dc converter. The energy efficiency is optimized using a proposed new automatic winding layout generator technique and a comprehensive loss model. The proposed optimization technique is experimentally validated on a 25 W (charging power) high voltage bidirectional flyback converter. The measured charge and discharge energy efficiencies of the converter, with PQ 20/20 core at an output voltage of 2.5 kV are 89% and 77.1%, respectively. For both optimized and smallest core designs, energy efficiency during discharge process is less compared to that during charge process, mostly due to the switching loss of the output capacitance of high voltage MOSFET.

TABLE VI
Comparison of Calculated and Measured Transformer Parameters for Smallest and Optimized Core Designs

Parameter of Transformer	SCD		OCD	
	Calculation	Measurement	Calculation	Measurement
Leakage inductance referred to primary L_{lkp}	3.22 μH	3.3 μH	818 nH	857 nH
Self-capacitance of secondary (high voltage) winding C_s	18.1 pF	21.62 pF	4.5 pF	6.23 pF
Dc resistance of secondary (high voltage) winding R_s	46.54 Ω	44 Ω	15.3 Ω	18.2 Ω

The important conclusions of this paper are as follows:

1) The proposed AWL technique is highly recommended for high input or high output voltage applications which need a transformer with many turns (primary or secondary). It automatically calculates and provides the necessary winding design data such as wire sizes, number of winding layers, number of turns per layer, and the number of parallel wires.
2) The AWL technique can be easily extended to interleaved and/or sectioned transformer structures.
3) Transformer parasitics are calculated for each set of outputs from AWL technique, which are needed to estimate the energy efficiency. By iteratively changing the spacing between secondary winding layers, the loss due to self-capacitance, leakage inductance and dc resistance of the transformer are balanced.
4) Providing a very thick insulating tape between the secondary winding layers reduces the self-capacitance. The self-capacitance can be reduced significantly by allocating more space (or height) for the secondary winding.
5) Non-sectioned bobbins with larger window height are suitable for minimizing the self-capacitance, hence are recommended for high voltage capacitor charge and discharge application.
6) The output of the proposed efficiency optimization (overall energy efficiency vs. core volume curve) gives the flexibility for the designer to choose the necessary core and winding configurations.

References

[1] Y. Bar-Cohen, Electroactive Polymer [EAP] Actuators as Artificial Muscles: Reality, Potential, and Challenges, 2nd Ed. Washington, DC: SPIE, 2004.

This article has been accepted for publication in a future issue of this journal, but has not been fully edited. Content may change prior to final publication. Citation information: DOI 10.1109/TPEL.2014.2379439, IEEE Transactions on Power Electronics

[2] R. E. Pelrine, R. D. Kornbluh, Q. Pei, J. P. Joseph, "High-speed electrically actuated elastomers with strain greater than 100%," *Science*, vol. 287, pp. 836–839, 2000.

[3] F. Carpi, D. DE Rossi, R. Kornbluh, R. Pelrine, P. Sommer-Larsen, Eds, "Dielectric Elastomer As Electromechanical Transducers," Amsterdam, The Netherlands: Elsevier, 2008.

[4] Danfoss PolyPower, Denmark, Online avilable: http://www.polypower.com/ [accessed 16 Oct. 2014].

[5] M. Tryson, H. E. Kiil, M. Benslimane, "Powerful tubular core free dielectric electro active polymer (DEAP) push actuator," in *Proc. SPIE*, vol. 7287, 2009.

[6] R. Sarban, B. Lassen, M. Willatzen, "Dynamic Electromechanical Modeling of Dielectric Elastomer Actuators With Metallic Electrodes," *IEEE/ASME Tran. Mechatronics*, vol. 17, no. 5, pp. 960-967, Oct. 2012.

[7] P. Thummala, H. Schneider, Z. Zhang, M. A. E. Andersen, R. Sarban, "A new Incremental Actuator based on Electro Active Polymer: Conceptual, Control and Driver Design Considerations," *IEEE/ASME Trans. Mechatronics* (under review process).

[8] P. Thummala, Z. Zhang, M. A. E. Andersen, S. Rahimullah, "Dielectric electro active polymer incremental actuator driven by multiple high-voltage bi-directional DC-DC converters," in *Proc. IEEE ECCE USA*, pp. 3837-3844, 2013.

[9] R. W. Erickson, D. Maksimovic, *Fundamentals of Power Electronics*, 2nd Ed., New York: Springer, 2001.

[10] J. Elmes, C. Jourdan, O. Abdel-Rahman, I. Batarseh, "High-Voltage, High-Power-Density DC-DC Converter for Capacitor Charging Applications," in *Proc. IEEE APEC*, pp. 433-439, 2009.

[11] T. Andersen, M. S. Rødgaard, O. C. Thomsen, M. A. E. Andersen, "Low voltage driven dielectric electro active polymer actuator with integrated piezoelectric transformer based driver," in *Proc.* SPIE, vol. 7976, p. 79762N, 2011.

[12] S. K. Chung, H. B. Shin, "High-voltage power supply for semi-active suspension system with ER-fluid damper," *IEEE Trans. Vehicular Technology*, vol. 53, no. 1, pp. 206- 214, Jan. 2004.

[13] L. Eitzen, T Hoffstadt, J. Maas, "Power electronics concepts for driving EAP actuators," in *Proc. SPIE, Electroactive Polymer Actuators and Devices (EAPAD)*, pp. 86870D, 2013.

[14] K. Venkatesan, "Current Mode Controlled Bidirectional Flyback Converter," in *Proc. IEEE PESC*, pp. 835-842, 1989.

[15] G. Chen, Y.-S. Lee, S.Y.R. Hui, D. Xu, Y. Wang, "Actively clamped bidirectional flyback converter," *IEEE Trans. on Industrial Electronics*, vol. 47, no. 4, pp. 770-779, Aug. 2000.

[16] T. Bhattacharya, V. S. Giri, K. Mathew, L. Umanand, "Multiphase Bidirectional Flyback Converter Topology for Hybrid Electric Vehicles," *IEEE Trans. Industrial Electronics*, vol. 56, no. 1, pp. 78-84, Jan. 2009.

[17] M. Karpelson, G. Y. Wei, R. J. Wood, "Driving high voltage piezoelectric actuators in microrobotic applications," *Sensors and Actuators A*, vol. 176, pp. 78– 89, 2012.

[18] F. Zhang, Y. Yan, "Novel Forward–Flyback Hybrid Bidirectional DC–DC Converter," *IEEE Trans. Industrial Electronics*, vol. 56, no. 5, pp. 1578-1584, May 2009.

[19] P. Thummala, Z. Zhang, M. A. E. Andersen, "High Voltage Bi-directional Flyback Converter for Capacitive Actuator", in *Proc. IEEE EPE*, pp. 1-10, 2013.

[20] P. Thummala, H. Schneider, Z. Ouyang, Z. Zhang, M. A. E. Andersen, "Estimation of transformer parameters and loss analysis for high voltage capacitor charging application," in *Proc. IEEE ECCE Asia*, pp. 704-710, 2013.

[21] C. W. T. McLyman, *Transformer and Inductor Design Handbook*, 3rd Ed., New York: Marcel Dekker, 2004.

[22] W. G. Hurley, W. H. Wolfle, Transformers and Inductors for Power Electronics: Theory, Design and Applications, 1st Ed., John Wiley and Sons Ltd., 2013.

[23] M. Kazimierczuk, *High-frequency magnetic components*, 2nd Ed., John Wiley and Sons Ltd., 2014.

[24] P. Thummala, H. Schneider, Z. Zhang, A. Knott, M. A. E. Andersen, "Optimization of a bi-directional flyback converter for a high voltage capacitor charging application," in *Proc. IEEE APEC*, pp. 2556-2563, 2014.

[25] H. Schneider, P. Thummala, L. Huang, A. Knott, Z. Zhang, M. A. E. Andersen, "Investigation of Transformer Winding Architectures for High Voltage Capacitor Charging Applications," in *Proc. IEEE APEC*, pp. 334-341, 2014.

[26] P. Thummala, D. Maksimovic, Z. Zhang, M. A. E. Andersen, "Digital control of a high-voltage (2.5 kV) bidirectional DC-DC converter for driving a dielectric electro active polymer (DEAP) based capacitive actuator," in *Proc. IEEE ECCE USA*, 14-18th Sept. 2014.

[27] N. O. Sokal, R. Redl, "Control algorithms and circuit designs for optimal flyback-charging of an energy storage capacitor (e.g., for flash lamp or defibrillator)," *IEEE Trans. Power Electronics*, vol. 12, no. 5, pp. 885-894, Sep. 1997.

[28] R. Prieto, J.A. Cobos, O. Garcia, R. Asensi, J. Uceda, "Optimizing the winding strategy of the transformer in a flyback converter," in *Proc. IEEE PESC*, pp. 1456-1462, 1996.

[29] C. R. Sullivan, T. Abdallah, T. Fujiwara, "Optimization of a flyback transformer winding considering two-dimensional field effects, cost and loss," in *Proc. IEEE APEC*, pp.116-122, 2001.

[30] H. K. Sang, D. Maksimovic, I. Cohen, "Efficiency Optimization in Digitally Controlled Flyback DC–DC Converters Over Wide Ranges of Operating Conditions," *IEEE Trans. Power Electronics*, vol. 27, no. 8, pp. 3734-3748, Aug. 2012.

[31] A. C. Nanakos, E.C. Tatakis, N. P Papanikolaou, "A Weighted-Efficiency-Oriented Design Methodology of Flyback Inverter for AC Photovoltaic Modules," *IEEE Trans. Power Electronics*, vol. 27, no. 7, pp. 3221-3233, July 2012.

[32] X. Zhou, T. G. Wang, F. C. Lee, "Optimizing Design for Low Voltage DC-DC Converters," in *Proc. IEEE APEC*, pp. 612-616, 2007.

[33] U. Badstuebner, J. Biela, J. W. Kolar, "An optimized, 99% efficient, 5 kW, phase-shift PWM DC-DC converter for data centers and telecom applications," in *Proc. IEEE IPEC*, pp.626,634, 21-24 June 2010.

[34] J. Biela, U. Badstuebner, J. W. Kolar, "Impact of Power Density Maximization on Efficiency of DC-DC Converter Systems," *IEEE Trans. Power Electronics*, vol. 24, no. 1, pp. 288-300, Jan 2009.

[35] E. C. Snelling, *Soft Ferrites-Properties and applications*, 2nd Ed. London, UK, Butterworth, 1988.

[36] L. Dalessandro, F. da Silveira Cavalcante, J. W. Kolar, "Self-Capacitance of High-Voltage Transformers," *IEEE Trans. Power Electronics*, vol. 22, no.5, pp. 2081-2092, Sept. 2007.

[37] J. Biela, J. W. Kolar, "Using Transformer Parasitics for Resonant Converters—A Review of the Calculation of the Stray Capacitance of Transformers," *IEEE Trans. Industry Applications*, vol. 44, no.1, pp. 223-233, 2008.

[38] W.G. Hurley, E. Gath, J. G. Breslin, "Optimizing the AC resistance of multilayer transformer windings with arbitrary current waveforms," *IEEE Trans. Power Electronics*, vol. 15, no. 2, pp. 369-376, Mar 2000.

[39] J. A. Ferreira, "Improved analytical modeling of conductive losses in magnetic components," *IEEE Trans. Power Electronics*, vol. 9, no. 1, pp. 127,131, Jan 1994.

[40] J. Vandelac, P. D. Ziogas, "A Novel Approach for Minimizing High-Frequency Transformer Copper Losses," *IEEE Trans. Power Electronics*, vol. 3, no. 3, pp. 266-277, Jul. 1988.

[41] S. H. Kang, "Efficiency Optimization in Digitally Controlled Flyback DC-DC Converters Over Wide Ranges of Operating Conditions," Ph.D. Thesis, Dept. Electrical, Computer and Energy Engineering, University of Colorado Boulder, USA 2011.

[42] LT3751 datasheet, "High voltage capacitor charger controller with regulation," Linear Technology Corporation, USA, Online available: http://cds.linear.com/docs/en/datasheet/3751fc.pdf [accessed 16 Oct. 2014].

[43] K. Venkatachalam, C. R. Sullivan, T. Abdallah, H. Tacca, "Accurate prediction of ferrite cores loss with nonsinusoidal waveforms using only Steinmetz parameters," in *Proc. IEEE Workshop Comput. Power Electron.*, pp. 36–41, 2002.

[44] M. T. Zhang, M. M. Jovanovic, F. C. Lee, "Design considerations and performance evaluations of synchronous rectification in flyback converters," in *Proc. IEEE APEC*, pp. 623-630, Feb 1997.

[45] C. P. Basso, *Switch-mode power supplies-spice simulations and practical designs*, 2nd Ed., McGraw Hill, 2008.

[46] Furukawa webpage, "Triple Insulated Wire: Standard Type TEX-E," Furukawa Electric, Japan, Online available: http://www.furukawa.co.jp/makisen/eng/product/texe_series.htm [accessed 16 Oct. 2014].

This article has been accepted for publication in a future issue of this journal, but has not been fully edited. Content may change prior to final publication. Citation information: DOI 10.1109/TPEL.2014.2379439, IEEE Transactions on Power Electronics

Prasanth Thummala (S'11) was born in India in 1987. He received the B.Tech. degree in electrical and electronics engineering from Acharya Nagarjuna University, Guntur, India, in 2008, and the M.Tech degree in control systems engineering, at the department of electrical engineering, from the Indian Institute of Technology Kharagpur, Kharagpur, India, in 2010. He was a Ph.D. student in the electronics group, department of electrical engineering, Technical University of Denmark (DTU), Denmark, from Nov. 2011 to Nov. 2014.

From Sept. 2013 to Jan. 2014, he was a Visiting PhD student in Colorado Power Electronics Center (CoPEC), at the University of Colorado Boulder, Boulder, CO, USA. He received the first prize UTRC best student paper award at the IEEE ECCE USA conference held in Denver, CO, USA, 2013. His research interests include modeling and control of power electronic converters, high-voltage switch-mode power converters for driving capacitive loads, magnetic design, digital control and system identification.

Henrik Schneider (S'11) was born in Denmark and received a master's degree in electrical engineering from the Technical University of Denmark in 2009. The following two years he worked as an R&D engineer within power electronics.

In 2011 he was enrolled as a Ph.D. at the Technical University of Denmark with a focus on switch mode power supplies and audio amplifiers. He received the best paper award at the IEEE ECCE Asia conference held in Melbourne, Australia, 2013 and a best presentation award at the IEEE APEC conference in Dallas, USA, 2014. His research interests include, efficiency and power density optimization of power electronics, audio system integration, magnetic design and finite element modeling.

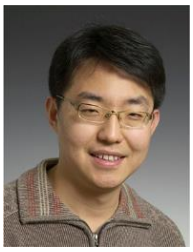

Zhe Zhang (S'07, M'11) received the B.Sc. and M.Sc. degrees in power electronics from Yanshan University, Qinhuangdao, China, in 2002 and 2005, respectively, and the Ph.D. degree from the Technical University of Denmark, Kgs. Lyngby, Denmark, in 2010.

He is currently an Associate Professor with the Department of Electrical Engineering, at the Technical University of Denmark. From 2005 to 2007, he was an Assistant Professor with Yanshan University. From June 2010 to August 2010, he was with the University of California, Irvine, CA, USA, as a visiting scholar. He was a Postdoctoral Researcher and Assistant Professor at the Technical University of Denmark between 2011 and 2014. He has authored or co-authored more than 70 transactions and conference papers. His current research interests include DC/DC converters, multiple-input converters, and multi-level inverters for renewable energy systems (RES), hybrid electric vehicles (HEV) and uninterruptable power supplies (UPS).

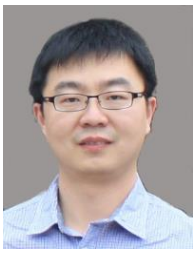

Ziwei Ouyang (S'07, M'11) received the B.S degree in electrical engineering from the Naval University of Engineering, Wuhan, China, in 2004, the M.S degree from the Tianjin University of Technology, Tianjin, China, in 2007, and the Ph.D. degree from the Technical University of Denmark (DTU), Denmark, in 2011. He worked as a Postdoctoral Researcher at DTU from 2011 to 2013 and is currently assistant professor in the Department of Electrical Engineering at DTU.

His current research interests include advanced magnetics design, modeling and integration in switch mode power supplies, dc/dc converters, and digital control in high-power reversible converters. He has over 30 peer-reviewed journal and conference publications and currently he is the holder of three US/EP/PCT patents. He received the Young Engineer Award at PCIM Asia 2014 and Best Paper Awards in ECCE-Asia conferences in 2010 and 2012, respectively. He is a member of the IEEE PELS, IES and Magnetics societies.

Arnold Knott (M'10) received the Diplom-Ingenieur (FH) degree from the University of Applied Sciences in Deggendorf, Germany, in 2004. From 2004 until 2009 he has been working with Harman/Becker Automotive Systems GmbH in Germany and USA, designing switch-mode audio power amplifiers and power supplies for automotive applications.

In 2010 he earned the Ph.D. degree from the Technical University of Denmark, Kongens Lyngby, Denmark working on a research project under the title "Improvement of out-of-band Behaviour in Switch-Mode Amplifiers and Power Supplies by their Modulation Topology". From 2010 to 2013 he was Assistant Professor and since 2013 Associate Professor at the Technical University of Denmark. His interests include switch-mode audio power amplifiers, power supplies, active and passive components, integrated circuit design, acoustics, radio frequency electronics, electromagnetic compatibility and communication systems.

Michael A. E. Andersen (M'88) received the M.Sc.E.E. and Ph.D. degrees in power electronics from the Technical University of Denmark, Kgs. Lyngby, Denmark, in 1987 and 1990, respectively. He is currently a Professor in power electronics and head of the Electronics group at the Technical University of Denmark (DTU). Since 2009 he has been the Deputy Head of the Department at the Department of Electrical Engineering, Technical University of Denmark.

He received the best poster prize in UPEC 1991 conference. He has authored and co-authored more than 280 publications. From 2010, he is serving as an Associate Editor of IEEE Transactions on Power Electronics. His research areas include switch mode power supplies, piezoelectric transformers, power factor correction, and switch mode audio power amplifiers.

Appendix I

Investigation of transformer winding architectures for high voltage capacitor charging applications

---

2014 IEEE Applied Power Electronics Conference and Exposition (APEC 2014)

Investigation of transformer winding architectures for high voltage capacitor charging applications

Henrik Schneider, Prasanth Thummala, Lina Huang, Ziwei Ouyang, Arnold Knott, Zhe Zhang, Michael A. E. Andersen
Electronics Group, Department of Electrical Engineering
Technical University of Denmark
2800 Kongens Lyngby, Denmark
hensc@elektro.dtu.dk, pthu@elektro.dtu.dk, huang@elektro.dtu.dk

***Abstract*—Transformer parameters such as leakage inductance and self-capacitance are rarely calculated in advance during the design phase, because of the complexity and huge analytical error margins caused by practical winding implementation issues. Thus, choosing one transformer architecture over another for a given design is usually based on experience or a trial and error approach. This work presents equations regarding calculation of leakage inductance, self-capacitance and AC resistance in transformer winding architectures, ranging from the common non-interleaved primary/secondary winding architecture, to an interleaved, sectionalized and bank winded architecture. The analytical results are evaluated experimentally and through FEM simulations. Different transformer winding architectures are investigated in terms of the losses caused by the transformer parasitics for a bi-directional high-voltage (~1500 V) flyback converter used to drive a dielectric electro active polymer based incremental actuator. The total losses due to the transformer parasitics for the best transformer architectures is reduced by more than a factor of ten compared to the worst case transformer architectures.**

I. INTRODUCTION

Dielectric electro active polymer (DEAP) is an emerging smart material that has experienced significant development and has gained increasing attention over the last decade [1], [2]. DEAP, when used as actuators, has the potential to be an effective replacement for many conventional actuators due to its unique properties such as high strain, light weight, low noise operation, low power consumption. However, a compact high voltage driver is required to charge and discharge the DEAP from 0 V to 2500 V DC supplied from a 24 V battery. The DEAP actuator applications require a bi-directional energy transfer capability, to increase the life time of the battery. The flyback converter topology is suitable for low power (< 150 W), and high voltage capacitor charging applications, as it can be made very compact with a low number of components.

The flyback transformer is the most critical component in terms of driver performance. The high voltage requirement demands a high turns ratio which calls for a large number of secondary turns. This may lead to a high winding self-capacitance resulting in severe capacitive switching loss and undesirable, resonating current spikes in the leading edge of the current waveform, which could lead to false triggering of the current limit during the turn-on process.

The leakage inductance of the transformer may cause undesirable voltage spikes on the drains of the primary and secondary MOSFETs during the charge and the discharge processes, respectively, which lead to use of active or passive snubber circuits in the converter. With active snubbers high energy efficiency can be achieved, at the expense of a higher cost and added control complexity whereas the passive snubbers result in switching loss due to the leakage inductance. The AC resistance is also an important parameter to consider, since the AC conduction loss is caused by high frequency skin and proximity effects in a flyback converter operating in boundary conduction mode (BCM) or in discontinuous conduction mode (DCM).

Thus, accurate estimation of the transformer parameters and their associated losses are required, to evaluate different transformer winding architectures (TWAs) from which the best TWA is selected to achieve high energy efficiency. Extensive research has been done on calculating the leakage inductance in conventional transformers [3]-[6], [17], and in [7]-[17], the capacitance calculation methods have been proposed for inductors, power, planar, and high voltage transformers. The influence of transformer parasitics for the low power flyback converter has been discussed in [24]. This paper investigates a number of TWAs providing a deep insight into transformer design and its impact on the total loss contribution of a bi-directional high-voltage flyback converter.

The paper is organized as follows: the TWAs are described and then calculations of self-capacitance, leakage inductance and AC resistance for different TWAs are provided. The calculated transformer parameters are evaluated via FEA simulation using ANSOFT Maxwell and

This work was sponsored by Danish National Advanced Technology Foundation.

the transformer paracitics for all TWAs are presented, followed by the conclusion.

II. TRANSFORMER WINDING ARCHITECTURES

This paper investigates the four known winding schemes (A, B, C and D) as shown in Fig. 1 [14], [16], [26], [27]. Winding scheme A is the most simple to implement since the next layer starts where the previous layer ended. In winding scheme B, the next layer starts just above the starting point of the previous layer. Winding scheme C split the winding into a number of sections that is individually wounded like winding scheme A. In winding scheme D, the turns progress in a vertical back angled way where turns are built on top of previous turns. It seems like winding scheme D achieves as many angled sections as there are turns in a layer without the penalty of reducing the fill factor due to the thickness of the section walls. Another advantage is that winding scheme D can be easily interleaved which is not the case for winding scheme C since it is hard to add section walls in-between windings. The difference in self-capacitance due to the winding schemes is severe because the voltage potentials between the turns in the winding are changed.

Several winding buildups (S/P, S/P/S, S/P/S/P/S/P/S; where S and P are is the secondary and primary windings, respectively) are investigated - see Fig. 2. Based on these configurations, seven high voltage transformer winding architectures (W_1-W_7) are derived and the winding information is summarized in Table 1. In order to simplify the implementation of the windings a low turns ratio of 10 is selected. The TWAs W_1-W_6 are wound with 10 primary turns and 100 secondary turns. W_7 deviates since it is only implemented with 9 primary turns due to the nature of the winding architecture.

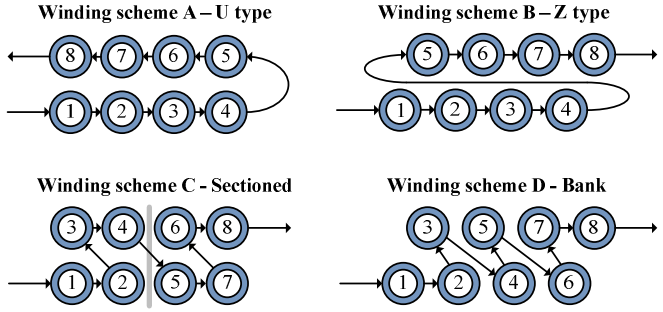

Figure 1. An overview of different winding schemes.

Winding scheme A is employed for the primary winding of all architectures. Moreover, all winding space of the bobbin is utilized to improve the fill factor and to reduce the winding resistance. Equal space allocation for primary and secondary winding is adopted for this investigation, thus the primary winding is wounded with a number of parallel wires.

III. SELF-CAPACITANCE

High voltage transformers tend to have a large number of turns in the high voltage side, which introduces a non-negligible parasitic self-capacitance. It is important to predict the self-capacitance in the design phase in order to avoid severe switching loss. In fact, the winding self-capacitance is a parameter representing the electric field energy stored in the winding and is considered as a shunt lumped element in most cases [14]. Due to a large number of turns per layer, the effect of the turn-to-turn capacitance can be neglected and the main

TABLE I. HIGH VOLTAGE TRANSFORMER ARCHITECTURES

Design	Winding buildup	Secondary winding		Primary winding
		Scheme	Parameters	Parameters
W_1	S/P	A	$N_s = 100$ $d_{is} = 0.3$ mm $d_{os} = 0.32$ mm $p_{TT} = 0.355$ mm $p_{LL} = 0.34$ mm $n_{ls} = 4$ $n_{pars} = 1$ Core / Material used: RM8 / N41	$N_p = 10$ $*d_{ip} = 0.7$ mm $*d_{op} = 0.8$ mm $n_{lp} = 2$ $n_{parp} = 2$
W_2	S/P	B		
W_3	S/P	C		
W_4	S/P	D		
W_5	S/P/S	B		
W_6	S/P/S	D		
W_7	S/P/S/P/S/P/S	B		$N_p = 9$ $*d_{ip} = 0.48$ mm $*d_{op} = 0.5$ mm $n_{lp} = 3$ $n_{parp} = 5$
Parameters interpretation				
N_s / N_p - number of secondary / primary turns; n_{ls} / n_{lp} - number of secondary / primary winding layers; n_{pars} / n_{parp} - number of secondary / primary parallel windings; d_{is} / d_{os} - inner / outer diameter of secondary winding; d_{ip} / d_{op} - inner / outer diameter of primary winding; p_{TT} / p_{LL} - turn-to-turn / layer-to-layer pitch of secondary winding; *In the practical transformer implementation triple insulated (TEX) windings are not used for the primary due to the unavailability of the wires;				

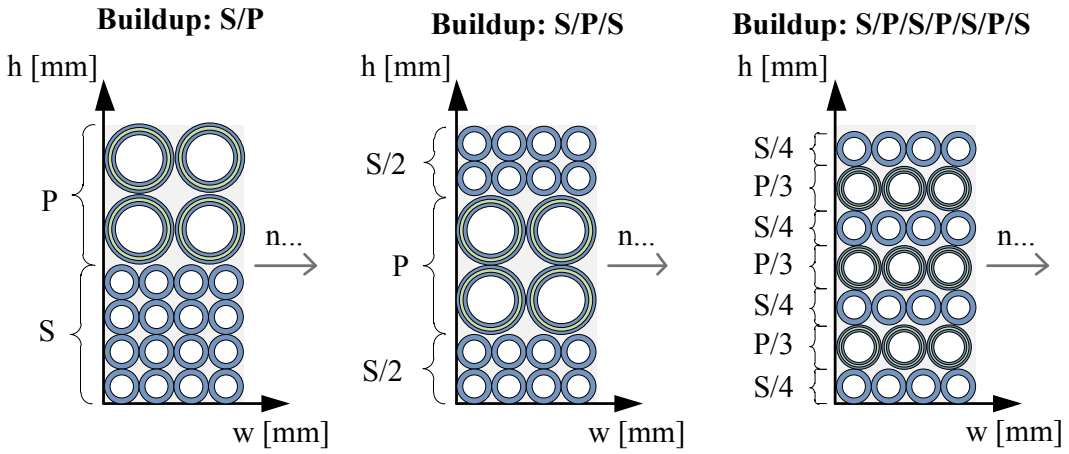

Figure 2. An overview of different winding buildups.

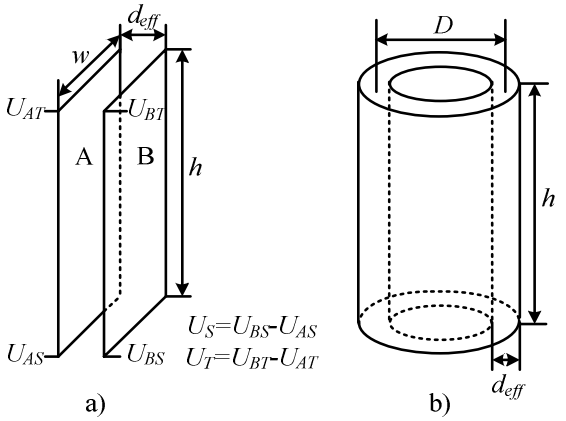

Figure 3. a) Two parallel plates with a linear potential distribution, b) Cylindrical capacitor model

contribution to the self-capacitance comes from the layer-to-layer capacitance, which can be calculated based on the simple parallel-plate or cylindrical capacitor model [14]-[16].

The self-capacitance in the transformer windings can be calculated using the electro static energy stored in the volume between the conductors [14], [16] and is given by

$$E_{Electric} = \frac{1}{2}\iiint_{Vol} \varepsilon\, E^2 dv = \frac{1}{2} C_S U_W^2 \tag{1}$$

where ε is the equivalent dielectric constant of the winding, E is the electric field strength, C_S is the self-capacitance, and U_W is the total voltage across the winding.

The energy stored in two adjacent conductive layers with a linear potential distribution, shown in Fig. 3a, can be calculated by (2), which is derived in [16]. The total stored energy is

$$E_{Stored} = \frac{C_l}{6}\left(U_S^2 + U_S U_T + U_T^2\right) \tag{2}$$

where U_S and U_T are the potential difference between the two surfaces at the bottom and top respectively, and C_l is the capacitance between the two surfaces and is considered as a parallel plate capacitance and can be calculated using (3)

$$C_l = \varepsilon_r \varepsilon_0 \frac{hw}{d_{eff}} \tag{3}$$

where ε_0 is the vacuum permittivity and is 8.854×10^{-12} F/m, ε_r is the relative permittivity of the dielectric material. The parameters h, w represents the dimensions of the plate and d_{eff} is the effective distance between two layers (which needs to be calculated for each TWA) and is given by

$$d_{eff} = p_{LL} - 1.15 d_{is} + 0.26 p_{TT} \tag{4}$$

where p_{LL}, d_{is} and p_{TT} are the layer to layer pitch, inner diameter, and turn to turn pitch, of the secondary winding, respectively. According to the methods given in [16], the expressions for calculating the self-capacitance for all above mentioned TWAs have been derived and are summarized in Table 2. Normally, the cylindrical shape, shown in Fig. 3b, is desired for most winding layers due to the simple winding technique as well as the short mean turn length [14]. If the distance between two layers is much less than the mean diameter for the two layers, the cylindrical capacitor can be considered to be a parallel plate capacitor and (3) can be employed to calculate the capacitance by replacing w with πD (see Fig. 3b).

TABLE II. SELF-CAPACITANCE EXPRESSIONS FOR DIFFERENT TWAS

TWA	Self-capacitance expression
W_1	$4\frac{(n_{ls}-1)}{n_{ls}^2}\frac{C_l}{3}$; $C_l = \varepsilon_r\varepsilon_0\frac{b_w l_{w1}}{d_{eff1}}$; $l_{w1} = \pi\left(D_i + n_{ls}d_{is} + (n_{ls}-1)h_{is}\right)$
W_2	$4\frac{(n_{ls}-1)}{n_{ls}^2}\frac{C_l}{4}$; $C_l = \varepsilon_r\varepsilon_0\frac{b_w l_{w1}}{d_{eff1}}$; $b_w = (T_{ls}-1)p_{TT} + d_{os}$
W_3	$\frac{4(n_{ls}-1)}{q_1 n_{ls}^2}\frac{C_l}{3}$; $C_l = \varepsilon_r\varepsilon_0\frac{\frac{b_{w2}}{q_1}l_{w1}}{d_{eff1}}$
W_4	$\varepsilon_r\varepsilon_0\frac{p_{TT}l_{w1}}{d_{eff2}}\frac{L}{b_w}$; $L = (n_{ls}-1)p_{LL} + d_{os}$ [7]
W_5	$\frac{\varepsilon_r\varepsilon_0 b_w}{n_{ls}^2}\left[\frac{l_{w2}}{d_{eff3}} + \frac{l_{w3}}{d_{eff3}} + \frac{l_{w4}}{d_{eff3} + n_{lp}d_p + (n_{lp}-1)h_{ip}}\right]$
W_6	$\varepsilon_r\varepsilon_0\left[\frac{p_{TT}(l_{w2}+l_{w3})}{d_{eff4}}\frac{L_1}{b_w} + \frac{p_{TT2}l_{w4}}{d_{eff4} + n_{lp}d_p + (n_{lp}-1)h_{ip}}\frac{L_2}{b_w}\right]$; $L_1 = \left(\frac{n_{ls}}{2}-1\right)p_{LL} + d_{os}$; $p_{TT2} = n_{lp}h_p + (n_{lp}-1)h_{ip} + d_{os}$; $L_2 = p_{TT2} + d_{os}$
W_7	$\frac{\varepsilon_r\varepsilon_0 b_w}{n_{ls}^2}\left[\frac{l_{w5}+l_{w6}+l_{w7}}{d_{eff5}}\right]$

Parameters interpretation

ε_0 / ε_r - relative permittivity of vacuum / dielectric material; $\varepsilon_r = 4$;
b_w - the width of the layer; T_{ls} is turns per layer of secondary winding;
D_i - inner diameter of the bobbin;
$d_{eff1,2,3,4,5}$ - effective thickness of dielectric between two layers [14] [16] for different TWAs;
l_{w1} - mean length turn for the TWAs W_1, W_2, W_3 and W_4;
l_{w2} / l_{w3} / l_{w4} - mean length turn between most inner two secondary (S_1, S_2) / most outer two secondary (S_3, S_4) / most outer secondary and the most inner secondary (S_2, S_3), layers for W_5 and W_6;
l_{w5} / l_{w6} / l_{w7} / l_{w8} / l_{w9} / l_{w10} - mean length turn between most inner two secondary (S_1, S_2) / middle two secondary (S_2, S_3) / most outer two secondary (S_3, S_4) layers for W_7
q_1 - number of sections for structure W_3 and $q_1 = 4$;
For remaining abbreviations refer Tables 1 and 3;

IV. LEAKAGE INDUCTANCE

The leakage inductance in a transformer is calculated using the energy stored in the magnetic field [16]. The total leakage energy stored in the magnetic field is given by

$$E_{Magnetic} = \frac{1}{2}\iiint_{Vol} \mu_0\, H^2\, dv = \frac{1}{2} L_{lk} I_p^2 \tag{5}$$

where H is the magnetic field strength which is proportional to the number of ampere turns linked by the flux path, L_{lk} is the leakage inductance, and I_p is the peak current in the winding. The fundamental principles used to calculate the leakage inductance are thoroughly investigated in [3], [4],

TABLE III. PRIMARY LEAKAGE INDUCTANCE EQUATIONS FOR DIFFERENT TWAS

TWA	Leakage inductance expression
W_1, W_2, W_3, W_4	$\mu_0 l_w N_p^2 \left[\frac{1}{b_w}\left(\frac{n_{lp}h_p}{3} + \frac{(2n_{lp}-1)(n_{lp}-1)}{6}\left(\frac{h_{ip}}{n_{lp}}\right) + h_i \right) + \frac{1}{b_{w2}}\left(\frac{n_{ls}h_s}{3} + \frac{(2n_{ls}-1)(n_{ls}-1)}{6}\left(\frac{h_{is}}{n_{ls}}\right) \right) \right]$ [17]
W_5, W_6	$\frac{\mu_o l_w N_p^2}{b_w} \left[\begin{array}{l} \frac{n_{ls1}^3 + n_{ls2}^3}{3(n_{ls1}+n_{ls2})^3}\left(n_{lp}h_p + (n_{ls1}+n_{ls2})h_s\right) + \frac{n_{ls1}^2 + n_{ls2}^2}{(n_{ls1}+n_{ls2})^2}h_i \\ \left\{ \frac{n_{ls1}(n_{ls1}-1)(2n_{ls1}-1) + n_{ls2}(n_{ls2}-1)(2n_{ls2}-1)}{6(n_{ls1}+n_{ls2})^2} \right\} h_{is} + \\ \left\{ \begin{array}{l} (n_{lp}-1)\left(\frac{n_{ls1}n_{lp}}{n_{ls1}+n_{ls2}}\right)^2 + \frac{n_{lp}(n_{lp}-1)(2n_{lp}-1)}{6} \\ -\frac{n_{ls1}^2 n_{lp}(n_{lp}-1)}{n_{ls1}+n_{ls2}} \end{array} \right\} \frac{h_{ip}}{n_{lp}^2} \end{array} \right]$
W_7	$\mu_0 \frac{l_w}{b_w} N_p^2 \left[\frac{3h_p + 4h_s}{72} + \frac{7}{36}h_i \right]$
Parameters interpretation	
μ_0 - permeability of free air; l_w - mean length turn (MLT); b_w - width of the layer; b_{w2} - width of the layer excluding the combined with of the sections walls for TWA W_3, $b_{w2} < b_w$; For W_1, W_2 and W_4, $b_w = b_{w2}$; $h_p = d_{op}$ and $h_s = d_{os}$; h_{ip} / h_{is} / h_i - insulation thickness between primary-to-primary layer, secondary-to secondary layer and primary-to-secondary layer; For W_5 and W_6, n_{ls1} and n_{ls2} are the number of secondary layers are at the top and bottom of a primary winding respectively, having n_{lp} primary layers. In Fig. 4c, n_{ls1}=2 and n_{ls2}=2; For remaining abbreviations refer Tables 1 and 2;	

and [16]. Based on those methods, the equations for calculating the leakage inductances for TWAs W_1-W_7 have been derived and are summarized in Table 3 [17]. The MMFs in each primary and secondary layer are $T_{lp}I_p$ and $T_{ls}I_s$, respectively. For the winding buildup shown in Fig. 4a, the energy stored in the magnetic field is derived in (AI) in Appendix.

V. AC RESISTANCE

The AC resistance is calculated using equations commonly found in the literature [18]-[19], [26]. The DC resistance of the primary/secondary winding can be calculated by

$$R_{DC} = \frac{\rho l_w N}{A\, n_{par}}, \quad A = \frac{\pi d_i^2}{4} \tag{6}$$

where ρ is the resistivity of copper at room temperature (ρ=17.24 nΩ/m at 20 °C), N is the total number of primary/secondary turns, l_w is the mean length turn of the winding, n_{par} is the number of parallel wires, A is the cross sectional area of the winding and d_i is the inner diameter of the winding excluding the insulation.

The AC resistance per layer of a given winding is given by

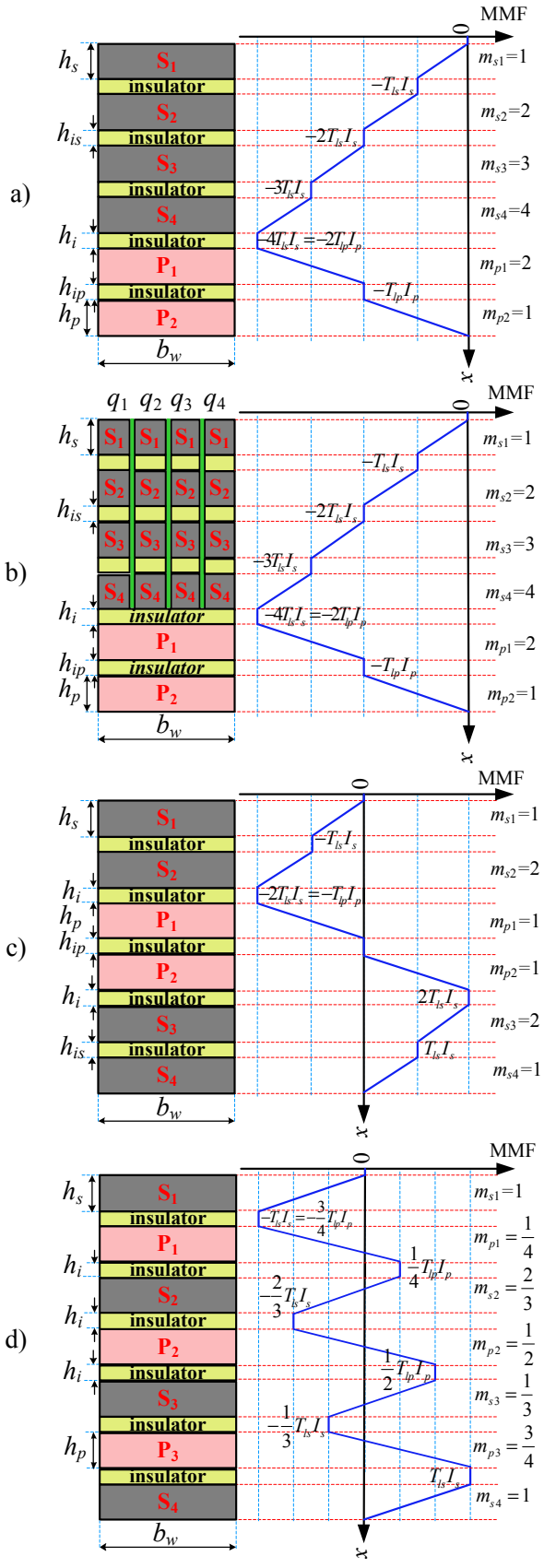

Figure 4. Analytical MMF distribution for, a) non-interleaved structure (S/P – W_1, W_2, W_4), b) non-interleaved structure (S/P – W_3), c) interleaved structure (S/S/P/P/S/S –W_5, W_6), d) fully interleaved structure (S/P/S/P/S/P/S –W_7)

$$R_{AC,\text{layer}} = R_{DC,layer} Q \left\{ \begin{array}{l} \left(2m^2 - 2m + 1\right) \dfrac{\sinh(2Q) + \sin(2Q)}{\cosh(2Q) - \cos(2Q)} - \\ 4\left(m^2 - m\right) \dfrac{\cos(Q)\sinh(Q) - \sin(Q)\cosh(Q)}{\cosh(2Q) + \cos(2Q)} \end{array} \right\} \quad (7)$$

Assume the variables Δ_1, Δ_2, Δ_3, and Δ_4 are assigned as in (8)

$$\Delta_1 = \frac{\sinh(2Q) + \sin(2Q)}{\cosh(2Q) - \cos(2Q)},\ \Delta_2 = \frac{\cos(Q)\sinh(Q) - \sin(Q)\cosh(Q)}{\cosh(2Q) + \cos(2Q)}$$
$$\Delta_3 = \frac{\sinh(Q) + \sin(Q)}{\cosh(Q) - \cos(Q)},\ \Delta_4 = \frac{\sinh(Q) - \sin(Q)}{\cosh(Q) + \cos(Q)} \quad (8)$$

The variable Δ_1 in terms of Δ_3 and Δ_4, and Δ_2 and Δ_4 is given by [19]

$$\Delta_1 = \frac{1}{2}\left(\Delta_3 + \Delta_4\right),\ \Delta_1 = \left(2\Delta_2 + \Delta_4\right) \quad (9)$$

Using (8), (9) in (7), the simplified AC resistance per layer is

$$R_{AC,\text{layer}} = R_{DC,layer} Q \left\{ \Delta_1 + 2\left(m^2 - m\right)\Delta_4 \right\} \quad (10)$$

$$R_{AC,\text{layer}} = R_{DC,layer} \frac{Q}{2} \left\{ \Delta_3 + \left(2m - 1\right)^2 \Delta_4 \right\} \quad (11)$$

The total AC resistance of M layers for the non-interleaved TWAs W_1-W_4 is given by

$$\begin{aligned} R_{AC,\text{total}} &= R_{DC,layer} Q \sum_{m=1}^{M} \left\{ \Delta_1 + 2\left(m^2 - m\right)\Delta_4 \right\} \\ &= \left(R_{DC,layer} M\right) Q \left\{ \Delta_1 + \frac{2}{3}\left(M^2 - 1\right)\Delta_4 \right\} \\ &= R_{DC,\text{total}} Q \left\{ \Delta_1 + \frac{2}{3}\left(M^2 - 1\right)\Delta_4 \right\} \end{aligned} \quad (12)$$

where $R_{DC,layer}$ and $R_{DC,total}$ are the DC resistance per layer and total DC resistance, respectively. The variable m represents the effective number of layers and is given by

$$m = \frac{F(h)}{F(h) - F(0)} \quad (13)$$

where $F(0)$ and $F(h)$ are the magneto motive forces (MMFs) at the start and end of each layer, respectively. The variable Q is the effective layer thickness normalized with the skin depth and is given by

$$Q = \frac{layer\ thickness}{penetration\ depth} = \frac{\frac{\pi}{4}^{3.5} d_i \sqrt{\frac{d_o T_l}{b_w}}}{\sqrt{\frac{\rho}{\pi \mu_0 f}}} \quad (14)$$

where d_i is the bare wire diameter, d_o is the overall wire diameter including insulation, T_l is the turns per layer of the given winding and f is the switching frequency.

To calculate the AC resistance per layer for the interleaved TWAs W_5-W_7, (10) or (11) needs to be used with the corresponding value of m for each layer. The total AC resistance is the sum of all AC resistances in each layer.

The total AC resistance referred to the primary is given by

$$R_{AC} = R_{AC,\text{total, P}} + \frac{R_{AC,\text{total, S}}}{n^2} \quad (15)$$

where n is the transformer turns ratio $R_{AC,total,\text{P}}$ and $R_{AC,total,\text{S}}$ are the total AC resistance of primary and secondary windings, respectively.

TABLE IV. ENERGY LOSS EXPRESSIONS OF TRANSFORMER PARACITICS

Name of energy loss	Loss expressions	
	Charge process (J)	Discharge process (J)
Switching loss due to self-capacitance	$E_{C1} = 0.5 C_P V_{dsP}^2$	$E_{C2} = 0.5 C_S V_{dsS}^2$
Snubber loss due to leakage inductance	$E_{L1} = \dfrac{0.5 L_{lkP} i_{pkP}^2 V_{snLV}}{V_{snLV} - \dfrac{V_{out}}{n}}$	$E_{L2} = \dfrac{0.5 L_{lkS} i_{pkS}^2 V_{snHV}}{V_{snHV} - V_{in} n}$
Winding loss due to AC and DC resistances	$E_{R1} = \left(\left[\begin{array}{l} I_{DCP}^2 R_{DCP} + \\ I_{RMSP}^2 R_{ACP} \end{array} \right] t_{onC} + \left[\begin{array}{l} I_{DCS}^2 R_{DCS} + \\ I_{RMSS}^2 R_{ACS} \end{array} \right] t_{offC} \right)$	$E_{R2} = \left(\left[\begin{array}{l} I_{DCP}^2 R_{DCP} + \\ I_{RMSP}^2 R_{ACP} \end{array} \right] t_{offD} + \left[\begin{array}{l} I_{DCS}^2 R_{DCS} + \\ I_{RMSS}^2 R_{ACS} \end{array} \right] t_{onD} \right)$
Parameters interpretation		
C_P / C_S – self capacitance referred to primary / secondary;		
V_{dsP} / V_{dsS} – drain to source voltage of primary / secondary MOSFET;		
L_{lkP} / L_{lkS} – leakage inductance referred to primary / secondary;		
i_{pkP} / i_{pkS} – primary / secondary peak current;		
V_{snLV} / V_{snHV} – RCD snubber capacitor voltage of primary / secondary;		
V_{out} / V_{in} – output / input voltage of the converter;		
I_{DCP} / I_{DCS} – DC current of primary / secondary;		
R_{DCP} / R_{DCS} – DC resistance of primary / secondary;		
I_{RMSP} / I_{RMSS} – RMS current of primary / secondary;		
R_{ACP} / R_{ACS} – AC resistance of primary / secondary;		
t_{onC} / t_{offC} – on / off time of the primary MOSFET during the charge process;		
t_{onD} / t_{offD} – on / off time of the HV MOSFET during the discharge process;		

VI. FINITE ELEMENT ANALYSES

The different winding architectures are simulated in Ansoft Maxwell to extract the value of the leakage inductance, self-capacitance and AC resistance. In Fig. 5 the electrostatic energy between the windings is shown for winding schemes B and D. It is noted that the energy density is high between layer to layer and low between turn to turn as expected in winding scheme B. In winding scheme D there is less electrostatic energy and thus it has lower self-capacitance.

Fig. 6 shows a close-up of the magneto static energy of the three investigated winding buildups. The leakage flux runs approximately vertically through the windings and the magneto static energy is highest in the space between the primary and secondary windings. The heavy interleaved buildup (S/P/S/P/S/P/S) has very low magneto static energy and thus it will have a very low leakage inductance.

The AC resistance at 100 kHz is also simulated for the three winding buildups. A standard mesh which is very fine compared to the skin depth is used to simulate the eddy effects in the winding. A close up plot of the mesh is shown in Fig. 7.a. The diameter of the secondary winding is 0.3 mm and the skin depth at 100 kHz is approximately 0.2 mm. It is

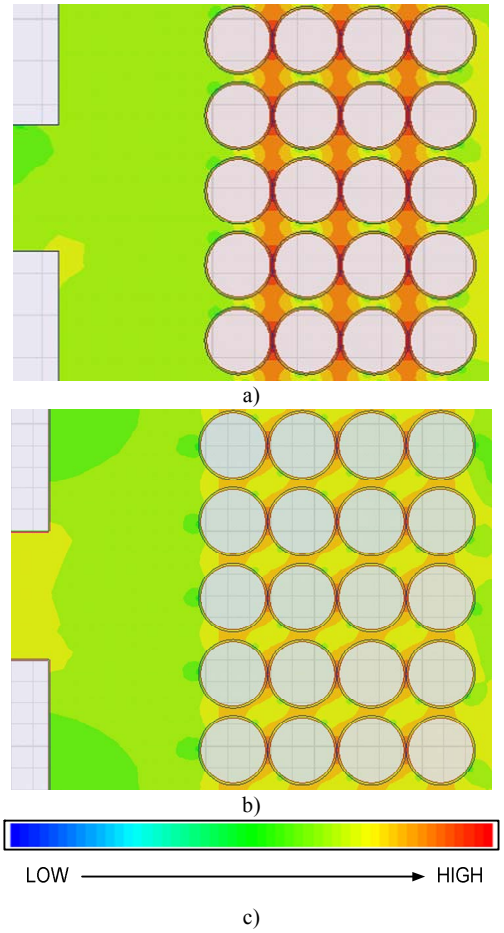

Figure 5. Plots from simulation of self-capacitance.
a) Energy distribution for winding scheme B. b) Energy distribution for winding scheme D. c) Density color bar

noted that the dimensions of the mesh is much lower than the diameter of the winding and the skin depth at 100 kHz. In Fig. 7. b-d, a close up of the current density for the three winding buildups is shown. It is noted that the current density in the non-interleaved buildup is much higher compared to the others and thus the AC resistance will also be higher.

VII. Experimental Results

The simulated, calculated and measured values of the self-capacitance, leakage inductance (measured at 10 kHz frequency using the impedance analyzer PSM1735) and AC resistance for the 7 TWA's are shown in the Tables 5, 6 and 7, respectively, from which it is clear that the measured, calculated and simulated transformer parameters for most of the TWAs closely matches. However, the differences in winding parameters such as an average layer to layer distance and mean length turn may cause errors around ±20 %. The measurement setup with 5 of the transformer prototypes is shown in Fig. 8. The energy loss expressions due to the transformer parasitics are summarized in Table 4. A plot of the loss distribution of the energy losses caused by the transformer parasitics), in a bi-directional flyback converter, used for charging and discharging an incremental DEAP actuator is shown in Fig. 9. The winding loss calculation for the flyback transformer is different from that of normal

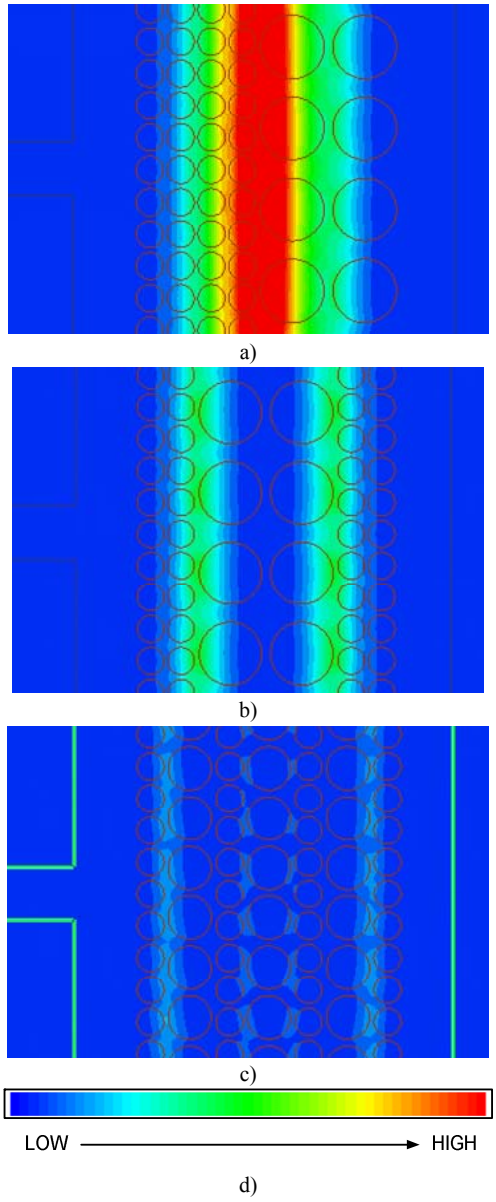

Figure 6. Plots from simulation of leakage inductance.
a) P/S. b) S/P/S. c) S/P/S/P/S/P/S. d) Density color bar.

transformer since the primary and secondary currents are out of phase, in [20] the winding loss is calculated for a flyback transformer with a non-interleaved structure. The same method can be used for the interleaved structures as well. However, due to limited space that is not included in this paper.

The calculated transformer parasitic values are used for calculating all losses, in order to provide a fair and useful comparison of the losses. The following specifications are used to calculate the losses in the bi-directional flyback converter [17], [20]-[23]: input voltage: 24V, output voltage: 1500 V, load capacitance: 200 nF, switching frequency during the charging and discharging process: 20-200 kHz, and 26 kHz, and primary peak current during charge and discharge processes: 2.12 A. The primary magnetizing inductance: 35 μH. From Fig. 9, it is clear that W_6 has the lowest loss among all TWAs followed by W_4, W_7 and W_3.

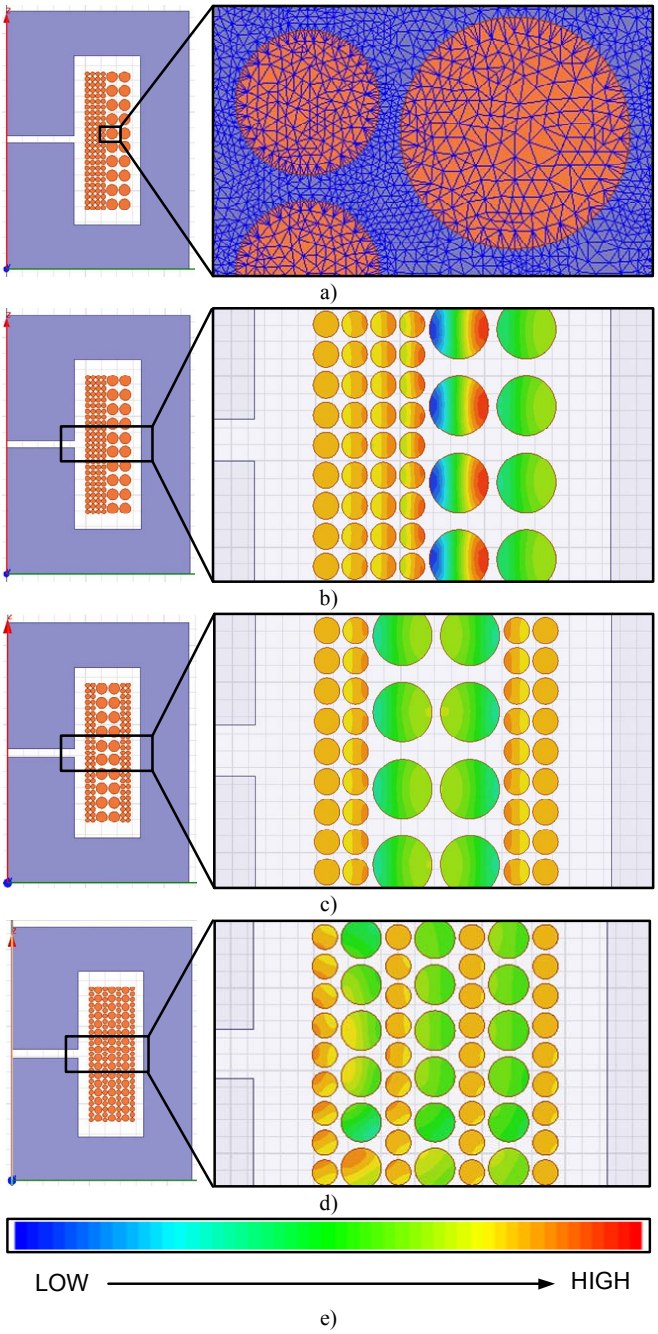

Figure 7. Plots from the simulations of AC resistance.
a) Default mesh, b) Current density of W_1-W_4, c) Current density of W_5-W_6, d) Current density of W_7, e) Density color bar

Thus the structure W_6 is highly recommended for high voltage capacitor charging application.

VIII. Conclusions

The analytical equations for calculating the transformer AC resistance, lekage inductance and self-capacitance for seven different winding architectures have been presented and evaluated experimentally and with FEA simulation. The main contribution to the errors is due to practical winding issues which are not accounted for in the equations. The transformer loss distribution is based on the calculated values, and it clearly shows that transformer winding architectures

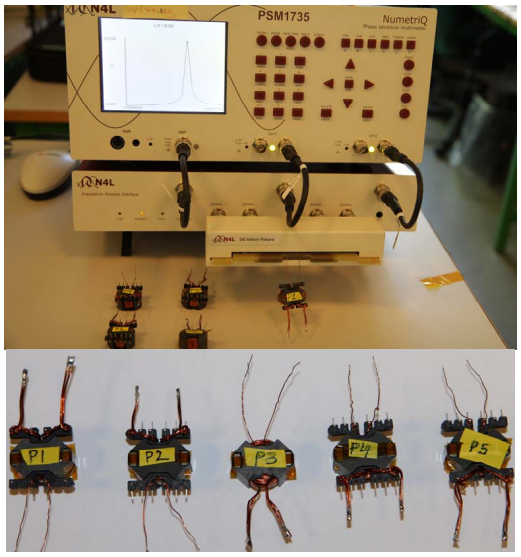

Figure 8. Measurement setup and five transformer prototypes with RM8 core

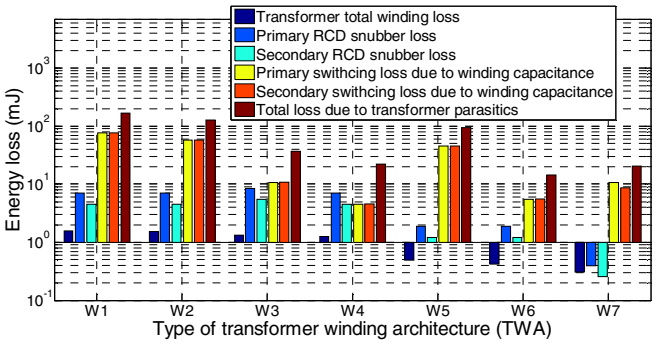

Figure 9. Energy loss distribution of the losses caused by transformer parasitics in the high voltage capacitor charging application.

where the self-capacitance is lowest are particularly suitable for high voltage charging applications. Future work involves the experimental validation of the proposed TWAs in the high voltage bi-directional dc-dc converter.

TABLE V. Self-capacitance of Secondary Winding at Resonance Frequency

TWA	Buildup	Winding scheme	Sim. (pF)	Calc. (pF)	Meas. (pF)
W_1	S/P	A	33	32	28
W_2	S/P	B	25	24	26
W_3	S/P	C	2.4	2	4.2
W_4	S/P	D	1.9	1	1.3
W_5	S/P/S	B	10	20	22
W_6	S/P/S	D	3.3	2.1	6
W_7	S/P/S/P/S/P/S	B	5	3.6	15

TABLE VI. Leakage Inductance Referred to Primary

TWA	Buildup	Winding scheme	Sim. (nH)	Calc. (nH)	Meas. (nH)
W_1	S/P	A	526	590	550
W_2	S/P	B			520
W_3	S/P	C			725
W_4	S/P	D			580
W_5	S/P/S	B	150	152	181
W_6	S/P/S	D			208
W_7	S/P/S/P/S/P/S	B	30	22	74

TABLE VII. AC RESISTANCE REFERRED TO PRIMARY AT 100 KHZ

TWA	Buildup	Winding scheme	Sim. (mΩ)	Calc. (mΩ)	Meas. (mΩ)
W_1	S/P	A	102	110	130
W_2	S/P	B			127
W_3	S/P	C			135
W_4	S/P	D			84
W_5	S/P/S	B	35	37	39
W_6	S/P/S	D			42
W_7	S/P/S/P/S/P/S	B	23	18	22

REFERENCES

[1] R. E. Pelrine, R. D. Kornbluh, Q. Pei, and J. P. Joseph, "High-speed electrically actuated elastomers with strain greater than 100%," in Proc. *Science*, vol. 287, pp. 836–839, 2000.

[2] R. E. Pelrine, R. D. Kornbluh, and J. P. Joseph, "Electrostriction of polymer dielectric with compliant electrodes as a means of actuation," in Proc. *Sens. Actuators A*, vol. 64, pp. 77–85, 1998.

[3] W. G. Hurley and D. J. Wilcox, "Calculation of leakage inductance in transformer windings," in Proc. *IEEE Trans. Power Electronics*, vol. 9, pp. 121-126, 1994.

[4] Z. Ouyang, Z. Zhang, O. C. Thomsen and M. A. E. Andersen, "Planar-integrated magnetics (PIM) module in hybrid bidirectional DC-DC converter for fuel cell application," in Proc. *IEEE Trans. Power Electronics*, vol.26, pp. 3254-3264, 2011.

[5] S. R. Cove, M. Ordonez, F. Luchino, and J. E. Quaicoe, "Applying Response Surface Methodology to Small Planar Transformer Winding Design," in Proc. *IEEE Trans. Industrial Electronics*, vol. 60, pp. 483-493, 2013.

[6] J. Zhang, Z. Ouyang, M. Duffy, M. A. E Andersen and W. G. Hurley "Leakage inductance calculation for planar transformer with magnetic shunt", in Proc. *ECCE USA* 2013.

[7] F. Blache, J-P. Keradec, B. Cogitore, "Stray capacitances of two winding transformers: equivalent circuit, measurements, calculation and lowering," in Proc. *IEEE Industry Applications Society Annual Meeting,* pp. 1211-1217 vol. 2, 2-6 Oct. 1994.

[8] W. T. Duerdoth, "Equivalent capacitance of transformer windings," in Proc. *Wireless Eng.*, vol. 23, pp. 161–167, Jun. 1946.

[9] A. Massarini and M. K. Kazimierczuk, "Self-capacitance of inductors," in Proc. *IEEE Trans. Power Electron.*, vol. 12, no. 4, pp. 671–676, Jul. 1997.

[10] T. Duerbaum and G. Sauerlander, "Energy based capacitance model for magnetic devices," in Proc. *APEC*, vol. 1, pp. 109–115, 2001.

[11] W. T. Duerdoth, "Equivalent capacitance of transformer windings," in Proc. *Wireless Eng.,* vol. 23, pp. 161–167, Jun. 1946.

[12] T. Duerbaum, "Capacitance model for magnetic devices," in Proc. *Power Electron. Spec. Conf.*, vol. 3, pp. 1651–1656, 2000.H. Y. Lu, J. Zhu, S. Y. R. Hui, and V. S. Ramseden, "Measurement and Modeling of stray capacitances in high frequency transformers," in Proc. *Power Electron. Spec. Conf.*, pp. 763–769, 1999.

[13] H. Y. Lu, J. G. Zhu, and S. Y. R. Hui, "Experimental determination of stray capacitances in high-frequency transformers," in Proc. *IEEE Trans. Power Electron.*, vol. 18, no. 5, pp. 1105–1112, Sep. 2003.

[14] L. Dalessandro, F. da Silveira Cavalcante, J. W. Kolar, "Self-Capacitance of High-Voltage Transformers," in Proc. *IEEE Trans. Power Electronics,* vol. 22, no. 5, pp. 2081-2092, Sept. 2007.

[15] J. Biela, J. W. Kolar, "Using Transformer Parasitics for Resonant Converters—A Review of the Calculation of the Stray Capacitance of Transformers," in Proc. *IEEE Trans. Industry Applications,* vol. 44, no. 1, pp. 223-233, 2008.

[16] E. C. Snelling, *Soft Ferrites-Properties and applications,* 2nd ed. London, UK, Butterworth, 1988.

[17] P. Thummala, H. Schneider, Z. Ouyang, Z. Zhang, M. A. E. Andersen, "Estimation of transformer parameters and loss analysis for high voltage capacitor charging application," in Proc. *IEEE ECCE Asia,* pp. 704-710, 3-6 Jun. 2013.

[18] W.G. Hurley, E. Gath, J. G. Breslin, "Optimizing the AC resistance of multilayer transformer windings with arbitrary current waveforms," in Proc. *IEEE Trans. Power Electronics*, vol. 15, no. 2, pp. 369-376, Mar 2000.

[19] J. A. Ferreira, "Improved analytical modeling of conductive losses in magnetic components," in Proc. *IEEE Transactions on Power Electronics*, vol. 9, no. 1, pp.127,131, Jan 1994.

[20] P. Thummala, H. Schneider, Z. Zhang, A. Knott, M. A. E. Andersen, "Optimization of a Bi-Directional Flyback Converter for a High Voltage Capacitor Charging Application," in Proc. *IEEE APEC,* pp., 16-20 Mar. 2014.

[21] K. Venkatesan, "Current Mode Controlled Bidirectional Flyback Converter," in Proc. *IEEE PESC*, pp. 835-842, 1989.

[22] T. Bhattacharya, V. S. Giri, K. Mathew, L. Umanand, "Multiphase Bidirectional Flyback Converter Topology for Hybrid Electric Vehicles,", in Proc. *IEEE Transactions on Industrial Electronics*, vol. 56, no.1, pp.78-84, Jan. 2009.

[23] P. Thummala, Z. Zhang, M. A. E. Andersen, "High Voltage Bi-directional Flyback Converter for Capacitive Actuator," in Proc. *European Power Electronics Conference (EPE),* pp. 3-6th Sept. 2013.

[24] G. Chen, Y.-S. Lee, S.Y.R. Hui, D. Xu, Y. Wang, "Actively clamped bidirectional flyback converter," in Proc. *IEEE Trans. Industrial Electronics*, vol. 47, no. 4, pp. 770-779, Aug. 2000.

[25] M. J. Prieto, A. Fernandez, J. M. Diaz, J. M. Lopera, J. Sebastian, "Influence of transformer parasitics in low-power applications," in Proc. *IEEE APEC*, vol. 2, pp. 1175-1180, 14-18th Mar. 1999.

[26] R. W. Erickson and D. Maksimovic, "Fundamentals of Power Electronics," 2nd ed. New York: Springer, 2001.

[27] John R. Barnes, "Robust electronic design reference book," Volume 1, Springer, 2004.

APPENDIX

$$E_{Mag}=\frac{\mu_0}{2}l_w b_w\int H^2(x)\,dx=\frac{\mu_0}{2}l_w b_w K_1;\; K_1=\left[\sum_{u=1}^{n_{ls}}\int_0^{h_s}H_{su}^2\,dx+\sum_{v=1}^{n_{lp}}\int_0^{h_p}H_{pv}^2\,dx+\sum_{a=1,b=a+1}^{n_{ls}-1}H_{sab}^2\,h_{is}+\sum_{c=1,d=c+1}^{n_{lp}-1}H_{pcd}^2\,h_{ip}+H_{sp}^2h_i\right]$$

$$H_{su}=\left[-\frac{(u-1)T_{ls}I_s}{b_w}-\frac{T_{ls}I_s}{b_w}\frac{x}{h_s}\right];H_{pv}=\left[-\frac{(n_{lp}-v+1)T_{lp}I_p}{b_w}+\frac{T_{lp}I_p}{b_w}\frac{x}{h_p}\right];H_{sab}=-\frac{uT_{ls}I_s}{b_w};H_{pcd}=-\frac{vT_{lp}I_p}{b_w};H_{sp}=-\frac{n_{ls}T_{ls}I_s}{b_w};$$

$$K_1=\left[\begin{array}{l}\int_0^{h_s}\left(-\frac{T_{ls}I_s}{b_w}\frac{x}{h_s}\right)^2dx+\int_0^{h_s}\left(-\frac{T_{ls}I_s}{b_w}-\frac{T_{ls}I_s}{b_w}\frac{x}{h_s}\right)^2dx+\int_0^{h_s}\left(-\frac{2T_{ls}I_s}{b_w}-\frac{T_{ls}I_s}{b_w}\frac{x}{h_s}\right)^2dx+\int_0^{h_s}\left(-\frac{3T_{ls}I_s}{b_w}-\frac{T_{ls}I_s}{b_w}\frac{x}{h_s}\right)^2dx+\left(-\frac{T_{lp}I_p}{b_w}\right)^2h_{ip}\\+\left[\left(-\frac{T_{ls}I_s}{b_w}\right)^2+\left(-\frac{2T_{ls}I_s}{b_w}\right)^2+\left(-\frac{3T_{ls}I_s}{b_w}\right)^2\right]h_{is}+\int_0^{h_p}\left(-\frac{2T_{lp}I_p}{b_w}+\frac{T_{lp}I_p}{b_w}\frac{x}{h_p}\right)^2dx+\int_0^{h_p}\left(-\frac{T_{lp}I_p}{b_w}+\frac{T_{lp}I_p}{b_w}\frac{x}{h_p}\right)^2dx+\left(-\frac{2T_{lp}I_p}{b_w}\right)^2h_i\end{array}\right] \quad \text{(AI)}$$

$$=\left(\frac{T_{ls}I_s}{b_w}\right)^2\left[4^3\frac{h_s}{3}+14h_{is}\right]+\left(\frac{T_{lp}I_p}{b_w}\right)^2\left[2^3\frac{h_p}{3}+h_{ip}+4h_i\right]=\left(\frac{N_pI_p}{b_w}\right)^2\left[\frac{2h_p+4h_s}{3}+\frac{7h_{is}}{8}+\frac{h_{ip}}{4}+h_i\right];\;\begin{array}{l}n_{lp}T_{lp}I_p=n_{ls}T_{ls}I_s\\N_pI_p=N_sI_s\end{array};$$

Appendix J

Investigation of Transformer Winding Architectures for High Voltage (2.5 kV) Capacitor Charging and Discharging Applications

---

About to Submit to IEEE Transactions on Power Electronics

Investigation of Transformer Winding Architectures for High Voltage (2.5 kV) Capacitor Charging and Discharging Applications

Prasanth Thummala, *Member*, *IEEE*, Henrik Schneider, *Student Member*, *IEEE*, Zhe Zhang, *Member*, *IEEE*,

Michael A. E. Andersen, *Member*, *IEEE*

Electronics Group, Department of Electrical Engineering,

Technical University of Denmark, 2800 Kongens Lyngby, Denmark

Email: pthu@elektro.dtu.dk, hensc@elektro.dtu.dk, zz@elektro.dtu.dk, ma@elektro.dtu.dk

***Abstract*—Transformer parameters such as leakage inductance and self-capacitance are rarely calculated in advance during the design phase, because of the complexity and huge analytical error margins caused by practical winding implementation issues. Thus, choosing one transformer architecture over another for a given design is usually based on experience or a trial and error approach. This paper presents equations regarding calculation of leakage inductance, self-capacitance and ac resistance in transformer winding architectures, ranging from the common non-interleaved primary/secondary winding architecture, to an interleaved, sectionalized and bank winded architecture. The analytical results are evaluated experimentally and through FEM simulations. Different transformer winding architectures for two different cores RM8 and EF25, are investigated in terms of the losses caused by the transformer parasitics for a bidirectional high-voltage flyback converter used to drive a electro active polymer based incremental actuator. The total losses due to the transformer parasitics for the best transformer architectures are reduced by more than a factor of ten compared to the worst case transformer architectures.**

***Index Term* —switch-mode power converters, high voltage dc-dc converters, digital control, energy efficiency, actuator**

The statement: *A part of this paper was presented and selected as an outstanding presentation at IEEE APEC 2014 (March 16–20th, 2014, Fort Worth, TX, USA). It is not currently under review for publication in any other journal.*

I. INTRODUCTION

Dielectric electro active polymer (DEAP) is an emerging smart material that has experienced significant development and has gained increasing attention over the last decade [1], [2]. DEAP, when used as actuators, has the potential to be an effective replacement for many conventional actuators due to its unique properties such as high strain, light weight, low noise operation, low power consumption. However, a compact high voltage driver is required to charge and discharge the DEAP from 0 V to 2500 V DC supplied from a 24 V battery. The DEAP actuator applications require a bi-directional energy transfer capability, to increase the life time of the battery. The flyback converter topology is suitable for low power (< 150 W), and high voltage capacitor charging applications, as it can be made very compact with a low number of components. The flyback transformer is the most critical component in terms of driver performance. The high voltage requirement demands a high turns ratio which calls for a large number of secondary turns. This may lead to a high winding self-capacitance resulting in the severe capacitive switching loss and undesirable, resonating current spikes in the leading edge of the current waveform, which could lead to false triggering of the current limit during the turn-on process.

The leakage inductance of the transformer may cause undesirable voltage spikes on the drains of the primary and secondary MOSFETs during the charge and the discharge processes, respectively, which lead to the use of active or passive snubber circuits in the converter. With active snubbers high energy efficiency can be achieved, at the expense of a higher cost and added control complexity, whereas the passive snubbers result in switching loss due to the leakage inductance. The AC resistance is also an important parameter to consider, since the AC conduction loss is caused by high frequency skin and proximity effects in a flyback converter operating in boundary conduction mode (BCM) or in discontinuous conduction mode (DCM).

Thus, accurate estimation of the transformer parameters and their associated losses are required, to evaluate different transformer winding architectures (TWAs) from which the best TWA is selected to achieve high energy efficiency. Extensive research has been done on calculating the leakage inductance in conventional transformers [3]-[6], [17], and in [7]-[17], the capacitance calculation methods have been proposed for inductors, power, planar, and high voltage transformers. The influence of transformer parasitics for the low power flyback converter has been discussed in [24]. This paper investigates a number of TWAs providing a deep insight into transformer design and its impact on the total loss contribution of a bi-directional high-voltage flyback converter. The paper is organized as follows: the TWAs are described and then the calculations of self-capacitance, leakage inductance and AC resistance for different TWAs are provided. The calculated

transformer parameters are evaluated via FEA simulation using ANSOFT Maxwell and the transformer parasitics for all TWAs are presented, followed by the conclusion.

II. TRANSFORMER WINDING ARCHITECTURES

This paper investigates the four known winding schemes (A, B, C and D) as shown in Fig. 1 [14], [16], [26], [27]. Winding scheme A is the most simple to implement since the next layer starts where the previous layer ended. In winding scheme B, the next layer starts just above the starting point of the previous layer. Winding scheme C split the winding into a number of sections that is individually wounded like winding scheme A. In winding scheme D, the turns progress in a vertical back angled way where turns are built on top of previous turns. It seems like winding scheme D achieves as many angled sections as there are turns in a layer without the penalty of reducing the fill factor due to the thickness of the section walls. Another advantage is that winding scheme D can be easily interleaved, which is not the case for winding scheme C since it is hard to add section walls in-between windings. The difference in self-capacitance due to the winding schemes is severe

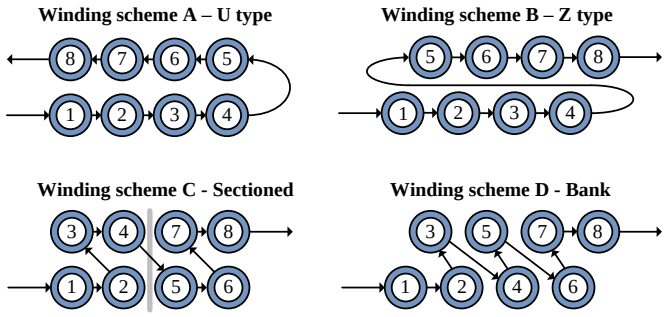

Figure 1. An overview of different winding schemes.

because the voltage potentials between the turns in the winding are changed.

TABLE I. HIGH VOLTAGE TRANSFORMER ARCHITECTURES

<table>
<tr><th rowspan="2">Design</th><th rowspan="2">Winding buildup</th><th colspan="2">Secondary winding</th><th>Primary winding</th></tr>
<tr><th>Scheme</th><th>Parameters</th><th>Parameters</th></tr>
<tr><td>W_1</td><td>S/P</td><td>A</td><td rowspan="6">N_s = 100
d_{is} = 0.3 mm
d_{os} = 0.32 mm p_{TT} = 0.355 mm
p_{LL} = 0.34 mm
n_{ls} = 4
n_{pars} = 1

Core / Material used:
RM8 / N41</td><td rowspan="6">N_p = 10
*d_{ip} = 0.7 mm
*d_{op} =0.8 mm
n_{lp} = 2 n_{parp} = 2</td></tr>
<tr><td>W_2</td><td>S/P</td><td>B</td></tr>
<tr><td>W_3</td><td>S/P</td><td>C</td></tr>
<tr><td>W_4</td><td>S/P</td><td>D</td></tr>
<tr><td>W_5</td><td>S/P/S</td><td>B</td></tr>
<tr><td>W_6</td><td>S/P/S</td><td>D</td></tr>
<tr><td>W_7</td><td>S/P/S/P/S/P/S</td><td>B</td><td>N_p = 9
*d_{ip} = 0.48 mm
*d_{op} = 0.5 mm
n_{lp} = 3
n_{parp} = 5</td></tr>
<tr><td colspan="5">Parameters interpretation</td></tr>
<tr><td colspan="5">N_s / N_p - number of secondary / primary turns;
n_{ls} / n_{lp} - number of secondary / primary winding layers;
n_{pars} / n_{parp} - number of secondary / primary parallel windings;
d_{is} / d_{os} - inner / outer diameter of secondary winding;
d_{ip} / d_{op} - inner / outer diameter of primary winding;
p_{TT} / p_{LL} - turn-to-turn / layer-to-layer pitch of secondary winding;
*In the practical transformer implementation triple insulated (TEX) windings are not used for the primary due to the unavailability of the wires;</td></tr>
</table>

Several winding buildups (S/P, S/P/S, S/P/S/P/S/P/S; where S and P are is the secondary and primary windings, respectively) are investigated - see Fig. 2. Based on these configurations, seven high voltage transformer winding architectures (W_1-W_7) are derived and the winding information is summarized in Table 1. In order to simplify the implementation of the windings a low turns ratio of 10 is selected. The TWAs W_1-W_6 are wound with 10 primary turns and 100 secondary turns. W_7 deviates since it is only implemented with 9 primary turns due to the nature of the winding architecture.

Winding scheme A is employed for the primary winding of all architectures. Moreover, all winding space of the bobbin is utilized to improve the fill factor and to reduce the winding resistance. Equal space allocation for primary and secondary

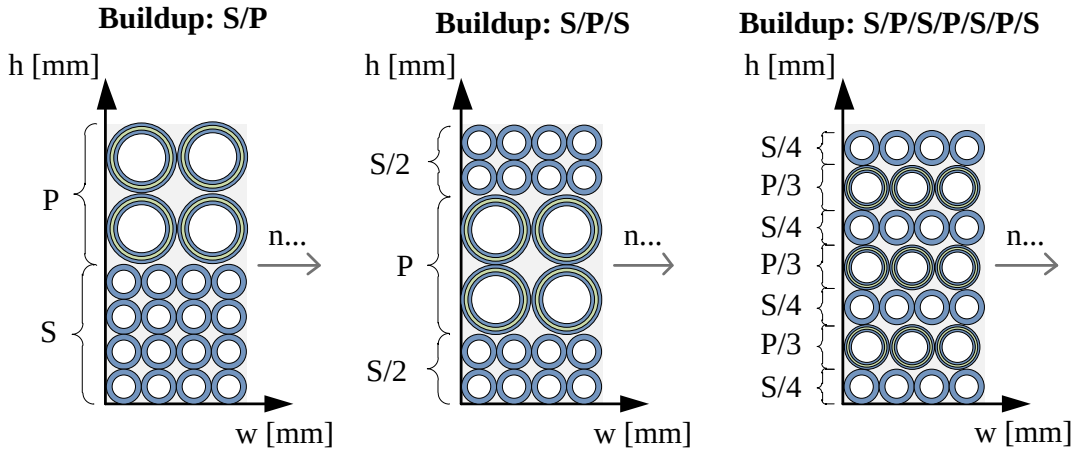

Figure 2. An overview of different winding buildups.

winding is adopted for this investigation, thus the primary winding is wounded with a number of parallel wires.

III. SELF-CAPACITANCE

High voltage transformers tend to have a large number of turns in the high voltage side, which introduces a non-negligible parasitic self-capacitance. It is important to predict the self-capacitance in the design phase in order to avoid severe switching loss. In fact, the winding self-capacitance is a parameter representing the electric field energy stored in the winding and is considered as a shunt lumped element in most cases [14]. Due to a large number of turns per layer, the effect of the turn-to-turn capacitance can be neglected and the main contribution to the self-capacitance comes from the layer-to-layer capacitance, which can be calculated based on the simple parallel-plate or cylindrical capacitor model [14]-[16].

The self-capacitance in the transformer windings can be calculated using the electro static energy stored in the volume

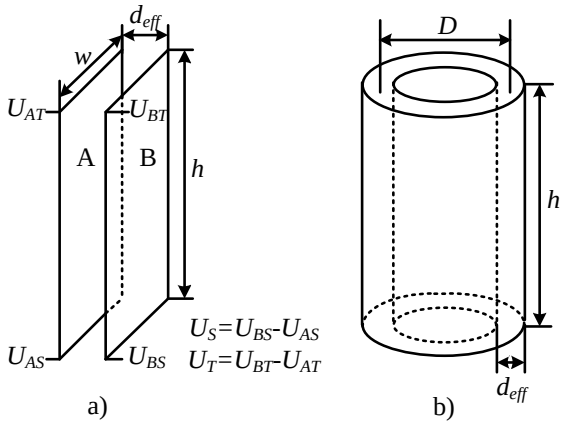

Figure 3. a) Two parallel plates with a linear potential distribution, b) Cylindrical capacitor model

between the conductors [14], [16] and is given by

$$E_{Electric} = \frac{1}{2}\iiint_{Vol} \varepsilon\, E^2 dv = \frac{1}{2} C_S U_W^2 \tag{1}$$

where ε is the equivalent dielectric constant of the winding, E is the electric field strength, C_S is the self-capacitance, and U_W is the total voltage across the winding.

The energy stored in two adjacent conductive layers with a linear potential distribution, shown in Fig. 3a, can be calculated by (2), which is derived in [16]. The total stored energy is

TABLE II. SELF-CAPACITANCE EXPRESSIONS FOR DIFFERENT TWAS

TWA	Self-capacitance expression
W_1	$4\frac{(n_{ls}-1)}{n_{ls}^2}\frac{C_l}{3};\ C_l=\varepsilon_r\varepsilon_0\frac{b_w l_{w1}}{d_{eff\,1}};\ l_{w1}=\pi\left(D_i+n_{ls}d_{is}+(n_{ls}-1)h_{is}\right)$
W_2	$4\frac{(n_{ls}-1)}{n_{ls}^2}\frac{C_l}{4};\quad C_l=\varepsilon_r\varepsilon_0\frac{b_w l_{w1}}{d_{eff\,1}};\quad b_w=(T_{ls}-1)p_{TT}+d_{os}$
W_3	$\frac{4(n_{ls}-1)}{q_1 n_{ls}^2}\frac{C_l}{3};\ C_l=\varepsilon_r\varepsilon_0\frac{\frac{b_{w2}}{q_1}l_{w1}}{d_{eff\,1}}$
W_4	$\varepsilon_r\varepsilon_0\frac{p_{TT}l_{w1}}{d_{eff\,2}}\frac{L}{b_w};\ L=(n_{ls}-1)p_{LL}+d_{os}$ [7]
W_5	$\frac{\varepsilon_r\varepsilon_0 b_w}{n_{ls}^2}\left[\frac{l_{w2}}{d_{eff\,3}}+\frac{l_{w3}}{d_{eff\,3}}+\frac{l_{w4}}{d_{eff\,3}+n_{lp}d_p+(n_{lp}-1)h_{ip}}\right]$
W_6	$\varepsilon_r\varepsilon_0\left[\frac{p_{TT}(l_{w2}+l_{w3})}{d_{eff\,4}}\frac{L_1}{b_w}+\frac{p_{TT2}l_{w4}}{d_{eff\,4}+n_{lp}d_p+(n_{lp}-1)h_{ip}}\frac{L_2}{b_w}\right];$ $L_1=\left(\frac{n_{ls}}{2}-1\right)p_{LL}+d_{os};\ p_{TT2}=n_{lp}h_p+(n_{lp}-1)h_{ip}+d_{os};$ $L_2=p_{TT2}+d_{os}$
W_7	$\frac{\varepsilon_r\varepsilon_0 b_w}{n_{ls}^2}\left[\frac{l_{w5}+l_{w6}+l_{w7}}{d_{eff\,5}}\right]$
Parameters interpretation	
ε_0 / ε_r - relative permittivity of vacuum / dielectric material; $\varepsilon_r = 4$; b_w - the width of the layer; T_{ls} is turns per layer of secondary winding; D_i - inner diameter of the bobbin; $d_{eff1,2,3,4,5}$ - effective thickness of dielectric between two layers [14] [16] for different TWAs; l_{w1} - mean length turn for the TWAs W_1, W_2, W_3 and W_4; l_{w2} / l_{w3} / l_{w4} - mean length turn between most inner two secondary (S_1, S_2) / most outer two secondary (S_3, S_4) / most outer secondary and the most inner secondary (S_2, S_3), layers for W_5 and W_6; l_{w5} / l_{w6} / l_{w7} / l_{w8} / l_{w9} / l_{w10} - mean length turn between most inner two secondary (S_1, S_2) / middle two secondary (S_2, S_3) / most outer two secondary (S_3, S_4) layers for W_7 q_1 - number of sections for structure W_3 and $q_1 = 4$; For remaining abbreviations refer Tables 1 and 3;	

$$E_{Stored}=\frac{C_l}{6}\left(U_S^2+U_S U_T+U_T^2\right) \tag{2}$$

where U_S and U_T are the potential difference between the two surfaces at the bottom and top respectively, and C_l is the capacitance between the two surfaces and is considered as a parallel plate capacitance and can be calculated using (3)

$$C_l=\varepsilon_r\varepsilon_0\frac{hw}{d_{eff}} \tag{3}$$

where ε_0 is the vacuum permittivity and is 8.854×10^{-12} F/m, ε_r is the relative permittivity of the dielectric material. The parameters h, w represents the dimensions of the plate and d_{eff} is the effective distance between two layers (which needs to be calculated for each TWA) and is given by

$$d_{eff}=p_{LL}-1.15d_{is}+0.26p_{TT} \tag{4}$$

where p_{LL}, d_{is} and p_{TT} are the layer to layer pitch, inner diameter, and turn to turn pitch, of the secondary winding, respectively. According to the methods given in [16], the expressions for calculating the self-capacitance for all above mentioned TWAs have been derived and are summarized in Table 2. Normally, the cylindrical shape, shown in Fig. 3b, is desired for most winding layers due to the simple winding technique as well as the short mean turn length [14]. If the distance between two layers is much less than the mean diameter for the two layers, the cylindrical capacitor can be considered to be a parallel plate capacitor and (3) can be employed to calculate the capacitance by replacing w with πD (see Fig. 3b).

IV. LEAKAGE INDUCTANCE

The leakage inductance in a transformer is calculated using the energy stored in the magnetic field [16]. The total leakage energy stored in the magnetic field is given by

$$E_{Magnetic} = \frac{1}{2}\iiint_{Vol} \mu_0 \, H^2 \, dv = \frac{1}{2} L_{lk} I_p^2 \tag{5}$$

where H is the magnetic field strength which is proportional to the number of ampere turns linked by the flux path, L_{lk} is the leakage inductance, and I_p is the peak current in the winding. The fundamental principles used to calculate the leakage inductance are thoroughly investigated in [3], [4], and [16]. Based on those methods, the equations for calculating the leakage inductances for TWAs W_1-W_7 have been derived and are summarized in Table 3 [17]. The MMFs in each primary and

TABLE III. PRIMARY LEAKAGE INDUCTANCE EQUATIONS FOR DIFFERENT TWAS

TWA	**Leakage inductance expression**
W_1, W_2, W_3, W_4	$\mu_0 l_w N_p^2 \left[\frac{1}{b_w} \left(\frac{n_{ip} h_p}{3} + \frac{(2n_{lp}-1)(n_{lp}-1)}{6} \left(\frac{h_{ip}}{n_{lp}} \right) + h_i \right) + \frac{1}{b_{w2}} \left(\frac{n_{ls} h_s}{3} + \frac{(2n_{ls}-1)(n_{ls}-1)}{6} \left(\frac{h_{is}}{n_{ls}} \right) \right) \right]$ [17]
W_5, W_6	$\frac{\mu_o l_w N_p^{\,2}}{b_w} \left[\frac{n_{ls1}^{\,3} + n_{ls2}^{\,3}}{3(n_{ls1}+n_{ls2})^3} \left(n_{lp} h_p + (n_{ls1}+n_{ls2}) h_s \right) + \frac{n_{ls1}^{\,2} + n_{ls2}^{\,2}}{(n_{ls1}+n_{ls2})^2} h_i \right.$ $\left. \left\{ \frac{n_{ls1}(n_{ls1}-1)(2n_{ls1}-1) + n_{ls2}(n_{ls2}-1)(2n_{ls2}-1)}{6(n_{ls1}+n_{ls2})^2} \right\} h_{is} + \left\{ \begin{array}{l} (n_{lp}-1)\left(\frac{n_{ls1} n_{lp}}{n_{ls1}+n_{ls2}} \right)^2 + \frac{n_{lp}(n_{lp}-1)(2n_{lp}-1)}{6} \\ -\frac{n_{ls1}^2 n_{lp}(n_{lp}-1)}{n_{ls1}+n_{ls2}} \end{array} \right\} \frac{h_{ip}}{n_{lp}^{\,2}} \right]$
W_7	$\mu_0 \frac{l_w}{b_w} N_p^2 \left[\frac{3h_p + 4h_s}{72} + \frac{7}{36} h_i \right]$
Parameters interpretation	
μ_0 - permeability of free air; l_w - mean length turn (MLT); b_w - width of the layer; b_{w2} - width of the layer excluding the combined with of the sections walls for TWA W_3, $b_{w2} < b_w$; For W_1, W_2 and W_4, $b_w = b_{w2}$; $h_p = d_{op}$ and $h_s = d_{os}$; h_{ip} / h_{is} / h_i - insulation thickness between primary-to-primary layer, secondary-to secondary layer and primary-to-secondary layer; For W_5 and W_6, n_{ls1} and n_{ls2} are the number of secondary layers are at the top and bottom of a primary winding respectively, having n_{lp} primary layers. In Fig. 4c, n_{ls1}=2 and n_{ls2}=2; For remaining abbreviations refer Tables 1 and 2;	

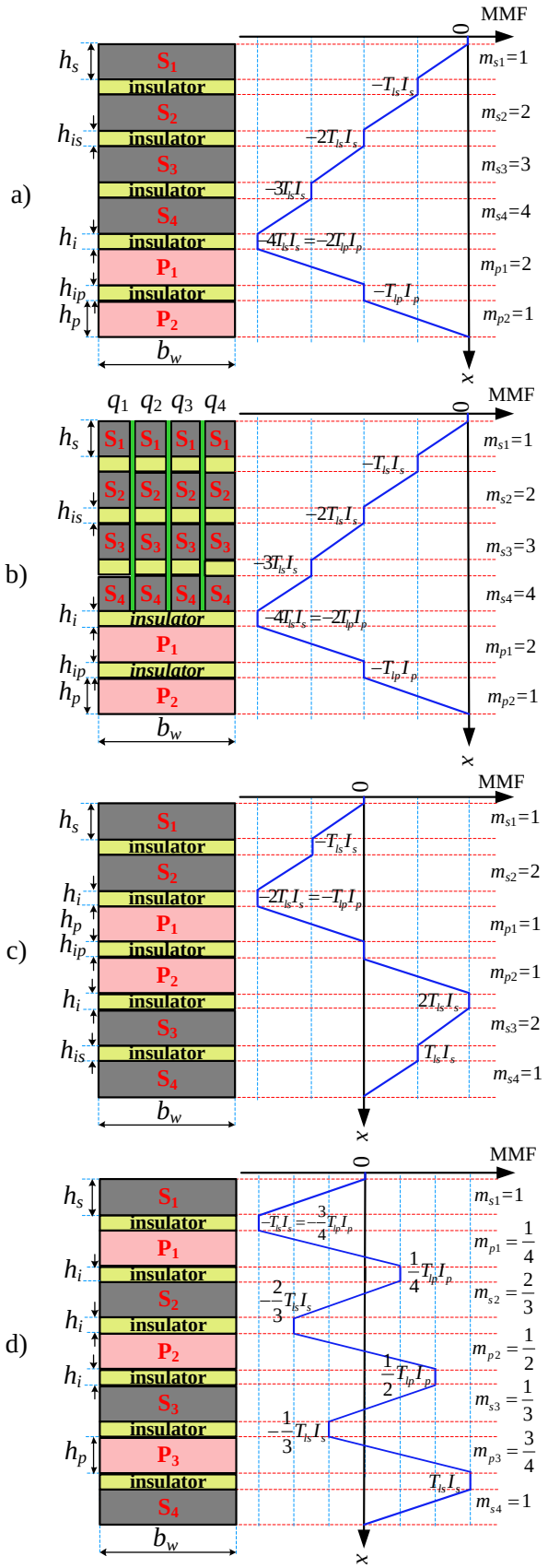

Figure 4. Analytical MMF distribution for, a) non-interleaved structure (S/P – W_1, W_2, W_4), b) non-interleaved structure (S/P – W_3), c) interleaved structure (S/S/P/P/S/S –W_5, W_6), d) fully interleaved structure (S/P/S/P/S/P/S –W_7)

secondary layer are $T_{lp}I_p$ and $T_{ls}I_s$, respectively. For the winding buildup shown in Fig. 4a, the energy stored in the magnetic field is derived in (AI) in Appendix.

V. AC RESISTANCE

The AC resistance is calculated using equations commonly found in the literature [18]-[19], [26]. The DC resistance of the primary/secondary winding can be calculated by

$$R_{DC} = \frac{\rho l_w N}{A\, n_{par}},\ A = \frac{\pi d_i^{\,2}}{4} \tag{6}$$

where ρ is the resistivity of copper at room temperature (ρ=17.24 nΩ/m at 20 °C), N is the total number of primary/secondary turns, l_w is the mean length turn of the winding, n_{par} is the number of parallel wires, A is the cross sectional area of the winding and d_i is the inner diameter of the winding excluding the insulation.

The AC resistance per layer of a given winding is given by

$$R_{AC,\text{layer}} = R_{DC,layer} Q\left\{\left(2m^2-2m+1\right)\frac{\sinh(2Q)+\sin(2Q)}{\cosh(2Q)-\cos(2Q)} - 4\left(m^2-m\right)\frac{\cos(Q)\sinh(Q)-\sin(Q)\cosh(Q)}{\cosh(2Q)+\cos(2Q)}\right\} \tag{7}$$

Assume the variables Δ_1, Δ_2, Δ_3, and Δ_4 are assigned as in (8)

$$\begin{aligned} \Delta_1 &= \frac{\sinh(2Q)+\sin(2Q)}{\cosh(2Q)-\cos(2Q)},\ \Delta_2 = \frac{\cos(Q)\sinh(Q)-\sin(Q)\cosh(Q)}{\cosh(2Q)+\cos(2Q)} \\ \Delta_3 &= \frac{\sinh(Q)+\sin(Q)}{\cosh(Q)-\cos(Q)},\ \Delta_4 = \frac{\sinh(Q)-\sin(Q)}{\cosh(Q)+\cos(Q)} \end{aligned} \tag{8}$$

The variable Δ_1 in terms of Δ_3 and Δ_4, and Δ_2 and Δ_4 is given by [19]

$$\Delta_1 = \frac{1}{2}\left(\Delta_3+\Delta_4\right),\ \Delta_1 = \left(2\Delta_2+\Delta_4\right) \tag{9}$$

Using (8), (9) in (7), the simplified AC resistance per layer is

$$R_{AC,\text{layer}} = R_{DC,layer} Q\left\{\Delta_1 + 2\left(m^2-m\right)\Delta_4\right\} \tag{10}$$

$$R_{AC,\text{layer}} = R_{DC,layer} \frac{Q}{2}\left\{\Delta_3 + \left(2m-1\right)^2 \Delta_4\right\} \tag{11}$$

The total AC resistance of M layers for the non-interleaved TWAs W_1-W_4 is given by

$$
\begin{aligned}
R_{AC,\text{total}} &= R_{DC,layer} Q \sum_{m=1}^{M} \left\{ \Delta_1 + 2\left(m^2 - m\right)\Delta_4 \right\} \\
&= \left(R_{DC,layer} M \right) Q \left\{ \Delta_1 + \frac{2}{3}\left(M^2 - 1\right)\Delta_4 \right\} \\
&= R_{DC,\text{total}} Q \left\{ \Delta_1 + \frac{2}{3}\left(M^2 - 1\right)\Delta_4 \right\}
\end{aligned} \tag{12}
$$

where $R_{DC,layer}$ and $R_{DC,total}$ are the DC resistance per layer and total DC resistance, respectively. The variable m represents the effective number of layers and is given by

$$
m = \frac{F(h)}{F(h) - F(0)} \tag{13}
$$

where $F(0)$ and $F(h)$ are the magneto motive forces (MMFs) at the start and end of each layer, respectively. The variable Q is the effective layer thickness normalized with the skin depth and is given by

$$
Q = \frac{\textit{layer thickness}}{\textit{penetration depth}} = \frac{\frac{\pi}{4}^{3.5} d_i \sqrt{\frac{d_o T_l}{b_w}}}{\sqrt{\frac{\rho}{\pi \mu_0 f}}} \tag{14}
$$

TABLE IV. ENERGY LOSS EXPRESSIONS OF TRANSFORMER PARASITICS

Name of energy loss	**Loss expressions**	
	Charge process (J)	**Discharge process (J)**
Switching loss due to self-capacitance	$E_{C1} = 0.5 C_P V_{dsP}^2$	$E_{C2} = 0.5 C_S V_{dsS}^2$
Snubber loss due to leakage inductance	$E_{L1} = \dfrac{0.5 L_{lkP} i_{pkP}^2 V_{snLV}}{V_{snLV} - \dfrac{V_{out}}{n}}$	$E_{L2} = \dfrac{0.5 L_{lkS} i_{pkS}^2 V_{snHV}}{V_{snHV} - V_{in} n}$
Winding loss due to AC and DC resistances	$E_{R1} = \left(\begin{bmatrix} I_{DCP}^2 R_{DCP} + \\ I_{RMSP}^2 R_{ACP} \end{bmatrix} t_{onC} + \begin{bmatrix} I_{DCS}^2 R_{DCS} + \\ I_{RMSS}^2 R_{ACS} \end{bmatrix} t_{offC} \right)$	$E_{R2} = \left(\begin{bmatrix} I_{DCP}^2 R_{DCP} + \\ I_{RMSP}^2 R_{ACP} \end{bmatrix} t_{offD} + \begin{bmatrix} I_{DCS}^2 R_{DCS} + \\ I_{RMSS}^2 R_{ACS} \end{bmatrix} t_{onD} \right)$
Parameters interpretation		
C_P / C_S – self capacitance referred to primary / secondary; V_{dsP} / V_{dsS} – drain to source voltage of primary / secondary MOSFET; L_{lkP} / L_{lkS} – leakage inductance referred to primary / secondary; i_{pkP} / i_{pkS} – primary / secondary peak current; V_{snLV} / V_{snHV} – RCD snubber capacitor voltage of primary / secondary; V_{out} / V_{in} – output / input voltage of the converter; I_{DCP} / I_{DCS} – DC current of primary / secondary; R_{DCP} / R_{DCS} – DC resistance of primary / secondary; I_{RMSP} / I_{RMSS} – RMS current of primary / secondary; R_{ACP} / R_{ACS} – AC resistance of primary / secondary; t_{onC} / t_{offC} – on / off time of the primary MOSFET during the charge process; t_{onD}/ t_{offD} – on / off time of the HV MOSFET during the discharge process;		

where d_i is the bare wire diameter, d_o is the overall wire diameter including insulation, T_l is the turns per layer of the given winding and f is the switching frequency.

To calculate the AC resistance per layer for the interleaved TWAs W_5-W_7, (10) or (11) needs to be used with the corresponding value of m for each layer. The total AC resistance is the sum of all AC resistances in each layer.

The total AC resistance referred to the primary is given by

$$R_{AC} = R_{AC,\text{total, P}} + \frac{R_{AC,\text{total, S}}}{n^2} \tag{15}$$

where n is the transformer turns ratio $R_{AC,total,\text{P}}$ and $R_{AC,total,\text{S}}$ are the total AC resistance of primary and secondary windings, respectively.

VI. FINITE ELEMENT ANALYSES

The different winding architectures are simulated in Ansoft Maxwell to extract the value of the leakage inductance, self-capacitance and AC resistance. In Fig. 5 the electrostatic energy between the windings is shown for winding schemes B and D. It is noted that the energy density is high between layer to layer and low between turn to turn as expected in winding scheme B. In winding scheme D there is a less electrostatic energy and thus it has lower self-capacitance.

Fig. 6 shows a close-up of the magneto static energy of the three investigated winding buildups. The leakage flux runs approximately vertically through the windings and the magneto static energy is highest in the space between the primary and secondary windings. The heavy interleaved buildup (S/P/S/P/S/P/S) has a very low magneto static energy and thus it will have a very low leakage inductance.

The AC resistance at 100 kHz is also simulated for the three winding buildups. A standard mesh which is very fine compared to the skin depth is used to simulate the eddy effects in the winding. A close up plot of the mesh is shown in Fig. 7.a. The diameter of the secondary winding is 0.3 mm and the skin depth at 100 kHz is approximately 0.2 mm. It is noted that the dimensions of the mesh is much lower than the diameter of the winding and the skin depth at 100 kHz. In Fig. 7. b-d, a close up of the current density for the three winding buildups is shown. It is noted that the current density in the non-interleaved buildup is much higher compared to the others and thus the AC resistance will also be higher.

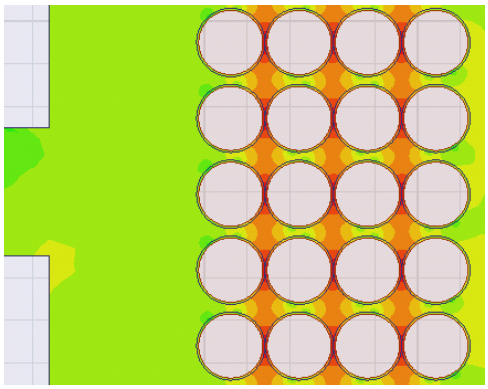

a)

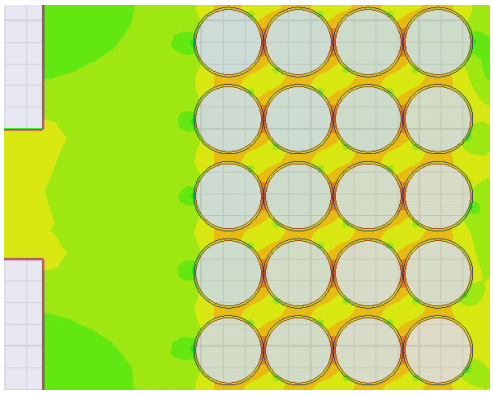

b)

c)

Figure 5. Plots from simulation of self-capacitance.

a) Energy distribution for winding scheme B. b) Energy distribution for winding scheme D. c) Density color bar

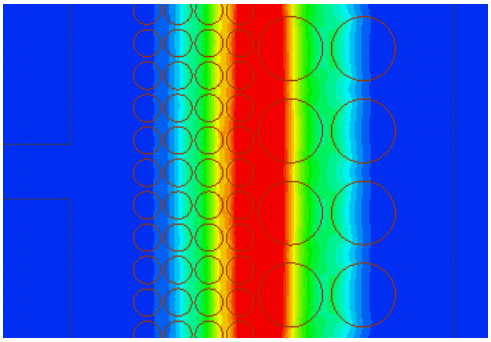

a)

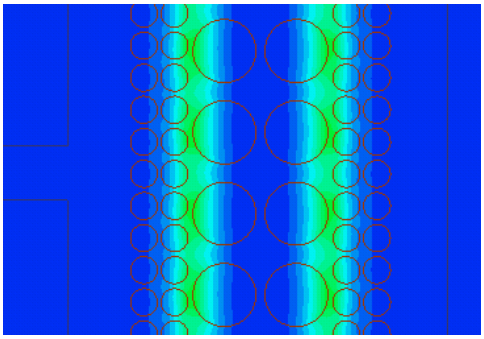

b)

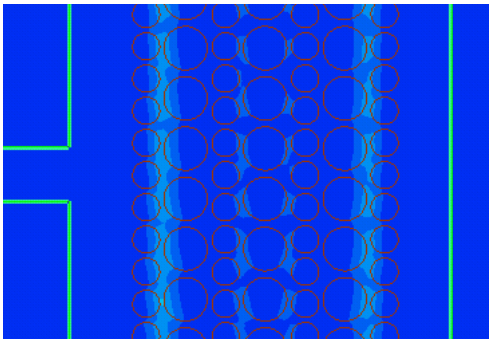

c)

d)

Figure 6. Plots from simulation of leakage inductance.

a) P/S. b) S/P/S. c) S/P/S/P/S/P/S. d) Density color bar.

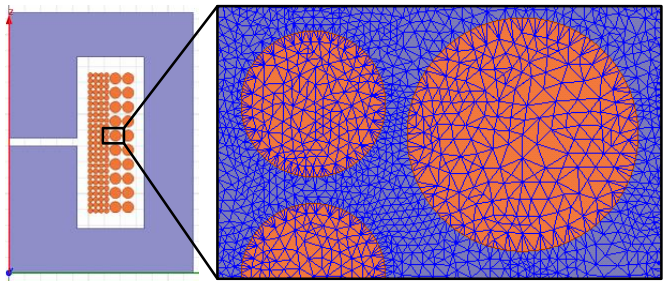

a)

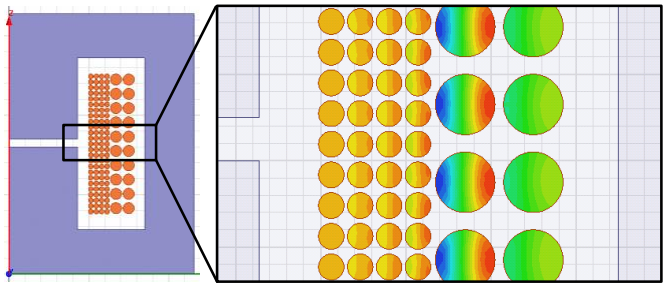

b)

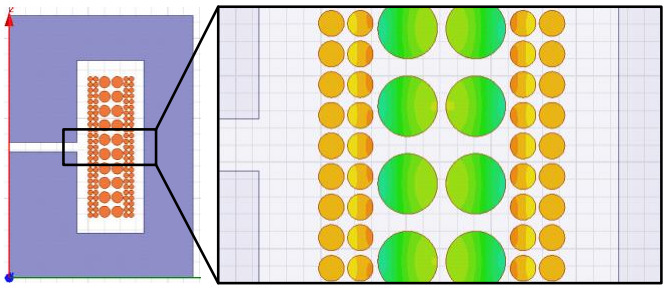

c)

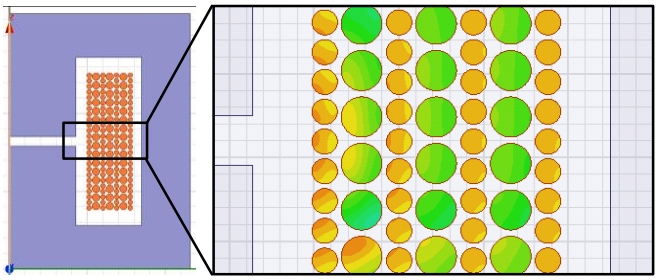

d)

e)

Figure 7. Plots from the simulations of AC resistance.

a) Default mesh, b) Current density of W_1-W_4, c) Current density of W_5-W_6, d) Current density of W_7, e) Density color bar

VII. EXPERIMENTAL RESULTS

The simulated, calculated and measured values of the self-capacitance, leakage inductance (measured at 10 kHz frequency using the impedance analyzer PSM1735) and AC resistance for the 7 TWAs are shown in the Tables 5, 6 and 7, respectively, from which it is clear that the measured, calculated and simulated transformer parameters for most of the TWAs closely matches. However, the differences in winding parameters such as an average layer to layer distance and mean length turn may cause errors around ±20 %. The measurement setup with 5 of the transformer prototypes is shown in Fig. 8. The energy loss expressions due to the transformer parasitics are summarized in Table 4. A plot of the loss distribution of the energy losses caused by the transformer parasitics), in a bi-directional flyback converter, used for charging and discharging an incremental DEAP actuator is shown in Fig. 9. The winding loss calculation for the flyback transformer is different from that of normal transformer, since the primary and secondary currents are out of phase, in [20] the winding loss is calculated for a flyback transformer with a non-interleaved structure. The same method can be used for the interleaved structures as well. However, due to the limited space that is not included in this paper.

The calculated transformer parasitic values are used for calculating all losses, in order to provide a fair and useful comparison of the losses. The following specifications are used to calculate the losses in the bi-directional flyback converter [17], [20]-[23]: input voltage: 24V, output voltage: 1500 V, load capacitance: 200 nF, switching frequency during the charging and discharging process: 20-200 kHz, and 26 kHz, and primary peak current during charge and discharge processes: 2.12 A.

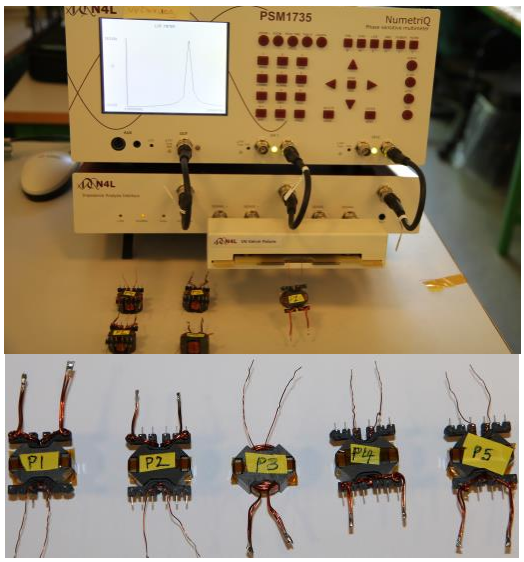

Figure 8. Measurement setup and five transformer prototypes with RM8 core

The primary magnetizing inductance: 35 μH. From Fig. 9, it is clear that W_6 has the lowest loss among all TWAs followed by W_4, W_7 and W_3. Thus the structure W_6 is highly recommended for high voltage capacitor charging application.

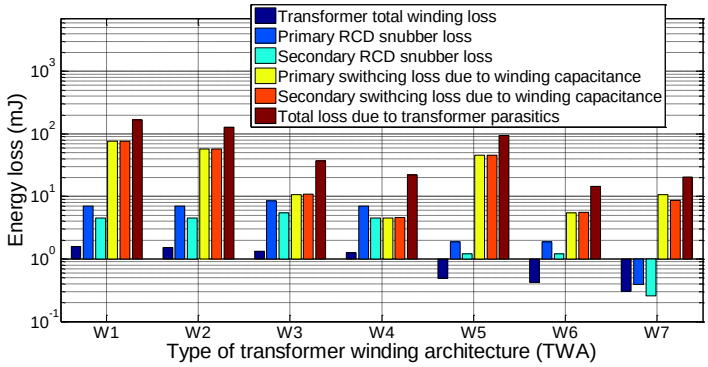

Figure 9. Energy loss distribution of the losses caused by transformer parasitics in the high voltage capacitor charging application.

TABLE V. SELF-CAPACITANCE OF SECONDARY WINDING AT RESONANCE FREQUENCY

TWA	**Buildup**	**Winding scheme**	**Sim. (pF)**	**Calc. (pF)**	**Meas. (pF)**
W_1	S/P	A	33	32	28
W_2	S/P	B	25	24	26
W_3	S/P	C	2.4	2	4.2
W_4	S/P	D	1.9	1	1.3
W_5	S/P/S	B	10	20	22
W_6	S/P/S	D	3.3	2.1	6
W_7	S/P/S/P/S/P/S	B	5	3.6	15

TABLE VI. LEAKAGE INDUCTANCE REFERRED TO PRIMARY

TWA	**Buildup**	**Winding scheme**	**Sim. (nH)**	**Calc. (nH)**	**Meas. (nH)**
W_1	S/P	A	526	590	550
W_2	S/P	B			520
W_3	S/P	C			725
W_4	S/P	D			580
W_5	S/P/S	B	150	152	181
W_6	S/P/S	D			208
W_7	S/P/S/P/S/P/S	B	30	22	74

TABLE VII. AC RESISTANCE REFERRED TO PRIMARY AT 100 KHZ

TWA	Buildup	Winding scheme	Sim. (mΩ)	Calc. (mΩ)	Meas. (mΩ)
W_1	S/P	A	102	110	130
W_2	S/P	B			127
W_3	S/P	C			135
W_4	S/P	D			84
W_5	S/P/S	B	35	37	39
W_6	S/P/S	D			42
W_7	S/P/S/P/S/P/S	B	23	18	22

VIII. INVESTIGATION USING EF 25 CORE

The transformer winding architectures (TWAs) investigated in the above sections using RM8 core are not suitable for generating the maximum voltage of 2.5 kV to drive the DEAP actuators. Hence, it is needed to investigate the parameters of the transformer further with a high turns ratio. From Section VII, the interesting TWAs are W_3, W_4, and W_6. When the secondary turns are very high, implementing the TWAs with bank winding scheme (W_4 and W_6) in the laboratory was extremely difficult, and hence it was not considered. Table VIII provides the details of transformer design using EF20 core. Four different TWAs such as non-interleaved and non-sectioned (W_2), interleaved and non-sectioned (W_5), non-interleaved and sectioned (W_3), and interleaved and sectioned (W_8, which is a new TWA) have been practically implemented. The measured parameters of the transformer for each TWA are provided in Tables IX, X, XI, and XII, respectively.

By comparing the transformer parasitics of all TWAs for EF25 core, the TWA non-interleaved and sectioned (W_3) has the lowest self and interwinding capacitances, followed by the interleaved and sectioned (W_8) TWA. The self-capacitances of TWAs W_8 and W_3 are comparable. Even though, the leakage inductance of W_8 is approximately half of W_3, due to very high interwinding capacitance, it might not be recommended for high voltage capacitor charge and discharge applications, due to conducted and radiated electromagnetic interference (EMI) problems.

TABLE VIII. DETAILS OF THE TRANSFORMER WITH A TURNS RATIO OF 20

Parameter	Value
Number of primary / secondary turns	18 / 360
Diameter of primary / secondary winding	0.4 mm (TEX [89]) / 0.14 mm
Number of layers of primary / secondary winding	3 / 4
Number of parallel wires of primary / secondary	3 / 1
Type of core / material	EF25 / N87

TABLE IX. PARAMETERS FOR NON-INTERLEAVED (P/S) AND NON-SECTIONED TRANSFORMER [W_2]

Parameter	Value
Magnetizing inductance of primary / secondary	53 μH / 23 mH
Leakage inductance referred to primary / secondary	1.2 μH / 490 μH
DC resistance of primary / secondary winding	42 mΩ / 16 Ω
AC resistance referred to primary / secondary winding at 50 kHz	98 mΩ / 39 Ω
AC resistance referred to primary / secondary winding at 100 kHz	130 mΩ / 52 Ω
Self-capacitance of the high voltage winding	42 pF
Interwinding capacitance	59 pF

TABLE X. PARAMETERS FOR INTERLEAVED (S/P/S) AND NON-SECTIONED TRANSFORMER [W_5]

Parameter	Value
Magnetizing inductance of primary / secondary	47 μH / 20 mH
Leakage inductance referred to primary / secondary	590 nH / 236 μH
DC resistance of primary / secondary winding	43 mΩ / 19 Ω
AC resistance referred to primary / secondary winding at 50 kHz	98 mΩ / 38 Ω
AC resistance referred to primary / secondary winding at 100 kHz	108 mΩ / 43 Ω
Self-capacitance of the high voltage winding	21.5 pF
Interwinding capacitance	160 pF

TABLE XI. PARAMETERS FOR NON-INTERLEAVED (P/S) AND SECTIONED (4 SECTIONS) TRANSFORMER [W_3]

Parameter	Value
Magnetizing inductance of primary / secondary	49 μH / 21 mH
Leakage inductance referred to primary / secondary	1 μH / 357 μH
DC resistance of primary / secondary winding	39 mΩ / 14 Ω
AC resistance referred to primary / secondary winding at 50 kHz	91 mΩ / 38 Ω
AC resistance referred to primary / secondary winding at 100 kHz	117 mΩ / 43 Ω
Self-capacitance of the high voltage winding	4.3 pF
Interwinding capacitance	44 pF

TABLE XII. PARAMETERS FOR INTERLEAVED (S/P/S) AND SECTIONED (4 SECTIONS) TRANSFORMER [W_8]

Parameter	Value
Magnetizing inductance of primary / secondary	49 μH / 21.5 mH
Leakage inductance referred to primary / secondary	420 nH / 175 μH
DC resistance of primary / secondary winding	43 mΩ / 19 Ω
AC resistance referred to primary / secondary winding at 50 kHz	90 mΩ / 39 Ω
AC resistance referred to primary / secondary winding at 100 kHz	100 mΩ / 43 Ω
Self-capacitance of the high voltage winding	6.8 pF
Interwinding capacitance	150 pF

IX. CONCLUSIONS

The analytical equations for calculating the transformer AC resistance, leakage inductance and self-capacitance for seven different winding architectures have been presented and evaluated experimentally and with FEA simulation. The main

contribution to the errors is due to practical winding issues which are not accounted for in the equations. The transformer loss distribution is based on the calculated values, and it clearly shows that transformer winding architectures where the self-capacitance is lowest are particularly suitable for high voltage charging applications. Another investigation has been made for EF25 core with a turns ratio of 25. Non-interleaved and Sectioned transformer could be most suitable for HV capacitor charge and discharge application as a good balance between the efficiency and EMI.

REFERENCES

[1] R. E. Pelrine, R. D. Kornbluh, Q. Pei, and J. P. Joseph, "High-speed electrically actuated elastomers with strain greater than 100%," in Proc. *Science*, vol. 287, pp. 836–839, 2000.

[2] R. E. Pelrine, R. D. Kornbluh, and J. P. Joseph, "Electrostriction of polymer dielectric with compliant electrodes as a means of actuation," in Proc. *Sens. Actuators A*, vol. 64, pp. 77–85, 1998.

[3] W. G. Hurley and D. J. Wilcox, "Calculation of leakage inductance in transformer windings," in Proc. *IEEE Trans. Power Electronics*, vol. 9, pp. 121-126, 1994.

[4] Z. Ouyang, Z. Zhang, O. C. Thomsen and M. A. E. Andersen, "Planar-integrated magnetics (PIM) module in hybrid bidirectional DC-DC converter for fuel cell application," in Proc. *IEEE Trans. Power Electronics*, vol.26, pp. 3254-3264, 2011.

[5] S. R. Cove, M. Ordonez, F. Luchino, and J. E. Quaicoe, "Applying Response Surface Methodology to Small Planar Transformer Winding Design," in Proc. *IEEE Trans. Industrial Electronics*, vol. 60, pp. 483- 493, 2013.

[6] J. Zhang, Z. Ouyang, M. Duffy, M. A. E Andersen and W. G. Hurley "Leakage inductance calculation for planar transformer with magnetic shunt", in Proc. *ECCE USA* 2013.

[7] F. Blache, J-P. Keradec, B. Cogitore, "Stray capacitances of two winding transformers: equivalent circuit, measurements, calculation and lowering," in Proc. *IEEE Industry Applications Society Annual Meeting*, pp. 1211-1217 vol. 2, 2-6 Oct. 1994.

[8] W. T. Duerdoth, "Equivalent capacitance of transformer windings," in Proc. *Wireless Eng.*, vol. 23, pp. 161–167, Jun. 1946.

[9] A. Massarini and M. K. Kazimierczuk, "Self-capacitance of inductors," in Proc. *IEEE Trans. Power Electron.*, vol. 12, no. 4, pp. 671–676, Jul. 1997.

[10] T. Duerbaum and G. Sauerlander, “Energy based capacitance model for magnetic devices,” in Proc. *APEC*, vol. 1, pp. 109–115, 2001.

[11] W. T. Duerdoth, “Equivalent capacitance of transformer windings,” in Proc. *Wireless Eng.*, vol. 23, pp. 161–167, Jun. 1946.

[12] T. Duerbaum, “Capacitance model for magnetic devices,” in Proc. *Power Electron. Spec. Conf.*, vol. 3, pp. 1651–1656, 2000.H. Y. Lu, J. Zhu, S. Y. R. Hui, and V. S. Ramseden, “Measurement and Modeling of stray capacitances in high frequency transformers,” in Proc. *Power Electron. Spec. Conf.*, pp. 763–769, 1999.

[13] H. Y. Lu, J. G. Zhu, and S. Y. R. Hui, “Experimental determination of stray capacitances in high-frequency transformers,” in Proc. *IEEE Trans. Power Electron.*, vol. 18, no. 5, pp. 1105–1112, Sep. 2003.

[14] L. Dalessandro, F. da Silveira Cavalcante, J. W. Kolar, “Self-Capacitance of High-Voltage Transformers,” in Proc. *IEEE Trans. Power Electronics*, vol. 22, no. 5, pp. 2081-2092, Sept. 2007.

[15] J. Biela, J. W. Kolar, “Using Transformer Parasitics for Resonant Converters—A Review of the Calculation of the Stray Capacitance of Transformers,” in Proc. *IEEE Trans. Industry Applications*, vol. 44, no. 1, pp. 223-233, 2008.

[16] E. C. Snelling, *Soft Ferrites-Properties and applications*, 2nd ed. London, UK, Butterworth, 1988.

[17] P. Thummala, H. Schneider, Z. Ouyang, Z. Zhang, M. A. E. Andersen, “Estimation of transformer parameters and loss analysis for high voltage capacitor charging application,” in Proc. *IEEE ECCE Asia*, pp. 704-710, 3-6 Jun. 2013.

[18] W.G. Hurley, E. Gath, J. G. Breslin, “Optimizing the AC resistance of multilayer transformer windings with arbitrary current waveforms,” in Proc. *IEEE Trans. Power Electronics*, vol. 15, no. 2, pp. 369-376, Mar 2000.

[19] J. A. Ferreira, “Improved analytical modeling of conductive losses in magnetic components,” in Proc. *IEEE Transactions on Power Electronics*, vol. 9, no. 1, pp.127,131, Jan 1994.

[20] P. Thummala, H. Schneider, Z. Zhang, A. Knott, M. A. E. Andersen, “Optimization of a Bi-Directional Flyback Converter for a High Voltage Capacitor Charging Application,” in Proc. *IEEE APEC*, pp., 16-20 Mar. 2014.

[21] K. Venkatesan, “Current Mode Controlled Bidirectional Flyback Converter,” in Proc. *IEEE PESC*, pp. 835-842, 1989.

[22] T. Bhattacharya, V. S. Giri, K. Mathew, L. Umanand, “Multiphase Bidirectional Flyback Converter Topology for Hybrid Electric Vehicles,”, in Proc. *IEEE Transactions on Industrial Electronics*, vol. 56, no.1, pp.78-84, Jan. 2009.

[23] P. Thummala, Z. Zhang, M. A. E. Andersen, “High Voltage Bi-directional Flyback Converter for Capacitive Actuator,” in Proc. *European Power Electronics Conference (EPE)*, pp. 3-6th Sept. 2013.

[24] G. Chen, Y.-S. Lee, S.Y.R. Hui, D. Xu, Y. Wang, "Actively clamped bidirectional flyback converter," in Proc. *IEEE Trans. Industrial Electronics*, vol. 47, no. 4, pp. 770-779, Aug. 2000.

[25] M. J. Prieto, A. Fernandez, J. M. Diaz, J. M. Lopera, J. Sebastian, "Influence of transformer parasitics in low-power applications," in Proc. *IEEE APEC*, vol. 2, pp. 1175-1180, 14-18th Mar. 1999.

[26] R. W. Erickson and D. Maksimovic, "Fundamentals of Power Electronics," 2nd ed. New York: Springer, 2001.

[27] John R. Barnes, "Robust electronic design reference book," Volume 1, Springer, 2004.

APPENDIX

$$E_{Mag}=\frac{\mu_0}{2}l_w b_w\int H^2(x)\,dx=\frac{\mu_0}{2}l_w b_w K_1;\; K_1=\left[\sum_{u=1}^{n_{ls}}\int_0^{h_s}H_{su}^2\,dx+\sum_{v=1}^{n_{lp}}\int_0^{h_p}H_{pv}^2\,dx+\sum_{a=1,\mathrm{b}=a+1}^{n_{ls}-1}H_{sab}^2\,h_{is}+\sum_{c=1,\mathrm{d}=c+1}^{n_{lp}-1}H_{pcd}^2\,h_{ip}+H_{sp}^2h_i\right]$$

$$H_{su}=\left[-\frac{(u-1)T_{ls}I_s}{b_w}-\frac{T_{ls}I_s}{b_w}\frac{x}{h_s}\right];H_{pv}=\left[-\frac{(n_{lp}-v+1)T_{lp}I_p}{b_w}+\frac{T_{lp}I_p}{b_w}\frac{x}{h_p}\right];H_{sab}=-\frac{uT_{ls}I_s}{b_w};H_{pcd}=-\frac{vT_{lp}I_p}{b_w};H_{sp}=-\frac{n_{ls}T_{ls}I_s}{b_w};$$

$$K_1=\left[\begin{array}{l}\int_0^{h_s}\left(-\frac{T_{ls}I_s}{b_w}\frac{x}{h_s}\right)^2dx+\int_0^{h_s}\left(-\frac{T_{ls}I_s}{b_w}-\frac{T_{ls}I_s}{b_w}\frac{x}{h_s}\right)^2dx+\int_0^{h_s}\left(-\frac{2T_{ls}I_s}{b_w}-\frac{T_{ls}I_s}{b_w}\frac{x}{h_s}\right)^2dx+\int_0^{h_s}\left(-\frac{3T_{ls}I_s}{b_w}-\frac{T_{ls}I_s}{b_w}\frac{x}{h_s}\right)^2dx+\left(-\frac{T_{lp}I_p}{b_w}\right)^2h_{ip}\\+\left[\left(-\frac{T_{ls}I_s}{b_w}\right)^2+\left(-\frac{2T_{ls}I_s}{b_w}\right)^2+\left(-\frac{3T_{ls}I_s}{b_w}\right)^2\right]h_{ls}+\int_0^{h_p}\left(-\frac{2T_{lp}I_p}{b_w}+\frac{T_{lp}I_p}{b_w}\frac{x}{h_p}\right)^2dx+\int_0^{h_p}\left(-\frac{T_{lp}I_p}{b_w}+\frac{T_{lp}I_p}{b_w}\frac{x}{h_p}\right)^2dx+\left(-\frac{2T_{lp}I_p}{b_w}\right)^2h_i\end{array}\right] \tag{AI}$$

$$=\left(\frac{T_{ls}I_s}{b_w}\right)^2\left[4^3\frac{h_s}{3}+14h_{is}\right]+\left(\frac{T_{lp}I_p}{b_w}\right)^2\left[2^3\frac{h_p}{3}+h_{ip}+4h_i\right]=\left(\frac{N_pI_p}{b_w}\right)^2\left[\frac{2h_p+4h_s}{3}+\frac{7h_{is}}{8}+\frac{h_{ip}}{4}+h_i\right];\;\begin{array}{c}n_{lp}T_{lp}I_p=n_{ls}T_{ls}I_s\\N_pI_p=N_sI_s\end{array};$$

Appendix K

Digital control of a high-voltage (2.5 kV) bidirectional DC-DC converter for driving a dielectric electro active polymer (DEAP) based capacitive actuator

---

2014 IEEE Energy Conversion Congress and Exposition USA (ECCE USA 2014)

Digital control of a high-voltage (2.5 kV) bidirectional DC-DC converter for driving a dielectric electro active polymer (DEAP) based capacitive actuator

Prasanth Thummala, Zhe Zhang, Michael A.E. Andersen
Electronics Group
Department of Electrical Engineering
Technical University of Denmark
DK-2800, Kongens Lyngby, Denmark
pthu@elektro.dtu.dk

Dragan Maksimovic
Colorado Power Electronics Center
Department of Electrical, Computer, and Energy Engineering
University of Colorado Boulder
Boulder, Colorado, USA-80309
maksimov@colorado.edu

***Abstract*—This paper presents a digital control technique to achieve valley switching in a bidirectional flyback converter used to drive a dielectric electro active polymer based incremental actuator. The incremental actuator consists of three electrically isolated, mechanically connected capacitive actuators. The incremental actuator requires three high voltage (~2.5 kV) bidirectional DC-DC converters, to accomplish the incremental motion by charging and discharging the capacitive actuators. The bidirectional flyback converter employs a digital controller to improve efficiency and charge/discharge speed using the valley switching technique during both charge and discharge processes, without the need to sense signals on the output high-voltage side. Experimental results verifying the bidirectional operation of a single high voltage flyback converter are presented, using a film capacitor as the load. Energy efficiency measurements are provided.**

NOMENCLATURE

C_{in}/C_{load}	Input/load capacitance
C_s	Self-capacitance of the high voltage winding of transformer
C_{oss1}/C_{oss2}	Output capacitance of MOSFET M_1/M_2
C_{D2}/C_{Db}	Junction capacitance of diode D_2/D_b
C_{lumpP}/C_{lumpS}	Equivalent lumped capacitance referred at the drain node of MOSFET M_1/M_2
D_2/D_b	High voltage (5 kV) diode which conducts during charge/discharge process
D_{b1}/D_{b2}	Body diodes of MOSFET M_1/M_2
f_{swC}/f_{swD}	Switching frequency during charge/discharge process
f_{r1}/f_{r2}	Charge/discharge process ringing frequency in discontinuous conduction mode (DCM)
$i_{in}/i_p/i_s$	Input /primary/secondary current
I_{ppkC}/I_{spkD}	Primary charging peak current / secondary discharging peak current
L_{mp}/L_{ms}	Primary/secondary magnetizing inductance
L_{lkp}/L_{lks}	Leakage inductance of transformer referred to primary side/secondary side
M_1	Low voltage MOSFET
M_2	High voltage (4 kV/4.5 kV) MOSFET
n	Turns ratio of the transformer from secondary to primary
N_p/N_s	Number of primary/secondary turns
R_p/R_s	Primary/secondary DC resistance of transformer
t_{onC}/t_{offC}	On-time/off-time of M_1 during charge process
t_{onD}/t_{offD}	On-time/off-time of M_2 during discharge process
T_{oss1}/T_{oss2}	Charge/discharge process oscillation period in DCM
t_{dcmC}/t_{dcmD}	Total DCM time duration during charge/discharge process
t_{vC}/t_{vD}	Time to reach the valley point during charge/discharge process
t_{dC}/t_{dD}	Delay time needed to reach the valley point during charge/discharge process after the comparator output becomes low/high
t_{dleak}	Delay time introduced to avoid the leakage inductance L_{lkp} effect during charge process
$V_{in}/\Delta V_{inD}$	Input voltage/ increment in the input voltage during discharge process
V_{outC}/V_{outD}	Variable load voltage during charge (0 V-2.5 kV) /discharge process (2.5 kV- 0 V)
V_{M1}/V_{M2}	Drain-to-source voltage of MOSFET M_1/M_2
V_{D2}/V_{Db}	Reverse voltage across diode D_2/D_b
V_{onD2}/V_{onDb}	Voltage drop of diode D_2/D_b
V_{leakD}	Voltage increment in M_2 due to leakage inductance L_{lks}
V_{comp}	Output of the comparator
δ	Capacitance ratio factor on the HV side

This work was sponsored by Danish National Advanced Technology Foundation.

I. INTRODUCTION

Dielectric electro active polymer (DEAP) is an evolving smart material that has experienced substantial development and has gained growing attention over the last decade [1]-[3]. DEAPs, when used as linear actuators, have the potential to be an effective replacement for many conventional linear actuators because of their unique properties, including light weight, low noise operation, high flexibility, low cost, large strain, and autonomous capability. The DEAP actuator, shown in Fig. 1(a), is ideally equivalent to a pure capacitive load [4]. The DEAP incremental actuator concept, recently proposed in [5], consists of two grippers at both ends (to enable gripping operation) and an extender (to move the grippers), as shown in Fig. 1(b). These grippers connect with the extender mechanically. The grippers A_1 and A_3, and the extender A_2 are similar to the DEAP actuator shown in Fig. 1(a). For moving the incremental actuator, the three DEAP actuators (which behave as electrically isolated capacitive loads) needs to be controlled. Details of the DEAP incremental actuator operation can be found in [5].

To drive a DEAP incremental actuator, high voltage (~ 2.5 kV) bidirectional DC-DC converters are required, to generate sufficient force and displacement for the three sub-actuators [5]. Prior work on high voltage (HV) drivers for the DEAP actuators demonstrated a low voltage piezoelectric transformer based DEAP solution which was incorporated into a coreless DEAP actuator [6], and a bidirectional flyback converter topology to drive the PolyPower Push Inlastor DEAP actuator [7], which utilized the control IC LT3751 [8] to achieve the charge and discharge operations, with boundary conduction mode (BCM) control and discontinuous conduction mode control (DCM), respectively. The objectives of this paper are to implement the valley switching technique using a digital controller, during both charge and discharge operations, in order to improve efficiency and charge/discharge speed, as well as to reduce electromagnetic interference (EMI). Furthermore, another objective is to eliminate the need to sense any signal (voltage or current) on the HV side.

The flyback converter is suitable for high voltage and low power applications due to its simple structure and low component count [11]. Control algorithms for optimal-flyback charging of a capacitive load have been proposed in [9]. In [12] an efficiency optimization technique is proposed for a bidirectional flyback converter [7] for a high voltage capacitor charging application. In [13] an efficiency optimization technique has been proposed for a flyback converter which employs the valley switching control. Valley switching/QR control has also been used in [14]-[17], to improve the efficiency of the switch mode power supplies by reducing the capacitive turn-on/switching losses, and to reduce EMI.

For the high voltage capacitor charging application, the capacitive switching losses [13], [19] due to the equivalent lumped capacitance, at the drain node of the primary MOSFET during charge process, and at the drain node of the HV MOSFET during discharge process dominates the total losses in the converter. Therefore, the approach followed in this paper is to reduce the capacitive switching losses by implementing the valley switching control for charging as well as discharging the capacitive load. The proposed valley switching technique requires only sensing of the low voltage side voltages (supply voltage and drain voltage) without the need to sense any HV side signals.

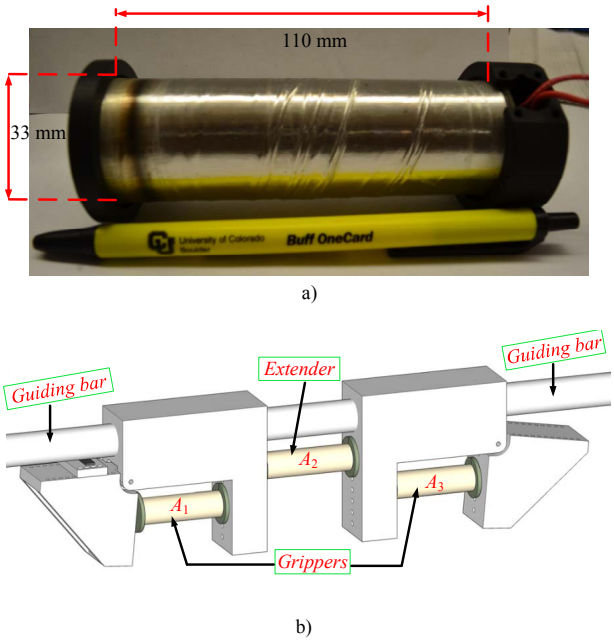

Figure 1. a) DEAP actuator; b) Incremental DEAP actuator.

This paper is organized as follows: Section II presents the theoretical analysis of the HV flyback converter in DCM, for achieving the valley switching during both charge and discharge modes. Section III discusses the proposed valley switching control technique. Section IV provides the experimental results followed by the conclusions in Section V.

II. QUASI RESONANT (QR) / VALLEY SWITCHING CONTROL IN BIDIRECTIONAL HV FLYBACK CONVERTER

The schematic of the HV bidirectional flyback converter for charging and discharging a capacitive actuator/load is shown in Fig. 2 [7]. This section provides the theoretical analysis, to detect the valley points in the drain voltage of the MOSFETs M_1 and M_2, respectively, with the assumption of $C_{load} >> C_s$ or C_{D2}.

A. Analysis during charge process

Figure 3 shows the drain-to-source voltage of the primary MOSFET M_1 during charge process, when the converter operates in DCM. The drain to source voltage V_{M1} when $V_{outC} < nV_{in}$ in DCM is [17]

$$V_{M1}(t) = V_{in} + \left[\frac{V_{outC} + V_{onD2}}{n}\right] e^{-\left[\frac{R_p}{2(L_{mp}+L_{lkp})}\right]t} \cos(w_{r1}t) \quad (1)$$

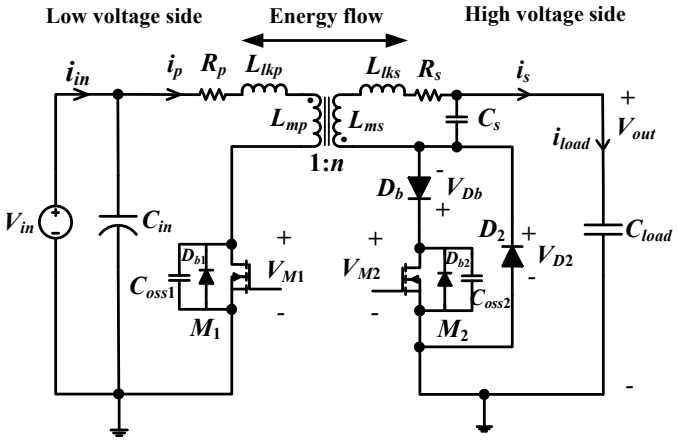

Figure 2. Schematic of the high voltage bidirectional flyback converter for driving a high voltage capacitive load.

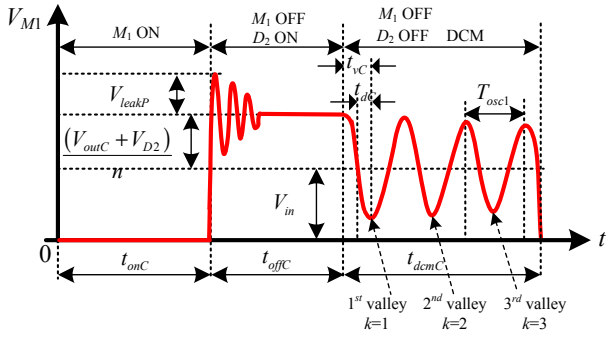

Figure 3. Voltage across low voltage MOSFET M_1 in DCM, during charge process when $V_{outC}<nV_{in}$.

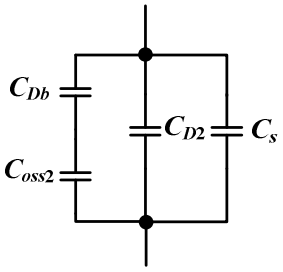

Figure 4. Equivalent circuit on the secondary side to calculate the lumped capacitance referred to primary or secondary.

The ringing frequency f_{r1} in DCM is given by

$$f_{r1}=\frac{w_{r1}}{2\pi}=\frac{1}{2\pi\sqrt{(L_{mp}+L_{lkp})C_{lumpP}}}=\frac{1}{T_{osc1}} \tag{2}$$

The lumped capacitance C_{lumpP} in terms of different capacitances in the converter is given by

$$C_{lumpP}\simeq C_{oss1}+n^2\left(C_s+C_{D2}+\frac{C_{Db}C_{oss2}}{C_{Db}+C_{oss2}}\right) \tag{3}$$

If the controller employs valley switching in DCM, the switching-node voltage V_{M1} at k^{th} valley point is given by

$$V_{M1}\big|_k=V_{in}-\left[\frac{V_{outC}+V_{onD2}}{n}\right]e^{-\left[\frac{R_p}{2(L_{mp}+L_{lkp})}(2k-1)\frac{T_{osc1}}{2}\right]} \tag{4}$$

The maximum number of valley points in terms of DCM period t_{dcmC} is given by [13]

$$k_{max}=round\left(\frac{t_{dcmC}}{T_{osc1}}\right) \tag{5}$$

The switching frequency at k^{th} valley point when the controller employs valley switching in DCM during charge process, is given by

$$\begin{aligned} f_{swC}\big|_k&=\frac{1}{t_{onC}+t_{offC}+(2k-1)\frac{T_{osc1}}{2}}\\ &=\frac{1}{\frac{L_{mp}I_{ppkC}}{V_{in}}+\frac{L_{mp}I_{ppkC}n}{V_{outC}}+(2k-1)\frac{T_{osc1}}{2}} \end{aligned} \tag{6}$$

At the end of each switching period, the energy stored in the non-linear lumped capacitance C_{lumpP} is dissipated when the MOSFET M_1 is turned on [13], [19]. This paper considers achieving valley switching for M_1 and M_2 at first valley point. However, it is possible to optimize the switching loss or other losses in the converter by switching at other valley points. The switching loss due the lumped capacitance at the drain node, when the converter employs the valley switching at the first valley point (k=1) is

$$P_{sw1}=\frac{1}{2}C_{lumpP}\left[V_{M1}\big|_{k=1}\right]^2\left[f_{swC}\big|_{k=1}\right] \tag{7}$$

Table I provides the comparison of different operating modes such as, continuous conduction mode (CCM), DCM without valley switching, and DCM with valley switching, during charge process, in terms of switching frequency and drain-to-source voltage. When $V_{outC}>nV_{in}$ zero voltage switching (ZVS) of M_1 occurs, and there is no energy loss due to the lumped capacitance, hence (7) is equal to 0 W.

B. Analysis during discharge process

Figure 5 shows the voltage across HV diode D_2, drain-to-source voltages of the primary and HV MOSFETs during discharge process, when the converter operates in DCM. All equations given below are derived with the assumption of $V_{outD}>nV_{in}$. The drain to source voltage across the primary MOSFET M_1 in DCM is [7]

$$V_{M1}(t)=V_{in}-V_{in}e^{-\left[\frac{R_s}{2(L_{ms}+L_{lks})}\right]t}\cos(w_{r2}t) \tag{8}$$

TABLE I. COMPARISON OF DIFFERENT OPERATING MODES IN A FLYBACK CONVERTER DURING CHARGE PROCESS

Operating Mode	Switching frequency during charge process f_{swC}	Drain-to-source voltage of M_1 (V_{M1}) at the beginning of next switching cycle during charge process
CCM	$\frac{1}{t_{onC}+t_{offC}}$	$V_{in}+\frac{V_{TC}}{n}$ $V_{TC}=V_{outC}+V_{onD2}$
DCM (without valley switching)	$\frac{1}{\left[t_{onC}+t_{offC}+t_{dcmC}\right]}$	$V_{in}+\frac{V_{TC}}{n}e^{-\Delta_1}\cos\left(w_{o1}t_{dcmC}\right)$ when $V_{outC}<nV_{in}$ $\Delta_1=\left[\frac{R_p}{2L_{Tp}}t_{dcmC}\right]$ $L_{Tp}=L_{mp}+L_{lkp}$
DCM (with valley switching at k^{th} valley point)	$\frac{1}{\left[t_{onC}+t_{offC}+(2k-1)\frac{T_{osc1}}{2}\right]}$	$\begin{cases}V_{in}-\frac{V_{TC}}{n}e^{-\Delta_2}, \text{ if } V_{outC}<nV_{in}\\ 0 \Rightarrow \text{ZVS}, \text{ if } V_{outC}>nV_{in}\end{cases}$ $\Delta_2=\left[\frac{R_p}{2L_{Tp}}(2k-1)\frac{T_{osc1}}{2}\right]$

The voltage across HV diode D_2 in DCM is [7]

$$V_{D2}(t)=\left(V_{outD}-V_{onDb}\right)+nV_{in}e^{-\left[\frac{R_s}{2(L_{ms}+L_{lks})}\right]t}\cos\left(w_{r2}t\right) \quad (9)$$

The voltage across HV diode D_b in DCM is

$$V_{Db}(t)=\left[\delta V_{leakD}+\delta nV_{in}\left\{1-e^{-\left[\frac{R_s}{2(L_{ms}+L_{lks})}\right]t}\cos\left(w_{r2}t\right)\right\}\right] \quad (10)$$

where $V_{leakD}=I_{spkD}\sqrt{\frac{L_{lks}}{C_{lumpS}}}$ and $\delta=\frac{C_{oss2}}{C_{oss2}+C_{Db}}$

The voltage across HV MOSFET M_2 in DCM is

$$V_{M2}(t)=\left[\begin{array}{l}\left(V_{outD}-V_{onDb}\right)+\delta V_{leakD}+\delta nV_{in}+\\ nV_{in}(1-\delta)e^{-\left[\frac{R_s}{2(L_{ms}+L_{lks})}\right]t}\cos\left(w_{r2}t\right)\end{array}\right] \quad (11)$$

The ringing frequency f_{r2} in DCM is given by

$$f_{r2}=\frac{w_{r2}}{2\pi}=\frac{1}{2\pi\sqrt{(L_{ms}+L_{lks})C_{lumpS}}}=\frac{1}{T_{osc2}} \quad (12)$$

The lumped capacitance C_{lumpS} in terms of different capacitances in the converter is given by

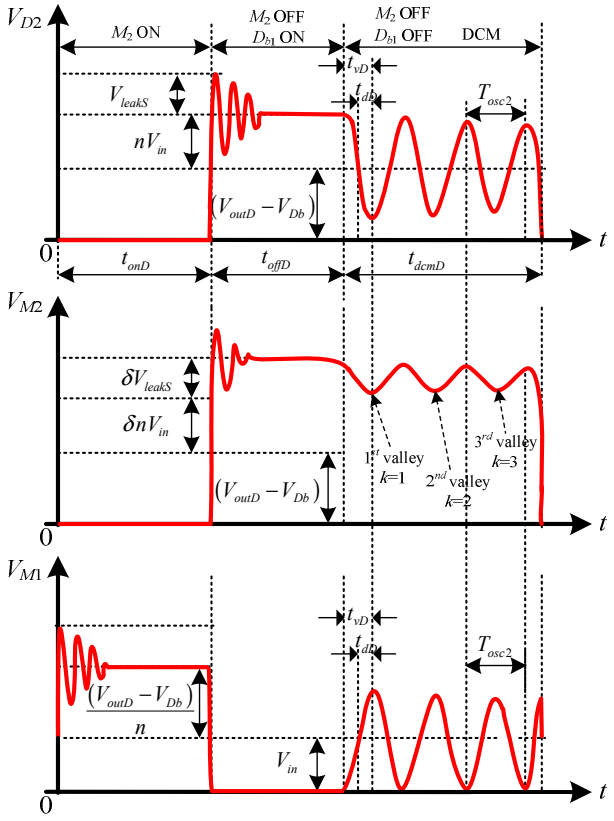

Figure 5. Voltages across D_2, M_2 and M_1 in DCM, during discharge process when $V_{outD}>nV_{in}$.

$$C_{lumpS}\simeq\left(C_s+C_{D2}+\frac{C_{Db}C_{oss2}}{C_{Db}+C_{oss2}}\right) \quad (13)$$

If the controller employs valley switching in DCM during discharge process, the switching-node voltage V_{M2} at k^{th} valley point is given by

$$V_{M2}\big|_k=\left[\begin{array}{l}\left(V_{outD}-V_{onDb}\right)+\delta V_{leakD}+\delta nV_{in}+\\ nV_{in}(1-\delta)e^{-\left[\frac{R_s}{2(L_{ms}+L_{lks})}(2k-1)\frac{T_{osc2}}{2}\right]}\end{array}\right] \quad (14)$$

The switching frequency at k^{th} valley point when the controller employs valley switching in DCM during discharge process, is given by

$$f_{swD}\big|_k=\frac{1}{t_{onD}+t_{offD}+(2k-1)\frac{T_{osc2}}{2}}=\frac{1}{\frac{L_{ms}I_{spkD}}{V_{outD}}+\frac{L_{mp}I_{spkD}n}{(V_{in}+\Delta V_{in})}+(2k-1)\frac{T_{osc2}}{2}} \quad (15)$$

At the end of each switching period, the energy stored in the non-linear lumped capacitance C_{lumpS} is dissipated when

the switch M_2 is turned-on. Valley switching at the first valley point is employed during the discharge process, to reduce the discharging time or to increase the discharge speed. The switching loss due the lumped capacitance at the drain node, when the converter employs the valley switching at the first valley point (k=1) is

$$P_{sw2} = \frac{1}{2} C_{lumpS} \left[V_{M2}\big|_{k=1} \right]^2 \left[f_{swD}\big|_{k=1} \right] \quad (16)$$

Table II provides the comparison of different operating modes during discharge process, in terms of switching frequency and drain-to-source voltage.

TABLE II. COMPARISON OF DIFFERENT OPERATING MODES IN A FLYBACK CONVERTER DURING DISCHARGE PROCESS

Operating Mode	Switching frequency during charge process f_{swD}	Drain-to-source voltage of M_2 (V_{M2}) at the beginning of the next switching cycle during the discharge process
CCM	$\frac{1}{t_{onD} + t_{offD}}$	$V_{TD} + \delta V_{leakD} + \delta n V_{in}$ $V_{TD} = V_{outD} - V_{onDb}$
DCM (without valley switching)	$\frac{1}{\left[t_{onD} + t_{offD} + t_{dcmD} \right]}$	$\left[V_{TD} + \delta V_{leakD} + \delta n V_{in} \right.$ $\left. n V_{in} (1-\delta) e^{-\Delta_3} \cos(w_{o2} t_{dcmD}) \right]$ $\Delta_3 = \left[\frac{R_s}{2L_{Ts}} t_{dcmD} \right]; L_{Ts} = L_{ms} + L_{lks}$
DCM (with valley switching at k^{th} valley point)	$\frac{1}{\left[t_{onD} + t_{offD} + (2k-1)\frac{T_{osc2}}{2} \right]}$	$\begin{cases} \left[V_{TD} + \gamma_1 + \gamma_2 - n V_{in} (1-\delta) e^{-\Delta_4} \right], & \text{if } V_{outD} > n V_{in} \\ -\delta V_{TD} + \gamma_1 + \gamma_2, & \text{if } V_{outD} < n V_{in} \end{cases}$ $\Delta_4 = \left[\frac{R_s}{2L_{Ts}} (2k-1) \frac{T_{osc2}}{2} \right]$ $\gamma_1 = \delta V_{leakD}; \quad \gamma_2 = \delta n V_{in}$

III. PROPOSED VALLEY SWITCHING CONTROL

A. Charge process

The bidirectional flyback converter with the control circuit to achieve the valley switching during charge and discharge processes is shown in Fig. 6. The input voltage and the drain voltage of primary MOSFET M_1, each scaled by a resistor divider network H_1 (3 kΩ and 90 kΩ), are compared using a high speed comparator TLV3501A. The comparator output becomes low (V_{comp}=0), when the drain voltage of M_1 is lower than the input voltage V_{in}. The output signal of the comparator V_{comp} is sent to the 16-bit microcontroller (PIC18F45K22) which detects the comparator output change, and produces a fixed on-time pulse to enable the gate driver 1 to drive the MOSFET M_1.

To introduce the control approach, Figs. 7-9 provide experimental results in the flyback converter during charge process, in the case when the converter is driven at a fixed frequency without valley switching. From Fig. 7, it can be observed that there is a delay time t_{dC} (~1.04 μs) between the time when the comparator output goes low and the first valley point (at which the next switching cycle should start to achieve valley switching), in the drain voltage of M_1 (V_{M1}). The microcontroller provides the delay time t_{dC} such that the next turn-on cycle of M_1 starts at the first valley point. The delay time t_{dC} can be calculated from the ringing frequency of V_{M1} in DCM. The delay time t_{dC} is half of the time to reach first valley point t_{vC} (k=1) when $V_{outC}<nV_{in}$ (see Fig. 3). The expression for t_{dC} in terms of DCM ringing frequency f_{r1} is given by

$$t_{dC} = \frac{t_{vC}}{2} = \frac{1}{4 f_{r1}} = \frac{\pi}{2} \sqrt{(L_{mp} + L_{lkp}) C_{lumpP}} \quad (17)$$

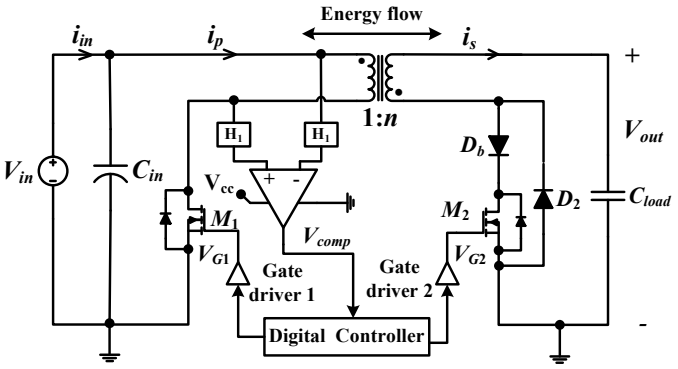

Figure 6. Schematic of the bidirectional flyback converter with the control circuit to achieve valley switching.

As mentioned before, M_1 is turned-on whenever the comparator output becomes low (V_{comp}=0), but the operation can be corrupted by ringing due to the leakage inductance L_{lkp}, which can also make the comparator output low (see Fig. 8). So, another delay time t_{dleak} (~1.5-2 μs) is provided by the microcontroller to disable the switching of M_1 during this interval. When $V_{outC}>nV_{in}$ the drain voltage V_{M1} reaches 0 V (with in 500 ns) before the delay time t_{dC}, which ensures zero voltage turn-on, as shown in Fig. 9. Hence, there is no capacitive switching loss during charge process when the output voltage $V_{outC}>nV_{in}$ (see Table I).

B. Discharge process

To achieve valley switching of HV MOSFET M_2 during discharge process, only the information of the comparator output V_{comp} is used. The comparator output becomes high (V_{comp}=5 V), when the drain voltage of M_1 is higher than the input voltage V_{in}. Similar to the charge process, the output signal of the comparator is sent to the microcontroller which produces a fixed or variable on-time pulse to enable the gate driver 2, to drive the MOSFET M_2. During the discharge process, since the output voltage decreases, the on-time t_{onD} of M_2 should be increased with the discharge time, to make the secondary discharge peak current I_{spkD} constant. Figures 10-12 provide experimental results in the flyback converter during discharge process, in the case when the converter is driven at a fixed frequency without valley switching. From Fig. 10, it can be observed that there is a delay time t_{dD} (~1.04 μs) between the time when the comparator output goes high and the first valley point (at which the next switching cycle should start to achieve valley switching), in the drain voltage of M_2 (V_{M2}). The microcontroller provides

the delay time t_{dD} such that the next turn-on cycle of M_2 starts at the first valley point, and it can be calculated from the ringing frequency of V_{M2} in DCM. The delay time t_{dD} is half of the time to reach first valley point t_{vD} (k=1) when $V_{outD}>nV_{in}$ (see Fig. 5). The expression for t_{dD} in terms of DCM ringing frequency f_{r2} is given by

$$t_{dD} = \frac{t_{vD}}{2} = \frac{1}{4f_{r2}} = \frac{\pi}{2}\sqrt{(L_{ms} + L_{lks})C_{lumpS}} \qquad (18)$$

When the HV probe is placed across D_2, the equivalent lumped capacitance C_{lumpS} is increased by ~9-10 pF due to the capacitance $C_{HVprobe}$ of the HV probe Lecroy PPE 4 kV. Due to this ringing frequency f_{r2} shown in Figs. 10 and 11 are different. When the HV probe is placed across M_2, C_{lumpS} remains unchanged, due to the series combination of D_b and M_2. When $V_{outD}<nV_{in}$ the drain voltage V_{M2} reaches $\sim \delta V_{TD} + \gamma_1 + \gamma_2$, whereas the voltage across D_2 becomes 0 V (see Table II) before the delay time t_{dD}, as shown Figs. 12 and 13, respectively.

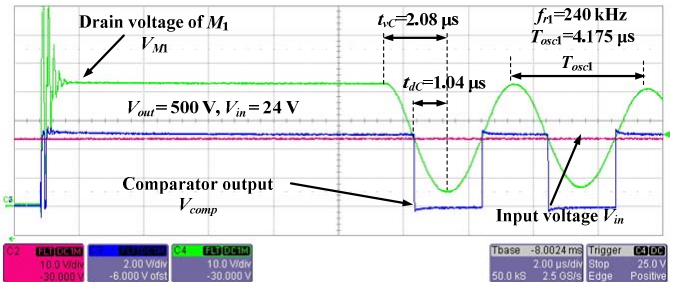

Figure 7. Experimental results when M_1 is driven with fixed frequency (V_{out}<600V) during charge process; CH2: V_{in}; CH3: V_{comp}; CH4: V_{M1}.

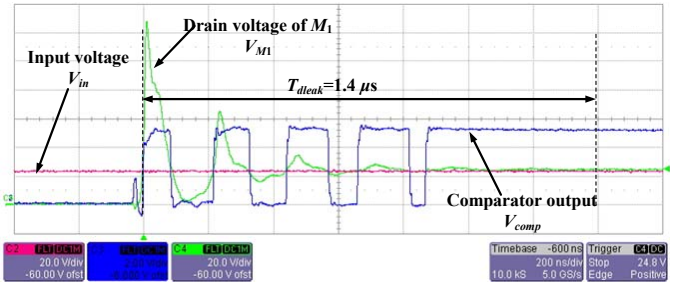

Figure 8. A zoomed view of Fig. 7 immediately after M_1 is turned-off.

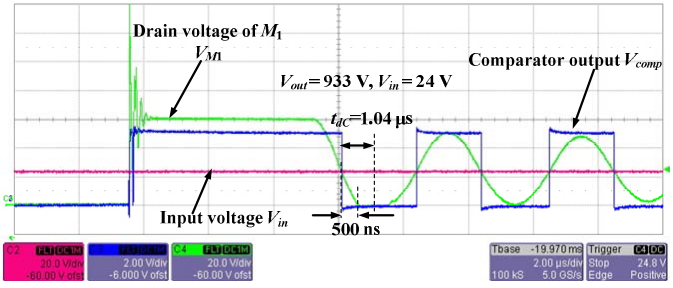

Figure 9. Experimental results when M_1 is driven with fixed frequency (V_{out}>600V) during charge process; CH2: V_{in}; CH3: V_{comp}; CH4: V_{M1}.

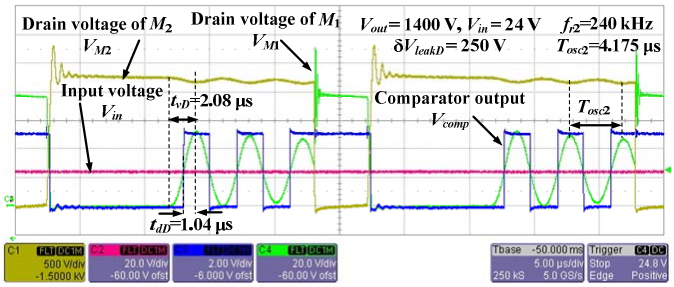

Figure 10. Experimental results when M_2 is driven with fixed frequency (V_{out}>600V) during discharge process; CH1: V_{M2}; CH2: V_{in}; CH3: V_{comp}; CH4: V_{M1}.

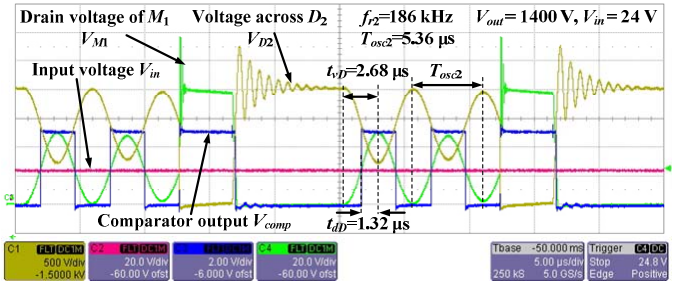

Figure 11. Experimental results when M_2 is driven with fixed frequency (V_{out}>600V) during discharge process; CH1: V_{D2}; CH2: V_{in}; CH3: V_{comp}; CH4: V_{M1}.

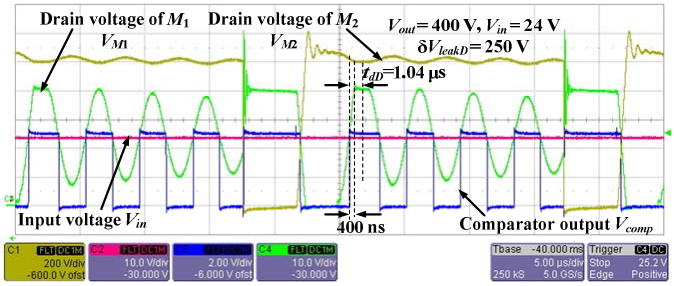

Figure 12. Experimental results when M_2 is driven with fixed frequency (V_{out}<600V) during discharge process; CH1: V_{M2}; CH2: V_{in}; CH3: V_{comp}; CH4: V_{M1}.

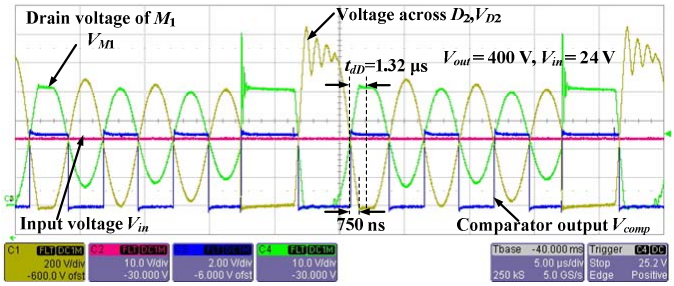

Figure 13. Experimental results when M_2 is driven with fixed frequency (V_{out}<600V) during discharge process; CH1: V_{D2}; CH2: V_{in}; CH3: V_{comp}; CH4: V_{M1}.

IV. Valley Switching Experimental Results

Tables II, III and IV provide the converter specifications, components used in the converter, and

flyback transformer parameters, respectively. The experimental prototype of the HV bidirectional flyback converter is shown in Fig. 14. The experimental results in the converter, tested with a film capacitive load of 400 nF, to validate the proposed valley switching technique are shown in Figs. 15-18. In Figs. 15 and 16, successful valley-switching operation at different output voltages during the charge process is shown. From Fig. 16, it is clear that the converter operates with zero voltage switching (ZVS) turn-on, and the primary current is negative before the switch is turned-on. In Fig. 17, successful valley-switching operation during discharge process is shown. As explained in Section III, the first valley voltage in the drain to-source voltage of M_2 is not very low, compared to the first valley voltage in HV diode voltage V_{D2} (due to the series combination of D_b and M_2). The capacitive switching loss is directly proportional to the voltage across the HV MOSFET when it is turned-on (7), (16). This is one of the reasons for the low energy efficiency during the discharge process.

TABLE III. SPECIFICATIONS OF THE BIDIRECTIONAL FLYBACK CONVERTER

Parameter	Value
Input voltage V_{in}	24 V
Output voltage V_{out}	0-2.5 kV
Capacitance of the load C_{load}	400 nF
On time of M_1 during charge process t_{onC}	9 μs
On times of M_2 during discharge process t_{onD}	[2 μs, 3 μs, 5 μs, 10 μs, 20 μs, 150 μs, 200 μs]

TABLE IV. COMPONENTS USED IN THE HV CONVERTER

Component	Value
Primary MOSFET M_1	250V, 16A [FQD16N25CTM]
HV MOSFET M_2	4.5 kV, 200 mA, 750 Ω [IXTA02N450HV] / 4 kV, 300 mA, 290 Ω [IXTV03N400S]
HV diode D_b / D_2	5 kV, 150 mA [SXF6525]
Gate driver	EL7104
Comparator	4.5 ns Rail-to-Rail, TLV3501A
Film capacitive load	400 nF, 3 kV [WIMA]

TABLE V. FLYBACK TRANSFORMER PARAMETERS

Parameter	Value
Core used / material used	PQ 20/20 / P type
Primary N_p / secondary turns N_s	12 / 300
Primary L_{mp} / secondary magnetizing inductance L_{ms}	47.5 μH / 30 mH
Leakage inductance referred to primary L_{lkp} / secondary L_{lks}	990 nH / 620 μH
Self-capacitance of secondary winding C_s (from the Impedance analyzer)	6 pF
Self-capacitance C_s from frequencies f_{r1}, f_{r2}	12.5 pF
Diameter of primary/secondary winding	0.5 mm (TEX-E)/ 0.11 mm
DC resistance of primary R_p /secondary R_s	62 mΩ / 14 Ω
Number of layers of primary/secondary	1 / 4

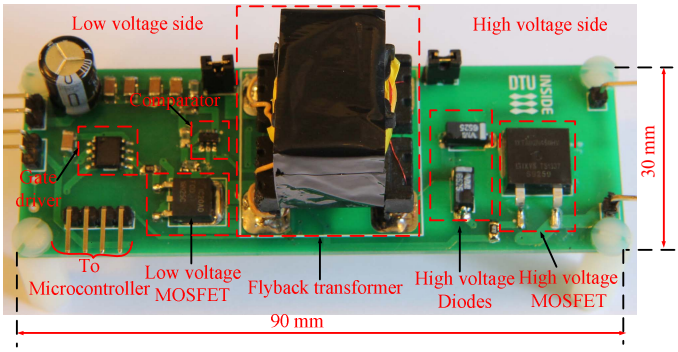

Figure 14. Experimental prototype of the HV bidirectional flyback converter with a 4.5 kV MOSFET on the HV side.

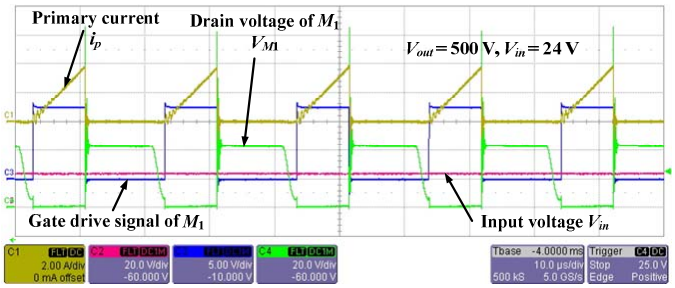

Figure 15. Experimental results when the converter is operated with valley switching during charge process; CH1: i_p; CH2: V_{in}; CH3: V_{G1}; CH4: V_{M1}.

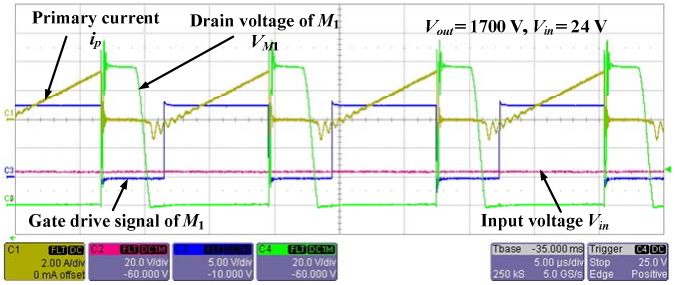

Figure 16. Experimental results with valley switching operation during the charge process; CH1: *IP*; CH2: V_{in}; CH3: V_{G1}; CH4: V_{M1}.

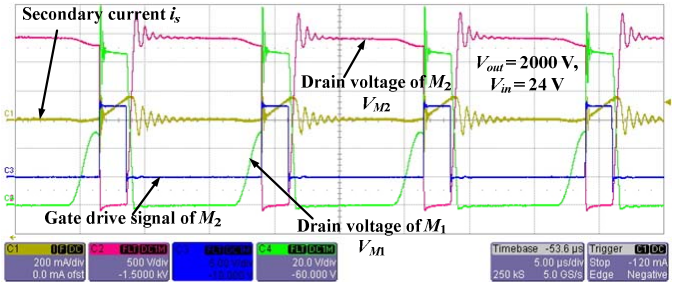

Figure 17. Experimental results with valley switching operation during discharge process; CH1: i_s; CH2: V_{M2}; CH3: V_{G2}; CH4: V_{M1}.

The bidirectional operation of the HV converter at 2.5 kV output voltage is shown in the Fig. 18. As provided in Table III, due to constant turn on-time t_{onC} for M_1 during charge process, the primary current I_{ppkC} is constant. During discharge process, employing variable turn on-time t_{onD} for M_2 makes the secondary current (hence the primary current) I_{spkC} almost constant. The energy efficiency measurements

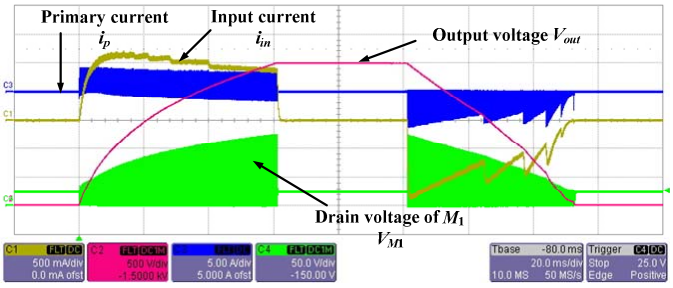

Figure 18. Experimental waveforms showing the bidirectional operation at 2.5 kV output voltage. CH1: i_{in}; CH2: V_{out}; CH3: i_p; CH4: V_{M1}.

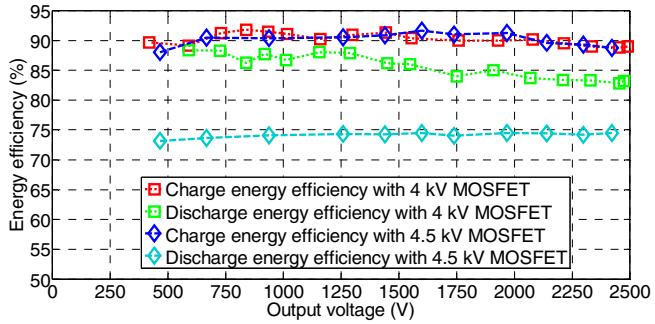

Figure 19. Energy efficiency measurements.

during charge and discharge processes [7] with 4 kV and 4.5 kV MOSFETs on the HV side are shown in Fig. 19. The charge energy efficiency for both 4 kV and 4.5 kV MOSFETs is above 90 %, for the output voltage range 750 V<V_{out}<2.2 kV, with a maximum efficiency of 92 %. The charge energy efficiency for the output voltage range 2.2 kV<V_{out}<2.5 kV is between 88-90 %. The discharge energy efficiency for 4 kV MOSFET is lower than the charge efficiency due to the fact that valley voltage in V_{M2} is not equal to valley voltage in V_{D2} during DCM. The junction capacitance of D_b is ~0.7 pF, the output capacitance of the HV MOSFET is ~10-12 pF. The lumped capacitances are C_{lumpP}=~9 nF and C_{lumpS}=~14 pF, respectively. Some of the reasons for very low discharge energy efficiency for 4.5 kV MOSFET are due to its high on resistance (750 Ω), high gate input resistance (76 Ω).

V. CONCLUSIONS

The valley switching technique for a bidirectional flyback converter, driving a capacitive load has been successfully implemented using a 16-bit microcontroller, during charge and discharge processes, respectively. Using the proposed simple valley switching technique, the flyback converter is able to charge and discharge the capacitor load within minimum time (or with maximum speed). To charge and discharge from 2.4 kV output voltage using a 4 kV MOSFET, the flyback converter has charge and discharge energy efficiencies of 89 % and 84 %, respectively. The future work involves further investigation of proposed control technique with 4.5 kV MOSFET, and testing the HV drivers with the incremental DEAP actuator.

REFERENCES

[1] R. E. Pelrine, R. D. Kornbluh, and J. P. Joseph, "Electrostriction of polymer dielectrics with compliant electrodes as a means of actuation," in *Proc. Sensors and Actuators A*, vol. 64, pp. 77–85, 1998.

[2] M. Tryson, H. E. Kiil, M. Benslimane, "Powerful tubular core free dielectric electro active polymer (DEAP) push actuator," in *Proc. SPIE, Electroactive Polymer Actuators and Devices (EAPAD)*, vol. 7287, 2009.

[3] R. Sarban, B. Lassen, M. Willatzen, "Dynamic Electromechanical Modeling of Dielectric Elastomer Actuators With Metallic Electrodes," *IEEE/ASME Transactions on Mechatronics,* vol. 17, no. 5, pp. 960-967, Oct. 2012.

[4] P. Thummala, Z. Zhang, M. A. E. Andersen, S. Rahimullah, "Dielectric electro active polymer incremental actuator driven by multiple high-voltage bi-directional DC-DC converters," in *Proc. IEEE ECCE USA,* pp. 3837-3844, 15-19 Sept. 2013.

[5] R. E. Pelrine, R. D. Kornbluh, Q. Pei, and J. P. Joseph, "High-speed electrically actuated elastomers with strain greater than 100%," in *Proc. Science*, vol. 287, pp. 836–839, 2000.

[6] T. Andersen, M. S. Rødgaard, O. C. Thomsen, M. A. E. Andersen, "Low voltage driven dielectric electro active polymer actuator with integrated piezoelectric transformer based driver," in Proc. SPIE, vol. 7976, p. 79762N, 2011.

[7] P. Thummala, Z. Zhang and M. A. E. Andersen, "Bi-directional Flyback Converter for Capacitive Actuator," in *Proc. EPE,* pp. 1-10, Sept. 2013.

[8] LT3751 datasheet, "High voltage capacitor charger controller with regulation," Linear Technology Corporation, USA, Online available: http://cds.linear.com/docs/en/datasheet/3751fc.pdf.

[9] N. O. Sokal, R. Redl, "Control algorithms and circuit designs for optimal flyback-charging of an energy storage capacitor (e.g., for flash lamp or defibrillator)," *IEEE Trans. on Power Electronics*, vol. 12, no. 5, pp. 885-894, Sep. 1997.

[10] M. Kazimierczuk, "High-Frequency Magnetic Components," 2nd Ed. John Wiley and Sons Ltd., 2014.

[11] R. W. Erickson and D. Maksimovic, "Fundamentals of Power Electronics," 2nd ed. New York: Springer, 2001.

[12] P. Thummala, H. Schneider, Z. Zhang, A. Knott, M. A. E. Andersen, "Optimization of a bi-directional flyback converter for a high voltage capacitor charging application," in *Proc. IEEE APEC*, pp. 2556-2563, March 2014.

[13] H. K. Sang, D. Maksimovic, I. Cohen, "Efficiency Optimization in Digitally Controlled Flyback DC–DC Converters Over Wide Ranges of Operating Conditions," *IEEE Trans. on Power Electronics*, vol. 27, no. 8, pp. 3734-3748, Aug. 2012.

[14] Y. Panov and M. M. Jovanovi´c, "Adaptive off-time control for variable frequency, soft-switched flyback converter at light loads," *IEEE Trans. Power Electronics*, vol. 17, no. 4, pp. 596–603, Jul. 2002.

[15] Y. Panov and M. M. Jovanovi´c, "Performance evaluation of 70-W two stage adapters for notebook computers," in *Proc. IEEE APEC*, 1999, pp. 1059–1065.

[16] Y. Park and H. Choi, "A efficiency improvement methodology for active mode efficiency regulation," in *Proc. IEEE Int. Symp. Electron. Environ.*, 2008, pp. 1–5.

[17] Z. Ling, T. Liang, L. Yang, and T. Li, "Design and implementation of interleaved quasi-resonant DC–DC flyback converter," in *Proc. IEEE Power Electron. Drive Syst.*, 2009, pp. 429–433.

[18] C. P. Basso, "Switch-mode power supplies spice simulations and practical designs," 2008.

[19] H. Schneider, P. Thummala, L. Huang, Z. Ouyang, A. Knott, Z. Zhang, M. A. E. Andersen, "Investigation of transformer winding architectures for high voltage capacitor charging applications," in *Proc. IEEE APEC*, pp. 334-341, March 2014.

Appendix L

Digital Control of a High Voltage (2.5 kV) Bidirectional DC-DC Converter for Driving a Capacitive Incremental Actuator

---

About to Submit to IEEE Transactions on Power Electronics

Digital Control of a High Voltage (2.5 kV) Bidirectional DC-DC Converter for Driving a Capacitive Incremental Actuator

Prasanth Thummala[*], *Student Member, IEEE*, Dragan Maksimovic[#], *Senior Member, IEEE*, Zhe Zhang[*], *Member, IEEE*, and Michael A. E. Andersen[*], *Member, IEEE*

[*]Electronics group, Department of Electrical Engineering, Technical University of Denmark, 2800 Kongens Lyngby, Denmark.

[#]Colorado Power Electronics Center, Department of Electrical, Computer, and Energy Engineering, University of Colorado Boulder, Boulder, 80309 Colorado, USA.

Email: pthu@elektro.dtu.dk, maksimov@colorado.edu

Abstract — **This paper presents a digital control technique to achieve valley switching in a bidirectional flyback converter used to drive a dielectric electro active polymer based incremental actuator. The incremental actuator consists of three electrically isolated, mechanically connected capacitive actuators. The incremental actuator requires three high voltage (2-2.5 kV) bidirectional dc-dc converters, to accomplish the incremental motion by charging and discharging the capacitive actuators. The bidirectional flyback converter employs a digital controller to improve efficiency and charge/discharge speed using the valley switching technique during both charge and discharge processes, without the need to sense signals on the output high-voltage side. The design of a low input (24 V) and variable high output voltage (0-2.5 kV) bidirectional dc-dc converter for driving a capacitive actuator is presented. Experimental results verifying the bidirectional operation of a single high voltage flyback converter are presented, using a film capacitor as the load. Energy efficiency measurements are provided.**

***Index Terms* — switch-mode power converters, high voltage dc-dc converters, digital control, energy efficiency, actuator**

Statement: *A part of this manuscript is presented at the IEEE ECCE USA 2014 conference. It is not currently under review for publication in any other journal. Compared with the conference paper, the detailed bidirectional flyback converter design and loss analysis results are included. Furthermore, the experimental results are updated.*

NOMENCLATURE

C_{in} / C_{load}	Input / load or actuator capacitance (F)
C_s	Self-capacitance of high voltage winding of transformer (F)
C_{ossp} / C_{osss}	Output capacitance of low voltage MOSFET M_p / high voltage MOSFET M_s (F)
C_{D2} / C_{Db}	Junction capacitance of high voltage freewheeling diode D_2 / blocking diode D_b (F)
C_{lumpP} / C_{lumpS}	Equivalent lumped capacitance referred at the drain node of MOSFET M_p / M_s (F)
D_2 / D_b	High voltage (5 kV) freewheeling diode / blocking diode
D_{bp} / D_{bs}	Body diode of MOSFET M_p / M_s
$D_{onC,min}$	Minimum on-duty cycle of M_p
$D_{offC,max}$	Maximum off-duty cycle of M_p
$D_{onD,max}$	Maximum on-duty cycle of M_s
f_{swC} / f_{swD}	Switching frequency during charge / discharge process (Hz)
f_{r1} / f_{r2}	Charge / discharge process ringing frequency in discontinuous conduction mode (DCM) (Hz)
i_{in} / i_p / i_s	Input / primary / secondary current (A)
I_{ppkC} / I_{spkD}	Primary peak charging current / Secondary peak discharging current (A)
I_{D2}/I_{Db}	Rated average current of diode D_2/D_b
I_{M2}	Rated average current of MOSFET M_s
L_{mp} / L_{ms}	Primary/secondary magnetizing inductance (H)
L_{lkp} / L_{lks}	Leakage inductance of transformer referred to primary / secondary side (H)
M_p	Low voltage MOSFET
M_s	High voltage (4 kV / 4.5 kV) MOSFET
n	Turns ratio of transformer from secondary to primary
N_p / N_s	Number of primary / secondary turns
R_p / R_s	Primary / Secondary dc resistance of transformer (Ω)
t_{onC} / t_{offC}	On-time / off-time of M_p during charge process (s)
t_{onD} / t_{offD}	On-time / off-time of M_s during discharge process (s)
T_{oss1} / T_{oss2}	Charge / discharge process oscillation period in DCM (s)
t_{dcmC} / t_{dcmD}	Total DCM time duration during charge / discharge process (s)
t_{vC} / t_{vD}	Time to reach the valley point in the drain voltage during charge / discharge process (s)

t_{dC} / t_{dD}	Delay time needed to reach the valley point during charge / discharge process after the comparator output changes (s)
t_{dleak}	Delay time introduced to avoid the leakage inductance L_{lkp} effect during charge process (s)
V_{in} / ΔV_{inD}	Input voltage / Increment in the input voltage during discharge process (V)
V_{outC} / V_{outD}	Variable load voltage during charge (0 V-2.5 kV) / discharge process (2.5 kV-0 V)
V_{Mp} / V_{Ms}	Drain-to-source voltage of MOSFET M_p / M_s (V)
V_{D2} / V_{Db}	Reverse voltage across diode D_2 / D_b (V)
V_{onD2} / V_{onDb}	Voltage drop of diode D_2 / D_b (V)
V_{BVM1} / V_{BVM2}	Breakdown voltage of MOSFET M_p / M_s
V_{BVD2}	Breakdown voltage of high voltage diode D_2 (or D_b)
β_{M1} / β_{M2} / β_{D2}	Margin factor (< 1) for V_{BVM1} / V_{BVM2} / V_{BVD2}
η	Power efficiency of the converter
V_{leakD}	Voltage increment in drain-to-source voltage of M_s due to leakage inductance L_{lks} (V)
V_{comp}	Output of the comparator (V)
δ	Capacitance ratio factor on the high voltage (HV) side

I. INTRODUCTION

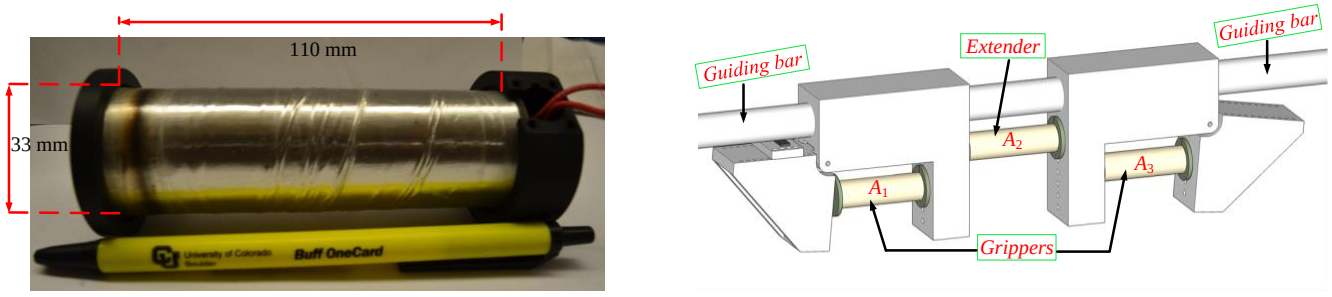

a) b)

Fig. 1. a) DEAP actuator; b) DEAP incremental actuator.

Dielectric electro active polymer (DEAP) is an evolving smart material that has experienced substantial development and has gained growing attention over the last decade [1]-[3]. DEAPs, when used as linear actuators, have the potential to be an effective replacement for many conventional linear actuators because of their unique properties, including light weight, low noise operation, high flexibility, low cost, large strain, and autonomous capability. The DEAP actuator, shown in Fig. 1(a), is ideally equivalent to a pure capacitive load [4]. The DEAP incremental actuator concept, recently proposed in [5], consists of

two grippers at both ends (to enable gripping operation) and an extender (to move the grippers), as shown in Fig. 1(b). These grippers connect with the extender mechanically. The grippers A_1 and A_3 and the extender A_2 are similar to the DEAP actuator shown in Fig. 1(a). For moving the incremental actuator, the three DEAP actuators (which behave as electrically isolated capacitive loads) needs to be controlled. Details of the DEAP incremental actuator operation can be found in [5].

To drive a DEAP incremental actuator, high voltage (~ 2.5 kV) bidirectional DC-DC converters are required, to generate sufficient force and displacement for the three sub-actuators [5]. Prior work on high voltage (HV) drivers for the DEAP actuators demonstrated a low voltage piezoelectric transformer based DEAP solution which was incorporated into a coreless DEAP actuator [6], and a bidirectional flyback converter topology to drive the PolyPower Push Inlastor DEAP actuator [7], which utilized the control IC LT3751 [8] to achieve the charge and discharge operations, with boundary conduction mode (BCM) control and discontinuous conduction mode control (DCM), respectively. The objectives of this paper are to implement the valley switching technique using a digital controller, during both charge and discharge operations, in order to improve efficiency and charge/discharge speed, as well as to reduce electromagnetic interference (EMI). Furthermore, another objective is to eliminate the need to sense any signal (voltage or current) on the HV side.

The flyback converter is suitable for high voltage and low power applications due to its simple structure and low component count [11]. Control algorithms for optimal-flyback charging of a capacitive load have been proposed in [9]. In [12] an efficiency optimization technique is proposed for a bidirectional flyback converter [7] for a high voltage capacitor charging application. In [13] an efficiency optimization technique has been proposed for a flyback converter which employs the valley switching control. Valley switching/QR control has also been used in [14]-[17], to improve the efficiency of the switch mode power supplies by reducing the capacitive turn-on/switching losses, and to reduce electro magnetic interference (EMI).

For the high voltage capacitor charging application, the capacitive switching losses [13], [19] due to the equivalent lumped capacitance, at the drain node of the primary MOSFET during charge process, and at the drain node of the HV MOSFET during discharge process dominates the total losses in the converter. Therefore, the approach followed in this paper is to reduce the capacitive switching losses by implementing the valley switching control for charging as well as discharging the capacitive load. The proposed valley switching technique requires only sensing of the low voltage side voltages (supply voltage and drain voltage) without the need to sense any HV side signals.

This paper is organized as follows: Section II describes the converter design considerations. Section III presents the theoretical analysis of the HV flyback converter in DCM, for achieving the valley switching during both charge and discharge

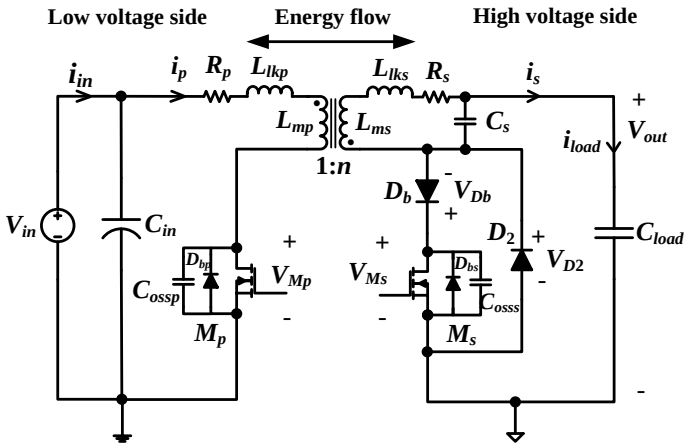

Fig. 2. Circuit configuration of the high voltage bidirectional flyback converter for driving a capacitive load.

TABLE I. SPECIFICATIONS OF BIDIRECTIONAL FLYBACK CONVERTER

Parameter	Value
Input V_{in}	24 V
Output voltage V_{out}	0-2.5 kV ($V_{out,max}$=2.5 kV)
Capacitance of the load C_{load}	400 nF
On time during charge process t_{onC}	9 μs
Target charging time T_{ch}	50 ms
Maximum flux density B_{maxC}	0.3 T

TABLE II. POWER STAGE COMPONENTS USED IN THE CONVERTER

Component	Value
Primary MOSFET M_p	250V, 25A [IPD600N25N3 G]
HV MOSFET M_s	4.5 kV, 200 mA, 750 Ω [IXTA02N450HV] / 4 kV, 300 mA, 290 Ω [IXTV03N400S]
HV diode D_b / D_2	5 kV, 150 mA [SXF6525]

modes. Section IV discusses the proposed valley switching control technique. Section V provides the experimental results followed by the conclusions in Section VI.

II. BIDIRECTIONAL DC-DC FLYBACK CONVERTER DESIGN CONSIDERATIONS

The schematic of the bidirectional flyback converter is shown in Fig. 2. The converter design considerations are discussed in this section. Specifications of the converter and power stage components are provided in Tables I and II, respectively.

A. Choice of turns ratio of the flyback transformer

For the capacitor charging application, the turns ratio is selected based on the maximum charging voltage of the capacitive load $V_{o,max}$. The typical voltage stress waveforms across MOSFETs M_p, M_s, and HV diode D_2 are shown in Figs. 3(a), 3(b) and 3(c), respectively.

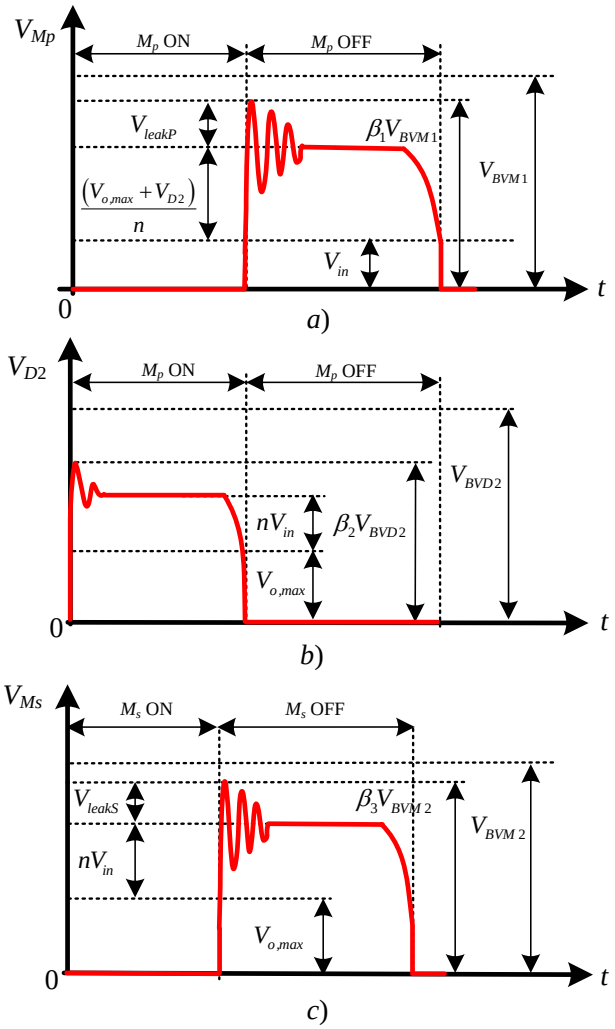

Fig. 3: Voltage stress when target output voltage ($V_{o,max}$) is reached across, a) M_p during charge process (BCM), b) D_2 during charge process (BCM), c) M_s during discharge process (BCM); BCM: Boundary Conduction Mode.

1) Charge process: The maximum and minimum turns ratios, from secondary to primary of the flyback transformer during charge process can be calculated to meet the device breakdown voltage constraints.

The voltage stress across the primary MOSFET M_p when turned off, should be less than its breakdown voltage V_{BVM1} (Fig. 3(a)), so

$$\left[V_{in}+\frac{\left[V_{o,max}+V_{onD2}\right]}{n}+V_{leakP}\right]<\beta_1 V_{BVM1} \tag{1}$$

where V_{leakP} is the increase in the drain voltage of primary MOSFET due to the leakage inductance L_{lkP}.

From (1), the transformer turns ratio

$$n > n_{min} \tag{2}$$

where n_{min} is the minimum turns ratio needed, to charge the capacitive load to $V_{o,max}$ and is given by

$$n_{min} = \frac{\left[V_{o,max} + V_{onD2}\right]}{\left[\left(\beta_1 V_{BVM1}\right) - V_{in} - V_{leakP}\right]} \tag{3}$$

For the given input specifications provided in Table I, by choosing V_{leakP}=70 V (this design value can be changed depending on the possible value of the leakage inductance referred to primary L_{lkP}), and choosing a margin factor of β_1=0.9 for a 250 V primary MOSFET (see Table II), with a high voltage diode drop V_{onD2}=7 V, the minimum turns ratio is n_{min}=20.

The voltage stress across the high voltage diode D_2 when M_p is turned on should be less than its breakdown voltage V_{BVD2} (Fig. 3(b)), so

$$\left[V_{o,max} + nV_{in}\right] < \beta_2 V_{BVD2} \tag{4}$$

From (4), the transformer turns ratio

$$n < n_{maxC} \tag{5}$$

where n_{maxC} is the maximum turns ratio needed for the charge process, and is given by

$$n_{maxC} = \left\lfloor \frac{\beta_2 V_{BVD2} - V_{o,max}}{V_{in}} \right\rfloor \tag{6}$$

By choosing a margin factor of β_2=0.8 for a 5 kV high voltage diode D_2, the maximum turns ratio is n_{maxC}=62.

2) Discharge process: The maximum turns ratio of the flyback transformer during discharge process can be calculated from the breakdown voltage of the secondary MOSFET M_s. The voltage stress across M_s when turned off should be less than its breakdown voltage V_{BVM2} (Fig. 3(c)), so

$$\left[V_{o,max} + nV_{in} + V_{leakS}\right] < \beta_3 V_{BVM2} \tag{7}$$

where V_{leakS} is the increase in the drain voltage of HV MOSFET due to the leakage inductance L_{lkS}.

From (7), the transformer turns ratio

$$n < n_{maxD} \tag{8}$$

where n_{maxD} is the maximum turns ratio needed for the discharge process, and is given by

$$n_{maxD} = \left\lfloor \frac{\beta_3 V_{BVM2} - V_{o,max} - V_{leakS}}{V_{in}} \right\rfloor \tag{9}$$

By choosing V_{leakS}=400 V, and by choosing a margin factor of β_3=0.9 (see Table II), the maximum turns ratios are 48 and 30 for 4.5 kV and 4 kV MOSFETs, respectively.

From (2), (5) and (8) the transformer turns ratio n must satisfy:

$$n=\begin{cases} n_{min}<n<n_{maxC}, \text{ if } V_{BVD2}<V_{BVM2} \\ n_{min}<n<n_{maxD}, \text{ if } V_{BVD2}>V_{BVM2} \end{cases} \tag{10}$$

Since $V_{BVM2}<V_{BVD2}$ (Table II), the turns ratio n should satisfy $20<n<48$, for 4.5 kV HV MOSFET, and $20<n<30$, for 4.5 kV HV MOSFET, respectively. To avoid complexity and difficulty in winding several secondary turns in the transformer, the turns ratio n is selected to be equal to 25. However, it is up to the designer to choose a different turns ratio, different margin factors, and different rating low voltage MOSFET for this application.

B. Selection of peak currents during charge and discharge processes

1) Charge process: The expression for primary peak current to charge the HV capacitive load from 0 V to $V_{o,max}$ in time T_{ch} is [8], [9]

$$I_{ppkC}=\frac{\left(2nV_{in}+V_{o,max}\right)C_{load}V_{o,max}}{\eta V_{in}\left(T_{ch}-T_{delay}\right)} \tag{11}$$

For the given input specifications, for a turns ratio of n=25, by choosing a power efficiency η=0.8, and for a delay time T_{delay}=5 ms, the approximate primary peak current is I_{ppkC}=4.28 A.

The expression for maximum secondary peak current $I_{spkC,max}$, to charge the HV capacitive load through HV diode D_2, when the converter is operating in BCM is

$$I_{spkC,max}<\frac{2I_{D2}}{\left(1-D_{onC,min}\right)}<\frac{2I_{D2}}{D_{offC,max}} \tag{12}$$

Equation (12) is derived based on the average current expression across HV diode D_2 during the charge process. The maximum secondary peak charging current, when a 5 kV HV diode, with a rated current of I_{D2}=150 mA is used, and for a maximum off-duty cycle during charge process $D_{offC,max}$=0.9 is $I_{spkC,max}$=333 mA. This corresponds to a maximum primary peak current of 8.3 A, for n=25.

2) Discharge process: During the discharge process, since the output voltage decreases in each switching cycle, to discharge the load with constant peak current i_{spkD}, the on-time t_{onD} should increase in each switching cycle. The expression for maximum secondary peak current $I_{spkD,max}$, to discharge the HV capacitive load, through the series combination of high voltage diode D_b and high voltage MOSFET M_s (Fig. 2) is

$$I_{spkD,max}<\frac{2I_{SD}}{D_{onD,max}} \tag{13}$$

where I_{SD} is the average current in the secondary side during discharge process, and is given by:

$$I_{SD} = \begin{cases} I_{Db}, \text{ if } I_{Db} < I_{M2} \\ I_{M2}, \text{ if } I_{Db} > I_{M2} \end{cases} \tag{14}$$

Since average current of D_b is less than that of M_2, i.e., $I_{Db}<I_{M2}$ (see Table II), $I_{SD}=I_{Db.}$ The maximum secondary peak discharging current, for a maximum discharge on-duty cycle $D_{onD,max}$=0.8 is $I_{spkD,max}$=375 mA. This corresponds to a maximum primary peak discharging current of 9.37 A, for n=25.

C. Design of primary and secondary turns

1) Charge process: The number of primary turns needed during charge process is

$$N_p = \frac{V_{in} t_{onC}}{B_{maxC} A_c} \tag{15}$$

The number of secondary turns needed is

$$N_{sC} = N_p n \tag{16}$$

By choosing a PQ 20/20 core with A_c=62 mm^2, and for the specifications shown in Table I, N_p=12 and N_{sC}=300.

2) Discharge process: The number of secondary turns needed during discharge process is

$$N_{sD} = \frac{V_{outD}\ t_{onD}}{B_{max\,D} A_c} = \frac{n\left(V_{in} + \Delta V_{inD}\right) t_{offD}}{B_{max\,D} A_c} \tag{17}$$

The same secondary turns ($N_s = N_{sC} = N_{sD}$) should meet both (15) and (16). The input capacitance of C_{in}=30 mF is chosen, such that the voltage increment during the discharge process ΔV_{inD} <2 V.

D. Design of primary magnetizing inductance

1) Charge process: When the converter operates in BCM during charge process, selecting fixed on-time t_{onC} ensures constant peak current. In this case, the duty cycle and the switching frequency are maximum at the final switching cycle (where the output voltage is close to the maximum target output voltage ($V_{o,max}$)), and minimum in the first switching cycle (where the output voltage is minimum or 0 V). The expression for the primary magnetizing inductance needed during charge process is

$$L_{mpC} = \frac{V_{in} t_{onC}}{I_{ppkC}} \tag{18}$$

For V_{in}=24 V, t_{onC}=9 μs, and I_{ppkC}=4.28 A the primary magnetizing inductance L_{mpC}=50.5 μH.

2) Discharge process: When the converter operates in BCM during discharge process, selecting variable on-time t_{onD} ensures constant peak current. In this case, the duty cycle and the switching frequency are maximum at the first switching

cycle (where the output voltage is close to the maximum target output voltage ($V_{o,max}$)), and minimum in the final switching cycle (where the output voltage is close to minimum discharge voltage or 0 V). When the capacitive load transfers the energy back to the source, the input voltage slightly increases by ΔV_{inD}. The magnitude of ΔV_{inD} depends on the value of the input capacitance C_{in}. The expression for the primary magnetizing inductance during discharge process is

$$L_{mpD} = \frac{\left(V_{in} + \Delta V_{inD}\right) t_{offD}}{I_{ppkD}} \tag{19}$$

The same primary magnetizing inductance ($L_{mp} = L_{mpC} = L_{mpD}$) should meet both (18) and (19).

From (15)-(19), it can be concluded that, if the number of secondary turns $N_s = N_{sC} = N_{sD}$ and the magnetizing inductance $L_{mp} = L_{mpC} = L_{mpD}$ then,

$$B_{max\,D} = \frac{I_{ppkD}}{I_{ppkC}} B_{maxC} = \frac{nI_{spkD}}{I_{ppkC}} B_{maxC} \tag{20}$$

The secondary discharge peak current I_{spkD} in any switching cycle limits the peak flux density B_{maxD} during the discharge process. Hence, from (20) suppose if a secondary discharge peak current of I_{spkD}=200 mA is chosen, then the flux density during discharge process becomes (for n=25, I_{ppkC}=4.26 A, B_{maxC}=0.3 T) B_{maxD}=0.35 T. The secondary discharge peak current i_{spkD} should be selected to avoid the core saturation.

III. QUASI RESONANT (QR) / VALLEY SWITCHING CONTROL

The schematic of the HV bidirectional flyback converter for charging and discharging a capacitive actuator/load is shown in Fig. 2 [7]. This section provides the theoretical analysis, to detect the valley points in the drain voltage of the MOSFETs M_p and M_s, respectively, with the assumption of C_{load}>>C_s or C_{D2}.

A. Analysis during charge process

Figure 4 shows the drain-to-source voltage of the primary MOSFET M_p during charge process, when the converter operates in DCM. The drain to source voltage V_{Mp} when V_{outC}<nV_{in} in DCM is [17]

$$V_{Mp}\left(t\right) = V_{in} + \left[\frac{V_{outC} + V_{onD2}}{n}\right] e^{-\left[\frac{R_p}{2\left(L_{mp}+L_{lkp}\right)}\right]t} \cos\left(w_{r1}t\right) \tag{21}$$

The ringing frequency f_{r1} in DCM is given by

$$f_{r1} = \frac{w_{r1}}{2\pi} = \frac{1}{2\pi\sqrt{(L_{mp} + L_{lkp})C_{lumpP}}} = \frac{1}{T_{osc1}} \tag{22}$$

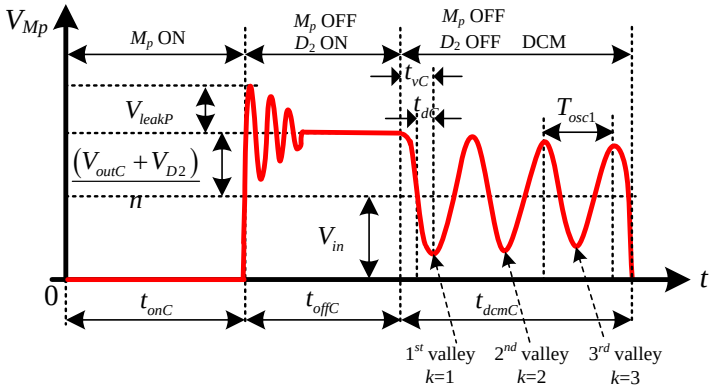

Fig. 4. Voltage across low voltage MOSFET M_p in DCM, during charge process when $V_{outC}<nV_{in}$.

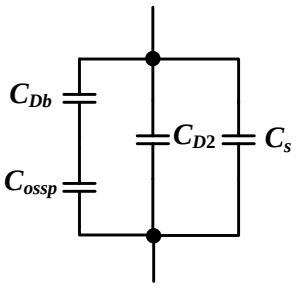

Fig. 5. Equivalent circuit on the secondary side to calculate the lumped capacitance referred to primary or secondary.

The lumped capacitance C_{lumpP} in terms of different capacitances in the converter is given by

$$C_{lumpP} \simeq C_{ossp} + n^2\left(C_s + C_{D2} + \frac{C_{Db}C_{osss}}{C_{Db} + C_{osss}}\right) \tag{23}$$

If the controller employs valley switching in DCM, the switching-node voltage V_{Mp} at k^{th} valley point is given by

$$V_{Mp}\big|_k = V_{in} - \left[\frac{V_{outC} + V_{onD2}}{n}\right] e^{-\left[\frac{R_p}{2(L_{mp}+L_{lkp})}(2k-1)\frac{T_{osc1}}{2}\right]} \tag{24}$$

The maximum number of valley points in terms of DCM period t_{dcmC} is given by [13]

$$k_{max} = round\left(\frac{t_{dcmC}}{T_{osc1}}\right) \tag{25}$$

The switching frequency at k^{th} valley point when the controller employs valley switching in DCM during charge process, is given by

$$f_{swC}\big|_k = \frac{1}{t_{onC} + t_{offC} + (2k-1)\dfrac{T_{osc1}}{2}} = \frac{1}{\dfrac{L_{mp} I_{ppkC}}{V_{in}} + \dfrac{L_{mp} I_{ppkC} n}{V_{outC}} + (2k-1)\dfrac{T_{osc1}}{2}} \tag{26}$$

At the end of each switching period, the energy stored in the non-linear lumped capacitance C_{lumpP} is dissipated when the MOSFET M_p is turned on [13], [19]. This paper considers achieving valley switching for M_p and M_s at first valley point. However, it is possible to optimize the switching loss or other losses in the converter by switching at other valley points. The switching loss due the lumped capacitance at the drain node, when the converter employs the valley switching at the first valley point (k=1) is

$$P_{sw1} = \frac{1}{2} C_{lumpP} \left[V_{Mp}\big|_{k=1} \right]^2 \left[f_{swC}\big|_{k=1} \right] \tag{27}$$

Table III provides the comparison of different operating modes such as, continuous conduction mode (CCM), DCM without valley switching, and DCM with valley switching, during charge process, in terms of switching frequency and drain-to-source voltage. When $V_{outC} > nV_{in}$ zero voltage switching (ZVS) of M_p occurs, and there is no energy loss due to the lumped capacitance, hence (27) is equal to 0 W.

TABLE III. COMPARISON OF DIFFERENT OPERATING MODES IN A FLYBACK CONVERTER DURING CHARGE PROCESS

Operating Mode	**Switching frequency during charge process f_{swC}**	**Drain-to-source voltage of M_p (V_{Mp}) at the beginning of next switching cycle during charge process**
CCM	$\dfrac{1}{t_{onC} + t_{offC}}$	$V_{in} + \dfrac{V_{TC}}{n}$ $V_{TC} = V_{outC} + V_{onD2}$
DCM (without valley switching)	$\dfrac{1}{\left[t_{onC} + t_{offC} + t_{dcmC} \right]}$	$V_{in} + \dfrac{V_{TC}}{n} e^{-\Delta_1} \cos(w_{o1} t_{dcmC})$ when $V_{outC} < nV_{in}$ $\Delta_1 = \left[\dfrac{R_p}{2L_{Tp}} t_{dcmC} \right]$ $L_{Tp} = L_{mp} + L_{lkp}$
DCM (with valley switching at k^{th} valley point)	$\dfrac{1}{\left[t_{onC} + t_{offC} + (2k-1)\dfrac{T_{osc1}}{2} \right]}$	$\begin{cases} V_{in} - \dfrac{V_{TC}}{n} e^{-\Delta_2}, \text{ if } V_{outC} < nV_{in} \\ 0 \ \Rightarrow \text{ZVS}, \ \text{ if } V_{outC} > nV_{in} \end{cases}$ $\Delta_2 = \left[\dfrac{R_p}{2L_{Tp}} (2k-1) \dfrac{T_{osc1}}{2} \right]$

B. Analysis during discharge proces

Figure 6 shows the voltage across HV diode D_2, drain-to-source voltages of the primary and HV MOSFETs during discharge process, when the converter operates in DCM. All equations given below are derived with the assumption of $V_{outD}>nV_{in}$. The drain to source voltage across the primary MOSFET M_p in DCM is [7]

$$V_{Mp}(t) = V_{in} - V_{in} e^{-\left[\frac{R_s}{2(L_{ms}+L_{lks})}\right]t} \cos(w_{r2}t) \tag{28}$$

The voltage across HV diode D_2 in DCM is [7]

$$V_{D2}(t) = (V_{outD} - V_{onDb}) + nV_{in} e^{-\left[\frac{R_s}{2(L_{ms}+L_{lks})}\right]t} \cos(w_{r2}t) \tag{29}$$

The voltage across HV diode D_b in DCM is

$$V_{Db}(t) = \left[\delta V_{leakD} + \delta n V_{in} \left\{ 1 - e^{-\left[\frac{R_s}{2(L_{ms}+L_{lks})}\right]t} \cos(w_{r2}t) \right\} \right] \tag{30}$$

where $V_{leakD} = I_{spkD}\sqrt{\frac{L_{lks}}{C_{lumpS}}}$ and $\delta = \frac{C_{oss2}}{C_{oss2}+C_{Db}}$

The voltage across HV MOSFET M_s in DCM is

$$V_{Ms}(t) = \left[(V_{outD} - V_{onDb}) + \delta V_{leakD} + \delta n V_{in} + nV_{in}(1-\delta) e^{-\left[\frac{R_s}{2(L_{ms}+L_{lks})}\right]t} \cos(w_{r2}t) \right] \tag{31}$$

The ringing frequency f_{r2} in DCM is given by

$$f_{r2} = \frac{w_{r2}}{2\pi} = \frac{1}{2\pi\sqrt{(L_{ms}+L_{lks})C_{lumpS}}} = \frac{1}{T_{osc2}} \tag{32}$$

The lumped capacitance C_{lumpS} in terms of different capacitances in the converter is given by

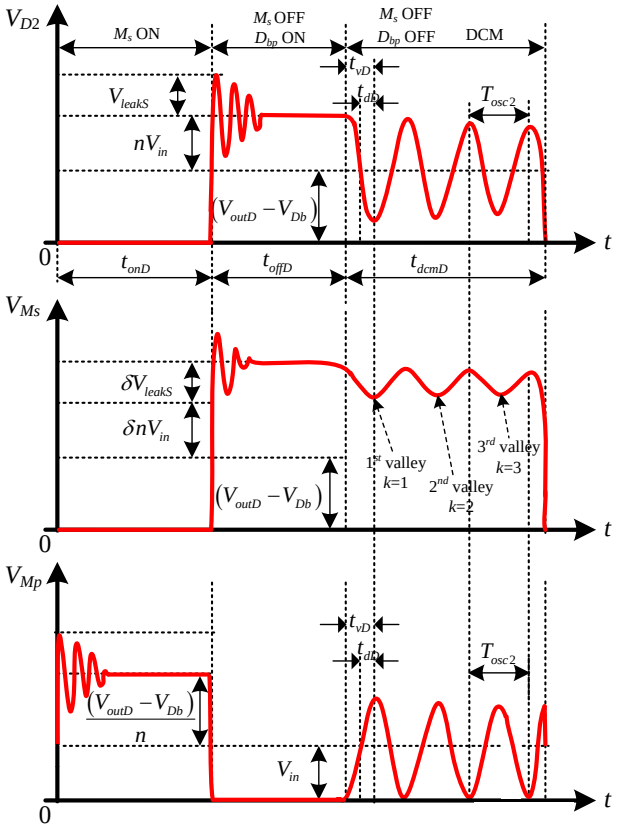

Fig. 6. Voltages across D_2, M_s and M_p in DCM, during discharge process when $V_{outD}>nV_{in}$.

$$C_{lumpS} \simeq \left(C_s + C_{D2} + \frac{C_{Db}C_{osss}}{C_{Db}+C_{osss}} \right) \tag{33}$$

If the controller employs valley switching in DCM during discharge process, the switching-node voltage V_{Ms} at k^{th} valley point is given by

$$V_{Ms}\big|_k = \left[\left(V_{outD} - V_{onDb}\right) + \delta V_{leakD} + \delta n V_{in} + nV_{in}\left(1-\delta\right) e^{-\left[\frac{R_s}{2\left(L_{ms}+L_{lks}\right)}\left(2k-1\right)\frac{T_{osc2}}{2}\right]} \right] \tag{34}$$

The switching frequency at k^{th} valley point when the controller employs valley switching in DCM during discharge process, is given by

$$\begin{aligned} f_{swD}\big|_k &= \frac{1}{t_{onD} + t_{offD} + \left(2k-1\right)\frac{T_{osc2}}{2}} \\ &= \frac{1}{\frac{L_{ms}I_{spkD}}{V_{outD}} + \frac{L_{mp}I_{spkD}n}{\left(V_{in}+\Delta V_{in}\right)} + \left(2k-1\right)\frac{T_{osc2}}{2}} \end{aligned} \tag{35}$$

At the end of each switching period, the energy stored in the non-linear lumped capacitance C_{lumpS} is dissipated when the switch M_2 is turned-on. Valley switching at the first valley point is employed during the discharge process, to reduce the discharging time or to increase the discharge speed. The switching loss due the lumped capacitance at the drain node, when the converter employs the valley switching at the first valley point (k=1) is

$$P_{sw2} = \frac{1}{2} C_{lumpS} \left[V_{M2}\big|_{k=1} \right]^2 \left[f_{swD}\big|_{k=1} \right] \tag{36}$$

Table IV provides the comparison of different operating modes during discharge process, in terms of switching frequency and drain-to-source voltage.

TABLE IV. COMPARISON OF DIFFERENT OPERATING MODES IN A FLYBACK CONVERTER DURING DISCHARGE PROCESS

Operating Mode	**Switching frequency during charge process f_{swD}**	**Drain-to-source voltage of M_s (V_{Ms}) at the beginning of the next switching cycle during the discharge process**
CCM	$\frac{1}{t_{onD} + t_{offD}}$	$V_{TD} + \delta V_{leakD} + \delta n V_{in}$ $V_{TD} = V_{outD} - V_{onDb}$
DCM (without valley switching)	$\frac{1}{\left[t_{onD} + t_{offD} + t_{dcmD}\right]}$	$\begin{bmatrix} V_{TD} + \delta V_{leakD} + \delta n V_{in} \\ n V_{in} (1-\delta) e^{-\Delta_3} \cos(w_{o2} t_{dcmD}) \end{bmatrix}$ $\Delta_3 = \left[\frac{R_S}{2L_{Ts}} t_{dcmD} \right]; L_{Ts} = L_{ms} + L_{lks}$
DCM (with valley switching at k^{th} valley point)	$\frac{1}{\left[t_{onD} + t_{offD} + (2k-1)\frac{T_{osc2}}{2}\right]}$	$\begin{cases} \begin{bmatrix} V_{TD} + \gamma_1 + \gamma_2 - \\ n V_{in} (1-\delta) e^{-\Delta_4} \end{bmatrix}, \text{if } V_{outD} > n V_{in} \\ \sim \delta V_{TD} + \gamma_1 + \gamma_2 \ , \quad \text{if } V_{outD} < n V_{in} \end{cases}$ $\Delta_4 = \left[\frac{R_S}{2L_{Ts}} (2k-1) \frac{T_{osc2}}{2} \right]$ $\gamma_1 = \delta V_{leakD}; \quad \gamma_2 = \delta n V_{in}$

IV. PROPOSED VALLEY SWITCHING CONTROL

A. Charge process

The bidirectional flyback converter with the control circuit to achieve the valley switching during charge and discharge processes is shown in Fig. 7. The input voltage and the drain voltage of primary MOSFET M_p, each scaled by a resistor divider network H_1 (3 kΩ and 90 kΩ), are compared using a high speed comparator TLV3501A. The comparator output becomes low (V_{comp}=0), when the drain voltage of M_p is lower than the input voltage V_{in}. The output signal of the comparator V_{comp} is sent to the 16-bit microcontroller (PIC18F45K22) which detects the comparator output change, and produces a fixed on-time pulse to enable the gate driver 1 to drive the MOSFET M_p.

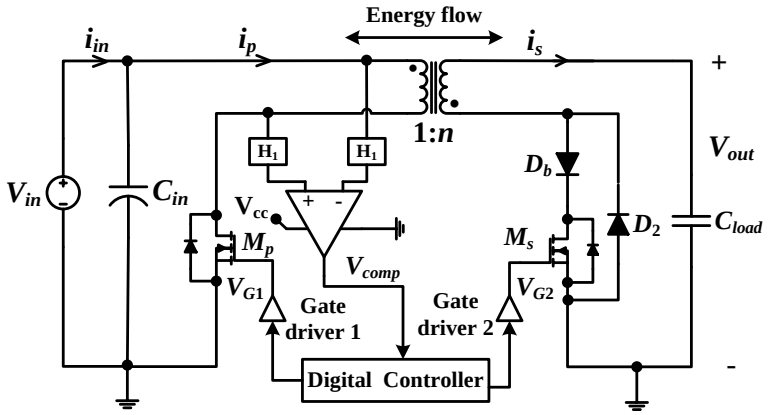

Fig. 7. Schematic of the bidirectional flyback converter with the control circuit to achieve valley switching.

To introduce the control approach, Figs. 8-10 provide experimental results in the flyback converter during charge process, in the case when the converter is driven at a fixed frequency without valley switching. From Fig. 8, it can be observed that there is a delay time t_{dC} (~1.04 μs) between the time when the comparator output goes low and the first valley point (at which the next switching cycle should start to achieve valley switching), in the drain voltage of M_p (V_{Mp}). The microcontroller provides the delay time t_{dC} such that the next turn-on cycle of M_p starts at the first valley point. The delay time t_{dC} can be calculated from the ringing frequency of V_{Mp} in DCM. The delay time t_{dC} is half of the time to reach first valley point t_{vC} (k=1) when $V_{outC}<nV_{in}$ (see Fig. 4). The expression for t_{dC} in terms of DCM ringing frequency f_{r1} is given by

$$t_{dC} = \frac{t_{vC}}{2} = \frac{1}{4 f_{r1}} = \frac{\pi}{2}\sqrt{\left(L_{mp} + L_{lkp}\right) C_{lumpP}} \tag{37}$$

As mentioned before, M_p is turned-on whenever the comparator output becomes low (V_{comp}=0), but the operation can be corrupted by ringing due to the leakage inductance L_{lkp}, which can also make the comparator output low (see Fig. 9). So, another delay time t_{dleak} (~1.5-2 μs) is provided by the microcontroller to disable the switching of M_p during this interval. When $V_{outC}>nV_{in}$ the drain voltage V_{Mp} reaches 0 V (with in 500 ns) before the delay time t_{dC}, which ensures zero voltage turn-on, as shown in Fig. 10. Hence, there is no capacitive switching loss during charge process when the output voltage $V_{outC}>nV_{in}$ (see Table III).

B. Discharge process

To achieve valley switching of HV MOSFET M_s during discharge process, only the information of the comparator output V_{comp} is used. The comparator output becomes high (V_{comp}=5 V), when the drain voltage of M_p is higher than the input voltage V_{in}. Similar to the charge process, the output signal of the comparator is sent to the microcontroller which produces a fixed or variable on-time pulse to enable the gate driver 2, to drive the MOSFET M_s. During the discharge process, since the output

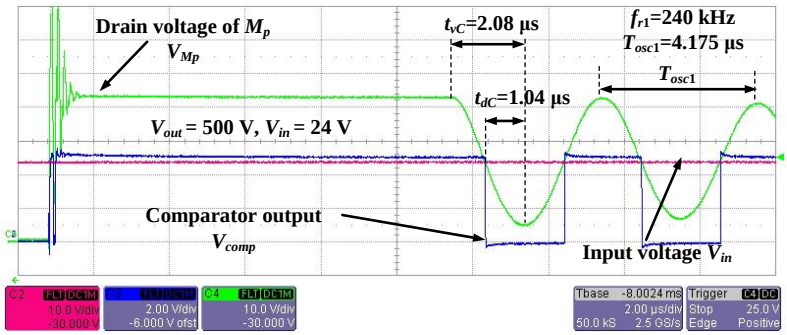

Fig. 8. Experimental results when M_p is driven with fixed frequency (V_{out}<600V) during charge process; CH2: V_{in}; CH3: V_{comp}; CH4: V_{Mp}.

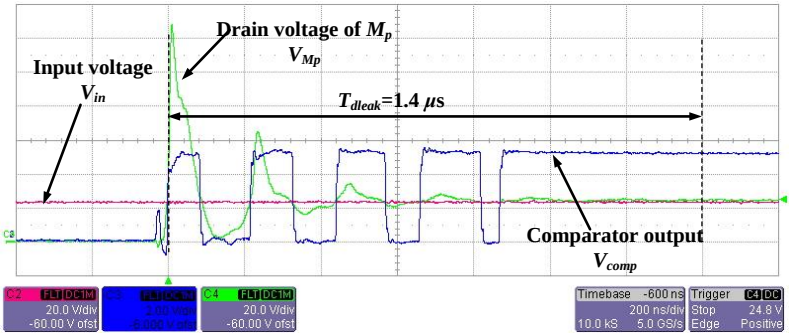

Figure 1. A zoomed view of Fig. 8 immediately after M_p is turned-off.

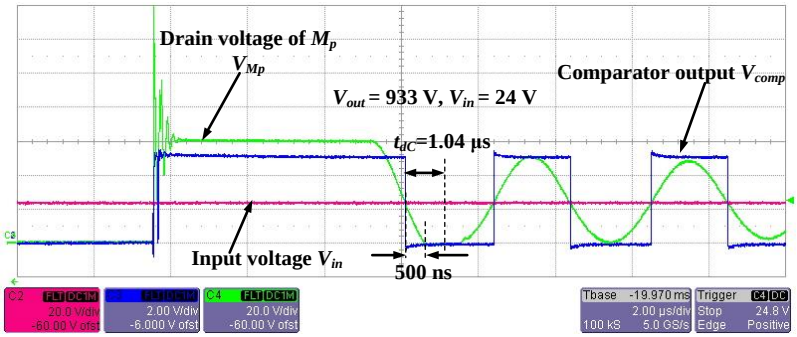

Fig. 10. Experimental results when M_p is driven with fixed frequency (V_{out}>600V) during charge process; CH2: V_{in}; CH3: V_{comp}; CH4: V_{Mp}.

voltage decreases, the on-time t_{onD} of M_s should be increased with the discharge time, to make the secondary discharge peak current I_{spkD} constant. Figures 11-14 provide experimental results in the flyback converter during discharge process, in the case when the converter is driven at a fixed frequency without valley switching. From Fig. 11, it can be observed that there is a delay time t_{dD} (~1.04 μs) between the time when the comparator output goes high and the first valley point (at which the next switching cycle should start to achieve valley switching), in the drain voltage of M_2 (V_{M2}). The microcontroller provides the delay time t_{dD} such that the next turn-on cycle of M_2 starts at the first valley point, and it can be calculated from the ringing

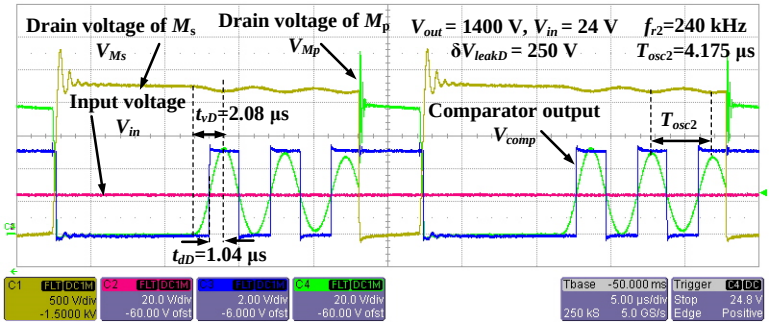

Fig. 11. Experimental results when M_s is driven with fixed frequency (V_{out}>600V) during discharge process; CH1: V_{Ms}; CH2: V_{in}; CH3: V_{comp}; CH4: V_{Mp}.

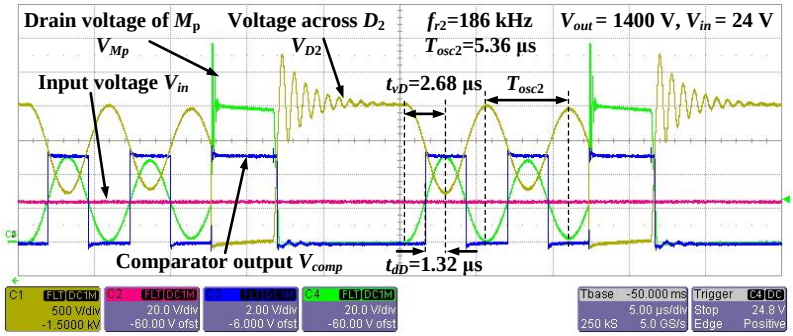

Fig. 12. Experimental results when M_s is driven with fixed frequency (V_{out}>600V) during discharge process; CH1: V_{D2}; CH2: V_{in}; CH3: V_{comp}; CH4: V_{Mp}.

frequency of V_{Ms} in DCM. The delay time t_{dD} is half of the time to reach first valley point t_{vD} (k=1) when V_{outD}>nV_{in} (see Fig. 6). The expression for t_{dD} in terms of DCM ringing frequency f_{r2} is given by

$$t_{dD} = \frac{t_{vD}}{2} = \frac{1}{4 f_{r2}} = \frac{\pi}{2}\sqrt{\left(L_{ms} + L_{lks}\right) C_{lumpS}} \tag{38}$$

When the HV probe is placed across D_2, the equivalent lumped capacitance C_{lumpS} is increased by ~9-10 pF due to the capacitance $C_{HVprobe}$ of the HV probe Lecroy PPE 4 kV. Due to this ringing frequency f_{r2} shown in Figs. 11 and 12 are different. When the HV probe is placed across M_s, C_{lumpS} remains unchanged, due to the series combination of D_b and M_s. When V_{outD}<nV_{in} the drain voltage V_{Ms} reaches $\sim \delta V_{TD} + \gamma_1 + \gamma_2$, whereas the voltage across D_2 becomes 0 V (see Table III) before the delay time t_{dD}, as shown Figs. 13 and 14, respectively.

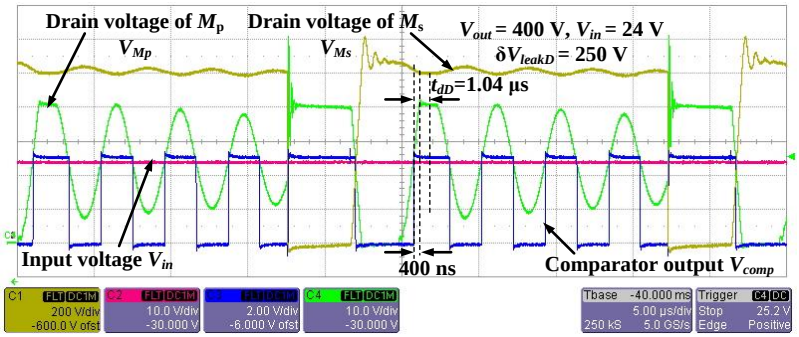

Fig. 13. Experimental results when M_s is driven with fixed frequency (V_{out}<600V) during discharge process; CH1: V_{Ms}; CH2: V_{in}; CH3: V_{comp}; CH4: V_{Mp}.

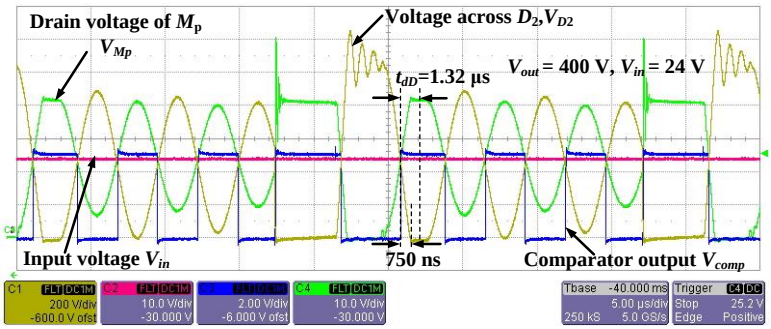

Fig. 14. Experimental results when M_s is driven with fixed frequency (V_{out}<600V) during discharge process; CH1: V_{D2}; CH2: V_{in}; CH3: V_{comp}; CH4: V_{Mp}.

V. VALLEY SWITCHING EXPERIMENTAL RESULTS

Tables V, VI and VII provide the converter specifications, components used in the converter, and flyback transformer parameters, respectively. The experimental prototype of the HV bidirectional flyback converter is shown in Fig. 15. The experimental results in the converter, tested with a film capacitive load of 400 nF, to validate the proposed valley switching technique are shown in Figs. 16-19. In Figs. 16 and 17, successful valley-switching operation at different output voltages during the charge process is shown. From Fig. 17, it is clear that the converter operates with zero voltage switching (ZVS) turn-on, and the primary current is negative before the switch is turned-on. In Fig. 18, successful valley-switching operation during discharge process is shown. As explained in Section III, the first valley voltage in the drain to-source voltage of M_s is not very low, compared to the first valley voltage in HV diode voltage V_{D2} (due to the series combination of D_b and M_s). The capacitive switching loss is directly proportional to the voltage across the HV MOSFET when it is turned-on. This is one of the reasons for the low energy efficiency during the discharge process.

TABLE V. SPECIFICATIONS OF THE BIDIRECTIONAL FLYBACK CONVERTER

Parameter	Value
Input voltage V_{in}	24 V
Output voltage V_{out}	0-2.5 kV
Capacitance of the load C_{load}	400 nF
On time of M_1 during charge process t_{onC}	9 μs
On times of M_2 during discharge process t_{onD}	[2 μs, 3 μs, 5 μs, 10 μs, 20 μs, 150 μs, 200 μs]

TABLE VI. COMPONENTS USED IN THE HV CONVERTER

Component	Value
Primary MOSFET M_1	250V, 16A [FQD16N25CTM]
HV MOSFET M_2	4.5 kV, 200 mA, 750 Ω 250V, 16A [FQD16N25CTM] [IXTA02N450HV] / 4 kV, 300 mA, 290 Ω [IXTV03N400S]
HV diode D_b / D_2	5 kV, 150 mA [SXF6525]
Gate driver	EL7104
Comparator	4.5 ns Rail-to-Rail, TLV3501A
Film capacitive load	400 nF, 3 kV [WIMA]

TABLE VII. FLYBACK TRANSFORMER PARAMETERS

Parameter	Value
Core used / material used	PQ 20/20 / P type
Primary N_p / secondary turns N_s	12 / 300
Primary L_{mp} / secondary magnetizing inductance L_{ms}	47.5 μH / 30 mH
Leakage inductance referred to primary L_{lkp} / secondary L_{lks}	990 nH / 620 μH
Self-capacitance of secondary winding C_s (from the Impedance analyzer)	6 pF
Self-capacitance C_s from frequencies f_{r1}, f_{r2}	12.5 pF
Diameter of primary/secondary winding	0.5 mm (TEX-E)/ 0.11 mm
DC resistance of primary R_p /secondary R_s	62 mΩ / 14 Ω
Number of layers of primary/secondary	1 / 4

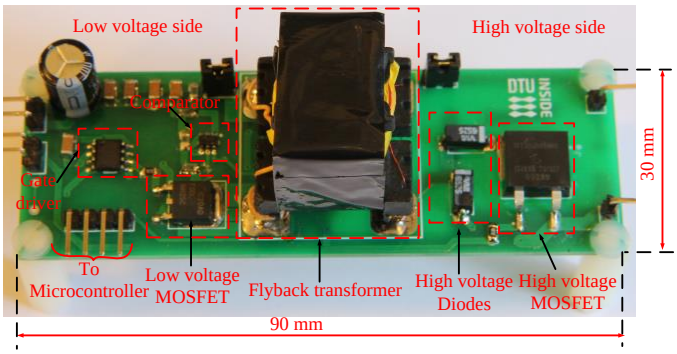

Fig. 15. Experimental prototype of the HV bidirectional flyback converter with a 4.5 kV MOSFET on the HV side.

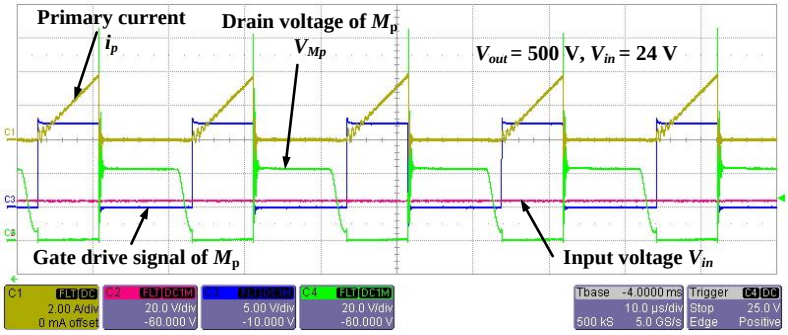

Fig. 16. Experimental results when the converter is operated with valley switching during charge process; CH1: i_p; CH2: V_{in}; CH3: V_{G1}; CH4: V_{Mp}.

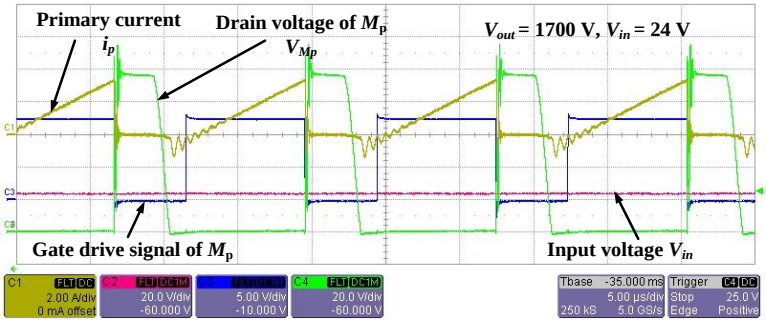

Fig. 17. Experimental results with valley switching operation during the charge process; CH1: i_p; CH2: V_{in}; CH3: V_{G1}; CH4: V_{Mp}.

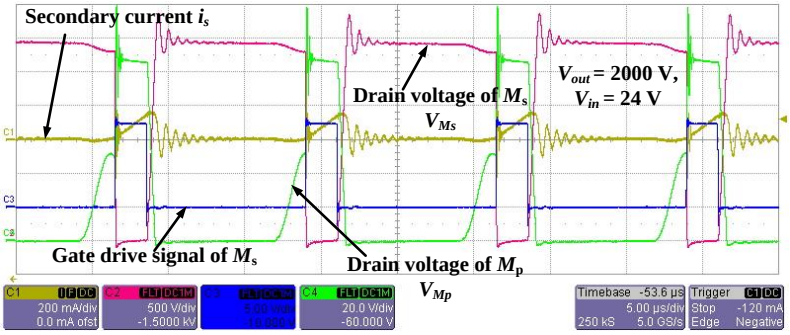

Fig. 18. Experimental results with valley switching operation during discharge process; CH1: i_s; CH2: V_{Ms}; CH3: V_{G2}; CH4: V_{Mp}.

The bidirectional operation of the HV converter at 2.5 kV output voltage is shown in the Fig. 19. As provided in Table V, due to constant turn on-time t_{onC} for M_p during charge process, the primary current I_{ppkC} is constant. During discharge process, employing variable turn on-time t_{onD} for M_s makes the secondary current (hence the primary current) I_{spkC} almost constant. The energy efficiency measurements

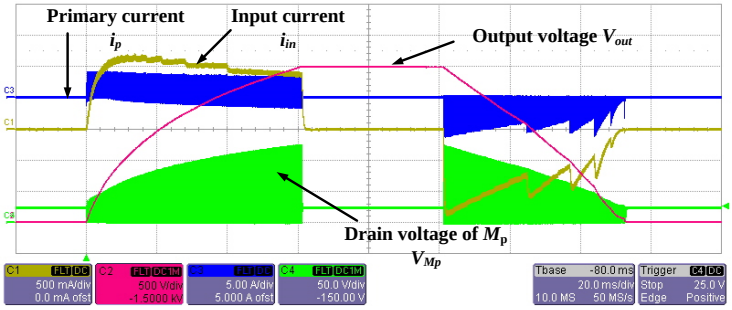

Fig. 19. Experimental waveforms showing the bidirectional operation at 2.5 kV output voltage. CH1: i_{in}; CH2: V_{out}; CH3: i_p; CH4: V_{M1}.

during charge and discharge processes [7] with 4 kV and 4.5 kV MOSFETs on the HV side are shown in Fig. 20. The charge energy efficiency for both 4 kV and 4.5 kV MOSFETs is above 90 %, for the output voltage range 750 V<V_{out}<2.2 kV, with a maximum efficiency of 92 %. The charge energy efficiency for the output voltage range 2.2 kV<V_{out}<2.5 kV is between 88-90 %. The discharge energy efficiency for 4 kV MOSFET is lower than the charge efficiency due to the fact that valley voltage in V_{M2} is not equal to valley voltage in V_{D2} during DCM. The junction capacitance of D_b is ~0.7 pF, the output capacitance of the HV MOSFET is ~10-12 pF. The lumped capacitances are C_{lumpP}=~9 nF and C_{lumpS}=~14 pF, respectively. Some of the reasons for very low discharge energy efficiency for 4.5 kV MOSFET are due to its high on resistance (750 Ω), high gate input resistance (76 Ω).

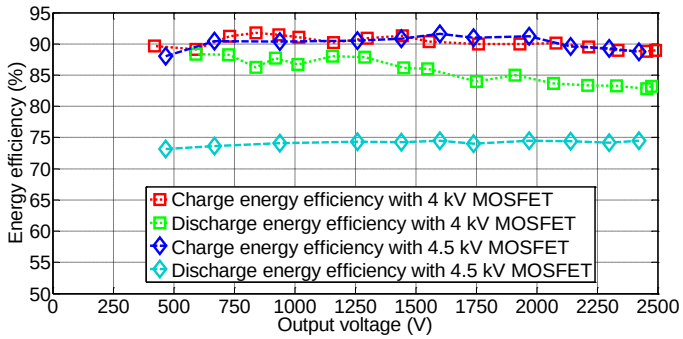

Fig. 20. Energy efficiency measurements.

VI. CONCLUSIONS

The valley switching technique for a bidirectional flyback converter, driving a capacitive load has been successfully implemented using a 16-bit microcontroller, during charge and discharge processes, respectively. Using the proposed simple valley switching technique, the flyback converter is able to charge and discharge the capacitor load within minimum time (or with maximum speed). To charge and discharge from 2.4 kV output voltage using a 4 kV MOSFET, the flyback converter has

charge and discharge energy efficiencies of 89% and 84%, respectively. The future work involves further investigation of proposed control technique with 4.5 kV MOSFET, and testing the HV drivers with the incremental DEAP actuator.

REFERENCES

[1] R. E. Pelrine, R. D. Kornbluh, and J. P. Joseph, "Electrostriction of polymer dielectrics with compliant electrodes as a means of actuation," in *Proc. Sensors and Actuators A*, vol. 64, pp. 77–85, 1998.

[2] M. Tryson, H. E. Kiil, M. Benslimane, "Powerful tubular core free dielectric electro active polymer (DEAP) push actuator," in *Proc. SPIE, Electroactive Polymer Actuators and Devices (EAPAD)*, vol. 7287, 2009.

[3] R. Sarban, B. Lassen, M. Willatzen, "Dynamic Electromechanical Modeling of Dielectric Elastomer Actuators With Metallic Electrodes," *IEEE/ASME Transactions on Mechatronics*, vol. 17, no. 5, pp. 960-967, Oct. 2012.

[4] P. Thummala, Z. Zhang, M. A. E. Andersen, S. Rahimullah, "Dielectric electro active polymer incremental actuator driven by multiple high-voltage bi-directional DC-DC converters," in *Proc. IEEE ECCE USA*, pp. 3837-3844, 15-19 Sept. 2013.

[5] R. E. Pelrine, R. D. Kornbluh, Q. Pei, and J. P. Joseph, "High-speed electrically actuated elastomers with strain greater than 100%," in *Proc. Science*, vol. 287, pp. 836–839, 2000.

[6] T. Andersen, M. S. Rødgaard, O. C. Thomsen, M. A. E. Andersen, "Low voltage driven dielectric electro active polymer actuator with integrated piezoelectric transformer based driver," in Proc. SPIE, vol. 7976, p. 79762N, 2011.

[7] P. Thummala, Z. Zhang and M. A. E. Andersen, "Bi-directional Flyback Converter for Capacitive Actuator," in *Proc. EPE*, pp. 1-10, Sept. 2013.

[8] LT3751 datasheet, "High voltage capacitor charger controller with regulation," Linear Technology Corporation, USA, Online available: http://cds.linear.com/docs/en/datasheet/3751fc.pdf.

[9] N. O. Sokal, R. Redl, "Control algorithms and circuit designs for optimal flyback-charging of an energy storage capacitor (e.g., for flash lamp or defibrillator)," *IEEE Trans. on Power Electronics*, vol. 12, no. 5, pp. 885-894, Sep. 1997.

[10] M. Kazimierczuk, "High-Frequency Magnetic Components," 2nd Ed. John Wiley and Sons Ltd., 2014.

[11] R. W. Erickson and D. Maksimovic, "Fundamentals of Power Electronics," 2nd ed. New York: Springer, 2001.

[12] P. Thummala, H. Schneider, Z. Zhang, A. Knott, M. A. E. Andersen, "Optimization of a bi-directional flyback converter for a high voltage capacitor charging application," in *Proc. IEEE APEC*, pp. 2556-2563, March 2014.

[13] H. K. Sang, D. Maksimovic, I. Cohen, "Efficiency Optimization in Digitally Controlled Flyback DC–DC Converters Over Wide Ranges of Operating Conditions," *IEEE Trans. on Power Electronics*, vol. 27, no. 8, pp. 3734-3748, Aug. 2012.

[14] Y. Panov and M. M. Jovanovi´c, "Adaptive off-time control for variable frequency, soft-switched flyback converter at light loads," *IEEE Trans. Power Electronics*, vol. 17, no. 4, pp. 596–603, Jul. 2002.

[15] Y. Panov and M. M. Jovanovi´c, "Performance evaluation of 70-W two stage adapters for notebook computers," in *Proc. IEEE APEC*, 1999, pp. 1059–1065.

[16] Y. Park and H. Choi, "A efficiency improvement methodology for active mode efficiency regulation," in *Proc. IEEE Int. Symp. Electron. Environ.*, 2008, pp. 1–5.

[17] Z. Ling, T. Liang, L. Yang, and T. Li, "Design and implementation of interleaved quasi-resonant DC–DC flyback converter," in *Proc. IEEE Power Electron. Drive Syst.*, 2009, pp. 429–433.

[18] C. P. Basso, "Switch-mode power supplies spice simulations and practical designs," 2008.

[19] H. Schneider, P. Thummala, L. Huang, Z. Ouyang, A. Knott, Z. Zhang, M. A. E. Andersen, "Investigation of transformer winding architectures for high voltage capacitor charging applications," in *Proc. IEEE APEC*, pp. 334-341, March 2014.

Appendix M

Parallel input parallel output high voltage bi-directional converters for driving dielectric electro active polymer actuators

---

SPIE Smart Structures/NDE on Electroactive Polymer Actuators and Devices (EAPAD) 2014

Parallel input parallel output high voltage bi-directional converters for driving dielectric electro active polymer actuators

P. Thummala*[a], Z. Zhang*[a], M. A. E. Andersen*[a], S. Rahimullah**[b]
[a]Technical University of Denmark, Electronics group, Dept. of Electrical Eng., Oersteds Plads, Building 349, Kgs. Lyngby, 2800 DENMARK;
[b]Danfoss PolyPower A/S, Nordborg, 6430 DENMARK;

ABSTRACT

Dielectric electroactive polymer (DEAP) actuators are capacitive devices which provide mechanical motions when charged electrically. The charging characteristics of a DEAP actuator depends on its size, voltage applied to its electrodes, and its operating frequency. The main idea of this paper is to design and implement driving circuits for the DEAP actuators for their use in various applications. This paper presents implementation of parallel input, parallel output, high voltage (~2.5 kV) bi-directional DC-DC converters for driving the DEAP actuators. The topology is a bi-directional flyback DC-DC converter incorporating commercially available high voltage MOSFETs (4 kV) and high voltage diodes (5 kV). Although the average current of the aforementioned devices is limited to 300 mA and 150 mA, respectively, connecting the outputs of multiple converters in parallel can provide a scalable design. This enables operating the DEAP actuators in various static and dynamic applications e.g. positioning, vibration generation or damping, and pumps. The proposed idea is experimentally verified by connecting three high voltage converters in parallel to operate a single DEAP actuator. The experimental results with both film capacitive load and the DEAP actuator are shown for a maximum charging voltage of 2 kV.

Keywords: dielectric electro active polymer, high voltage power converters, capacitive actuator, energy efficiency, flyback converter

1. INTRODUCTION

Dielectric electro active polymer (DEAP) is a very thin incompressible silicone elastomer film sandwiched between two metallic electrodes [1], [2]. The polymer film expands in area and contracts in thickness, as a result of the electrostatic pressure generated by the applied voltage to the electrodes [3]. The thickness of the polymer film is ~40 μm and the DEAP material requires high electric field strength of ~60 V/μm [4], [5], hence the DEAP actuator requires high DC voltage (~2.5 kV) to generate sufficient force and displacement. DEAP can be considered as a pure capacitive load with very low leakage current (~0.2-1 nA/nF). DEAP when actuated, changes its capacitance which is proportional to the strain.

DEAP actuators have the potential to be an effective replacement for many conventional actuators for example piezo, hydraulic, and pneumatic actuators, because of their unique characteristics such as large strain, light weight, low noise operation, and high flexibility [6]. Some of the prospective applications for the DEAP actuator are in line heating valves, loudspeakers, and wind turbine flaps, etc. Moreover, the DEAP actuator technology has the potential to be used in several industries such as automotive, aeronautics, space and medicine.

While the focus has been given to establish the electromechanical characteristics [7] and application-based designs of the actuators, less research has been done in implementing the necessary electrical drivers for different DEAP actuator applications. Commercially available laboratory equipment such as high voltage (HV) power supplies [8] and/or HV amplifiers are often used to operate the DEAP actuators. Although such HV equipment provides the necessary signals for laboratory experiments, they are quite inadequate in real applications as they are expensive and bulky. Furthermore, a new incremental DEAP actuator proposed in [9] requires HV bi-directional DC-DC converters to discharge the actuators besides transferring some of the energy stored in the capacitive actuators to the source [10], [11]. Consequently, HV drivers specifically designed to operate the DEAP actuators while being compatible with the real applications are needed. Scalability of such HV drivers is of outmost importance for their use in various applications with different operational requirements.

*{pthu, zz, ma}@elektro.dtu.dk; http://www.ele.elektro.dtu.dk/; **sarban@danfoss.com; http://www.polypower.com/;

Electroactive Polymer Actuators and Devices (EAPAD) 2014, edited by Yoseph Bar-Cohen, Proc. of SPIE Vol. 9056, 90561N · © 2014 SPIE · CCC code: 0277-786X/14/$18 · doi: 10.1117/12.2044887

Previous work on HV drivers for the DEAP actuators demonstrated a low voltage piezoelectric transformer based DEAP solution [12], and a HV bi-directional flyback converter [11] topology to drive the incremental DEAP actuator [9], which utilized the control IC LT3751 [13] to achieve charge (boundary conduction mode control) and discharge (discontinuous conduction mode control) operations. The bi-directional flyback converter implemented in [11] utilized the commercially available HV MOSFET (IXTV03N400S: 4 kV, 300 mA) and HV diode (SXF6525: 5 kV, 150 mA), for charging and discharging the capacitive actuator.

The flyback converter is suitable for high voltage and low power applications due to its simple structure and low component count [13]. Control algorithms for optimal-flyback charging of a capacitive load have been proposed in [14]. Figure 1 provides the circuit diagram of the HV bi-directional flyback converter [15]. In Fig. 1, V_{in}, V_{out}, C_{in}, C_{load}, i_p, i_s, L_p, L_s, n, M_p and M_s are input voltage, output voltage, input capacitance, load capacitance or capacitance of the actuator, primary current, secondary current, primary magnetizing inductance, secondary magnetizing inductance, transformer turns ratio, primary MOSFET and secondary HV MOSFET, respectively. Figure 2 shows the ideal switching waveforms of a single bi-directional HV flyback converter. In Fig. 2, I_{ppkC}, I_{spkC}, I_{ppkD}, I_{spkD}, and T_{delay} are primary and secondary peak currents during charge process, primary and secondary peak currents during discharge process, and the delay time between charge and discharge processes, respectively.

The capacitive load C_{out} during charge process is charged to high voltage (0 V→2.5 kV) through the HV diode D_s. The reason for using the HV diode D_s instead of utilizing the body diode of M_s is due to the high reverse recovery time (2.8 µs) of the body diode. Another HV diode D_b is added in series with M_s to block the current through the body diode of M_s during charge process. During charge process, the converter operates with boundary conduction mode (BCM) control, constant on-time and variable switching frequency, and during discharge process the converter operates with discontinuous conduction mode (DCM) control, constant off-time and constant switching frequency [11].

As the primary peak current I_{ppkC} increases, the energy stored in the transformer primary magnetizing inductance ($0.5L_p i_{ppkC}^2$) increases when M_p is turned on. Ideally, the same energy is transferred to the capacitive load ($0.5C_{load}\Delta V_{out}^2$) when M_p is turned-off, where ΔV_{out} is the absolute difference between initial and final output voltages in any off-switching cycle during charge process. Therefore, as the peak current I_{ppkC} during charge process increases, the capacitive actuator is charged to higher voltage in each switching cycle, which ultimately decreases the total charging time (to charge C_{load} from 0 V→2.5 kV) T_{charge} of the capacitive actuator. The total charging time T_{charge} during charge process is inversely proportional to the peak primary current I_{ppkC} when M_p is turned-on. When M_p is turned-off, the current i_s flows through D_s on the secondary side and charges the capacitive load C_{load}. Similarly, the total discharging time (to discharge C_{load} from 2.5 kV→0 V) $T_{discharge}$ during discharge process is inversely proportional to the peak secondary current I_{spkD} when M_s is turned-on.

The current i_s flows through the series combination of the HV diode D_b and the high voltage MOSFET M_s, when M_s is turned-on. Therefore, for a given charge and discharge control strategy, how fast the DEAP actuator can be charged or discharged depends on the maximum peak current that the HV semiconductors (D_s, D_b and M_s) on the secondary side of the HV bi-directional flyback converter can withstand. The maximum average currents of the HV MOSFET M_s and the HV diode D_s (= D_b, same HV diode) are 300 mA and 150 mA, respectively.

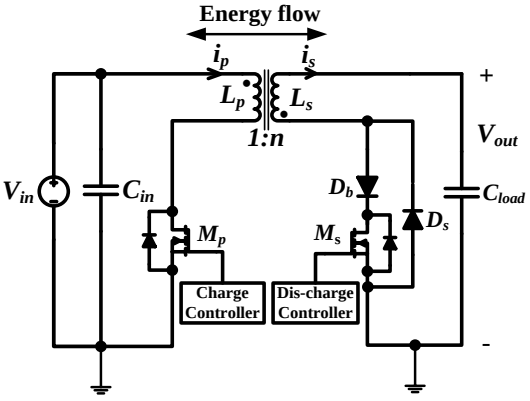

Figure 1. Circuit diagram of the high voltage bi-directional flyback converter for driving a capacitive actuator.

The maximum peak current on the secondary side during charge process I_{spkC} is limited by the HV diode D_s. Likewise, the maximum peak current on the secondary side during discharge process I_{spkD} is limited only by the HV diode D_b, but

not by the HV MOSFET M_s, since during discharge process secondary current i_s flows through the series combination of HV diode D_b and HV MOSFET M_s. Hence, minimum achievable charging and discharging times of the proposed bi-directional flyback converter depend only on the current rating of the HV diode used in the converter.
Operating the DEAP actuators at high frequency needs lower charging and discharging times. The two possible solutions for are: by connecting multiple HV bi-directional flyback converters in parallel (Fig. 3) or by connecting and controlling the HV semiconductors in parallel (Fig. 5). This paper focuses only on the first solution, i.e. by connecting the outputs of the multiple HV converters in parallel with the same power source. Therefore, the main objective of this paper is to quickly charge and discharge the capacitive actuator by connecting multiple high voltage converters in parallel. A comparison of the aforementioned two solutions is given in Table 1.
This paper is organized as follows: Section 2 describes the proposed HV driving circuits. Section 3 provides the simulation results of the HV bi-directional converters connected in parallel. Section 4 discusses the specifications of the converters and the HV transformers, details of the experimental setup, and the experimental results followed by the conclusion in Section 5.

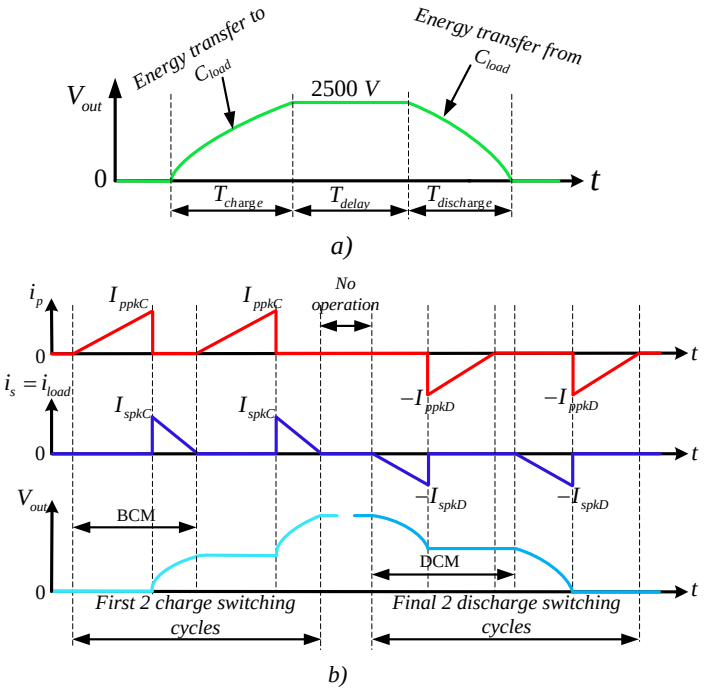

Figure 2. Ideal switching waveforms of a single high voltage bi-directional flyback converter, a) output voltage variation in the complete charge and discharge processes, b) Two switching cycles during charge and discharge processes; BCM- boundary conduction mode, DCM- discontinuous conduction mode.

2. PROPOSED HIGH VOLTAGE DRIVING CIRCUITS

If a given DEAP actuator application demands much lower charging and discharging times than those obtained from a single HV bi-directional flyback converter, it is simple and more convenient to parallel connect a number of bi-directional converter modules, since for a given specification it is more flexible to change the number of parallel converter modules. In Fig. 3 the circuit diagram of the two input-parallel and output-parallel [17] HV bi-directional converters is shown. The assumption associated with these parallel converters is that the two HV converters are almost identical. However, it is practically impossible to design identical HV transformers with exactly same parameters, viz. DC/AC resistances, leakage inductances, and self-capacitances. Since the capacitive actuator charges and discharges with constant peak current control during both charge and discharge processes, respectively, it is expected that the current supplied to and drawn from the actuator would be shared between the two high voltage DC-DC converters. Figure 4 provides the ideal switching waveforms for the two parallel HV bi-directional flyback converters. Ideally, the

current supplied to the load during charge process and the current drawn from it during discharge process are doubled, but practical HV transformers will have a small difference in their parameters, hence, the secondary currents are not represented in phase as shown in Fig. 4 b) (see Figs. 25 and 26). The total charging and discharging times with two parallel converters become half of those with a single converter, due to increase in the output voltage for each secondary current pulse.

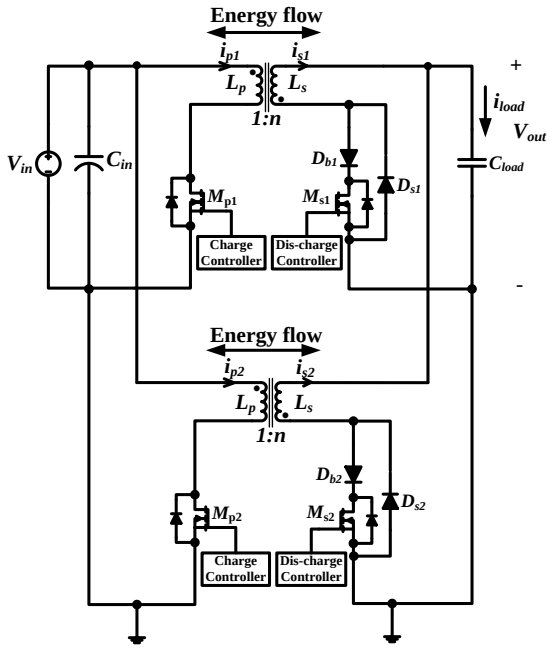

Figure 3. Circuit diagram of two parallel input parallel output high voltage bi-directional converters to drive a single capacitive load.

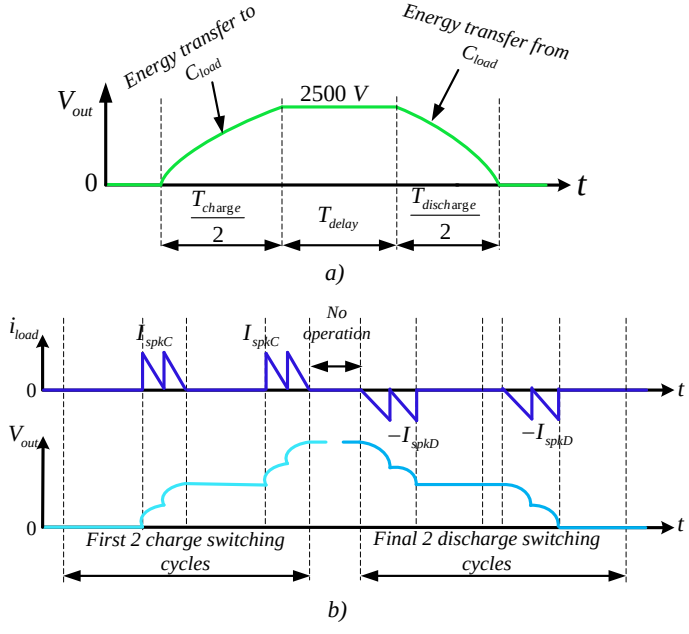

Figure 4. Ideal switching waveforms of two parallel input parallel output high voltage bi-directional flyback converters, a) output voltage variation in the complete charge and discharge processes, b) Two switching cycles during charge and discharge processes.

The capacitive actuator can also be charged and discharged quickly by employing the converter as shown in Fig. 5, in which the HV semiconductors are connected in parallel on the secondary side. The assumptions associated with this topology is that the secondary current is equally shared between the HV diodes D_{s1} and D_{s2} during charge process, also the secondary current is equally shared between the series combination of the HV diodes D_{b1} and D_{b2} with the HV MOSFETS M_{s1} and M_{s2}, respectively during discharge process, finally the HV MOSFETs M_{s1} and M_{s2} are synchronously controlled during discharge process. The HV transformer in the converter shown in Fig. 5 needs to be designed to handle twice the peak current of the converter shown in Fig. 3 is designed for. In Fig. 5, the new primary and secondary inductances, and the turns ratio of the HV transformer are L_{p1}, L_{s1}, and n_1 respectively. Even though the topology mentioned in Fig. 5 requires less number of components compared to the topology shown in Fig. 3, achieving synchronizing control of M_{s1} and M_{s2} and current sharing through HV diodes is very complex. Figure 6 provides the ideal switching waveforms of the topology mentioned in Fig. 5.

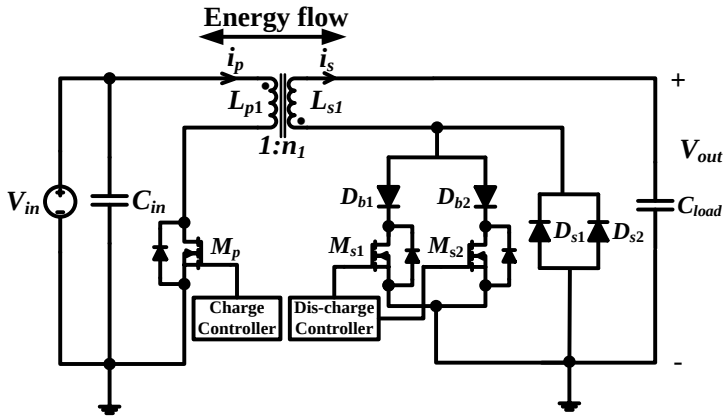

Figure 5. Circuit diagram of a bi-directional flyback with high voltage semiconductors connected in parallel on the secondary side to drive a capacitive load (n_1>n).

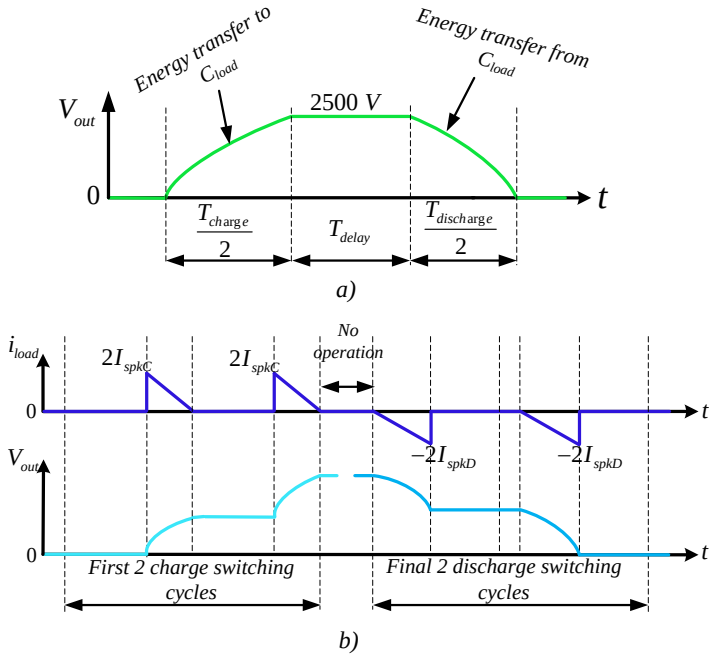

Figure 6. Ideal switching waveforms of two high voltage bi-directional flyback converters connected in parallel, a) output voltage variation in the complete charge and discharge process, b) Two switching cycles during charge and discharge processes (i_{Ds1C}=i_{Ds2C}=I_{spkC} ; i_{Ds1D}=i_{Ds2D}=I_{spkD} ; C, D-stands for charge and discharge processes, respectively).

An input parallel connected and outputs series connected modular converter system is proposed in [18] for energy harvesting application. Figure 7 provides a modular parallel input parallel output HV bi-directional flyback converter circuit, in which *p* modules are connected in parallel to charge the DEAP actuator. In the Fig. 8, the ideal switching waveforms are shown. Due to the non-identical HV transformers, the load current with the *p* converters is drawn as shown in Fig. 8 b).

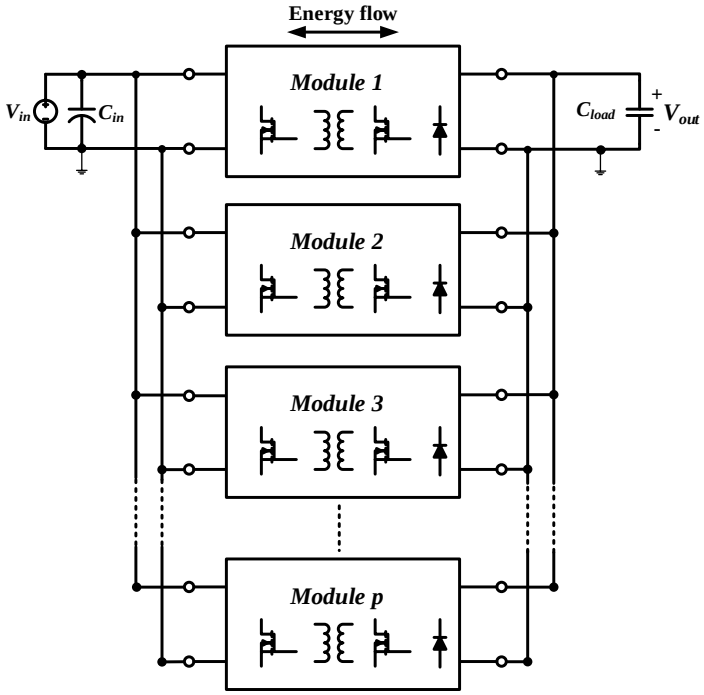

Figure 7. Proposed conceptual block diagram with *p* parallel input parallel output, high voltage bi-directional converters to drive a single capacitive load.

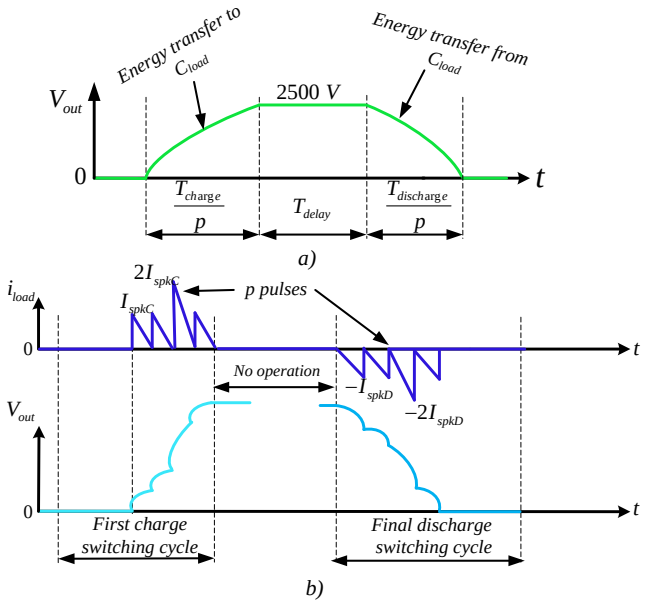

Figure 8. Ideal switching waveforms of *p* high voltage bi-directional flyback converters connected in parallel: a) output voltage variation in the complete charge and discharge process, b) Two switching cycles during charge and discharge processes.

Table 1. Comparison of the p parallel input parallel output bi-directional flyback converters (solution 1) and the bi-directional flyback with q high voltage semiconductors combinations (parallel connection of D_s, with series connection of D_b and M_s) connected in parallel on the secondary side (solution 2), for the same power level

Comparing parameters	Solution 1	Solution 2
Number of low voltage MOSFETs	p	1
Number of high voltage MOSFETs	p	q
Number of high voltage diodes	$2p$	$2q$
Number of transformers	p	1
Cost of implementation	High	High
Complexity with winding high voltage transformers	Very high	Low
Control complexity	Low	Very high
Filter size requirement	Low	High
Electromagnetic interference (EMI)	Low	High

3. SIMULATION RESULTS

The bi-directional flyback converter is simulated in the LTSpice software. In the simulation a maximum number of p=3 HV converter modules are used. The specifications of the converter, the simulation and experimental parameters of the high voltage transformers, and the components used in each converter are shown in Tables 2, 3 and 4, respectively. The simulations are performed without adding any leakage inductance and self-capacitances. In the simulations, the Spice-models of HV diode and HV MOSFET models are used. Figure 9 provides the simulation results for a single HV bi-directional flyback converter, for a maximum output voltage of ~ 2 kV. In Fig. 10, the simulation results of the three parallel input parallel output bi-directional high voltage converters are shown.

The zoomed simulation results of three parallel input parallel output HV bi-directional flyback converters are shown in Fig. 11. Since the high voltage transformers are slightly different (see Table 2), the currents and the voltages of three HV converters are not synchronized and have a small phase-shift among them as shown in Figs. 11 a) and b).

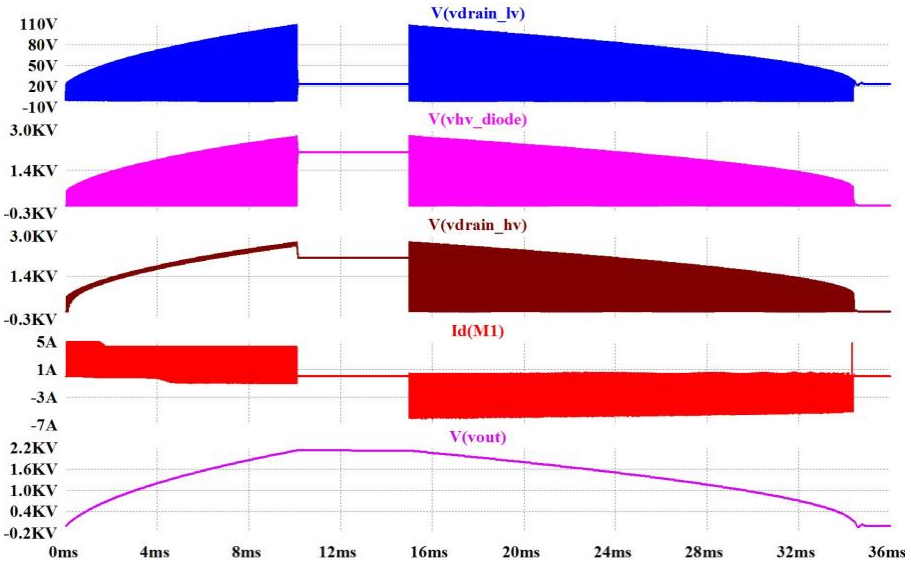

Figure 9. Simulation results of a single HV bi-directional flyback converter. V(vout) – Output voltage; Id(M1) – current through primary MOSFET; V(vdrain_hv) – drain voltage across high voltage MOSFET; V(vhv_diode) – voltage across high voltage diode D_s; V(vdrain_lv) – drain voltage across low voltage MOSFET;

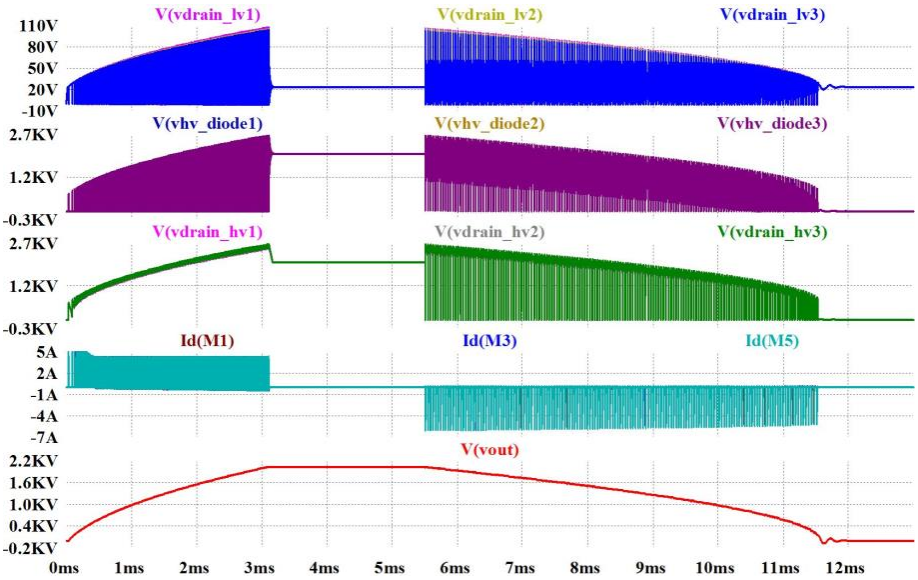

Figure 10. Simulation results of three parallel input parallel output high voltage bi-directional flyback converters. V(vout) – Output voltage; Id(M1), Id(M3) , Id(M5) – currents through primary MOSFET 1, 2 and 3 respectively; V(vdrain_hv) – drain voltage across high voltage MOSFET; V(vhv_diode) – voltage across high voltage diode D_s; V(vdrain_lv) – drain voltage across low voltage MOSFET; The numbers 1, 2 and 3 in the above three voltages stands for HV converter 1, 2 and 3, respectively;

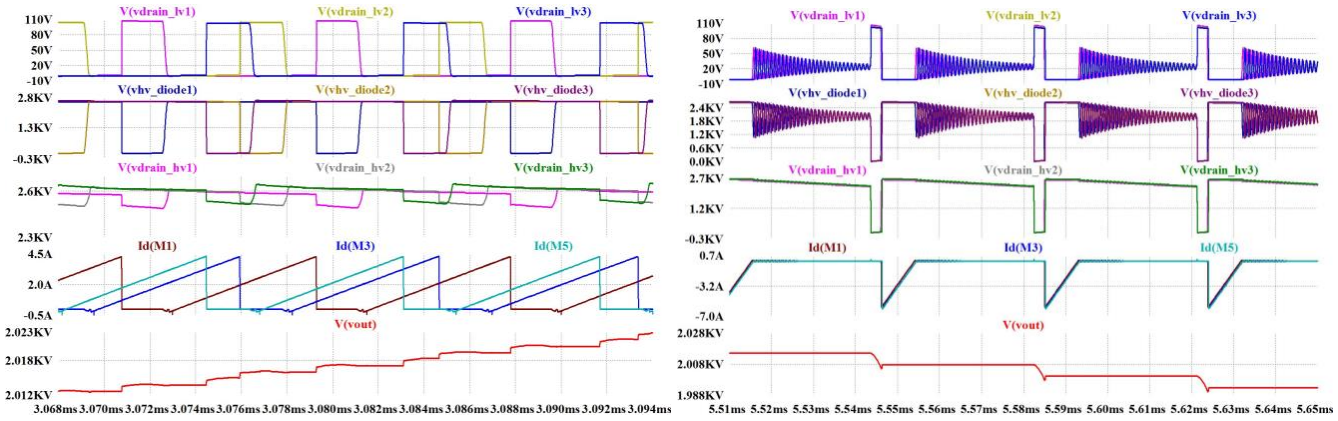

(a) (b)

Figure 11. Zoomed simulation results of three parallel input parallel output high voltage bi-directional flyback converters, a) during charge process and b) during discharge process.

4. EXPERIMENTAL RESULTS

The proposed idea to quickly charge and discharge the capacitive load using the parallel input parallel output high voltage bi-directional DC-DC converters is experimentally verified. Both film capacitive load and the DEAP actuator have been tested with the high voltage parallel input parallel output drivers. The experimental setup of the three parallel input parallel output HV converters to charge the film capacitive load is shown in Fig. 12. In Fig. 13, the experimental setup of the three parallel input parallel output HV converters to drive the DEAP actuator is shown. As discussed earlier in Section 1, charge and discharge processes of each converter will be performed by the control IC LT3751, which needs an enable signal to initiate charge or discharge process. The enable signals for each HV bi-directional converter are provided by the microcontroller PIC18F2550.

The high voltage film capacitors with a capacitance of ~133 nF (four 33 nF in parallel) from KEMET have been used as a film capacitive load. The DEAP actuator which has a capacitance of ~133 nF is a PolyPower Inlaster PUSH type

actuator manufactured by Danfoss PolyPower. The high voltage transformer parameters provided in Table 3 have been measured by the Impedance analyzer PSM1735. The high voltage (4 kV) MOSFET IXTV03N400S used in each converter is manufactured by IXYS and is currently out of production. At present, IXYS is producing 4.5 kV MOSFETs (IXTA02N450HV). The 5 kV high voltage (SXF6525) diode manufactured by VMI has been used in all converters.

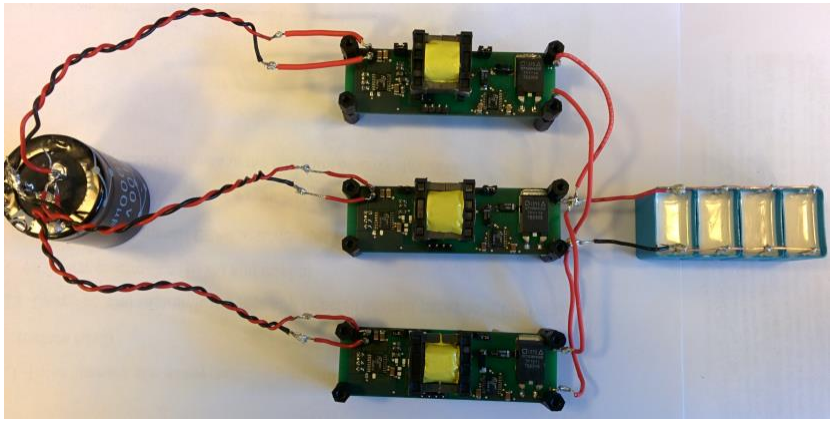

Figure 12. Experimental setup with film capacitive load.

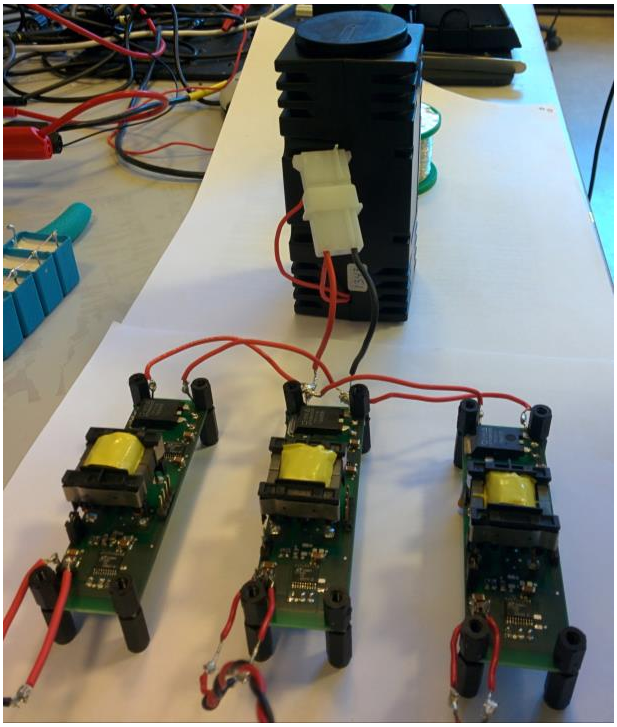

Figure 13. Experimental setup with DEAP actuator.

Table 2. Specifications of the bidirectional flyback converter

Parameter	Value
Input voltage	24 V
Output voltage	0 – 2500 V
Capacitance of the DEAP actuator / film capacitive load	133 nF
Stored energy in the load at 2.5 kV	0.416 J
Primary peak current during charge / discharge process	4.2 A / 5.3 A

Table 3. Parameters of the high voltage transformers

Parameter	Transformer1	Transformer2	Transformer3
Core / Material used	EF 20 / N 87	EF 20 / N 87	EF 20 / N 87
Primary / Secondary turns	15 / 375	16 / 400	16 / 400
Primary / Secondary inductance	30 μH / 19 mH	33 μH / 21 mH	28 μH / 18 mH
Leakage inductance referred to primary	1.1 μH	1.2 μH	1.25 μH
Self-capacitance of secondary	17 pF	19 pF	22 pF
DC resistance of primary / secondary	62 mΩ / 28 Ω	85 mΩ / 41 Ω	84 mΩ / 40 Ω
Diameter of primary / secondary	0.5 mm / 0.1 mm	0.65 mm / 0.1 mm	0.65 mm / 0.1 mm
Number of layers of primary / secondary	1 / 5	2 / 5	2 / 5

Table 4. Components used in the bi-directional flyback converter

Component	Value
Primary / High voltage MOSFET	250V, 25A [IPB600N25N3G] / 4 kV, 300 mA [IXTV03N400S]
High voltage diode (D_b or D_s)	5 kV, 150 mA [SXF6525]
Microcontroller	PIC18F2550
Film capacitor	33 nF (3 kV), 4 of them in parallel

The experimental test results are provided in Figs. 14-26. In each of Figs. 14-26, all sub figures a) corresponds to film capacitive load and sub figures b) corresponds to the DEAP actuator. The experimental results of a single HV bi-directional converter are shown in Figs. 14-19, and the experimental results of three parallel input parallel output HV bi-directional converters are shown in Figs. 20-26. As shown in Fig. 14, during charge process the output voltage increases, and primary and secondary currents are positive, and during discharge process the output voltage decreases, and primary and secondary currents are negative. The zoomed waveforms of Fig. 14, during charge and discharge processes are shown in Figs. 15 and 16, respectively. Figure 17 provides the drain voltages across primary and secondary MOSFETs, voltage across the HV diode which conducts during charge process. The zoomed waveforms of Fig. 17, during charge and discharge processes are shown in Figs. 18 and 19, respectively.

In Fig. 20, primary currents of the parallel input parallel output HV converters are shown together with the output voltage. The zoomed waveforms of Fig. 20, during charge and discharge processes are shown in Figs. 21 and 22, respectively. In Fig. 23, secondary currents of the parallel input parallel output HV converters are shown together with the output voltage. The zoomed waveforms of Fig. 23, during charge and discharge processes are shown in Figs. 24, 25 and 26, respectively.

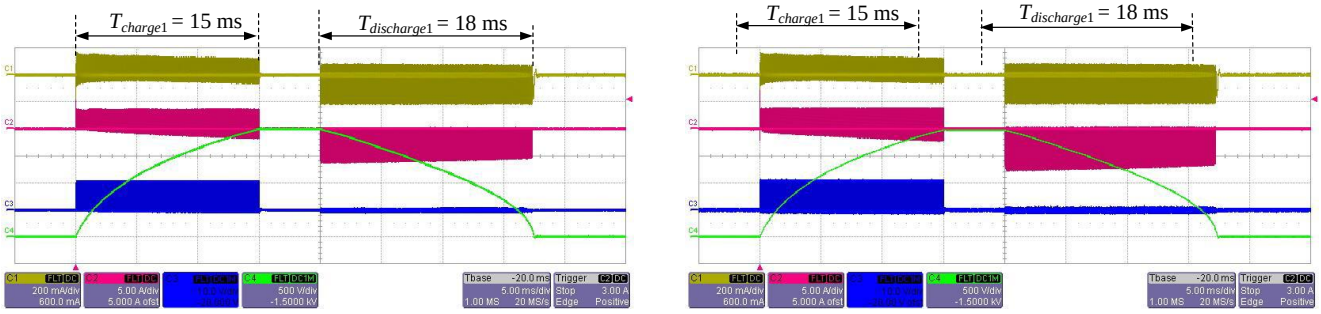

(a) (b)

Figure 14. Experimental results of a single HV bi-directional converter, a) with film capacitive load, b) with DEAP actuator; CH1: Secondary current in the converter; CH2: Primary current in the converter; CH3: primary MOSFET gate drive signal; CH4: Output voltage across the load; $V_{out,max}$ = 2 kV.

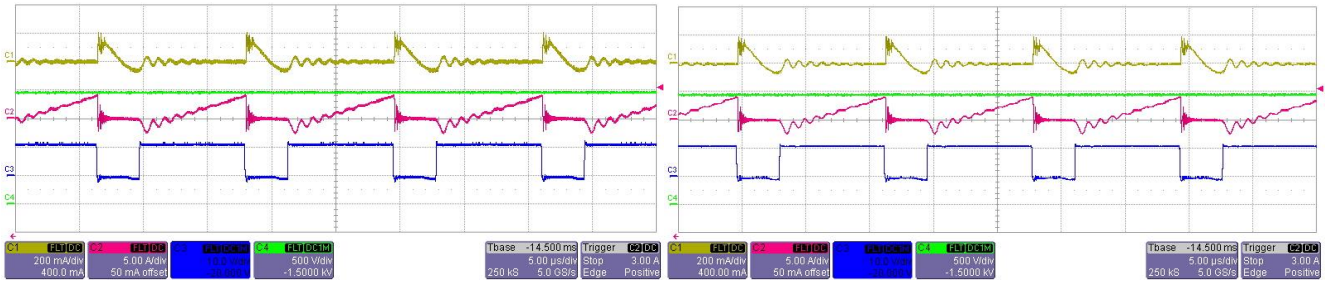

(a) (b)

Figure 15. Zoomed view of Fig. 14 during charge process, a) with film capacitive load, b) with DEAP actuator.

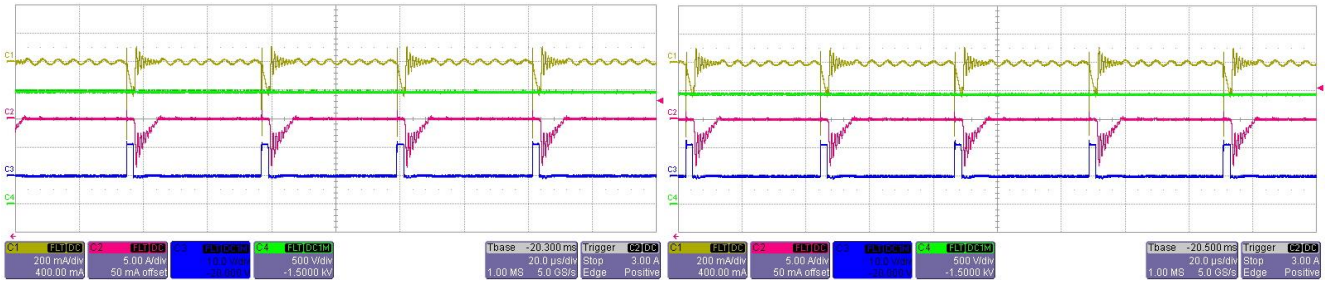

(a) (b)

Figure 16. Zoomed view of Fig. 14 during discharge process, a) with film capacitive load, b) with DEAP actuator; CH4 - secondary MOSFET gate drive signal.

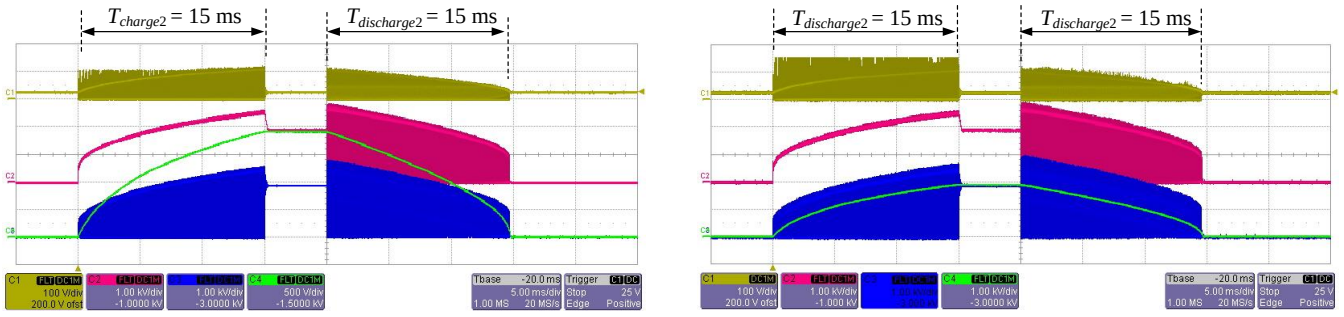

(a) (b)

Figure 17. Experimental results of a single HV bi-directional converter, a) with film capacitive load, b) with DEAP actuator; CH1: drain voltage across primary MOSFET; CH2: drain voltage across secondary MOSFET; CH3: voltage across high voltage diode D_s; CH4: Output voltage across the load; $V_{out,max}$ < 2 kV (due to placing the high voltage [3 kV, 50 MΩ, < 6 pF] probe across D_s).

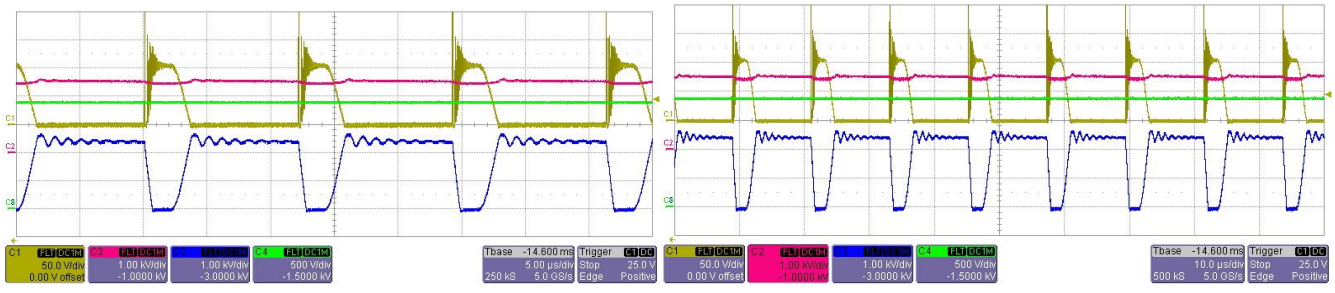

(a) (b)

Figure 18. Zoomed view of Fig. 17 during charge process, a) with film capacitive load, b) with DEAP actuator.

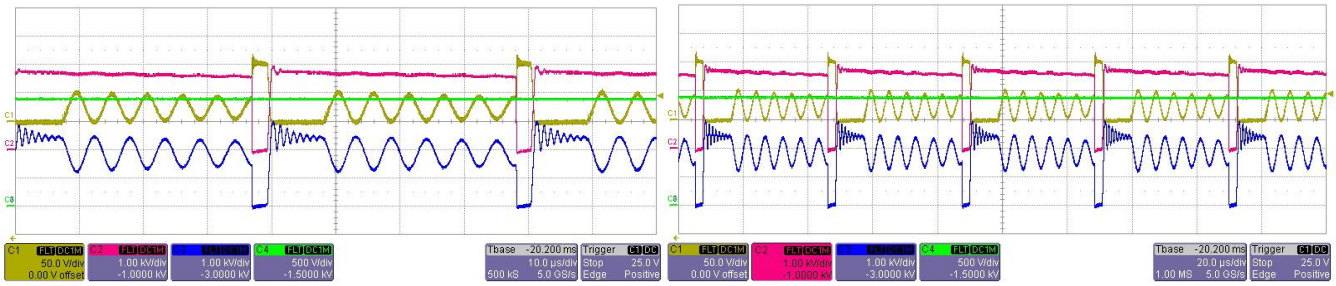

(a) (b)

Figure 19. Zoomed view of Fig. 17 during discharge process, a) with film capacitive load, b) with DEAP actuator.

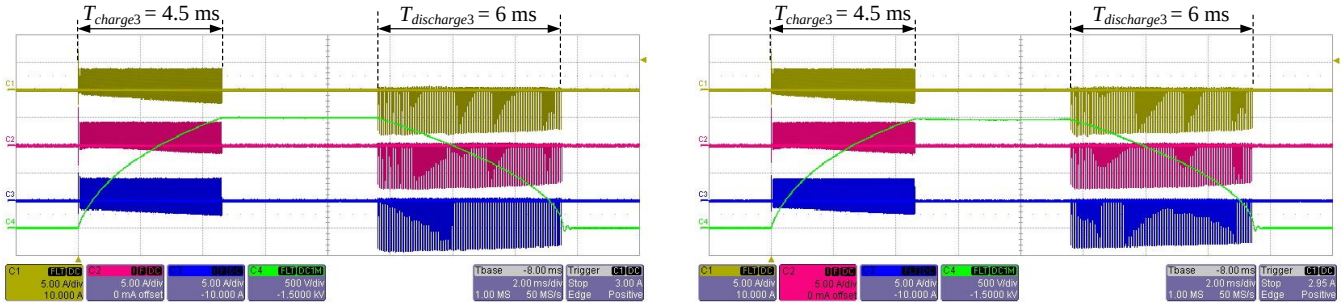

(a) (b)

Figure 20. Experimental results of three parallel input parallel output HV bi-directional converters, a) with film capacitive load, b) with DEAP actuator; CH1: Primary current in converter 1; CH2: Primary current in converter 2; CH3: Primary current in converter 3; CH4: Output voltage across the load; $V_{out,max}$ = 2 kV.

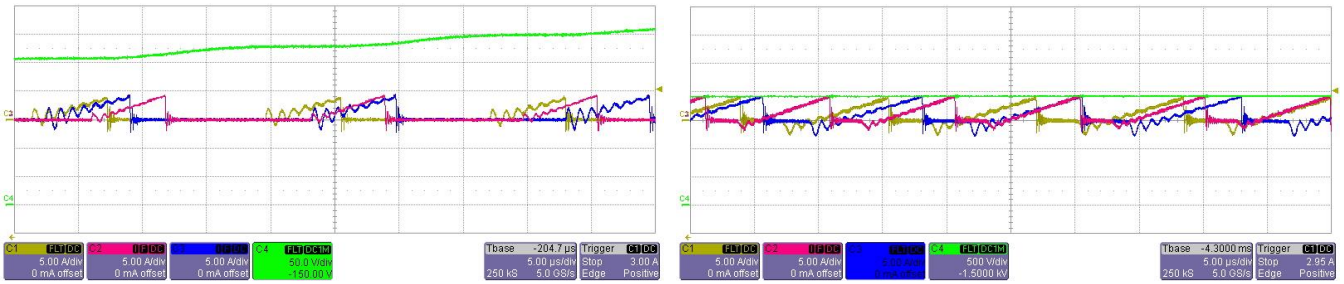

(a) (b)

Figure 21. Zoomed view of Fig. 20 during charge process, a) with film capacitive load, b) with DEAP actuator.

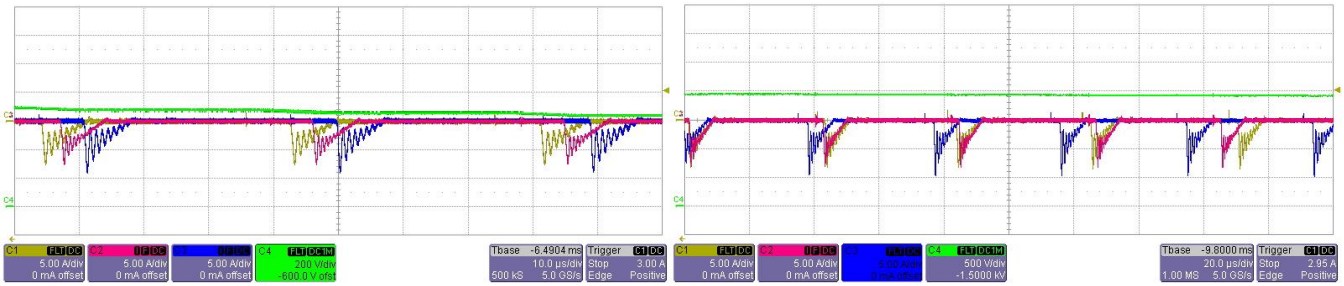

(a) (b)

Figure 22. Zoomed view of Fig. 20 during discharge process, a) with film capacitive load, b) with DEAP actuator.

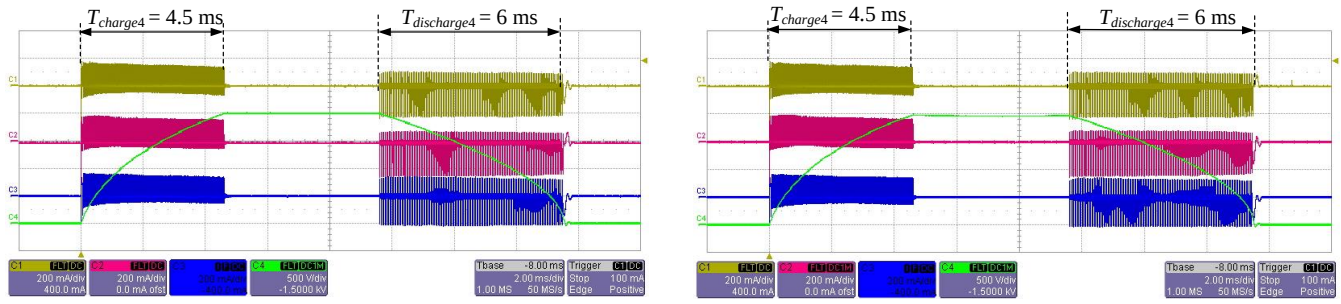

(a) (b)

Figure 23. Experimental results of three parallel input parallel output HV bi-directional converters, a) with film capacitive load, b) with DEAP actuator; CH1: Secondary current in converter 1; CH2: Secondary current in converter 2; CH3: Secondary current in converter 3; CH4: Output voltage across the load; $V_{out,max}$ = 2 kV.

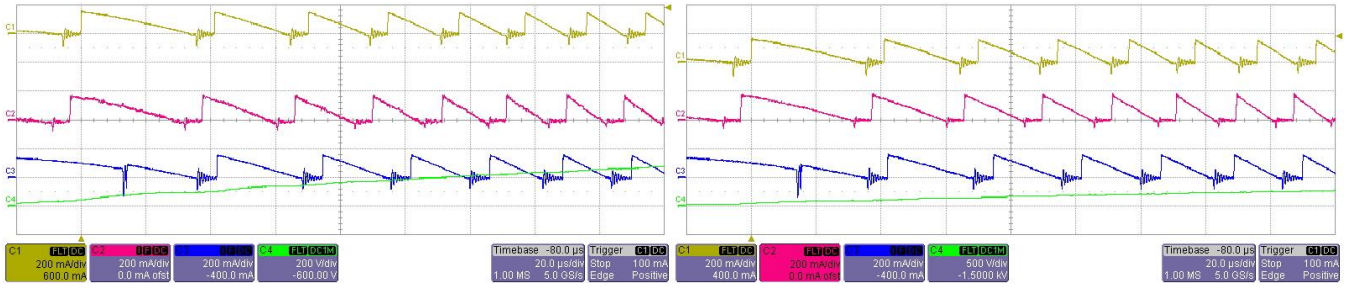

(a) (b)

Figure 24. Zoomed view of Fig. 23 during charge process at low output voltage, a) with film capacitive load, b) with DEAP actuator.

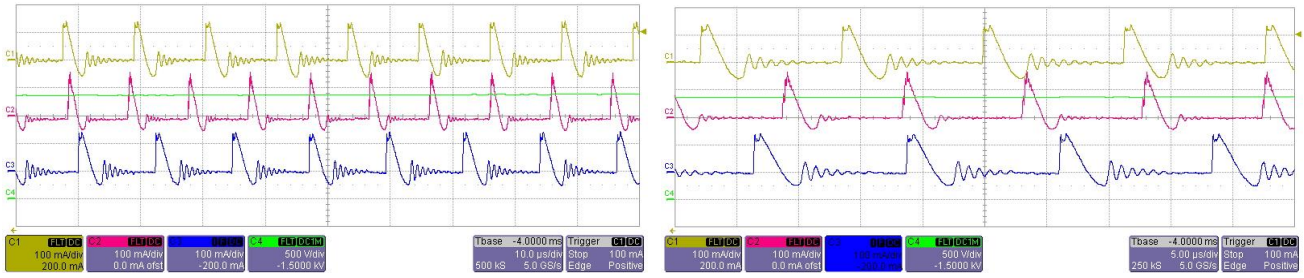

(a) (b)

Figure 25. Zoomed view of Fig. 23 during charge process at high output voltage, a) with film capacitive load, b) with DEAP actuator.

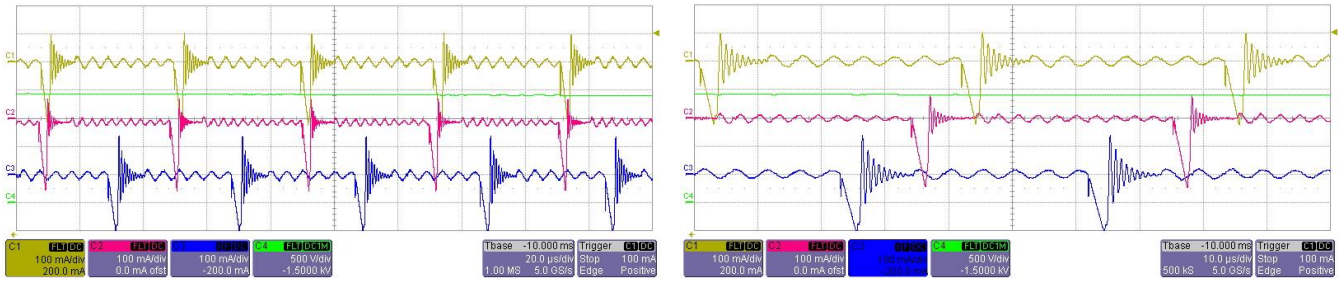

(a) (b)

Figure 26. Zoomed view of Fig. 23 during discharge process, a) with film capacitive load, b) with DEAP actuator.

5. CONCLUSION

Parallel input parallel output high voltage bi-directional flyback converters have been designed and implemented, and their operation has been successfully verified with both film capacitive load and the DEAP actuator. Even though, the DEAP actuator could able to withstand 2.4 kV output voltage, only a maximum voltage of 2 kV is applied to the actuator to avoid any potential damage to it. Similarly, all simulation results are shown for a maximum output voltage of 2 kV. The proposed idea of reducing the charge and discharge times is verified by connecting a maximum of 3 modules in parallel. With the practical experience, it is expected that even more modules (> 3) could be easily connected in parallel. Practically, a single converter is able to charge and discharge the actuator to and from 2 kV within 15 ms and 17.5 ms, respectively. The 3 parallel input parallel output HV modules are able to charge and discharge the actuator to and from 2 kV within 4.5 ms and 6 ms, respectively. This can increase the maximum operating frequency of the DEAP actuator from 30 Hz to 90 Hz by assuming the delay time between charge and discharge processes T_{delay} equal to 0 ms.

REFERENCES

[1] Pelrine, R. E., Kornbluh, R. D., Pei, Q. and Joseph, J. P., "High-speed electrically actuated elastomers with strain greater than 100%," Proc. Science, 287, 836–839 (2000).

[2] Pelrine, R. E., Kornbluh, R. D. and Joseph, J. P., "Electrostriction of polymer dielectric with compliant electrodes as a means of actuation," Proc. Sens. Actuators A, 64, 77–85 (1998).

[3] Danfoss PolyPower website, http://www.polypower.com/Technology/Overview/DEAP+in+General/.

[4] Tryson, M., Kiil, H. E., Benslimane, M., "Powerful tubular core free dielectric electro activate polymer (DEAP) push actuator," Proc. SPIE, 7287, 72871F1-11(2009).

[5] Benslimane, M. Y., Kiil H. E. and Tryson, M. J., "Dielectric electro-active polymer push actuators: performance and challenges," Proc. Polymer International, 59 (3), 415-421 (2010).

[6] Technical document from Danfoss PolyPower, http://www.polypower.com/NR/rdonlyres/8C3F4F8B-3F60-417B-94B6-378042EF169B/0/094F5002WhitepaperDEAPActuatorElements.pdf.

[7] Sarban, R., Lassen, B., Willatzen, M., "Dynamic Electromechanical Modeling of Dielectric Elastomer Actuators with Metallic Electrodes," IEEE/ASME Transactions on Mechatronics, 17(5), 960-967 (2012).

[8] Technical document from Danfoss PolyPower, http://www.polypower.com/NR/rdonlyres/DA0AC752-6FE7-40F0-B973-6A2C264F7AEF/0/094F0439_Charger_Engineering_sheet.pdf.

[9] Thummala, P., Zhang, Z., Andersen, M. A. E. and Rahimullah, S. "Dielectric electro active polymer incremental actuator driven by multiple high-voltage bi-directional DC-DC converters," Proc. IEEE Energy Conversion Congress and Exposition (ECCE) USA, 3837-3844 (2013).

[10] Eitzen, L., Graf, C. and Maas, J., "Bidirectional power electronics for driving dielectric elastomer transducers," Proc. SPIE, 8340, (2012).

[11] Thummala, P., Zhang Z. and Andersen, M. A. E., "Bi-directional Flyback Converter for Capacitive Actuator," Proc. European Power Electronics (EPE) conference, 1-10 (2013).

[12] Andersen, T., Rødgaard, M. S., Thomsen, O. C. and Andersen, M. A. E., "Low voltage driven dielectric electro active polymer actuator with integrated piezoelectric transformer based driver," Proc. SPIE, 7976, 79762N1-12 (2011).

[13] LT3751 datasheet, "High voltage capacitor charger controller with regulation," Linear Technology Corporation, USA, http://cds.linear.com/docs/en/datasheet/3751fc.pdf.

[14] Erickson, R. W. and Maksimovic, D., [Fundamentals of Power Electronics], 2nd ed. Springer, New York (2001).

[15] Sokal, N. O. and Redl. R., "Control Algorithms and Circuit Designs for Optimal Flyback-Charging of and Energy-Storage Capacitor (e.g. for Flash Lamp or Defibrillator)," IEEE Transactions on Power Electronics, 885-894 (1997).

[16] Venkatesan, K., "Current Mode Controlled Bidirectional Flyback Converter," Proc. 20th Annual IEEE Power Electronics Specialists Conference, 835-842 (1989).

[17] Cheng, P., Shi, J. and He, X., "A Novel Input-Parallel Output-Parallel Connected DC-DC Converter Modules with Automatic Sharing of Currents," Proc. IEEE 7th International Power Electronics and Motion Control Conference - ECCE Asia, 1871-1876 (2012).

[18] Eitzen, L., Graf, C., Maas, J., "Modular DC-DC converter system for energy harvesting with EAPs," Proc. SPIE 8687, 86870P 1-14 (2013).

Appendix N

Bidirectional Flyback Converter with Multiple Series Connected Outputs for High Voltage Capacitive Charge and Discharge Applications

---

2015 IEEE Applied Power Electronics Conference and Exposition(APEC 2015)

Bidirectional Flyback Converter with Multiple Series Connected Outputs for High Voltage Capacitive Charge and Discharge Applications

Prasanth Thummala, Henrik Schneider, Zhe Zhang and Michael A. E. Andersen
Electronics Group, Department of Electrical Engineering
Technical University of Denmark
Kongens Lyngby, DK-2800 Denmark
Web: http://www.ele.elektro.dtu.dk/
Email: pthu@elektro.dtu.dk, hensc@elektro.dtu.dk

***Abstract*—This paper evaluates two different implementations of a bidirectional flyback converter for driving a capacitive electro active actuator, which must be charged and discharged from 0 V to 2.5 kV DC and vice versa, supplied from a 24 V battery. In one implementation, a high voltage MOSFET (4 kV) in series with a high voltage blocking diode is added, in parallel with a high voltage freewheeling diode of a conventional flyback topology, to enable bidirectional operation. Experimental result from a digitally controlled bidirectional flyback converter shows that the discharge energy efficiency is limited by the parasitics of the high voltage active components, which also prevent full utilization of valley switching during discharge process. A second implementation is therefore proposed, where the secondary of flyback transformer winding is split into multiple windings which are connected in series by lower voltage rating MOSFETs driven by a gate drive transformer. Simulation results to compare the operation of conventional and proposed converters are provided. The advantages of proposed implementation are improved energy efficiency and lower cost. Experimental results with two series connected secondary windings are provided to validate the proposed implementation.**

NOMENCLATURE

C_{in}/C_{load}	Input capacitance / Load capacitance.
C_{out1}	Balancing capacitor across a series combination of one of the splitted secondary winding and a secondary MOSFET.
C_{ossp}	Output capacitance of the low voltage MOSFET M_p.
C_{osss}	Output capacitance of the high voltage MOSFET M_s.
C_{osss1}	Output capacitance of one of the several series connected MOSFETs (M_{s1}) on the secondary high voltage side.
C_j	Junction capacitance of the high voltage diodes D_2 or D_b.
C_s	Self capacitance of secondary high voltage winding of the flyback transformer.
C_{s1}	Self capacitance of one of the secondary high voltage splitted windings of the flyback transformer.
D_2	High voltage (5 kV) freewheeling diode which conducts while charging the capacitive load.
D_b	High voltage (5 kV) blocking diode which conducts while discharging the capacitive load.
D_{bp}/D_{bs}	Body diode of the MOSFET M_p/M_s.
D_{bs1}	Body diode of one of the several series connected MOSFETs (M_{s1}) on the secondary high voltage side.
$i_{in}/i_p/i_s$	Input / Primary / Secondary current.
i_{load}	Current through the load.
L_{mp}/L_{ms}	Primary / Secondary magnetizing inductance of a non-splitted flyback transformer.
L_{ms1}	Secondary magnetizing inductance of one of the splitted winding of the flyback transformer.
L_{lkp}/L_{lks}	Leakage inductance referred to primary / secondary of a non-splitted flyback transformer.
L_{lks1}	Leakage inductance referred to secondary of one of the splitted winding of the flyback transformer.
M_p/M_s	Low voltage / High voltage (4 kV) MOSFET.
M_{s1}	One of the several series connected MOSFETs on the secondary high voltage side.
n	Turns ratio from secondary to primary of the non-splitted flyback transformer.
n_1	Turns ratio from one of the splitted secondary to primary of the splitted flyback transformer.
N_p/N_s	Number of primary / secondary turns of the non-splitted flyback transformer.
N_{s1}	Number of secondary turns on one of the splitted secondary winding of the flyback transformer.
R_p/R_s	DC resistance of low voltage / high voltage winding of the transformer.
R_{s1}	DC resistance of one of the splitted secondary high voltage winding of the flyback transformer.
V_{Db}/V_{D2}	Voltage across the high voltage (5 kV) blocking / freewheeling diode.
V_{Mp}/V_{Ms}	Voltage across the low voltage / high voltage (4 kV) MOSFET.
V_{Ms1}	Voltage across one of the several series connected MOSFETs (M_{s1}) on the secondary high voltage side.
V_{in}/V_{out}	Input voltage / Output or load voltage.

I. Introduction

Dielectric electro active polymer (DEAP) is an emerging smart material that has experienced substantial improvement and has gained increasing attention over the last decade from the researchers [1]–[3]. The DEAP material is a very thin (40 μm) incompressible silicone elastomer film with a compliant electrode layer on both sides [5], [7]. DEAP can be considered as a pure capacitive load from an electrical perspective [6]. The basic behaviour of the DEAP actuator is the reduction in the polymer thickness and the increment in its area, due to an applied electric field (40-60 V/μm) [7], [8]. The axial DEAP actuator as shown in Fig. 1 is ideally equivalent to a capacitive load. When a DEAP actuator is driven with high voltage (2-2.5 kV), it converts a portion of the electrical energy into mechanical displacement, which is of the order of mm (1-1.5 mm) [4], [5]. Three of such axial DEAP actuators are used to create a DEAP incremental actuator [9] as shown in Fig. 2. DEAP, when used as linear incremental actuators, has the potential to be an effective replacement for many conventional (e.g., piezo, pneumatic and hydraulic) linear actuators due to its unique properties such as large strain, light weight, and high flexibility.

Fig. 1. A linear DEAP actuator manufactured by Danfoss PolyPower A/S.

The DEAP actuator applications [10], [11] require high voltage (HV) bidirectional power electronic converters, to charge and discharge the actuator, and to transfer part of the energy stored in it to the source. Switch-mode power supplies for charging the capacitive loads have been implemented in [12]–[15]. The flyback converter is suitable for low power ($<$ 150 W) and high voltage (2.5 kV) applications, due to its simple structure and low component count [16]. In [17], [30], [32]–[36], [44], [45] bidirectional flyback converters with various power stages and control techniques, for charging and discharging DEAP actuators have been proposed and implemented. The proposed converter with multiple series connected secondary windings is different from aforementioned converters, since it is aimed for bidirectional operation, by replacing the diode with a MOSFET on the secondary HV side. This paper is organized as follows: Section II describes the conventional and proposed HV drivers. Section III provides the simulation results. Section IV discusses the gate driver for the secondary HV side. Section V provides the experimental results and efficiency measurements. Section VI concludes the paper followed by the futur work in Section VII.

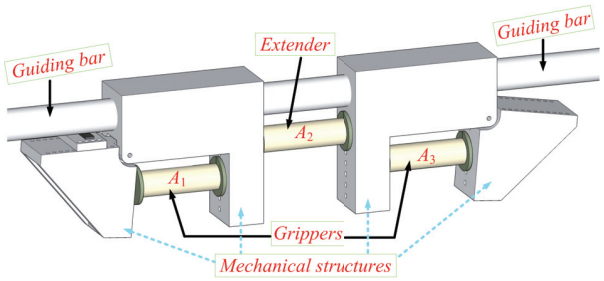

Fig. 2. A DEAP incremental actuator.

II. High Voltage Drivers: Conventional and Proposed

High efficient flyback based converters have been widely investigated and implemented by researchers [18]–[24]. Several bidirectional flyback converter topologies have been proposed and implemented in [25]–[29]. The conventional high voltage bidirectional flyback converter [30], [31], for driving (charging and discharging) a DEAP actuator with a certain actuation frequency, is shown in Fig. 3.

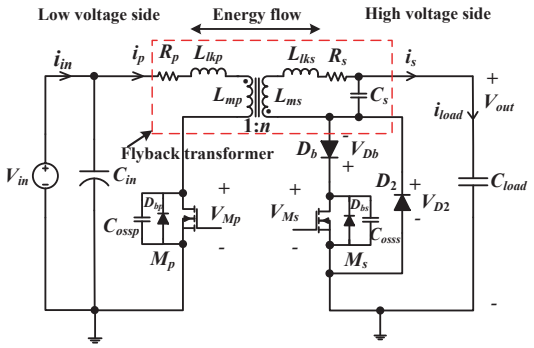

Fig. 3. Conventional HV bidirectional flyback converter.

An efficiency optimization technique has been proposed in [32], [33] to improve the energy efficiency of the converter. Investigation of different transformer winding architectures (TWAs) for the same topology is proposed in [34]. A new digital control technique to achieve the valley switching during both charge and discharge processes in a bidirectional flyback converter is proposed in [35], for better energy efficiency and improved charge and discharge speed. Primary parallel, secondary series flyback converter with multiple transformers is proposed in [36], to reduce the equivalent self-capacitance on the secondary HV side. The HV converter used in [9], [30], [32], [35], requires a HV (4 or 4.5 kV) MOSFET M_s and two HV (5 kV) diodes D_2 and D_b as shown in Fig. 3.

The 4 kV, 300 mA high voltage IXYS MOSFET [37] has the following features:

- high on-resistance of 290 Ω.
- high output capacitance of 19 pF.
- high reverse recovery time of 2.8 μs.

The 5 kV, 150 mA VMI high voltage diode [38] has the following features:

- on-state voltage drop of 7 V.
- junction capacitance of 3 pF.
- reverse recovery time of 70 ns.

Therefore, using a HV MOSFET M_s and two HV diodes D_2 and D_b on the secondary side of the HV bidirectional DC-DC converter, make it very expensive and inefficient.

To reduce the voltage rating of the high voltage MOSFETs, series input and parallel output DC-DC converters have been proposed and implemented in [39]–[43]. The proposed HV bidirectional flyback converter is shown in Fig. 4. Using this topology, it is possible to series connect several lower voltage ($<$ 4 kV) rated MOSFETs each having a better body diode (with less reverse recovery time).

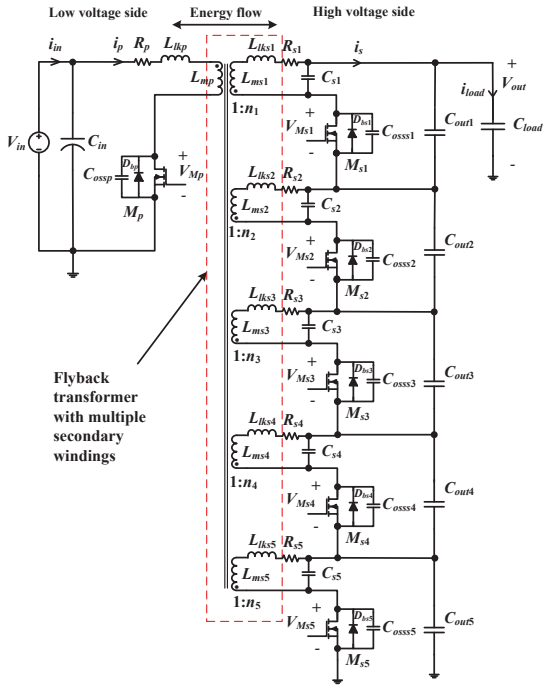

Fig. 4. Proposed HV bidirectional flyback converter with 5 series connected secondary transformer windings and MOSFETs on the secondary HV side.

The advantages of the proposed topology are:

- reduction in the voltage rating and price of the HV MOSFET.
- elimination of blocking and freewheeling HV diodes.
- possibility to achieve perfect valley switching of HV MOSFET, unlike the semi-valley switching [35] (due to series connection of HV diode D_b and HV MOSFET M_s during the discharge process).
- improved overall (charge and/or discharge) energy efficiency.

However, the difficulties associated with the proposed converter are:

- the need of high side gate drivers for driving some of the secondary MOSFETs.
- synchronous switching of secondary MOSFETs.
- voltage sharing among the secondary windings and the secondary MOSFETs.

III. Simulation Results

Simulations have been performed in PSpice software to validate the proposed method, and the results are provided in Figs. 5 and 6.

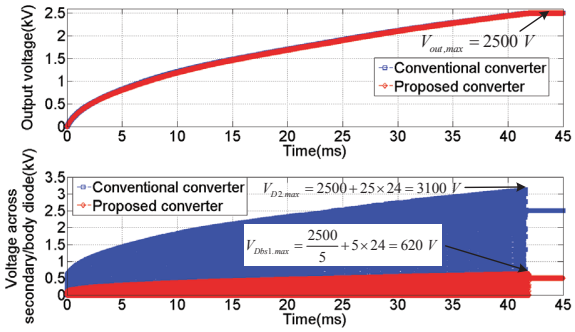

Fig. 5. Simulation results during charge process for $p = 5$ stages.

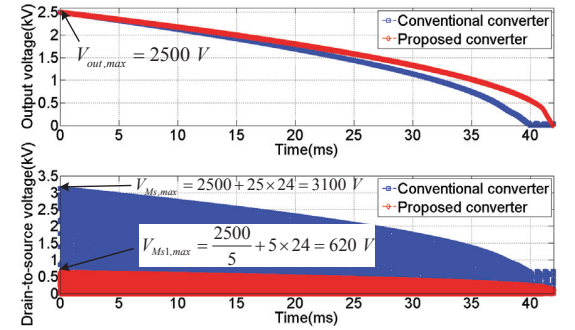

Fig. 6. Simulation results during discharge process for $p = 5$ stages.

The simulation parameters used for the conventional flyback converter (Fig. 3) are: V_{in}=24 V, C_{load}=400 nF, L_{mp}=48 μH, L_{ms}=30 mH, R_p=60 mΩ, n=25, R_s=13 Ω. Peak current control has been implemented during both charge (with current limit 5 A) and discharge (with current limit 200 mA) processes with a fixed time period of 22 μs (switching frequency f_{sw}=45.54 kHz). The simulation parameters used for the proposed flyback converter (Fig. 4) are the same as above, except the turns ratio (n_1=5) and the secondary magnetizing inductance (L_{ms1}=1.2 mH). In the simulations, the leakage inductance and self-capacitance are ignored and ideal switches and diodes are being used. Figure 5, provides the comparison between the output voltages, and the voltage across the secondary HV free wheeling diode V_{D2}, and body diode V_{Ms1}, for the conventional and proposed converters,

during charge process. Figure 6, provides the comparison of the output voltages and the drain-to-source voltage across the secondary MOSFET, for the conventional and proposed converters, during discharge process.

When p series connected transformer and MOSFET stages are used in the secondary HV side of the proposed converter:

- the turns ratio n_1 is reduced by p.
- the magnetizing inductance L_{ms1} is reduced by p^2.
- the drain-to-source voltage across the body diode of the secondary MOSFETs during the charge process is reduced by p.
- the drain-to-source voltage across the secondary MOSFETs during the discharge process is reduced by p.

Hence, to charge and discharge the capacitive load to and from 2.5 kV output voltage, the 4 kV or 4.5 kV MOSFET on the secondary HV side, could be easily replaced by a 800 V MOSFET, when $p = 5$ stages are used in the secondary side.

Table I provides the comparison between the conventional and proposed converters in terms of losses due to the HV active components (at the maximum output voltage during both charge and discharge modes). Table II provides the comparison between the conventional and proposed converters in terms cost and the volume occupied, when the real MOSFETs and HV diodes are used in the converter.

TABLE I. LOSS COMPARISON BETWEEN THE CONVENTIONAL AND PROPOSED CONVERTERS

Converter Type	Loss during charge process (W)	Loss during discharge process (W)	Total loss (W)
Conventional	$P_{loss1} = 0.168$	$P_{loss3} = 0.133$ $P_{loss4} = 4.9$	5.201
Proposed	$P_{loss2} = 0.192$	$P_{loss5} = 0.61$	0.8

TABLE II. COST AND VOLUME COMPARISON BETWEEN THE CONVENTIONAL AND PROPOSED CONVERTERS

Converter Type	Cost ($) *low quantity prices	Volume occupied (mm^3)	Total cost ($)	Total volume (mm^3)
Conventional	20 (*10 for each HV diode) *30 (HV MOSFET)	128 (64 each diode) 1034 (MOSFET)	50	1162
Proposed	5 (1 for each MOSFET), 3 (for gate driver)	440 (88 each MOSFET), 560 (gate driver)	8	1000

In Table I the loss expressions are given by:
$P_{loss1} = i_{avgC} V_{onD2}$ (for HV diode D_2);
$P_{loss2} = p i_{avgC} V_{onDbs}$ (for $p = 5$ HV body diodes);
$P_{loss3} = i_{avgD} V_{onDb}$ (for HV diode D_b);
$P_{loss4} = i^2_{rmsD} R_{dsons} + 0.5 C_{osss} V^2_{Ms,max} f_{sw} + V_{gs} f_{sw} Q_{gs}$ (for 4 kV MOSFET M_s);
$P_{loss5} = p(i^2_{rmsD} R_{dsons1} + 0.5 C_{osss1} V^2_{Ms1,max} f_{sw} + V_{gs} f_{sw} Q_{gs1})$ (for p series connected MOSFETs M_{si}, $i = 1, 2...p$);

The parameters used are: i_{avgC}= 24 mA, i_{avgD} =19 mA, i_{rmsD}=52 mA, V_{onD2}=V_{onDb}=7 V, V_{onDbs}=1.6 V, $R_{dsons} =$ 290 Ω (4 kV MOSFET), $R_{dsons1} = 13$ Ω (800 V MOSFET), C_{osss}=19 pF, $C_{osss1} = 9.5$ pF, V_{Ms}=3100 V, V_{Ms1}=620 V, V_{gs}=12 V, Q_{gs}=16.3 nC, Q_{gs1}=7.7 nC;

In the above i_{avgC}, i_{avgD}, i_{rmsD} are the average current during charge and discharge modes, and RMS current during discharge mode, respectively. Those values are extracted from the PSpice simulations. Also V_{onD2}, V_{onDb}, and V_{onDbs} are the on-state diode drops of diodes D_2, D_b and D_{bs1}, respectively.

IV. DRIVING THE SECONDARY SERIES CONNECTED MOSFETS USING A GATE DRIVE TRANSFORMER (GDT)

In the proposed topology as shown in Fig. 4, the secondary HV side MOSFETs, need to be driven with $p-1$ high side gate drivers, for p series connected stages. It is possible to drive all secondary MOSFETs using a gate drive transformer (GDT). Figure 7a) provides the full schematic of the gate driver for 2 series connected stages ($p = 2$). The microcontroller generates enable signals for the dual low-side gate driver, whose outputs are fed to the GDT. The GDT as shown in Fig. 7a) has a single primary and two secondary windings with 1:1 turns ratio.

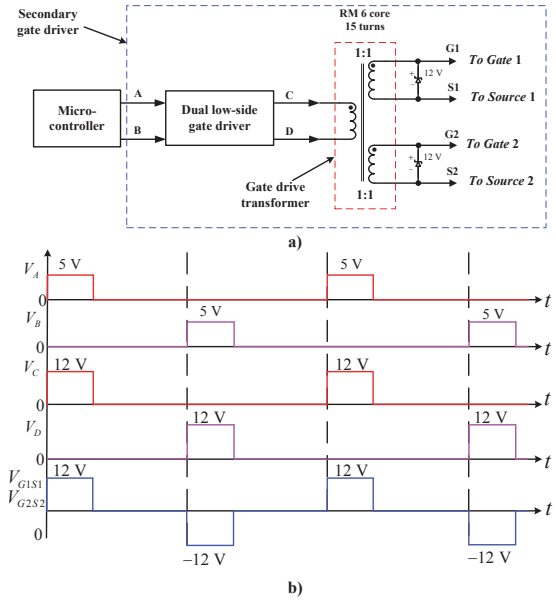

Fig. 7. a) Schematic of the gate driver for driving two secondary series connected MOSFETs; b) Driving signals at different nodes in the gate driver schematic.

The GDT is made using a RM 6 core, each winding has 15 turns with 0.2 mm diameter. The two isolated outputs of the GDT are used to drive the 2 secondary series connected MOSFETs. To protect the secondary MOSFETs from the voltage spikes, a 12 V Zener diode is placed across the gate to source terminals of the two MOSFETs. Driving signals at different nodes in the secondary gate driver are shown in Fig. 7b). The two primary winding terminals of gate drive transformer (nodes C and D) are driven with two out-of-phase signals. Positive signal at the primary dot terminal of GDT (node C), produces positive gate-to-source driving signals, and positive signal at the primary non-dot terminal of GDT (node D), produces negative gate-to-source driving signals, for the two MOSFETs, respectively. In Fig. 7b), G_1, G_2, S_1

and S_2 represents the gate nodes and source nodes of the two MOSFETs, respectively. The idea of driving the two series connected MOSFETs, using a GDT described above, can be used to drive more than 2 series connected MOSFET stages ($p > 2$). However, the type of core used for the GDT can be changed depending on the number of stages.

V. Experimental Results

The experimental prototype of the conventional HV bidirectional flyback converter is shown in Fig. 8 [35]. The experimental results showing the bidirectional operation at 2.5 kV output voltage are provided in Fig. 9. The primary MOSFET M_p is 250 V, 16 A [FQD16N25CTM], the secondary side MOSFETs are 4 kV, 300 mA, 290 Ω [IXTV03N400S] and 4.5 kV, 200 mA, 750 Ω [IXTA02N450HV], and the HV diodes D_2 and D_b are 5 kV, 150 mA [SXF6525]. However, for evaluating the conventional and proposed converters, only 4 kV MOSFET is considered. The secondary MOSFET used in the proposed converter is 800 V, 1 A, 13 Ω [STN1NK80Z, [46]].

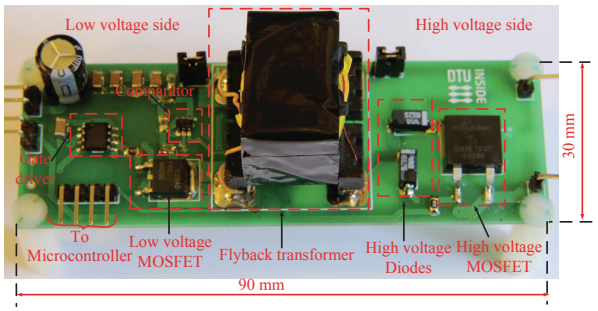

Fig. 8. Experimental prototype of the digitally controlled conventional HV bidirectional flyback converter with 4.5 kV MOSFET on the HV side [35].

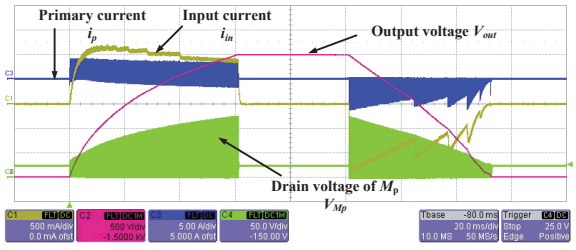

Fig. 9. Experimental results showing a single charge (0 V to 2.5 kV) and discharge cycle (2.5 kV to 0 V) [35]; CH1: 500 mA/div, CH2: 500 V/div, CH3: 5 A/div, CH4: 50 V/div, Time scale: 20 ms/div.

A digital control technique was recently proposed in [35] to achieve valley switching control during both charge and discharge processes. In Fig. 9 a full charge/discharge cycle is shown. Figure 10 confirms the valley switching operation in charge mode. However, during discharge mode the valley voltage of the drain of HV MOSFET M_s is limited by the series connected HV diode D_b as seen in Fig. 11. The energy efficiency measurements during both charge and discharge modes as a function of output voltage are provided in Fig. 12. The proposed converter is expected to achieve ideal valley

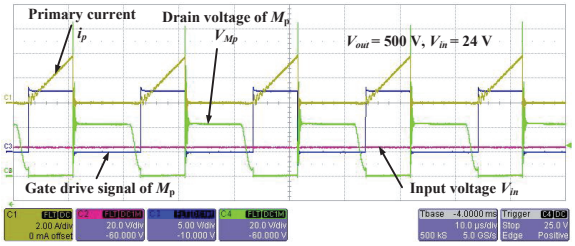

Fig. 10. Experimental waveforms when the converter is operated with valley switching during charge process; CH1: 2 A/div, CH2: 20 V/div, CH3: 5 V/div, CH4: 20 V/div, Time scale: 5 μs/div.

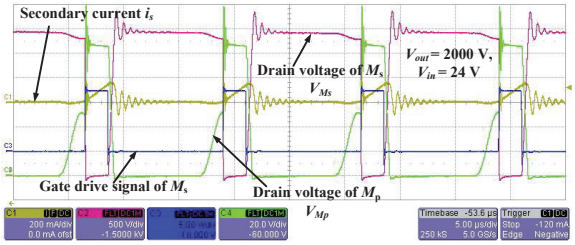

Fig. 11. Experimental waveforms when the converter is operated with valley switching during discharge process; CH1: 200 mA/div, CH2: 500 V/div, CH3: 5 V/div, CH4: 20 V/div, Time scale: 5 μs/div.

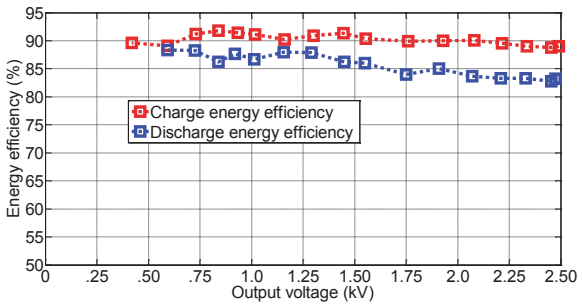

Fig. 12. Energy efficiency measurements with a 4 kV MOSFET on HV side.

switching during the discharge process leading to improved energy efficiency.

The proposed converter specifications are provided in Table III. The details of flyback transformer are shown in Table IV. To verify the concept of proposed converter, only two series connected secondary stages are considered. The 300 secondary turns are split into two, for each series connected secondary winding ($N_{s1} = 150$). The parameters of the flyback transformer are provided in Table V.

The flyback transformer used for the experiment is of non-interleaved and non-sectioned, and it is not propoerly optimized. However, for this application, transformer with multiple sections would be better choice to reduce the self-capacitance. The experimental results from the proposed converter with 2 series connected secondary stages ($p = 2$) are shown in Figs. 13, 14 and 15, respectively.

Figure 13 provides a single charge and discharge cycle us-

ing the proposed topology, when the capacitor load is charged and discharged from 0 V to 200 V, and vice versa. To verify the proposed concept, during both charge and discharge processes, the converter is driven with fixed switching frequency. During the charge process the switching time period is 59 μs, and during the discharge process, the switching time period is 100 μs. In Figs. 14 and 15, a comparison of drain-to-source voltage across the two secondary MOSFETs during a charge and discharge switching cycle are provided.

TABLE III. CONVERTER SPECIFICATIONS

Parameter	Value
Input voltage	24 V
Capacitance of load	400 nF
On-time of primary MOSFET during the charge process	9 μs

TABLE IV. DETAILS OF THE SPLITTED FLYBACK TRANSFORMER WITH A TURNS RATIO OF 25

Parameter	Value
Number of primary / secondary turns	12 / 300
Diameter of primary / secondary winding	0.5 mm / 0.12 mm
Number of layers of primary / secondary winding	1 / 4
Type of core / material	EF25 / N87

TABLE V. PARAMETERS OF THE SPLITTED FLYBACK TRANSFORMER

Parameter	Value
Primary / Each splitted secondary magnetizing inductance	42 μH / 6.3 mH
Secondary non-splitted magnetizing inductance	25 mH
Leakage inductance referred to primary / splitted secondary	1.1 μH / 53 μH
Leakage inductance referred to non-splitted secondary	721 μH
Primary / Secondary splitted winding DC resistance	64 mΩ / 6.3 Ω
Secondary non-splitted winding DC resistance	12.4 Ω
Self-capacitance of each splitted secondary winding	78.2 pF
Self-capacitance of non-splitted secondary winding	37 pF

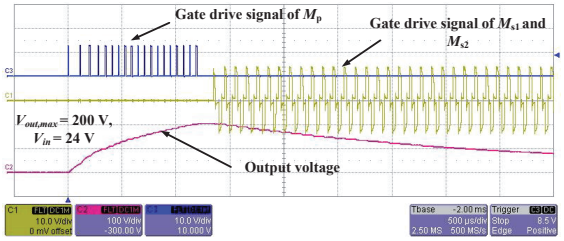

Fig. 13. A charge and discharge cycle with the proposed topology; CH1: 10 V/div, CH2: 100 V/div, CH3: 10 V/div, Time scale: 500 μs/div.

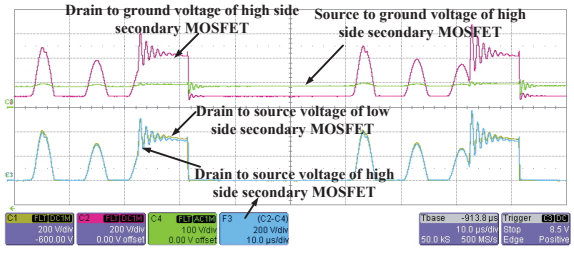

Fig. 14. Comparison of the voltage stress across the two secondary MOSFETs during the charge process using the proposed topology; CH1: 200 V/div, CH2: 200 V/div, CH4: 100 V/div,F3=C2-C4: 200 V/div, Time scale: 10 μs/div.

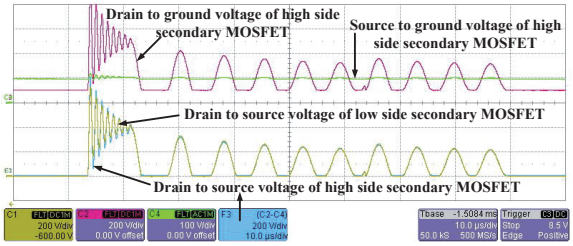

Fig. 15. Comparison of the voltage stress across the two secondary MOSFETs during the discharge process using the proposed topology; CH1: 200 V/div, CH2: 200 V/div, CH4: 100 V/div,F3=C2-C4: 200 V/div, Time scale: 10 μs/div.

VI. CONCLUSION

In this paper, a bidirectional flyback converter with multiple series connected outputs is proposed, for high voltage drive of capacitive DEAP actuators. Simulation results (output voltages and voltage stresses across the secondary MOSFETs/diodes) during both charge and discharge processes are provided, to show a comparison between the proposed and conventional implementations. A theoretical comparison shows that the proposed converter has the potential to improve efficiency and lower the cost. The detailed implementation of secondary gate driver, using a gate drive transformer is provided. Experimental results from the conventional (for full operating voltage range 0-2.5 kV) and the proposed (0-200 V) bidirectional converters are provided. The experimental waveforms of the drain-to-source voltages of the two secondary MOSFETs confirm the voltage sharing across the two secondary MOSFETs.

VII. FUTURE WORK

Due to lack of time the converter operation for full operating voltage range (0-2.5 kV), and with $p = 5$ series connected secondary stages are not verified. However, the future work regarding the proposed converter involves:

- implementing the valley switching control during both charge and discharge processes.
- design and implementation of the gate drive transformer for $p = 5$ stages.
- design of the efficient flyback trasformer with very low self-capacitance.
- investigating the coupling factor of different winding strategies interms of voltage sharing.

REFERENCES

[1] Y. Bar-Cohen, *Electroactive Polymer [EAP] Actuators as Artificial Muscles: Reality, Potential, and Challenges*, 2nd ed. Washington, DC: SPIE, 2004.

[2] R. E. Pelrine, R. D. Kornbluh, Q. Pei, and J. P. Joseph, "High-speed electrically actuated elastomers with strain greater than 100%," *Science*, vol. 287, pp. 836–839, 2000.

[3] F. Carpi, D. DE Rossi, R. Kornbluh, R. Pelrine, and P. Sommer-Larsen, *Dielectric Elastomer As Electromechanical Transducers*, Amsterdam, Netherlands: Elsevier, 2008.

[4] M. Tryson, H. E. Kiil, M. Benslimane, "Powerful tubular core free dielectric electro active polymer (DEAP) push actuator," in *Proc. SPIE*, vol. 7287, 2009.

[5] R. Sarban, B. Lassen, M. Willatzen, "Dynamic Electromechanical Modeling of Dielectric Elastomer Actuators With Metallic Electrodes," *IEEE/ASME Trans. on Mechatronics*, vol. 17, no. 5, pp. 960–967, Oct. 2012.

[6] L. Huang, P. Thummala, Z. Zhang, M. A. E. Andersen, "Battery Powered High Output Voltage Bidirectional Flyback Converter for Cylindrical DEAP Actuator," in *Proc. IEEE IPMHVC*, Jun. 2012, pp. 454–457.

[7] Danfoss PolyPower, http://www.polypower.com/, [accessed 18 Nov. 2014].

[8] LEAP Technology, http://www.leaptechnology.com/, [accessed 20 Nov. 2014].

[9] P. Thummala, Z. Zhang, M. A. E. Andersen, S. Rahimullah, "Dielectric electro active polymer incremental actuator driven by multiple high-voltage bi-directional DC-DC converters," in *Proc. IEEE ECCE USA*, Sept. 2013, pp. 3837–3844.

[10] R. D. Kornbluh, R. Pelrine, Q. Pei, R. Heydt, S. Stanford, S. Oh, J. Eckerle,"Electroelastomers: applications of dielectric elastomer transducers for actuation, generation, and smart structures," in *Proc. SPIE*, vol. 4698, pp. 254-270, 2002.

[11] I. A. Anderson, T. A. Gisby, T. G. McKay, B. M. OBrien, E. P. Calius, "Multi-functional dielectric elastomer artificial muscles for soft and smart machines," *Journal of Applied Physics*, 112, 041101, 2012.

[12] S. K. Chung, H. B. Shin, "High-voltage power supply for semi-active suspension system with ER-fluid damper," *IEEE Trans. Vehicular Technology*, vol. 53, no. 1, pp. 206–214, Jan. 2004.

[13] J. Elmes, C. Jourdan, O. Abdel-Rahman, I. Batarseh, "High-Voltage, High-Power-Density DC-DC Converter for Capacitor Charging Applications," in *Proc. IEEE APEC*, Feb. 2009, pp. 433–439.

[14] T. Andersen, M. S. Rodgaard, O. C. Thomsen, M. A. E. Andersen, "Low voltage driven dielectric electro active polymer actuator with integrated piezoelectric transformer based driver," in *Proc. SPIE Electroactive Polymer Actuators and Devices (EAPAD)*, vol. 7976, pp. 79762N, 2011.

[15] N. O. Sokal, R. Redl, "Control algorithms and circuit designs for optimal flyback-charging of an energy storage capacitor (e.g., for flash lamp or defibrillator)," *IEEE Trans. Power Electronics*, vol. 12, no. 5, pp. 885–894, Sep. 1997.

[16] R. W. Erickson and D. Maksimovic, *Fundamentals of Power Electronics*, 2nd ed. New York: Springer, 2001.

[17] L. Eitzen, C. Graf, J. Maas, "Cascaded bidirectional flyback converter driving DEAP transducers," in *Proc. IEEE IECON*, Nov. 2011, pp. 1226–1231.

[18] S. H. Kang, D. Maksimovic, I. Cohen, "Efficiency Optimization in Digitally Controlled Flyback DCDC Converters Over Wide Ranges of Operating Conditions" *IEEE Trans. Power Electronics*, vol. 27, no. 8, pp. 3734–3748, Aug. 2012.

[19] L. Chen, H. Hu, Q. Zhang, A. Amirahmadi, I. Batarseh, "A Boundary-Mode Forward-Flyback Converter With an Efficient Active LC Snubber Circuit," *IEEE Trans. Power Electronics*, vol. 29, no. 6, pp. 2944–2958, June 2014.

[20] J. Park, Y.-S. Roh, Y.-J. Moon, C. Yoo, "A CCM/DCM Dual-Mode Synchronous Rectification Controller for a High-Efficiency Flyback Converter," *IEEE Trans. Power Electronics*, vol. 29, no. 2, pp. 768–774, Feb. 2014.

[21] Y.-H. Kim, Y.-H. Ji, J.-G. Kim, Y.-C. Jung, C.-Y. Won, "A New Control Strategy for Improving Weighted Efficiency in Photovoltaic AC Module-Type Interleaved Flyback Inverters," *IEEE Trans. Power Electronics*, vol. 28, no. 6, pp. 2688–2699, June 2013.

[22] A. Radic, A. Straka, A. Prodic, "Low-volume stackable flyback converter with near minimum deviation controller," in *Proc. IEEE APEC*, March 2014, pp. 1948–1953.

[23] J.-W. Shin, S.-J. Choi, B.-H. Cho, "High-Efficiency Bridgeless Flyback Rectifier With Bidirectional Switch and Dual Output Windings," *IEEE Trans. Power Electronics*, vol. 29, no. 9, pp. 4752–4762, Sept. 2014.

[24] N. Sukesh, M. Pahlevaninezhad, P. K. Jain, "Analysis and Implementation of a Single-Stage Flyback PV Microinverter With Soft Switching," *IEEE Trans. Industrial Electronics*, vol. 61, no. 4, pp. 1819–1833, April 2014.

[25] K. Venkatesan, "Current mode controlled bidirectional flyback converter," in *Proc. IEEE PESC*, pp. 835–842 vol.2, 26-29 Jun 1989.

[26] T. Bhattacharya, V. S. Giri, K. Mathew, L. Umanand, "Multiphase Bidirectional Flyback Converter Topology for Hybrid Electric Vehicles" *IEEE Trans. Industrial Electronics*, vol. 56, no. 1, pp.78–84, Jan. 2009.

[27] T. Anno, H. Koizumi, "Double Input Bidirectional DC/DC Converter Using Cell Voltage Equalizing with Flyback Transformer," *IEEE Trans. Power Electronics*, April 2014.

[28] G. Chen, Y.-S. Lee, S.Y.R. Hui, D. Xu, Y. Wang, "Actively clamped bidirectional flyback converter," *IEEE Trans. Industrial Electronics*, vol. 47, no. 4, pp. 770–779, Aug. 2000.

[29] F. Zhang, Y. Yan, "Novel ForwardFlyback Hybrid Bidirectional DC-DC Converter," *IEEE Trans. Industrial Electronics*, vol. 56, no. 5, pp. 1578–1584, May 2009.

[30] P. Thummala, Z. Zhang, M. A. E. Andersen, "High Voltage Bi-directional Flyback Converter for Capacitive Actuator," in *Proc. European Power Electronics (EPE) Conference*, Sept. 2013, pp. 1–10.

[31] L. Huang, Z. Zhang, M.A.E. Andersen, "Design and development of autonomous high voltage driving system for DEAP actuator in radiator thermostat," in *Proc. IEEE APEC*, pp. 1633–1640, 16-20 March 2014.

[32] P. Thummala, H. Schneider, Z. Zhang, A. Knott, M. A. E. Andersen, "Optimization of a bi-directional flyback converter for a high voltage capacitor charging application," in *Proc. IEEE APEC*, Mar. 2014, pp. 2556–2563.

[33] P. Thummala, H. Schneider, Z. Zhang, Z. Ouyang, A. Knott, M. A. E. Andersen, "Efficiency Optimization by Considering the High Voltage Flyback Transformer Parasitics using an Automatic Winding Layout Technique," *IEEE Trans. Power Electronics*, accepted, 2014.

[34] H. Schneider, P. Thummala, L. Huang, Z. Ouyang, A. Knott, Z. Zhang, M. A. E. Andersen, "Investigation of transformer winding architectures for high voltage capacitor charging applications," in *Proc. IEEE APEC*, Mar. 2014, pp. 334–341.

[35] P. Thummala, D. Maksimovic, Z. Zhang, M. A. E. Andersen, "Digital control of a high-voltage (2.5 kV) bidirectional DC-DC converter for driving a dielectric electro active polymer (DEAP) based capacitive actuator," in *Proc. IEEE ECCE USA*, Sept. 2014, pp. 3435–3442.

[36] R. Pittini, L. Huang, Z. Zhang, M. A. E. Andersen, "Primary parallel secondary series flyback converter (PPSSFC) with multiple transformers for very high step-up ratio in capacitive load charging applications," in *Proc. IEEE APEC*, Mar. 2014, pp. 1440–1447.

[37] IXYS, Online available, http://ixapps.ixys.com/DataSheet/DS100214A-(IXTH_V03N400_S).pdf, [accessed 18 Nov. 2014].

[38] VMI, Online available, http://www.voltagemultipliers.com/pdf/SXF6521_25.pdf, [accessed 18 Nov. 2014].

[39] J.-W. Kim, J.-S. Yon, B.-H. Ch, "Modeling, control, and design of input-series-output-parallel-connected converter for high-speed-train power system," *IEEE Trans. Industrial Electronics*, vol. 48, no. 3, pp. 536–544, Jun 2001.

[40] R. Ayyanar, R. Giri, N. Mohan, "Active input-voltage and load-current sharing in input-series and output-parallel connected modular DC-DC converters using dynamic input-voltage reference scheme," *IEEE Trans. Power Electronics*, vol. 19, no. 6, pp. 1462–1473, Nov. 2004.

[41] J. W. Kimball, J. T. Mossoba, P. T. Krein, "Control Technique for Series Input-Parallel Output Converter Topologies" in *Proc. IEEE PESC* pp. 1441–1445, June 2005.

[42] X. Ruan, W. Chen, L. Cheng, C.K. Tse, H. Yan, T. Zhang, "Control Strategy for Input-SeriesOutput-Parallel Converters," *IEEE Trans. Industrial Electronics*, vol. 56, no. 4, pp. 1174–1185, April 2009.

[43] H. Fan, H. Li, "A distributed control of input-series-output-parallel bidirectional dc-dc converter modules applied for 20 kVA solid state transformer," in *Proc. IEEE APEC*, pp. 939–945, 6-11 March 2011.

[44] P. Thummala, D. Maksimovic, Z. Zhang, M. A. E. Andersen, R. Sarban, "Design of a High Voltage DC-DC Converter for Driving the Capacitive Incremental Actuators usable in Electric Vehicles (EVs)," in *Proc. IEEE IEVC*, Dec. 2014.

[45] P. Thummala, Z. Zhang, M. A. E. Andersen, R. Sarban, "Parallel input parallel output high voltage bi-directional converters for driving dielectric electro active polymer actuators," in *Proc. SPIE EAPAD*, vol. 9056, pp. 90561N-90561N-15, Mar. 2014.

[46] STM, Online available, http://www.st.com/st-web-ui/static/active/en/resource/technical/document/datasheet/CD00058073.pdf, [accessed 18 Nov. 2014].

Appendix O

Dielectric Electro Active Polymer Incremental Actuator Driven by Multiple High-Voltage Bi-directional DC-DC Converters

---

2013 IEEE Energy Conversion Congress and Exposition USA (ECCE USA 2013)
→ ***Best Student Paper Award***

Dielectric Electro Active Polymer Incremental Actuator Driven by Multiple High-Voltage Bi-directional DC-DC Converters

Prasanth Thummala, Zhe Zhang, Michael A.E. Andersen
Department of Electrical Engineering
Technical University of Denmark
DK-2800 Kongens Lyngby, Denmark
pthu@elektro.dtu.dk

Sarban Rahimullah
Danfoss PolyPower A/S
DK-6430 Nordborg, Denmark
sarban@danfoss.com

Abstract— **This paper presents driving circuit for a recently invented dielectric electro active polymer (DEAP) incremental actuator. The basic operation of such an actuator is bio-inspired from the movement of an inchworm. The actuator consists of three electrically isolated, and mechanically connected capacitive sub-actuators. It needs to be driven by three high voltage (~2.5 kV) DC-DC converters, to achieve the linear incremental motion. The topology used for this application is a bi-directional flyback DC-DC converter. The control of the incremental actuator involves, implementation of digital controller used for controlling charge and discharge sequences of the individual sub-actuators, and monitoring and adjustment of the output voltages of three high voltage DC-DC converters to provide over-voltage protection capability. Three power stages of the proposed converter were experimentally tested. The experimental results and efficiency measurements are shown.**

NOMENCLATURE

V_{in}	Input voltage
C_{in}	Input capacitance
C_{A_1}, C_{A_2}, C_{A_3}	Capacitances of the actuators A_1, A_2, and A_3
i_{p_1}, i_{p_2}, i_{p_3}	Primary currents of converters 1, 2 and 3
i_{s_1}, i_{s_2}, i_{s_3}	Secondary currents of converters 1, 2 and 3
n_1, n_2, n_3	Turns ratios of converters 1, 2 and 3
$AC_{1,\,2,\,3,\,4,\,5,\,6}$	Analog controllers 1, 2, 3, 4, 5 and 6
$V_{ch_{1,\,2,\,3,\,4,\,5,\,6}}$	Enable signals for the analog controllers 1, 2, 3, 4, 5 and 6
M_1, M_3, M_5	Low voltage MOSFETS of converters 1, 2 and 3
M_2, M_4, M_6	High voltage MOSFETS of converters 1, 2 and 3
$D_{HV_{1,\,2,\,3,\,4,\,5,\,6}}$	High voltage diodes of converters 1,2 and 3
V_{A_1}, V_{A_2}, V_{A_3}	Output voltages of the actuators A_1, A_2 and A_3 / capacitive loads
V_{FB_1}, V_{FB_2}, V_{FB_3}	Feedback voltages of the actuators A_1, A_2 and A_3 / capacitive loads

INTRODUCTION

Dielectric electro active polymer (DEAP) is an emerging smart material that has experienced substantial development and has gained increasing attention over the last decade [1], [2]. The DEAP material is a very thin (~40 μm) incompressible elastomer film with a compliant electrode layer on both sides [3]. The basic behavior of the DEAP material is the reduction in the polymer's thickness and increment in its area, due to an applied electric field (~60 V/μm). DEAP, when used as actuators, has the potential to be an effective replacement for many conventional actuators due to its unique properties, such as large strain, light weight, noiseless operation, low power consumption, high flexibility, and power density. Actuators providing linear motion are used in a vast range of applications ranging from large size machineries (e.g. cranes), to small scale MEMS devices used for micro positioning. Linear actuators are typically characterized by their maximum stroke, force, speed, and precision. The strokes of many linear actuators are limited to their initial geometrical dimensions. This characteristic of conventional linear actuators limits their use in applications where large strokes, and low size and weight of the actuators are desired. DEAP incremental actuators are an alternative design to overcome these limitations by providing an inchworm-like actuation.

The DEAP incremental actuator concept is the latest invention from Danfoss PolyPower [4] that consists of two grippers (to enable gripping operation) and an extender (to move the grippers). These grippers connect with the extender using the mechanical structures, so the incremental actuator is equivalent to three independent capacitive actuators with electrical isolation between them. Fast and precise adjustment, low noise operation, and high energy efficiency are the key advantages of the DEAP incremental actuator. Some potential applications for the DEAP incremental actuator are transportation of equipment at industrial production facilities, pipe monitoring and cleaning, and search and rescue robots. In addition to the above, the DEAP incremental actuator technology has the

Danish National Advanced Technology Foundation

Figure 1: PolyPower axial DEAP actuator.

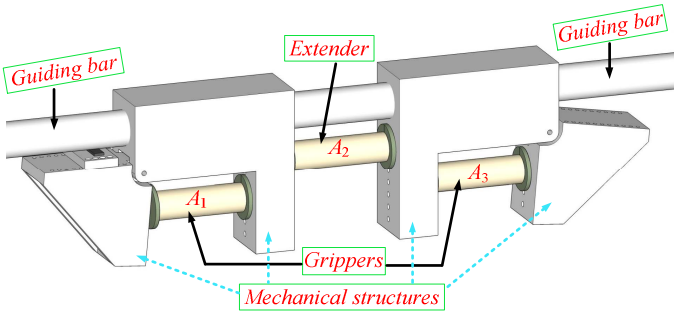

Figure 2: Conceptual diagram of the DEAP incremental actuator.

potential to be used in various industries, e.g. automotive, aeronautics, space and medicine. Table I provides a short comparison of the DEAP and Piezo incremental actuator technologies.

TABLE I. COMPARISON OF DEAP AND PIEZO INCREMENTAL ACTUATOR TECHNOLOGIES

Parameter	Piezo Technology	DEAP Technology
Strain	Small (~0.02-0.1 %)	Large (~5-100 %)
Force density	High (~20 N/mm^2)	Medium (~0.5 N/mm^2)
Structural flexibility	Low (Young's Modulus Y=~40-60 GPa)	High (Young's Modulus Y=~1.1 MPa)
Linear velocity per unit length = Strain×actuation frequency	Medium (~20-100 Hz)	High (~100-1500 Hz)

Driving the DEAP incremental actuator has three main challenges from a power electronics standpoint. Firstly, it requires high voltages of approximately 2.5 kV at relatively low currents [5], to generate sufficient force and displacement for the sub-actuators. Suitable energy sources for the incremental actuator application are lithium batteries with voltage range 9-24 V; this necessitates the need of high voltage step-up circuits as a driving mechanism for the DEAP actuator. Secondly, DEAP actuators convert only a small fraction of the input electrical energy into mechanical work, while they store the remainder in the capacitive structure of the actuator and must be recovered to maximize the system efficiency; this necessitates the need of bi-directional converters [6]-[8], [11]. Finally, control of charge and discharge cycles of three sub-actuators to achieve the required incremental motion.

Prior work on the high voltage drivers for the DEAP actuators demonstrated a world's first low voltage piezoelectric transformer based DEAP solution, and it was integrated into a core less DEAP actuator [9], and a flyback converter topology to drive the PolyPower Push Inlastor DEAP actuator for wind turbine flaps application [10], without energy recovery circuits in both topologies. Bi-directional, high voltage DC-DC converter topology for capacitive charging application has been recently proposed and implemented in [13], and the detailed loss analysis of the same converter has been discussed in [14]. The overall goal of this paper is the design, control and implementation of the three high voltage DC-DC converters.

The paper is organized as follows. Section II describes the basic idea and operational diagrams of the DEAP incremental actuator concept. Section III presents high voltage driving circuits for the incremental actuator. Section IV discusses the experimental results, and the implementation issues, followed by the conclusion in Section V.

INCREMENTAL DEAP ACTUATOR

The PolyPower axial DEAP actuator and the DEAP incremental actuator conceptual diagrams are shown in Figs. 1 and 2, respectively. The DEAP incremental actuator consists of three axial DEAP actuators viz., one extender (A_2) and two grippers (A_1 and A_3) at either end. Each gripper that is connected to mechanical supports on either side, expands and clamps to the guiding bar surface when charged, and unclamp from it, when discharged. The extender expands axially along the axis of the guiding bar. When in operation, one gripper holds the guiding bar while the other gripper is in the released position. The extender either pushes or pulls the released gripper. The incremental actuation sequence of steps, and the driving voltage waveforms of the grippers and the extender are shown in Figs. 3-5, respectively. The incremental actuator undergoes 6 steps of different operations (Fig. 3), to achieve a single incremental actuation stroke.

A. The moving sequence of steps for the linear incremental motion towards the positive x-axis (right) direction

- *Start:* All actuators are in the discharged state.
- *Step 0:* A_1 is charged and clamps to the guiding bar. A_2 and A_3 are in the discharged state.
- *Step 1:* A_1 remains in the charged state. A_2 is charged and pushes the mechanical structure towards right, and A_3 remains in the discharged state.
- *Step 2:* A_1 and A_2 still remain in the charged state. A_3 is charged.
- *Step 3:* A_1 is discharged and is in the released position. A_2 and A_3 still remain in the charged state.
- *Step 4:* A_1 remains in the discharged state. A_2 is discharged, and A_3 remains in the charged state.
- *Step 5:* A_1 is charged. A_2 remains in the discharged state, and A_3 remains in the charged state.

- *Step 6:* A_1 remains in the charged state. A_2 remains in the discharged state, and A_3 is discharged.
- End: All actuators are discharged at the end.

The Step 0 is used only for charging the actuator A_1. The Steps 1-6 repeat for achieving continuous incremental actuations.

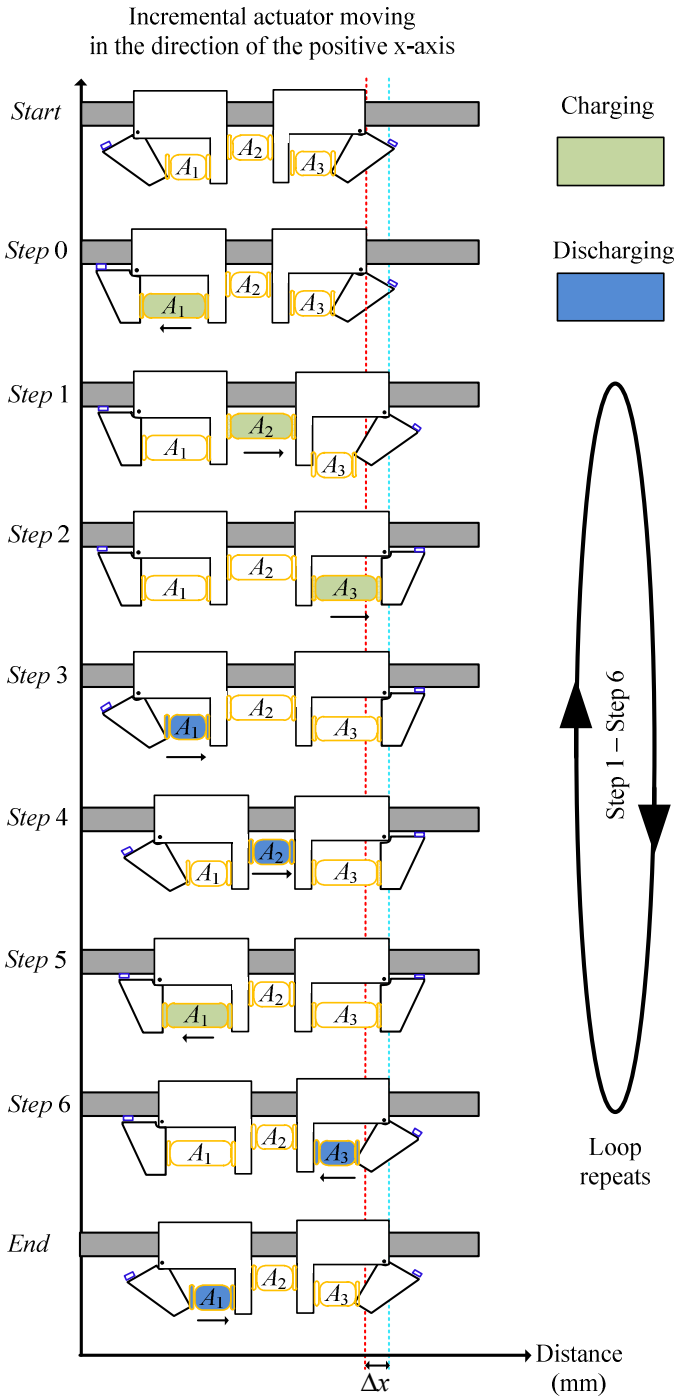

Figure 3: Moving sequence of the incremental actuator for moving towards the positive x-axis direction.

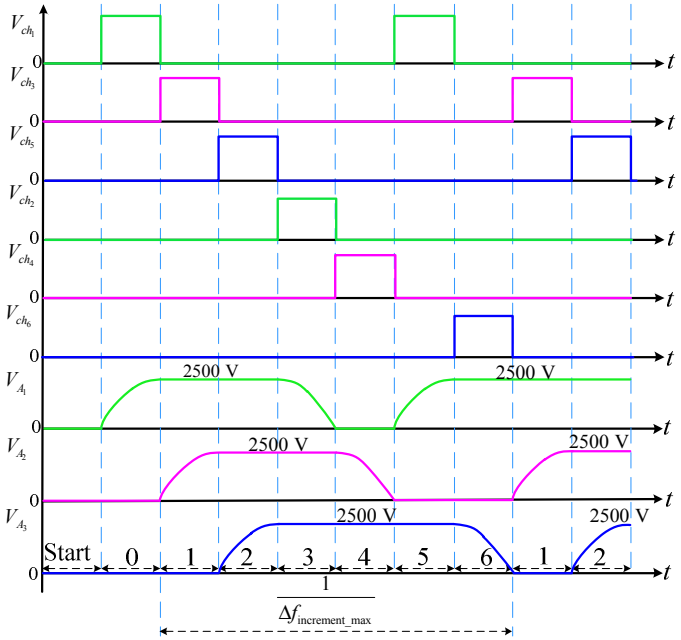

Figure 4: Driving voltages of the sub-actuators for moving towards the positive x-axis direction with maximum speed.

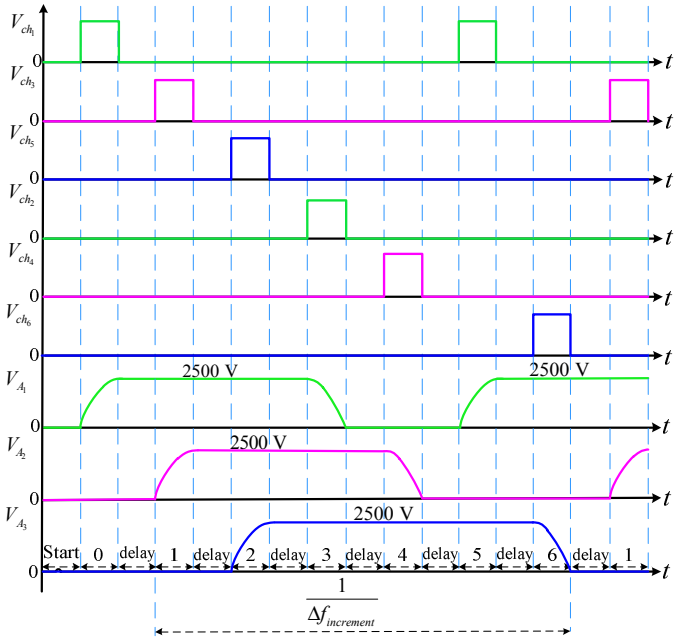

Figure 5: Driving voltages of the sub-actuators for moving towards the positive x-axis direction with variable speed.

The moving sequence of steps for the linear incremental motion towards the negative x-axis (left) direction can be easily drawn similar to Fig. 3. In Fig. 4, Δx is the stroke of the incremental actuator for one incremental actuation movement. The driving voltages for moving with the maximum frequency (speed) are shown in Fig. 4, where no delay is provided between the actuator charge and discharge cycles. The incremental actuator speed can be changed, by proving delay between the actuator charge and discharge

cycles as shown in Fig. 5. However, when the incremental actuator is loaded when in operation, the delay between the Steps 1 and 2 can be skipped, to prevent the actuator being led the load. This can prevent the pulling of the incremental actuator by the load when actuator A_2 is charged. In Figs. 4 and 5 $\Delta f_{\text{increment\_max}}$ and $\Delta f_{\text{increment}}$ are the maximum and variable incremental actuation frequencies, respectively.

III. High Voltage Drivers for Incremental DEAP Actuator

The basic block diagram of the high voltage driving circuits to drive the DEAP incremental actuator is shown in Fig. 6. The complete circuit schematic of the DEAP incremental actuator driven by multiple bi-directional high voltage DC-DC converters is shown in Fig. 7. The topology is a peak current controlled bi-directional flyback converter. Three bi-directional flyback converters are powered by the same source. Each converter independently controls the charge and discharge operations of the three axial sub-actuators (two grippers and an extender) in the incremental actuator. The basic theory of operation of the proposed circuit is described below.

B. Bi-directional flyback converter

1) Charge process: To transfer the energy from the source to the actuator A_1, M_1 is turned ON by the analog controller 1 (AC_1) [12], which is enabled by the enable signal V_{ch_1}, provided by the digital controller, causing the current in the primary winding L_{mp_1} of the flyback transformer to increase to the peak value I_{ppk1}. When M_1 is turned OFF, the energy stored in the transformer core is transferred to the capacitive actuator C_{A_1} via secondary winding L_{ms_1} and diode D_{HV_1}, causing the output voltage V_{A_1} to increase. C_{A_2} and C_{A_3} are charged independently, in a similar fashion through the DC-DC converters 2 and 3, respectively.

The energy balance equation for the converter 1, during the charging process is:

$$\frac{L_{mp_1} I_{ppk_1}^2}{2} - E_{loss_1} = \frac{C_{A_1}}{2}\left(V_{\text{A}_1\_final}^2 - V_{\text{A}_1\_initial}^2\right) \quad (1)$$

where E_{loss_1} is the dissipated energy in the flyback converter, $V_{A_1\_initial}$ and $V_{A_2\_final}$ are the values of output voltage V_{A_1} at the beginning and end of a switching cycle.

2) Discharge process: To transfer the energy back to the source from the actuator A_1, M_2 (is turned ON by the analog controller 2 (AC_2), which is enabled by the enable signal V_{ch_2}, provided by the digital controller, causing the current in the secondary winding L_{ms_1} of the flyback transformer to increase to the peak value $-I_{spk1}$. When M_2 is turned OFF, the energy stored in the transformer core is transferred to the source via primary winding L_{mp_1} and the body diode of M_1, i.e., D_{b_1}, causing the output voltage V_{A_1} to decrease. C_{A_2} and C_{A_3} are discharged independently, in a similar fashion through the DC-DC converters 2 and 3, respectively.

The energy balance equation for the converter 1, during the discharging process is:

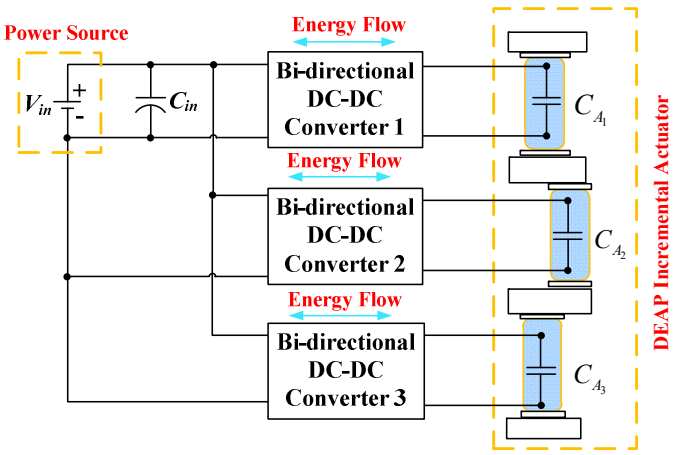

Figure 6: Block diagrams of multiple high voltage bi-directional DC-DC converters and digital controller.

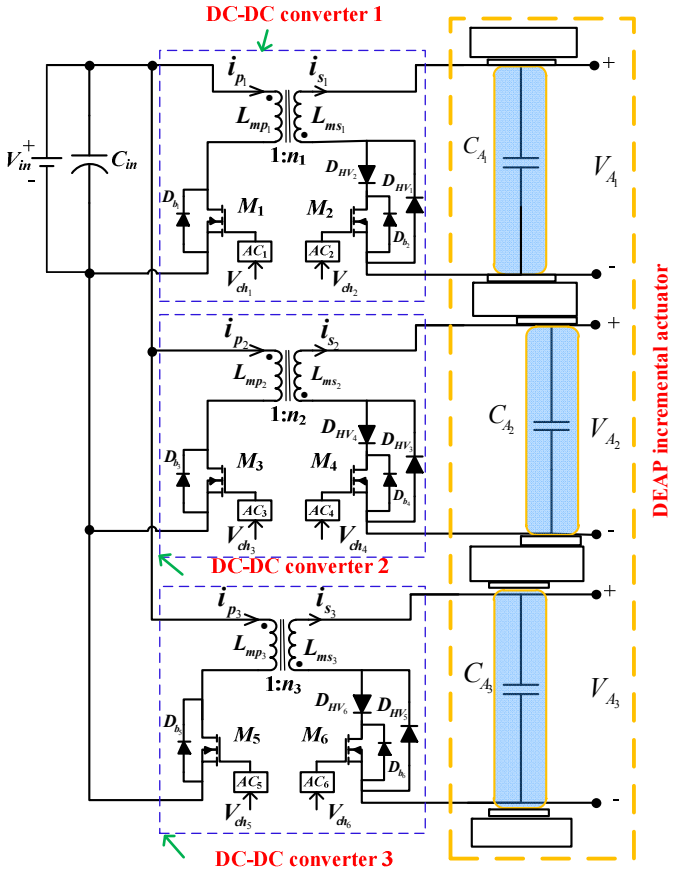

Figure 7: Circuit schematic of the DEAP incremental actuator driven by multiple high voltage bi-directional DC-DC converters.

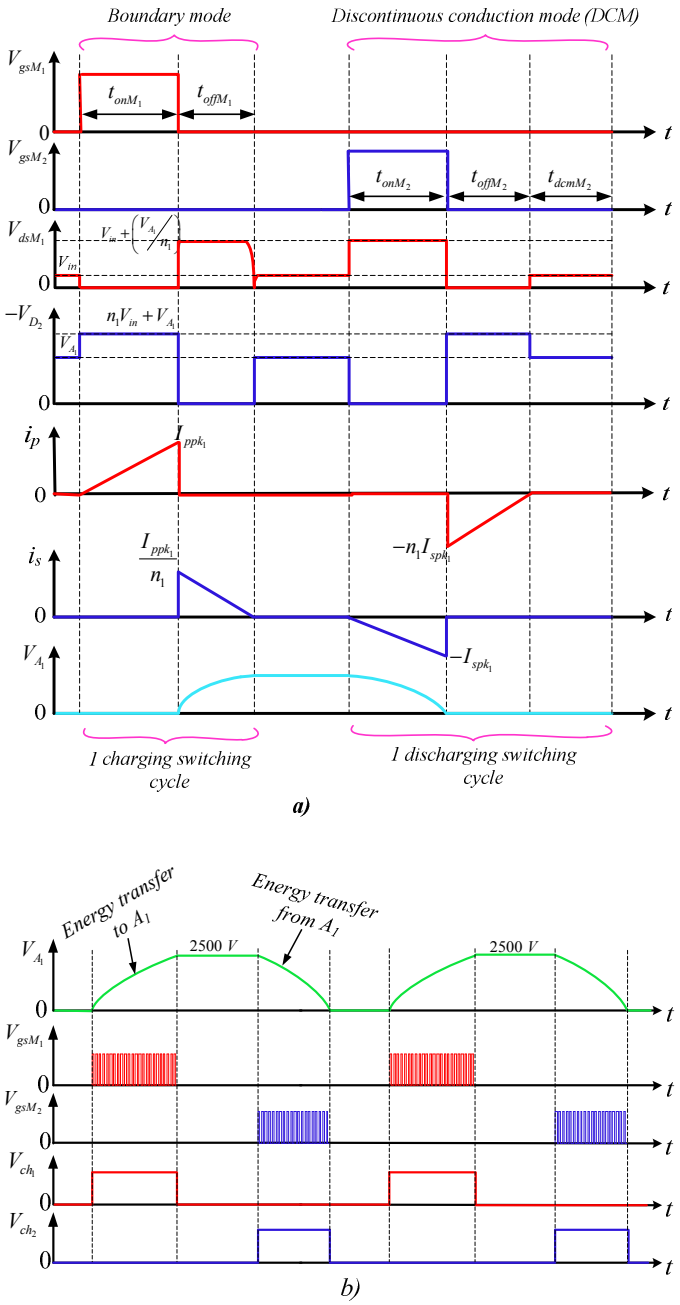

Figure 8a): Ideal switching waveform of the bi-directional flyback converter 1; 8b): Driving signal for the sub-actuator A_1

$$\frac{L_{ms_1} I_{spk_1}^2}{2} - E_{loss_2} = \frac{C_{A_1}}{2}\left(V_{A_1\_initial}^2 - V_{A_1\_final}^2\right) \quad (2)$$

where E_{loss_2} is the dissipated energy in the flyback converter during a discharging switching cycle. The same principles apply for the converters 2 and 3. The ideal bi-directional flyback converter waveforms during energy transfer and energy recovery processes are shown in Fig. 8. In any DC-DC converter of Fig. 7, the low voltage MOSFET is used during energy transfer from source to load, while high voltage MOSFET is used during energy recovery from load to source. More details about the bi-directional flyback converter topology and analysis can be obtained from [13].

C. Digital controller

For controlling the incremental actuator, the 16-bit microcontroller PIC18F2550 has been used. The block diagram of the digital controller is shown in Fig. 9.

The main functions of the microcontroller are:

- To control the charge and discharge sequences of the individual sub-actuators
- Monitoring the high voltage to provide the over voltage protection for all converters
- To change the direction of movement of incremental actuator
- To change the speed of movement of the incremental actuator

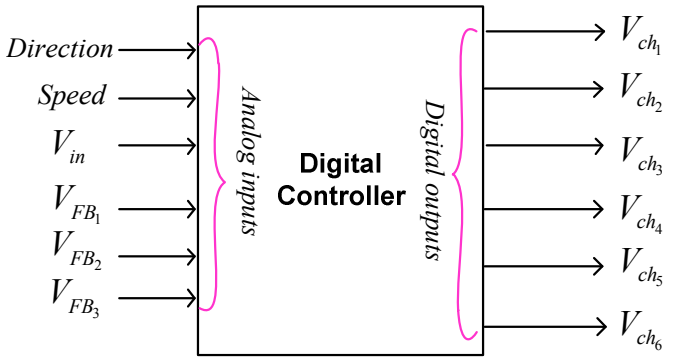

Figure 9: Block diagram of the digital controller to control the 3 high voltage DC-DC converters.

D. High voltage measurement

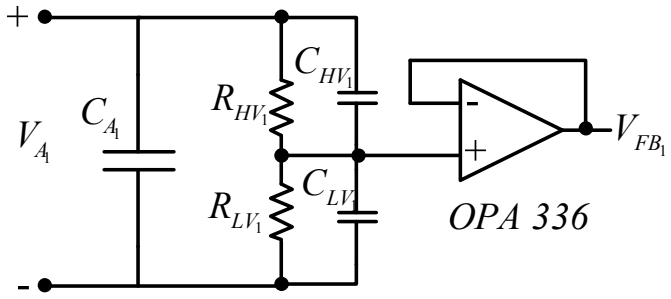

Figure 10: High voltage measurement circuit of converter 1 with resistive and capacitive voltage divider.

The high voltage measurement circuit for DC-DC converter 1, with resistive and capacitive voltage dividers is shown in Fig. 10. The feedback voltage is buffered by an operational amplifier having a very high input impedance (>10 TΩ), and the outputs of the buffer is used as the feedback signal to the digital controller which provides the over voltage protection.

The low frequency or steady state relationship between the feedback signals and the output voltages are given by

$$V_{FB_i} = V_{A_i}\left[\frac{R_{LV_i}}{R_{HV_i} + R_{LV_i}}\right]; \; i=1,\ 2 \text{ and } 3 \tag{3}$$

To eliminate the impact of the parasitic capacitors, without increasing the static discharge of the DEAP actuator, a capacitive voltage divider is added. By using relatively large capacitors in the divider the impact from the parasitic capacitors is neglected.

The frequency dependent feedback voltages for the combined resistive and capacitive voltage dividers is given in (4).

$$V_{FB_i} = V_{A_i}\left[\frac{\dfrac{R_{LV_i}}{1 + j\omega R_{LV_i} C_{LV_i}}}{\dfrac{R_{HV_i}}{1 + j\omega R_{HV_i} C_{HV_i}} + \dfrac{R_{LV_i}}{1 + j\omega R_{LV_i} C_{LV_i}}}\right] \tag{4}$$

$i = 1,\ 2 \text{ and } 3$

The frequency dependent feedback voltages can become frequency independent, if

$$R_{LV_i} C_{LV_i} = R_{HV_i} C_{HV_i}; \; i = 1,\ 2 \text{ and } 3 \tag{5}$$

The frequency independent feedback voltages are

$$V_{FB_i} = V_{A_i}\left[\frac{R_{LV_i}}{R_{HV_i} + R_{LV_i}}\right] = V_{A_i}\left[\frac{C_{HV_i}}{C_{LV_i} + C_{HV_i}}\right] \tag{6}$$

$i = 1,\ 2 \text{ and } 3$

where R_{HV_i}, R_{LV_i}, C_{HV_i} and C_{LV_i} are the high voltage (3 kV), low voltage resistors, high voltage (3 kV, C0G/NP0 type) and low voltage capacitors used in the high voltage sensing network, respectively. For each converter, $R_{HV} = 5\ G\Omega$, $R_{LV} = 5.1\ \text{M}\Omega$, $C_{HV} = 33\ \text{pF}$, and $C_{HV} = 33\ \text{nF}$.

IV. Experimental Results

Three high voltage bi-directional flyback converters were experimentally tested. The experimental results are shown in Figs. 11 and 14. The maximum energy efficiency of the converters during charging operation (transferring the input energy to the actuator) was 87 %, and during discharging operation (transferring the actuator energy back to the source) it was 80 %, for an output energy of 0.62 J. The converter specifications are provided Table II. The parameters of the flyback transformers 1, 2 and 3 are given in Tables III, IV and V respectively. The measurement of transformer parameters is described below.

E. Measurement of Transformer parameters using the Impedance Analyser

1) Magnetizing inductance (L_m): Magnetizing inductance of the primary/secondary side can be obtained by opening the secondary/primary winding and measuring the inductance across the primary/secondary winding at the frequency of interest.

2) Leakage inductance (L_{lk}): Leakage inductance referred to the primary/secondary side can be obtained by shorting the secondary/primary winding and measuring the inductance across the primary/secondary winding.

3) Self capacitance (C_s): Self capacitance of the secondary winding can be obtained by measuring the resonant frequency (f_{rs}) of the secondary winding from its impedance plot. Then, self-capacitance C_s is given by

$$C_s = \frac{1}{\left(2\pi f_{rs}\right)^2 L_{ms}} \tag{7}$$

where L_{ms} is the secondary winding magnetizing inductance.

4) Interwinding capacitance: Interwinding capacitance can be obtained, by shorting both primary and secondary windings, and measuring the capacitance across the shorted primary and secondary windings.

F. Discussion

During charging process the converter operates in the boundary mode, and during discharging it operates in the discontinuous conduction mode. The energy loss is mainly contributed as the capacitive switching loss caused by the transformer parasitic winding capacitance, and the leakage loss due to the transformer's leakage inductance. Research is still ongoing to optimize the flyback converter to obtain very high energy efficiency in the entire operating range.

Practical experience reveals that careful design of the flyback transformer with low leakage inductance and low stray capacitance is required for achieving continuous high voltage bi-directional operation. In the current market the available high voltage MOSFETs for this application are 4 kV, IXTV400NS (used in the current research) and 4.5 kV, IXTA02N450HV MOSFETs. Improper flyback transformer designs may lead to failure of the converter during the discharging operation. The experimental prototype is shown in Fig. 15. The charging and discharging energy efficiency [13] measurement results are provided in Figs. 16 and 17.

TABLE II. Converter Specifications

Parameter	Value
Input voltage	24 V
Output voltage	0-2500 V
Stored energy at 2.5 kV output voltage	0.62 J
Capacitance of each sub-actuator/film capacitor load	200 nF
Incremental actuation frequency	~ 1-5 Hz
Primary peak current during charging/discharging process	4.2 A / 5.3 A
Input filter capacitor	3900 μF

TABLE III. FLYBACK TRANSFORMER 1 PARAMETERS

Parameter	Value
Flyback transformer core type / Material	EF20 / N87
Primary (L_{mP}) / Secondary magnetizing inductance (L_{mS})	29.5 μH / 16 mH
Primary turns (N_P) / Secondary turns (N_S)	16 / 375
Leakage inductance of transformer primary (L_{lkP}) / secondary (L_{lkS})	1.11 μH / 633 μH
Secondary winding self (C_s) / Interwinding capacitance (C_{int})	17 pF / 41 pF
DC resistance of primary (R_{dcP}) / secondary winding (R_{dcS})	62 $m\Omega$ / 28.5 Ω
Primary (n_{lp}) / Secondary layers (n_{ls})	1 / 5
Each layer primary (h_p) / secondary winding thickness (h_s)	0.5 mm / 0.1 mm

TABLE IV. FLYBACK TRANSFORMERS 2 PARAMETERS

Parameter	Value
Flyback transformer core type / Material	EF20 / N87
Primary (L_{mP}) / Secondary magnetizing inductance (L_{mS})	33.5 μH / 20.8 mH
Primary turns (N_P) / Secondary turns (N_S)	16 / 400
Leakage inductance of transformer primary (L_{lkP}) / secondary (L_{lkS})	1.2 μH / 728 μH
Secondary winding self (C_s) / Interwinding capacitance (C_{int})	19.4 pF / 33.5 pF
DC resistance of primary (R_{dcP}) / secondary winding (R_{dcS})	85 $m\Omega$ / 41 Ω
Primary (n_{lp}) / Secondary layers (n_{ls})	2 / 5
Each layer primary (h_p) / secondary winding thickness (h_s)	0.65 mm / 0.1 mm

TABLE V. FLYBACK TRANSFORMERS 3 PARAMETERS

Parameter	Value
Flyback transformer core type / Material	EF20 / N87
Primary (L_{mP}) / Secondary magnetizing inductance (L_{mS})	28 μH / 17 mH
Primary turns (N_P) / Secondary turns (N_S)	16 / 400
Leakage inductance of transformer primary (L_{lkP}) / secondary (L_{lkS})	1.25 μH / 710 μH
Secondary winding self (C_s) / interwinding capacitance (C_{int})	22.6 pF / 35 pF
DC resistance of primary (R_{dcP}) / secondary winding (R_{dcS})	84 $m\Omega$ / 41 Ω
Number of primary (n_{lp}) / secondary layers (n_{ls})	2 / 5
Each layer primary (h_p) / secondary winding thickness (h_s)	0.65 mm / 0.1 mm

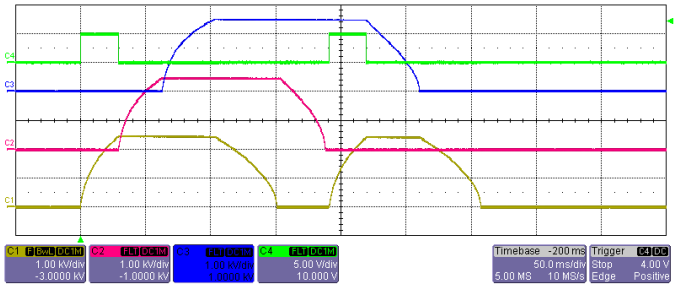

Figure 11: Experimental result with the 3 dc-dc converters with 1 incremental actuation cycle; CH1: V_{A_1} ; CH2: V_{A_2} ; CH3: V_{A_3} ; CH4: V_{ch_1} ; $\Delta f_{increment\_max} = 4.3$ Hz

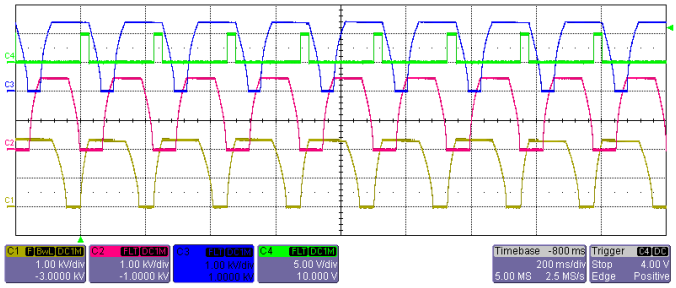

Figure 12: Experimental result with the 3 dc-dc converters with several incremental actuation cycles; CH1: V_{A_1} ; CH2: V_{A_2} ; CH3: V_{A_3} ; CH4: V_{ch_1} ; $\Delta f_{increment\_max} = 4.3$ Hz

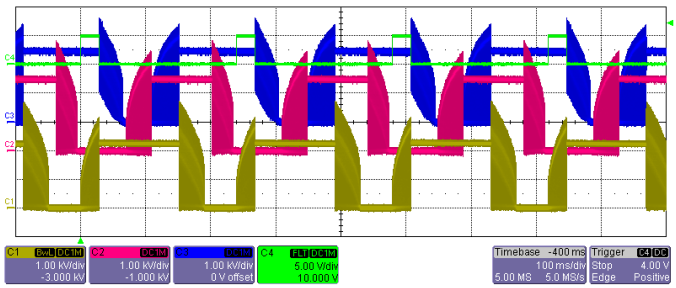

Figure 13: Experimental result with the 3 dc-dc converters; CH1: $-V_{D_{HV_1}}$; CH2: $-V_{D_{HV_2}}$; CH3: $-V_{D_{HV_3}}$; CH4: V_{ch_1} ;

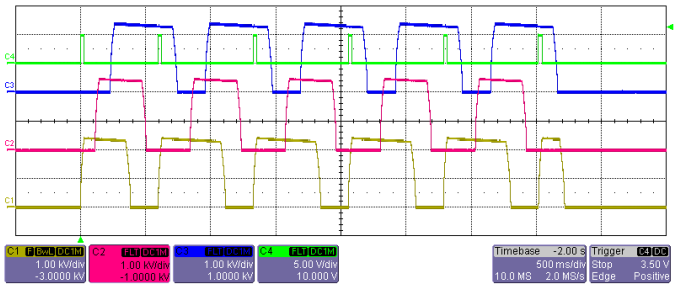

Figure 14: Experimental result with the 3 dc-dc converters with several incremental actuation cycles; CH1: V_{A_1} ; CH2: V_{A_2} ; CH3: V_{A_3} ; CH4: V_{ch_1} ; $\Delta f_{increment} = 1.5$ Hz.

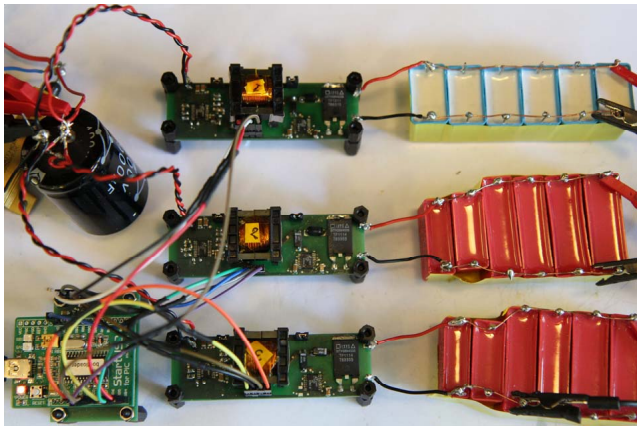

Figure 15: Experimental setup picture.

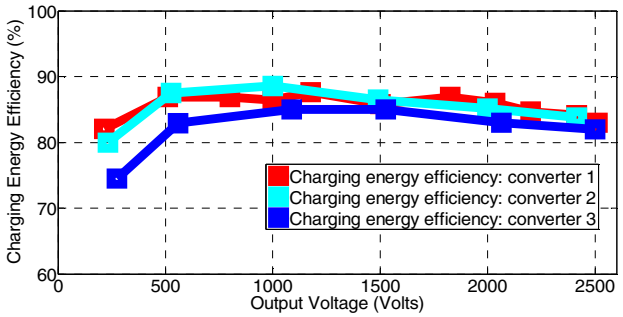

Figure 16: Charging energy efficiency measurement results of three high voltage converters.

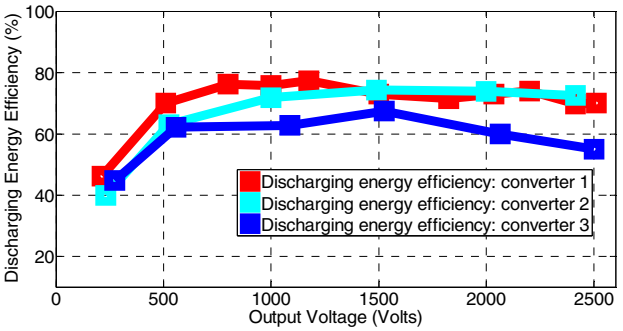

Figure 17: Discharging energy efficiency measurement results of three high voltage converters.

V. CONCLUSIONS

In this paper, the concept of world's first DEAP incremental actuator is introduced. The driving circuit and the control concepts for the DEAP incremental actuator are discussed. Experimental results for three high voltage bi-directional DC-DC converter power stages are presented. The maximum charging energy efficiency of converter 2, for a non-optimized flyback transformer was 87%. It is expected to achieve higher energy efficiency by optimizing the flyback converter. The digital controller is implemented to change the increment actuator speed and direction of movement. The proposed converters with the required control for the DEAP incremental actuator concept, were successfully tested with the film capacitive loads. Due to unavailability of the actuators, the driving circuits will be tested with the DEAP incremental actuator in the future. It is expected that the converter's performance will be the same for both film capacitive load and the incremental actuators. The final conclusion is that the proposed new DEAP incremental actuator will have promising and demanding applications in the future.

REFERENCES

[1] R. E. Pelrine, R. D. Kornbluh, Q. Pei, and J. P. Joseph, "High-speed electrically actuated elastomers with strain greater than 100%," *in Proc. of Science*, vol. 287, pp. 836–839, 2000.

[2] R. E. Pelrine, R. D. Kornbluh, and J. P. Joseph, "Electrostriction of polymer dielectric with compliant electrodes as a means of actuation," *in Proc. of Sens. Actuators A*, vol. 64, pp. 77–85, 1998.

[3] R. Sarban, B. Lassen, M. Willatzen, "Dynamic Electromechanical Modeling of Dielectric Elastomer Actuators With Metallic Electrodes," in Proc. *IEEE/ASME Transactions on Mechatronics,* vol. 17, no. 5, pp. 960-967, Oct. 2012.

[4] http://www.polypower.com/

[5] M. Tryson, H.E. Kiil, M. Benslimane, "Powerful tubular core free dielectric electro activate polymer (DEAP) push actuator," *in Proc. of SPIE*, vol. 7287, 2009.

[6] L. Huang, P. Thummala, Z. Zhang, and M. A. E. Andersen, "Battery powered high output voltage bidirectional flyback converter for cylindrical DEAP actuator*," in Proc. International Power Modulator and High Voltage Conference (IPMHVC)*, 3-7 June 2012.

[7] L. Eitzen, C. Graf, and J. Maas, "Cascaded bidirectional flyback converter driving DEAP transducers," *in Proc. Annual Conference on IEEE Industrial Electronics Society (IECON 2011)*, pp.1226-1231, 7-10 Nov. 2011.

[8] L. Eitzen, C. Graf, and J. Maas, "Bidirectional power electronics for driving dielectric elastomer transducers," *in Proc. of SPIE,* vol. 8340, p.834018 1-12, 2012.

[9] T. Andersen, M. S. Rødgaard, O. C. Thomsen and M. A. E. Andersen, "Low voltage driven dielectric electro active polymer actuator with integrated piezoelectric transformer based driver," *in Proc. of SPIE Electroactive Polymer Actuators and Devices (EAPAD)*, vol. 7976, p. 79762N, 2011.

[10] P. Thummala, Z. Zhang, M. A. E. Andersen, and O. C. Thomsen, "A high voltage DC-DC converter driving a Dielectric Electro Active Polymer actuator for wind turbine flaps," *in Proc. Universities Power Engineering Conference (UPEC),* pp. 1-7, 4-7 Sept. 2012.

[11] M. Karpelson, G. Y. Wei, and R. J. Wood, "Driving high voltage piezoelectric actuators in microrobotic applications," *in Proc. of Sensors and Actuators A*, vol. 176, pp. 78– 89, 2012.

[12] Linear Technology, "LT3751 High Voltage Capacitor Charger with Regulation", Linear Technology Corporation, USA. http://cds.linear.com/docs/Datasheet/3751fc.pdf

[13] P. Thummala, Z. Zhang, M. A. E. Andersen, "High Voltage Bi-directional Flyback Converter for Capacitive Actuator," in Proc. *European Power Electronics Conference (EPE),* pp. 3-6th Sept. 2013.

[14] P. Thummala, H. Schneider, Z. Ouyang, Z. Zhang, M. A. E. Andersen, "Estimation of transformer parameters and loss analysis for high voltage capacitor charging application," in Proc. *IEEE ECCE Asia,* pp. 704-710, 3-6 Jun. 2013.

Appendix P

A new Incremental Actuator based on Electro Active Polymer: Conceptual, Control and Driver Design Considerations

---

Revision Submitted to IEEE Transactions on Mechatronics

A new Incremental Actuator based on Electro Active Polymer: Conceptual, Control and Driver Design Considerations

Prasanth Thummala[*], *Student Member, IEEE,* Henrik Schneider[*], *Student Member, IEEE,* Zhe Zhang[*], *Member, IEEE,* Michael A. E. Andersen[*], *Member, IEEE,* Sarban Rahimullah[#], *Member, IEEE*

***Abstract*—This paper presents an overview of the widely used conventional linear actuator technologies and existing electro active polymer based linear and rotary actuators. It also provides conceptual, control and driver design considerations for a new dielectric electro active polymer (DEAP) based incremental actuator. The proposed actuator consists of three independent DEAP actuators with a unique cylindrical design that potentially simplifies mass production and scalability compared to existing DEAP actuators. To accomplish the incremental motion, each actuator is independently charged and discharged by a high voltage bidirectional DC-DC converter. The topology used for the high voltage driver is a peak-current controlled bidirectional flyback converter. The scalability of the proposed incremental actuator is discussed and the estimated speed and force of various designs are provided. The high voltage drivers are experimentally tested with both capacitive loads and a prototype of the DEAP incremental actuator. The prototype moves with a maximum velocity of 1.5 mm/s, at 2.87 Hz incremental driving frequency, when all actuators are driven with 1.8 kV.**

***Index Terms*—linear actuators, switch-mode power supplies, DC-DC power converters, actuators, energy efficiency, dielectric electro active polymer (DEAP)**

I. INTRODUCTION

ACTUATORS providing linear motion are used in a vast variety of applications ranging from large size machineries (e.g., cranes) to small scale micro-electro-mechanical system (MEMS) devices used for micro positioning. Linear actuators are typically characterized by their maximum stroke length, force, speed, and precision (or resolution). The typical linear actuators include electro-mechanical, hydraulic, pneumatic, piezo, and electro active polymer, etc.

This work was supported by the Danish National Advanced Technology Foundation under the "Highly efficient low cost energy generation and actuation using disruptive DEAP technology" project, managed by Danfoss PolyPower A/S, Denmark.

Part of this paper was presented and selected as a best student paper award at IEEE Energy Conversion Congress and Exposition (ECCE) USA'13 conference (Sept. 15-19th, 2013, Denver, CO, USA).

[*]The authors are with the Department of Electrical Engineering, Technical University of Denmark, DK-2800 Kongens Lyngby, Denmark (e-mail: pthu@elektro.dtu.dk, hensc@elektro.dtu.dk, zz@elektro.dtu.dk, ma@elektro.dtu.dk).

[#]The author is with LEAP Technology, Science and Technology Park, DK-2800 Kongens Lyngby, Denmark (e-mail: Rahim@leaptechnology.com).

An electromechanical linear actuator uses a DC motor or a stepper motor to control a linear-action shaft output, as shown in Fig. 1. The rotary motion of the motor is converted to linear displacement through a belt drive, a gearing, a threaded rod and a nut connected to a shaft. The advantages are high force, high speed and high precision which all can be tailored via high design flexibility. The disadvantages are mechanical complexity, weight, size and cost. Pneumatic linear actuators as shown in Fig. 2 operate with an external source of compressed air. They are efficient, but relatively complex to control via pressure valves and compressor manipulation.

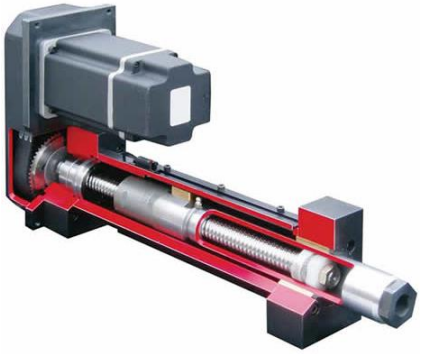

Fig. 1. An electro-mechanical linear actuator [1].

Hydraulic linear actuators are used in many industrial applications requiring higher levels of force than provided through equivalently sized electromechanical systems. Hydraulic actuators not only allow the generation of large forces, but also capable of closed-loop velocity controlling or highly precise positioning of heavy loads. A hydraulic linear

Fig. 2. A pneumatic linear actuator [2].

actuator as shown in Fig. 3 requires an external source for fluid pressurization. Unlike pneumatic actuators, a leak from hydraulic equivalents can foul equipment and require additional clean up procedures depending on the type of fluid used. Control is complex, involving compressor control and hydraulic valves. All the aforementioned standard linear actuators are mechanically complex systems, hence are not suitable for some applications.

Fig. 3. A hydraulic linear actuator [3].

Piezo actuators convert electrical energy directly into mechanical energy and vice versa. The actuators typically operate in a clamp and push configuration and allow for motions in the sub-nanometer range. Besides a high resolution the piezo actuator as shown in Fig. 4 has other advantages such as small size, light weight, operation under magnetic fields, and low wear and tear. The disadvantages are low force, low speed, high cost, low shock robustness and high driving voltage (~100-200 Vac) [4].

Fig. 4. A piezo linear actuator [5].

Dielectric electro active polymer (DEAP) is an emerging smart material that has experienced substantial development and has gained increasing attention by the researchers from academia and industry [6]-[8]. The DEAP material consists of a very thin (35-55 μm) incompressible silicone elastomer film with a compliant electrode layer on both sides [9]-[12]. DEAP can be used in actuation, sensing and energy harvesting applications. The basic behavior of the DEAP is the reduction in the polymer's thickness and increase in its area, due to an applied electric field to its electrodes. The unique properties of DEAP are large strain (5-100%), light weight (7 times lighter than steel), high flexibility (100,000 times less stiff than steel), low noise operation, and low power consumption. DEAP, when used as actuators, have the potential to be an effective replacement for many conventional actuators viz. electro-mechanical, pneumatic, hydraulic, piezo etc. The linear DEAP actuator shown in Fig. 5 is ideally equivalent to a pure capacitive load [12], [13].

Fig. 5. A prototype of linear DEAP actuator.

Several researchers have investigated and implemented electro active polymer based linear and rotary type actuators. Numerous applications of dielectric elastomers including an inchworm robot and rotary motors have been described in [14]. The robotic inchworm as shown in Fig. 6 uses electrostatic clamps which enable it to travel over both vertical and horizontal surfaces, for tasks such as inspection in narrow pipes [14]. A segmented DE-driven inchworm concept has been described in [15], and each segment consists of a single tube, two DE membranes and a coupling fluid. The walking robot using a multi-functional electro elastomer (MER) spring roll as each of the robot's six legs is shown in Fig. 7 [16]. Each spring roll leg was a linear actuator, with 3-6 mm stroke at 1-10 Hz frequency. The speed was as high as 2.7 in/s. A rotary motor made with a pair of bow tie elastomer actuators as shown in Fig. 8, with an output power of 4 W at 100 RPM has been demonstrated in [14]. The emerging DE technology has been thoroughly reviewed and presented exciting possibilities across a wide range of applications including soft robotics [17]. An earthworm robot as shown in Fig. 9 has been made using a novel soft actuator based on a dielectric elastomer. It has been demonstrated that the actuator moved with 1 mm/s at 5 Hz [18]. A simple rotary motor based on dielectric elastomers as shown in Fig. 10, has been proposed in [19]. A new way to achieve the rotary motion using the DEAP actuators has been reported in [20]. Furthermore,

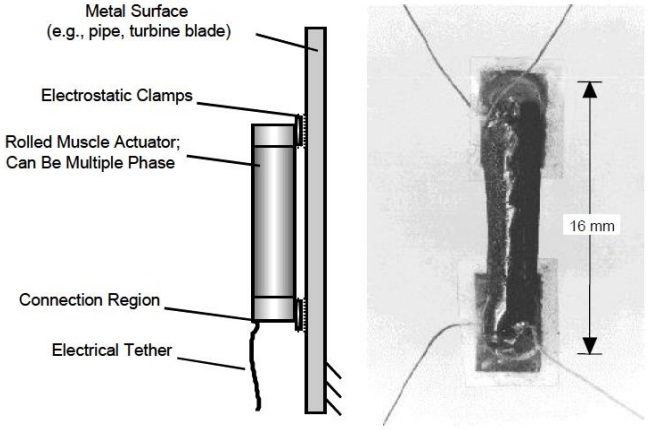

Fig. 6. An inchworm robot with a dielectric elastomer body [14].

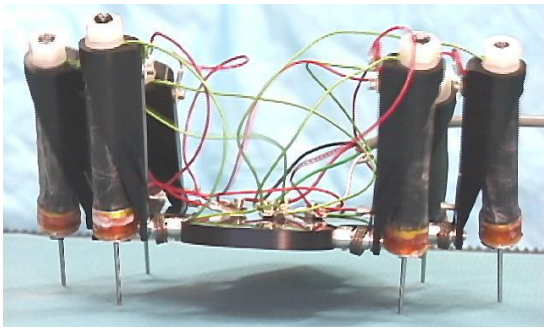

Fig. 7. A walking robot with MER spring rolls as legs [16].

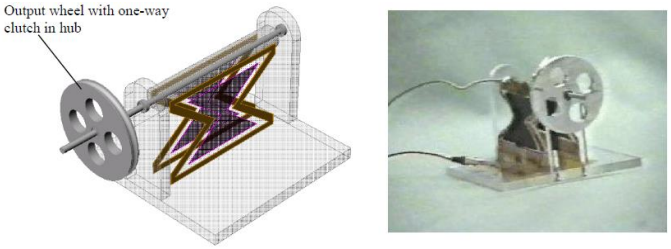

Fig. 8. A simple rotary motor based on dielectric elastomers [14].

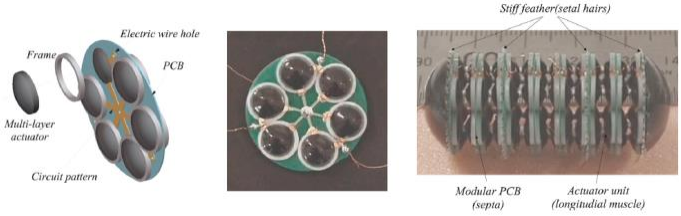

Fig. 9. The earthworm robot with the actuator module [17], [18].

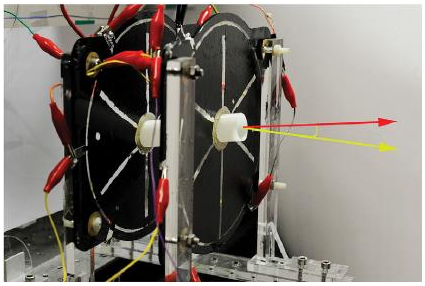

Fig. 10. A simple rotary motor based on dielectric elastomers [19].

several researchers have investigated piezo, pneumatic and hydraulic based actuators. The gain scheduling control of a walking piezo actuator is proposed in [21]. Bipolar piezo electric actuators are proposed in [22]. High-accuracy tracking control of hydraulic actuators is discussed in [23].

The DEAP incremental actuator concept, recently proposed in [24], consists of two grippers at both ends (to enable gripping operation) and an extender (to move the grippers), as shown in Fig. 11. These grippers connect with the extender mechanically. The grippers A_1 and A_3 and the extender A_2 are similar to the DEAP actuator shown in Fig. 5. For moving the DEAP incremental actuator, the three DEAP actuators (which behave as electrically isolated capacitive loads) need to be controlled. Details of the DEAP incremental actuator operation can be found in [24]. The DEAP incremental actuator technology has the potential to be used in various industries, e.g., automotive, space and medicine. Table I, provides a short comparison of the DEAP and piezo incremental actuator technologies. To summarize, the DEAP incremental actuator technology has a coarser resolution and a lower force density, but has the potential for higher velocity, higher structural flexibility and robustness compared to piezo technology. The DEAP technology is still a new technology and future performance improvements are expected.

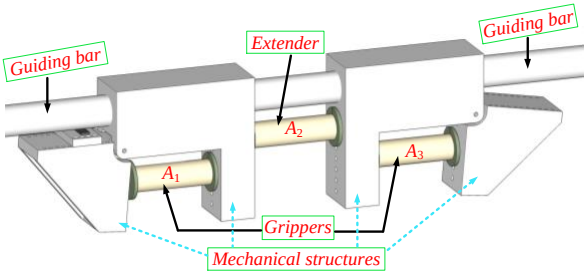

Fig. 11. Conceptual diagram of the proposed DEAP incremental actuator.

TABLE I
COMPARISON BETWEEN DEAP AND PIEZO INCREMENTAL ACTUATOR TECHNOLOGIES

Parameter	Piezo Technology	DEAP Technology
Strain (Resolution)	Small (~ 0.02-0.1%)	Large (~ 1-100%)
Force density	High (~ 20 N/mm^2)	Medium (~ 0.5 N/mm^2)
Structural flexibility	Low (Young's Modulus Y= ~ 40-60 GPa)	High (Young's Modulus Y= ~ 1.1-1.8 MPa)
Incremental actuation frequency	~ 100-5000 Hz	~ 1-15 Hz
Linear velocity per unit length = Strain×incremental actuation frequency	Medium (~ 20-500 Hz)	High (~ 1-1500 Hz)

Driving the DEAP incremental actuator has three main challenges from a power electronics standpoint. Firstly, it requires high voltages (2-2.5 kV), to generate sufficient force and stroke from each DEAP actuator. Suitable energy sources for this application are lithium batteries with a voltage range: 9-24 V DC. This necessitates the need of high voltage step-up circuits as a driving mechanism for the DEAP actuator. Secondly, DEAP actuators convert only a small fraction of the input electrical energy into mechanical work, while they store the remainder in the capacitive structure of the actuator, and must be recovered to maximize the system efficiency. This necessitates the need of bidirectional converters [25]-[27]. Finally, to move the incremental actuator with a required

speed and direction, the three DEAP actuators needs to be driven by a specific sequence of high voltage signals.

The flyback converter is suitable for high voltage and low power applications due to its simple structure and low component count [28]. Control algorithms for optimal-flyback charging of a capacitive load have been proposed in [29]. High voltage switch-mode power supplies for charging the capacitive loads have been implemented in [30], [31]. The bidirectional flyback converters are proposed in [32]-[34] to transfer the power in both directions. Prior work on the high voltage drivers for the DEAP actuators demonstrated a low voltage piezoelectric transformer based DEAP solution, and it was incorporated into a coreless DEAP actuator [35], and a bidirectional flyback converter topology to drive the PolyPower Push Inlastor DEAP actuator [36], [37]. In [38] an efficiency optimization technique is proposed for a bidirectional flyback converter in a high voltage capacitor charging application. Several transformer winding architectures (TWAs) have been investigated in [39] for the high voltage capacitor charge and discharge application. Experimental study of DEAP actuator energy conversion efficiency is performed in [40]. Intelligent control of electro active polymer actuators based on fuzzy and neuro fuzzy methodologies is proposed in [41]. Geometry optimization of tubular dielectric elastomer actuators with anisotropic metallic electrodes is discussed in [42]. Digital control of the bidirectional flyback converter is proposed in [43] for driving capacitive actuators.

The main objectives of this paper are, to provide the conceptual design and scalability of the DEAP actuators used in the incremental motor, and the necessary control and high voltage (HV) driving circuits for the newly proposed DEAP incremental actuator. The paper is organized as follows: Section II provides new concepts for the DEAP incremental actuators. Section III discusses the conceptual design of an axial DEAP actuator, followed by the scalability of DEAP actuators in Section IV. Section V describes the basic idea and operational diagrams of the DEAP incremental actuator concept. Section VI presents high voltage driving circuits for the incremental actuator, and the experimental results. Section VII provides the system integration, followed by the conclusions in Section VIII.

II. New Concepts of DEAP Incremental Actuators

Three new concepts (1, 2 and 3) of DEAP incremental actuators are provided in this section. Each concept has its unique characteristics which can demonstrate various unique properties of DEAP as described in earlier sections.

A. Concept 1

Figure 12(a) shows the concept 1 of the DEAP incremental actuator. It is designed to operate outside a cylindrical bar and consists of three sub components, namely one extender and two grippers at either end. The corrugation profile of the extender and the grippers are 90° shifted. When in operation, one gripper holds the bar while the other gripper is in the released position. The extender either pushes or pulls the released gripper.

The grippers are rolled on a core with radial tension. Rigid mechanical connections are subsequently applied. The extender sub component can be realized by simply using cylindrical actuator. The grippers and extender are joined by gluing or screwing their mechanical connections together (green plates in Fig. 12(a)). Mechanical constrainers can be applied to the grippers in order to avoid the axial extension of the grippers when in operation. Such constrainers enable the gripper to exhibit only radial movements. Soft encapsulation for protection and/or aesthetics can be applied as shown in Fig. 12(b).

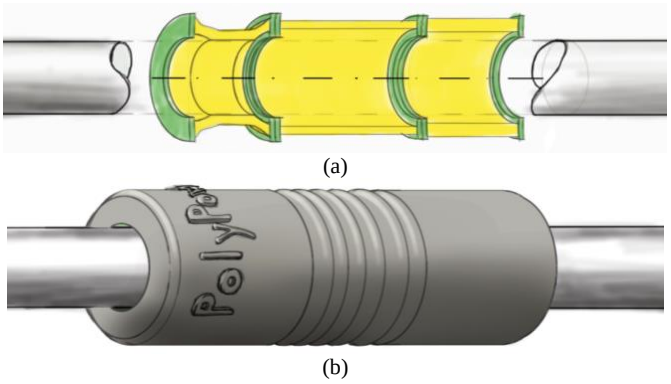

Fig. 12. Concept 1 of DEAP incremental actuator. (a) Cross section view of the actuator, (b) incremental actuator with protective and/or aesthetic encapsulation.

B. Concept 2

Concept 2 is designed to operate inside a cylindrical tube as opposed to Concept 1. Concept 2 consists of one extender and two grippers on either end. Both the grippers and the extender of Concept 2 are cylindrical actuators. Additional gripping mechanisms are applied to the grippers (red structures in Fig. 13). The gripping mechanism extends or contracts radially when the grippers are, respectively, contracting or extending axially as illustrated by the arrows in Fig. 13. The three cylindrical actuators are joined together, at their mechanical connections, by gluing or screws.

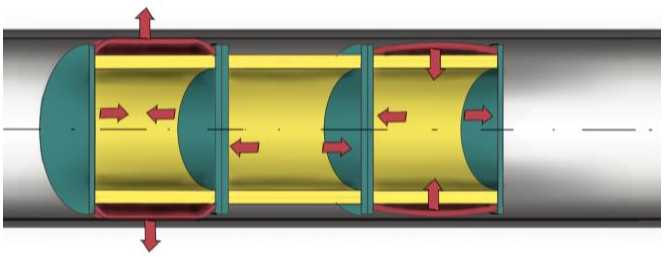

Fig. 13. Concept 2 of DEAP incremental actuator: Cross section view of the actuator with operation arrows.

C. Concept 3

The concept 3 as shown in Fig. 14(a) is based on 3 DEAPs in axial configuration. It consists of 1 extender and 2 blocking DEAPs. When the blocking DEAP is extended the wedges are driven toward the guide rod, thereby creates a blocking force.

Here three cylindrical transducers are used to facilitate the incremental motion. Auxiliary mechanics as shown in Figs. 14(b) and 14(c) are attached to the transducer enabling them to grip, release and extend on a solid rod.

The DEAP incremental actuator concept as shown in Fig. 11, is chosen as the first iteration of this feasibility study, due to its transparent motion which can be easily understood and demonstrated. However, the three concepts described in this section are the potential concepts for the DEAP based incremental motors in the future. Simple design, fast and precise adjustment, low noise operation, high energy efficiency, and low cost are the key advantages of the proposed DEAP incremental actuators compared to other linear incremental actuators or other sliding dielectric elastomer actuators.

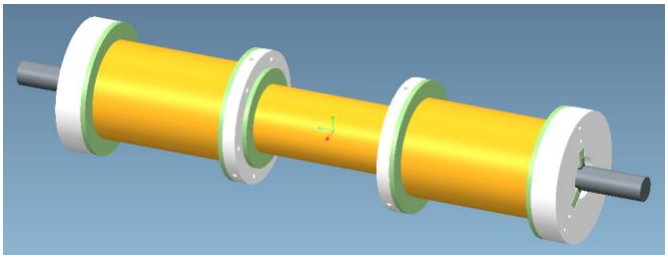

(a)

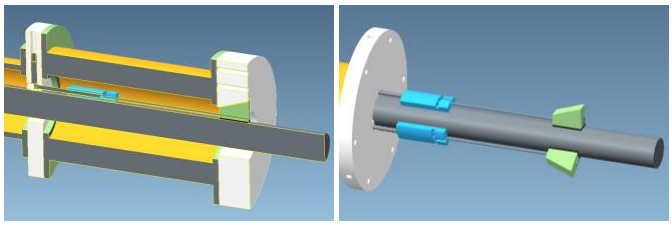

(b) (c)

Fig. 14. (a) Concept 3 of DEAP incremental actuator; (b) Side view; (c) Break system.

III. Conceptual Design of an Axial DEAP Actuator

An axial DEAP actuator is a tubular structure being formed by rolling a DEAP sheet as shown in Fig. 15(a) and 15(b). The main design parameters of such structure are its active height H_a, passive height H_p, the inner dimensions a and b, the wall thickness t, and the number of laminate layers n_l. The laminated DE film consists of two DE sheets laminated together. As shown in Fig. 15(c), only one of the DE sheets of a DE laminate is metallized at either lateral end to the left and to the right. This is to realize a safe electrical connection in the actuator by avoiding short circuiting. Some of the design parameters are assumed before the design and the remaining parameters are calculated using the known parameters and the mechanical and electrical constants of the actuator which are provided in Table II.

The capacitance of the DEAP actuator at no applied voltage is given by

$$C_{DEAP} = \varepsilon_0 \varepsilon_r \frac{WH_a}{d_0} = 399 \text{ nF} \quad (1)$$

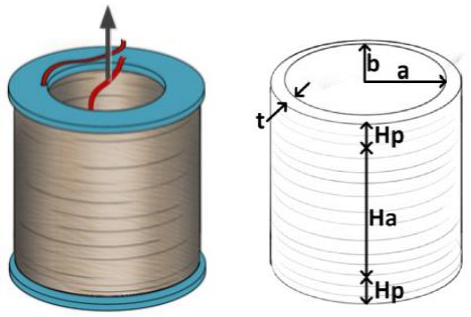

(a) (b)

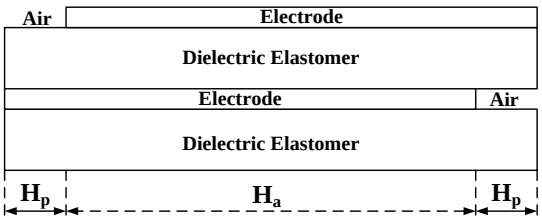

(c)

Fig. 15. Conceptual drawing of an axial DEAP actuator. (a) finished actuator with end mounts and connecting wires; (b) Dimensional drawing of the DEAP cylindrical design; (c) Schematic of a laminated film cross-section with active and passive ends.

TABLE II
Mechanical and Electrical Constants and Design Parameters of the Actuator

Parameter	Value
Permittivity of vacuum ε_0	8.854×10^{-12} F/m
Relative permittivity of the dielectric material ε_r	2.9
Young's modulus of the transducer Y_t	2.7 MPa
The sum of Mooney constants for the transducer $C_1+C_2 = Y_t/8$	0.34 MPa
Initial thickness of the polymer film d_0	45 μm
Active height of the transducer H_a	70 mm
Height of each passive end H_p	20 mm
Total width of the rolled DEAP sheet W	10 m
Maximum operating electric field strength E	45 V/μm
Maximum operating voltage $V_{applied,max}$	2025 V
Center hole diameter of the actuator D_i	25 mm

The number of laminate layers n_l is calculated using the following expression

$$n_l = \frac{D_o - D_i}{2d_0} = \frac{\sqrt{\frac{4}{\pi}WH_a + D_i^2} - D_i}{2d_0} = 107 \quad (2)$$

The outer diameter of the rolled actuator is given by

$$D_o = D_i + 2n_l d_0 = 35 \text{ mm} \quad (3)$$

The cross-sectional area of the active material is given by

$$A_c = Wd_0 = 450 \text{ mm}^2 \quad (4)$$

The volume of the polymer material is given by

$$V_c = Wd_0\left(H_a + H_p\right) = 49.5\ \text{cm}^2 \tag{5}$$

The equation governing the electrostatic $F_{Electrostatic}$, elastic $F_{Elastic}$ and load forces F_{load} in a DEAP actuator system as shown in Fig. 16, during static operation is given by

$$F_{Electrostatic} - F_{Elastic} = F_{load} \tag{6}$$

Equation (6) can be simplified as [6], [44], [45]

$$\varepsilon_0\varepsilon_r\left(\frac{V_{DEAP}}{d_0}\right)^2 \alpha^2 A_c - 2(C_1 + C_2)\left(\alpha^2 - \alpha^{-2}\right)A_c = F_{load} \tag{7}$$

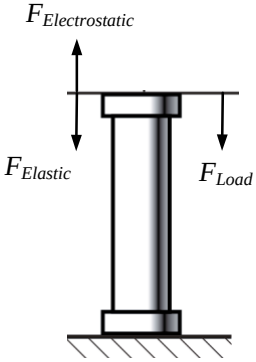

Fig. 16. Force balance of DEAP actuator element in static operation.

V_{DEAP} is the applied voltage to the DEAP actuator, α represents the stretch (elongation) ratio and is defined as, α=1+s, where s is the strain in the compliant direction. In this case, the influence of passive ends has been ignored, as the displacement between passive ends and active area is much smaller than the stroke of the transducer.

$$\varepsilon_0\varepsilon_r\left(\frac{V_{DEAP}}{d_0}\right)^2 \alpha^2 - 2(C_1 + C_2)\left(\alpha^2 - \alpha^{-2}\right) = \frac{F_{load}}{A_c}\alpha \tag{8}$$

The output force of the actuator is given by

$$F_{output} = \left[\varepsilon_0\varepsilon_r\left(\frac{V_{DEAP}}{d_0}\right)^2 \alpha^2 - 2(C_1 + C_2)\left(\alpha^2 - \alpha^{-2}\right) - \frac{F_{load}}{A_c}\alpha\right]\frac{A_c}{\alpha} \tag{9}$$

Since the displacement between the active area and passive area is limited, so we could assume that they are linear material, and passive area has the same modulus of elasticity as that of active area. In the equilibrium position, the stress on the passive area should be equal to the stress of the active area:

$$Y_t\frac{\Delta L}{H_p} = \varepsilon_0\varepsilon_r\left(\frac{V_{DEAP}}{d_0}\right)^2 - Y_t\frac{2\Delta L}{H_a} \tag{10}$$

The displacement ΔL between the active area and the passive end is

$$\Delta L = \frac{\varepsilon_0\varepsilon_r\left(\frac{V_{DEAP}}{d_0}\right)^2}{Y_t\left(\frac{1}{H_p} + \frac{2}{H_a}\right)} \tag{11}$$

Blocking force can be reduced by passive ends of the transducer, due to the displacement between the passive area and the active area. The blocking force is given by the following expression,

$$F_{blocking} = \left(\varepsilon_0\varepsilon_r\left(\frac{V_{DEAP}}{d_0}\right)^2 - Y_t\frac{2\Delta L}{H_a}\right)\cdot Wh_0 = Y_t\frac{\Delta L}{H_p}\cdot Wh_0 \tag{12}$$

The operating region of a DEAP actuator can be represented by the relationship between its force, stroke and applied voltage (or electric field strength). The force-stroke, stroke-voltage and force-electric field strength characteristics of the axial DEAP actuator which is designed above, are shown in Figs. 17, 18 and 19, respectively. As shown in Fig. 17, to achieve a certain stroke, the output force of the actuator decreases with the applied voltage. Also, for a given applied voltage, the output force drops as the actuator elongates. The variation of the stroke and strain of the DEAP actuator as a function of the applied voltage are shown in Fig. 18. The

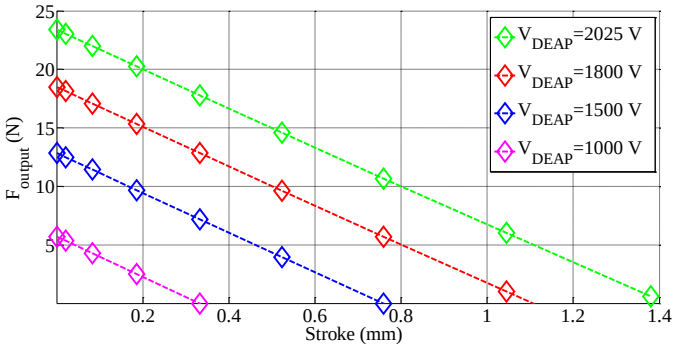

Fig. 17. Modelled actuator output force as a function of stroke for different maximum applied voltages (F_{load}=0 N).

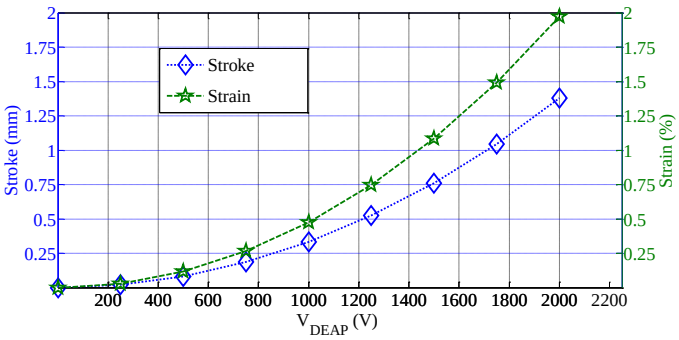

Fig. 18. Modelled actuator stroke and strain as a function of applied voltage.

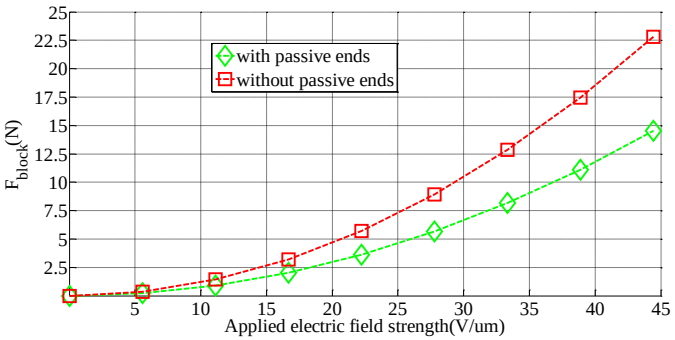

Fig. 19. Modelled blocking force as a function of applied electric field strength.

blocking forces of the actuator with and without passive ends in the design of actuator are shown in Fig. 19. From Fig. 19, it is clear that the blocking force is lower for the actuator which has passive ends, compared to the actuator without passive ends.

IV. Scalability of DEAP Actuators

One of the unique features of DEAP actuator elements is their ease of scaling. DEAP actuator elements can be scaled up to provide larger actuation forces by increasing the cross section areas as shown in Figs. 20(a) and 20(b), i.e. rolling more DEAP material. Similarly, DEAP actuator elements can be scaled up easily to provide larger actuation stroke by increasing the length of the DEAP actuator element (Fig. 20). The up scaling can also be achieved by connecting multiple actuator elements in series or parallel resulting in larger stroke or force, respectively.

To investigate the scalability of the DEAP incremental actuator, 3 designs as shown in Table III, are considered. The reference design parameters are provided in Section III. In the design 1, the actuator's height is reduced by 10 times, by keeping the area of cross-section same as the reference design. In the design 2, the area of cross-section of the actuator is reduced by 10 times, by keeping its length the same as the reference. The design 3 is made by reducing both the actuator's length and its area of cross-section by 10 times. The characteristics of designs 1 and 2 are shown in Figs. 21, 22, and 23, 24, respectively. Similarly, the characteristics of design 3 are provided in Fig. 25.

For the design 1, since the actuator's length is reduced by 10 times, the stroke as shown in Fig. 21 is very low, even at 2 kV. Since the area of cross-section is not changed the output force is not reduced as shown in Fig. 22. For the design 2, since the area of cross-section is reduced by 10 times, the output force is reduced as shown in Fig. 23, but the stroke remains the same as the reference design. The blocking force is also reduced for the design 2, as shown in Fig. 24. Similarly, for the design 3, the force-stroke characteristics are shown in Fig. 25, in which the stroke and force both are reduced. In Fig. 25, the actuator when driven with 1.8 kV can only produce 1 N output force for a stroke of 0.05 mm.

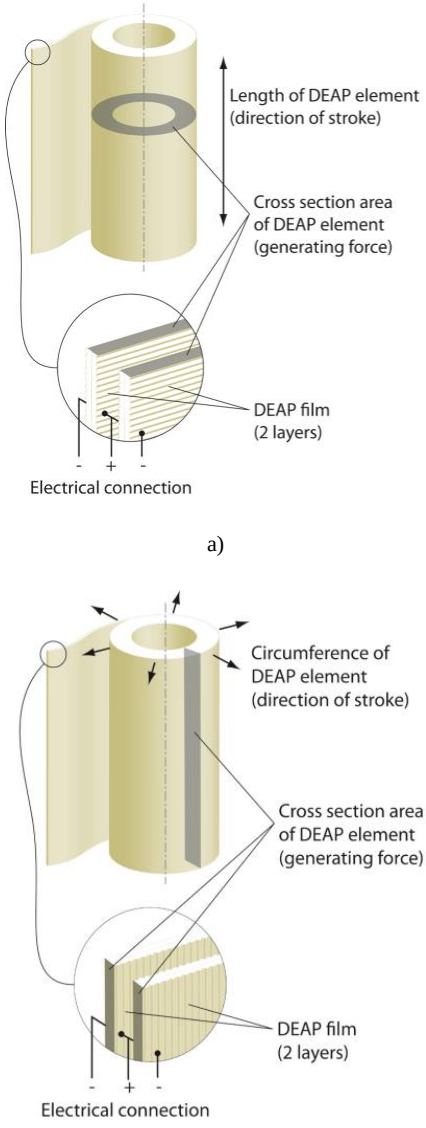

Fig. 20. Rolled structure construction, a) Electrode elasticity allows axial actuation. b) Electrode elasticity allows radial actuation.

TABLE III
Design Parameters of the Scaled DEAP Actuator

Parameter	Scaled design 1	Scaled design 2	Scaled design 3
Active height of the transducer H_a	7 mm	70 mm	7 mm
Height of each passive end H_p	2 mm	20 mm	2 mm
Total width of the rolled DEAP sheet W	10 m	1 m	1 m
Center hole diameter of the actuator D_i	25 mm	4 mm	4 mm
The outer diameter of the actuator D_o	35 mm	9 mm	9 mm
Capacitance of the actuator C_{DEAP}	39.9 nF	39.9 nF	3.99 nF
Number of layers of laminate n_l	107	51	51
Area of cross section of active DEAP A_c	450 mm^2	45 mm^2	45 mm^2

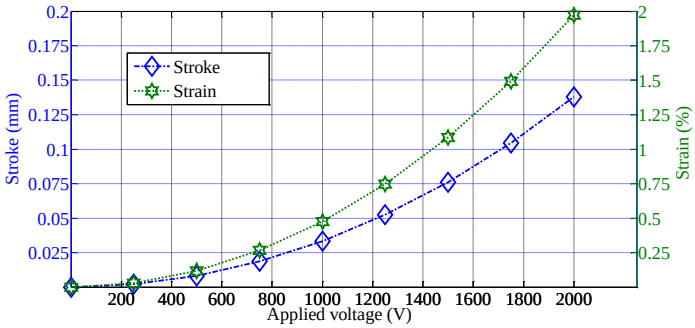

Fig. 21. Actuator stroke and strain as a function of applied voltage for the scaled design 1.

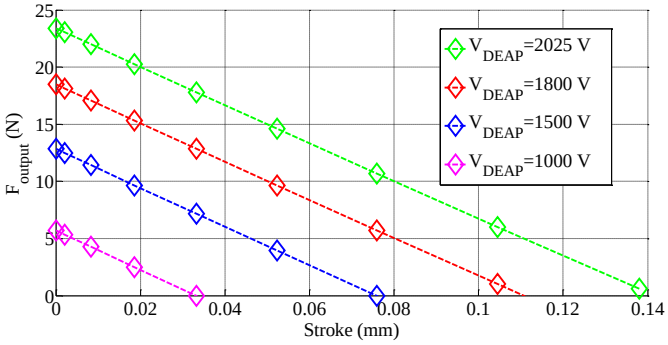

Fig. 22. Actuator output force as a function of stroke for different maximum applied voltages for the scaled design 1.

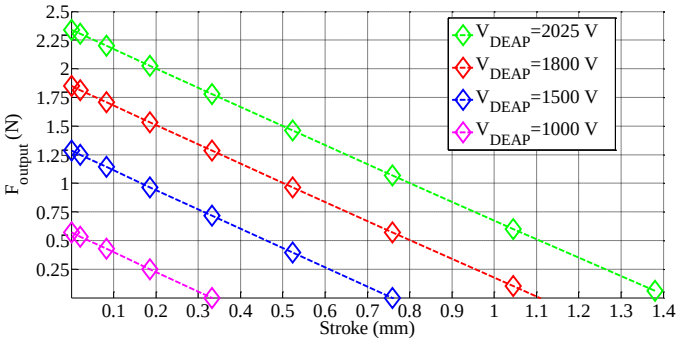

Fig. 23. Actuator output force as a function of stroke for different maximum applied voltages for the scaled design 2.

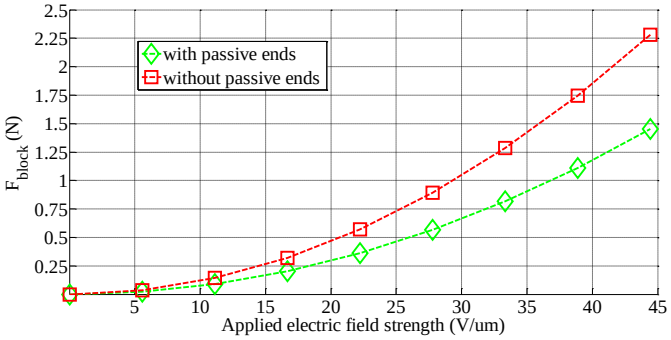

Fig. 24. Blocking force as a function of applied electric field strength for the scaled design 2.

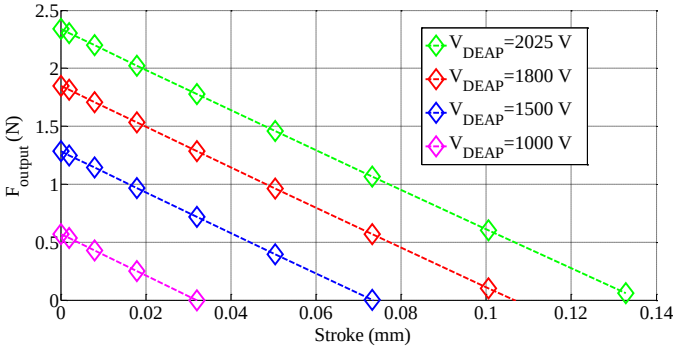

Fig. 25. Actuator output force as a function of stroke for different maximum applied voltages for the scaled design 3.

V. Control of Incremental Motor

The DEAP incremental actuator consists of three axial DEAP actuators (one extender and two grippers). The incremental actuation sequence and the driving voltage waveforms for the grippers and the extender are shown in Figs. 26 and 27, respectively [24]. Each gripper is connected to mechanical supports on either side. It expands and clamps to the guiding bar (e.g., a rod) surface when charged (with high voltage), and unfastens from it, when discharged. The extender expands axially along the guiding bar. During the operation, one gripper holds the guiding bar while the other gripper is in a released position. The extender either pushes or pulls the released gripper. The incremental actuator performs 6 different steps, to achieve a single incremental actuation stroke Δx as shown in Fig. 26.

A. Moving sequence of the linear incremental motion towards the positive x-axis direction

1. *Start*: All actuators are in the discharged state.
2. *Step* 0 (S_0): A_1 is charged and clamps to the guiding bar. A_2 and A_3 are in the discharged state.
3. *Step* 1 (S_1): A_1 remains in the charged state. A_2 is charged and pushes the mechanical structure towards right, and A_3 remains in the discharged state.
4. *Step* 2 (S_2): A_1 and A_2 still remain in the charged state. A_3 is charged.
5. *Step* 3 (S_3): A_1 is discharged and is in the released position. A_2 and A_3 still remain in the charged state.
6. *Step* 4 (S_4): A_1 remains in the discharged state. A_2 is discharged, and A_3 remains in the charged state.
7. *Step* 5 (S_5): A_1 is charged. A_2 remains in the discharged state, and A_3 remains in the charged state.
8. *Step* 6 (S_6): A_1 remains in the charged state. A_2 remains in the discharged state, and A_3 is discharged.
9. *End*: All actuators are discharged at the end.

The Step 0 is only used for charging the actuator A_1. The Steps 1-6 (S_1-S_6) repeat for achieving continuous incremental

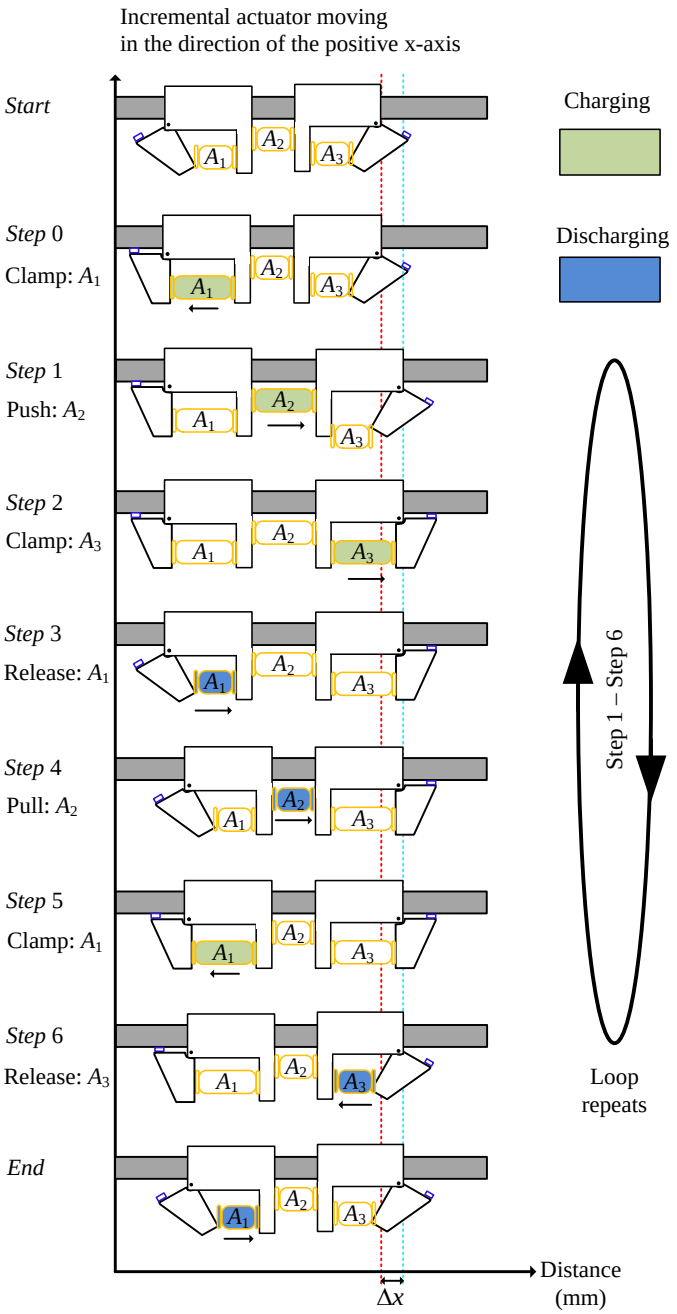

Fig. 26. Moving sequence of the DEAP incremental actuator for incremental motion towards the positive x-axis direction.

actuation cycles. The End step is used to discharge all actuators. The moving sequence for the reverse linear incremental motion towards the negative x-axis direction can be easily drawn similar to Fig. 26. For moving towards the negative x-axis (reverse) direction, the driving voltages of actuators A_1 and A_3 need to be reversed, without changing the driving voltage of actuator A_2. The driving voltages for moving with the certain incremental driving frequency are shown in Fig. 27. To move the actuator with maximum incremental frequency, zero delay (t_D=0) needs to be provided between the charge and discharge cycles of actuators A_1, A_2 and A_3.

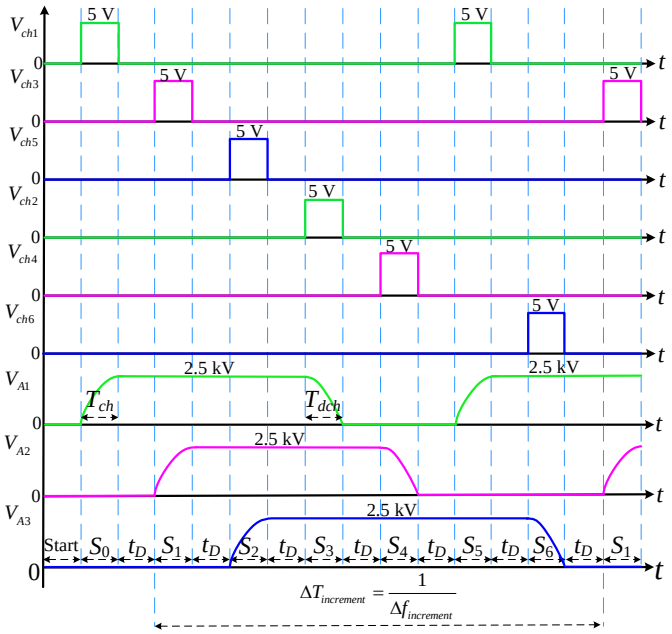

Fig. 27. Enable signals and driving voltages of all DEAP actuators, to achieve the incremental motion with variable speed, towards the positive x-axis direction.

B. *Incremental driving frequency*

Assuming the same charging T_{ch} and discharging T_{dch} times for all DEAP actuators, the maximum incremental driving frequency $\Delta f_{increment\_max}$ or minimum incremental period $\Delta T_{increment\_min}$ is given by

$$\Delta f_{increment\_max} = \frac{1}{6\left(T_{ch} + T_{dch}\right)} = \frac{1}{\Delta T_{increment\_min}} \tag{13}$$

The incremental actuator speed can be changed, by proving a delay t_D between the charge and discharge cycles of actuators A_1, A_2, and A_3. The expression for the variable incremental driving frequency $\Delta f_{increment}$ or variable incremental period $\Delta T_{increment}$ is given by

$$\Delta f_{increment} = \frac{1}{6\left(T_{ch} + T_{dch}\right) + 6t_D} = \frac{1}{\Delta T_{increment}} \tag{14}$$

When the DEAP incremental actuator is loaded during the operation, the delay between the steps S_1 and S_2 can be skipped. This can prevent pulling of the incremental actuator by the load when actuator A_2 is charged.

It is very interesting to estimate the velocity of the DEAP incremental actuator for the scaled axial DEAP actuators. Figure 28 provides the estimated velocity as a function of the incremental drive frequency (see Eq. (14)) for all designs discussed in Sections III and IV. The viscous effects of the polymer material have been neglected. The speed of the incremental motor for the reference design and each scaled design is estimated when all actuators are driven with 1.8 kV. Furthermore, the speed is estimated at a given output force and

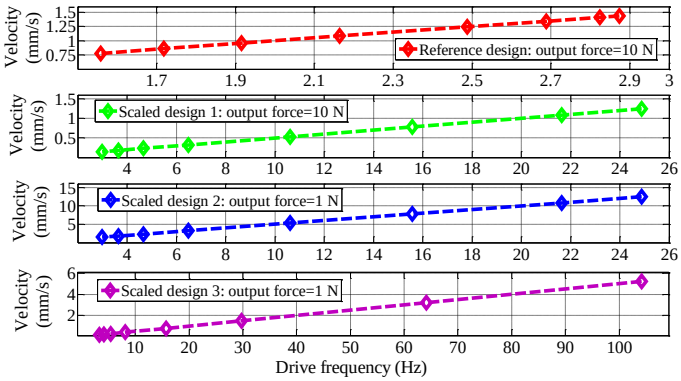

Fig. 28. Estimated velocity of the DEAP incremental actuator for different designs, for a driving voltage of 1.8 kV.

stroke for each design. The output force for each design has been marked on each subplot of Fig. 28.

For the reference design to produce an output force of 10 N, the velocity of the actuator varies between 0.78-1.44 mm/s, as shown in Fig. 29. For the scaled design 1, for an output force of 10 N, the velocity varies between 0.15-1.24 mm/s. Similarly, for the scaled design 2, for an output force of 1 N, the velocity varies between 1.5-12.4 mm/s. Finally, for the scaled design 3, for an output force of 1 N, the velocity varies between 0.16-5.2 mm/s.

The scaled design 1 produces relatively high output force, at a relatively low speed. The scaled design 2 produces relatively low output force, at a relatively high speed. Likewise, the scaled design 3 produces relatively low output force, at a relatively medium speed. The drive frequency for all designs is different, since the capacitance of the DEAP actuator is not the same. The simulated charge and discharge times for the designs with capacitances 399 nF, 39.9 nF and 3.99 nF are 21 ms, 2.1 ms and 240 μs, and 36 ms, 3.6 ms and 360 μs, respectively. The delay times (t_D) used for the calculation of the driving frequency for each design are 1 ms, 2 ms, 5 ms, 10 ms, 20 ms, 30 ms, 40 ms, and 50 ms, respectively.

VI. Power Electronics: HV Drivers

The complete circuit diagram of the DEAP incremental actuator driven by multiple bidirectional high voltage DC-DC converters is shown in Fig. 29. The topology is a peak current controlled bidirectional flyback converter. Three bidirectional flyback converters are powered by the same source. Each converter independently controls the charge and discharge operations of the three axial DEAP actuators (two grippers and an extender) in the incremental actuator.

Three high voltage bidirectional flyback converters are experimentally tested with both film capacitor loads and the DEAP incremental actuator. The picture of the experimental prototype with film capacitor loads is shown in Fig. 30. The setup of the DEAP incremental actuator with the axial DEAP actuators is shown in Fig. 31. The converter specifications are provided in Table IV. The parameters of the three flyback transformers used in the three DC-DC converters are provided in Table V. The capacitance of each film capacitor load is 200

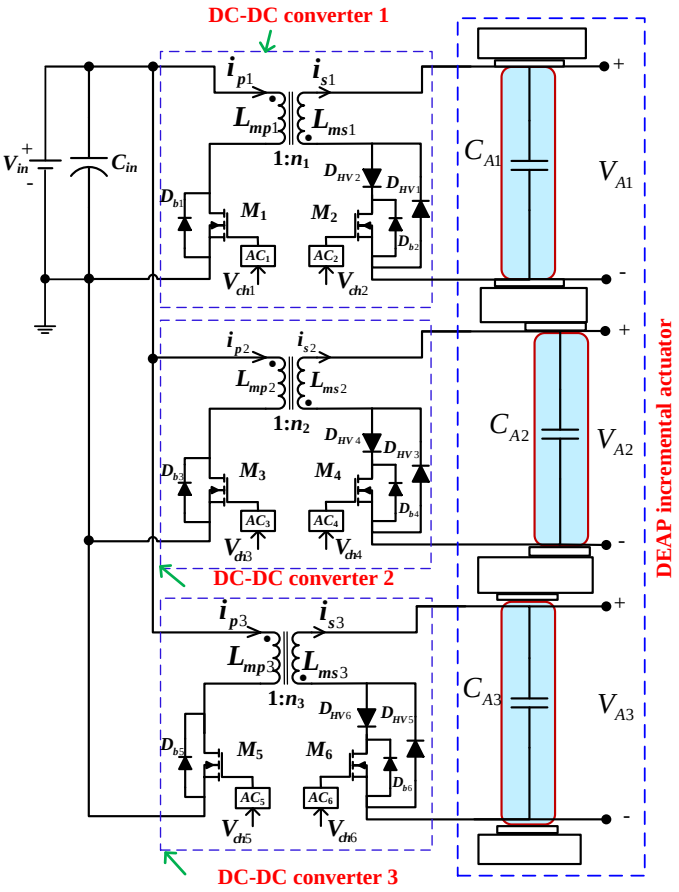

Fig. 29. Circuit schematic of the DEAP incremental actuator driven by multiple high voltage bidirectional DC-DC converters [24].

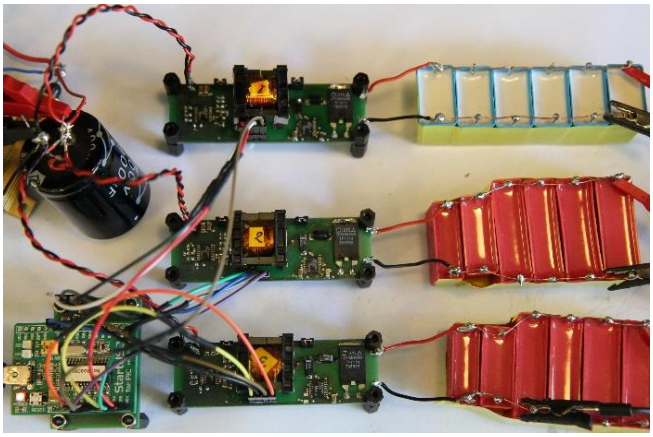

Fig. 30. Experimental setup picture with film capacitive loads.

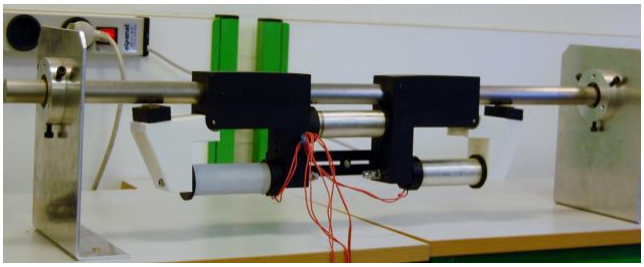

Fig. 31. Setup of the DEAP incremental actuator driven by three high voltage drivers.

TABLE IV
CONVERTER DESIGN SPECIFICATIONS

Parameter	Value
Input voltage	24 V
Output voltage	0-2500 V
Capacitance of each DEAP acator in the DEAP incremental actuator setup	400 nF
Capacitance of each film capacitor load	200 nF
Incremental driving frequency	~ 1-5 Hz
Primary peak current during charging/discharging process	4.2 A / 5.3 A

TABLE V
FLYBACK TRANSFORMER PARAMETERS

Parameter	Trans. 1	Trans. 2	Trans. 3
Flyback transformer core type / Material	EF20 / N87	EF20 / N87	EF20 / N87
Primary / Secondary magnetizing inductance	29.5 μH / 16 mH	33.5 μH / 20.8 mH	28 μH / 17 mH
Number of primary turns / secondary turns	16 / 375	16 / 400	16 / 400
Leakage inductance of transformer referred to primary / secondary	1.11 μH / 633 μH	1.2 μH / 728 μH	1.25 μH / 710 μH
Secondary winding self / Interwinding capacitance	17 pF / 41 pF	19.4 pF / 33.5 pF	22.6 pF / 35 pF
DC resistance of primary / secondary winding	62 mΩ / 28.5 Ω	85 mΩ / 41 Ω	84 mΩ / 41 Ω
Number of primary / secondary layers	1 / 5	2 / 5	2 / 5
Diameter of primary / secondary winding	0.5 mm / 0.1 mm	0.65 mm / 0.1 mm	0.65 mm / 0.1 mm

nF. The capacitance of each axial DEAP actuator in the setup shown in Fig. 31 is 400 nF. The detailed design of the bidirectional flyback converter for driving a capacitive load is discussed in [46].

The experimental test results with the film capacitor loads are provided in Figs. 32-34. During the charging process the converter operates in a boundary conduction mode (BCM), and during the discharge process it operates in discontinuous conduction mode (DCM) using a control IC LT 3751 [36], [47]. In Fig. 32, the output voltages of all converters are shown when the film capacitor loads are driven with a single incremental cycle (similar to Fig. 26, with t_D=0) with a maximum driving voltage of 2.5 kV. The maximum incremental driving frequency $\Delta f_{increment\_max}$ with 200 nF capacitive loads is 4.34 Hz. Since the real DEAP actuators have a capacitance of 400 nF, the maximum incremental driving frequency is less than 4.34 Hz, and it is explained in the following sections.

In Fig. 33, the output voltages of all converters are shown when the film capacitor loads are driven by multiple incremental actuation cycles with a maximum driving voltage of 2.5 kV. In Fig. 34, the film capacitor loads are driven with multiple incremental actuation cycles with a maximum driving voltage of 2.5 kV, and with a delay time t_D of 100 ms. The incremental actuation frequency $\Delta f_{increment}$ in this case is 1.4 Hz.

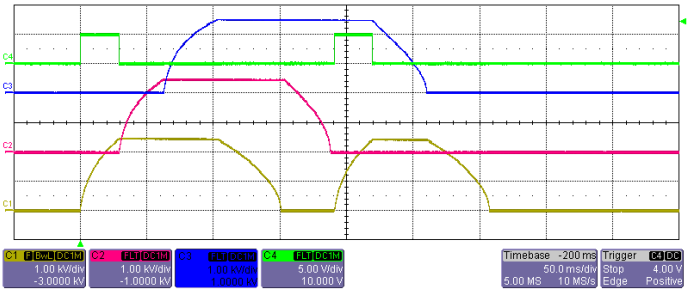

Fig. 32. Experimental results for demonstrating a single incremental actuation cycle, when the 3 HV DC-DC converters are driving the film capacitor loads; CH1 (1 kV/div): V_{A1} ; CH2 (1 kV/div): V_{A2} ; CH3 (1 kV/div): V_{A3} ; CH4 (5 V/div): V_{ch1} ; Time scale: 50 ms/div; $\Delta f_{increment\_max}$ = 4.34 Hz.

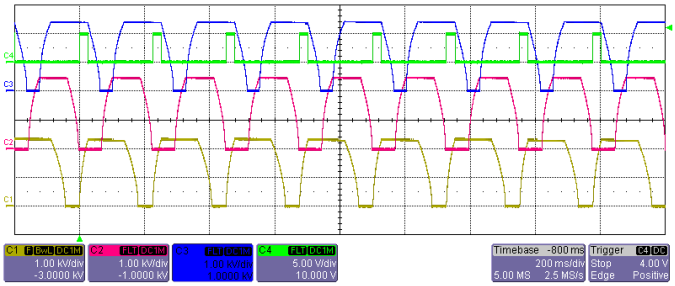

Fig. 33. Experimental results for demonstrating multiple incremental actuation cycles,when the 3 dc-dc converters are driving the film capacitor loads; CH1 (1 kV/div): V_{A1} ; CH2 (1 kV/div): V_{A2} ; CH3 (1 kV/div): V_{A3} ; CH4 (5 V/div): V_{ch1} ; Time scale: 200 ms/div; $\Delta f_{increment\_max}$ = 4.34 Hz.

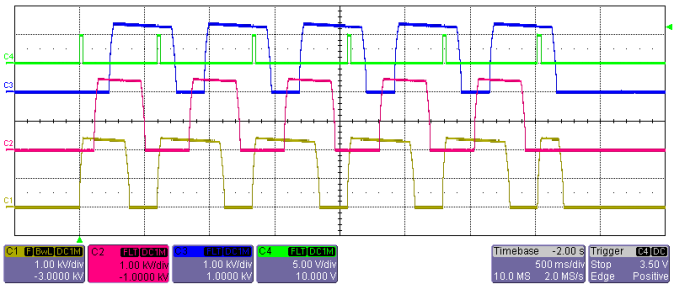

Fig. 34. Experimental results for demonstrating multiple incremental actuation cycles,when the 3 dc-dc converters are driving the film capacitor loads with a delay time t_D=100 ms; CH1 (1 kV/div): V_{A1} ; CH2 (1 kV/div): V_{A2} ; CH3 (1 kV/div): V_{A3} ; CH4 (5 V/div): V_{ch1} ; Time scale: 500 ms/div; $\Delta f_{increment}$ = 1.4 Hz.

The energy efficiency [36] is measured for all converters with film capacitors as loads. The charging and discharging energy efficiency measurement results with film capacitor loads are provided in Figs. 35 and 36, respectively. The maximum energy efficiency of the converters during charging operation (transferring the input energy to the actuator) is 87%, and during discharging operation (transferring the actuator energy back to the source) it is 79%. As shown in Figs. 35 and 36, the energy efficiency of all converters is not identical, because the transformer designs shown in Table V are not identical. For any DC-DC converter, the discharge energy efficiency is less than the charge energy efficiency, due to very high conduction losses, switching loss due to leakage

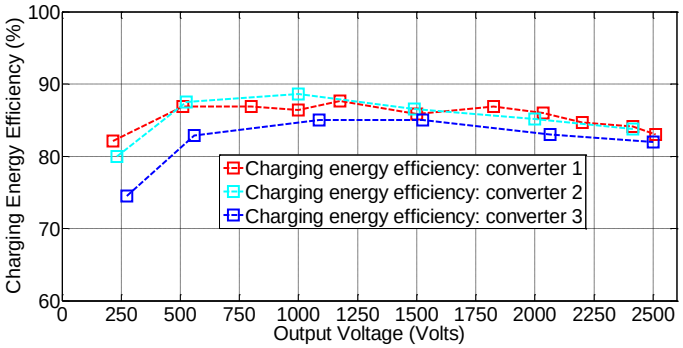

Fig. 35. Charging energy efficiency measurement results of three high voltage converters.

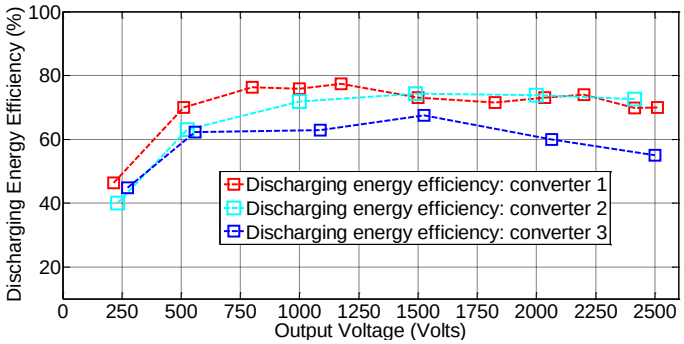

Fig. 36. Discharging energy efficiency measurement results of three high voltage converters.

inductance and capacitive switching losses of the HV MOSFET.

Practical experience reveals that careful design of the flyback transformer with low leakage inductance and low self-capacitance is required for achieving high energy efficiency in high voltage bidirectional operation. The HV MOSFET used for this research is IXTV03N400S (4 kV, 300 mA, 290 Ω) [48]. The available high voltage MOSFET for this application, in the current market is IXTA02N450HV (4.5 kV, 200 mA, 750 Ω) [49]. The HV diode used in the converter is SXF 6525 (5 kV, 150 mA, 70 ns (t_{rr})) [50]. The improper HV flyback transformer designs may lead to failure of the HV MOSFET during the discharging operation.

VII. System Integration

A. Incremental motion with different speeds

The integrated system as shown in Fig. 31 is tested for its variable speed and repeatability. 100 increments are generated using the digital controller, and the total displacement and travel time are recorded. The applied voltage level is fixed to a maximum of 1.8 kV to avoid any potential damage to the transducers. Table VI provides the acquired data of the experiments. It can be seen that the system has a repeatability within 5% (of stroke) for different speeds.

B. Bidirectional motion:

The above test is repeated with a maximum voltage of 1.7 kV for bidirectional motion at three different speed settings (delay times t_D) in the controller. Table VII provides the results which indicate a larger total displacement in the forward motion compared to the reverse motion.

TABLE VI
Experimental data of DEAP incremental actuator moving with different speeds to achieve 100 increments/steps

Total travel* (mm)	Total travel time (s)	Delay time t_D (ms)	Average Speed (mm/s)	Increment size / stroke per step (mm)	Incremental driving frequency $\Delta f_{increment}$ (Hz)
39	50	50	0.78	0.39	1.55
39	45	40	0.86	0.39	1.72
39	40	30	0.97	0.39	1.91
38	35	20	1.07	0.38	2.16
40	30	10	1.33	0.40	2.49
40	28	5	1.43	0.40	2.68
39	25	2	1.56	0.39	2.82
39	26	1	1.50	0.39	2.87

*All 3 DEAP actuators are driven with a maximum voltage of 1.8 kV. Charging time T_{ch}=22 ms, discharging time T_{dch}=36 ms.

TABLE VII
Experimental data from Bidirectional DEAP Incremental Actuator Tests for 100 Increments

Direction of movement	Total travel* (mm)	Total travel time (s)	Delay time t_D (ms)	Average Speed (mm/s)	Incremental driving frequency $\Delta f_{increment}$ (Hz)
Forward	40	71	100	0.56	1.08
Forward	44	35	10	1.26	2.60
Forward	43.7	32	1	1.36	3.03
Reverse	37	71	100	0.52	1.08
Reverse	41	41	10	1.00	2.60
Reverse	35	37	1	0.94	3.03

*All 3 DEAP actuators are driven with a maximum voltage of 1.7 kV. Charing time T_{ch}=21 ms, discharging time T_{dch}=33 ms.
Forward: positive x-axis direction.
Reverse: negative x-axis direction.

C. Discussion

In Fig. 37 the sequential DEAP incremental actuator images are provided when it moved with a maximum speed of 1.5 mm/s. The DEAP incremental actuator system indicated a non-repeatable motion when operated bidirectional resulting in a drift from original position. This drift increased with the number of bidirectional iterations resulting in an even larger drift from original position. Such drift might be primarily caused by non-identical grippers differing in their gripping force. As the extending transducer is activated, it excites both grippers with the same force. The activated gripper should have enough gripping force, to not slip backward due to transient forces generated by the extender. If the two grippers have different gripping force, the one with smaller force will exhibit larger backward slipping resulting cumulatively in a drift of the whole system from the original position. The performance specifications of the several designed incremental motors are summarized in Table VIII. The reference design has the highest volume, maximum output force, and the scaled design 3 has the lowest volume and minimum output force. The scaled design 2 has maximum

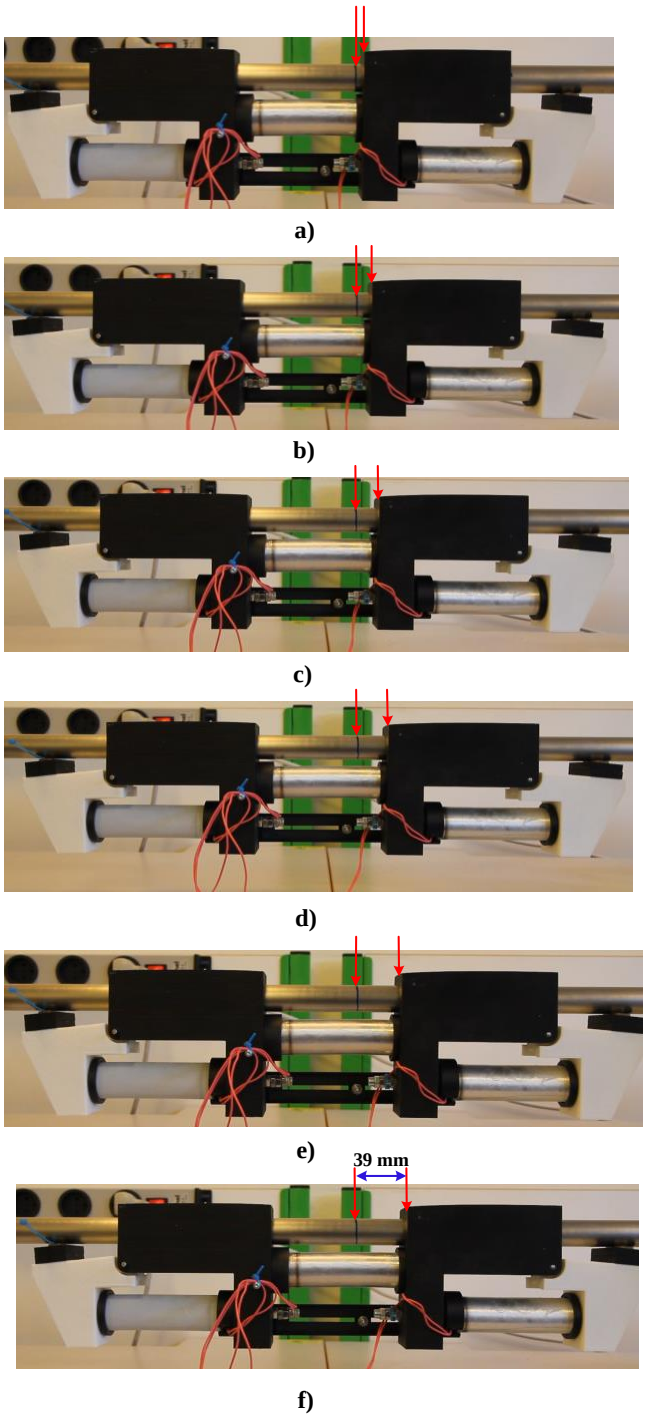

Fig. 37. Sequential DEAP incremental actuator images at different instants of time, when moving with a maximum speed (driven at 2.87 Hz): a) time=2 s, b) time=5 s, c) time=10 s, d) time=14 s, e) time=20 s, f) time=24 s.

velocity at low push/pull and holding force of 1 N. The resolution is the stroke of the extender in a single incremental step; it is high for the reference and scaled design 2.

D. Future work

Subsequent iteration of the DEAP incremental actuator will consider the improvement of both the mechanical and electronics concepts. Specific attention will be given to the design of the grippers to, i) achieve a more identical performance, and ii) have enough grip force to overcome the inertial effects and as such increased speed and repeatability. The focus will be given to develop a more compact and autonomous system where the electronics are carried by the actuator. The weight and form factor of DEAP are to be exploited and demonstrated. This is potentially achieved by reducing the actuator size, redesigning the auxiliary mechanics, and integrating the electronics on a single PCB print. Moreover, the form factor can be demonstrated by developing a concept which can travel on curved and inclined paths which is challenging for other technologies to achieve. The final conclusion is that the proposed new DEAP incremental actuator will have promising and demanding applications in the future.

TABLE VIII
PERFORMANCE SPECIFICATIONS OF THE DESIGNED DEAP INCREMENTAL ACTUATORS

Incremental motor performance specifications at 1.8 kV applied voltage	**Reference design**	**Scaled design 1**	**Scaled design 2**	**Scaled design 3**
Velocity	0.78-1.44 mm/s	0.15-1.24 mm/s	1.5-12.4 mm/s	0.16-5.2 mm/s
Push/Pull force	10 N	10 N	1 N	1 N
Holding force	10 N	10 N	1 N	1 N
Resolution	0.5 mm	0.05 mm	0.5 mm	0.05 mm
Total volume	4950 mm^2	495 mm^2	495 mm^2	49.5 mm^2

VIII. CONCLUSIONS

An overview of the widely used conventional linear actuator technologies, and their advantages and disadvantages are discussed. Different concepts of the DEAP incremental actuators and their unique features are discussed. One of the proposed DEAP incremental actuator concepts has been designed, built and tested. It is demonstrated that the DEAP is feasible for providing incremental motion with variable speed and bidirectional motion.

The conceptual design considerations and scalability of an axial DEAP actuator are discussed. The estimated velocities of the incremental motor for all scaled designs are provided. The control of the incremental actuator using the HV drivers is discussed. The control and HV driving circuits demonstrated good performance in providing the appropriate stimuli to the transducers with reasonable efficiency and compactness. Experimental test results with the three high voltage bidirectional DC-DC converters are presented. The proposed DEAP incremental actuator moves with a maximum velocity of 1.5 mm/s, at a 2.87 Hz incremental driving frequency, when all actuators are driven with 1.8 kV.

ACKNOWLEDGEMENT

The authors would like to thank the industrial partner Danfoss PolyPower A/S for providing the actuators and system integration set up. The authors also express thanks to Lina Huang and Jonas T. Smith for their help in the system integration.

REFERENCES

[1] JenaTec, Online available: http://www.jena-tec.co.uk/linear-actuators.php [accessed 14 Nov. 2014].

[2] AGI American Grippers, Online available: http://localautomation.com/featured/agi-pneumatic-linear-actuator-agi-american-grippers-inc.html [accessed 14 Nov. 2014].

[3] Stemulate, Online available: http://www.stemulate.org/2012/07/02/solid-learning-robot-linear-actuators/ [accessed 14 Nov. 2014].

[4] Piezodrive, Online available: http://www.piezodrive.com/products.html [accessed 06 Jan. 2015].

[5] PI, Online available: http://www.linear-actuator.net/Vacuum_Linear_Actuators.php [accessed 14 Nov. 2014].

[6] Y. Bar-Cohen, "Electroactive Polymer [EAP] Actuators as Artificial Muscles: Reality, Potential, and Challenges," 2nd ed. Washington, DC: SPIE, 2004.

[7] R. E. Pelrine, R. D. Kornbluh, Q. Pei, J. P. Joseph, "High-speed electrically actuated elastomers with strain greater than 100%," *Science*, vol. 287, pp. 836–839, 2000.

[8] F. Carpi, D. DE Rossi, R. Kornbluh, R. Pelrine, P. Sommer-Larsen, Eds, "Dielectric Elastomer As Electromechanical Transducers," Amsterdam, The Netherlands: Elsevier, 2008.

[9] Danfoss PolyPower, Denmark, Online available: http://www.polypower.com/ [accessed 20 Oct. 2014].

[10] LEAP Technology, Denmark, Online available: http://leaptechnology.com/ [accessed 20 Oct. 2014].

[11] M. Tryson, H. E. Kiil, M. Benslimane, "Powerful tubular core free dielectric electro active polymer (DEAP) push actuator," in *Proc. SPIE*, vol. 7287, 2009.

[12] R. Sarban, B. Lassen, M. Willatzen, "Dynamic Electromechanical Modeling of Dielectric Elastomer Actuators With Metallic Electrodes," *IEEE/ASME Trans. Mechatronics*, vol. 17, no. 5, pp. 960-967, Oct. 2012.

[13] L. Huang, P. Thummala, Z. Zhang, M. A. E. Andersen, "Battery powered high output voltage bidirectional flyback converter for cylindrical DEAP actuator," in *Proc. IEEE IPMHVC*, pp. 454-457, 3-7 June 2012.

[14] R. D. Kornbluh, R. Pelrine, Q. Pei, R. Heydt, S. Stanford, S. Oh, J. Eckerle, "Electroelastomers: applications of dielectric elastomer transducers for actuation, generation, and smart structures," in *Proc. SPIE*, vol. 4698, pp. 254-270, 2002.

[15] A. T. Conn, A. D. Hinitt, P. Wang, "Soft segmented inchworm robot with dielectric elastomer muscles," in Proc. SPIE, Electroactive Polymer Actuators and Devices (EAPAD), vol. 9056, pp. 90562L, 2014.

[16] Q. Pei, R. Pelrine, S. Stanford, R. D. Kornbluh, M. S. Rosenthal, K. Meijer, R. J. Full, "Multifunctional electroelastomer rolls and their application for biomimetic walking robots," in *Proc. SPIE*, vol. 4698, 2002.

[17] I. A. Anderson, T. A. Gisby, T. G. McKay, B. M. O'Brien, E. P. Calius, "Multi-functional dielectric elastomer artificial muscles for soft and smart machines," *Journal of Applied Physics*, 112, 041101, 2012.

[18] K. Jung, J. C. Koo, J. -do Nam, Y. K. Lee, H. R. Choi, "Artificial annelid robot driven by soft actuators," *Journal of Bioinspiration and Biomimetics*, vol. 2, pp. S42-S49, 2007.

[19] I. A. Anderson, T. C. H. Tse, T. Inamura, B. M. O'Brien, T. McKay, T. Gisby, "A soft and dexterous motor," *Journal of Applied Physics*, 98, 123704, 2011.

[20] R. Wache, D. N. McCarthy, S. Risse, G. Kofod, "Rotary Motion Achieved by New Torsional Dielectric Elastomer Actuators Design," *IEEE/ASME Trans. Mechatronics*, vol. 99, pp. 1-3, Feb. 2014.

[21] R. J. E. Merry, J. L. Holierhoek, M. J. G. van de Molengraft, M. Steinbuch, "Gain Scheduling Control of a Walking Piezo Actuator," *IEEE/ASME Trans. Mechatronics*, vol. 19, no. 3, pp. 954-962, June 2014.

[22] D. M. Neal, H. H. Asada, "Bipolar Piezoelectric Buckling Actuators," *IEEE/ASME Trans. Mechatronics*, vol. 19, no. 1, pp. 9-19, Feb. 2014.

[23] Y. Jianyong, J. Zongxia, M. Dawei, Y. Liang, "High-Accuracy Tracking Control of Hydraulic Rotary Actuators With Modeling Uncertainties," *IEEE/ASME Trans. Mechatronics*, vol. 19, no. 2, pp. 633-641, April 2014.

[24] P. Thummala, Z. Zhang, M. A. E. Andersen, S. Rahimullah, "Dielectric electro active polymer incremental actuator driven by multiple high-voltage bi-directional DC-DC converters," in *Proc. IEEE ECCE USA*, pp. 3837-3844, 15-19 Sept. 2013.

[25] M. Karpelson, G. Y. Wei, R. J. Wood, "Driving high voltage piezoelectric actuators in microrobotic applications," *Sensors and Actuators A*, vol. 176, pp. 78– 89, 2012.

[26] L. Eitzen, C. Graf, J. Maas, "Cascaded bidirectional flyback converter driving DEAP transducers," in *Proc. IEEE IECON*, pp. 1226-1231, 7-10 Nov. 2011.

[27] L. Eitzen, C. Graf, J. Maas, "Bidirectional power electronics for driving dielectric elastomer transducers," in *Proc. SPIE*, vol. 8340, p. 834018 1-12, 2012.

[28] R. W. Erickson, D. Maksimovic, "Fundamentals of Power Electronics," 2nd ed. New York: Springer, 2001.

[29] N. O. Sokal, R. Redl, "Control algorithms and circuit designs for optimal flyback-charging of an energy storage capacitor (e.g., for flash lamp or defibrillator)," *IEEE Trans. Power Electronics*, vol. 12, no. 5, pp. 885-894, Sep. 1997.

[30] J. Elmes, C. Jourdan, O. Abdel-Rahman, I. Batarseh, "High-Voltage, High-Power-Density DC-DC Converter for Capacitor Charging Applications," in *Proc. IEEE APEC*, pp. 433-439, 2009.

[31] S. K. Chung, H. B. Shin, "High-voltage power supply for semi-active suspension system with ER-fluid damper," *IEEE Trans. Vehicular Technology*, vol. 53, no. 1, pp. 206- 214, Jan. 2004.

[32] T. Bhattacharya, V. S. Giri, K. Mathew, L. Umanand, "Multiphase Bidirectional Flyback Converter Topology for Hybrid Electric Vehicles," *IEEE Trans. Industrial Electronics*, vol. 56, no. 1, pp. 78-84, Jan. 2009.

[33] G. Chen, Y.-S. Lee, S.Y.R. Hui, D. Xu, Y. Wang, "Actively clamped bidirectional flyback converter," *IEEE Trans. Industrial Electronics*, vol. 47, no. 4, pp. 770-779, Aug. 2000.

[34] F. Zhang, Y. Yan, "Novel Forward–Flyback Hybrid Bidirectional DC-DC Converter," *IEEE Trans. Industrial Electronics*, vol. 56, no. 5, pp. 1578-1584, May 2009.

[35] T. Andersen, M. S. Rødgaard, O. C. Thomsen, M. A. E. Andersen, "Low voltage driven dielectric electro active polymer actuator with integrated piezoelectric transformer based driver," in *Proc. SPIE EAPAD*, vol. 7976, p. 79762N, 2011.

[36] P. Thummala, Z. Zhang, M. A. E. Andersen, "High Voltage Bi-directional Flyback Converter for Capacitive Actuator," in *Proc. IEEE European Power Electronics conference*, pp. 3-6 Sept. 2013.

[37] L. Huang, Z. Zhang, M. A. E Andersen, "Design and development of autonomous high voltage driving system for DEAP actuator in radiator thermostat," in *Proc. IEEE Applied Power Electronics Conference and Exposition (APEC)*, pp. 1633-1640, 16-20 March 2014.

[38] P. Thummala, H. Schneider, Z. Zhang, Z. Ouyang, A. Knott, M. A. E. Andersen, "Efficiency Optimization by Considering the High Voltage Flyback Transformer Parasitics using an Automatic Winding Layout Technique," *IEEE Trans. Power Electronics.*

[39] H. Schneider, P. Thummala, L. Huang, Z. Ouyang, A. Knott, Z. Zhang, M. A. E. Andersen, "Investigation of transformer winding architectures for high voltage capacitor charging applications," in *Proc. IEEE APEC*, pp. 334-341, 16-20 March 2014.

[40] J. P. L. Bigue, J. S. Plante, "Experimental Study of Dielectric Elastomer Actuator Energy Conversion Efficiency," *IEEE/ASME Trans. Mechatronics*, vol. 18, no. 1, pp. 169-177, Feb. 2013.

[41] C. M. Druitt, G. Alici, "Intelligent Control of Electroactive Polymer Actuators Based on Fuzzy and Neurofuzzy Methodologies," *IEEE/ASME Trans. Mechatronics*, vol. 19, no. 6, pp. 1951-1962, Dec. 2014.

[42] B. Rechenbach, M. Willatzen, R. Sarban, C. Liang, B. Lassen, "Geometry optimization of tubular dielectric elastomer actuators with anisotropic metallic electrodes," in *Proc. SPIE Electroactive Polymer Actuators and Devices (EAPAD)*, vol. 9056, pp. 905606-905606-13, Mar. 2014.

[43] P. Thummala, D. Maksimovic, Z. Zhang, M. A. E. Andersen, "Digital control of a high-voltage (2.5 kV) bidirectional DC-DC converter for driving a dielectric electro active polymer (DEAP) based capacitive actuator," in *Proc. IEEE ECCE USA*, pp. 3435-3442, 14-18 Sept. 2014.

[44] Y. H. Iskandarani, R. W. Jones, E. Villumsen, "Modeling and experimental verification of a dielectric polymer energy scavenging cycle", in *Proc. SPIE EAPAD*, vol. 7287, pp. 72871Y-1–72871Y-12, 2009.

[45] M. Tryson, H. -E. Kiil, M. Benslimane, "Powerful tubular core free dielectric electro activate polymer (DEAP) push actuator," in *Proc. SPIE EAPAD*, vol. 7287, pp. 72871F-72871F-11, April, 2009.

[46] P. Thummala, D. Maksimovic, Z. Zhang, M. A. E. Andersen, S. Rahimullah, "Design of a High Voltage Bidirectional DC-DC Converter for Driving Capacitive Incremental Actuators Usable in Electric Vehicles (EVs)," in *Proc. IEEE IEVC*, 14-18 Dec. 2014.

[47] Linear Technology, "LT3751 High Voltage Capacitor Charger with Regulation," Linear Technology Corporation, USA. http://cds.linear.com/docs/en/datasheet/3751fc.pdf [accessed 20 Oct. 2014].

[48] IXYS, IXTV03N400S, 4 kV MOSFET, Online available: http://ixapps.ixys.com/DataSheet/DS100214A-(IXTH_V03N400_S).pdf [accessed 20 Oct. 2014].

[49] IXYS, IXTA02N450HV, 4.5 kV MOSFET, Online available: http://ixapps.ixys.com/DataSheet/DS100498(IXTA-T02N450HV).pdf [accessed 20 Oct. 2014].

[50] VMI, SXF 6525, 5 kV diode, Online available: http://www.voltagemultipliers.com/pdf/SXF6521_25.pdf [accessed 20 Oct. 2014].

www.elektro.dtu.dk

Department of Electrical Engineering
Electronics Group (ELE)
Technical University of Denmark
Oersteds Plads bygning 349
DK-2800 Kgs. Lyngby
Denmark
Tel: (+45) 45 25 25 25
Fax: (+45) 45 88 01 17
Email: info@elektro.dtu.dk